# ANTARCTIC ICE SHEET EVOLUTION OVER THE LAST GLACIAL CYCLE: A DATA-CONSTRAINED LARGE-ENSEMBLE MODELLING APPROACH

ROBERT D. BRIGGS

# Antarctic Ice Sheet evolution over the last glacial cycle: A data-constrained large-ensemble modelling approach.

by

©Robert D. Briggs

A Thesis submitted to the School of Graduate Studies in partial fulfillment of the requirements for the degree of

**Doctor of Philosophy**

**Department of Physics and Physical Oceanography**

Memorial University of Newfoundland

**Aug 2012**

St. John's Newfoundland

# Abstract

The Antarctic Ice Sheet (AIS) is an important component of the global climate system and has been identified as a major source of uncertainty to future sea level change. It is also one of the slowest components; much of the interior reacts on timescales greater than 10,000 years. To better understand the role Antarctica played in the global climate, the observed contemporaneous change, and to make predictions of its future behaviour, reconstructions of past ice sheet evolution are required. Furthermore, to interpret reconstructions with any degree of confidence, meaningful uncertainty estimates should be attributed.

Glaciological modelling is an effective tool to generate continental-scale reconstructions over glacial cycles, but the models depend on parametrisations to account for the deficiencies (*e.g.*, missing physics, poorly represented sub-grid processes, uncertain boundary conditions) inherent in any numerical model. These parameters, considered together, form a parameter-space from which sets of parameters can be sampled; each set corresponds to an ice sheet reconstruction. Previous modelling studies have relied upon a limited exploration of this space, furthermore few studies have employed the available observations to constrain the reconstructions. Large ($\mathcal{O}(1000)$ member) ensemble analysis techniques have been effectively employed to explore the phase-space of models configured for other Quaternary ice sheets, but have yet to be applied to the AIS.

This thesis documents a large-ensemble data-constrained study of the evolution of the AIS over the last glacial cycle. The contemporaneous glacial system model I use has been modified through the definition of 31 ensemble parameters that explore the uncertainty in the ice-physics, the climate forcing, and the ice-ocean interaction. A database of constraint data with an associated evaluation methodology is used to compute probability distributions for ice sheet evolution.

The reconstructions predict that the Last Glacial Maximum (LGM) in Antarctica occurred at ~24 ka BP, with deglaciation commencing after ~18 ka BP, and that during the LGM the AIS contained 8.9 m equivalent sea level (mESL) in excess ice when compared to present day (with a $1\sigma$ upper and lower range of 5.8-12.2 mESL).

# Acknowledgements

I am grateful to my supervisor, Dr Lev Tarasov, for providing the opportunity to study this engrossing subject and for always being available to discuss problems. Many thanks also to my supervisory committee, Dr Trevor Bell and Dr Len Zedel. They always made time to give me guidance and advice.

I am very appreciative to Dave Pollard, without his ice sheet model and his prompt and efficient responses this project would have taken much more time than it did. Pippa Whitehouse was kind enough to host me for a visit to Durham University for extensive discussions and made comments of an early draft of paper 2. Steven Livingston provided the marine core dataset. Many people took time to respond to my questions and requests including, Catherine Ritz, Dan Zwartz, Erik Ivins, Greg Balco, Andrey Salamatin, Gary Clow, Claus-Dieter Hillenbrand, and Anne LeBrocq. I thank them.

Thanks are made to the glacial systems dynamics group, especially Tristan Hauser and Alec Melanson, for moral and scientific support. I am also grateful to the post-docs, Martina Schäfer and Andrew Keats, who came and went during my time.

I am eternally thankful to the Nautilus running and triathlon club; knowing that, regardless of the weather, there will be a group to run with every Monday, Wednesday, Friday, and Saturday maintained my sanity.

Most importantly, to Stephanie, gratitude for everything: for always finding time

to cook delicious food with me, no matter what time I came home, and for helping me experience this beautiful island of Newfoundland. I hope you know how important you are to me.

Financial support was from Canadian Foundation for Innovation, the National Science and Engineering Research Council and ACEnet. Without this support, it would not have been possible to pursue this research on a full-time basis.

# Table of Contents

**Abstract** ii

**Acknowledgments** iv

**Table of Contents** xi

**List of Tables** xiii

**List of Figures** xxiii

**Nomenclature** xxiv

**1 Introduction** 1

1.1 Motivation and overview . . . . . 2

1.2 Background . . . . . 5

1.2.1 Physical characteristics of the Antarctic ice sheet . . . . . 5

1.2.2 Late Quaternary period . . . . . 10

1.2.3 The role of past ice sheet evolution in present sea-level change 11

1.2.4 Paleo-climatic studies . . . . . 13

1.3 Literature review . . . . . 14

1.3.1 Glaciological modelling . . . . . 14

1.3.2 Data constrained-ensemble analysis . . . . . 17

1.3.3 Types of observational constraints . . . . . 19
1.3.4 Last Glacial Maximum . . . . . 22
1.3.5 AIS deglaciation from the observational record . . . . . 24
1.3.6 Meltwater pulse events and abrupt climate change . . . . . 26
1.3.7 Last Interglacial (Eemian period) . . . . . 27
1.4 Objectives . . . . . 28
1.5 Thesis Overview . . . . . 30
1.6 Co-authorship statement . . . . . 31

**2 A glacial systems model configured for large ensemble analysis of Antarctica deglaciation 34**

2.1 Abstract . . . . . 35
2.2 Introduction . . . . . 37
2.3 Model description . . . . . 39
2.3.1 Model setup . . . . . 40
2.3.2 Ice dynamics . . . . . 42
2.3.3 Ice rheology factor . . . . . 43
2.3.4 Basal drag . . . . . 44
2.3.5 Grounding line treatment . . . . . 47
2.3.6 Sub shelf pinning points . . . . . 48
2.3.7 Bedrock response and relative sea level computation . . . . . 48
2.3.8 Geothermal heat flux . . . . . 49
2.3.9 Climate forcing . . . . . 50
2.3.9.1 Temperature forcing . . . . . 51
2.3.9.2 Precipitation forcing . . . . . 53
2.3.10 Ice-ocean interface . . . . . 55
2.3.10.1 Calving . . . . . 56

2.3.10.2 Sub-shelf melt . . . . . 58
2.3.11 Spin up and initialization of the model . . . . . 73
2.4 Sensitivity study . . . . . 75
2.4.1 Discussion of parameter/metric sensitivity . . . . . 81
2.5 Summary and Conclusion . . . . . 82
2.6 References . . . . . 84

**3 How to evaluate model derived deglaciation chronologies: A case study using Antarctica** **95**

3.1 Abstract . . . . . 96
3.2 Introduction . . . . . 97
3.3 Development of a constraint database . . . . . 99
3.4 AntICEdat constraint database . . . . . 102
3.4.1 Present-day ice-sheet configuration (PD) . . . . . 104
3.4.2 Paleo data . . . . . 106
3.4.2.1 Relative sea level (RSL) . . . . . 108
3.4.2.2 Past ice thickness (ELEV) . . . . . 113
3.4.2.3 Extent data: grounding line retreat/open marine conditions (EXT) . . . . . 115
3.4.2.4 Density, spatial, and temporal spread of paleo-data . 116
3.4.2.5 Format of paleo-data spreadsheet. . . . . 116
3.5 Evaluation Process . . . . . 118
3.5.1 Comment on structural error and the evaluation process . . . 120
3.5.2 Paleo-data misfit computations and observational error models 121
3.5.3 Weighting . . . . . 124
3.5.3.1 Intra-Data-Type weighting . . . . . 125
3.5.3.2 Inter-Data-Type weighting (volume of influence) . . . 127

3.5.4 Sieves . . . 128
3.5.5 Scoring and scoring schemes . . . 130
3.5.6 Assessment of scoring schemes . . . 131
3.6 Discussion: relating model output to data . . . 139
3.7 Summary, Future Work and outstanding issues . . . 143
3.8 References . . . 147

**4 A data-constrained large-ensemble analysis of Antarctica over the last glacial cycle 156**

4.1 Abstract . . . 157
4.2 Introduction . . . 159
4.3 Methods . . . 162
4.3.1 Parameter distributions and ensemble overview . . . 163
4.3.2 Ensemble scoring . . . 165
4.3.3 Generation of distributions . . . 167
4.4 Results . . . 173
4.4.1 Present-day reconstructions . . . 173
4.4.2 Paleo-data: RSL results . . . 178
4.4.3 Paleo-data: ELEV results . . . 182
4.4.4 Paleo-data: EXT results . . . 187
4.4.5 Paleo-data misfit by sector . . . 189
4.4.6 Antarctic deglaciation chronology and LGM reconstruction . . 195
4.4.6.1 LGM (24 ka) reconstruction . . . 197
4.4.6.2 18 ka to present-day snapshots . . . 200
4.4.7 Meltwater pulse 1a/b contributions . . . 202
4.4.8 Eemian configuration . . . 204
4.4.9 Evolution of AIS since the Eemian . . . 208

4.5 Discussion . . . . . 208
4.5.1 Reconstruction misfits . . . . . 210
4.5.2 LGM . . . . . 213
4.5.3 LGM to present-day evolution . . . . . 216
4.5.4 Meltwater pulses . . . . . 218
4.5.5 Eemian configuration and subsequent evolution . . . . . 219
4.6 Conclusion . . . . . 220
4.7 References . . . . . 223

**5 Conclusions** **233**
5.1 Summary . . . . . 233
5.2 Future work . . . . . 236

**Bibliography** **239**

**A A glacial systems model configured for large ensemble analysis of Antarctica deglaciation** **267**
A.1 Supplementary tables . . . . . 268
A.2 References . . . . . 273

**B How to evaluate model derived deglaciation chronologies: A case study using Antarctica** **275**
B.1 Interpolation of ALBMAP . . . . . 276
B.2 Site notes . . . . . 279
B.2.1 RSL sites . . . . . 279
B.2.2 ELEV sites . . . . . 286
B.3 Site maps and age-altitude plots . . . . . 296
B.3.1 RSL sites . . . . . 296

B.3.2 ELEV sites . . . . . 305
B.4 References . . . . . 332

**C A data-constrained large-ensemble analysis of Antarctica over the last glacial cycle** **336**

C.1 Appendix: Parameter distribution . . . . . 337
C.2 Appendix: Exploration of $\sigma_f$ for generation of weighted average - Probability Distribution . . . . . 340
C.3 Appendix: ELEV site maps and age-altitude plots . . . . . 343
C.4 References . . . . . 370

# List of Tables


2.1 Ensemble parameters . . . . . 41

2.2 Table showing dimensions of the 4 major shelves and the calculated aspect ratio . . . . . 66

3.1 Table of abbreviations . . . . . 100

3.2 Paleo data constraint type summary . . . . . 109

3.3 Drainage basin sector code . . . . . 110

3.4 Summary table of scoring schemes . . . . . 133

4.1 Details of key scoring schemes from Briggs and Tarasov (2012). This study predominantly uses the schemes emphasised in bold. . . . . 166

4.2 Summary of present-day grounded volumes (mESL) for observations, key individual runs and from the mean of the distributions . . . . . 178

4.3 Summary of the AIS, the WAIS, and the EAIS LGM (24 ka) contributions to eustatic sea level relative to present-day, $\Delta\xi$, from the $W_{09}$ , $N_{10}$ , and $N^{*}_{10}$ distributions. . . . . 197

4.4 AIS $\Delta\zeta$ (maximum contribution to eustatic sea level relative to present-day) at 114 ka for the AIS, the WAIS, and the EAIS. . . . . 205

A.1 Symbols and constants . . . . . 269

A.2 Tables of thickness (H) and melt rates for the (a) AMY and (b) RON ice shelves . . . . . 270

A.3 SSM observations as extracted from the literature . . . . . 271

A.4 Processed SSM observations used for verification purposes . . . . . 272

A.1 Grid locations and pre/post-adjustment values of $hb_{40}$ . . . . . 277

B.2 RSL site notes . . . . . 279

B.3 ELEV site notes . . . . . 286

B.1 Range of $\sigma_f$ values (only results until $\sigma_f$ =0.25 are tabulated) and the resultant probabilities and volg metrics for scoring scheme PDcPaSea and PDcPaSeb. Bold font indicates the sigma values that are used in Fig. 4.2 and discussed in Section 4.3.3. . . . . 341

B.2 Results of incremental changes to $\sigma_f$ and resultant probabilities and volg metrics for scoring scheme PDcPbSeb . . . . . 342

# List of Figures

1.1 Map of key geographic features and locations discussed in introductory text. Mountainous or rocky regions (*e.g.*, Transantarctic Mountains) are highlighted in dark grey . . . . . 6

1.2 Variation of sea level over the last 140 kyr, adopted from (Lisiecki, 2005) 10

2.1 AMY and RON transects and melt rate vs thickness plots . . . . . 63

2.2 SSM implementation flowchart . . . . . 64

2.3 Thickness and melt rate transect and melt rate maps for large shelves 70

2.4 Comparison plot showing net melt amounts from observations and the predicted melt amount from the SSM component for each of the five shelf regions; two observations that are for the cumulative RON-FIL are also show. The OTHER observation has been clipped as the maximum, estimated from Jacobs et al. (1996), peaks at 675 Gt $yr^{-1}$ (see Table A.4). 71

2.5 Melt rate maps generated from lower (9164) and upper (9165) SSM parameter values . . . . . 74

2.6 Lisiecki (2005) stacked benthic $\delta 18O$ record as proxy for global ice volume showing key times for spin up run. For the generation of the spin up ensemble (see text for details), ice dynamics is only intermittently active from 391 ka (red) until 205 ka (green). For the ensemble proper, initialization starts at 205 ka. Approximate period of the Eemian is highlighted in grey. . . . . 76
2.7 Sensitivity results for present-day WAIS (upper) and EAIS (lower) grounded ice volume . . . . . 78
2.8 Sensitivity results for total the AIS grounded volume (upper) at LGM and ROS grounding line position (lower) . . . . . 79
2.9 Sensitivity results for ROS (upper) and RON-FIL (lower) present-day area. . . . . 80

3.1 Location maps showing sectors and data sites . . . . . 105
3.2 Temporal distribution of WAIS and EAIS data-points . . . . . 117
3.3 Conceptual diagram showing the evaluation process . . . . . 119
3.4 Intra-site weighting . . . . . 126
3.5 Averaged volg time series . . . . . 135
3.6 Hdiff plots . . . . . 137
3.7 Comparison of ELEV sites . . . . . 140
3.8 Comparison of RSL sites . . . . . 142

4.1 Distribution of scores . . . . . 170

4.2 Exploration of $\sigma_f$ for schemes PDcPaSE[a/b]. Upper plots (a and c) show distribution of run probabilities, $P_n$ for ranked runs (sorted by $P_n$) for different values of $\sigma_f$, threshold values are highlighted in colour. Lower (b and d) plots show sensitivity plots of grounded ice volume at 20 k and 0 k (and associated errors) against $\sigma_f$. Coloured vertical lines represent the threshold $\sigma_f$ values. . . . . 172

4.3 Composite map of names and locations of mentioned in the text, RSL (yellow squares) and ELEV (yellow triangles) constraint data points (with id numbers), and basal topography and bathymetry (colour filled image), contoured surface elevations (1000 m black, 500 m grey), present-day grounding line (green) and coastline (red). The orange lines are taken from the Livingstone et al. (2012) LGM grounding line extent reconstructions. Based on the data they compiled and assessed, the reconstructions were categorised into high confidence segments (solid orange line in this plot) and speculative segments (dotted orange). . . 174

4.4 Present-day characteristics and differences for run 2679 and present day observation: (a) modelled magnitude of surface velocity overlaid with contours of surface elevation (1000 m thin black, 500 m light grey), (b) as (a) except using observations, (c) difference plot of modelled ice thickness minus observed ice thickness. (d) difference plot of modelled surface velocity and observed surface velocity. In both difference plots red indicates model overestimation. The present-day $ALB_{40}$ grounding line (black) and modelled grounding (blue) are show in all plots. . . . 175

4.5 (a) difference between mean of the thickness field, as computed by $N_{10}$ , and $ALB_{40}$ (b) One way $1\sigma$ standard deviation. . . . . 176

4.6 RSL data points and sea level curves for the EAIS sites. Observed RSL data points are colour coded according to the constraint they provide: two-way (light blue, dated past sea level); one-way lower-bounding (mauve, past sea level above or maximum age of beach) or one-way upper-bounding (orange, past sea level below or minimum age of beach). One-way error bars are generally indeterminate in their non-bounded direction, though not shown as such to avoid clutter. For a detailed description of the RSL dataset and its processing refer to Briggs and Tarasov (2012). . . . . 180

4.7 RSL data points and sea level curves for the TAM/ROS RSL sites (9401, 9402) and the Antarctic Peninsula sites (9601, 9602). Figure notes as for Fig. 4.6. . . . . 181

4.8 ELEV observations, ensemble results, upper and lower bounds from $W_{09}$ and $N_{10}$ , and computed misfits for Dronnig Maud and Enderby land (DMEL) and Lambert-Amery Ice Shelf (LAIS) sectors. . . . . 184

4.9 ELEV observations, ensemble results, upper and lower bounds from $W_{09}$ and $N_{10}$ , and computed misfits for Ross (ROS) and Admunsen sea (AS) sectors. . . . . 185

4.10 ELEV observations, ensemble results, upper and lower bounds from $W_{09}$ and $N_{10}$ , and computed misfits for Antarctic Peninsula (AP) and Weddell Sea (WS) sectors. . . . . 186

4.11 EXT observations and ensemble results. Core identifiers 1-21 are grounding line retreat (GLR) two-way constraint types, 22-27 are open marine conditions (OMC) one-way constraint. Black horizontal lines and associated labels segregate and identify the different sectors. . . . . 188

4.12 EAIS (upper) and WAIS (lower) grounded ice volume evolution with $1\sigma$ error bars generated from mean for $W_{09}$ , $N_{10}$ and $N^*_{10}$ . . . . . 195

4.13 Eustatic sea level contributions, relative to present-day, from the drainage sectors computed from the $N_{10}$ mean. . . . . 196

4.14 AIS LGM (24 ka) characteristics from $N_{10}$ and run 2679. For reference the modelled LGM grounding line (blue) is shown in all plots. (a) shows, in addition to the modelled LGM grounding line, the Livingstone et al. (2012) reconstructed (purple) and speculative (dashed purple, see text for details), LGM grounding line Livingstone et al. (2012), the observed (black) and modelled (red) present-day grounding line. To aid misfit estimates, the graticules have a resolution of 80 km, thus 2x model resolution. Symbols representing the ability of the ensemble to recreate the EXT observation are plotted at the location of the marine cores (see text for details of the typology). (b) magnitude of surface velocity (from run 2679) overlain with surface elevation (1000 m contours black, 500 m grey) from $N_{10}$ , modelled LGM grounding line (blue) and Livingstone et al. (2012) reconstructed grounding line (purple). Also shown are the Livingstone et al. (2012) paleo-ice-stream locations (cyan). (c) $N_{10}$ 20 ka ice thickness minus present-day (modelled) ice thickness, modelled LGM (blue) and observed present-day (black) grounding line. (d) One way $1\sigma$ standard deviation of $N_{10}$ . The cells with the largest variance are regions that would most benefit from additional constraint and could provide a focus location for future field campaigns. . . . . 198

4.15 Antarctic deglaciation snapshots between time-slices from LGM to PD showing surface elevation, thickness change (Red indicates thinning), migration of the grounding line, and WAIS and EAIS eustatic contributions. The 1000 m surface contours and black grounding line are from the youngest time-slice of the given interval. The grey grounding line is extracted from the oldest time-slice in the interval. Sea level contribution (mESL) between time-slices is presented at the base of each plot for WAIS (W) and EAIS (E). All fields and scalars are computed from $N_{10}$ probability distribution. For reference, the LGM grounding line is presented in the 20-16 ka plot and the present-day observed grounding line is presented in the 3-0 ka plot. The dated green circles are grounding line retreat dates, see Discussion section (Section 4.5). Graticule is at 1000 km intervals. . . . . 201

4.16 Run scores plotted against the MWP-1a and 1b contributions for the $W_{09}$ wide and $N_{10}$ narrow schemes. The crosses represent all the runs for each of the schemes, and circles are the runs that fall within the $P_{90}$ target, highlighted by their fill colour, according to their ranking. 203

4.17 AIS evolution chronologies for the period before, during and after the Eemian presented as $\Delta\zeta$ (contribution to eustatic sea level relative to present-day). The global sea level departure from present (Lisiecki, 2005) is presented for timing and magnitude reference; for comparison the lower plot presents the full range of global sea level change over the same time period. . . . . 206

4.18 Upper plots show AIS surface elevation snapshots from $N_{10}$ , relative to global sea level inferred from the Lisiecki (2005) stacked $\delta_{18}$ records. Contribution to eustatic sea level from WAIS and EAIS is shown in each plot. Lower plots present thickness difference from the Eemian to present-day. Modelled grounding line position (red) is shown in all plots, and for reference, the present-day modelled $ALB_{40}$ (upper plots in black, lower plots in green) grounding line and shelf front. In the lower plots blue signifies thinner ice at Eemian. . . . . 207

4.19 Grounded volume evolution of WAIS (lower) and EAIS (middle), represented as eustatic sea level contribution relative to present-day from $W_{09}$ ,$N_{10}$ and $N^*_{10}$ . Note the x-axes are the same range. Upper plot is the sea level departure from present (from stacked benthic $\delta^{18}O$ records of Lisiecki, 2005) and mean annual insolation departure from present (at $80^oS$). . . . . 209

4.20 AIS surface elevation at 90 ka (left) and ice thickness difference between 90 ka and present-day. Modelled grounding line position (red) is shown in both plots. For reference, the present-day modelled $ALB_{40}$ (left plot in black, right plot in green) grounding line and shelf front. Blue signifies thinner ice at 90 ka. . . . . 210

4.21 Thickness difference plot between mean $N_{10}$ and present-day, overlaid with topographic and bathymetric contours, present-day and LGM observed grounding lines and site locations for ELEV and RSL. . . . . 211

B.1 ALBMAP interpolation . . . . . 278

B.2 RSL site:9101 Syowa Coast (SC) . . . . . 297

B.3 RSL site:9201 Larsemann Hills (LH) . . . . . 298

B.4 RSL site:9202 Vestfold Hills (VH) . . . . . 299

B.5 RSL site:9301 Windmill Islands (WI) . . . . . 300
B.6 RSL site:9401 Terra Nova Bay (TNB) . . . . . 301
B.7 RSL site:9402 Southern Scott Coast (SSC) . . . . . 302
B.8 RSL site:9601 Marguerite Bay (MB) . . . . . 303
B.9 RSL site:9602 King George Island (KGI) . . . . . 304
B.10 PHS site:1101 Lutzow-Holm Bay (LHB) . . . . . 306
B.11 PHS site:1201 Framnes Mts. 1 (FM1) . . . . . 307
B.12 PHS site:1202 Framnes Mts. 2 (FM2) . . . . . 308
B.13 PHS site:1203 Framnes Mts. 3 (FM3) . . . . . 309
B.14 PHS site:1204 Grove Mts. (GM) . . . . . 310
B.15 PHS site:1205 Prince Charles Mts. 1 (PCM1) . . . . . 311
B.16 PHS site:1206 Prince Charles Mts. 2 (PCM2) . . . . . 312
B.17 PHS site:1207 Prince Charles Mts. 3 (PCM3) . . . . . 313
B.18 PHS site:1401 Reedy Glacier 1 (RG1) . . . . . 314
B.19 PHS site:1402 Reedy Glacier 2 (RG2) . . . . . 315
B.20 PHS site:1403 Reedy Glacier 3 (RG3) . . . . . 316
B.21 PHS site:1404 Hatherton glacier (HG) . . . . . 317
B.22 PHS site:1405 Clark Mtn (CLM) . . . . . 318
B.23 PHS site:1406 Allegheny Mtn (ALM) . . . . . 319
B.24 PHS site:1407 Western Sarnoff Mts (WSM) . . . . . 320
B.25 PHS site:1408 Eastern Fosdick Mts (EFR) . . . . . 321
B.26 PHS site:1501 Executive Committee Range (ECR) . . . . . 322
B.27 PHS site:1502 Pine Island Bay 1 (PIB1) . . . . . 323
B.28 PHS site:1503 Pine Island Bay 2 (PIB2) . . . . . 324
B.29 PHS site:1601 West Palmer Land (WPL) . . . . . 325
B.30 PHS site:1602 Alexander Island South (AXS) . . . . . 326

B.31 PHS site:1603 Alexander Island North (AXN) . . . . . 327
B.32 PHS site:1701 Behrendt Mts (BM) . . . . . 328
B.33 PHS site:1702 Ellsworth Mts. (EM) . . . . . 329
B.34 PHS site:1703 Shackleton Range 1 (SR1) . . . . . 330
B.35 PHS site:1704 Shackleton Range 2 (SR2) . . . . . 331

C.1 Parameter distributions I. Histograms bin size=50. Light grey is the wide ensemble set, dark grey is the narrow set. The cumulative total is the stepped black line. Vertical black lines represent the value of the paramter for the best four runs as scored by PDcPbSEb and run 3506. For a complete explanation of the paramters refer to Briggs et al. (2013).337
C.2 Parameter distributions II (see Fig. C.1 caption for notes). . . . . 338
C.3 Parameter distributions III (see Fig. C.1 caption for notes). . . . . 339
C.4 Parameter distributions IV (see Fig. C.1 caption for notes). . . . . 339
C.5 PHS siteMisfit:1101 Lutzow-Holm Bay (LHB) . . . . . 344
C.6 PHS siteMisfit:1201 Framnes Mts. 1 (FM1) . . . . . 345
C.7 PHS siteMisfit:1202 Framnes Mts. 2 (FM2) . . . . . 346
C.8 PHS siteMisfit:1203 Framnes Mts. 3 (FM3) . . . . . 347
C.9 PHS siteMisfit:1204 Grove Mts. (GM) . . . . . 348
C.10 PHS siteMisfit:1205 Prince Charles Mts. 1 (PCM1) . . . . . 349
C.11 PHS siteMisfit:1206 Prince Charles Mts. 2 (PCM2) . . . . . 350
C.12 PHS siteMisfit:1207 Prince Charles Mts. 3 (PCM3) . . . . . 351
C.13 PHS siteMisfit:1401 Reedy Glacier 1 (RG1) . . . . . 352
C.14 PHS siteMisfit:1402 Reedy Glacier 2 (RG2) . . . . . 353
C.15 PHS siteMisfit:1403 Reedy Glacier 3 (RG3) . . . . . 354
C.16 PHS siteMisfit:1404 Hatherton glacier (HG) . . . . . 355
C.17 PHS siteMisfit:1405 Clark Mtn (CLM) . . . . . 356

C.18 PHS siteMisfit:1406 Allegheny Mtn (ALM) . . . . . 357
C.19 PHS siteMisfit:1407 Western Sarnoff Mts (WSM) . . . . . 358
C.20 PHS siteMisfit:1408 Eastern Fosdick Mts (EFR) . . . . . 359
C.21 PHS siteMisfit:1501 Executive Committee Range (ECR) . . . . . 360
C.22 PHS siteMisfit:1502 Pine Island Bay 1 (PIB1) . . . . . 361
C.23 PHS siteMisfit:1503 Pine Island Bay 2 (PIB2) . . . . . 362
C.24 PHS siteMisfit:1601 West Palmer Land (WPL) . . . . . 363
C.25 PHS siteMisfit:1602 Alexander Island South (AXS) . . . . . 364
C.26 PHS siteMisfit:1603 Alexander Island North (AXN) . . . . . 365
C.27 PHS siteMisfit:1701 Behrendt Mts (BM) . . . . . 366
C.28 PHS siteMisfit:1702 Ellsworth Mts. (EM) . . . . . 367
C.29 PHS siteMisfit:1703 Shackleton Range 1 (SR1) . . . . . 368
C.30 PHS siteMisfit:1704 Shackleton Range 2 (SR2) . . . . . 369

# Nomenclature

## Abbreviations

| | |
|---|---|
| AIS | Antarctic Ice Sheet |
| ACZ | Accumulation zone |
| ALM | Allegheny Mts |
| AMY | Amery Ice Sshelf |
| AP | Antarctic Peninsula |
| AS | Admunsen Sea |
| AXN | Alexander Island North |
| AXS | Alexander Island South |
| BM | Behrendt Mts |
| CDW | circumpolar deep water |
| CLM | Clark Mts |
| DMEL | Dronning Maud-Enderby Land |
| EAIS | East Antarctic Ice Sheet |
| ECR | Executive Committee Range |
| EFM | Eastern Fosdick Mts |
| ELEV | Past ice elevation (constraint data-type) |
| EM | Ellsworth Mts |
| EOF | Empirical orthogonal function |
| EXT | Past ice extent (constraint data-type) |
| Et | total (combined grounded and floating) ice for the EAIS |
| FIL | Filchner Ice Shelf |
| FM | Framnes Mts |
| GCM | General circulation model/Global climate model |
| GHF | Geothermal heat flux |
| GIA | Glacial isostatic adjustment |
| GLR | Grounding line retreat (constraint data-type) |
| GLZ | Grounding line zone |
| GM | Grove Mts |
| GRACE | Gravity Recovery and Climate Experiment |
| GSM | Glacial systems model |
| HG | Hatherton Glacier |
| HSSW | high-salinity continental shelf water |
| IPCC | Intergovernmental Panel on Climate Change |
| ISM | Ice sheet model |
| ISW | ice-shelf water |
| KGI | King George Island |

| | |
|---|---|
| LAIS | Lambert-Amery Ice System |
| LGM | Last Glacial Maximum |
| LH | Larsemann Hills |
| LHB | Lutzow-Holm Bay |
| MB | Marguerite Bay |
| Mts | Mountains |
| MSE | Mean square error |
| MUN | Memorial University |
| MWP | Melt water pulse |
| NADW | North Atlantic Deep Water |
| OMC | Open marine conditions (constraint data-type) |
| PCM | Prince Charles Mts |
| PD | Present day |
| PDD | Positive Degree Day |
| PIB | Island Bay |
| PIG | Pine Island Glacier |
| PMIPII | Paleo-Modelling Intercomparison Project II |
| PSU | Penn State University |
| RG | Reedy Glacier |
| RISgl | Ross ice shelf grounding line position |
| RMS | Root Mean Square |
| RON | Ronne Ice Shelf |
| ROS | Ross Ice Shelf |
| RS | Ross Sea |
| RSL | Relative sea level (constraint data-type) |
| SC | Syowa Coast |
| SED | surface exposure dating |
| SFZ | Shelf front zone (for SFZ) |
| SIA | Shallow ice approximation |
| SR | Shackleton Range |
| SSA | Shallow shelf approximation |
| SSC | Southern Scott Coast |
| SSM | Sub-shelf melt |
| ShfAr | Shelf area |
| TAM | Transantarctic Mountains |
| TNB | Terra Nova Bay |
| VH | Vestfold Hills |
| WAIS | West Antarctic Ice Sheet |
| WI | Windmill Islands |
| WPL | West Palmer Land |
| WS | Weddell Sea |
| WSM | Western Sarnoff Mts |
| WVL | Wilkes-Victoria Land |
| Wf | Floating ice in the WAIS |
| Wg | Grounded ice in the WAIS |
| volg | Grounded ice volume for all the AIS |
| vol0g | Grounded ice volume at present day (0 ka) |
| vol20g | Grounded ice volume at 20 ka |
| vol0ge | Grounded ice volume for the EAIS |
| vol0gw | Grounded ice volume for the WAIS |
| mESL | (meters) Equivalent sea level |
| $SEb_{10}$ | Probability distribution from PDcPaSEa |

| | |
|---|---|
| $SEbb_{10+}$ | Probability distribution from PDcPaSEb |
| $SEa_{09}$ | Probability distribution from PDcbSEb |
| PDc | Baseline present day |
| PDcPa | PDc and paleo-data (Pa) |
| PDcPaSEa | As PDcPa and with wide Eemian sieve (SEa) |
| PDcPaSEb | As PDcPa and with narrow Eemian sieve(SEb) |
| PDcbSEb | As PDcPaSEb but with double paleo-data (Pb) weighting |
| ka | $1x10^3$ years before present *i.e.*, marking the time of a past event |
| Ma | $1x10^6$ years before present *i.e.*, marking the time of a past event |
| kyr | a period of time lasting $1x10^3$ years |

## Symbols

| | |
|---|---|
| $(\mathbf{X})$ | Horizontal dimensions |
| $H$ | Ice thickness |
| $H_{flot}$ | Maximum buoyant thickness for tidewater calving |
| $Hcrit2$ | Ice shelf calving minimum thickness threshold |
| $I$ | Glacial index, derived from either $T_{epica}$ |
| $P$ | Interpolated (blended) precipitation |
| $P_{LGM}$ | Reference LGM precipitation field |
| $P_{PD}$ | Reference PD precipitation field |
| $Pave_{LGM}$ | PMIPII average LGM precipitation field |
| $Peof1,2_{LGM}$ | PMIPII reference LGM precipitation EOFs |
| $Pf_{1,2,3}$ | Individual precipitation fields |
| $Pfac$ | Scaled precipitation glacial index |
| $Pwa$ | Precipitation blending |
| $Pwb$ | Precipitation blending 2 |
| $Se$ | Sediment presence exponent |
| $Slk$ | Sediment likelihood parameter |
| $T$ | Interpolated (blended) temperature |
| $T_{Cmn}$ | Minimum critical $T_s$ for tidewater calving |
| $T_{Cmx}$ | Maximum critical $T_s$ for tidewater calving |
| $T_{LGM}$ | Reference LGM temperature field |
| $T_{PD}$ | Reference PD temperature field |
| $T_m$ | Melting temperature of ice |
| $T_s$ | Sea-surface mean summer temperature |
| $Tave_{LGM}$ | PMIPII averaged LGM temperature |
| $Teof_{LGM}$ | PMIPII LGM temperature EOFs |
| $Tf_{1,2,3}$ | Individual temperature fields |
| $Twa$ | Temperature blending 1 |
| $Twb$ | Temperature blending 2 |
| $U_{Cmx}$ | Maximum calving velocity |
| $U_c$ | Tidewater calving velocity |
| $\Delta q_s$ | Annual orbital insolation anomaly from present day at 80 S |
| $\Delta s$ | $\delta^{18}$O O sea level departure from present |
| $\Delta_{\mathrm{Halb}}$ | Ice thickness model-obs misfit |
| $\dot{C}$ | Calving rate |

| | |
|---|---|
| $\dot{M}a$ | Sub-shelf melt rate for accumulation zone |
| $\dot{M}g$ | Sub-shelf melt rate for grounding line zone |
| $\dot{M}g_{AMY}$ | Reference SSM rate for AMY grounding line zone |
| $\dot{M}g_{RON}$ | Reference SSM rate for RON grounding line zone |
| $\dot{M}s$ | SSM rate for shelf front zone |
| $\epsilon_{AMY}$ | AMY shelf aspect ratio |
| $\epsilon_{RON}$ | RON shelf aspect ratio |
| $\epsilon_{shf}$ | Shelf aspect ratio |
| $\sigma_{hb}$ | Sediment roughness |
| $\tau_b$ | Basal stress |
| $calvF$ | Ice shelf calving sub $Hcrit2$ enhancement factor |
| $calvrate_{Ts}$ | Ice shelf calving rate |
| $crh$ | Basal sliding co-efficient (between bed and ice) |
| $crhcrit$ | SSA-SIA critical threshold |
| $fDragmod$ | Model-obs ice thickness misfit scaling |
| $fPeof1$ | LGM precipitation EOF fields ($Pf_3$ only) |
| $fPeof2$ | LGM precipitation EOF fields ($Pf_3$ only) |
| $fTeof$ | LGM temperature EOF field ($Tf_3$ only) |
| $fbedGHF$ | Geothermal heat flux input blending |
| $fcalvVmx$ | Maximum calving velocity, tidewater glacier |
| $fcalvwater$ | Thin ice calving temperature dependant scaling |
| $fdesfac$ | Desert elevation effect factor |
| $fhbPhif$ | Scaling of sediment presence after isostatic unloading |
| $fnGLz1$ | Grounding line zone SSM factor (large shelves) |
| $fnGLz2$ | Grounding line zone SSM factor (other shelves) |
| $fnPdexp$ | Phase factor for precipitation |
| $fnPin$ | Pinning Factor |
| $fnPre$ | Glacial index interpolation scaling factor for precipitation |
| $fnSfz1$ | Shelf front SSM factor (large shelves) |
| $fnTdfscale$ | Glacial index interpolation scaling factor for temperature |
| $fnflow$ | Flow enhancement factor for grounded ice |
| $fnsed$ | Soft bed enhancement factor |
| $fnshcalv$ | Ice shelf calving scaling factor |
| $fnshelf$ | Flow enhancement factor for shelf flow |
| $fnslid$ | Hard bed enhancement factor |
| $fnzclimsfz$ | Shelf front melt climate dependence scaling |
| $hb$ | Basal elevation, relative to sea level |
| $hs$ | Ice surface elevation |
| $hs_{PD}$ | Reference present day ice surface elevation |
| $n_{edge}$ | Number of grid-cell edges that meet tidewater conditions |
| $powfstdsed$ | Subgrid roughness exponent for drag modification of sediment |
| $powfstdslid$ | Subgrid roughness exponent for drag modification of sliding |
| $rlapseR$ | Lapse Rate factor |
| $t$ | Time |
| $u, v$ | Total horizontal velocities |
| $u_b, v_b$ | Horizontal basal velocities |
| $z$ | Vertical dimension dimensions (positive upwards) |
| $zcrhsed$ | Basal sliding co-efficient for soft bed (sediment) |
| $zcrhslid$ | Basal sliding co-efficient for hard bed (bare rock) |
| $\|\phi\|$ | Latitude |
| $\Delta\xi$ | Equivalent sea-level rise of AIS at LGM, relative to present day (*i.e.*, eustatic sea level locked u |

| | |
|---|---|
| $\Delta\zeta$ | Eemian contribution to eustatic sea level, relative to present day (*i.e.*, eustatic sea level release |
| $\sigma_f$ | Scaling factor for probability distributions |
| $P_{max}$ | Probability of the best run |
| $P_{90}$ | Number of runs required to achieve >90% coverage (of the total probability |
| $P_{tot}$ | Total probability |

# Chapter 1

# Introduction

In this chapter I provide supporting material to the three articles that document the body of work performed for this thesis. In the first section I discuss the motivation behind the study and present an overview of the work undertaken. The second section presents background material for readers who might be less familiar with (1) the physical characteristics of Antarctica, (2) the late Quaternary period of Earth history and the relation between it, the Antarctic Ice Sheet (AIS) and the other Quaternary ice sheets, (3) the role past ice sheet behaviour plays in understanding present and future sea-level change and (4) paleo-climatic studies. The last two topics are not directly addressed in the thesis, but as they have a strong dependency on ice sheet reconstructions they, in part, motivate the work.

The third section presents a literature review of the foundation topics of this thesis: (1) the current state of continental scale ice sheet modelling with a focus on the modelling deficiencies highlighted by the IPCC AR4 report and how they have been addressed in recent developments, (2) previous studies that employ ensemble techniques, (3) a description of the types of observational data that can be used for constraining the evolution of the AIS, (4) the LGM period, (5) AIS deglaciation from

the observational record, (6) Meltwater pulse events and abrupt climate change, and finally (7) the Eemian period. The last four are key periods and events from the last glacial cycle that I investigate with the reconstructions.

## 1.1 Motivation and overview

The Antarctic ice sheet (AIS) is the largest ice sheet on Earth, if melted there is sufficient volume of ice to raise sea levels 60-70 m (Siegert, 2001). Furthermore, it plays an important role in the global climate, having significant influence on, and being influenced by, atmospheric circulation, ocean circulation, and global sea level (King and Turner, 1997). It is also one of the slowest components in the climate system. It can take over 10,000 yrs for the ice sheet to reach equilibrium after an accumulation rate increase (Alley and Whillans, 1984) and, depending on the size of the perturbation, it can take more than a glacial-interglacial cycle for the ice-sheet to reach thermomechanical equilibrium after a temperature change (Ritz et al., 2001).

As such, to understand the role the AIS has played in the past global climate, the observed contemporaneous change, and to make predictions of future evolution, reconstructions of historical ice sheet behaviour are required. This requirement for quantifying past AIS evolution motivates the work documented in this thesis.

Reconstructions of past ice sheet extent and behaviour can be derived from geological constraints, but the observations are temporally and spatially spartan, especially in regions where ice still exists such as in Antarctica. Numerical ice sheet models are an effective tool for producing quantitative reconstructions and for 'filling in' the spatial and temporal holes in the observational record (Siegert, 2001; Cuffey and Paterson, 2010). The models, however, are inherently flawed due to the discrete representation of a continuous natural system, missing or poorly understood physics, and uncertain

boundary conditions. As with any numerical model, the ice sheet models implicitly and explicitly employ parameters to account for these uncertainties and limitations. Each parameter has a range of values that might generate realistic output. As the complexity of the models grows, so to does the number of parameters increasing the phase-space of possible reconstructions.

Past numerical reconstructions of the Antarctic ice sheet have predominantly relied either on (1) the application of geophysical inversion techniques that are glaciologically inconsistent (*e.g.*, Peltier, 2004)* or, (2) on a small number of simulations using hand-tuned glaciological models that are generally poorly integrated with the available geological data. In addition, most reconstructions lack meaningful assessments of their uncertainty making it difficult to interpret them with any degree of confidence.

The goal for this thesis is to address these deficiencies and produce data-constrained reconstructions of past AIS evolution with meaningful error bars. The AIS reconstructions are then used to investigate: (1) the timing and configuration at the Last Glacial Maximum (LGM); (2) the pattern of deglaciation from the LGM until present day; (3) the contribution the AIS made to melt water pulses; and (4) the configuration during the last interglacial.

In addition to addressing the above questions, AIS reconstructions provide valuable forcing or boundary conditions to other disciplines, primary examples being glacial isostatic adjustment (GIA) modelling and paleo-climatic studies. Determination of contemporaneous ice mass changes from geodetic measurements requires removal of long-term glacial isostatic adjustment signals to accurately disentangle contemporaneous change from past loading and unloading of ice (Ivins and James,

*Geophysical inversion techniques reconstruct the evolution of ice sheets using geophysical and/or geological data to infer what the ice loads might have been. They contain no glacial physics to model the dynamics of the ice. A further deficiency is that there is an ambiguity in isostatic response between the magnitude of the load and timing of load removal and thus other constraints are required (Tarasov and Peltier, 2004).

2005; Bentley, 2010). Paleo-climatic studies with coupled ocean-atmosphere models such as those of the Paleo-Modelling Intercomparison Project II (PMIPII, Braconnot et al., 2007)* require ice sheet reconstructions to provide boundary conditions such as freshwater flux and orography.

This thesis documents the work undertaken to generate the reconstructions and their application in investigating AIS evolution over the last glacial cycle. Building on earlier work for other major Quaternary ice sheets (Tarasov and Peltier, 2004, 2006; Tarasov et al., 2012), a well proven glacial system model (Pollard and DeConto, 2007; Pollard and DeConto, 2009; Pollard and DeConto, 2012b) has been heavily modified for large ensemble analysis. The model has 31 ensemble parameters to account for uncertainty in the ice physics, the climate forcing and the mass loss through ice-ocean interaction. Thousands of runs are generated by automatically sampling parameter sets from the parameter space; each run being a different reconstruction of AIS evolution. Using a diverse set of constraint data compiled for this study and a misfit-to-observation based evaluation methodology, each reconstruction is attributed a misfit score. The evaluation method addresses the challenges of using heterogeneous spatial and temporal observations, that also contain measurement uncertainty, in constraining model results. The scores attributed by the evaluation method are in effect probabilities and can be used to define probability distributions of the past evolution of the ice sheet. Weighted mean values and uncertainty estimates of key metrics (e.g. grounded ice volume) are computed. Both individual and weighted average reconstructions are used to investigate the ice sheet configurations and contributions to sea-level change from the Last Glacial Maximum, the deglaciation history of the AIS from LGM to present day and during the last interglacial, all crucial events and periods over the last glacial cycle.

*http://pmip2.lsce.ipsl.fr/

To date there has been no large-ensemble data-constrained study of AIS evolution. The probability distributions of reconstructions are an important contribution to improve confidence in the understanding the ice sheet evolution. Furthermore, the issues tackled in the evaluation methodology are not restricted to AIS reconstructions, rather, any study that wishes to constrain model derived glaciological reconstructions with diverse observational data will need to address similar challenges. To my best knowledge, in a ice sheet modelling context, these issues have not received such focused attention as found in this thesis. In addition to producing the reconstructions, the database of constraint data is made freely available to other researchers. As such it is hoped that both products will be valuable to the scientific community beyond the confines of this thesis.

## 1.2 Background

### 1.2.1 Physical characteristics of the Antarctic ice sheet

The Antarctic ice sheet (AIS) covers an area of $\sim 14 \times 10^6$ km$^2$ (Canada has an area of approximately $10 \times 10^6$ km$^2$) and contains around 90% of the worlds freshwater ice (King and Turner, 1997). As mentioned in the introduction, if the entire ice sheet where to melt it would cause 60-70 m of global sea level rise (Siegert, 2001). The Antarctic (defined as the ocean and landmass south of latitude 60°S ) is an important component in the global climate system (Antarctica is defined as the landmass). The ice sheet is the oldest on Earth, existing to some degree since at least 35 Ma (Greenland arrived at around ~3 Ma, the other large northern hemisphere ice sheets grew in the cold glacial periods of the Quaternary and disappeared during the interglacials) (Cuffey and Paterson, 2010). It has significant influence on, and is influenced by, atmospheric circulation, ocean circulation, and global sea level. The Antarctic Ice

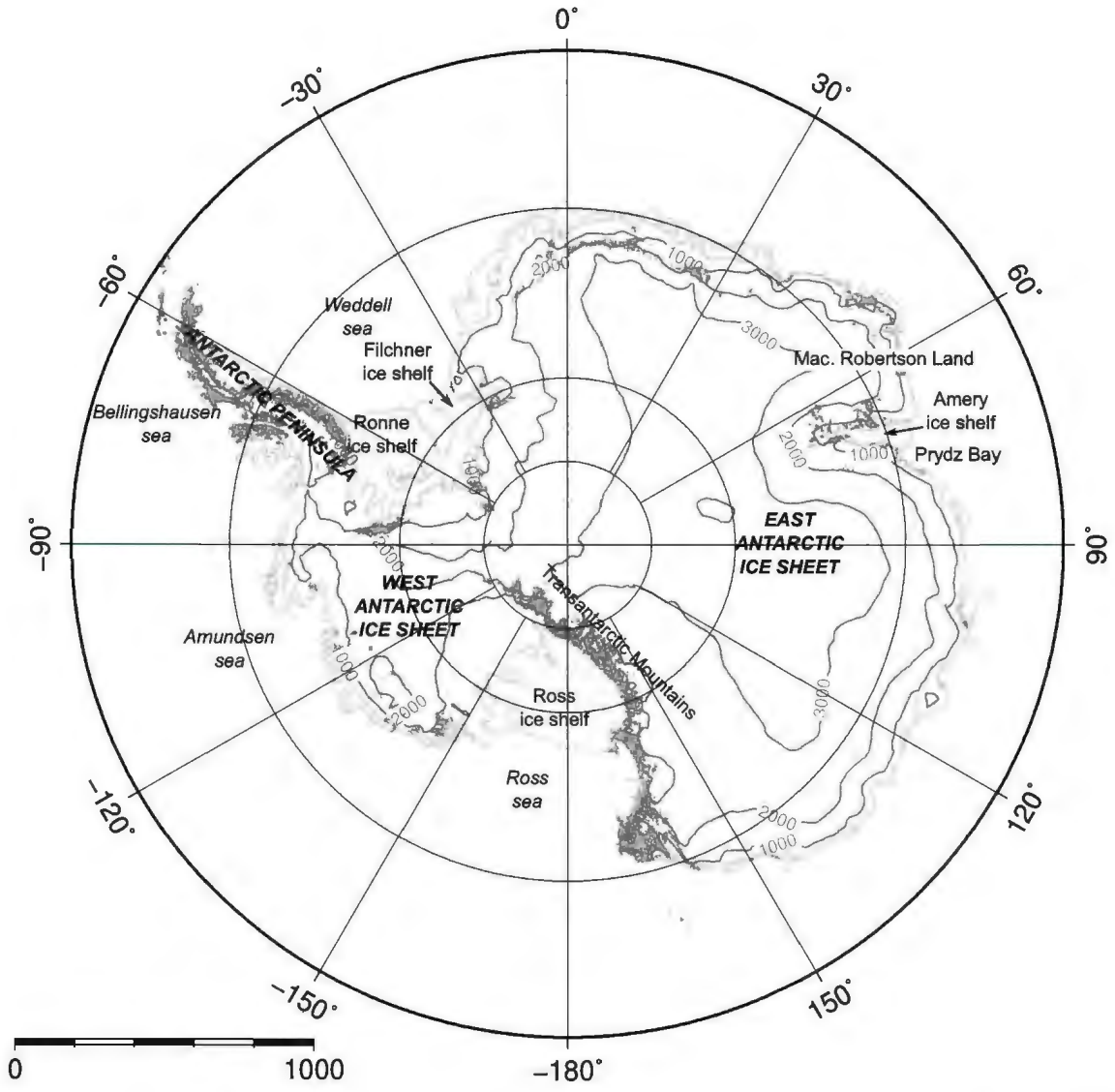


Figure 1.1: Map of key geographic features and locations discussed in introductory text. Mountainous or rocky regions (*e.g.*, Transantarctic Mountains) are highlighted in dark grey

Sheet is made up of two main grounded ice sheets, the East Antarctic Ice Sheet, the West Antarctica Ice Sheet, and a relatively smaller ice cap on the Antarctic Peninsula.

The East Antarctic ice sheet (EAIS) contains 86.5% of the total volume of ice of the AIS (King and Turner, 1997). Much of the interior is at elevations greater than >2000m (Fig. 1.1), rising to >4000 m in the centre. The EAIS is predominantly a terrestrial ice sheet, if ice were to be removed from the EAIS and the bedrock were allowed to relax back into is equilibrium elevation, the majority of the bedrock would be above sea-level.

The West Antarctic ice sheet (WAIS) is much smaller (11.5% of ice volume), with average elevations of around 850 m. WAIS and EAIS are separated by the Transantarctic Mountains (TAM), whose peaks rise to elevations greater than 4000 m. The WAIS is a marine based ice sheet, if the ice were to be removed and the bedrock was allowed to adjust for isostatic rebound, much of the bedrock would still remain under water.

The marine ice remains in place because it has sufficient thickness to keep it grounded. Ice flux has a strong (to the power of 5) non-linear dependence on the thickness (Chapter 8 Cuffey and Paterson, 2010)). The grounding line is the point where the grounded ice has insufficient weight to overcome the condition for flotation, the ice begins to float and so decouples from the bed. The majority of the ice in the WAIS is grounded on a reverse slope *i.e.*, the margin is higher that the interior. Given these conditions, if the grounding line were to retreat (caused for example by a warming ocean eroding away at the grounding line or thinning of the ice sheet upstream) the ice would thicken, increasing the flux of ice out of the grounded ice mass. This would promote thinning in the interior, thus causing further retreat of the grounding line (until, for example, the grounding line meets a upward slope, stopping the retreat). This positive feedback loop makes the WAIS potentially unstable; with

4-6 m of potential sea level rise locked up in the ice and evidence of past WAIS collapse it is the one of the most pressing concerns in AIS research (Mercer, 1978; Oppenheimer, 1998; Pollard and DeConto, 2009; Bamber et al., 2009b; Joughin and Alley, 2011).

The relatively mountainous Antarctic Peninsula contains a series of glaciers and small connected icecaps. It juts outs from the main body of the WAIS into the Southern Ocean as far north as 63°S . It has a mean height of 1500 m and an average width of 70 km. The peninsula is a significant barrier impacting the zonal atmospheric and oceanographic flow regimes and producing contrasting climatic conditions in the Bellingshausen Sea to the west and the Weddell Sea to the east (King and Turner, 1997).

Global atmospheric circulation can be thought of as a heat engine transporting surplus heat in the tropics to the polar regions (due to the incident angle of the sun the tropics receive more solar radiation that the poles). The Antarctic is the heat sink for the southern hemisphere—further enhanced by the high albedo of ice coverage that reflects back more solar radiation that would bare rock or ocean—and exerts significant control on the high and mid-latitude atmospheric circulation in the southern hemisphere. The enhanced albedo can also promote a positive feedback, a decrease in temperature is likely to lead to increased ice coverage, primarily through an increase in sea ice coverage (in the case of Antarctica), increasing the albedo and thus promoting more cooling (King and Turner, 1997). There is also a negative feedback; increased sea-ice also has the effect of moving the moisture source (the open ocean) further away from the land, reducing the amount of accumulation that can reach the interior (Huybrechts, 2002).

Strong cooling over the high plateaus of the interior promotes persistent katabatic winds that transport cold air from the interior out toward the coasts. In addition to

influencing the high-latitude atmospheric circulation (possibly extending its influence into the mid-latitudes (King and Turner, 1997)), this cooling plays an important role in the formation of dense, saline ocean bottom water (Hay, 1993) which in turn become part of the global thermohaline circulation (Clark et al., 2002b). The cooled surface waters are made more dense through increasing salinification caused by brine rejection in the formation of sea ice. The dense surface waters sink to become bottom water that subsequently moves northwards to become part of, and effect, the global ocean circulation (King and Turner, 1997). The Weddell sea and the Ross Sea are the key locations were deep water formation occurs (Hay, 1993).

As the largest body of ice on Earth (and comparable in size to the North American ice sheet complex (Tarasov et al., 2012)), AIS has the potential to greatly influence global sea level. As with any ice sheet the mass balance can either be in a positive, negative, or balanced state. This depends on the relative magnitudes of the integrated accumulation against the total loss through surface melt and the loss of ice into the ocean, either through iceberg calving and/or ocean melt. A positive balance causes water to be removed, through evaporation and precipitation, from the ocean and locked into a growing ice sheet; a negative balance releases water into the global ocean.

The range of temporal responses to external forcing in the AIS is diverse: locally and regionally it can be on the order of years to decades, whereas vast areas of the interior respond on much longer timescales (Bamber et al., 2007). Alley and Whillans (1984) estimate the time it takes for the ice mass to reach a new state of equilibrium after a perturbation to sea-level change to be ~8 kyr, to accumulation-rate increase to be ~10 kyr and much longer times for a response to temperature change (Ritz et al., 2001). As such, it is one of the slowest components in the climate system, changes to the forcings that occurred over 10,000 years ago may only now be

expressing themselves in the behaviour of the ice-sheet.

### 1.2.2 Late Quaternary period

During the Quaternary period (1.8 Ma to present day), sea level change has been primarily driven by the cyclic growth and decay of the ice sheets (Lambeck and Chappell, 2001). For most of the past 1 Ma this has been on a quasi-periodic 100 kyr cycle. Evidence of past sea level change is inferred from sources such as the Barbados coral record (Peltier and Fairbanks, 2006) and oxygen-isotope ratio recorded in fossilised benthic foraminfera ('forams') (Lisiecki, 2005). The change in ice volume, presented as inferred change global sea level over the last glacial cycle from the foraminera record is shown in Fig 1.2.

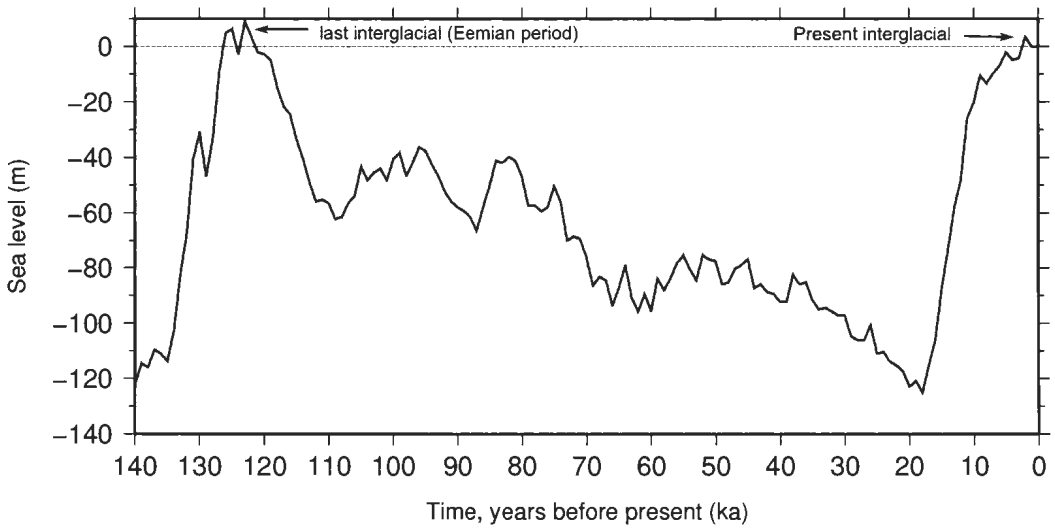


Figure 1.2: Variation of sea level over the last 140 kyr, adopted from (Lisiecki, 2005)

The glacial cycles are characterised by alternating glacial-interglacial periods. We are currently in an interglacial period, an uninterrupted warm interval during which the average global temperatures are warmer than the pre-industrial temperatures. Similarly, the last interglacial, or Eemian period, had temperatures warmer (and sea

levels higher) than today (Berger, 2002).

The asynchronous saw-tooth trend of slow global ice growth followed by rapid decay is a major feature of the 100 kyr cycle. At the peak of the Last Glacial Maximum (LGM) there was sufficient ice volume to remove 120-130 m of equivalent sea-level. This was predominantly locked up in the AIS, Greenland ice sheet (GIS), the North American ice sheet (NAIS), and the Eurasia ice sheets (EIS). At the termination of the glacial cycle the NAIS and EIS underwent rapid and practically complete disintegration. The majority of the 120-130 m excess ice was returned to the global ocean within about 8 kyr (Cuffey and Paterson, 2010). Furthermore, during that period of deglaciation, large and abrupt changes to sea level, caused by melt water pulses from the deglaciating ice sheets have been seen. The two most extreme examples of these events, meltwater pulse 1a and 1b (MWP-1a, MWP-1b), occurred around 14 ka and 11.3 ka. MWP-1a was characterised by a sea level rise of about 15 m or more in less than 500 yrs, the smaller MWP-1b by a rise of 5m in 400 yrs (Fairbanks, 1989; Bard et al., 1990). The timing, provenance–the predominant source of the MWP pulses has been attributed both to the northern hemisphere (Fairbanks, 1989; Peltier, 2005; Peltier and Fairbanks, 2006; Tarasov et al., 2012) and the southern hemisphere (Bard et al., 1996; Stanford et al., 2006)–and exact amplitudes of these events remains controversial, the importance of correctly untangling the climatic interactions and potential triggers of such rapid events is incontrovertible (e.g. Clark, 2002; Bard et al., 2010; Deschamps et al., 2012).

### 1.2.3 The role of past ice sheet evolution in present sea-level change

Ten percent (~600 million) of the world's population live in zones along the coast that are located less than 10 m above present day mean sea level and more than 100

million of those people live within 1 m (Douglas and Peltier, 2002; McGranahan et al., 2007). Even a small increase in sea level rise will have significant socio-economic impact through coastal erosion and shoreline retreat, loss of arable land, increased susceptibility to storm surges and groundwater contamination (Meier and Wahr, 2002; Alley et al., 2005). Accurate forecasts of sea-level change over decadal and centennial timescales are essential for the planning, design and engineering of effective responses. Estimates of sea level rise that are too high may result in over-engineered solutions, misdirecting limited resources, whereas underestimates of the rise may leave coastal populations under prepared for change (Pfeffer et al., 2008).

There are two primary processes controlling long term eustatic* sea level change over Quaternary time scales: an increase in the mass of water (glacio-eustatic component), caused primarily by the melting of terrestrial ice, and an increase in the volume of the ocean without a change to its mass (the steric component), caused by thermal expansion of the oceans (Meier and Wahr, 2002). The measurement of contemporaneous eustatic sea level change and long term trends is achieved through a global network of tide gauges (in a few cases there are datasets that are over 100 years old) and in recent decades by satellite (Cazenave and Nerem, 2004). At a regional scale, the (relative) sea level can be influenced by glacial isostatic adjustment (GIA), the vertical movement of the Earth's crust in response to the unloading (and loading) of the ice sheets due to mass loss (or gain) (Peltier and Tushingham, 1991; Douglas, 1991; Davis and Mitrovica, 1996). GIA is measured by GPS stations and, since its launch in 2002, the Gravity Recovery and Climate Experiment (GRACE) (GRACE actually measures the redistribution of mass, so also measures groundwater changes, ice mass, water mass etc.) which provides global estimates of the temporal changes in the Earth's gravitational field (effectively through the redistribution of water mass)

*Eustatic sea level change is a global change that results from either a change in the volume of seawater, or a change in the size of the ocean basin that contains it.

(Cazenave and Nerem, 2004).

The major contributors to 20th century eustatic sea level rise are thought to have been the result of ocean thermal expansion and the melting of glaciers and ice caps, whereas ice sheet melting is thought to have played a minor role. In the future, under the predicted warming climate, ice sheets may potentially be the larger contributor, however they also have the greatest uncertainty (Church et al., 2008).

GIA is a slow process that still has a major influence today, for example very long tide gauge records around Fennoscandia indicate relative sea level is actually falling by about 10 mm $yr^{-1}$ as the region under goes post-glacial rebound due to the unloading of the Fennoscandia ice sheet (Douglas and Peltier, 2002). One of the major difficulties in making future predictions of eustatic sea level change is separating out the glacio-eustatic, the steric signal and the GIA signal. Accurate deglaciation chronologies are required to quantify past loading and unloading of ice to provide loading histories for decontamination of the measured GIA rates (Ivins and James, 2005; Bentley, 2010).

### 1.2.4 Paleo-climatic studies

The study of past climates that are analogous or partially analogous to predicted future climatic scenarios–such as the last interglacial period when temperatures were warmer and sea levels higher–is of particular importance as a tool to aid their interpretation and guide climatic policy (Turney et al., 2006). For example the Paleo-Modelling Intercomparison Project II (PMIPII, Braconnot et al., 2007)* uses coupled ocean-atmosphere (sometimes including vegetation components) models to recreate key climatic periods in the past. These experiments require ice sheet reconstructions to provide essential boundary conditions and forcing such as orography and fresh water flux.

*http://pmip2.lsce.ipsl.fr/

## 1.3 Literature review

### 1.3.1 Glaciological modelling

For the purposes of this thesis I define a glacial system model as comprising a thermo-mechanically coupled ice sheet model core integrated with a bedrock response component (that simulates the response of the Earth to the loading and unloading of the ice sheet as it grows and shrinks), a climate forcing component and an ice-ocean component.

The generation of ice sheet models (ISM) that provided the results for the IPCC AR4 report were unable to capture many of the processes now thought to be most responsible for the variability and evolution of the ice sheets, especially those occurring over decadal or centennial scales. The areas of concern that were identified as high priority for future research efforts were: accurate modelling of the coupling between the ocean and ice shelf, accurate modelling of the transition zone between the ice shelf and ice sheet and inclusion of sub-glacial hydrology (Marshall, 2005; Payne et al., 2006).

The interaction between grounded ice, floating ice and the surrounding oceans is key to controlling its evolution. Two concerns are paramount to modelling this interface: (1) proper representation of the basal melting below the ice shelf due to the interaction between the ocean and the shelf; and the ability to accurately capture the migration of the grounding line, the point at which the ice detaches from the bedrock and begins to float (Payne et al., 2006; Vieli and Payne, 2005). Sub-shelf melting and calving are important as they constitute the main cause of mass loss from the AIS (Huybrechts, 1991; Jacobs et al., 1992). The causal link is indirect because they evolve the geometry of the ice shelf—either through melting at grounding line directly or changing the back stress provided by the shelf configuration—which af-

fects the grounded ice sheet through retreat of the grounding line, as ice crosses the grounding line, it floats and becomes part of the ocean system, positively contributing to sea level rise (Pattyn et al., 2006; Schoof, 2007). The processes that control calving and sub-shelf melt (discussed in greater detail in Chapter 2) are still poorly understood; therefore, mass loss rates in the models are either prescribed (*e.g.*, Pollard and DeConto, 2009), computed from ad-hoc implementations (*e.g.*, Tarasov and Peltier, 2004) or calculated based on empirical evidence (*e.g.*, Alley et al., 2008).

Ice streams, rivers of fast flowing ice (ca. 0.8 km/year, 50 km wide, 300 km long), laterally restricted by topography or by areas of slower moving ice are seen as the dominant force in determining the variability in present-day Antarctica (Payne et al., 2006). They are likely responsible for at least 90% of the discharge of ice and sediment from within the ice sheet (Bamber, 2000). Of significant concern was that the stress regimes believed to operate within the ice streams, their tributaries and at their margins were not being represented in the last generation of ISM (Payne et al., 2006). The inclusion of these regimes is now considered critical; the response of an ice sheet to changes within an adjoining ice shelf is believed to rely heavily on the propagation of longitudinal stresses transmitted through the ice stream (Hindmarsh, 2006).

Grounded ice sheet flow is dominated by vertical shear, whilst ice shelf flow is dominated by longitudinal stretching and lateral shear. The two regimes couple together across a mechanically complex zone near the grounding line where neither regime dominates and both the longitudinal stretching and the shear stresses are important (Schoof, 2007). This transition zone can be large, such as in an ice stream or small, such as at an abrupt ice sheet/ice shelf junction (Pattyn et al., 2006). The dynamics of this transition zone control the rate of outflow of ice across the grounding line. The horizontal extent of this transition zone is the distance over which longitudinal

stresses from the ice shelf are transmitted into the ice sheet. This process is poorly resolved in models (the process frequently occurs at the sub-grid scale) as the process may only be a few ice thicknesses (in he AIS 1-2 km) in length (Schoof, 2007) *i.e.*, even a large ice stream with a width of approximately 40 km is barely resolved in a continental scale ice sheet model which typically operate on a 20-40 km horizontal resolution (Payne et al., 2006). The concurrent modelling of both the ice stream flow and the slower, adjacent ice sheet flow is not trivial. Full 3D continental-scale model that are capable of capturing both regimes within reasonable run-times have only started to become available in recent years (*e.g.*, Pollard and DeConto, 2007; Pollard and DeConto, 2009; Martin et al., 2010).

It should be noted that the methods employed to model these processes in the present generation of models are quite different and can give differing results; for example, the way the grounding line is numerically treated can heavily influence the solution (Vieli and Payne, 2005). Model intercomparison projects such as EISMINT and ISMIP will continue to be useful benchmarks to assess the capabilities of the different methods being employed (Huybrechts et al., 1996; Pattyn et al., 2008).

The other major area of concern, not explicitly addressed in this thesis but noted for completeness in this review, is the proper treatment of sub-glacial hydrology. The omission of sub-glacial hydrology and its effect on the rheology of the sub-glacial sediment in the models is a large concern as it has an important influence on the stability of the ice streams and thus the evolution of the ice sheet (Payne et al., 2006). An increase in the availability of water at the base of the ice will enhance basal sliding and if present increase the amount of water-saturated sub-glacial sediment promoting bedrock deformation and faster ice flow (Hooyer and Iverson, 2002).

There have only been a few studies that have produced continental scale-glacial cycle reconstructions. The first thermomechanically coupled model used for AIS evo-

lution studies was produced by Huybrechts (1991); Huybrechts and Wolde (1999); Huybrechts (2002). Thermomechanical coupling is important because the final ice configuration depends heavily on the mutual interactions of the ice temperature and the flow. (Ritz et al., 2001) advanced on this by produced a GSM with separate treatment of ice sheet flow and ice stream/shelf flow. They modelled AIS evolution over the last 420 kyr. The next significant improvement came from a heuristically combined set of equations that model sheet/stream/shelf flow (Pollard and DeConto, 2007; Pollard and DeConto, 2009; Pollard and DeConto, 2012b). The core of the Pollard and DeConto (2009) ice sheet model was used in this study. Recently, a number of higher order models have been produced that are configured for AIS, but have yet to be used to generate glacial cycle reconstructions (*e.g.*, Martin et al., 2010; Larour et al., 2012; Martin et al., 2012).

### 1.3.2 Data constrained-ensemble analysis

This thesis builds on the sequence of data-model integration techniques initiated by Tarasov and Peltier (2002, 2004). They first applied a data-constrained ensemble approach to produce deglaciation chronologies of the NAIS (Tarasov and Peltier, 2004), using a SIA based thermo-mechanical GSM model with 20 ensemble parameters to generate the reconstructions. The constraint data included ice margin chronologies, relative sea level histories, a single geodetic uplift observation, and a traverse of absolute gravity measurements. The basis of the evaluation methodology was RMS scoring, subjective weighing for critical data-points and 'sieves' that would accept or reject runs based on some criteria *e.g.*, runs outside the range of the observed range of uncertainty for the uplift measurement would be rejected from subsequent scoring.

Tarasov and Peltier (2006) built on that initial study to produce a Bayesian calibrated drainage chronology. The Bayesian methodology generated a posterior distri-

bution for the parameters and therefore the reconstructions, given the observational data sets. In addition, improvements were made to the model, including the introduction of two extra ensemble parameters. Further enhancements to the NAIS deglaciation reconstructions were made recently (Tarasov et al., 2012), with a number of model improvements, an increase to 39 ensemble parameters, and a larger set of constraint data, including a deglaciation ice margin chronology constraint.

The most comprehensive data-constrained deglaciation chronology, to date, for the AIS was produced by Whitehouse et al. (2012). Their objective was to produce a loading history for a glacial isostatic model. Using the open-source ice sheet model Glimmer (Rutt et al., 2009), at a resolution of 20 km, they generated different AIS configurations at five time-slices (20, 15, 10, 5, 0 ka*). The reconstructions were produced by fixing the grounding line extent, based on marine geophysical and marine geological data-sets, and adjusting the bed sliding parameter and the boundary conditions (climate inputs, relative sea level, isostatic behaviour and geothermal heat flux). Each configuration generated was then evaluated using terrestrial constraint data for past ice sheet elevation and 'no-ice' zones. The model to observation misfit was evaluated (using RMS misfit, mean error, standard deviation of mean error, and a correlation coefficient; see Whitehouse et al. (2012) for details) for each configuration. Weighting was applied using inverse distance and a subjective data quality factor. Using the maximum, minimum and smallest misfit, a upper, lower and best AIS contribution from LGM to AIS was estimated

A small number of other researchers are also starting to use ensemble techniques to explore model and parametric sensitivities (Hebeler et al., 2008; Stone et al., 2010; Applegate et al., 2011) but with no data-model integration. To the authors best knowledge there is no data-constrained large-ensemble study of the AIS (especially

*ka defined as 1000 calendar years before present, whereas kyr is a time period of 1000 yrs

with fully coupled ice shelves).

### 1.3.3 Types of observational constraints

Constraint data is extracted from a range of sources that includes geological and glaciological proxies, date-able organic matter recovered in-situ or from on-shore or off-shore sediment cores, marine geophysical data, and geodetic measurements. In the following paragraphs I describe these sources and, more importantly, describe the type of constraint that they provide, categorised as: grounding line extent and retreat data, relative sea level and past ice thickness indicators, rate of present day uplift, past ice surface elevation data and biological refugia that identify ice free areas. In this study only grounding line extent and retreat data, relative sea level and past ice thickness indicators were used to evaluate the reconstructions. The other data-types were considered and subsequently rejected for reasons discussed in the text. Future investigations will, ideally, include this data.

The maximum extent of the grounding line has been identified though multi-beam echo sounding mapping of subglacial bedforms (swath bathymetry) in locations such as Pyrdz Bay (Domack et al., 1998; O'Brien et al., 1999), the Ross Sea (Domack et al., 1999; Shipp et al., 1999), Pine Island Bay (Lowe, 2002a), and around the Antarctic Peninsula (Pudsey et al., 1994; Heroy, 2005). Bathymetric surveys identify geomorphological features such as grounding line wedges (Anderson, 1999) that mark the furthest extent that the grounding line advanced to. Although a strong constraint, the maximum extent as recovered from swath bathymetry alone does not provide an associated age constraint and thus has restrictions on its usage. In conjunction with dating of sediment cores recovered from the continental shelf, however, a history of the grounding line retreat from its maximum position can be reconstructed (Anderson, 2002; Heroy, 2005).

The retreat of the grounding line across the continental shelf is recorded in the underlying sediment and, although a non-trivial exercise, can be interpreted from stratigraphic analysis of the sediment recovered in marine cores (Anderson, 2002; Heroy and Anderson, 2007; Hillenbrand et al., 2010). If organic matter can be sampled a date may be obtained. The ideal stratigraphic succession to record the migration of the grounding line would reflect three distinct environments: sub-glacial, glacial-proximal and open marine (Heroy and Anderson, 2007). Identifying and dating the contact between the underlying sub-glacial facies and the overlying glacial-proximal facies provides a date on the age of grounding line retreat. It is often the case that there is insufficient dateable organic matter in the sub-glacial facies, however, onset of open marine conditions, providing a theoretical minimum age for the grounding line retreat, might be obtained by dating organic matter recovered above the transition zone in the overlying post-glacial glacial-marine muds and/or the diatom rich open marine sediments (Anderson, 2002; Heroy and Anderson, 2007; Livingstone et al., 2012).

Dated organic matter (*e.g.*, penguin or whale remains, shells) recovered from paleo-beaches or from sediment cores recovered from isolation basins (present day lakes that were once inundated by the ocean but, due to GIA, have rebounded above sea level, thus containing both marine and lacustrine sediment) can be used as indicators for past sea level. By gathering sufficient data-points from the same area a relative sea level RSL curve can be reconstructed (*e.g.*, Baroni and Hall, 2004; Hall, 2004). RSL curves provide a constraint on the earths response to loading and unloading relative to sea level, thus are a proxy to past changes to the ice sheet (Bassett et al., 2007). Most RSL data is younger than the Holocene (10 ka) so does not constraint as far back as the LGM. RSL observations combined with reconstructed RSL curves, generated from coupled ice sheet-earth response model, provide a strong constraint both to

magnitudes and timings of deglaciation histories (*e.g.*, Bassett et al., 2007; Bentley and Hodgson, 2009; Tarasov et al., 2012).

The maximum altitude and thinning history of the ice-sheet surface can be recovered through surface exposure dating (SED) of glacial geomorphological features and glacially transported erratics. SED, or cosmogenic dating, exploits the amount of time material has been uncovered by ice and exposed to cosmic radiation. The technique is capable of dating samples that are over 1 Ma old (*e.g.*, Storey et al., 2010). The maximum elevation of the ice sheet is recorded when the past ice surface either erodes up to a certain elevation leaving trimlines on nunataks (rock outcrops or mountain peaks that protrude above the ice) or previously entrained boulders are deposited on exposed bedrock as the ice recedes (or previously covered bedrock becomes exposed)deposits glacial erratics. Thinning can be recorded as through two or more cosmogenically dated observations enabling an age-elevation plot to be constructed (*e.g.*, Stone et al., 2003; Mackintosh, 2007).

Surface elevation changes derived from isotopic and gas analysis of ice cores (e.g. Martinerie et al. (1994); Delmotte et al. (1999); Steig et al. (2001); Parrenin et al. (2007); Price et al. (2007)) can be used to provide a direct glaciological constraint (Whitehouse et al., 2012). Their interpretation is dependant, however, on methods that themselves are dependent on parametrisations (e.g. inferring the surface changes due to air-pressure deviations from air content analysis or through glaciological modelling). In addition they lack appropriate uncertainty estimations.

A compilation of GPS based present-day uplift data was recently made available (Thomas et al., 2011) which, for the first time, offers sufficient signal strength to be employed as a model constraint for the AIS. Rates of present-day uplift have been used as a major constraint for the deglaciation of the last North American (Tarasov et al., 2012) and Eurasian ice sheets. The GRACE record also provides a powerful

constraint data-set (Peltier, 2004; Tapley et al., 2004). Both these data-sets, however are highly sensitive to recent changes in surface load making the characterisation of uncertainty a challenge.

Biological refugia have the potential to be a constraint on the long term (Myr) evolution of the ice sheet (Convey et al., 2009). Paleobiological studies of Antarctic terrestrial, marine and freshwater fauna that require ice free conditions have found evidence of habitation for up to tens of millions of years in coastal locations and on nunataks such as the South Shetland islands, Victoria Land, and the Larsemann hills (Newman et al., 2009). This data type was not included in this initial study as the oases are generally much smaller the model resolution of 40 km and, in addition, there is uncertainty as in the age of ice-free conditions *i.e.*, ice-free conditions may have existed for longer than the occupation of the fauna (Hiller et al., 1988). Future incorporation of this data-type will require close collaboration with data specialists.

### 1.3.4 Last Glacial Maximum

Most Quaternary ice sheets had grown to their maximum extent by 26.5 ka and began to retreat after 18.0-19.0 ka, during this LGM period sea levels were 120-130m lower than present day (Clark et al., 2009). The global sea-level signal (shown in Fig. 1.2) is an integrated signal that does not distinguish between the hemispheric or local glacial maximas, determining the individual contributions is an on-going challenge. Accurate estimates of the local LGM timing and the associated sea level contribution from the AIS will aid in constraining the timing and magnitudes of the other Quaternary ice sheets and in understanding ice sheet sensitivity to global and regional climate change and identifying ice sheet–climate feedbacks (Clark et al., 2009; Weber et al., 2011). Furthermore, of particular importance is trying to understand the triggers (*e.g.*, warming ocean or atmosphere vs sea level rise) that initiated deglaciation

and the subsequent role those triggers played in deglaciation; tackling these question requires individual reconstructions of ice sheets (Clark et al., 2009).

Especially intriguing is the 'missing water' problem (Andrews, 1992); it has been an ongoing challenge to make the total sum of estimates for equivalent sea level locked up in the LGM ice sheets add up to the ~120-130 m global total. Furthermore, as estimates for some of the LGM ice sheet volumes are being refined the individual contributions are decreasing (Bentley, 2010), the AIS being a prime example. Most of the estimates from the 1980s and the early 1990s estimated >20 m equivalent sea-level rise was locked up in the larger LGM ice-sheet. Since then estimates have been decreasing, most, certainly predict less than 20 m with many estimating less than 10–15m (See Table 1 of Bentley, 2010, for an comprehensive summary table of LGM volume estimates and the methods used to generate them).

The configuration of the AIS during the LGM is believed to have been (1) a slightly thinner or unchanged EAIS interior, thought to be caused by extended sea ice coverage pushing the moisture source further away than at present day (Huybrechts, 2002) with thicker margins and a minor grounding line advance; (2) major migration of the ROS grounding line in front of the present day ice shelf position and out onto the continental shelf and an associated thickening; (3) grounding line advancement and limited thickening of the interior WAIS; (4) thickening and migration of the grounding line onto the shelf (maybe as far as the shelf edge (Lowe, 2002b)) for the AP, and in the Weddell Sea/RON-FIL region, due to lack of evidence, there is uncertainty as to if the present day RON-FIL grounding line was able to migrate to the continental shelf break or was hampered from advancing due to the presence of the deep Crary trough underneath and in front of the present day ice shelf (Bentley, 1999; Denton and Hughes, 2002; Anderson, 2002; Heroy and Anderson, 2007; Bentley et al., 2010; LeBrocq et al., 2011; Hein et al., 2011).

The most recent glaciological modelling studies have made AIS LGM sea-level equivalent estimates of 12 mESL (Pollard and DeConto, 2009), 10 mESL (Mackintosh et al., 2011), 9±1.5 mESL (with a prediction of 8 mESL contribution from a minimum misfit model) (Whitehouse et al., 2012), and 1.6 mESL (3.5 mESL from WAIS and -1.9 mESL from EAIS, because of increased accumulation) (Pollard and DeConto, 2012b)) respectively. The Mackintosh et al. (2011) study reconstructed a local LGM as having occurred at 14 ka.

### 1.3.5 AIS deglaciation from the observational record

The deglaciation of the AIS is believed to have commenced at ~18 ka in response to atmospheric warming (Jouzel et al., 2001; Heroy and Anderson, 2007), however, this single estimate simplifies the issue greatly. The observations that record the maximum extent, the subsequent retreat and the thinning interior show considerable variability both in the dynamics of retreat and the timing of retreat from sector to sector (Sugden et al., 2006).

The ages for grounding line retreat from marine cores range from 31-8 ka BP, with the majority of ages occurring between 18-8 ka BP (Livingstone et al., 2012). Heroy and Anderson (2007) estimated similar ages for the onset of deglaciation in the Antarctic peninsula, retreat beginning at ~18 ka from the outer shelf edge, first in the North then later in the South of the Peninsula and reached its current configuration by 9.5 ka (Bentley et al., 2005). Retreat of the grounding line in the Ross Sea is thought to have occurred relatively smoothly, following a swinging gate pattern hinged at the eastern side of the sea, from ~15 ka until it reached its present location at around ~3 ka (Conway et al., 1999; McKay et al., 2008). The retreat in the EAIS is less well constrained and, where there is a constraint, there is a significant difference in the timing. For example, in the Eastern Weddell Sea, retreat started prior to the LGM

(Anderson, 2002), whereas in Mac. Robertson Land retreat started from the outer shelf at around ~14 ka (Mackintosh et al., 2011), with the Prydz bay ice-streams retreating sometime afterwards at around ~12 ka.

Similarly, there is variability, within the same sector, in the thinning histories recorded by the cosmogenically dated samples. The deglaciation history from Frammes Mts west of the Lambert-Amery ice shelf system and close to the edge of the EAIS has undergone a gradual thinning of ~350 m from ~22 ka until it reached the present day altitude at ~6 kyr (Mackintosh, 2007). Whereas, in the Grove Mountains, behind the Lambert-Amery ice shelf system and deeper in the interior the observations record no thinning for at least the past ~50 ka (Lilly et al., 2010). Sites in the TAM Mts constrain the glaciologically dynamic glaciers that drain the EAIS through complex topography of the mountains into the WAIS and Ross ice shelf (Todd et al., 2010). The samples, located mid-way and at progressively higher elevations record an 'up-glacier' propagating wave of thickening at 17-14 ka, 14.7-10.2 ka and 9.1-7.7 ka, respectively, followed by subsequent thinning caused by the retreating grounding line of the Ross ice shelf (15-3 ka (Conway et al., 1999; McKay et al., 2008). In Marie Bryd land in the WAIS, 700 m of thinning has occurred over the past ~10 kyr and is containing today. In the Pine Island Bay, ongoing thinning has been seen since ~14.5 ka (Johnson et al., 2008). AP exhibits similar behaviour to the Frammes Mts, reaching its current elevation at around 9.6 ka (Bentley et al., 2006). On the AP side of the Weddell sea sector samples in the Ellsworth Mountains have progressively thinned between 230-480 m since 15 ka (Bentley et al., 2010). On the EAIS side of the Weddell Sea in the Shackleton Range, the measurements suggest that the ice streams in the Slessor and Recovery glaciers were not significantly thicker than present day at the time of the LGM (hypothesises because the grounding line was not able to migrate beyond the Crary trough (Bentley et al., 2010; Hein et al., 2011).

### 1.3.6 Meltwater pulse events and abrupt climate change

Melt water pulse (MWP) events are periods of accelerated sea level rise caused by rapid melting events. In the Barbados coral record, at least two major MWP events (MWP-1a and MWP-1b) are recognisable since the LGM, MWP-1a occurred around 14 ka and was characterised by a global mean sea level rise of about 20 m in less than 500 yrs (Fairbanks, 1989; Liu and Milliman, 2004; Deschamps et al., 2012), the smaller MWP-1b occurred ~11.3 ka, the smaller MWP-1b saw was by a rise of 5-15 m in 400 yrs (Fairbanks, 1989; Bard et al., 2010; Deschamps et al., 2012).

Published dates for the onset of MWP-1a range from around 14.6 ka (Hanebuth et al., 2000) to 14.0 ka (Stanford et al., 2006). The likely sources for MWP-1a are the Laurentide Ice sheets and/or the Antarctic Ice Sheet. There is no evidence that the Eurasia Ice Sheet was a primary source for MWP-1a (Clark et al., 1996; Peltier, 2005). Two major climatic events occurred within the MWP-1a time-frame; the Bølling warming event begin at ~14.6 ka, which was abruptly ended by the Older Dryas cold event which begin ~14.0 ka (Rasmussen et al., 2006).

The timing, provenance—the predominant source of the MWP pulses has been attributed both to the northern hemisphere (Fairbanks, 1989; Peltier, 2005; Peltier and Fairbanks, 2006) and the southern hemisphere (Bard et al., 1996; Stanford et al., 2006)—and exact amplitudes of these events remains controversial, but the importance of correctly untangling the climatic interactions and potential triggers of such rapid events is incontrovertible (e.g. Clark, 2002; Bard et al., 2010; Deschamps et al., 2012). Correlating an Antarctica sourced meltwater event with the possible inception of the Bølling warming event has a very different implication to correlating a Northern Hemisphere source with the possible inception of the Older Dryas cooling event. Accurate deglaciation chronologies will facilitate understanding of the potential triggers and the response of the AIS, and other ice sheets, to such abrupt events.

### 1.3.7 Last Interglacial (Eemian period)

The Eemian (last interglacial period) began approximately 129±1 ka and lasted until at least 118 ka (Overpeck et al., 2006); it was characterised by globally averaged warmer temperatures, (e.g. ~1.5 °C Turney and Jones, 2010)†, sea levels higher than present day (6.6 - 9.4 m higher Kopp et al., 2009)‡, a smaller Greenland Ice Sheet (GIS) and likely also a smaller West Antarctic Ice Sheet (WAIS) (Cuffey and Marshall, 2000; Overpeck et al., 2006; Kopp et al., 2009). As such, the study of this period is of interest because of its similarity to predicted future climatic conditions and, being geologically recent, high resolution records are available against which models of future climate change can be tested (Overpeck et al., 2006; Meehl et al., 2007; Kopp et al., 2009).

The probabilistic study by Kopp et al. (2009) concluded that the Southern Hemisphere contributed at least 2.5 m of eustatic sea level increase. Through glaciological modelling, Tarasov and Peltier (2003) estimated the conservative contribution from Greenland to be 2-5.2 mESL with a more likely range of 2.7-4.5 mESL. This requires a conservative minimum from the AIS of 1.4 mESL and a more likely minimum of 2.1 mESL. Ackert et al. (2011) place constraints on WAIS geometry that limit the WAIS contribution to the higher sea levels observed during the last interglacial to ~3 mESL. The end of the Eemian has been aligned to the end of Marine isotope stage 5e at 116.1±0.9 ka (Shackleton, 2003).

To the authors knowledge only Ritz et al. (2001) and Huybrechts (2002) have published glaciological modelling based estimates of AIS configuration during the Eemian. The snapshots at 120 ka both have a similar appearance, with substantially reduced Ross and Ronne-Filchner grounding lines. The Huybrechts (2002) reconstruction pre-

†Other estimations range from 0.1 °C to >2 °C warmer than present.

‡Higher than 6.6 m with 95% certainty, higher than 8.0 m with 68% certainty and likely no more than 9.4 m (33 %).

dicts that the AIS contributed 1.4 mESL during the Eemian. Ritz et al. (2001) does not make an explicit contribution assessment.

## 1.4 Objectives

**Objective 1: Development of a glacial systems model for large ensemble analysis of AIS evolution** The first objective, documented in Chapter 2, was to produce a glacial systems model configured for generating a large ensemble of AIS reconstructions over glacial timescales.

The GSM must incorporate state-of-the-art developments in ice sheet modelling theory (as discussed in Section 1.3.1) and be able to produce continental-scale results over 100 kyr timescales. Furthermore, to generate the ensemble, parameters must be defined that allow the uncertainty in the individual components of the model to be explored. The computing resource available was about 1000 processor cores* shared processors, thus the GSM needs to be computationally efficient, runs need to be complete in days rather than weeks and allowing 2000-4000 ensemble runs to be generated within reasonable time-scales

**Objective 2: Development of a constraint database and associated evaluation methodology** The second objective of the study, documented in Chapter 3 has two parts, (1) the compilation of a database of observational data to constrain the reconstructions and (2) the development of an evaluation methodology to assess the AIS reconstructions using the constraint data.

The constraint database must contain sufficient high quality observational data

*This study used the Placentia cluster of ACEnet (Atlantic Canada high performance computing facility) http://www.ace-net.ca/wiki/Compute_Resources; individual model runs took between 2-6 days, depending on the load from other users a 3000 run ensemble would take approximately 10 days to complete.

points to provide spatial and temporal coverage (within the limits of the available data) for constraining the AIS reconstructions. The evaluation methodology, based on work for the other major Quaternary ice sheets (Tarasov and Peltier, 2002, 2003; Tarasov et al., 2012), must be adopted for this GSM and the AIS observational data. The outcome from the evaluation methodology is a misfit-to-observation score for each run. A crucial part of the evaluation methodology is that the uncertainties in the system (model and observational uncertainties and irregular spatial and temporal distribution of the constraint observations) are captured and addressed so that they can be propagated into the final results.

**Objective 3: Evaluation of the reconstruction misfits** An essential part of the evaluation process is the assessment of the dominant characteristics and misfit patterns in the reconstructions and therefore, by proxy, the GSM. Understanding the strengths and weaknesses of the reconstructions must be considered in discussing the reconstructed AIS behaviour (see objective 1.4 and to guide future work and efforts. Specifically, I address the following:

- Is there any correlation (linear or non-linear) between parameters and the key metrics?
- What are the dominant patterns of misfit from the reconstructions?
- How can the GSM model be improved?
- Are there any key regions in need of further constraint?

**Objective 4: Investigation of AIS evolution using the reconstructions** The final objective addresses the questions specific to the evolution of AIS, predominantly

from LGM to present day but also during the Eemian period. The question I specifically explore are:

- Based on the reconstructions when did the local LGM of the AIS occur?
- What is[are] the eustatic contribution of the AIS, and different sectors of the AIS, from LGM to present day?
- When did deglaciation start and what was the pattern of deglaciation?
- What was the contribution from AIS to the MWP events *i.e.*, could the AIS have been a predominant contributor to MWP-1a or 1b?
- What was the configuration of AIS during the Eemian and what was its contribution to global sea level?
- How did the reconstructed AIS evolve over the glacial cycle?

## 1.5 Thesis Overview

This thesis is written in manuscript format as opposed to a traditional thesis format. Content is presented in the style of three journal articles that have either been submitted for publication or are being prepared for submission. Because they are written as standalone articles they may contain material that has will already have been presented in the introduction. To meet the requirements of Memorial University thesis guidelines each article is presented with its associated bibliography and, in addition, there is a bibliography for the entire thesis. The appendices and supplementary material for each of the articles is appended after thesis bibliography.

The original research papers of this thesis appear in Chapters 2, 3 and 4. An overall summary to the body of work and comments on envisioned future efforts are

presented in Chapter 5.

## 1.6 Co-authorship statement

Authorship for all research papers presented in Chapters 2 to 4 is listed in the following order: Robert Briggs (thesis author), Dr Lev Tarasov (thesis supervisor). Dr Lev Tarasov is an Associate Professor with the Department of Physics and Physical Oceanography at Memorial University and holds a Canada Research Chair.

Dr Lev Tarasov developed the initial idea and direction of the project. The core of the ice sheet model was provided by Dr Dave Pollard from Penn State University. The model was modified for ensemble analysis predominantly by Mr Briggs with guidance, help and input from Dr Tarasov and Dr Pollard. Mr Briggs developed the new sub-shelf melt component. Dr Tarasov designed and implemented the basal drag component. The constraint database was compiled and prepared by Mr Briggs. The evaluation methodology was developed by Rob Briggs (EXT and ELEV data) and Dr Tarasov (RSL, overall concept, and statistical methodology). Data analysis was performed by Mr Briggs. Finally, Mr Briggs performed all duties associated with preparing each manuscript, except for the following sections which were provided by Dr Tarasov: Chapters 2; Bedrock response and relative sea level computation section and initial draft of the Basal drag and the Calving section; Chapter 3 initial draft of Inter-Data-Type weighting section.

Dr Tarasov critically reviewed all three chapters. Dr Len Zedel and Dr Trevor Bell provided comments on all three papers. Chapter 3 was also critically reviewed by Dr Pippa Whitehouse.

# Connecting Text

The first research article addresses objective 1. It describes the GSM and the sensitivity tests performed on the ensemble parameters.

The dynamical core of the GSM is based on a proven state-of-the art ISM which models sheet/stream/shelf ice flow and has a sub-grid grounding-line flux parametrisation (Pollard and DeConto, 2007; Pollard and DeConto, 2009; Pollard and DeConto, 2012b). To this core, as part of this study, the following were added: a parametrised basal drag coefficient that accounts for sediment likelihood, boundary condition downscaling, and systematic model-to-observation thickness misfit; a variety of climate forcing methodologies (removing reliance on a single methodology); a visco-elastic bedrock response component; a calving component which can compute both tide water glacier calving and ice shelf calving; and, a newly developed, physically based sub-shelf melting component. The GSM includes 31 ensemble parameters used to explore the uncertainties in the climate forcing, mass-balance processes and ice dynamics. The article describes each of the ensemble parameters in turn, in doing so, documents the modifications made to the core ISM and details the newly developed components and forcings.

In addition, the paper discusses the sensitivity study performed on the ensemble parameters. The sensitivity of six key metrics (metrics are key model outputs pertinent to monitoring the AIS reconstructions, *e.g.*, the grounded ice volume for EAIS

and WAIS at present day, and for the AIS at 20ka) to maximum and minimum parameter values was assessed. As such the following important conclusions are made: (1) within the range of the maximum and minimum values, each ensemble parameter has significant influence over at least one of the metrics, (2) combined and as best can be done with 31 parameters in a non-linear system, the parameter ranges are able to produce output that approximately brackets reality. These conclusions justify the effort required to generate and analyse a full ensemble.

The research paper has been written with the intention of being submitted to the *Geoscientific Model Development*[*] journal.

[*] http://www.geoscientific-model-development.net/

# Chapter 2

# A glacial systems model configured for large ensemble analysis of Antarctica deglaciation

## 2.1 Abstract

This article describes the Memorial University of Newfoundland/Penn State University (MUN/PSU) glacial systems model (GSM) that has been developed specifically for large-ensemble data-constrained analysis of past Antarctic Ice Sheet evolution. Our approach emphasizes the introduction of a large set of model parameters to explicitly account for the uncertainties inherent in the modelling of such a complex system.

At the core of the GSM is a 3D thermo-mechanically coupled ice sheet model that solves both the shallow ice and shallow shelf approximations. This enables the different flow regimes of ice sheet (vertical shear stresses), ice shelves (longitudinal stretching and essentially zero basal traction), and ice streams (longitudinal stretching and basal traction) to be represented. The grounding line is modelled through an analytical sub-grid flux parametrisation. To this dynamical core the following have been added: a heavily parametrised basal drag coefficient component; a visco-elastic isostatic adjustment solver; a diverse set of climate forcing mechanisms (to remove any reliance on any single method); tidewater and ice shelf calving functionality; and a new physically-motivated empirically-derived sub-shelf melt component. To assess the accuracy of the sub-shelf melt component we compare the predicted shelf melt values against a compilation of published observations. The GSM has 31 parameters that account (as best can be done with 31 parameters) for the uncertainty in the ice-physics, the climate forcing, and the ice-ocean interaction. Each of these parameters can be explored over a range of values and thus an ensemble can be generated.

The results and assessment of a 125 run sensitivity analysis, specifically generated to evaluate the parameter sensitivity, are presented. It is shown that each of the 31 ensemble parameters (with their associated parameter ranges), have an impact over one or more key model output metrics. Thus, when considered together, the

ensemble parameters approximately bound reality (in so far as is possible with 31 parameters). This justifies the expenditure of resources required to generate and subsequently evaluate a full ensemble with the given configuration.

## 2.2 Introduction

The Antarctic Ice Sheet (AIS) is identified as one of the major sources of uncertainty in predicting global sea level change (Meehl et al., 2007). The range of temporal responses to external forcing (*e.g.*, climate, sea-level change) is diverse: locally it can be on the order of decades if not less, whereas vast areas of the interior respond over $10^3 \rightarrow 10^4$ yrs (Alley and Whillans, 1984; Bamber et al., 2007). Without properly attributing the extent to which the behaviour of the glacial system is an artifact of past climate versus an ongoing response to the present climate, the scientific community will struggle to accurately predict how the AIS will respond to future climatic change and what the contribution to eustatic sea level might be (Huybrechts, 2004; Bentley, 2010). As such, there an urgent requirement for quantitatively evaluated reconstructions with associated uncertainty estimates.

Ice-sheet models, like other numerical model, suffer limitations from simplified or missing physics (e.g. reduced equations due to computational restrictions or poorly understood processes that have no physical law), boundary condition uncertainties, and inherent numerical modelling approximations. Parametrizations offer a way to address these issues (even the simplest models may hide many implicit parameters). Most parameters employed in the model have a range of possible values that can produce plausible output*. Exploration of these parameter ranges can be performed to generate an ensemble of results, as such we term them ensemble parameters. The interaction of ensemble parameters, considered together, creates a phase-space of possible reconstructions. More complex models invariably have more parametrisations and a larger phase space.

Even with a handful of ensemble parameters, the traditional method of hand-tuning models with a small number of runs [$\mathcal{O}(10)$] is restrictive and limits exploration

*Some parameters, such as gravity or ice density are tightly constrained thus are not explored

of the parameter space. Depending on the non-linearity of the system and the number of parameters, even the generation of relatively large ensembles [$\mathcal{O}$(1000-10000)] may still be far from adequate. With such large numbers of model runs, a quantitative and systematic means to compare and contrast runs is critical.

The plausibility of each model run can be assessed by comparisons against observations. Thus, each run can be evaluated in relation to its misfit to the observational data, and a 'misfit score' can be attributed allowing runs to be ranked. Runs can then be combined (for example as weighed averages, using the scores as weights) to produce composite deglaciation chronologies. In addition, by capturing the observational, parametric, and structural uncertainties and propagating them into the evaluation process the cumulative uncertainties can be computed and presented along with the reconstructions (Briggs and Tarasov, 2012). A similar approach has been applied to the other major Quaternary ice sheets (Tarasov and Peltier, 2003, 2004; Tarasov et al., 2012) and is now being developed for the AIS.

This model description and sensitivity assessment paper is the first in a suite of three articles documenting the steps undertaken to produce a data-constrained deglaciation chronology, with associated uncertainties, for the AIS using a large ensemble analysis approach (2000-3000 runs per ensemble). The second article presents a database of observational data and describes a method that can be employed to evaluate model output using the constraint data (Briggs and Tarasov, 2012). The generation of the ensemble and subsequent analysis of the generated chronologies is described in Briggs et al. (2013).

The MUN/PSU has been developed specifically for ensemble analysis of AIS deglaciation. The dynamical core of MUN/PSU is based on the Penn State University ice sheet model (Pollard and DeConto, 2007; Pollard and DeConto, 2009; Pollard and DeConto, 2012b). In this paper we document how MUN/PSU differs from the

PSU model and describe 31 ensemble parameters that allow exploration of a set of uncertainties in the GSM. We also assess model sensitivity to parameter variations.

## 2.3 Model description

The dynamical core of the MUN/PSU is the PSU ice-sheet model (Pollard and DeConto, 2012b, and references therein)). The original PSU was developed as a continental scale model that operates over long [$\mathcal{O}(10^6)$ yrs] periods. It has been used in many studies for the AIS and other ice-sheets (see Pollard and DeConto, 2012b, for a complete list) over a range of spatial and temporal scales and has been a part of the ISMIP-HEINO, ISMIP-HOM, and MISMIP intercomparison tests.

The key features of the MUN/PSU GSM are (items marked with an asterisk deviate significantly from the PSU model):

- treatment of both shallow ice and shallow shelf/stream regimes, including Schoof grounding line condition
- a standard coupled thermodynamic solver including horizontal advection, vertical diffusion and heat generated from deformation work
- * parametrised basal drag coefficient that accounts for subgrid topographic roughness, sediment likelihood (based on some specific assumptions), and systematic model-to-observation ice thickness misfit
- * visco-elastic bedrock response component
- * parametrised climate forcing that generates three separate temperature and precipitation fields concurrently, these are subsequently merged, through further ensemble parameters, to produce a final 'blended' set of climate fields (developed to avoid dependence on a single climate forcing method)

- * separate models for treatment of tidewater and shelf front calving
- * a new physically-motivated empirical approach to sub-shelf melt (SSM)

The 31 parameters used to account for the uncertainty in the GSM are summarised in Table 2.1. They are listed in the order they are discussed in the text and organised in accordance with the model functionality they effect: ice dynamics (10 parameters), climate forcing (11 parameters) and ice-ocean mass loss through calving and sub-shelf melt (8 parameters). The evolution of the parameter range and justifications for choosing/excluding parameters are discussed in greater detail in Section 2.4. The ranges presented in Table 2.1 contains three values, the upper bound, the value of the parameter from the baseline run, and the lower bound. The baseline run is used and discussed fully in the sensitivity assessment (Section 2.4); briefly, the baseline run is one of the runs with the smallest misfit-to-observation score as identified through the application of the constraint data and the evaluation scheme (Briggs and Tarasov, 2012). Table A.1 in the appendix provides a full list of all the variables and non-ensemble parameters discussed in the text.

### 2.3.1 Model setup

We adopt the same discretisation methodology as the PSU (Pollard and DeConto, 2009, 2012b). In summary, the MUN/PSU operates at a resolution of 40 km in the horizontal direction and uses a finite-difference Arakawa-C grid. In the vertical the grid has 10 uneven layer, spaced closer at the surface and base of the ice. The horizontal velocities $u, v$ are located between the grid points (*i.e.*, staggered half a grid cell) whereas the ice geometry (*e.g.*, ice thickness $H$, surface elevation $hs$), vertical velocities, and temperatures are located at the grid centres.

Table 2.1: Ensemble parameters

| | Definition | Parameter | Range LB [BA] UB[1] | Units |
|---|---|---|---|---|
| **Ice dynamics** | | | | |
| 1 | Flow enhancement factor for grounded ice | $fnflow$ | 3.50 [4.84] 5.50 | |
| 2 | Flow enhancement factor for shelf flow | $fnshelf$ | 0.40 [0.57] 0.65 | |
| 3 | Hard bed enhancement factor | $fnslid$ | $1 \cdot 10^{-10}$ [$2.57 \cdot 10^{-9}$] $1 \cdot 10^{-8}$ | m $a^{-1}Pa^{-2}$ |
| 4 | Soft bed enhancement factor | $fnsed$ | $5 \cdot 10^{-7}$ [$5.15 \cdot 10^{-6}$] $3 \cdot 10^{-5}$ | m $a^{-1}Pa^{-2}$ |
| 5 | Scaling of sediment presence after isostatic unloading | $fhbPhif$ | 0.001 [0.19] 1.00 | |
| 6 | Model-obs ice thickness misfit scaling | $fDragmod$ | 0.00 [3.01] 9.99 | |
| 7 | Subgrid roughness exponent for drag modification of sediment | $powfstdsed$ | 0.00 [0.47] 1.20 | |
| 8 | Subgrid roughness exponent for drag modification of sliding | $powfstdslid$ | 0.00 [0.67] 1.20 | |
| 9 | Pinning Factor | $fnPin$ | 0.01 [0.085] 0.1 | |
| 10 | Geothermal heat flux input blending | $fbedGHF$ | 0.00 [0.85] 1.00 | |
| **Climate Forcing** | | | | |
| 11 | Glacial index interpolation scaling factor for temperature | $fnTdfscale$ | 0.75 [1.19] 1.30 | |
| 12 | Lapse Rate factor | $rlapseR$ | 5.00 [8.31] 11.00 | C $km^{-1}$ |
| 13 | LGM temperature EOF field ($Tf_3$ only) | $fTeof$ | -0.50 [-0.44] 0.50 | |
| 14 | Temperature blending 1 | $Twa$ | 0.00 [0.46] 1.00 | |
| 15 | Temperature blending 2 | $Twb$ | 0.00 [0.03] 1.00 | |
| 16 | Phase factor for precipitation | $fnPdexp$ | 0.50 [1.94] 2.00 | |
| 17 | LGM precipitation EOF fields ($Pf_3$ only) | $fPeof1$ | -0.50 [0.16] 0.50 | |
| 18 | LGM precipitation EOF fields ($Pf_3$ only) | $fPeof2$ | -0.50 [-0.44] 0.50 | |
| 19 | Glacial index interpolation scaling factor for precipitation | $fnPre$ | 0.50 [1.67] 2.00 | |
| 20 | Precipitation blending 1 | $Pwa$ | 0.00 [0.86] 1.00 | |
| 21 | Precipitation blending 2 | $Pwb$ | 0.00 [0.34] 1.00 | |
| 22 | Desert elevation effect factor | $fdesfac$ | 0.00 [1.97] $2.00 \cdot 10^{-3}$ | |
| **Ice-ocean interface (Sub-shelf melt (SSM) and calving parameters)** | | | | |
| 23 | Ice shelf calving scaling factor | $fnshcalv$ | 0.50 [1.40] 2.50 | |
| 24 | Ice shelf calving minimum thickness threshold | $Hcrit2$ | 10.00 [89.5] 150.00 | $myr^{-1}$ |
| 25 | Ice shelf calving sub $Hcrit2$ enhancement factor | $calvF$ | 0.00 [0.08] 0.20 | $yr^{-1}$ |
| 26 | Maximum calving velocity, tidewater glacier | $fcalvVmx$ | 0.10 [0.79] 10.00 | km $yr^{-1}$ |
| 27 | Thin ice calving temperature dependant scaling | $fcalvwater$ | 3.00 [7.92] 10.00 | m $yr^{-1}$ |
| 28 | Grounding line zone SSM factor (large shelves) | $fnGLz1$ | 0.50 [1.51] 2.50 | m $yr^{-1}$ |
| 29 | Grounding line zone SSM factor (other shelves) | $fnGLz2$ | 0.50 [1.56] 3.00 | m $yr^{-1}$ |
| 30 | Shelf front SSM factor (large shelves) | $fnSfz1$ | 0.50 [1.70] 2.50 | m $yr^{-1}$ |
| 31 | Shelf front melt climate dependence scaling | $fnzclimsfz$ | 0.00 [0.65] 1.18 | |

[1] LB = lower bound, BA = baseline and UB = upper bound. Values are rounded to 2 decimal places.

The standard model run start time is from 205 ka*, to present day (the initialization conditions are described in Section 2.3.11). The model has adaptive time stepping functionality that, if numerical instabilities occur, enables the GSM to backtrack to a previous state (the state is recorded by a rolling buffer) and re-attempt the calculations with reduced time steps (50% reduction upon each back-track). After 300 yrs under reduced time-step conditions, the time-step is doubled. On initialization the ice dynamics are set to be computed every 0.5 yrs, thermodynamics every 10 yrs, and bedrock response every 100 yrs.

### 2.3.2 Ice dynamics

Grounded and floating ice have the same fundamental rheology, but the large scale (simplified) equations that describe them are different. Three regimes classify the type of ice flow: sheet flow, stream flow and shelf flow. Sheet flow, using the zero-order shallow-ice approximation (SIA), is valid for an ice mass with a small aspect ratio (height scale « length scale) and where the flow is dominated by vertical shear stress *i.e.*, much of the interior of the AIS, and is the simplest type of flow. It has a large basal traction (the retaining force due to friction at the interface between an ice sheet and the underlying bed). The flow is dominated by vertical shear ($\partial u/\partial z$, where $u$ is velocity and $z$ is the vertical co-ordinate within the ice thickness) determined locally by the driving stress. The driving stress is a function of the surface gradient and the thickness; steeper slopes and/or thicker ice beget larger driving stresses. In shallow shelf flow (SSA), the driving stress is balanced by longitudinal and horizontal shear stress gradients. Stream flow is similar to shelf flow, except for the presence of basal drag, and the basal topographic boundary condition (MacAyeal, 1997).

The PSU model offers three approaches to modelling these two different regimes.

*ka is defined as $10^3$ calendar years before present whereas kyr is a time interval of $10^3$ yrs

Computationally, the most costly implements a combined set of SIA-SSA equations over the whole ice sheet. The internal shear and longitudinal stretching is combined–through strain-softening terms that are dependant on the velocities in the other set of equations–into one set, which is applied at all locations. As a consequence, the viscosity is a function of the velocity gradients. Thus the set of equations is non-linear in the velocity terms, as well as dependent on the state of the ice (*e.g.*, ice thickness, temperatures etc.). To address the nonlinearity, an iterative approach is taken, whereby the viscosity term is computed based on the previously calculated velocity. The new viscosity term is then used to update the velocities. This is repeated until the difference between the velocities is less than a predetermined convergence criterion (Pollard and DeConto, 2007, 2012b). Significant savings in CPU time, with virtually no impact on the results can be earned by limiting the combined SIA-SSA equations to cells where SSA flow is predisposed to dominate due to low basal drag; above a critical threshold (the majority of the East Antarctic Ice Sheet (EAIS) the flow is limited to SIA (Pollard and DeConto, 2009). Further reductions in computing resource can be achieved by removing completely the strain softening terms and calculating either SIA or SSA based on the critical threshold. This has a slight impact on the results (Pollard and DeConto, 2012b). Because the large ensemble approach is computationally costly (each ensemble contains 2000-3000 runs, each run can take 2-5 days), the latter method is employed for this study.

### 2.3.3 Ice rheology factor

The sheet and shelf flow enhancement factors, used to implicitly allow some softening due the unresolved grain-scale characteristics (*e.g.*, ice crystal size, orientation, impurities) of the ice (Cuffey and Paterson, 2010, p. 71) adjust the ice rheology (Pollard and DeConto, 2012b, eqs. 16a and 16b) and are explored through ensemble parameters

$fnflow$ and $fnshelf$. The parameters have a range that gives enhancement values between $3.5 \rightarrow 5.5$ for sheet flow and $0.4 \rightarrow 0.65$ for shelf flow. This approximately follows the bounds defined in Ma et al. (2010). Physically they manifest themselves as a control on the height-to-width ratio of the ice sheet (Huybrechts, 1991).

### 2.3.4 Basal drag

Though a consensus is developing towards the validity of Coulomb plastic basal drag from subglacial sediment deformation (Cuffey and Paterson, 2010), the Schoof grounding line flux condition (Schoof, 2007) used in the core ISM is only defined for power law forms. We therefore retain the exponent two basal drag of Pollard and DeConto (2007, 2012b),

$$u_b = crh \cdot \tau_b^2 \tag{2.1}$$

where $u_b$ is the basal sliding velocity, $crh$ is the basal sliding coefficient, and $\tau_b$ is the basal stress.

To capture the large uncertainty in subglacial basal stress regimes, we have introduced a number of ensemble parameters that are used to determine the basal sliding coefficient.

Firstly, following Pollard and DeConto (2012b), we define two basal drag values for different bed characteristics: $10^{-10}$m a$^{-1}$Pa$^{-2}$ for hard bed ($zcrhslid$; bare rock, predominantly under EAIS) and $10^{-6}$m a$^{-1}$Pa$^{-2}$ for soft bed ($zcrhsed$; sediment coverage, predominantly under the West Antarctic Ice Sheet (WAIS)). We adopt these values but they are adjusted respectively by ensemble parameters $fnslid$ (giving a range of $10^{-11} \rightarrow 1.08 \times 10^{-9}$) and $fnsed$ ($10^{-8} \rightarrow 3 \times 10^{-6}$)

The parametrisation has three key dependencies. First, as per Pollard and De-

Conto (2012b), we assume that subglacial sediment thickness is largely related to the surface elevation of the unloaded subglacial topography. Areas that are still submerged after glacial unloading are likely to have soft sedimentary surface lithology, and therefore are a precursor for subglacial sediment. With some allowance for uncertainty in the resultant unloaded ice (dependant on ground surface elevations, thus uncertainty in ALBMAP, earth rheology etc.) under the control of a parameter $fhbPhif$ (0.001→1), we define a sediment likelihood parameter

$$Slk = \frac{\text{unloaded water depth in km} - fhbPhif}{fhbPhif} \tag{2.2}$$

and use this to set a sediment presence exponent, $Se$, that controls the transition from $zcrhslid$ to $zcrhsed$ (bare rock to sediment):

$$Se = \begin{cases} 1, & \text{if } Slk > 0 & \text{thick sediment cover} \\ 1 + Slk, & \text{if } -1 < Slk < 0 & \text{some sediment} \\ 0, & \text{if } Slk < -1 & \text{no sediment} \end{cases} \tag{2.3}$$

The second dependence is on subgrid roughness, given by the standard deviation of the 5 km resolution ALBMAP (LeBrocq et al., 2010)* basal topography for each GSM grid cell ($\sigma_{hb}$, in dekametres). We assume an increasing degree of basal drag for combinations of sediment thickness and surface roughness. Any site with sediment cover will have much reduced basal drag compared to sites without sediment cover. For regions with thicker sediment cover, as described by $Se$, we assume that higher roughness will lead to increased basal drag. For minimal or no sediment cover, we

*The ALBAMP dataset is provided at a resolution of 5 km. To be used in the GSM it must be upscaled to the model resolution of 40 km; the steps taken to upscale the dataset, whilst preserving grounding-line positions and key pinning points, are described in the supporting on-line material (SOM) of Briggs and Tarasov (2012). Unless explicitly stated (as in this case for subgrid roughness) in the text any references to ALBMAP implicitly refers to the upscaled dataset at 40 km.

assume that enhanced surface roughness increases the surface area available to erosion, promoting trapping of eroded sediments, leading to reduced basal drag.

The final dependence takes into account the ice thickness difference, $\Delta H_{alb}$ between the present-day field from an early test run and ALBMAP thickness $H_{ALB}$, thus we allow some observation-model misfit into the adjustment of $crh$. This is a similar, albeit much simpler, approach to the inverse method employed by (Pollard and DeConto, 2012a) to adjust the values of $crh$ to reduce model misfit. The $\Delta H_{alb}$ is scaled by parameter $fDragmod$ (range 0→9.99).

The basal sliding coefficient $crh$ is set as:

$$crh = \max\left[\min\left[zcrhslid\left(\frac{zcrhsed}{zcrhslid}\right)^{Se} \cdot fstd \cdot fDragmod^{(0.8\cdot\Delta_{Halb})}, zcrhMX\right], zcrhMN\right] \tag{2.4}$$

where $fstd$, which introduces the sediment roughness, is given by:

**if** $Se > 0.67$ **then** ▷ deeper sediment

  **if** $\sigma_{hb} >= 0.75$ **then** ▷ rougher sub-grid topography

    $fstd = (0.75/\sigma_{hb})^{powfstdsed}$

  **else** ▷ smoother sub-grid topography

    $fstd = (1 + (0.75 - \sigma_{hb})/0.69)^{powfstdsed}$

  **end if**

**else if** $Se < 0.5$ **then** ▷ shallower sediment

  $fstd = \max\left[1, \sigma_{hb}^{powfstdslid}\right]$

**else**

  $fstd$=1

**end if**

The ensemble parameters $powfstdsed$ and $powfstdslid$ both have ranges of $0 \rightarrow 1.2$.

Numerical coefficients were selected from initial sensitivity analyses while maintaining numerical continuity.

Mass fluxes for grounded ice with *crh* values greater than a critical threshold *crhcrit*= $10^{-8}$m $a^{-1}Pa^{-2}$ are determined by the SSA ice shelf equations with basal drag otherwise the SIA is active. The basal sliding coefficient is smoothly increased from an essentially zero ($10^{-20}$) value as the basal temperature approaches the pressure melting point except at the grounding line where a warm base is always imposed.

### 2.3.5 Grounding line treatment

At the locality of the grounding line (the point where the ice detaches from the underlying bed and starts to float) and in ice streams with very little basal traction, a combination of both flow regimes exist (Pollard and DeConto, 2007).

The grounding line treatment in the model is based on Schoof (2007) who showed that to capture the grounding line accurately, either the grounding zone boundary layer must be resolved at a very high resolution (~0.1 km, impractical on a continental scale), or an analytical constraint on the flux, $q_g$, across the grounding line must be applied. The flux is a function of the longitudinal stress across the grounding line, the ice thickness at the grounding line, and a form of the basal sliding law adjusted by a tuned basal sliding coefficient (Schoof, 2007). The longitudinal stress is calculated by the stress balance equation and also takes into account back stress at the grounding line caused by buttressing from pinning points, downstream islands or side-shear due to slower moving ice or rock walls.

The analytically calculated ice flux $q_g$ and height at the grounding line $H_g$, found through linear interpolation, are then used ($u_g = q_g/H_g$) to compute the depth-averaged velocity at the grounding line $u_g$. The calculated $u_g$ is imposed as an internal boundary condition for the shelf-flow equations and is used to overwrite the velocity

solution calculated for that position from the stress balance equations (Pollard and DeConto, 2007, 2012b).

### 2.3.6 Sub shelf pinning points

Pinning points, sometimes manifest in the form of small ice rises, are found below the ice shelves, generally toward the grounding line. Grounding of the ice shelf onto such pinning points causes additional back stresses that influence the migration of the grounding line upstream (Pollard and DeConto, 2012b). These pinning points are too small to be resolved on a 40 km grid so are parametrised to be a percentage of the equivalent basal drag for grounded ice as a function of the water depth (Pollard and DeConto, 2009). Ensemble parameter $fnPin$ (range $0.01 \rightarrow 0.1$) scales the computed pinning point drag.

### 2.3.7 Bedrock response and relative sea level computation

The bedrock response component of the GSM is taken from Tarasov and Peltier (2004) but modified to use the VM5a earth rheology of Peltier and Drummond (2008) which still retains a 90 km thick elastic lithosphere (as previously, the earth rheology is spherically symmetric). The bedrock displacement is computed every 100 years from a space-time convolution of surface load changes and a radial displacement Greens function, at degree and order 256.

Ice chronologies from the model are then post-processed (at the location of the sites defined in the constraint database (Briggs and Tarasov, 2012)), using an approximation to a gravitationally self-consistent theory (Peltier, 1998) to generate RSL chronologies. As detailed in Tarasov and Peltier (2004), the approximation invokes eustatic load changes during changes in marine extent (otherwise gravitational effects are accounted for). Rotational components of RSL are not taken into account. The

generated RSL curves are then assessed with the RSL constraint data in accordance to the evaluation methodology of Briggs and Tarasov (2012).

This study considers the glaciological and climatic uncertainties in the GSM, thus we employ a single Earth model that has reasonable fits to geophysical observations from North America (Peltier and Drummond, 2008, earth model VM5a). For a preliminary examination of the impact of Earth model uncertainty on inferred Antarctica deglacial history see Whitehouse et al. (2012). Variations in the earth rheology will have some impact on ice evolution, but that will get swamped by the other uncertainties *e.g.*, the climate forcing.

### 2.3.8 Geothermal heat flux

Geothermal heat flux (GHF) is a spatially varying, temporally fixed boundary condition. There are very few direct measurements of GHF for the AIS. Those that do exist are usually derived from direct temperature measurements in ice cores (Pattyn, 2010), as such, continental scale GHF reconstructions must be derived from proxies. This study employs two GHF datasets which are interpolated through ensemble parameter $fbedGHF$ (in effect blending the two fields). The Shapiro and Ritzwoller (2004) dataset uses a global seismic model of the crust and upper mantle to extrapolate available measurements to regions where they are non-existent or sparse. The Maule et al. (2005) dataset was estimated from satellite measured magnetic data. The datasets are corrected, around a Gaussian area of influence, so that the reconstructions match the observations where available (Pattyn, 2010). The observations are taken from ice-core temperature profiles and based on the location of sub-glacial lakes (the ice/bedrock interface can be considered to be at the pressure melting thus the minimum GHF can be computed (Pattyn, 2010)).

### 2.3.9 Climate forcing

Climate forcing over glacial cycles is one of the most difficult components in the GSM to constrain (Tarasov and Peltier, 2004); in the GSM, 11 of the 31 ensemble parameters adjust the climate forcing. The GSM requires both temperature and precipitation fields. For large ensemble analysis, coupled climate-glacial systems model are computationally too expensive, as such the GSM uses parametrised climate forcing. Three different methodologies, each of which has one or more ensemble parameters, are used to concurrently generate the temperature ($Tf_{1,\ 2,\ 3}$) and precipitation ($Pf_{1,\ 2,\ \ 3}$) fields.

The spatial distribution of the fields are obtained either through empirical parametrisations or from published observational datasets (*e.g.*, Arthern et al., 2006).

For $Tf_3$ a from the Paleo-Modelling Intercomparison Project II (PMIPII, Braconnot et al., 2007)* modelling study.

The fields are then projected backwards in time using a ice- or deep sea-core time series (Ritz et al., 2001; Huybrechts, 2002; Tarasov and Peltier, 2006; Pollard and DeConto, 2009). Finally, the different fields are combined together using a weighed sum, the weight determined by ensemble parameters, to generate the final climate fields that force the GSM.

This approach ensures there is no reliance on a single climate methodology and that each method has one or more ensemble parameter. This affords the model a much larger degree of freedom (with respect to climate forcing) than the single climate forcing methodology with limited parametrisation employed in other studies (*e.g.*, Pollard and DeConto, 2012b; Whitehouse et al., 2012).

*http://pmip2.lsce.ipsl.fr/

#### 2.3.9.1 Temperature forcing

$Tf_1$ models the spatial and altitudinal variation of the temperature field as a function of latitude, height, and lapse rate (Huybrechts, 1993; Pollard and DeConto, 2009). Using the annual orbital insolation anomaly ($\Delta q_s$) at 80°S (W m$^{-2}$) and sea level departure from present ($\Delta s$), the modern day temperature field is adjusted to generate a paleo-temperature field. Annual orbital insolation is calculated from Laskar et al. (2004) and, following Tarasov and Peltier (2004), it is weighted by ensemble parameter $fnTdfscale$ (range 0.75 $\rightarrow$ 1.3) to account for the uncertainty inherent in using this method to drive the transition between a glacial to interglacial state. The sea level departure from present is taken from stacked benthic $\delta^{18}$O O records Lisiecki (2005). The field[†] is computed as

$$Tf_1(\mathbf{X},t) = T_m + 30.7 - 0.0081\,hs(\mathbf{X},t) - 0.6878|\Phi|(\mathbf{X}) + fnTdfscale\,\Delta q_s(t) + \frac{10\Delta s(t)}{125}, \tag{2.5}$$

where $T_m$ is the melting temperature of ice (0 °C ), $hs$ is modelled surface height (m), and $\Phi$ is latitude ($^o$). To avoid overly low temperatures over the ice-shelves, we follow Martin et al. (2010) and remove the dependence on surface elevation when it is below 100 m,

$$Tf_1(\mathbf{X},t) = T_m + 29.89 - 0.6878|\Phi| + fnTdfscale\,\Delta q_s(t) + \frac{10\Delta s(t)}{125} \quad \text{when } hs(\mathbf{X},t) < 100 \text{ m}. \tag{2.6}$$

The second temperature forcing field, $Tf_2$, uses the Comiso (2000) present-day surface air temperature map (available as part of ALBMAP) for AIS ($T_{PD}$) adjusted using the insolation anomaly $\Delta q_s$. $T_{PD}$ are corrected from the present-day topography

[†] $\mathbf{X}$ is the x,y location for each grid cell

($hs_{PD}$), via an ensemble parameter lapse rate ($rLapseR$), to the modelled surface-elevation ($hs$). The lapse rate range is 5-11 C km$^{-1}$ (compared with, for example 9.14 C km$^{-1}$ (Ritz et al., 2001; Pollard and DeConto, 2009) and 8.0 C km$^{-1}$ (Pollard and DeConto, 2012b)). Then,

$$Tf_2(\mathbf{X},t) = T_{PD}(\mathbf{X}) + fnTdfscale \cdot \Delta q_s + rLapseR\,[hs(\mathbf{X},t) - hs_{PD}(\mathbf{X})] \quad (2.7)$$

where $\Delta q_s$ and $hs$ are as for $Tf_1$.

Following Tarasov and Peltier (2004), $Tf_3$ is calculated by interpolating between PD surface temperature (Comiso, 2000) and a Last Glacial Maximum (LGM) air surface temperature field generated from an amalgam of five high resolution PMIPII (Braconnot et al., 2007) -21 ka simulations/snapshots (CCSM, HadCM3M2, IPSL-CM4-V1-MR, MIROC3.2 and ECHAM53). The 5 datasets are averaged together ($Tave_{LGM}$) and we also use the first empirical orthogonal basis function (EOF) of inter-model variance for the LGM snapshots. * The first EOF ($Teof_{LGM}$) captures 64% of the total variation and is incorporated through ensemble parameter $fTeof$ (range -0.5→0.5) into a run specific reference dataset $T_{LGM}$ when the model is initialised,

$$T_{LGM}(\mathbf{X}) = Tave_{LGM}(\mathbf{X}) + fTeof \cdot Teof_{LGM}(\mathbf{X}). \quad (2.8)$$

As with $Tf_2$, the present-day and LGM temperature fields are adjusted, through the parametrised lapse rate, to account for the difference between the modelled surface elevation, $hs$, and the reference surface elevation fields $hs_{PD}$ and $hs_{LGM}$ (the PMIPII files are supplied with an associated LGM orthography). The interpolation between

*This is a numerical technique to decompose in this case the maps of LGM temperature from the set of PMIP GCM runs into a series of orthogonal spatial maps, ordered with respect to minimizing the residual variance of the subsequent maps in the series. Thus the first EOF captures in some sense the maximum mode of inter-model differences.

Comiso (2000) present-day temperature field and the model derived LGM temperature is weighted using the glacial index, $I$, derived from the EPICA temperature record $T_{epica}$ (Jouzel and Masson-Delmotte, 2007),

$$I(t) = \frac{T_{epica}(t) - T_{epica}(0)}{T_{epica}(LGM) - T_{epica}(0)}, \tag{2.9}$$

and adjusted using ensemble parameter $fnTdfscale$ giving

$$\begin{aligned} Tf_3(\mathbf{X},t) = &\left[(T_{PD}(\mathbf{X}) + rLapseR \cdot (hs(\mathbf{X},t) - hs_{PD}(\mathbf{X}))\right](1 - (fnTdfscale \cdot I(t)) \\ &+ \left[(T_{LGM}(\mathbf{X}) + rLapseR \cdot (hs(\mathbf{X},t) - hs_{LGM}(\mathbf{X}))\right](fnTdfscale \cdot I(t)) \end{aligned} \tag{2.10}$$

The three temperature fields are then combined in accordance with two ensemble parameters, $Twa$ and $Twb$ (both range 0→1), to produce the final temperature field,

$$T(\mathbf{X},t) = (1-Twb)\left[Twa \cdot Tf_1(\mathbf{X},t) + (1 - Twa)Tf_2(\mathbf{X},t)\right] + Twb \cdot Tf_3(\mathbf{X},t). \tag{2.11}$$

#### 2.3.9.2 Precipitation forcing

The precipitation forcing is also subject to a weighted almalgam of three different forcings. $Pf_1$ assumes precipitation is driven by temperature (Huybrechts, 1993),

$$Pf_1(\mathbf{X},t) = 1.5 \times 2^{\frac{T(\mathbf{X},t)-T_m}{10}}. \tag{2.12}$$

where $T$ is the blended temperature (Pollard and DeConto, 2009). The exponent is used in the precipitation calculations because of the exponential behaviour of the saturation vapour pressure on temperature.

$Pf_2$ is computed in a similar manner to $Tf_2$; at run-time, an observational dataset ($P_{PD}$) of present-day precipitation (Arthern et al., 2006) is adjusted using the annual

orbital insolation anomaly. Ensemble phase factor, $fnPdexp$, (range 0.5→2) accounts for some phase uncertainty in using the insolation anomaly (Tarasov and Peltier, 2004),

$$Pf_2(\mathbf{X},t) = P_{PD}(\mathbf{X}) \times 2^{fnPdexp\frac{\Delta q_3(t)}{10}}. \tag{2.13}$$

In a similar manner to $Tf_3$, $Pf_3$ is computed using $I(t)$ to interpolate between the present-day dataset $P_{PD}$ and an LGM precipitation field, generated from an amalgam of the PMIPII LGM precipitation simulations. Two EOFs are used. The first ($Peof1$) captures 62% of the inter-model variance, the second ($Peof2$) captures 23%. As for $Tf_3$ the EOFs are introduced at model initialization thorough parameters $fPeof1$ and $fPeof2$ (range -0.5→0.5) to create a run specific reference dataset,

$$P_{LGM}(\mathbf{X}) = Pave_{LGM}(\mathbf{X}) + fPeof1 \cdot Peof1_{LGM}(\mathbf{X}) + fPeof2 \cdot Peof2_{LGM}(\mathbf{X}). \tag{2.14}$$

This is scaled and adjusted using ensemble parameter $fnPre$ (range 0.5→>2),

$$Pf_3(\mathbf{X},t) = P_{PD}(\mathbf{X}) \left( fnPre \frac{P_{LGM}(\mathbf{X})}{P_{PD}(\mathbf{X})} \right)^{Pfac}, \tag{2.15}$$

where $Pfac$ is the glacial index scaled by ensemble parameter $fnPdexp$ (range 0.5->2),

$$Pfac = \text{sign}\left[1.0, \mathrm{I(t)}\right] |\mathrm{I(t)}|^{\mathrm{fnPdexp}}. \tag{2.16}$$

The final precipitation field is then summed and interpolated using two ensemble parameters $Pwa$ and $Pwb$,

$$P(\mathbf{X},t) = q_{des} \cdot \tag{2.17}$$

$$\{(1 - Pwb)\left[(Pwa \cdot Pf_1(\mathbf{X},t) + (1 - Pwa)Pf_2(\mathbf{X},t)\right] + Pwb \cdot Pf_3(\mathbf{X},t)\}, \tag{2.18}$$

where $q_{des}$ accounts for the elevation-desert effect (reduced amount of moisture the atmosphere can hold at elevation)(Marshall et al., 2002; Tarasov and Peltier, 2004). It is simulated as a function of the modelled elevation anomaly from present-day,

$$q_{des} = \exp^{-fdesfak \cdot (hs(\mathbf{X},t) - hs_{PD}(\mathbf{X}))}, \tag{2.19}$$

and ensemble parameter $fdesfak$ $(0 \rightarrow 2 \times 10^{-3})$.

The final 'blended' temperature and precipitation fields are used to calculate the fraction of precipitation that falls as snow and the annual surface melt. Given the small amount of surface melt over AIS (p136 ch 4 Cuffey and Paterson, 2010) a simplified positive-degree-day method (PDD) is used with a melt factor of 5 mm/PDD.

### 2.3.10 Ice-ocean interface

The vast majority of mass lost from the AIS occurs from the ice shelves, either due to calving at the ice margin, or from submarine melting beneath the ice shelf (Jacobs et al., 1992). The ice shelves play a crucial role in restricting (buttressing) the upstream flow of ice(Dupont and Alley, 2005). Reduction or removal of the shelves allows the upstream grounded ice to accelerate, drawing down the ice in the interior. Thus, changes at the ice-ocean interface can have an impact hundreds of kilometres inland (Payne et al., 2004).

Although iceberg calving is the largest contributor to mass loss, Jacobs et al. (1992) apportioned a loss of 2016 Gt $yr^{-1}$ to calving against 544 Gt $yr^{-1}$ to sub shelf melt (the uncertainty estimates for these number are large, ±33% for iceberg calving and ±50% for ice-shelf), there is growing concern and evidence that the sub shelf melt rate is a primary control on the mass loss (Pritchard et al., 2012). Both processes are modelled in the GSM.

#### 2.3.10.1 Calving

Marine ice margins can either terminate as a floating ice shelf or as a tidewater glacier. The GSM uses two distinct parametrizations to calculate mass loss from either of these regimes, in addition there is an ad-hoc treatment for thin ice.

**Ice shelf calving** Though there have been significant efforts towards a fully constrained physically based calving model for ice shelves (*e.g.*, Alley et al., 2008; Albrecht et al., 2010; Amundson and Truffer, 2010), we have found none to be stable for the relatively coarse grid of the GSM. For the present configuration, ice shelf calving is based on a steady state approximation of Amundson and Truffer (2010, eq. 25) which corresponds to the insertion of the Sanderson (1979) relationship for ice-shelf half-width into the empirical relation of Alley et al. (2008). Due to the coarse grid, it was necessary to upstream, by an extra grid cell from the terminus, the stress and ice thickness gradients used in the parametrisation. The calving is computed along each exposed face of the marginal grid-cell. The calving velocity (in the x-direction) is computed as,

$$U_c = -3H_0\dot{\epsilon}_{xx}\left(\frac{\partial h}{\partial x}\right)^{-1} \tag{2.20}$$

where $H_0$ is the terminus thickness and $\dot{\epsilon}_{xx}$ is the along flow spreading rate. The calving rate (ice loss per grid cell area), adjusted by ensemble parameter $fnshcalv$ (0.5→2.5), is computed as (x-direction),

$$\dot{C} = fnshcalv \cdot U_c \cdot \frac{H \cdot \partial y}{\partial x \cdot \partial y}. \tag{2.21}$$

Once calculated $\dot{C}$ is used in the mass balance equation (Pollard and DeConto, 2012b, eq. 14).

For ice thinner than 300 m the calving rate computed above is enhanced. Given the present-day correspondence between average shelf front and the mean annual -5 °C isotherm (Mercer, 1978), for ice thinner than 300 m and thicker than ensemble parameter $Hcrit2$ (10→150 m), we impose a simple temperature dependent ($T_s$, sea-surface mean summer temperature in °C ) parametrisation. For ice thinner than $Hcrit2$, calving is enhanced by a term $calvF \cdot H$, where ensemble parameter $calvF$ ranges from 0→0.2 $\mathrm{yr}^{-1}$. Thus, the ice shelf calving rate is,

$$\dot{C}_{IS} = \begin{cases} \dot{C} & \text{if } H > 300 \\ \dot{C} + (T_s + 3)\frac{H}{5} \cdot 1yr^{-1} & \text{if } Hcrit2 < H < 300 \\ \dot{C} + calvF \cdot H & \text{if } H < Hcrit2 \end{cases} \tag{2.22}$$

**Tidewater calving** For grounded marine ice margins (*i.e.*, large scale tidewater glaciers), we use a slight variant of the temperature-dependant proximity to the flotation model of Tarasov and Peltier (2004). Three conditions are imposed for such calving: 1) an adjacent ice-free grid-cell with water depth greater than 20 m, 2) $T_s$ above a critical minimum value $T_{Cmn}$ and 3) ice thickness less than 1.15 times the maximum buoyant thickness, $H_{flot}$. When the above conditions are met, the calving velocity is given by:

$$\begin{aligned} U_c = fcalvVmx \cdot n_{edge} \cdot \min\left[1, \left(\frac{1.15H_{flot} - H}{0.35H_{flot}}\right)^2\right] \\ \times \left(\exp\left(\frac{3 \cdot (T_s - T_{Cmx})}{T_{Cmx} - T_{Cmn}}\right) - \exp(-3)\right) / (1 - \exp(-3))^{0.5}. \end{aligned} \tag{2.23}$$

Calving velocity is proportional to the number of grid-cell edges ($n_{edge}$) meeting the first calving condition above and uses the maximum calving velocity, $fcalvVmx$,

as the single ensemble parameter (range 0.1→10 km $yr^{-1}$). Based on best fits from previous ensembles and sensitivity analyses, $T_{Cmn}$ is set to -5 °C and $T_{Cmx}$ to 2 °C . We also invoke an *ad hoc* extrapolation of ice thickness at the margin for conversion of calving velocity to a mass-balance term. The marginal ice thickness for this conversion is computed as a quadratic reduction of the grid-cell thickness for ice thicker than 400 m with a maximum effective marginal ice thickness of 900 m for grid cells with ice thicker than 1400 m.

**Thin ice treatment** The shelf calving modules, and the sub-shelf component described in the next section, were not designed for excessively thin (in this case < 10 m thick) ice and we found it necessary to add a separate parametrisation for this case. Again using the present-day correspondence between average shelf front and the -5 °C isotherm (Mercer, 1978), we imposed a simple temperature dependent parametrisation. For marine ice < 10 m thick, the calving rate is

$$\dot{C}_r = \max\left[\text{calving rate from other modules}, 0.3 + zclim(t) \cdot fcalvwater\right], \quad (2.24)$$

where $fcalvwater$ is a calibration parameter with a range 3→10 m $yr^{-1}$ and $zclim$ is the glacial index factor computed, as in $Tf_{1,2}$, from the sea level departure from present ($\Delta s$) and some influence from annual orbital insolation ($\Delta q_s$)

$$zclim(t) = \max\left[0, \min\left[1.5, 1 + \frac{\Delta s(t)}{85} + \max\left[0, \frac{\Delta q_s(t)}{4}\right]\right]\right]. \quad (2.25)$$

#### 2.3.10.2 Sub-shelf melt

Sub-shelf melt (SSM) is a reaction to a complex interaction of bathymetric, oceanographic, and glaciological conditions and processes. The newly developed SSM component used in MUN/PSU is a physically motivated implementation based on empirical

observations, as such we provide a brief review of the SSM process to justify the implementation.

Three modes of melt have been identified (Jacobs et al., 1992). Mode 1 melt occurs in the grounding line zone of the larger shelves; driven by thermohaline circulation, it is triggered by the formation of high-salinity continental shelf water (HSSW). As sea ice forms near the shelf edge, brine rejection occurs producing the dense HSSW. The water mass sinks and, upon reaching the continental shelf, drifts underneath the ice-shelf (the continental shelves generally slope down toward the grounding line due to isostatic depression) into the grounding line cavity. Due to the pressure dependence of the freezing point of water, the *in situ* melting point of the ice shelf base is lower than the temperature of the HSSW (formed at sea-surface temperatures *e.g.*, ~-1.9 °C ); the encroaching water mass, acting as a heat delivery mechanism, melts away at the ice shelf base (Jacobs et al., 1992; Rignot and Jacobs, 2002; Joughin and Padman, 2003; Holland et al., 2008). The melting ice freshens (and cools) the surrounding water mass producing buoyant ice-shelf water (ISW), which, if not advected away, rises up and shoals along the base of the ice shelf. As the water mass rises the ambient pressure decreases, increasing the in-situ freezing point until refreezing occurs, and new marine ice accrets onto the base of the ice shelf (Jacobs et al., 1992; Joughin and Padman, 2003).

The three largest shelves, Amery (AMY), Ross (ROS), and Ronne-Filchner (RONFIL) differ greatly in draught and cavity geometry, and have distinct melt regimes (Horgan et al., 2011). The long narrow AMY is smallest by area but has a relatively deep draught of $\sim$ 2200 m (Fricker et al., 2001). Grounding line melt rates of $31 \pm 5$ m $yr^{-1}$ have been estimated and accreted marine ice with a thickness up to 190 m have been calculated (Rignot et al., 2008; Fricker et al., 2001). The ROS is the largest shelf by area but is much shallower with a draught of about 800 m, the melt rates

are greatly reduced as is the marine ice accretion (10 m (Neal, 1979; Zotikov et al., 1980)). The RON and FIL both have deep grounding lines $\sim$ 1400 m and melt rates that can exceed 5 m $yr^{-1}$ at some locations, the accreted marine ice can exceed $>$ 300 m under RON, but, unlike the AIS it does not persist until the shelf front (Thyssen et al., 1993; Lambrecht et al., 2007).

Mode 2 and mode 3 melting occur both under the smaller shelves that fringe the AIS (*e.g.*, those that face the Amundsen, Weddell, and Bellingshausen Seas) and proximal to the zone near the calving margin of the larger shelves. Mode 2 melting is associated with the intrusion of 'warm' circumpolar deep water (CDW) at intermediate depths (Jacobs et al., 1992; Jacobs et al., 1996; Joughin and Padman, 2003). The degree of melt is dependant on the amount of heat that can be delivered into the ice cavity, itself a function of oceanographic conditions and the proximity of the ice base to the continental shelf edge. The highest melt rates occur at the grounding lines of the Pine Island (40 m $yr^{-1}$) and Thwaites (30 m $yr^{-1}$) glaciers that discharge into the Amundsen Sea. The grounding lines, at a depth of about 1000 m, are melted by the intrusion of CDW water that is almost 4 °C above the in-situ melting point (Rignot and Jacobs, 2002). Mode 3 melting is produced by seasonally warm surface water being advected against and underneath the shelf edge, though the action of tidal pumping and coastal currents (Jacobs et al., 1992). Melt rates of 2.8 m $yr^{-1}$, decaying exponentially down to zero around 40 km up-shelf from the calving margin, have been estimated for the ROS. This is 10-40% of the published total melt estimates for ROS (Horgan et al., 2011).

There is clear evidence that regional oceanographic forcing of the contemporary AIS is important (e.g., Pine Island, Western AP) and growing evidence that similar regional forcing occurred during deglaciation (*e.g.*, Nicholls et al., 2009; Walker et al., 2008; Jenkins et al., 2010; Pritchard et al., 2012). To accurately model SSM over

glacial cycles would require a high resolution coupled GSM and ocean model that are able to represent the major components (*e.g.*, evolving cavity geometry; heat and salt flux exchange between the ice base, the cavity water masses, and the open ocean) of the SSM process (Holland et al., 2003; Payne et al., 2007; Olbers and Hellmer, 2010; Dinniman et al., 2011). This approach is at present not computationally feasible. Recent studies with GSMs configured for the AIS have used either parametrised *ad hoc* implementations (Pollard and DeConto, 2009) or derivations of the melt equation proposed by Beckmann (2003) (Martin et al., 2010; Pollard and DeConto, 2012b). The Beckmann equation was developed to model the ice-shelf ocean-interface in climate models. It yields a melt rate dependant on the heat flux between the shelf bottom and the ocean. PISM-PIK used a variant of this law–forced by an continental-wide constant ocean temperature that is adjusted by the pressure-dependant freezing point of the ocean water–to produce an SSM spatial distribution dependant on the draught of the shelf (Martin et al., 2010). The PSU GSM evolved the PISM-PIK method by, amongst other changes, introducing specific regions of ocean temperatures based on observations; this reportedly gives quite reasonable modern day SSM values (Pollard and DeConto, 2012b). For paleo-climatic simulations the regional ocean temperatures were hindcast backward proportional to the Lisiecki (2005) stacked benthic $\delta^{18}$O O records. The Beckmann law does not capture the freeze-on nor the effect of enhanced shelf front melt.

For the MUN/PSU GSM, a SSM component was developed that did not have a strong dependence on oceanic temperatures. This removed the associated parameters required to provide both regional tuning of the shelves and paleo-adjustment. The new SSM component is a physically-motivated empirical approach that captures both the melt-freeze-melt regimes of the larger shelves and the simpler melt regimes of the peripheral shelves. There are three ensemble parameters to provide some degrees of

freedom in the component. The geometry of the larger shelves is used to adjust the strength of the melt aspect ratio allowing some regional, and temporal evolution. For verification purposes, we present spatial-melt plots and make comparisons between observations and predictions.

**SSM implementation** We merge the exponential shelf front melt law published by Horgan et al. (2011)* with quadratic fits to distance-from-grounding line transects for the melt rate and the shelf ice thickness measured for AMY (Wen et al., 2007)† and RON (Jenkins and Doake, 1991)‡. A flowchart of the implementation is shown in Fig. 2.2.

The SSM component models three regimes under the larger shelves: a draught dependent grounding line zone (GLZ) of melt, an accretion zone (ACZ) where freeze-on occurs, and a zone of melt at the shelf front (SFZ). The smaller shelves only have regions of GLZ and SFZ melt occurring (being on the periphery of the continent, they lack the embayment protection that the larger shelves have, as such the sub-shelf environment is not sufficiently quiescent to allow the mode 1 melt water to freeze-on underneath the shelf). To manage this, the floating ice is divided into five regions (shown in Fig. 2.5a) pertaining to the four large shelves (AMY, ROS, RON, and FIL) and, the ice that is not part of the large shelves (*e.g.*, the smaller shelves of the Amundsen, Weddell, and Bellingshausen Seas and the remaining unnamed

*The exponential shelf melt law was derived from spatial and temporal variations, measured by ICESat laser altimetry data, of the ice surface at the front of the shelf. The surface changes were attributed to enhanced basal melt within 60 km of the shelf front (Horgan et al., 2011).

†The AMY transects were computed from in-situ and remote sensing datasets; a flow line set of flux-gates were defined using the datasets. From the flux gates the mass budgets, basal melting, and freezing rates were derived (Wen et al., 2007).

‡The RON transects were derived from a glaciological field study of 28 sites that lie along flow lines extending from the grounding line to the shelf front. The objective of the study was to derive ice-ocean interaction behaviour from surface measurements. Physical characteristics, including the thickness data, were measured at each site and the data was used in a kinematic steady state model to derive the basal mass flux (and other fields) (Jenkins and Doake, 1991).

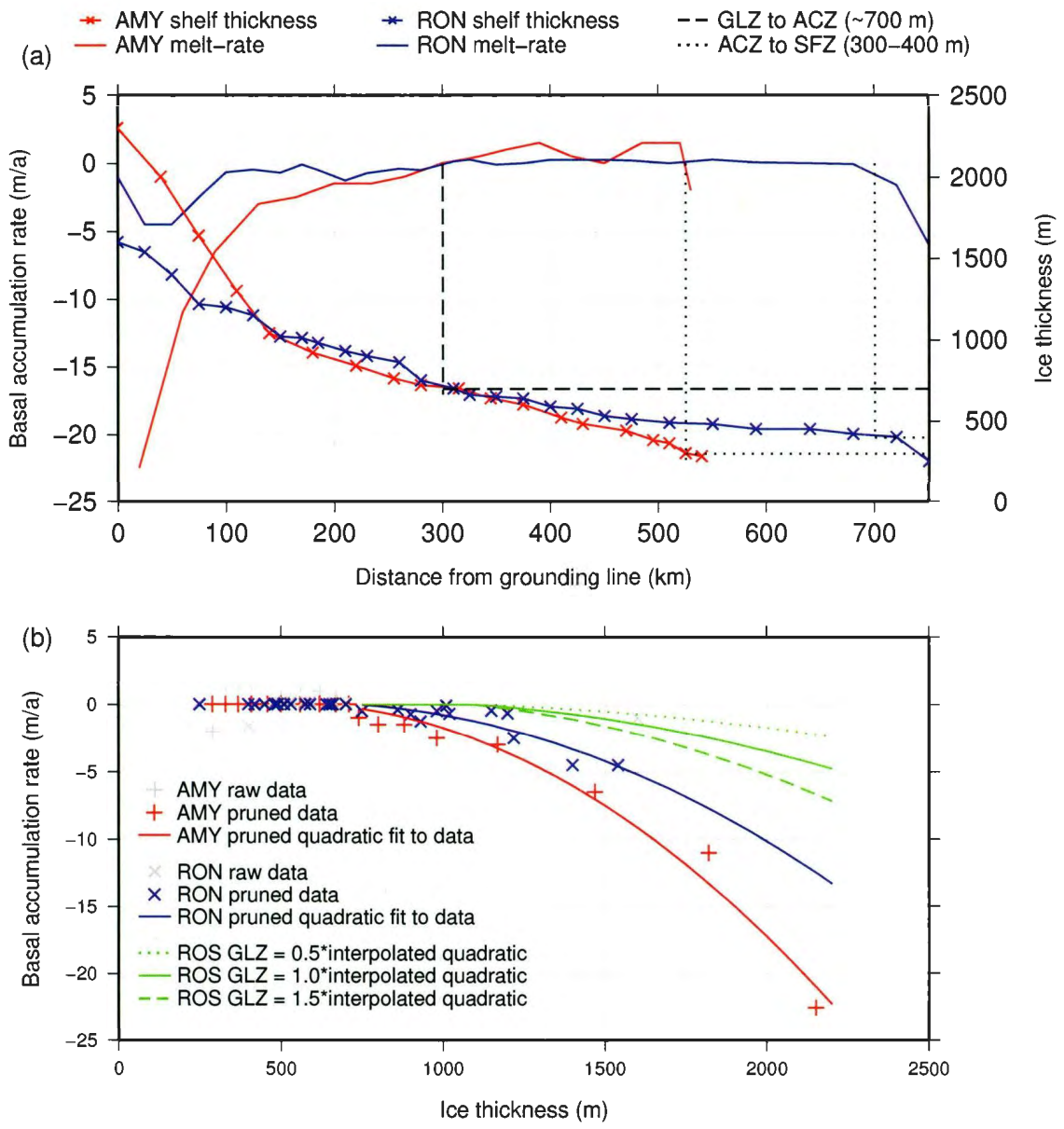


Figure 2.1: Plots showing the (a) melt rate and thickness transects and (b) the GLZ quadratic law. The transects are as extracted from source publications for AMY (Wen et al., 2007) and for RON (Jenkins and Doake, 1991). The transitions, from which the threshold thicknesses are estimated, between GLZ to ACZ and ACZ to SFZ are shown in plot (a). For the quadratic fits, once the basal mass-balance rate >0 m $yr^{-1}$ (*i.e.*, becomes freeze-on and thus part of the ACZ), the remaining data points are all set to zero. The quadratic fit is made to this pruned dataset.

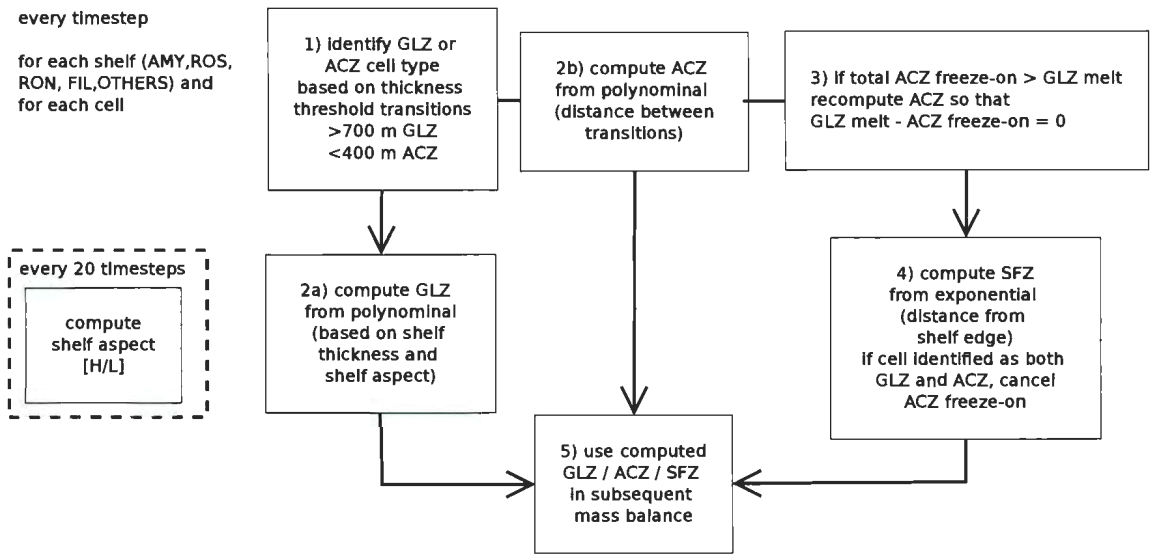


Figure 2.2: SSM implementation flowchart

shelves), is classified as OTHER.

The transitions between the zones were estimated from the AMY and RON transects, shown in Fig. 2.1a. The raw data for these transects, given in Table A.2 of the Appendix, were extracted from Wen et al. (2007, Fig. 4 and Fig. 6) for the AMY and from Jenkins and Doake (1991, Fig. 9 and Fig. 10) for the RON.

The transition from GLZ to ACZ in the larger shelves occurs at a shelf thickness of ~700 m. Similarly the transition from the ACZ to the SFZ occurs at a shelf thickness of approximately 300-400 m. The melt-accretion-melt pattern can also be seen, albeit approximately, when comparing the 700 m and/or 300 m contour from ALBMAP (Fig. 2.3) and the satellite derived melt distribution patterns of the AMY (Fricker et al., 2001, Fig. 3), the FIL (Joughin and Padman, 2003, Fig. 2), and the modelling study of the ROS (Holland et al., 2003, Fig. 10)). Sensitivity tests were made adjusting the transition thicknesses within the range of uncertainty in the transects. However, because the melt/accumulation rates before and after the transition zones are very small–the dominant melt rates occur at the grounding lines

and at the shelf front (Jacobs et al., 1992; Horgan et al., 2011)–there was little impact. As such the transition thicknesses are held constant in the SSM component.

The melt rate in the GLZ is modelled as a function of ice shelf thickness and the aspect ratio of the shelf. Plotting the melt rate as a function of thickness (Fig. 2.1b) allows a quadratic best-fit to be made (the raw data was pruned so that the quadratic fit is only made with the data that is upstream of the GLZ to ACZ transition thickness threshold *i.e.*, where H $<$ 700m the melt rate is set to zero); each transect has a different fit, thus each shelf has a different melt rate thickness function. We hypothesise that, because the larger shelves have distinct cavity geometries that effect the oceanographic processes within them (Fricker et al., 2001; Horgan et al., 2011), the melt function is proportional to the physical dimensions of the shelf. We define a thickness to length aspect ratio, $\epsilon = [H]/[L]$, to reflect the cavity dimensions. Table A.2 below summarises the physical characteristics, computed from ALBMAP$_{40}$, used for defining the aspect ratio. The average length is computed as the average minimum distance from each grid cell to open ocean without encountering land or grounded ice. The shelf average melt rate magnitudes are taken from Table A.3 of the appendix. The stronger melt rates are seen under the AMY (thick and short) and FIL (thickest and shortest) which have larger aspect ratios than the RON (thick and long). The ROS (thin and long) has the smallest melt rate.

computed and the sequence is unchanged.

Using the present-day AMY and RON aspect ratios ($\epsilon_{AMY}, \epsilon_{RON}$) and associated quadratic laws as reference melt functions ($\dot{M}g_{AMY}, \dot{M}g_{RON}$), the melt rate ($\dot{M}g$) for a shelf of thickness $H$ with aspect ratio ($\epsilon_{shf}$) can be computed using $\epsilon_{shf}$ as a weighting factor and interpolating between the two reference functions.

Table 2.2: Table showing dimensions of the 4 major shelves and the calculated aspect ratio, $\epsilon = [H]/[L]$. Area, average length (see text), and thickness are computed from ALBMAP. Melt rates given in italics are derived estimates (see SSM verification discussion and Table. A.4.)

| code | area $10^3 km^2$ | average H m | max H m | average length km | $\epsilon$ | average melt rate m $a^{-1}$ | melt rate estimate source |
|---|---|---|---|---|---|---|---|
| AMY | 57 | 580 | 1508 | 198 | 2.9 | $0.51 \pm 0.13$ | (Yu et al., 2010) |
| ROS | 483 | 395 | 783 | 295 | 1.3 | 0.1 | (Reddy et al., 2010) |
| RON | 348 | 646 | 1538 | 298 | 2.2 | *0.19* | (Joughin and Padman, 2003) |
| FIL | 77 | 792 | 1107 | 163 | 4.9 | *0.25*-0.35 | (Joughin and Padman, 2003; Grosfeld et al., 1998) |
| other | 459 | 285.57 | 1478 | n/a | n/a | n/a | |

$$\dot{M}g_{AMY} = -7.95 \times^{-06} H^2 + 8.38 \times^{-03} H - 2.19,$$
$$\dot{M}g_{RON} = -5.10 \times^{-06} H^2 + 5.92 \times^{-03} H - 1.62.$$

The shelf weighting factor is computed as

$$W_{shf} = \frac{\epsilon_{shf} - \epsilon_{AMY}}{\epsilon_{RON} - \epsilon_{AMY}}. \tag{2.26}$$

The final melt rate is computed from:

$$\dot{M}g = fnGLzN \left[\dot{M}g_{AMY} + W_{shf} \left[\dot{M}g_{RON} - \dot{M}g_{AMY}\right]\right], \tag{2.27}$$

where ensemble parameter $fnGLzN$ allows the strength of the computed melt to be adjusted: $fnGLz1$ (range 0.5→3) for the larger shelves and $fnGLz2$ (range 0.5→2.5) for the OTHER shelves. The aspect ratio for the OTHER shelves is always set to be

the maximum of the large shelves, motivated by the fact that they are closer to the CDW so will likely suffer stronger melt for a given thickness. As the shelves evolve over time, the aspect ratio will also evolve, reducing or increasing the amount of melt proportionally. The calculation of length is computationally costly, as such, it is only performed every 20 years.

The basal accretion in the ACZ is modelled using a quadratic function that increases from zero at the two transition zones to a maximum near the centre:

$$\dot{M}a = -\frac{1}{45000}(H - 550)^2 + 0.5\,. \tag{2.28}$$

The maximum is set to be 0.5 m $yr^{-1}$ for all shelves[†]. ACZ accumulation, being a product of the GLZ mode 1 melt, should not exceed $\dot{M}g$. If this does occur, the total $\dot{M}a$ is recomputed to be equal to $\dot{M}g$ melt and is re-distributed over the ACZ area. For present-day this condition only occurs in the ROS where, because of the shallow draught, the total GLZ melt is very low. Thus, because of the large area of the ACZ, the redistribution can produce freeze-on amounts that approach 0 m/yr (see Figure 2.5).

The SFZ melt is modelled in accordance with the exponential law presented in Horgan et al. (2011). Within the front 60 km of the shelf the melt follows the law,

$$\dot{M}s = fzclimsfz \times 2.0 \exp^{\left(\frac{-x}{11900}\right)}\,, \tag{2.29}$$

where x is distance from the shelf front and $fzclimsfz$,

$$fzclimsfz = 1 + fnzclimsfz \times (zclim - 1)\,, \tag{2.30}$$

[†]From the transects and the RON (Joughin and Padman, 2003, Fig. 2) and ROS melt maps (Holland et al., 2003, Fig. 10), the accretion is generally very low [0.5 m $yr^{-1}$]. Only for the AMY do they get significantly higher, with a maximum of 1.5 m $yr^{-1}$.

is a shelf front melt climate dependence scaling factor. With the current 40 km resolution of the GSM, the integral is evaluated over the first and second (isf1, isf2 respectively) grid cells at the ice-shelf front to produce two constants of SFZ melt,

$$\dot{Ms} = \begin{cases} -0.574 & \text{isf1, if cell is shelf edge} \\ -0.019 & \text{isf2, if cell is proximal to isf1}\,. \end{cases} \tag{2.31}$$

Ensemble parameter, $fnSfz1$, is used to scale $\dot{Ms}$ if the region is a large shelf. For the smaller shelves the melt is held constant (in earlier assessments of the GSM, adjustment of the SFZ for the smaller shelves had little impact, as such the parameter was removed). In the event of the ACZ grid cells encroaching into the SFZ (ice thickness in the grid cells at the shelf front being $>$ 400 m) the accretion is set to 0 m/yr. We reason that, at the shelf front, ISW would be advected away by CDW and/or coastal currents (Jacobs et al., 1992). The shelf front melt for all types of shelves is then further adjusted by climate dependence factor $fnzclimsfz$ (range 0$\rightarrow$1.18) following the logic of the *zclim* for thin ice (section 2.3.10.1).

The output from the SSM component is presented in Fig. 2.3, 2.4, and 2.5. Fig. 2.3 shows transects and melt maps for AMY(a & d), RON(b & e), and ROS(c & f). The observed and computed melt rates from the high ($H_5$ from ALBMAP$_5$) and low ($H_{40}$ from ALBMAP$_{40}$) resolution thickness transects is shown for the AMY and RON. Both $H_5$ and $H_{40}$ are presented to compare the effect of the resolution change. All the computed melt rates used SSM ensemble parameters set to unity thus removing their influence. Given there are no observations for ROS only the computed melt rate is shown (*i.e.*, by interpolating between the two references functions using the aspect ratio computed from the estimated length scale and $H_5$ thickness).

The melt rate spatial distributions, again calculated using $H_5$ thickness and with the ensemble parameters set to unity, of the major shelves are shown in Fig. 2.3(d,e

& f). The 400 m and 700 m zone transition thresholds are shown on the melt maps; the spatial distribution can be compared with the published melt maps for FIL (Fig. 2 of Joughin and Padman, 2003) and ROS (Fig. 10 of Holland et al., 2003). There is no melt map for AMY, but a comparison can be made with the marine-ice thickness map (Fricker et al., 2001, Fig. 3), *e.g.*, to delineate between the GLZ and ACZ.

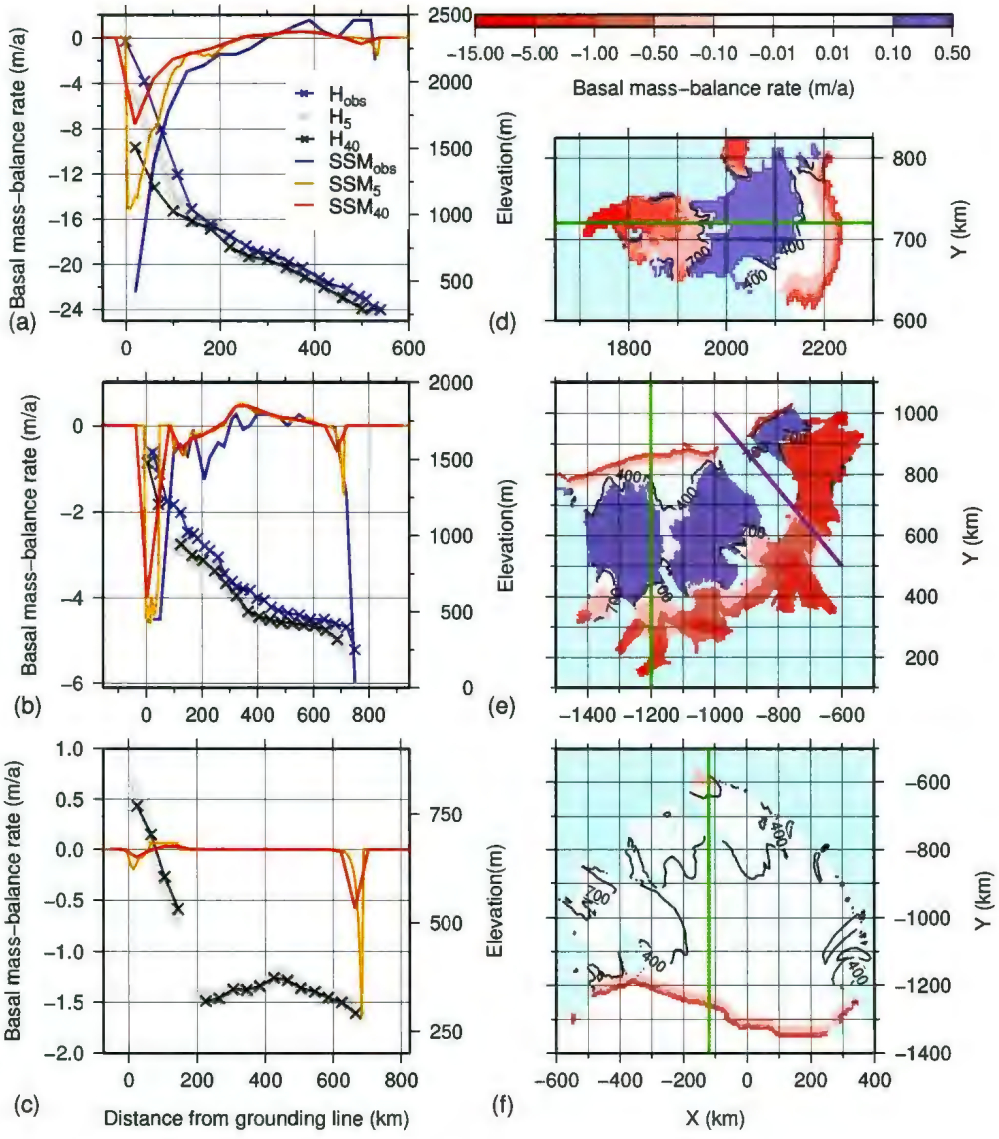


Figure 2.3: Thickness and melt transects and spatial melt maps for the three major shelves: AMY (a & d), ROS (b & e), RON-FIL (c & f) computed from the SSM law with unity parameters (see text). Green lines on the melt maps show the locations of the transects. The purple lines demarcate the divide between the FIL and RON shelves at 47°W .

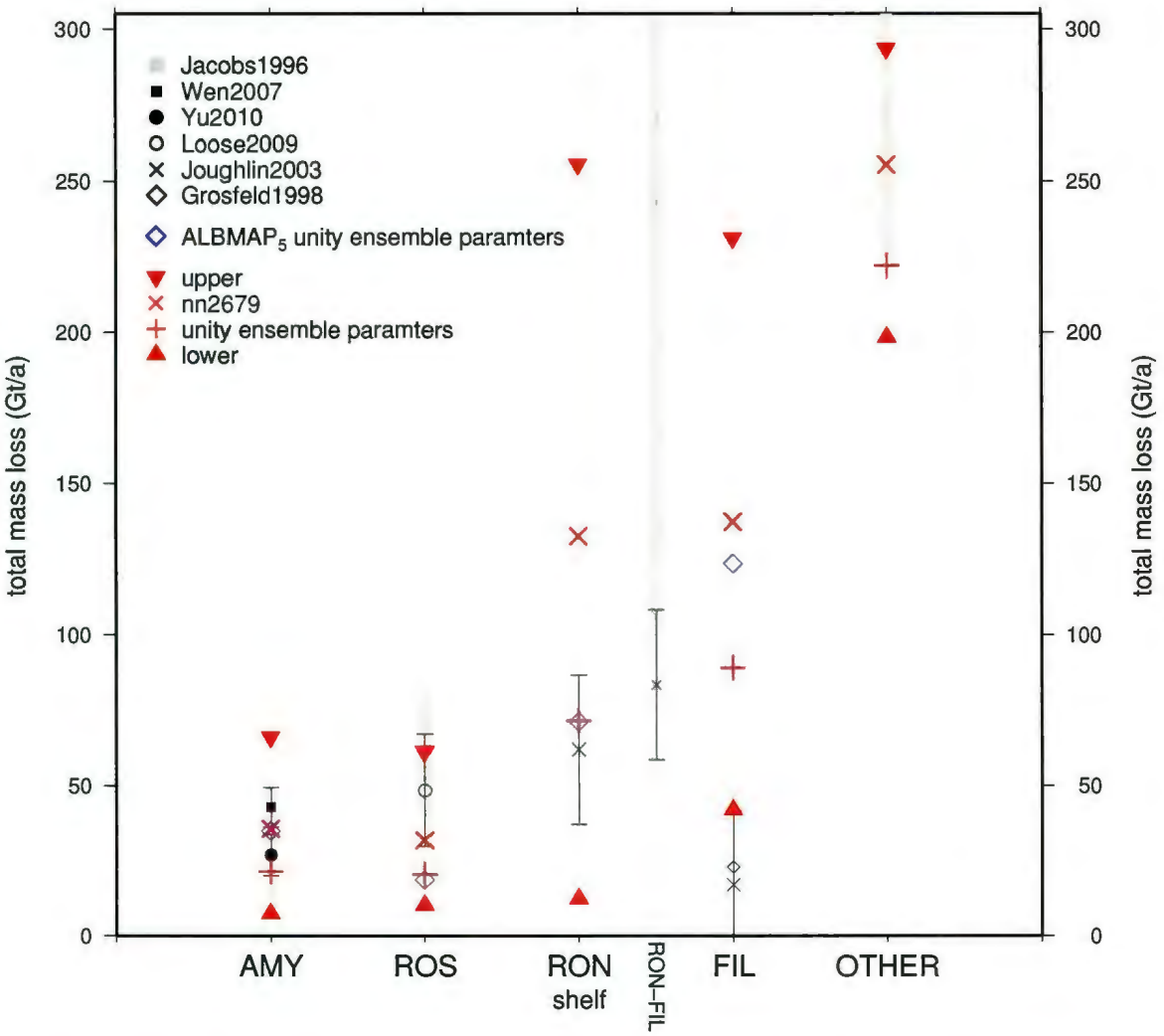


Figure 2.4: Comparison plot showing net melt amounts from observations and the predicted melt amount from the SSM component for each of the five shelf regions; two observations that are for the cumulative RON-FIL are also show. The OTHER observation has been clipped as the maximum, estimated from Jacobs et al. (1996), peaks at 675 Gt yr$^{-1}$ (see Table A.4).

**SSM verification** To verify the SSM component, we make comparisons with the available observations. Obtaining direct SSM measurements is understandably difficult given the environment in which it occurs (Heimbach and Losch, 2012). A variety of techniques, including oceanographic (e.g. Jacobs et al., 1992; Jacobs et al., 1996), geochemical (e.g. Jacobs et al., 1992; Smethie and Jacobs, 2005; Loose et al., 2009), remote sensing (e.g. Fricker et al., 2001; Joughin and Padman, 2003; Lambrecht et al., 2007), borehole (e.g. Zotikov et al., 1980; Nicholls et al., 1991), and modelling studies (e.g. Holland et al., 2003; Payne et al., 2007) have been employed to obtain SSM volumes, magnitudes, and spatial distributions. The observations, as extracted from the literature, are presented in Table A.3, some processing and conversion was performed to convert the raw data into a dataset that could be used for verification, shown in Table A.4. Because of the diversity in the format of the observations is unsurprising given the complexity of the SSM processes, the spatial and temporal variability in the forcing mechanism, and the numerous measurement (and modelling) techniques employed to obtain them.

SSM component are presented in the Appendix in Table A.3. The range and type of published observations is diverse; unsurprising given the complexity of the SSM processes, the spatial and temporal variability in the forcing mechanism, and the numerous measurement (and modelling) techniques employed to obtain them. Some conversion were performed to convert the raw data into a dataset that could be used for verification, shown in Table A.4.

The observed and predicted net mass loss for the shelf regions are shown in Fig. 2.4. Five sets of model derived SSM magnitudes are shown. The melt rates computed using the $H_5$ thickness dataset (and unity ensemble parameters) for Fig. 2.3; and four computed using the GSM initialised with $H_{40}$ and with different parameter settings (no ice-dynamic computations were performed, only the shelf melt component is exe-

cuted, to generate the data): upper bound parameters, unity parameters, run nn2679 parameter values and lower bound values.

The unity parameter run removes the influence of the ensemble parameters. Apart from the FIL, the modelled total melt is similar to observations. The upper and lower bound runs have all ensemble parameters set to the highest and lowest values respectively as defined in Table 2.1 and are presented to show the maximum and minimum range the SSM component is capable of. Run nn2679 is the baseline run used in the sensitivity assessment (see Section 2.4). Values from the SSM component bracket observational inferences for the AMY, the ROS, and, although biased high, the RON. The component generates excessive melt for the FIL. The higher melt produced by RON and FIL is caused through excess GLZ melt. For the OTHER shelves, the SSM component is at the lower bound of the observations.

The spatial melt-map produced by the runs with upper (run 9164) and lower (run 9165) bound parameters are presented in Fig. 2.5. The $H_{40}$ run (with parameters set to unity) melt map is similar to the high resolution melt map shown in Fig. 2.3 thus is not shown.

### 2.3.11 Spin up and initialization of the model

Initialization of the GSM and choosing a model run start time is a non-trivial task and the following factors need to be considered. Firstly, a full suite of self consistent boundary conditions (*e.g.*, bedrock elevation and characteristics, ice thickness, internal ice temperature and velocity fields, geothermal heat flux etc.) must to be prescribed for the time at which the GSM is to be initialised. Secondly, the thermodynamical response time of the ice sheet operates on order 100 kyr time scales; the model must be run for at least a glacial cycle for the initial temperature condition, and the associated uncertainties, to be 'forgotten' by the ice (Ritz et al., 2001). The time of initialization

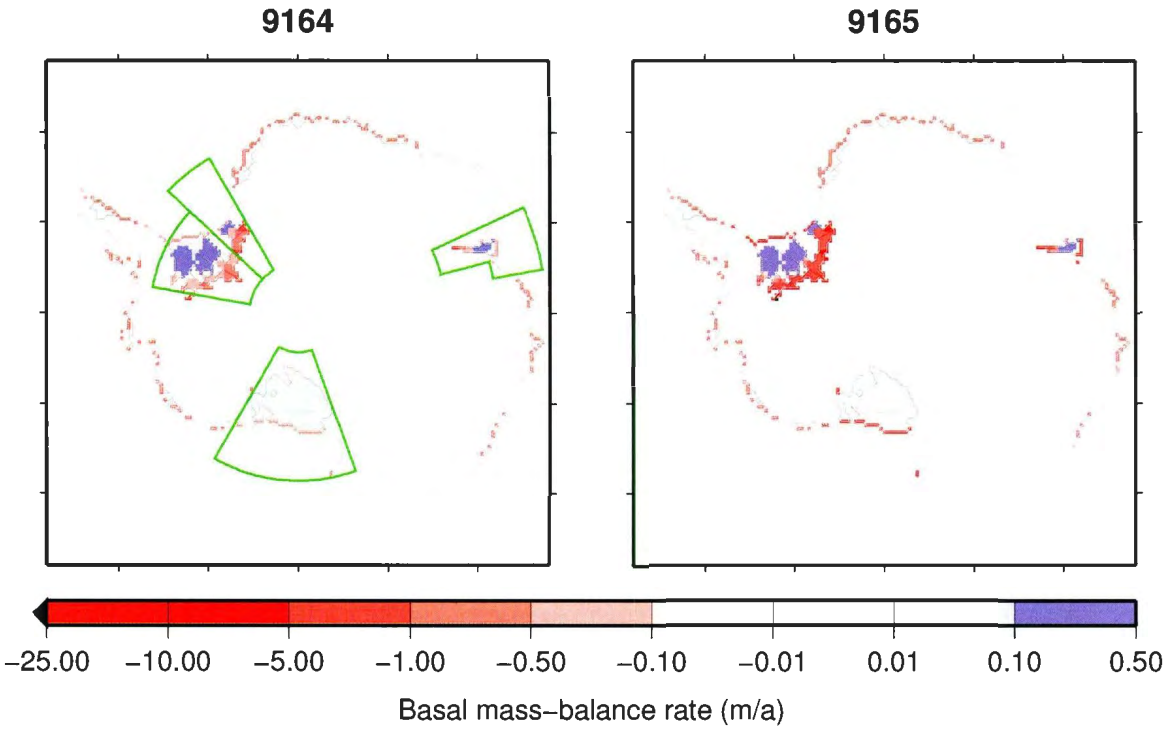


Figure 2.5: Melt rate maps generated from lower (9164) and upper (9165) SSM parameter values. The large shelf regions are outlined in green (the latitude, $\Phi$, and longitude, $\lambda$, boundaries are: AMY=$\Phi(-75,-65), \lambda(65,75)$ and $\Phi(-75,-70), \lambda(75,80)$; ROS=$\Phi(-86,-73), \lambda(160,210)$; RON=$\Phi(-85,-75), \lambda(280,313)$ and FIL=$\Phi(-72,-85), \lambda(313,330)$)

must account for this. Finally, part of the evaluation methodology to constrain the ensemble of runs produced by this GSM uses Eemian (~120 ka) sea level estimates (Briggs and Tarasov, 2012), thus to meet the second requirement we require a start time that must be at least one fully coupled glacial cycle prior to the Eemian. To meet these requirements and based on previous ensembles, 205 ka was identified as an appropriate start time to begin each model run (sea level and the modelled AIS volume being close to present-day).

Generation of the spin up configuration was performed as follows. (1) an initial internal ice sheet temperature regime was computed as an equilibrium temperature produced under diffusive heat transport and ALBMAP ice-sheet configuration with the surface temperature defined at 391 ka and basal temperature set to -6$^oC$. An

adhoc attempt to better account for advection (via proximity to the pressure melting point) while avoiding potential initial numerical instabilities from basal ice at the pressure melting point guided our choice of the basal thermal boundary condition. The initial geothermal temperature profile was also set to equilibrium for the given basal temperature and deep geothermal heat flux as boundary conditions. 391 ka has a temperature/Deuterium value which best matches mean temperature between 418ka→205ka, (418 ka has a match to present-day temperature and is approximately 200 kyr before 205 ka (the advection timescale on the interior of the AIS is ∼200kyr [thickness/accumulation rate = 4 km/2cm], giving a timescale for thermal equilibration), *i.e.*, , initial surface temperature used to set initial ice temperature is set to the average value over 418ka→205ka. (2) an internal velocity configuration is generated by initialising the GSM with ALBMAP assuming isostatic equilibrium and the internal temperature computed in step 1. (3) Starting from the above configuration, a small ensemble of 134 runs was generated (the parameter ranges were determined from previous runs) that ran from 391 ka to present-day with transient climate forcing and full thermodynamics. However, from 391 ka until 200 ka ice-dynamics is only active every 25 kyr for a period of just 100 yr. From 200 ka to present, ice-dynamics was continuously active. The output of these runs were assessed and the best run (closest to present-day configuration) was used as the starting configuration for the ensemble at 205 ka.

## 2.4 Sensitivity study

In the context of large ensemble analysis, the objective of the sensitivity study is to verify that each parameter: (a) has a discernible effect over some characteristic of the model output (*e.g.*, total grounded ice volume), (b) does not produce incon-

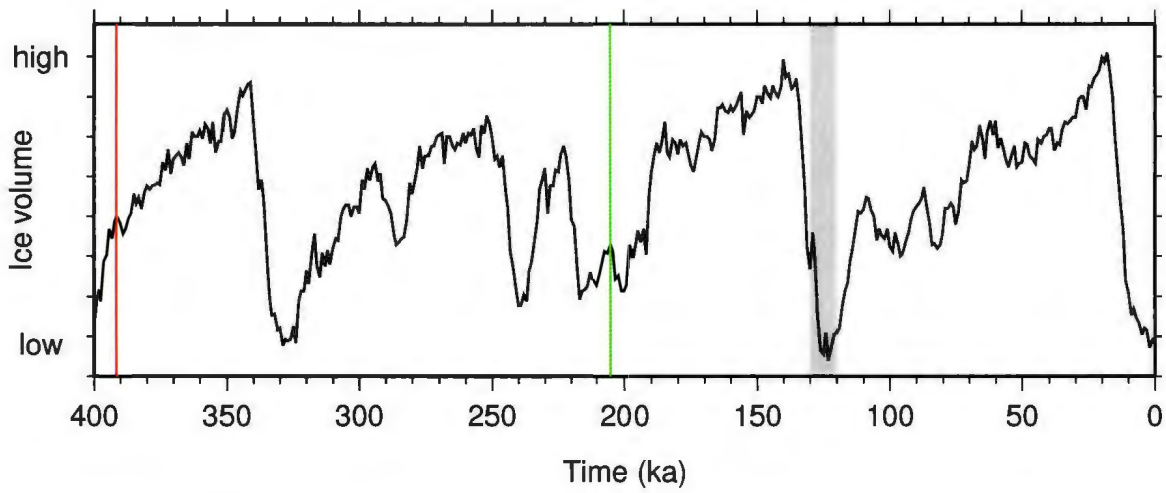


Figure 2.6: Lisiecki (2005) stacked benthic $\delta 18O$ record as proxy for global ice volume showing key times for spin up run. For the generation of the spin up ensemble (see text for details), ice dynamics is only intermittently active from 391 ka (red) until 205 ka (green). For the ensemble proper, initialization starts at 205 ka. Approximate period of the Eemian is highlighted in grey.

sistent (neither numerical instabilities nor physically implausible) results, and that (c)collectively the parameter ranges provide adequate coverage to bracket the observed ice sheet metrics (characteristics).

The appropriate choice of metrics is driven by the scientific question being addressed, in this case, the evaluation of a deglaciation chronology, discussed in (Briggs and Tarasov, 2012)*. For the purposes of this sensitivity study, we use 6 metrics: grounded ice volume (in eustatic sea level equivalent, mESL† ) for present-day WAIS (vol0gw), for EAIS (vol0ge)‡, total grounded ice volume for the LGM (vol20g), the zonal position of the Ross shelf grounding line (RISgl) along the 81°S line of latitude§,

*Briggs and Tarasov (2012) present a constraint database of present-day (derived from ALBMAP) and paleo data (Eemian volume estimates, relative sea level curves, past ice surface indicators and grounding line retreat data) for Antarctica. They describe a structured method of applying this data to a large ensemble of model runs. The evaluation process they present addresses the uncertainties found in the observational measurements, some of the structural error in the model, and the problems that must be addressed in integrating them together.

†Conversion factor of $1e6km^3$ of ice = 2.519 mESL

‡WAIS and EAIS are separated along a line-arc-line, defined as 30°W -> 85°S -> 170°W

§observed grounding line along the 81°S line of latitude (present-day location taken as 81°S , 155°W )

and the shelf areas for ROS and RON-FIL.

Finding the appropriate range for each parameter is an iterative process. Initially the parameter ranges are set using best guess values, either taken from the literature or from experience gained during the development of the components (*e.g.*, the SSM component). From these initial ranges, sensitivity ensembles are generated, evaluation of which potentially refines the ranges and, if required, might provoke the incorporation of new parameters to provide more freedom in the model or, conversely, removal of superfluous parameters.

Once the parameters and associated ranges have been verified to achieve the requirements of (a), (b), and (c) there is, ideally, sufficient confidence to justify the computational expenditure required to generate (and evaluate) a full ensemble. Deeper analysis of the full ensemble results can then be used to verify that full coverage has been achieved (within the parameter-space created by the 31 parameters).

Sensitivity plots (Figs. 2.7, 2.8 and 2.9) present the impact each parameter has on the selected metrics. Each parameter is explored using five values: a baseline value, and–whilst holding all the other parameters to their respective baseline values–an upper bound, a lower bound, an intermediate point between the upper bound and the baseline, and an intermediate point between the lower bound and the baseline. The baseline run (nn2679) is one of the 'better' runs *i.e.*, has the smallest misfits, as identified through the application of the constraint database and the evaluation methodology (Briggs and Tarasov, 2012). The intermediate values are presented as they can give a sense of the non-linearity of a parameter.

Although the baseline run used as the control for the sensitivity test is bias to be have excess volume (seen in Fig. 2.7, there is <0.5 mESL difference between the metric and the model output which, assuming ~50 mESL for EAIS, is <2.5% error) and similarly the shelf areas are smaller than the metrics, the ranges are able to produce

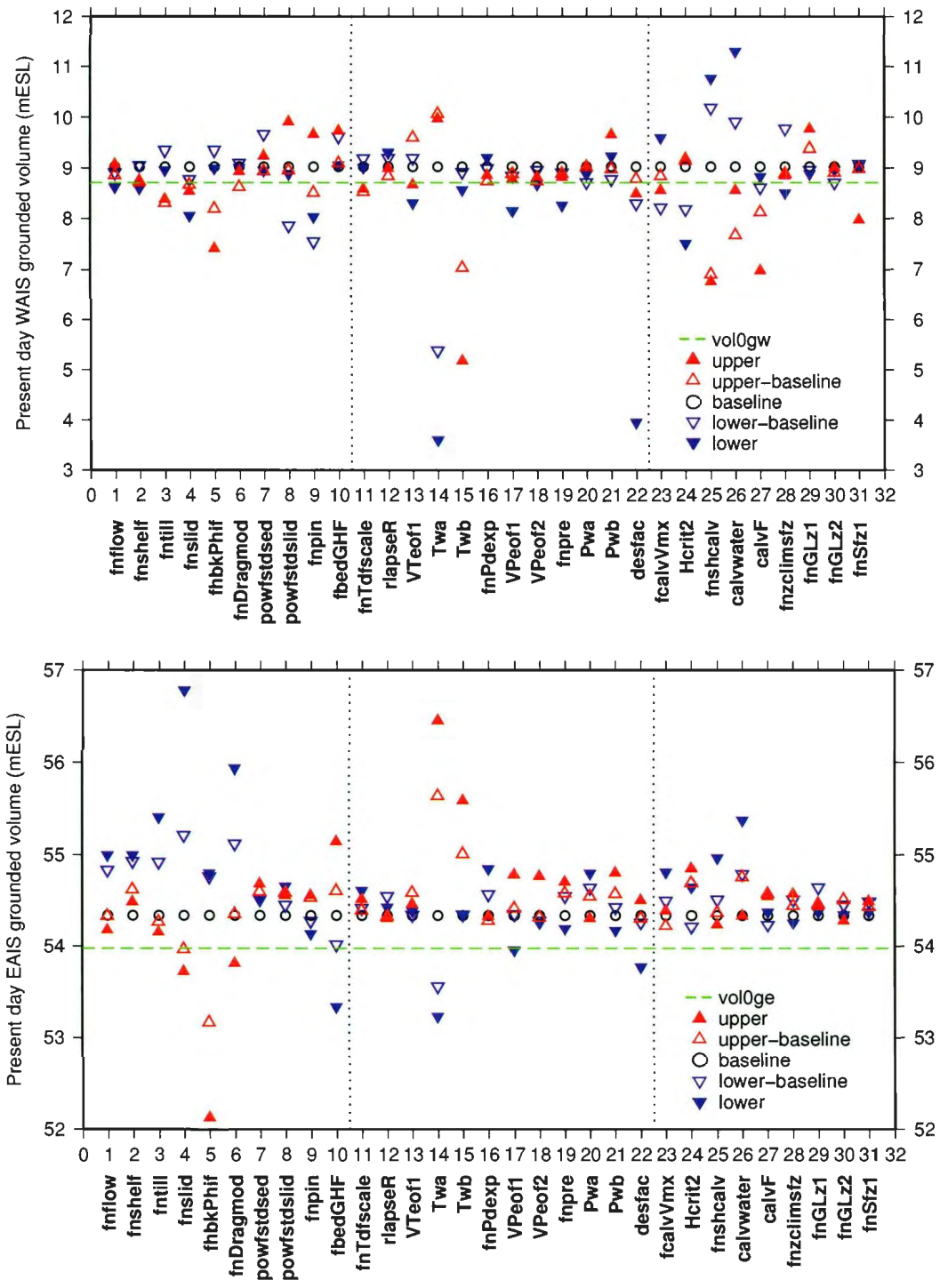


Figure 2.7: Sensitivity results for present-day WAIS (upper) and EAIS (lower) grounded ice volume. The dotted lines segregate the parameters into blocks pertaining to ice physics, climate forcing and ice-ocean forcing. Observational metrics values are computed from $H_{40}$.

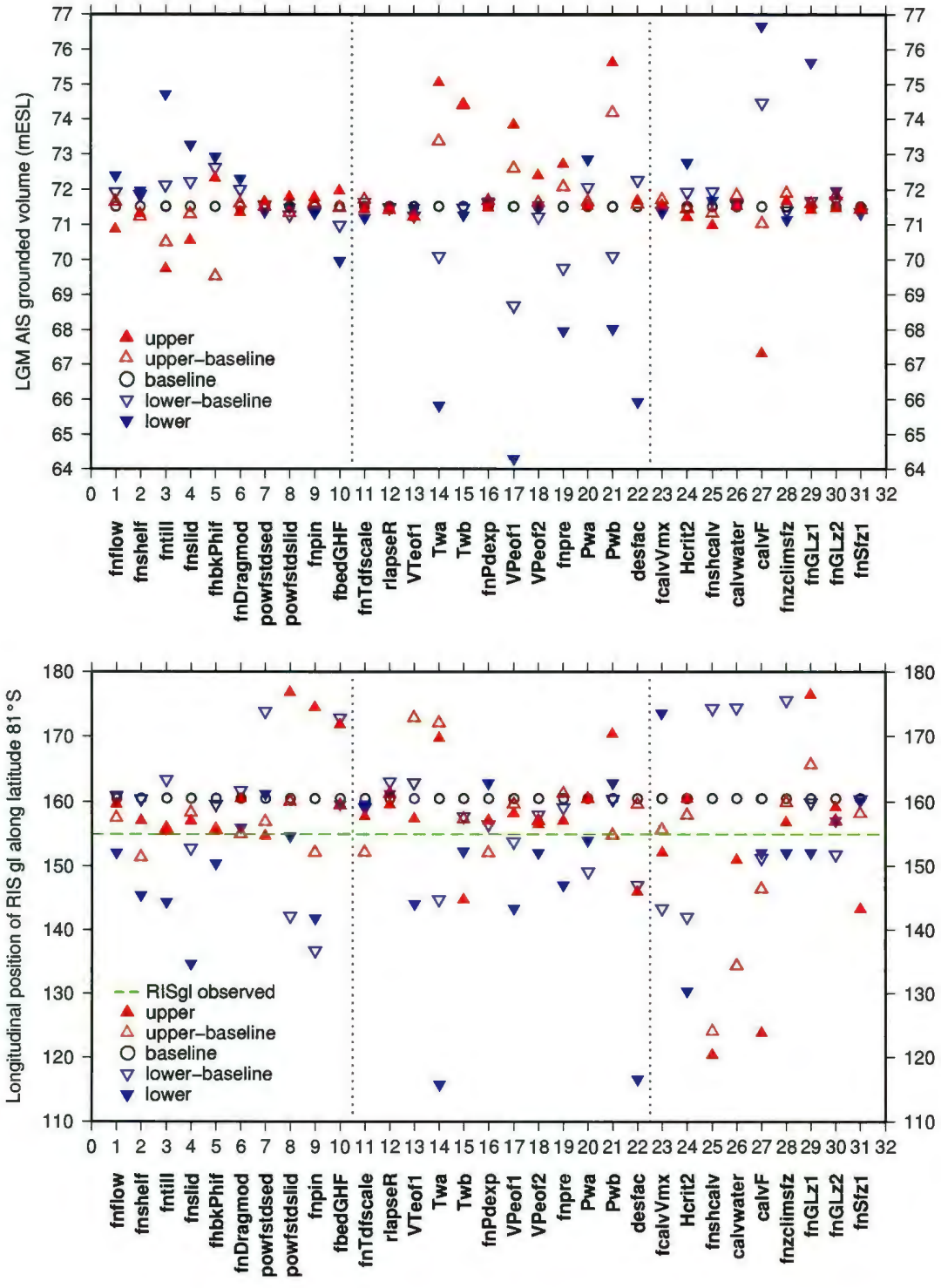


Figure 2.8: Sensitivity results for total AIS grounded volume (upper) at LGM and ROS grounding line position (lower). Note the latter metric misfit from observation for the baseline run is ~100 km, which equates to 2-3 grid cells.

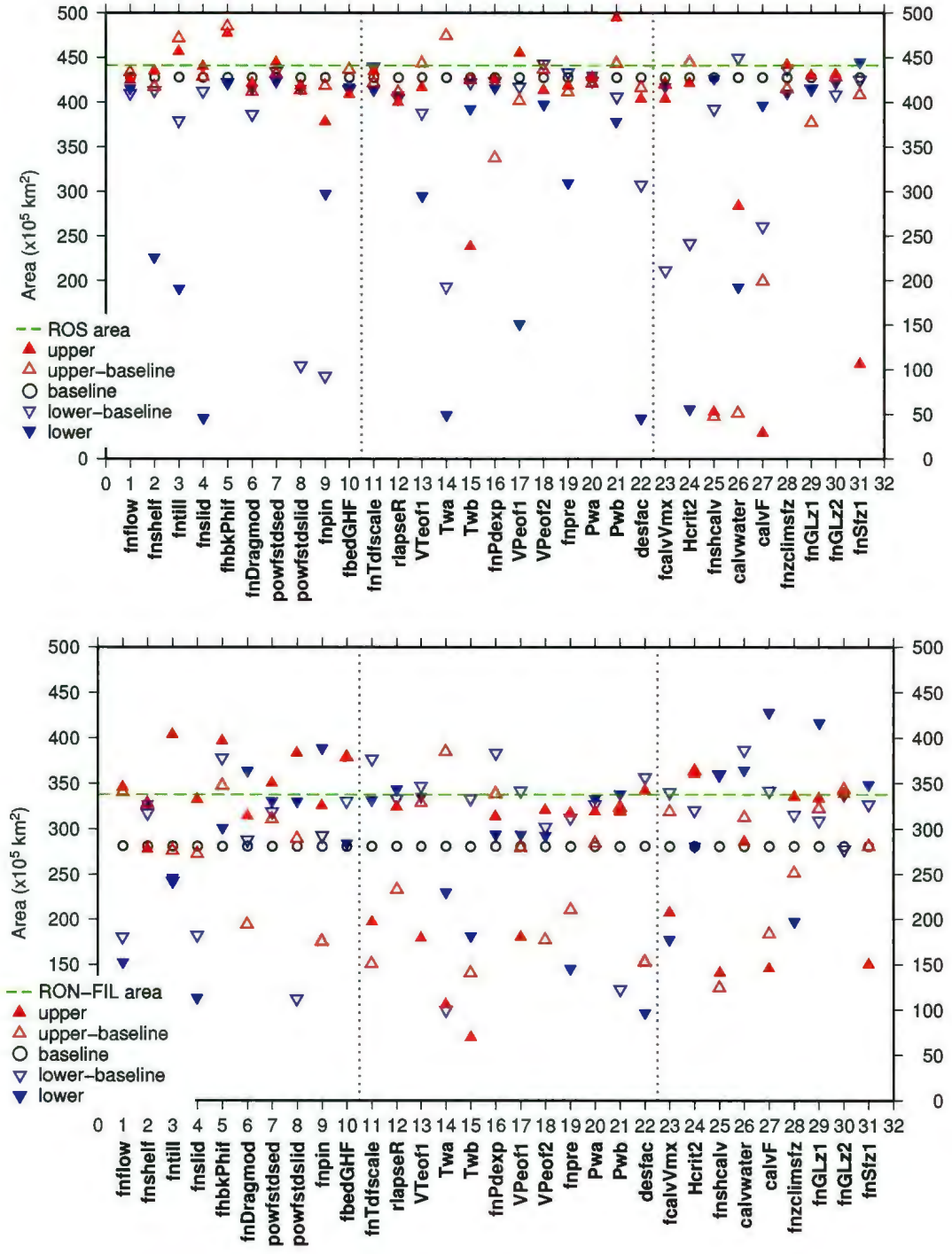


Figure 2.9: Sensitivity results for ROS (upper) and RON-FIL (lower) present-day area.

smaller AIS configurations and larger shelves thus we have confidence that the ranges are wide enough and physically realistic (initially the parameter ranges where wider than those presented here and, as the development ensembles were executed, the ranges were narrowed if implausible results were obtained at the extrema). Inevitably there will always be inherent model structural problems.

### 2.4.1 Discussion of parameter/metric sensitivity

Many of the parameters exhibit non-linear behaviour in the outcome of one or more of the metrics. For instance, the impact of increasing the shelf pinning parameter ($fnpin$) on ROS and RON-FIL shelf areas is non-monotonic. Furthermore, the impact is qualitatively different for each of the two shelf areas.

Over the range of parameters, vol0gw is more sensitive than vol0ge ($\sim$9 m in comparison to $\sim$5 m), furthermore only a few of the parameters cause this spread (predominately calving and climate parameters), the majority of parameters produce less than $\pm$1 mESL of deviation for both metrics. The shelf flow having less influence on vol0gw than on vol0ge is unexpected. The vol0ge metric is sensitive to the choice of the GHF.

The ice-ocean parameters have more impact on the present-day WAIS rather than EAIS or during the LGM (*i.e.*, when the shelf area was reduced). The shelf melt parameters have less impact that the calving parameters, except on the shelf area metrics. $fnGLz2$ is the least influential of the melt parameters.

The climate forcing parameters have much more impact on vol20g than on vol0gw and vol0ge as many of the climate parameters are inactive during present-day. Parameter $Twa$ is one of the few parameters with a strong influence over all metrics. $Twb$ is also influential but to a lesser degree; $Tf2$ and $Tf3$ both depend on the same present-day observational field, whereas $Tf1$ is a parametrised climate, as such has a

more distinct response (during the development ensembles, the better runs, as scored by the Briggs and Tarasov (2012) methodology have a spread of mid values for the Twa parameter; there is no pattern to say a dominant $Tf1$ or $Tf2$ produces better runs). Ensemble parameter $rlapseR$ only has significant impact on the RON-FIL shelf. This may be because the results are more sensitive to the $Tf1$ forcing, which does not employ $rlapse$, rather than $Tf2$ and $Tf3$. In addition, given the non-linear behaviour of the model, the impact of $rlapseR$ could be being masked behind other model parameters.

The plots confirm that each parameter has an impact on one or more of the metrics *e.g.*, vol0gw is quite insensitive to $fnslid$, whereas vol0ge has much larger response (understandable behaviour given $fnslid$, which parametrizes bare rock, is much more predominant under EAIS). Considered together, the results show that the parameter ranges bracket the observed metric values.

## 2.5 Summary and Conclusion

We have modified the PSU ice sheet model through the inclusion of six climate forcing mechanisms, a basal drag coefficient that accounts for sediment likelihood, boundary condition downscaling and systematic model-to-observation thickness misfit, a visco-elastic earth solver, tidewater and ice-shelf calving functionality, and a newly developed SSM component. To perform ensemble analysis 31 ensemble parameters are used to explore the uncertainty in the ice physics (predominately the definition of the basal coefficients), the climate forcing, and the ice-ocean interface.

The SSM component captures the melt-freeze-melt regime of the larger shelves and the simpler melt-melt regime of the smaller, peripheral, ice-shelves. The grounding line zone melt-rate is a function of the depth and the shelf aspect ration, the shelf

front melt-rate is derived from an exponential law mediated by the -5 °C isotherm. The accumulation due to basal freeze-on is a simple parabolic law. The SSM component produces total melt comparable to published SSM observations for the AMY, ROS, and RON, but produces too much melt for the FIL and too little for the RON. The melt pattern is similar to melt patterns in other published studies. Except for the use of the -5 degC isotherm to mediate the shelf front melt, the SSM component and thus the GSM, does not account for the spatially or temporally diverse regime of oceanographic forcing. However, given that, the melt law is not driven by ocean temperature, rather by the shape/thickness of the shelf, the current SSM implementation does not preclude regional variability in shelf melt regimes. Future studies will need to examine the impact of marine temperature variations on sub-shelf melt behaviour and associated shelf evolution.

Through the sensitivity study we have verified that for the 31 parameters described, each has some influence over at least one of the 6 model metrics. The sensitivity study also highlights the non-linear behaviour of many of the parameters. Considered together this gives us confidence that the parameter ranges provide some coverage of the model phase-space and thus warrant the effort required to generate (and analyse) a large ensemble.

## 2.6 References

Albrecht, T., Martin, M., Haseloff, M., Winkelmann, R., Levermann, A., 2010. Parameterization for subgrid-scale motion of ice-shelf calving-fronts. The Cryosphere Discussions 4 (3), 1497–1523.

Alley, R. B., Horgan, H. J., Joughin, I., Cuffey, K. M., Dupont, T. K., Parizek, B. R., Anandakrishnan, S., Bassis, J., 2008. A Simple Law for Ice-Shelf Calving. Science 322, 1344.

Alley, R. B., Whillans, I. M., 1984. Response of the East Antarctica Ice Sheet to Sea-Level Rise. Journal of Geophysical Research 89, 6487–6493.

Amundson, J. M., Truffer, M., 2010. A unifying framework for iceberg-calving models. Journal of Glaciology 56 (199), 822–830.

Arthern, R. J., Winebrenner, D. P., Vaughan, D. G., 2006. Antarctic snow accumulation mapped using polarization of 4.3-cm wavelength microwave emission. Journal of Geophysical Research 111 (D10), 6107.

Bamber, J. L., Alley, R. B., Joughin, I., 2007. Rapid response of modern day ice sheets to external forcing. Earth and Planetary Science Letters 257, 1–13.

Beckmann, A., 2003. A parameterization of ice shelf-ocean interaction for climate models. Ocean Modelling 5 (2), 157–170.

Bentley, M. J., 2010. The Antarctic palaeo record and its role in improving predictions of future Antarctic Ice Sheet change. Journal of Quaternary Science 25 (1), 5–18.

Braconnot, P., Otto-Bliesner, B., Harrison, S., Joussaume, S., Peterchmitt, J., Abe-Ouchi, A., Crucifix, M., Driesschaert, E., Fichefet, T., Hewitt, C. D., Kageyama,

M., Kitoh, A., Laine, A., Loutre, M., Marti, O., Merkel, U., Ramstein, G., Valdes, P., Weber, S. L., Yu, Y., Zhao, Y., 2007. Results of PMIP2 coupled simulations of the Mid-Holocene and Last Glacial Maximum - Part 1: experiments and large-scale features. Climate of the Past 3 (2), 261–277.

Briggs, R., Pollard, D., Tarasov., L., 2013. A data-constrained large-ensemble analysis of Antarctica over the last glacial cycle. in prep.

Briggs, R., Tarasov, L., 2012. How to evaluate model derived deglaciation chronologies: A case study using Antarctica. Submitted to Quaternary Science Reviews.

Comiso, J. C., 2000. Variability and trends in antarctic surface temperatures from in situ and satellite infrared measurements. Journal of Climate 13 (10), 1674–1696.

Cuffey, K., Paterson, W., 2010. The Physics of Glaciers. Academic Press. Butterworth-Heinemann/Elsevier.

Dinniman, M. S., Klinck, J. M., Smith, Jr., W. O., 2011. A model study of Circumpolar Deep Water on the West Antarctic Peninsula and Ross Sea continental shelves. Deep Sea Research Part II: Topical Studies in Oceanography 58, 1508–1523.

Dupont, T. K., Alley, R. B., 2005. Assessment of the importance of ice-shelf buttressing to ice-sheet flow. Geophysical Research Letters 32, 4503.

Fricker, H. A., Popov, S., Allison, I., Young, N., 2001. Distribution of marine ice beneath the Amery Ice Shelf. Geophysical Research Letters 28 (11), 2241–2244.

Grosfeld, K., Hellmer, H., Jonas, M., Sandhäger, H., Schulte, M., Vaughan, D., 1998. Marine ice beneath Filchner Ice Shelf Evidence from a multi-disciplinary approach. In: Jacobs, S., Weiss, R. (Eds.), Ocean, ice and atmosphere Interactions at the

Antarctic continental margin. Vol. 75 of Antarct Res Ser. AGU, Washington DC„ pp. 319–339.

Heimbach, P., Losch, M., 2012. Adjoint sensitivities of sub-ice-shelf melt rates to ocean circulation under the Pine Island Ice Shelf, West Antarctica. Annals of Glaciology 53, 59–69.

Holland, D. M., Jacobs, S. S., Jenkins, A., 2003. Modelling the ocean circulation beneath the Ross Ice Shelf. Antarctic Science 15 (1), 13–23.

Holland, P. R., Jenkins, A., Holland, D. M., 2008. The Response of Ice Shelf Basal Melting to Variations in Ocean Temperature. Journal of Climate 21, 2558.

Horgan, H., Walker, R., Anandakrishnan, S., Alley, R., 2011. Surface elevation changes at the front of the Ross Ice Shelf: Implications for basal melting. Journal of Geophysical Research (Oceans) 116 (15), 2005.

Huybrechts, P., 1991. The Antartic ice sheet and enviromental change: a three-dimensional modelling study. Ph.D. thesis, Alfred Wegener Institute for Polar and Marine Research.

Huybrechts, P., 1993. Glaciological Modelling of the Late Cenozoic East Antarctic Ice Sheet: Stability or Dynamism? Geografiska Annaler. Series A, Physical Geography 75 (4), 221–238.

Huybrechts, P., 2002. Sea-level changes at the LGM from ice-dynamic reconstructions of the Greenland and Antarctic ice sheets during the glacial cycles. Quaternary Science Reviews 21, 203–231.

Huybrechts, P., 2004. Antarctica: modelling. In: Bamber, J., Payne, A. (Eds.), Mass balance of the cryosphere: observations and modelling of contemporary and future changes. Cambridge: Cambridge University Press, pp. 491–523.

Jacobs, S., Hellmer, H., Jenkins, A., 1996. Antarctic ice sheet melting in the Southeast Pacific. Geophysical Research Letters 23, 957–960.

Jacobs, S., Hellmer, H. H., Doake, C. S. M., Jenkins, A., Frolich, R., 1992. Melting of ice shelves and the mass balance of Antarctica. Journal of Glaciology 38(130), 375–387.

Jenkins, A., Doake, C. S. M., 1991. Ice-ocean interaction on Ronne Ice Shelf, Antarctica. Journal of Geophysical Research 96, 791–813.

Jenkins, A., Dutrieux, P., Jacobs, S. S., McPhail, S. D., Perrett, J. R., Webb, A. T., White, D., 2010. Observations beneath Pine Island Glacier in West Antarctica and implications for its retreat. Nature 3 (7), 468–472.

Joughin, I., Padman, L., 2003. Melting and freezing beneath Filchner-Ronne Ice Shelf, Antarctica. Geophysical Research Letters 30 (9), 1477.

Jouzel, J., Masson-Delmotte, V., 2007. EPICA Dome C Ice Core 800KYr Deuterium Data and Temperature Estimates. IGBP PAGES/World Data Center for Paleoclimatology Data Contribution Series 2007-091.

Lambrecht, A., Sandhäger, H., Vaughan, D., Mayer, C., 2007. New ice thickness maps of Filchner-Ronne Ice Shelf, Antarctica, with specific focus on grounding lines and marine ice. Antarctic Science 19 (04).

Laskar, J., Robutel, P., Joutel, F., Gastineau, M., Correia, A. C. M., Levrard, B., 2004. A long-term numerical solution for the insolation quantities of the Earth. Astronomy and Astrophysics 428, 261–285.

LeBrocq, A. M., Payne, A. J., Vieli, A., 2010. An improved Antarctic dataset for high resolution numerical ice sheet models (ALBMAP v1). Earth System Science Data 2 (3), 247–260.

Lisiecki, L. E., 2005. A Pliocene-Pleistocene stack of 57 globally distributed benthic $\delta$18O records. Paleoceanography 20, 1003.

Loose, B., Schlosser, P., Smethie, W. M., Jacobs, S., 2009. An optimized estimate of glacial melt from the Ross Ice Shelf using noble gases, stable isotopes, and CFC transient tracers. Journal of Geophysical Research (Oceans) 114 (C13), 8007.

Ma, Y., Gagliardini, O., Ritz, C., Gillet-Chaulet, F., Durand, G., Montagnat, M., 2010. Enhancement factors for grounded ice and ice shelves inferred from an anisotropic ice-flow model. Journal of Glaciology 56 (199), 805–812.

MacAyeal, D. R., 1997. EISMINT: Lessons in Ice-Sheet Modeling.

Marshall, S. J., James, T. S., Clarke, G. K. C., 2002. North American Ice Sheet reconstructions at the Last Glacial Maximum. Quaternary Science Reviews 21 (1-3), 175–192.

Martin, M. A., Winkelmann, R., Haseloff, M., Albrecht, T., Bueler, E., Khroulev, C., Levermann, A., 2010. The Potsdam Parallel Ice Sheet Model (PISM-PIK) - Part 2: Dynamic equilibrium simulation of the Antarctic ice sheet. The Cryosphere Discussions 4 (3), 1307–1341.

Maule, C. F., Purucker, M. E., Olsen, N., Mosegaard, K., 2005. Heat flux anomalies in Antarctica revealed by satellite magnetic data. Science 309 (5733), 464–467.

Meehl, G., Stocker, T., Collins, W., Friedlingstein, P., Gaye, A., Gregory, J., Kitoh, A., Knutti, R., Murphy, J., Noda, A., Raper, S., Watterson, I., Weaver, A., Zhao, Z.-C., 2007. Climate Change 2007: The Physical Basis: Contributions of Working Group 1 to the Fourth Assessment Report of the Intergovernmental Panel on Climate Change. Cambridge University Press Cambridge, New York, Melbourne, Madrid, Cape Town, Singapore, São Paulo, Delhi, Ch. 10.

Mercer, J. H., 1978. West Antarctic ice sheet and $CO_2$ greenhouse effect: a threat of disaster. Nature 271, 321–325.

Neal, C. S., 1979. The dynamics of the Ross Ice Shelf revealed by radio echo-sounding. Journal of Glaciology 24, 295–307.

Nicholls, K. W., Makinson, K., Robinson, A. V., 1991. Ocean circulation beneath the Ronne ice shelf. Nature 354, 221–223.

Nicholls, K. W., Østerhus, S., Makinson, K., Gammelsrød, T., Fahrbach, E., Jul. 2009. Ice-ocean processes over the continental shelf of the southern Weddell Sea, Antarctica: A review. Review of Geophysics 47 (3), RG3003.

Olbers, D., Hellmer, H., 2010. A box model of circulation and melting in ice shelf caverns. Ocean Dynamics 60, 141–153.

Pattyn, F., 2010. Antarctic subglacial conditions inferred from a hybrid ice sheet/ice stream model. Earth and Planetary Science Letters 295, 451–461.

Payne, A. J., Holland, P. R., Shepherd, A. P., Rutt, I. C., Jenkins, A., Joughin, I., 2007. Numerical modeling of ocean-ice interactions under Pine Island Bay's ice shelf. Journal of Geophysical Research (Oceans) 112 (C11), 10019.

Payne, A. J., Vieli, A., Shepherd, A. P., Wingham, D. J., Rignot, E., 2004. Recent dramatic thinning of largest West Antarctic ice stream triggered by oceans. Geophysical Research Letters 31, 23401.

Peltier, W. R., 1998. Postglacial variations in the level of the sea: implications for climate dynamics and solid-earth geophysics. Review of Geophysics 36 (4), 603–689.

Peltier, W. R., Drummond, R., 2008. Rheological stratification of the lithosphere: A direct inference based upon the geodetically observed pattern of the glacial isostatic adjustment of the North American continent. Geophysical Research Letters 35 (L16314), 16314.

Pollard, D., DeConto, R. M., 2007. A Coupled Ice-Sheet/Ice-Shelf/Sediment Model Applied to a Marine-Margin Flowline: Forced and Unforced Variations. Special Publication International Association of Sedimentologists 39, 37–52.

Pollard, D., DeConto, R. M., 2009. Modelling West Antarctic ice sheet growth and collapse through the past five million years. Nature 458, 329–332.

Pollard, D., DeConto, R. M., 2009. Modelling West Antarctic ice sheet growth and collapse through the past five million years-Supplementry. Nature 458 (7236), 329–32.

Pollard, D., DeConto, R. M., 2012a. A simple inverse method for the distribution of basal sliding coefficients under ice sheets, applied to Antarctica. The Cryosphere Discussions 6, 1405–1444.

Pollard, D., DeConto, R. M., 2012b. Description of a hybrid ice sheet-shelf model, and application to Antarctica. Geoscientific Model Development Discussions 5, 1077–1134.

Pritchard, H. D., Ligtenberg, S. R. M., Fricker, H. A., Vaughan, D. G., van den Broeke, M. R., Padman, L., 2012. Antarctic ice-sheet loss driven by basal melting of ice shelves. Nature 484 (7395), 502–505.

Reddy, T. E., Holland, D. M., Arrigo, K. R., 2010. Ross ice shelf cavity circulation, residence time, and melting: Results from a model of oceanic chlorofluorocarbons. Continental Shelf Research 30, 733–742.

Rignot, E., Bamber, J. L., van den Broeke, M. R., Davis, C., Li, Y., van de Berg, W. J., van Meijgaard, E., 2008. Recent Antarctic ice mass loss from radar interferometry and regional climate modelling. Nature Geoscience 1, 106–110.

Rignot, E., Jacobs, S. S., 2002. Rapid Bottom Melting Widespread near Antarctic Ice Sheet Grounding Lines. Science 296, 2020–2023.

Ritz, C., Rommelaere, V., Dumas, C., 2001. Modeling the evolution of Antarctic ice sheet over the last 420,000 years: implications for altitude changes in the Vostok region. Journal of Geophysical Research-Atmospheres 106 (D23), 31943–31964.

Sanderson, T., 1979. Equilibrium profile of ice shelves. Journal of Glaciology 22 (88), 435–460.

Schoof, C., 2007. Ice sheet grounding line dynamics: Steady states, stability, and hysteresis. Journal of Geophysical Research 112 (F3), F03S28.

Shapiro, N. M., Ritzwoller, M. H., 2004. Inferring surface heat flux distributions guided by a global seismic model: particular application to Antarctica. Earth and Planetary Science Letters 223 (1-2), 213–224.

Smethie, Jr., W., Jacobs, S., 2005. Circulation and melting under the Ross Ice Shelf: estimates from evolving CFC, salinity and temperature fields in the Ross Sea. Deep Sea Research Part II: Topical Studies in Oceanography 52, 959–978.

Tarasov, L., Dyke, A. S., Neal, R. M., Peltier, W. R., 2012. A data-calibrated distribution of deglacial chronologies for the North American ice complex from glaciological modeling. Earth and Planetary Science Letters 315, 30–40.

Tarasov, L., Peltier, W. R., 2003. Greenland glacial history, borehole constraints and Eemian extent. Geophysical Research Letters 108 (83), 2124–2143.

Tarasov, L., Peltier, W. R., 2004. A geophysically constrained large ensemble analysis of the deglacial history of the North American ice sheet complex. Quaternary Science Reviews 23 (3–4), 359–388.

Tarasov, L., Peltier, W. R., 2006. A calibrated deglacial drainage chronology for the North American continent: Evidence of an Arctic trigger for the Younger Dryas. Quaternary Science Reviews 25 (7-8), 659–688.

Thyssen, F., Bombosch, A., Sandhäger, H., 1993. Elevation, ice thickness and structure mark maps of the central part of the Filchner-Ronne Ice Shelf. Polarforschung 62 (1), 17–26.

Walker, R. T., Dupont, T. K., Parizek, B. R., Alley, R. B., Sep. 2008. Effects of basal-melting distribution on the retreat of ice-shelf grounding lines. Geophysical Research Letters 35 (17), L17503.

Wen, J., Jezek, K. C., ó, B. M. C., Herzfeld, U. C., Farness, K. L., Huybrechts, P., 2007. Mass budgets of the Lambert, Mellor and Fisher Glaciers and basal fluxes beneath their flowbands on Amery Ice Shelf. Science in China Series D: Earth Sciences 50 (11), 1693–1706.

Whitehouse, P. L., Bentley, M. J., Brocq, A. M. L., 2012. A deglacial model for Antarctica: geological constraints and glaciological modelling as a basis for a new model of Antarctic glacial isostatic adjustment. Quaternary Science Reviews 32 (16), 1–24.

Yu, J., Liu, H., Jezek, K. C., Warner, R. C., Wen, J., 2010. Analysis of velocity field, mass balance, and basal melt of the Lambert Glacier-Amery Ice Shelf system by incorporating Radarsat SAR interferometry and ICESat laser altimetry measurements. Journal of Geophysical Research (Solid Earth) 115 (B14), 11102.

Zotikov, I. A., Zagorodnov, V. S., Raikovsky, J. V., 1980. Core Drilling through the Ross Ice Shelf (Antarctica) Confirmed Basal Freezing. Science 207, 1463–1465.

# Connecting Text

The second paper discusses the general question of how to evaluate model derived ice sheet reconstructions against observational constraints (Objective 2). It was written using Antarctica as an example, but the issues addressed are pertinent to any ice sheet reconstruction. The paper examines in detail the issues involved in assessing thousands of model runs against observational data and proposes an evaluation methodology. Critically, the evaluation methodology accounts for all categories of uncertainty in the system (model and observational uncertainties and irregular spatial and temporal distribution of the constraint observations) and propagates them into the evaluation results. The subject matter is cross disciplinary and, as such was written to appeal to both data providers and data users such as modellers. It highlights the importance of providing sufficient information in source publications to ensure maximum value can be extracted from observational data. The compiled database of published constraint data is provided in spreadsheet form, facilitating automated processing. To the best of my knowledge, this is the first time an Antarctica database developed for model evaluation is made available in such a usable format.

The article was submitted to *Quaternary Science Reviews* * in July 2012.

*http://www.journals.elsevier.com/quaternary-science-reviews/

# Chapter 3

# How to evaluate model derived deglaciation chronologies: A case study using Antarctica

## 3.1 Abstract

We address the evaluation of model-derived deglaciation chronologies using observational data. The study has been undertaken using the Antarctic ice sheet as the focus, however, the issues addressed and the methods described are applicable to the evaluation of other ice sheet reconstructions. Within this context, we present an initial database of observational data for constraining Antarctic ice sheet deglaciation chronologies (AntICEdat). The database constrains present-day ice sheet configuration, relative sea level, past ice thickness and grounding line retreat and is made available as a spreadsheet. We consider the non-trivial translation of an observation to model-applicable constraint data. Through observational error models and data-weighting we address the main issues that arise from evaluating modelled reconstructions–generated with a glacial systems model that has, like all such models, inherent structural deficiencies–using heterogeneous observational data. The evaluation method uses observational error models to quantify model to observational misfits that also incorporate the measurement uncertainties for each data-point. The data-point misfits are adjusted by data-weighting and combined to generate a score for the model output. As such, different chronologies can be evaluated and compared. We examine the sensitivity of the score to the different data-types and associated weighting using model-derived reconstructions. In addition, suggested reporting requirements are proposed to ensure that maximum value can be extracted from observational data.

## 3.2 Introduction

Like any numerical model of complex environmental systems, the glacial system models (GSMs) that are used to produce deglaciation chronologies necessarily invoke simplifications in their representation of physical processes (e.g. due to computational restrictions and incomplete understanding). Such chronologies therefore have little meaning without a clear account of uncertainties. Further uncertainties arise in the boundary conditions imposed (such as assumed climate forcings, subglacial topographies,..). By employing adjustable parameters, a modeller can account to a varying (but incomplete) degree for these uncertainties. Each set of model parameters defines a model glacial chronology and therefore is a sample out of a phase-space of possible reconstructions.

Exploration of this phase-space generally requires an ensemble of model runs and subsequent comparison of each run against observations to assess its plausibility. In this article we address the non-trivial question of how to quantitatively evaluate model generated deglaciation chronologies using observational data. Deglaciation chronologies are crucial to aid our understanding of ice sheet dynamics (be it past, present, or future), and global sea level change (e.g. (Bentley, 2010; Kopp, 2012)). Furthermore, associated uncertainty estimations are essential to ensure that the reconstructions can be interpreted with the appropriate degree of confidence.

A data-constrained large ensemble analysis technique has been employed in reconstructions of Greenland (Tarasov and Peltier, 2003), the North American ice sheet complex (Tarasov and Peltier, 2004), Eurasia (in prep.), and is now being employed in generating Antarctic ice sheet (AIS) reconstructions. This required the compilation of a AIS constraint database and an associated evaluation methodology for assessing each reconstruction against the observations, provoking this article.

Other data-model approaches have been used to evaluate ice sheet reconstructions.

For the Greenland ice sheet (GrIS), Simpson et al. (2009) compared model generated configurations against relative sea level (RSL) and past ice extent data. By adjusting the lithosphere, upper and lower mantle thicknesses of the Earth viscosity structure, and the grounding line extent of the ice sheet model they produced different ice sheet configurations. Through assessment of the model to observations misfit they explored the sensitivity ranges of the results.

A recent AIS glaciological modelling study (Whitehouse et al., 2012) with the objective of producing a loading history for a glacial isostatic model, has produced a data constrained-deglaciation chronology with range estimated uncertainties of sea level contributions. They used the community ice sheet model Glimmer (Rutt et al., 2009) at a resolution of 20 km, to generate different AIS configurations at five time-slices (20, 15, 10, 5, 0 ka*). The reconstructions were produced by fixing the grounding line extent, defined using marine geophysical and marine geological data-sets, and adjusting the boundary conditions (climate inputs, bed sliding parameters, relative sea level, isostatic behaviour and geothermal heat flux). Each configuration generated was then evaluated using terrestrial constraint data for past ice sheet elevation and 'no-ice' zones. The model to observation misfit was then scored (see Whitehouse et al. (2012) for details) for each configuration. Weighting was applied using inverse distance and a subjective data quality factor.

However, no article to date (to our knowledge) has adequately addressed observational error models, data-weighting issues, and model scoring for glaciological reconstruction. The task of using observations to constrain model output requires both observational and modelling issues to be tackled, as such this article is targeted toward both communities. Although the focus of this study is the AIS, the issues that are addressed and the methods described are applicable to any ice sheet reconstruction.

*Within this article ka is defined as $10^3$ calendar years before present whereas kyr is a time period of $10^3$ yrs

The structure of the article is as follows: first a brief overview of the development of the constraint database is given, this is followed by a description of the compilation, sorting, and processing of published data so that it can be employed as constraint data for AIS. The subsequent section presents the deglaciation chronology evaluation process. Next, the issues that are raised in applying the data to glacial reconstructions for the purposes of constraint are discussed. Finally a summary and discussion of future work and outstanding issues is given. To prevent the text becoming unwieldy many abbreviations are used and are listed in Table 3.1 for ease of reference.

## 3.3 Development of a constraint database

The Antarctic ICesheet Evolution database (AntICEdat) presented in this article has been developed to contain sufficient high quality data to provide spatial and temporal coverage (within the limits of the available data) for constraining modelled AIS deglaciation chronologies at continental and regional scales. This initial version is intended as the start of a community database that will evolve in both size and ease of access and update. As such, to ensure that AntICEdat is future-proof and flexible enough to be adopted for other purposes, a survey, summarized below, of existing constraint databases for Antarctica and other Quaternary ice sheets was performed. Their strengths and weaknesses were identified and used to guide the design of AntICEdat.

A comprehensive but unfortunately stale resource is the Antarctica Glaciological Geological Database (AGGD) (Kluiving and van der Wateren, 2001), a collection of geological, geomorphological and glaciological constraints taken from nearly 250 references, the most recent being 2001. The database format is a html website navigable by geographic locale; useful for viewing the data, but does not lend itself to auto-

Table 3.1: Table of abbreviations

| | |
|---|---|
| AIS | Antarctic Ice sheet |
| AGGD | Antarctica Glaciological Geological Database |
| $ALBMAP_{40}$ | ALBMAP dataset resampled to 40 km dataset as described in the supporting on-line material |
| $ALBMAP_5$ | ALBMAP dataset at 5 km resolution |
| AntICEdat | Antarctic ICesheet Evolution database |
| EAIS | East Antarctic ice sheet |
| ELEV | data-type: thickness from elevation markers |
| EXT | data-type: ice sheet extent |
| Et | total (grounded + floating) ice in EAIS |
| GLR | grounding line retreat (variant of EXT) |
| MSE | mean squared error |
| OMC | open marine conditions (variant of EXT) |
| PALa | only paleo data-types (with the baseline inter-data-type-weighting) |
| PD | data-type: present-day ice sheet configuration, |
| PDx | present-day constraints, x is a unique identifier for the scheme |
| PDxPx | schemes use both present day and paleo-data, x's are unique identifiers |
| PDxPxSEy | employs all data [just paleo-data] and sieve y. |
| PxSEy | employs just paleo-data and sieve y. |
| RISgl | Ross ice shelf grounding line |
| RSL | data-type:relative sea level |
| SE | squared errors |
| SOM | supporting on-line material |
| ShfAr | ice shelf area |
| WAIS | West Antarctic ice sheet |
| Wf | floating ice in WAIS |
| Wg | grounded ice in WAIS |
| volg | grounded ice volume |
| vol0g | present day grounded ice volume |
| vol20g | LGM grounded ice volume |
| $\Delta\xi$ | equivalent sea level contribution (vol20g-vol0g) |

mated processing and manipulation/searching by a user. The database includes all data-points from the original referenced studies including data that is inconsistent or that provides superfluous constraint information. For each site (which generally pertains to a single reference) there is a summary page presenting a table of data and a site description. Bentley and Hodgson (2009) provide an overview of on-shore and off-shore studies, made since 2000, effectively filling in the gap left by the AGGD.

Other resources are more data-type specific. As part of a study to explore the provenance of meltwater pulse 1A, Bassett et al. (2007) present a textual summary of eight relative sea level (RSL) sites from around Antarctica, all those sites are used in AntICEdat. Following on from work focused in the Antarctic Peninsula by Heroy and Anderson (2007), Livingstone et al. (2012) presented an overview of AIS paleo-ice streams and, as part of that work, they compiled an exhaustive database of marine cores that provide ice extent data. The cores are made available in tabular form and as a spreadsheet.

The deglaciation study published by Whitehouse et al. (2012) presents a well-referenced suite of constraint data of differing types, organized by region and site. As a consequence of the modelling/evaluation methodology they employ, the data has been binned into 5 ka time slices. From this a minimum, maximum, and likely constraint is inferred. Individual data-points in their source form, as required by the evaluation method we present, are not available, nor are the temporal and spatial uncertainties provided.

Of the non-AIS database surveyed, two RSL databases were particularly useful in developing the format for this constraint database. Brooks and Edwards (2006) present a RSL database for Ireland compiled from existing publications, available for download as a spreadsheet. The database contains 206 data-points distributed (unevenly) around 22 regional sites. Because of the discordant nature of the data (as

extracted from the source publications), they categorized the data into four groups based on the data quality and its utility. The large ensemble analysis of the North America ice sheet complex by Tarasov et al. (2012) was constrained using a RSL and marine limit database freely available in spreadsheet form (Dyke, unpublished). The data is organized such that each worksheet in the spreadsheet corresponds to a region, each region/worksheet containing one or many sites. There are over 500 sites in the spreadsheet.

Based on the survey of the other databases, and past experience with model calibration, the following design criteria were adopted for AntICEdat. Superfluous, low quality or inconsistent data are excluded, *i.e.*, the data should have a high signal strength relative to data uncertainty. Each paleo data-point requires an associated uncertainty estimation. Primarily this should be taken from the source publication. If no explicit uncertainty estimate is provided for what on other grounds appears to be a high-quality data-point, it is attributed an appropriate default uncertainty value taken from similar data-types in the database. The database should be in a simple open-source format that facilitates bulk-processing and manipulation. Where relevant, data-types should be categorized following the naming terminology (see Section 3.4.2) commonly used by the Antarctica community (e.g. Hall and Denton (1999); Bassett et al. (2007)).

## 3.4 AntICEdat constraint database

AntICEdat contains four primary data-sets that are used to produce misfit scores: present-day ice sheet configuration (PD) and three classes of paleo-data. The latter are relative sea level indicators (RSL), past ice sheet thickness from elevation (ELEV) markers, and ice sheet extent (EXT) from grounding line retreat and open marine

conditions data. A fifth class of data used as an accept/reject criteria during the evaluation process is described in Section 3.5.4.

Three other potential constraint data classes were not included. Rates of present-day uplift offer major constraint for the deglaciation of the last North American (Tarasov et al., 2012) and Eurasian ice sheets. A new compilation (Thomas et al., 2011), for the first time, offers sufficient signal strength to potentially merit inclusion. The GRACE (Gravity Recovery and Climate Experiment) record provides a powerful constraint (Peltier, 2004; Tapley et al., 2004). However, both of these data sets are highly sensitive to recent changes in surface load which lack adequate uncertainty characterization. Surface elevation changes derived from isotopic and gas analysis of ice cores (e.g. Martinerie et al. (1994); Delmotte et al. (1999); Steig et al. (2001); Parrenin et al. (2007); Price et al. (2007)) were also considered. The interpretation of the constraint information is dependant on methods that themselves are dependent on parameterizations (e.g. inferring the surface changes due to air-pressure deviations from air content analysis or through glaciological modelling). As such, along with the lack of appropriate uncertainty estimation, they were rejected for this initial study.

To be useful for producing a misfit score a data-point must have three pieces of information: location data (latitude, longitude), age data (contemporaneous or paleo, obtained through the application of some dating technique) and finally an indicative relationship between the sample, the age and the characteristic being constrained (*e.g.*, elevation of an RSL sample has some known relationship to past sea level; sediment analysis performed on a marine core identifies the transition from sub-glacial to glacial-proximal conditions indicating a grounding line migration). The attributes, issues and steps required to process each data-type into constraining data are described in the following subsections.

### 3.4.1 Present-day ice-sheet configuration (PD)

The ALBMAP dataset (LeBrocq et al., 2010) is used as the present-day constraint. Present-day ice thickness and topography provide the strongest spatial constraint of all data-types and also offer some late Holocene temporal constraint, as discussed in Section 3.5.3.2. ALBMAP is an update to the BEDMAP (Lythe and Vaughan the BEDMAP Consortium, 2001) dataset. It corrects numerous inconsistencies and is augmented by data collected since the publication of BEDMAP (LeBrocq et al., 2010).

The fit to present-day constraint is decomposed into 5 metric components. The three most discriminating are mean-squared-errors (MSE) of modelled vs observed ice thickness for grounded ice in the WAIS (Wg), floating ice in the WAIS (Wf), and total (combined grounded and floating) ice for the EAIS (Et) *. The remaining two metric components are the squared-errors (SE) for the Ross Ice Shelf grounding line position (RISgl) and the squared-errors for the area of the four largest ice shelves (ShfAr). The RISgl error is the misfit between modelled and present-day observed grounding line along the 81°S line of latitude (present-day location taken as 81°S , 155°W ) shown in Fig. 3.1. This approach permits selectivity in investigating WAIS and major ice shelves in accord with the concern about, and scientific interest in, past and potential future dynamical instabilities.

As ALBMAP (and BEDMAP) are constructed from the integration of numerous other data-sets, collected using different techniques, and at differing spatial resolutions and areal coverage, inevitably there are uncertainties both with the source data-sets and the final product. Quantification of those uncertainties was not an objective of the ALBMAP authors (LeBrocq et al., 2010) and is also beyond the scope of this study.

*WAIS and EAIS are separated along a line-arc-line shown in Fig 3.1, defined as 30°W ->85°S ->170 °W .

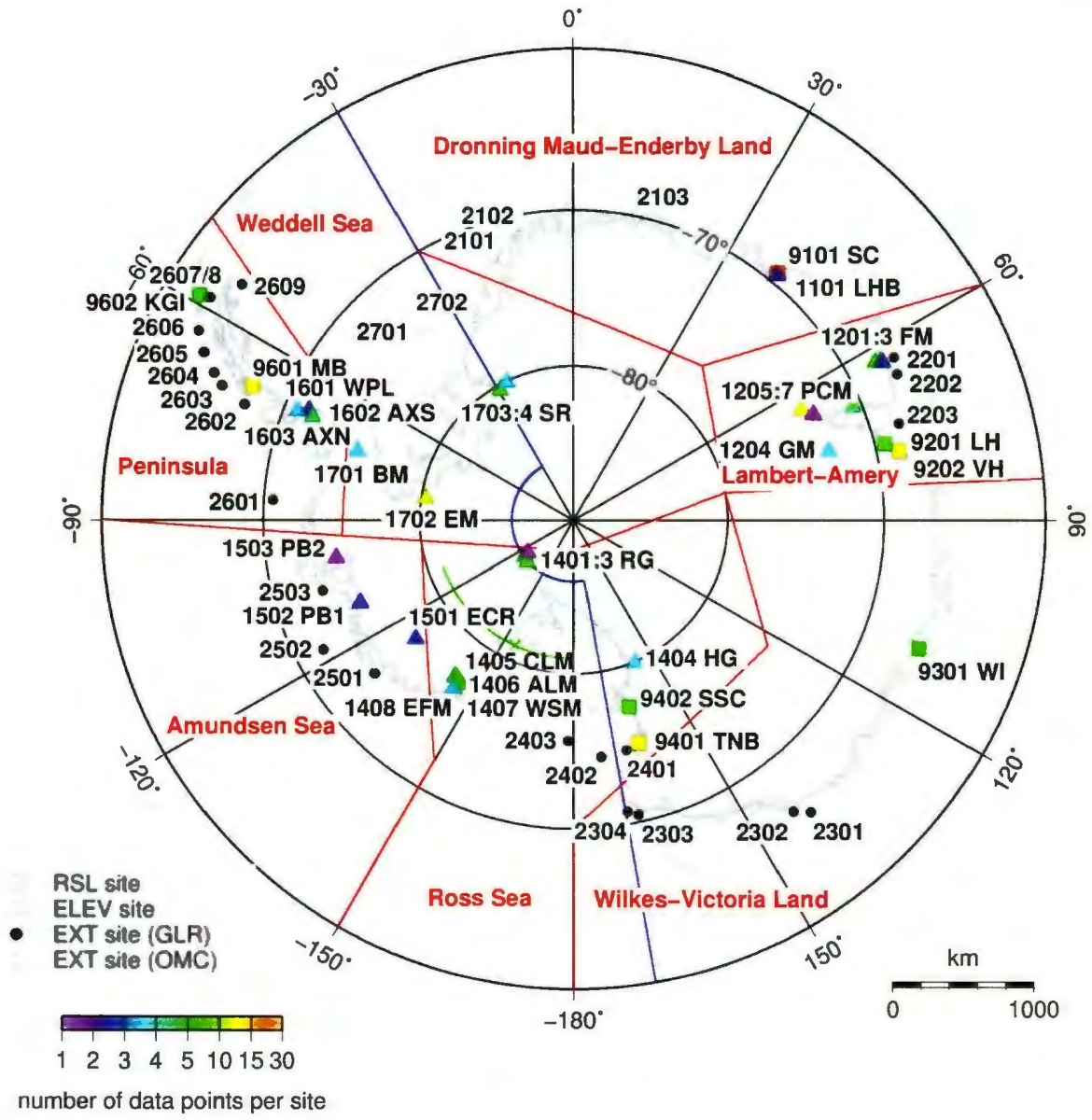


Figure 3.1: Location map showing sites and site data density for constraint data types. Red lines delineate sector divisions, blue line dissects WAIS and EAIS, and green line shows the 81°S track line for computing Ross ice-shelf grounding line misfit. RSL sites are (squares, clockwise from top right): Syowa Coast (SC), Larsemann Hills (LH), Vestfold Hills (VH), Windmill Islands (WI), Terra Nova Bay (TNB), Southern Scott Coast (SSC), Marguerite Bay (MB) and King George Island (KGI). ELEV sites (triangles, clockwise from top right): Lutzow-Holm Bay (LHB), Framnes Mts (FM), Grove Mts (GM), Prince Charles Mts (PCM), Reedy Glacier (RG), Hatherton Glacier (HG), Clark Mts (CLM), Allegheny Mts (ALM), Western Sarnoff Mts (WSM), Eastern Fosdick Mts (EFM), Executive Committee Range (ECR), Pine Island Bay (PB1, PB2), West Palmer Land (WPL), Alexander Island South (AXS), Alexander Island North (AXN), Behrendt Mts (BM), Ellsworth Mts (EM), Shackleton Range (SR). EXT sites are identified only by code, filled circles provide a dated grounding line retreat, unfilled circles are onset of open marine conditions (minimum ages for grounding line retreat).

As such (with one exception as described below), the present-day configuration does not have any spatial variation in the uncertainty attributed. A scalar (*i.e.*, spatially independent) uncertainty is implicit in the intra-data-type weighting described in Section 3.5.3.1, though this is far from satisfactory.

ALBMAP is provided at a resolution of 5 km (herein named $\text{ALBMAP}_5$). To be used as constraint data it must be upscaled to the model resolution of 40 km (referred to as $\text{ALBMAP}_{40}$). As part of the process corrections were made to ensure grounding-line positions and key pinning points were preserved. Details of the upscale resampling is described in the supporting on-line material (SOM).

Motivated by unavoidable biases when upscaling the grounding line area, along with the larger uncertainties associated with remote sensing grounding line positions, a one sigma uncertainty estimate for each ice shelf area (ShfAr) was set to be the sum of: (a) 0.5× the upscaled area of the associated grounding-line mask uncertainty from the ALBMAP data set*, (b) 10 km × the approximate length of the grounding line†, and (c) 5 km × the length of the calving margin‡. These uncertainties assume some accounting for systematic error (as discussed below).

### 3.4.2 Paleo data

The paleo-data covers a range of proxies including geological, glaciological, dateable organic matter and both on-shore and off-shore sediment cores. Table 3.2 provides a overview of the paleo-data types. The data is managed on a site by site basis, each site containing 1 or more data-points of the same data-type within an $\sim$ 20 km catchment region. This corresponds to the minimal size of a single grid cell

*The ALBMAP grounding-line mask uncertainty field is total (two-sided) uncertainty, thus 0.5 factor.

†The 10 km comes from an adhoc choice of 2 ALBMAP grid cells.

‡ALBMAP can only resolve the calving margin to within 2.5 km, we chose to double this to 5km.

(20-40km) in contemporaneous continental scale ice sheet models (Ritz et al., 2001; Huybrechts, 2002; Pollard and DeConto, 2009; Martin et al., 2010; Whitehouse et al., 2012). Furthermore, geophysical constraints such as RSL and present-day uplift do not provide any higher spatial resolution of constraint (in good part due to the smoothing effect of the lithosphere on isostatic response). In the majority of cases the study area from which the data was collected meets this criteria. As such, the sites as they are organized in AntICEdat will generally match the sites as they are published. If however, the source data of the publication is spread over a wider geographic area, as is common with the ELEV data, it is split into separate sites in AntICEdat. The site specific details of these processing steps for the RSL and ELEV data-types is documented in Table 2 and 3 of the SOM. The position location, used in Fig. 3.1, is computed as the average location of all the data points for that site. EXT data is extracted from the marine core database compiled by Livingstone et al. (2012). There is sufficient geographic separation between the cores used in AntICEdat that each core pertains to a separate site, thus the site location is the same as the core location. The RSL and ELEV sites have been derived from publications surveyed up until July 2011. The most recent reference from the EXT database is Jan 2012.

Normally, in the source publications, the authors process and assess the data as individual data-points then, prior to interpreting the history of the region, data identified as incongruent is excluded. Data identified as such by the authors are excluded from AntICEdat. To further avoid bloating of the database, observations that do not increase the signal strength for a given site have also been excluded. Examples of redundant data are given in the data-type descriptions that follow. The specific cases are described in the Table of the SOM.

The uncertainties considered and how they have been addressed (or not) for each data-type are described in the following data-type overviews. The observational error

model that dictates how the observations and the associated uncertainties (either observational, or due to interpretation) are translated into a constraint data-point are discussed as part of the evaluation process, described in Section 3.5.2.

Each data-site has a unique four digit integer identifier within AntICEdat, the format is ABCC, where A is the constraint data type, 1 for ELEV data, 2 for EXT data and 9 for RSL data. B identifies the sector of Antarctica in which the site is located (Table 3.3 and Fig. 3.1). The sectors approximately demarcate the major ice drainage basins, loosely based on Rignot et al. (2011). CC identifies the site. Each data-point within a site is identified using the sample name or identifier as taken from the source publication.

#### 3.4.2.1 Relative sea level (RSL)

A RSL data-point provides a proxy record of past sea level (either an exact, a maximum, or a minimum bound) for a specific time at a location. By gathering sufficient data-points from the same area an RSL curve can be reconstructed. AntICEdat contains RSL data-points radiocarbon-dated using two methods: by dating sediment recovered from isolation basins with known sill heights and by dating organic matter (e.g. penguin guano, seal remains, shells) found on, or in, direct indicators of former sea level, such as raised beaches (Verleyen, 2005).

RSL data provides three types of constraint (1) a two way constraint *i.e.*, past sea level was at the height of the sample, (2) a one way upper constraint *i.e.*, a sea-level maximum, or (3) a one way lower constraint *i.e.*, a sea-level minimum. However, depending if the data can be used directly or must be adjusted due to interpretation requirements, it is actually classified into six types: unadjusted two-way (type t1), unadjusted one-way upper (t2a), unadjusted one-way lower (t2b), adjusted two-way (t3), adjusted one-way upper (t4a) and adjusted one-way lower (t4b). These are

| id | constraint type | material | notes |
|---|---|---|---|
| **RSL** | | | |
| t1 | two-way | marine/lacustrine or lacustrine/marine sediment | Dated RSL. Derived from sediment transition and sill elevation (measured from present-day sea level) from isolation basin. |
| t2a | one-way | marine sediment | Date of inundation, RSL minimum (RSL above). Derived from dated marine sediment and sill elevation from isolation basin. RSL was above sill elevation. |
| t2b | one-way | lacustrine sediment | Date of isolation, RSL maximum (RSL was below). Derived from dated lacustrine sediment and sill elevation from isolation basin. RSL was below sill elevation. |
| t3 | two-way adjusted | mollusc fragments, seal skin/hairs, penguin bone | Close age of RSL, dated organic matter buried within the beach because of storm event. RSL at sample height - storm beach adjustment factor. |
| t4a | one-way adjusted | in-situ molluscs | Maximum age of beach, RSL minimum (RSL was above). Molluscs needed 1-2 m ocean depth minimum to survive. RSL at least above sample height + adjustment factor. |
| t4b | one-way adjusted | seal remains, penguin remains, and guano | Minimum age of beach, RSL maximum (RSL below). Seal remains, penguin remains and guano, sufficiently high above beach to avoid disruption from storm surges. RSL at least below sample height - storm beach adjustment factor. |
| **ELEV** | | | |
| | two-way | erratic or bedrock | Cosmogenic dating of glacially transported erratic or glacially scoured bedrock yields a paleo-ice surface elevation relative to present-day ice free surface and thus past ice thickness. |
| **EXT** | | | |
| | two-way | sub-glacial and glacial-proximal facies | Sediment transition records time and position of grounding line retreat. |
| | one-way | glacial-marine mud | Records onset of open marine conditions (proxy for minimum age of grounding line retreat, but given uncertainty, in this study only open marine event used). |

Table 3.2: Paleo data constraint type summary

Table 3.3: Drainage basin sector code

| id | sector code | sector description | site range |
|---|---|---|---|
| 1 | DMEL | Dronning Maud-Enderby Land | 101-199 |
| 2 | LAIS | Lambert-Amery Ice System | 201-299 |
| 3 | WVL | Wilkes-Victoria Land | 301-399 |
| 4 | RS | Ross Sea | 401-499 |
| 5 | AS | Admunsen Sea | 501-599 |
| 6 | AP | Antarctic Peninsula | 601-699 |
| 7 | WS | Weddell Sea | 701-799 |

discussed below and presented in Table 3.2.

Isolation basins provide an excellent record of RSL. They are formed by a sequence of marine inundation of near-shore ponds or lakes followed by isolation from the marine source. Thus the basin accumulated either marine sediment, or through freshwater influx they were flushed and accumulated lacustrine sediments. By measuring the controlling sill height and identifying and dating the sediment, three types of constraint can be derived (Zwartz, 1998).

- t1: a marine-lacustrine/lacustrine-marine contact (or transition) provides a precise sea level record.
- t2a: marine sediments provide a sea level minimum (past sea level was above) from when the basin was inundated.
- t2b: lacustrine sediments record when the basin was isolated from marine waters providing a dated sea level maximum as past sea level was below the sill.

For type 1 contact points, the type of sediment that is dated determines if there needs to be a marine reservoir correction applied or not. The elevation and elevation uncertainty of the data-point is the isolation basin sill height (above present day sea

level) and associated measurement error. Published elevation errors are in the range 0.1-2 m (e.g Zwartz 1998; Hall 2009).

Buried organic matter in raised beaches–paleo-beaches situated above the present-day shoreline–also provide a dated sea level record. Depending on the type of organic material dated (and the local conditions) a sea level maximum or minimum, with an associated minimum age or maximum age is obtained; in rare cases a close age of the beach can be derived (Bassett et al., 2007; Hall and Denton, 1999).

- t3: at two sites, 9401 and 9402, noted in the SOM, some of the organic samples were recovered from deep within the storm beaches (Hall and Denton, 1999; Baroni and Hall, 2004). The authors report that the samples can be interpreted as having been deposited during a storm event and not at later time providing a close age on the beach.

- t4a: the molluscs *Laternua Elliptica* and *Adamussium colbecki* live at a range of depths, from hundreds of meters, to just below the sea-ice in 1-2 m of water (Baroni and Hall, 2004; Bassett et al., 2007). When found in-situ in marine sediment the shells are interpreted to be a sea level minimum and thus a maximum age constraint on the beach. They provide a record of past sea level being above the samples at deposition; the beach cannot be older than the age of the shell.

- t4b: seal remains, penguin remains, and guano found on the surface of raised beaches provide a maximum sea level constraint and minimum age for the beach; past sea level was below the samples at deposition and the beach must be at least as old as the samples. Modern day penguins in Terra Nova Bay, live at least 2 m above the level of the storm beach.

Following Baroni and Hall (2004) and Bassett et al. (2007) we assume that sea

level was 2 ± 1m below the elevation from where the samples were recovered*.

Published uncertainties are used, except in the case of two sites whose samples have no published elevation error (Zhang and Peterson, 1984; Miura et al., 1998). Both of these are for shells recovered from within marine sediment. They are assigned a sample elevation uncertainty of ± 1 m as this is the largest error for this sample type taken from the other studies (Hall and Denton, 1999).

The radiocarbon dates extracted from the source publications were calibrated using the CALIB program v6.0 (Stuiver et al., 2005) and, depending on the material being dated, either the IntCal04 or Marine04 radiocarbon calibration curves (Reimer et al., 2009) were used. Marine samples were corrected using a reservoir correction value specific for each material, 1424 ± 200 yr for whale and seal bone (Berkman and Forman, 1996), 1300 ± 100 yr for molluscs (Ingólfsson et al., 1998), 1300 ± 100 yr for marine sediment (Berkman, 1998) and 1130 ± 134 yr for penguin bone (Berkman and Forman, 1996). The calibrated $^{14}C$ ages* of the data-points in the spreadsheet are presented with both $\pm 1\sigma$ and $\pm 2\sigma$ dating uncertainties. It remains a task for the community to refine the above reservoir values taking into account both location and material type.

To make some allowance for tidal uncertainty, up to 1.0 m uncertainty is added to all data-points with measurement uncertainty < 2m †. Whether this adequately accounts for paleo variations in tidal ranges must await detailed modelling.

There are subtleties that have to be assumed to be accounted for in the source publications. For example, dates based on lacustrine organisms directly above a marine-lacustrine contact may have lived in a largely marine carbon pool; some degree

*Unless otherwise indicated, stated uncertainties are $1\sigma$ values.

*All dates discussed in the main body of this article are calibrated ages. Distinctions between uncorrected, corrected and calibrated $^{14}C$ ages are only made in the spreadsheet.

†To be precise, for measurement uncertainty $\Delta M < 2m$, it is replaced by $\min(2m, \Delta M + 1m)$. At Terra Nova bay Baroni and Hall (2004) estimate 0.3 m uncertainty in mean sea level due to tidal range variations. In the Vestfold Hills maximum peak-to-peak height is 1.75 m (Zwartz, 1998).

of reservoir correction may have to be applied, the amount of correction will depend on the sedimentation rate, compaction rate and sample height above the transition etc. See Zwartz (1998) for more detail.

#### 3.4.2.2 Past ice thickness (ELEV)

As an ice sheet retreats, bedrock becomes exposed, or materials that were previously entrained within the ice become deposited on the bedrock and then exposed. By determining the amount of time since the glacially transported erratic or bedrock was last covered by ice (exposure age) and recording the altitude at which it was found, a proxy for the paleo-ice surface relative to present day bedrock is obtained. As such, this constrains past ice thickness. If a number of erratics can be dated from a similar geographical location it is possible to infer a history of the ice sheet evolution in that area (Mackintosh, 2007).

The exposure age is calculated using surface exposure dating. This technique exploits the build up of radioactive nuclides, typically $^{10}Be$ and $^{26}Al$, created when cosmic rays (neutrons) interact with the atoms of a near-surface ($<\sim$ 2 m below the surface) rock, producing radioactive nuclides. The concentration of the nuclides in the rock, after being corrected for radioactive decay, yields the length of time the rock has been exposed to cosmic radiation (Ackert et al., 1999).

The technique assumes that the sample has been subject to simple and continuous cosmogenic exposure, which due to glaciological and geological processes might not be the case. An erratic that has been supra-glacially transported and then deposited by the retreating ice sheet will yield an older age than that of a sub-glacially deposited erratic. An erratic that has undergone repeated exposures and re-burials will also yield a complex exposure age that is older than the true deposition date. Conversely, an erratic that has suffered erosion or shielding after deposition will yield a younger

age than the age of deposition. Techniques and methods exist that can be employed to identify samples that truly represent the deposition age and reject those that do not (e.g. careful selection of samples that indicate clear signs of sub-glacial transport; using two isotopes of differing half lives that decay at differing rates to identify if a sample has been subject to burial and re-exposure). A full description of the dating technique and issues can be found in other publications (e.g. Bentley et al. (2006); Mackintosh (2007); Storey et al. (2010); Balco (2011)).

After samples with complex histories have been identified and rejected, the remaining samples (assuming there is more than one sample remaining), may or may not provide a clear record of the past ice surface behaviour. If the younger samples are lower than the older samples, *i.e.*, chronostratigraphically consistent, they can be used without further processing. If, however, the older samples are lower than the younger samples, further processing must be performed. Two methods are currently employed in the literature to remedy this. The most common method is to treat the youngest erratic at the highest elevation as the most likely age of deglaciation (Bentley et al., 2006). The second method aggregates the cluster of samples into a weighted, or unweighted mean age (Todd et al., 2010).

The ages and uncertainties for the ELEV data-points are extracted directly from the source publications; no recalibration has taken place prior to inclusion in AntICE-dat as this would require access to the raw sample measurements (sample thickness, sample density, shielding correction, erosion rate etc.) for all the data-points. Often this information is not available in the source publication. Only three publications provide altitude measurement uncertainties, Bentley et al. (2006) state an error of 2%, which for the range of altitudes in the database has a max of $\sim$ 20m and an average of $\sim$ 10m. Bentley et al. (2010) state an altitude error of $\pm$ 10m and Todd et al. (2010) state $\pm$ 3-4 m. If no error uncertainty has been supplied in the source

publication ± 10 m is applied.

#### 3.4.2.3 Extent data: grounding line retreat/open marine conditions (EXT)

The record of past ice extent out onto the continental shelf and its subsequent retreat is recorded in the underlying sediment and, although a non-trivial exercise, the grounding line retreat (GLR) history can be interpreted from stratigraphic analysis of the sediment recovered in marine cores (Anderson, 2002; Heroy and Anderson, 2007; Hillenbrand et al., 2010). The ideal stratigraphic succession to record the migration of the grounding line would reflect three distinct environments: sub-glacial, glacial-proximal and open marine (Heroy and Anderson, 2007). Identifying and dating the contact between the underlying sub-glacial facies and the overlying glacial-proximal facies provides a date on the age of GLR. The transitional glacial-marine sediment is notorious for having a paucity of dateable organic matter making this an elusive, but nonetheless valuable constraint. Onset of open marine conditions (OMC), providing a theoretical minimum age for GLR, can be obtained by dating organic matter recovered above the transition zone in the overlying post-glacial glacial-marine muds and/or the diatom rich open marine sediments (Anderson, 2002; Heroy and Anderson, 2007; Livingstone et al., 2012). Although the OMC provide a qualitative minimum age for GLR, the interpretation is different for each core. For example a core might have glacial till at the base of the sediment but no dateable material, using sedimentation rates, an estimated upper and lower bound might be obtained. Another core from a different location might have no identifiable glacial-till, as such no upper or lower bound can be obtained. As there is no consistent way to apply the minimum GLR constraint we only use the OMC constraint.

The data in AntICEdat used to constrain grounded ice extent and retreat history were obtained directly from a review of paleo-ice streams (Livingstone et al., 2012).

As part of that study a comprehensive database of published Antarctica marine ice cores was compiled. The cores that provide the most reliable deglaciation ages ($^{14}C$ dating) were identified. Only cores flagged as reliable ages for initial retreat (see Fig 8a (Livingstone et al., 2012)) and with associated age errors are included in AntICEdat. All the cores from the Livingstone database were calibrated using CALIB v6.0 (Stuiver et al., 2005; Livingstone et al., 2012), the ages are replicated here.

#### 3.4.2.4 Density, spatial, and temporal spread of paleo-data

The paleo-data distribution is both spatially and temporally uneven. The spatial distribution of the sites and a color representation of the data-point density per site are shown in Fig. 3.1. There are 8 RSL sites (depicted as squares) with a total of 96 data-points and 26 ELEV sites (triangles) with 106 data-points. Of the 27 marine cores, 21 provide a dated constraint (filled circles) on grounding line retreat and the remaining 6 (open circles) record the onset of open marine conditions. The temporal distribution of the paleo-data is shown in Figure 3.2 along with key statistics. To aid data-type comparison the plot has been clipped at 30 ka. The RSL data constraint is concentrated around $\sim$ 5.0 ka for EAIS and $\sim$ 3.8 ka for WAIS, and extends no further back than $\sim$ 12.3 ka and $\sim$ 7.4 ka respectively. ELEV data is less concentrated but has much greater spread, going back as far as $\sim$ 120 ka for EAIS and $\sim$ 40.9 ka for WAIS. The marine cores are focused around $\sim$ 14.5 ka and $\sim$ 17.5 ka. The issue of heterogeneity in space-time coverage is addressed in section 3.5.3.

#### 3.4.2.5 Format of paleo-data spreadsheet.

The suites of paleo data are made available in the SOM as spreadsheets (one per data-type). They contain the source data as extracted from the publications and the associated data (if required) to convert each observation into a data-point that

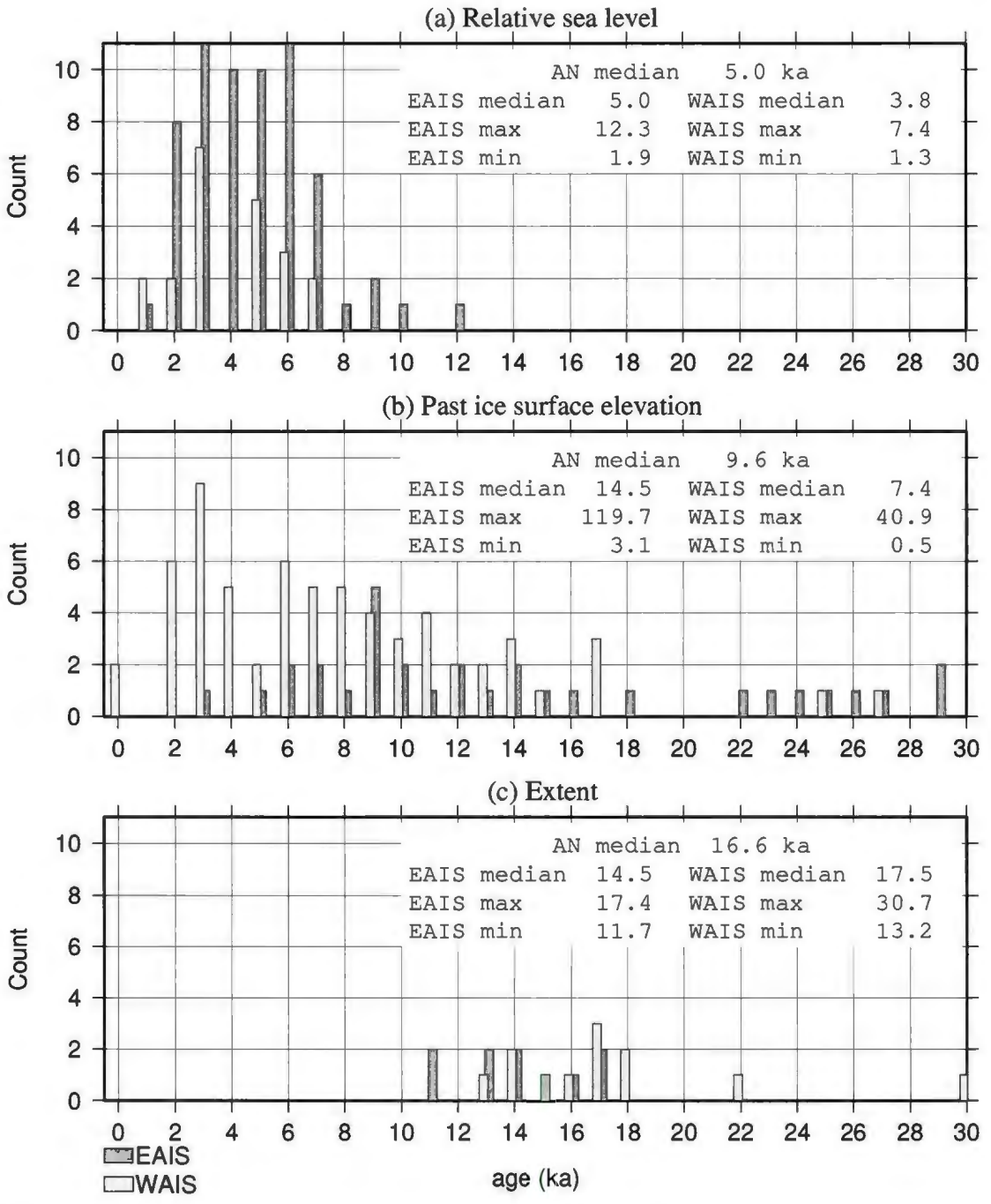


Figure 3.2: Temporal distribution (1 ka bins) and key statistics (in ka) of WAIS and EAIS data-points presented by data-type. To aid comparison between the data-types, the x axis range has been limited to 30 ka, the y axis to a count of 11. The EAIS RSL count goes to 18 and 17 at 3 ka and 6 ka respectively. ELEV data-points have an extra 11 data-points, dispersed around 32 ka (EAIS), 40 ka (WAIS), 50 ka (EAIS), 80 ka (EAIS) and 115 ka (EAIS) are thus not seen. They have been included in the statistics presented.

can be used in the evaluation process. For RSL and EXT data-types, along with the corrected and re-calibrated dates, the $^{14}C$ radiocarbon dates are also provided allowing recalibration to be performed at a later date if required. As discussed previously, there is often insufficient raw data in the ELEV publications for recalibration to be performed, as such only the published calibration date is given.

## 3.5 Evaluation Process

The evaluation process quantitatively compares model-derived chronologies against observational constraints. The following brief description is given as an overview, details are presented in the subsequent subsections. There are two primary steps: sieving (Section 3.5.4) and scoring (Section 3.5.5). Sieving is an accept/reject step used to identify clearly bad model runs based on chosen criteria. Runs that pass the sieve are then scored. The scoring process computes misfits for each data-point and combines them into data-site, data-type, and finally a misfit score for each run. For paleo-data, an observational error model (Section 3.5.2) is used to account for the inferred relationship between data and model output (combination of measurement and any observation interpretation uncertainty). The misfit scores are also weighted (Section 3.5.3) to compensate for the inequalities in the spatio-temporal density and constraint potential of the data. Each combination of sieves and weights defines a scoring scheme. This scoring process, excluding sieving, is conceptually summarised in Fig. 3.3.

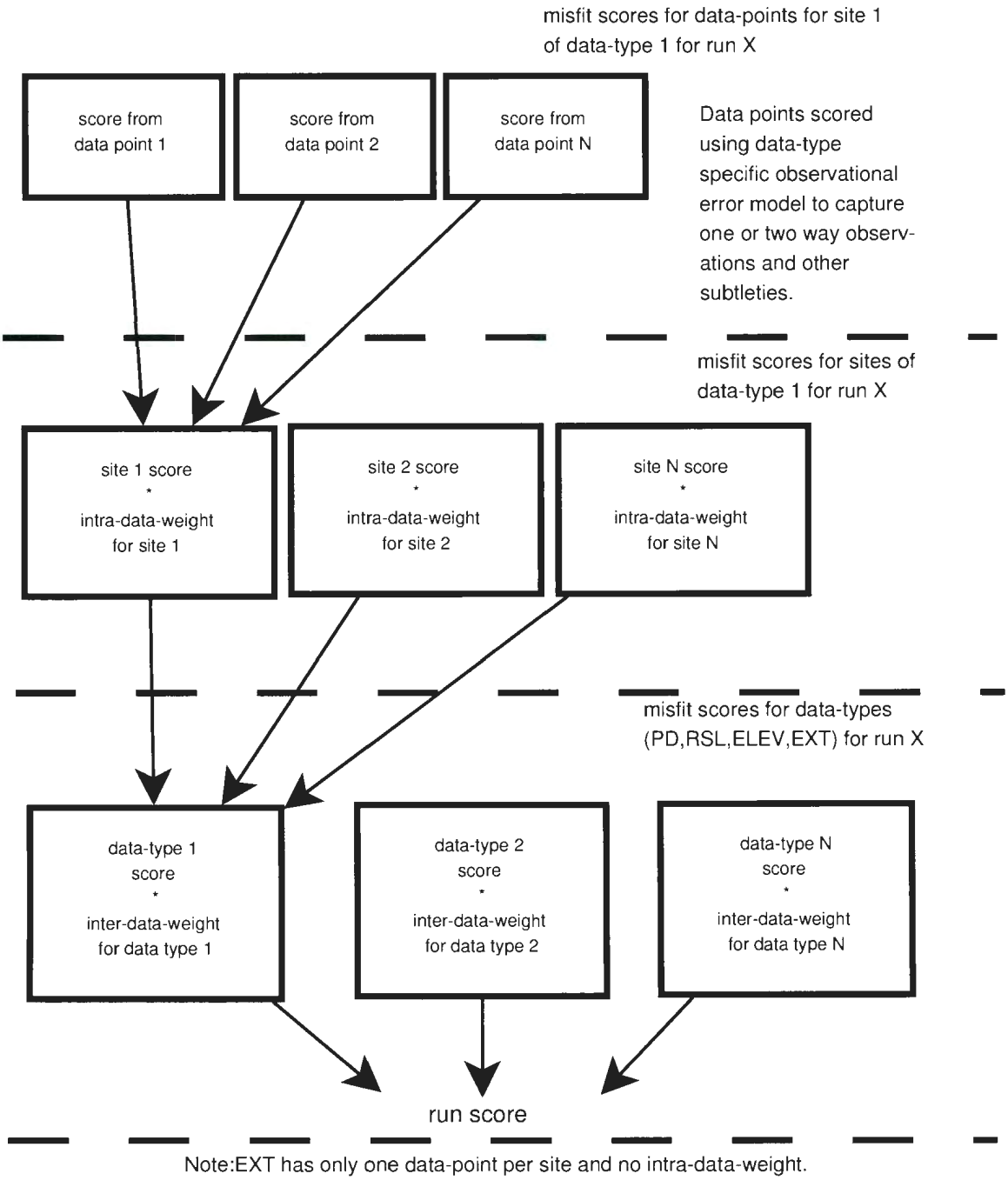


Figure 3.3: Conceptual diagram showing the evaluation process

### 3.5.1 Comment on structural error and the evaluation process

Numerical models of complex environmental systems are necessarily approximations of the real world. As such they are subject to structural uncertainty, *i.e.*, model-to-measurement misfit not attributed to measurement noise nor to uncertainty in the value of model parameters due to the inherent imperfections of a numerical model. As a result, for example, without appropriate weighting a high density of data in the Pine Island Bay region could skew the ensemble evaluation and favour runs that had strong fits to that region and poor fits everywhere else. This concept is differentiated from parametric uncertainty, *i.e.*, that due to having non-optimal values for whatever tunable parameters the model may have. Parametric uncertainty is addressed through model calibration (Hauser et al., 2011; Tarasov et al., 2012). The structural error in the GSM must be considered in the evaluation process to ensure accurate estimation of the likelihood or acceptability of each model run*.

We use a number of techniques as an (imperfect) means to account for structural error. The primary method is through data-weighting, discussed in section 3.5.3. On an intuitive level, weighting can be understood as a means to compensate for the varying spatial-temporal volume of effective constraint offered by each data-point. In addition, some allowance for structural error is made in the misfit and observation error models and in the sieves, discussed in those sections respectively.

*From a statistical point of view, the need to choose data weights arises from the lack of a complete structural error model. Such a model would fully account for the lack of statistical independence of model errors (*i.e.*, with respect to the "real world") between different data sites and data types, and thereby effectively set appropriate weights. More concretely, it would provide a population covariance matrix if there were an underlying multivariate Gaussian error structure. However, even in this case, subjective adjustments to effective weighting could still be made to further emphasize regions of interest (such as the WAIS).

### 3.5.2 Paleo-data misfit computations and observational error models

For most data, a generic form of the model versus constraint data misfit for each paleo-data-point is given by:

$$misfit = \left( \frac{mod - obs}{\sigma} \right)^2 \tag{3.1}$$

where *mod* is the model predicted observation, *obs* is the observation and $\sigma$ is the observational uncertainty. This form assumes a Gaussian error distribution.

The RSL data has the most complex error model in this study. Given non-Gaussian uncertainties with respect to marine reservoir effects and also to introduce some accounting for structural errors (especially with respect to the assumed visco-elastic structure of the earth), the RSL observational error model is implemented in a two stage approach. First, the time within the calibrated $^{14}C \pm 2\sigma$ confidence interval that gives the best model fit to observations is selected. Then a split Gaussian error model is applied. For the one-way error bounds (sea level minimum [maximum], type 2a,b [type 4a,b]) the default $\sigma$ for the lower [upper] bound is 2 m. The upper [lower] bound $\sigma$ defaults to 50 m (unless a larger value is in the database). Furthermore the component of the residual outside the 1-way error bound (*i.e.*, with the 2 m default and not the wide 50 m bound) is doubled. This doubling was found to improve results for previous calibrations of North American (Tarasov et al., 2012) and Eurasian deglaciation models. For two-way bounds the error model is assumed to be Gaussian. For type 1, the observational uncertainty is used as the misfit $\sigma$. For type 3, misfit $\sigma$ is the observational uncertainty + the uncertainty in the adjustment factor. The error model assumes that RSL data collection minimizes other potential errors, for instance, by ensuring that molluscs were found in a living position.

Each ELEV data-point provides two constraints that, combined, record thinning history. Firstly, each data-point effectively provides an ice thickness constraint at time of initial sample exposure. Secondly, because of the (assumed) continuous exposure of the sample, ELEV data-points provide a maximum thickness constraint from the age of exposure until present day. The misfit score, $misfit_{ELEV}$, for each constraint data-point is computed by calculating the smallest misfit to the observation for all past ice surface elevations identified as being part of a thinning trend. In detail, for each data site, a time-series of ice surface elevation with sea level and glacial isostatic adjustment components removed, $h(t)$, is extracted from the model output:

$$h(t) = H(t) + hb(0), \tag{3.2}$$

where $t$ is the time corresponding to the model output, $H$ is the ice thickness, and $hb(0)$ is the modelled present-day bedrock surface elevation. Both $H$ and $hb(0)$ are linearly interpolated from the model grid down to the sample location. Secondly, to ensure that the misfit is only computed against an overall deglaciating trend we identify just the thinning segments of the modelled chronology with some allowance for structural error, $\Delta h$, (so that a degree of thickening is allowed, the magnitude described below). For each site, the interpolated model ice surface elevation time series is extracted, starting at present-day working back. Ice surface elevations below the maximum ice surface elevation at that site since present-day (less the uncertainty $\Delta h$) are excluded. To compute $\Delta h$ fror each site we impose a two standard deviation elevation uncertainty, $\Delta h = \sqrt{2{\sigma_h}^2}$, with $\sigma_h$ being an adjusted observational error,

$${\sigma_h}^2 = \sigma_{hsam}^2 + (min[100, \mathcal{E}_d])^2 \,, \tag{3.3}$$

where $\sigma_{hsam}$ is the uncertainty in the sample elevation and $\mathcal{E}_d$ is a downscaling un-

certainty computed from the difference between $\text{ALBMAP}_5$ and $\text{ALBMAP}_{40}$ at the sample location. The downscaling uncertainty is on average a factor of 20 times larger than the sample error, we restrict it to a maximum of 100 m*. Finally, the misfit ELEV score, $misfit_{ELEV}$ is computed as the minimum of*:

$$misfit_{ELEV}(t) = \left(\frac{h(t) - h_{sam}}{\sigma_h}\right)^2 + \left(\frac{t - D_{sam}}{\sigma_{Dsam}}\right)^2, \tag{3.4}$$

where $h_{sam}$ is the sample elevation, $D_{sam}$ and $\sigma_{Dsam}$ are the sample age and age uncertainty respectively.

The EXT data-points provide either a two-way constraint that records the grounding line retreat (GLR) or a nominally one-way constraint that provides a date for the onset of open marine conditions (OMC). The misfit score for the GLR constraint is computed from the residual between the observed and modelled age of the GLR event. The modelled age, computed from a floating/grounded ice mask, is the time of the most recent transition from grounded ice to floating ice. The flotation criteria is computed using the Lisiecki (2005) stacked deep-sea-core $\delta^{18}$O record as a proxy for sea level departure from present (Pollard and DeConto, 2009), the modelled ice thickness $H$, and basal elevation $hb$ (corrected for isostasy in the GSM)†. As with the ELEV misfit calculation, $H$ and $hb$, are computed by linearly interpolating from the model grid down to the core location. To improve the misfit resolution, the 1 kyr model output is linearly interpolated to 100 yr. The misfit $\sigma_{GLR}$ is computed as,

$${\sigma_{GLR}}^2 = \sigma_{obs}^2 + \sigma_{struct}^2, \tag{3.5}$$

*For the 106 ELEV samples in the database the mean of $\mathcal{E}_d$ is 191 m, the maximum is 504 m. The mean measurement uncertainty is 10 m.

*This is the Mahalanobis distance.

†As opposed to that of the RSL calculation, the gravitational components of sea level change are currently not taken into account for determination of the flotation condition for the EXT scoring. This potentially induces a sea level error of up to approximately 20 m (Weber et al., 2011).

where $\sigma_{obs}$ is the dating uncertainty (calibrated $^{14}C$ age $1\sigma$ confidence interval) and $\sigma_{struct}$ ($\pm$ 250 yr) is included to give some allowance for structural error and bathymetric uncertainty. As more such data accrues with resultant increased weighting, consideration should be given towards a more complete error model that fully takes into account upscaled bathymetric uncertainties along with full accounting of the gravitational components of sea level change.

For the OMC one-way constraint we again use a split Gaussian error model. A floating ice/ocean mask is used to locate the model time of the most recent transition to open marine conditioms. If the modelled OMC event occurs after the observation age we use a smaller $\sigma_{OMC}$ in the same manner as for $\sigma_{GLR}$, but with a larger structural error allowance of 500 yr *i.e.*, half the model output resolution. If the modelled event occurs earlier than the observation an additonal temporal uncertainty, $\sigma_{1way}$ (500 yr) is added to account for the larger uncertainty in the relation of the date to the onset of OMC conditions. This gives,

$$\sigma^2_{OMC} = \begin{cases} \sigma^2_{obs} + \sigma^2_{struct} & \text{transition to OMC later then observation age} \\ \sigma^2_{obs} + \sigma^2_{struct} + \sigma^2_{1way} & \text{transition to OMC earlier than observation age.} \end{cases} \tag{3.6}$$

### 3.5.3 Weighting

Given the lack of a complete structural error model, weighting necessarily involves a judgement component. Given the resultant added layer of uncertainty from such judgements, plausible weight ranges are chosen and evaluation sensitivity to variations in weights are assessed. We differentiate between two types of weighting: intra- and inter-data-type weighting. Intra-data-type weighting accounts for the difference in

the data density within each data-type, at each site, and inter-data-type accounts for the different constraint data-types.

#### 3.5.3.1 Intra-Data-Type weighting

The intra-data-weighting accounts for the differences in data density within the data-types. This is predominantly a problem for RSL and ELEV data where the effective spatial-temporal volume of constraint of individual data-points overlap (as inferred from Fig.3.1).

Inverse areal density weighting is applied to account for differences in the spatial density of data-points (of the same data-type) between sites that are located in close proximity to each other. Following Tarasov et al. (2012), the relative site weight is computed as the square root of the number of data-points at a site divided by the square root of the number of regional data-points. The square root dependence is chosen to better reflect the relation between the effective constraint value and the number of data points at each site. The region size ($10^o$ of longitude by $5^o$ of latitude) is approximately the characteristic scale-size of visco-elastic response. To reduce grid dependence, the final weight is computed from an average of four such weight determinations, the region shifted at each computation by $5^o$ of longitude and $2.5^o$ of latitude. The inverse areal density weighting is only applied to the ELEV and RSL data-types. These data-types have an uneven site distribution and data-density with sites in close spatial proximity. The computed weighting can be seen in Figure 3.4. Once computed and applied, the intra-data-type weighting are not adjusted.

EXT sites all comprise a single core per site, are relatively well spaced. As such no intra-data weighting is computed for EXT data.

PD data is decomposed into five components. The MSE for Wg, Wf, and Et are calculated from ice thickness data and each given unit weighting. The squared mis-

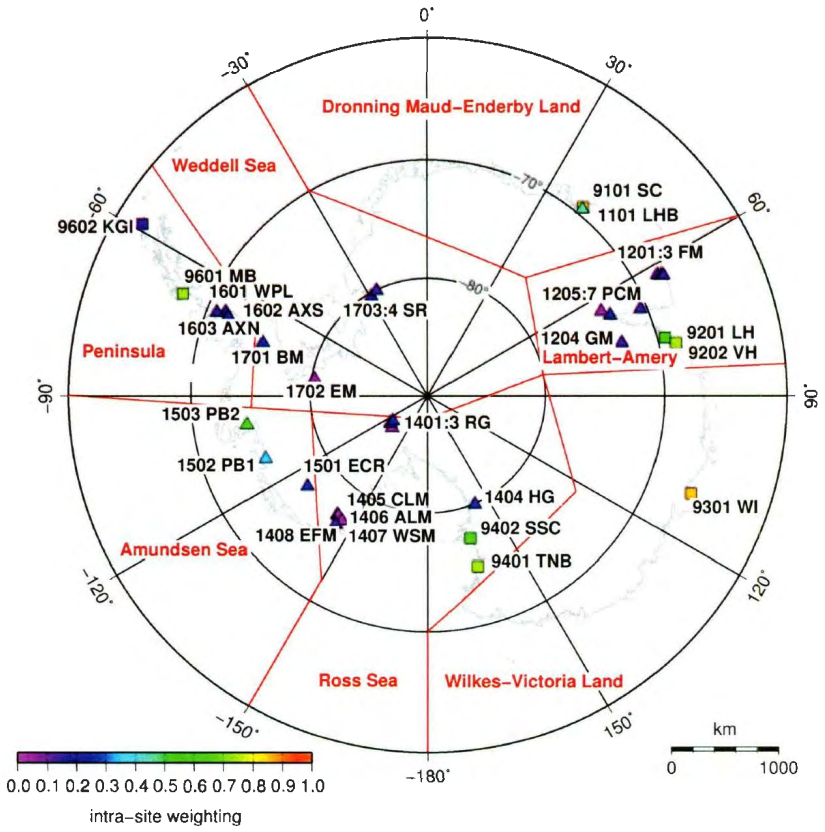


Figure 3.4: Intra-data-type weighting as calculated by the inverse areal density weighting method. Note, although RSL (squares) and ELEV (triangles) use the same color scale, the weighting is computed separately for each data-type. There is no intra-site-weighting for EXT as each site is a single point and in nearly all cases there is sufficient separation between the sites to nullify the need for weighting

fits (SE) for ShfAr and RISgl position are each given a default weighting of 0.333. The extra weight accorded to floating ice and grounding line position (*i.e.*, relative to weighting in proportion to area coverage) was chosen in the context of current concern over the dynamic stability of those components. As noted above, these weightings implicitly include an unquantified uncertainty (*i.e.*, $\sigma$ in the Gaussian error model). When/if uncertainty estimates for the ALBMAP dataset become available, their explicit incorporation into the PD error models would therefore entail an adjustment to the above weightings.

#### 3.5.3.2 Inter-Data-Type weighting (volume of influence)

To compute the relative amount of constraint provide by different data-types, we introduce the concept of a volume of influence; the approximate space-time volume of grid-cells (*i.e.*, $\int\int\int dxdydt$ over model output) that are highly correlated with one or more given grid-cells containing the constraint data over the temporal range of the data. Thus the larger space-time volume of the ice sheet linearly constrained by the data, the larger the volume of influence. Relative weights for different sets of data can then be assigned in proportion to their relative volumes of influence.

In detail, relative weights for constraint data-types were determined as follows. First the volume of 90% influence for each data-point was computed using an initial "best-fit" sub-ensemble of 400 model runs (selected on the various subjective weighting and sieve conditions). For each one ka time-slice, the dimensions of the spatial area of influence were approximated by the 90% correlation length scales in the latitudinal and longitudinal directions. As implemented, these length scales were determined by finding the grid-points for which ice thickness or ground elevation correlations with the grid-point covering the data-site had a value closest to 90%. These correlation grid-points thereby bound a rectangle of grid-cells which are highly correlated with

the data-site grid-cell. For any time-slice, the area of this rectangle provides a relative measure of the constraint potential of the data-point for that time. These correlation areas were then summed over all one kyr time-slices (i.e. correlations were computed against the grid-cell and time-slice covering the data-point)*.

For each data-type, the total volume of influence was then set to the sum of associated data-point volumes of influence. Intersecting volumes of influence were partitioned equally to the associated sites so that no double counting of volume occured. Inter-data-type weights were then set in proportion to their corresponding total volumes of influence.

This process could have been disaggregated to the determination of individual weights assigned to each data-point. However, given a number of associated issues such as the extent to which spatially-temporally proximate (i.e. within 90% correlation) constraint data-points are not redundant, we chose the current approach. Using the above approach, the following weights are computed: present-day (MSE + SE)=0.83; RSL=0.08; ELEV=0.07, and EXT=0.02† We define these values as the baseline weighting. As part of the scoring scheme assessment below, we test the scoring sensitivity to variations in these relative weights.

### 3.5.4 Sieves

Sieves reject runs that do not meet a specified criteria. Sieves are difficult to defend on a statistical ground except for a fundamentally non-continuous characteristic. For any continuous characteristic (such as eustatic sea level contribution at some time),

*Mathematically, for the case of ice thickness $H$, the volume of influence for a constraint data point with space-time location $(x_p, y_p, t_p)$ is $\int\int\int dxdydt$ over the set of x, y, t, such that Correlation$(H(x,y,t), H(x_p,y_p,t_p)) \sim\geqq 90\%$. Statistically, this can be viewed as a very approximate approach to diagonalize the structural error matrix.

†An 80% correlation cutoff was also tested, but it further increased the PD relative weight to 0.86.

it is highly unlikely that there is a threshold below which scientific understanding of relevant processes and data uncertainties would lead to absolute rejection of model runs and above which absolute acceptance with no penalty. However, the abrupt nature of sieves permits clearer conceptual analysis and on that account they merit consideration.

The sieve used in this study is for Eemian (the last interglacial period beginning approximately 129±1 ka, lasting until at least 118 ka (Overpeck et al., 2006)) eustatic sea level. Unless an assumption is made about present-day thermodynamic equilibrium, glaciological modelling of Antarctica necessarily must be initiated a few glacial cycles prior to present. The GSM used in this study (description in prep.) models the AIS from an equilibrated start at 391 ka to present-day and therefore Eemian sea level estimates can provide a useful sieve criteria. The most recent probabilistic estimate for maximum mean Eemian sea level change relative to present (Kopp et al., 2009) is greater than 6.6 m with 95% confidence and greater than 8.0 m with a 67% and unlikely to be greater than 9.4 m. That study also estimated with 95% confidence, that the maximum Southern (therefore mostly AIS) contribution was greater than 2.5 m. When interpreting these estimates, it should be noted that the associated confidence intervals do not take into account the structural uncertainties due to the approximations invoked. Maximum Greenland Eemian contributions have been conservatively estimated to be 2-5.2 m with a more likely range of 2.7-4.5 m (Tarasov and Peltier, 2003). It is unlikely however, that minimal ice Eemian ice volumes for the two ice sheets occurred synchronously.

With these considerations along with some allowance for structural model errors, we use two sieves for the maximum Eemian (130 ka to 120 ka) ESL contribution relative to the (modelled) present-day value. The wide sieve acceptance range is -1 to 10 mESL, the narrow is 1 to 8 mESL. Runs that have a maximum ESL contribution

within the sieve range at anytime between 130 ka and 120 ka will pass the sieve. It is worth noting that the maximum contribution in current ensembles is less than 6 mESL, so the upper bound for acceptance has no impact.

### 3.5.5 Scoring and scoring schemes

Each run that passes the sieve(s) is attributed a score that represents the misfit to the observations (see Fig. 3.3). The score for each run is calculated as follows. First, the mean-squared-error (MSE) for the paleo data-sites is computed from the individual data-points at that site. This is calculated in accordance to the error model (Section 3.5.2). To account for differences in the data density of observations at each site, the resultant site score is scaled by the intra-data-type weighting (Section 3.5.3.1). The weighted site scores are then summed to produce a misfit score for each data-type*. The present-day constraints are treated as as a single data-type (all originating from the ALBMAP data-set). The scores for each of the 5 subsets of the present-day constraints are individually normalized across the ensemble and then combined to provide a present-day data-type misfit score.

To compute the final run score, each data-type score is normalized to the mean of the scores for that data-type. Thus unit variance on each data-type score across the ensemble is imposed. Inter-data-type weighting is then applied in proportion to the inferred spatial-temporal volume of influence of each data-type (Section 3.5.3.2). The weighted data-type scores are then summed to produce the final run score. Considered together, this gives a set of misfit scores (lower scores meaning better fitting runs) for that combination of sieves (if used) and weights. The choice of weightings (weighting factors can be set to zero to exclude data-types) and sieves that are used to evaluate

*The MSE for the sites are treated as log-likelihoods of assumed underlying multivariate Gaussian error models and as such can be directly summed.

the runs define a single scoring scheme.

### 3.5.6 Assessment of scoring schemes

Given the uncertainties in weighting and thereby its tentative nature, it is important to assess sensitivity to the choice of weighting scheme and the extent to which past and present-day data provide a coherent set of constraints. We have applied a range of scoring schemes to the same ensemble of 2929 runs from the Memorial University/Penn State University GSM (in prep.) configured for the AIS*. The scoring schemes are named to reflect the data-types, weighting and/or sieves they employ. PDx schemes use only present-day constraints (Wg, Wf, Et, ShfAr and RISgl), where x is a unique identifier for the scheme, e.g. Scheme PDa is unique from scheme PDb. PDxPx schemes use both present day and paleo-data (RSL, ELEV, EXT), again x is unique identifier. To examine the correlation between the impact of past and present constraints we also define a scheme, PALa, which employs only the combined paleo data-types (with the baseline inter-data-type weighting). Scheme PDxPxSEy employs all data and one of the sieves, the sieve identified by y. PxSEy only uses a sieve and paleo-data. To explore the sensitivity of the paleo-data weighting we use scheme PDcPaSEb as the baseline scheme (all constraint data, baseline intra-data-weight weightings and the narrow Eemian sieve), and adjust the individual paleo-data type weightings around that reference. These paleo-data sensitivity schemes are identified as PDcPaDdSEb, where D is the data-type and d is the weighting.

*The GSM includes a 3-D thermo-mechanically coupled dynamical core that models the sheet/stream/shelf flow regimes (with shallow ice or shallow shelf representations as appropriate) (Pollard and DeConto, 2009), a sub-grid grounding line flux parameterization (Schoof, 2007), and visco-elastic bedrock response. It currently has 31 ensemble parameters to capture uncertainties in the glacial cycle climate, the mass-balance processes, and in the ice dynamics. An ensemble of 3000 random parameter vectors was generated via Latin hypercube sampling from univariate distributions chosen to cover plausible parameter ranges. From the original ensemble of 3000 runs, 71 suffered numerical instability and were aborted.

The sensitivity of mean AIS grounded ice volume in meters eustatic sea level equivalent (mESL)[†] to various scoring schemes is presented in the time-series plots of Fig. 3.5 and in the summary of results given in Table 3.4. The table also includes a description of the scoring scheme characteristics. We have chosen total grounded ice volume (volg) as a summary statistic given the high current scientific and societal interest in past and future eustatic sea level contributions from Antarctica (in the summary Table 3.4 the volumes for present day [vol0g] and LGM [vol20g] are presented). The grounded ice volume is computed as a unweighted average from the lowest scoring (best) 10 runs, as evaluated by each scoring scheme. Given the relatively small random ensemble, unweighted averages offer a more robust characterization of sub-ensembles that could otherwise get skewed by the existence of a single highest scoring run if weighted averages were used. The 10-run cut-off was arbitrarily selected as per experience with the analysis of previous ensembles.

The vol20g sensitivities to the scoring schemes in Table 3.4 are generally less than 1.5 mESL (relative to the base PDcPaSEb scheme with narrow sieve) except for the 2.6 mESL vol20g difference for the scheme with reduced RSL weighting (PDcPaR04SEb). For all schemes that include present-day components, the values for LGM excess relative to present day ($\Delta\xi$) are within 1.2 mESL of the 7.23 mESL value for the base PDcPaSEb (with the same PDcPaR04SEb exception as above). The EXT component has no impact even when assigned a weight value of 0.04, double that inferred from its computed volume of influence. This is perhaps not surprising given the geographically peripheral nature of such data which is reflected in its relatively low volume of influence.

[†]We use a conversion factor of 2.519 x $10^6$ $km^3$ of ice = 1 mESL.

Table 3.4: Summary table of scoring schemes presenting scheme characteristics, grounded ice volumes (mESL) computed from the average of the best 10 runs for 20 ka (vol20g) and 0 ka (vol0g), and the equivalent sea level contribution ($\Delta\xi$) from AIS between 20 ka and 0 ka ($vol20g - vol0g$ ). To facilitate comparison between schemes, the difference between volg computed by each scheme and a reference volg (ALBMAP at 0 ka and PDcPaSEb at 20 ka is also presented. All volumes and differences are in mESL. Note that the apparent total lack of sensitivity to certain weight variations would not occur if weighted averages were displayed (*e.g.*, PDcPaR16SEb and PDcPaEL035SEb both select the same ten lowest scoring runs, but the scores, and order of runs, are different)

| name | characteristics | vol20g mESL | vol20g(scheme) - vol20g(PDcPaSEb) mESL | vol0g mESl | vol0g(scheme) - vol0g(ALBMAP) mESL | $\Delta\xi$ mESL |
|---|---|---|---|---|---|---|
| ALBMAP | | - | - | 62.62 | - | - |
| PDa | Equal weighting per unit area for the MSE metrics Wg, Wf & Et | 71.59 | 1.16 | 63.96 | 1.34 | 7.63 |
| PDb | Equal weighting ofthe MSE metrics Wg, Wf & Et (1:1:1) | 71.34 | 0.91 | 63.73 | 1.11 | 7.61 |
| PDc | As PDb for Wg, Wf & Et and 1/3 weighting for both ShfAr & RISgl (1:1:1:1/3:1/3) | 71.21 | 0.78 | 63.63 | 1.01 | 7.58 |
| PDcPa | 0.83*PDc+0.08*RSL+0.07*ELEV+0.02*EXT | 69.88 | -0.55 | 62.40 | -0.22 | 7.48 |
| PDcPb | 0.83*PDc+2*(0.08*RSL+0.07*ELEV+0.02*EXT) | 70.46 | 0.03 | 62.04 | -0.58 | 8.41 |
| PALa | 0.08*RSL+0.07*ELEV+0.02*EXT | 69.40 | -1.03 | 58.94 | -3.68 | 10.45 |
| PDcPaSEa | PDcPa+Eemian wide | 70.23 | -0.20 | 62.65 | 0.03 | 7.58 |
| PDcPaSEb | PDcPa+Eemian narrow | 70.43 | - | 63.20 | 0.58 | 7.23 |
| PDcPaR04SEb | as PDcPaSEb but 04*RSL | 73.03 | 2.59 | 63.28 | 0.66 | 9.75 |
| PDcPaR16SEb | as PDcPaSEb but 16*RSL | 69.12 | -1.31 | 62.77 | 0.15 | 6.35 |
| PDcPaEL035SEb | as PDcPaSEb but 035*ELEV | 69.12 | -1.31 | 62.77 | 0.15 | 6.35 |
| PDcPaEL14SEb | as PDcPaSEb but 14*ELEV | 71.79 | 1.36 | 63.40 | 0.78 | 8.39 |
| PDcPaEX01SEb | as PDcPaSEb but 01*EXT | 70.43 | 0.00 | 63.20 | 0.58 | 7.23 |
| PDcPaEX04SEb | as PDcPaSEb but 04*EXT | 70.43 | 0.00 | 63.20 | 0.58 | 7.23 |
| PDcPbSEb | PDcPb+Eemian narrow | 70.20 | -0.23 | 62.82 | 0.20 | 7.38 |
| PaSEb | PALa+Eemian narrow | 70.48 | 0.05 | 61.29 | -1.33 | 9.19 |
| PDdPaSEb | 1:1:1:1:1/3 + PaSEb | 70.41 | -0.03 | 63.50 | 0.88 | 6.90 |
| PDePaSEb | 1:1:1:0:1/3 + PaSEb | 71.69 | 1.26 | 63.10 | 0.48 | 8.59 |

The ice volume chronologies in Fig. 3.5a show the impact of the different present day data only (PDx) schemes, the composite paleo-data schemes including those with the Eemian sieves (PDxPx, PDxPxSEy) and the scheme that does not use present-day data (PALa,PALaEy). Fig. 3.5b focuses on the impact of the individual paleo data-types.

The first set of schemes, PDx (Fig. 3.5a) use various combinations of present-day metrics (Wg, Wf, Et, ShfAr and RISgl) to score the runs. Three schemes are shown: PDa using equal weighting per unit area (and therefore simply the unweighted MSE for the whole ice sheet), PDb with equal weighting of the three MSE metrics (*i.e.*, after normalization across the whole ensemble) and PDc, equal weighting of the three MSE metrics and additional constraint provided by RISgl and ShfAr. The proximity of the mean vol0g to that of ALBMAP improves sequentially with these metric refinements, with the PDc selected sub-ensemble having a vol0g value within $\sim$ 1 mESL of ALBMAP.

The second group of schemes in Fig. 3.5a highlight the impact of employing the paleo-data with baseline weighting (PDcPa), 2x baseline weighting (PDcPb), and with the exclusion of the present-day data (PALa). The importance of employing the present day constraint is clearly seen in scheme PALa as the final volg0 is $>$ 3m from ALBMAP. As a contrast, the addition of paleo-data with baseline weighting to present-day constraints (*i.e.*, PDcPa as compared to PDc) draws the mean vol0g closer to the ALBMAP reference*. However, the LGM contribution is similarly reduced; the net impact on the $\Delta\xi$ in comparison with PDc is therefore small (<0.1 mESL). Doubling the baseline paleo weighting (PDcPb) drives vol0g lower than the value with baseline weighting and, conversely, increases the LGM contribution. This pushes $\Delta\xi$

*Those puzzled but such behaviour need to remember that vol0g is not a part of the present-day constraints. One should not, however, infer that the addition of paleo constraints will necessarily improve vol0g fits for any random ensemble.

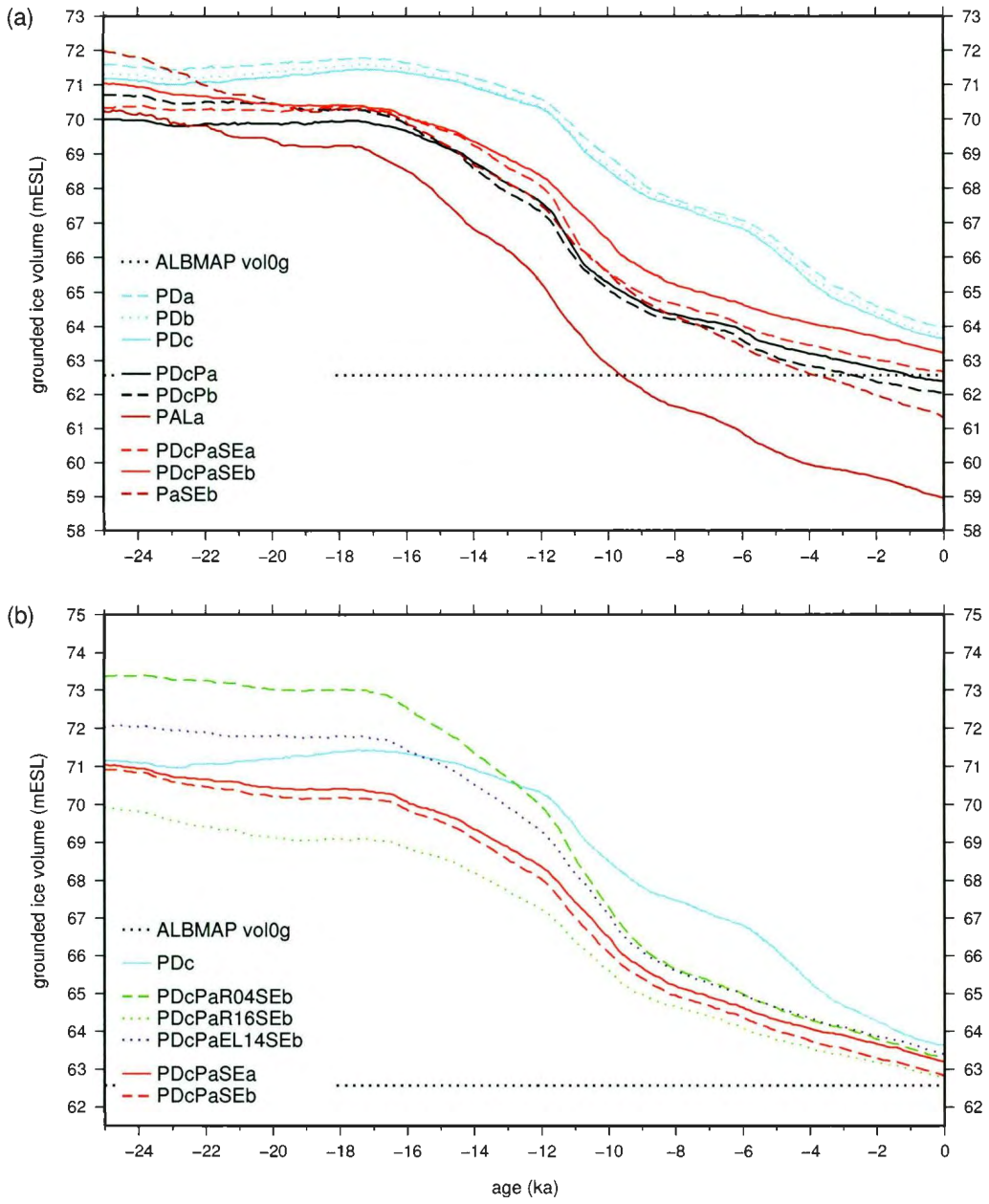


Figure 3.5: Time series of volg (mESL) generated from unweighted average of lowest scoring 10 runs as evaluated by scoring schemes listed in the legend. Upper plot (a) shows present-day data schemes (PDx), all data schemes PDxPx, all data plus the Eemian sieves (PDxPxSEy) and just paleo data (PALa & PaSEb). Lower plot (b) focuses on the combined and individual paleo-data types. ALBMAP vol0g, PDc, PDcPaSEb (the baseline scheme) and PDcPaSEa are presented in both plots to aid reference.

to 8.4 mESL, nearly 1 mESL larger than PDcPa.

The third group of schemes in Fig. 3.5a utilize the sieves. Of the total 2929 runs, 1868 pass the wide sieve and only 214 runs pass the narrow sieve. The wide sieve further improves the predicted vol0g, $\Delta\xi$ is within 0.1 mESL of PDa and PDaPc. The narrow sieve PDcPaSEb, used as the reference scheme, draws the mean vol0g away from the ALBMAP target by 0.6 mESL and decreases $\Delta\xi$ to 7.2 mESL. The importance of including present day constraint is re-illustrated in scheme PaSEb although, the resultant vol0g is much improved over scheme PALa.

The schemes presented in Fig. 3.5b were chosen to assess the impact of the paleo data-types using PDcPaSEb as the base. The sensitivity of the scores to each data-type is explored by halving and doubling the baseline weightings for a single data-type whilst holding the weighting for the other types constant. Three schemes that are shown in Table. 3.4 are not plotted as they have an identical trajectory to other schemes: PDcPaEX01SEb and PDcPaEX04SEb both overlie PDcPaSEb, PDcPaEL035SEb overlies PDcPaR16SEb. This is consequence of using the unweighted average. The schemes produce different scores but the same ten runs are selected, thus the same trajectory is generated. The non-linear response of vol20g to the various constraints is evident in Fig. 3.5b and Table 3.4, for instance, increasing the weight of the RSL data decreases vol20g, whereas increasing the weight of ELEV causes an increase in vol20g.

To further illustrate the importance and impact of metric components on resultant best runs from scored sub-ensembles, Fig. 3.6 shows the difference plots between present-day modelled ice thickness (H) and $\text{ALBMAP}_{40}$ thickness for four top runs from various schemes. Run nn3506 (top left) had the best score from PDcPa and PDcPaSEa (*i.e.*, with and without the wide Eemian sieve) but did not pass the narrow Eemian sieve. Run nn2679 was the top run with base scoring scheme (PDcPaSEb,

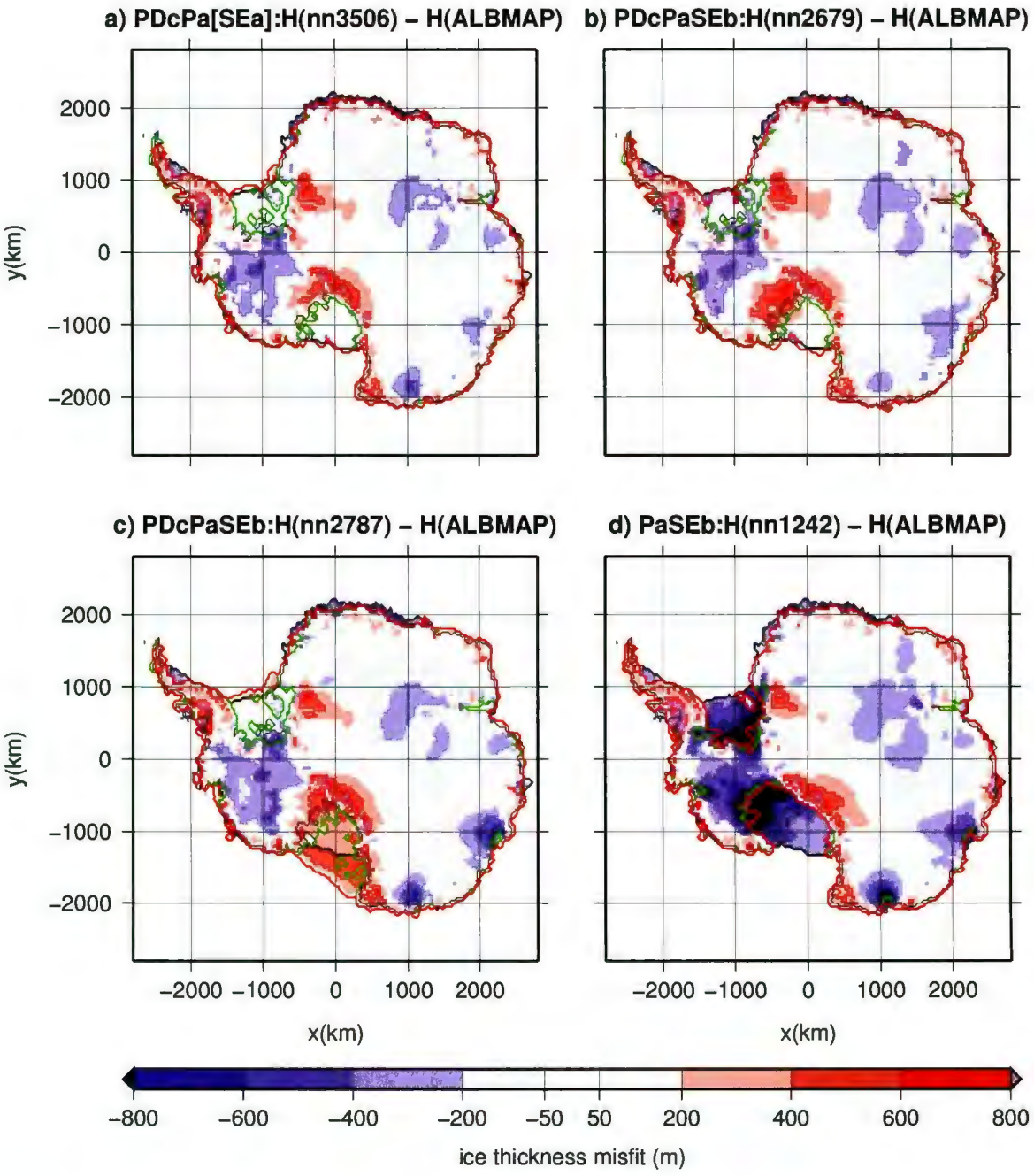


Figure 3.6: Modelled present day minus observed present day ice thickness for (a) the best run as scored by schemes PDcPa[SEa], (b) by scheme PDcPaSEb. The necessity for a shelf area metric is shown by run nn2787 (c). Run nn1242 (d) highlights the importance of present day data; scheme PaSEb does not use the present day constraint. Black line is ALBMAP grounding line and shelf edge, green line is modelled grounding line and red line is modelled shelf edge.

*i.e.*, with narrow Eemian sieve).

Run nn2787* was also within the 10 best subset for PDcPaSEb and illustrates the importance of the ice shelf area metric, ShfAr. It is the only run within the top best 10 subset with a large misfit in present-day ice shelf extent. Without the ShfAr metric component (PDePaSEb, summarized in Table 3.4), there are a total of four runs with such large (or larger) misfits of ice shelf extent within the best 10 runs. Increasing the relative weighting of the ice shelf area metric from 1/3 to unit value (PDdPaSEb, so that ShfAr misfit has the same weight as each of the three MSE components for present-day ice thickness) eliminates nn2787 from the top 10 subset. A future consideration would be to add a metric component that compares mean marine margin misfit.

Run nn1242 was the third best run for PaSEb (no present-day constraints, with Eemian narrow sieve) and illustrates the lack of positive correlation between fit to past and present-day constraints and thus the important of employing both present and paleo-date. The majority of other runs identified as good by PaSEb have a similar 'reduced WAIS' configuration, likely provoking the low vol0g seen in Fig.3.5 and Table 3.4 especially when Eemian sieves are not imposed (PALa). Indeed the top two runs for PALa, not shown, have fully collapsed WAIS configurations. The baseline present-day constraint component (PDc) has 0.0 correlation with the total paleo component (PALa) across the whole ensemble, and a weak negative (-0.4 to -0.2) correlation when only the top 10 or top 100 runs are considered (as selected by PDcPaSEb). Therefore, on the full raw ensemble scale, the two classes of constraints are statistically independent (at least in a linear sense). Under scoring (including sieving), the weak negative correlation implies that there is a trade-off between fits to past constraints and present-day (topographic) constraints. This therefore underlines

*nn stands for neural-network as the runs are part of a neural-network based model calibration.

the importance of a clearly specified (and justified to the extent possible) weighting scheme and documented sensitivity analysis thereof.

For the context of ensemble evaluation, it makes sense to include all data-types (especially given the lack of positive correlation between PALa and PDc scores). Given the relatively small weight (17%) assigned to paleo constraints, we have chosen an uncertainty range for scoring schemes to be given by the set: PDcPaSEb (base set with weights as per volume of influence), PDcPbSEb (base with doubled weight on paleo data), and PDcPaSEa (base with wide Eemian sieve). Although the narrow Eemian sieve has some allowance for structural error, lacking clear bounds on both model structural error and Eemian sea level estimation uncertainty (Lambeck et al., 2012) we judged it necessary to include one scheme with a wide Eemian sieve. From Table 3.4, these 3 schemes have a maximum difference in $\Delta\xi$ of only 0.35 mESL.

## 3.6 Discussion: relating model output to data

A data-centric view further illustrates some of the issues involved in relating model output to paleo observations that led to the above methodology. Fig. 3.7 and 3.8 show paleo-data observations and corresponding sample model results from two ELEV sites and from four RSL sites. The model results were chosen to provide examples of runs selected by schemes that use all the constraint data (best run from PDcPa[SEa] and PDcPaSEb), using no paleo-data (PDc), and without present-day data (PALa).

Fig 3.7 is a comparison of ELEV sites 1502 and 1404. The maps of the topography, taken from the ADD (SCAR, 2006) dataset are overlain with the 40 km GSM grid. Site 1404, Hatherton Glacier is located in the middle of the Transantarctic mountains in a complex region of outcrops, ridges and sub-grid fast flowing glaciers. ALBMAP is at a resolution of 5 km and thus will not resolve much of the described detail of

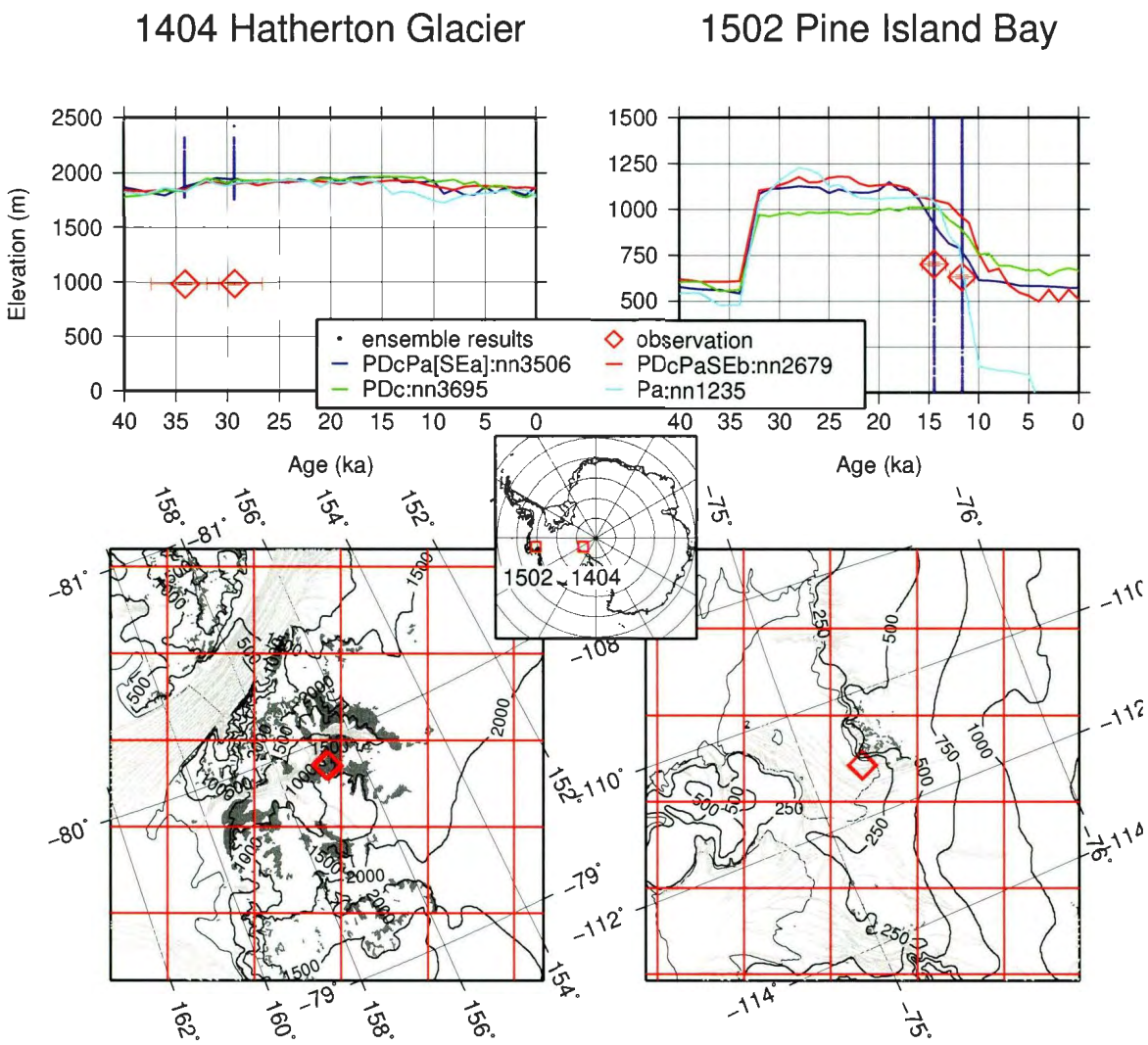


Figure 3.7: Plots showing maps and age-altitude plots for ELEV site 1404, a topographically complex region and ELEV site 1502, a topographically simple region. The maps are overlayed with the 40 km model grid, highlighting the disparity between reality and the GSM. The observations, proxies for the past ice sheet surface elevation, are indicated as red diamonds. The map inset shows the location of the sites on the Antarctic Continent. The upper age-altitude plots display the past ice surface observations (red diamonds), the ensemble of modelled ice surface elevation results (spread of blue dots) and the evolution of the modelled ice surface at that site for the best run as identified by PDcPa[SEa], PDcPaSEb, PDc and PALa.

this location. Once the dataset has been interpolated to 20 or 40 km, any detail will likely have been obliterated. In contrast, site 1502 at Pine Island Bay, is topographically simpler with gentler gradients. The age-elevation plots above the maps show the ELEV observations and associated uncertainties, and the corresponding set of modelled ice surface elevations, relative to present day topography.

At site 1404, no runs are able to achieve a modelled past ice surface elevation that is $< \sim$ 750m above the present-day ice sheet surface indicated by the observations. There is also little variation in the best four runs. At site 1502 the spread of ensemble results (clipped at the axis) is about three times larger than that of site 1404. The systematic model misfit of site 1404 suggests that the large scale impacts of its regional basal topographic complexity cannot be captured by the model. This misfit implies that the data at site 1404 has lesser constraint value in contrast to that of site 1502. Conversely, as a possible indicator of systematic model error, site 1404 could have value in the formulation of a structural error model for the GSM. In this specific case, the impact of excluding present-day data constraints is evident in the lower present-day elevation of run nn1235 at site 1502.

Model generated RSL curves (taken from the same runs as presented in Fig. 3.7) and the RSL constraint data for four sites are shown in Fig. 3.8. Three of the sites have been selected as their data is (relatively) homogeneous in providing either one-way lower (site 9101, type 4a, mollusc), one-way upper (site 9601, type 4b, penguin bones recovered from a raised beach) or two-way bounds (site 9402, type 3, shell fragments deposited on a raised beach, providing a close age on the beach). Site 9201 contains a mixture of all three bounds (type 1, 2a and 2b retrieved from sediment cores). Site 9402, at the foot of the Transantarctic mountains, is in the vicinity of ELEV site 1404 show in Fig 3.7, where there is a bias for the model to have excess ice. This site, with these runs, demonstrates the impact of using only paleo-data or only

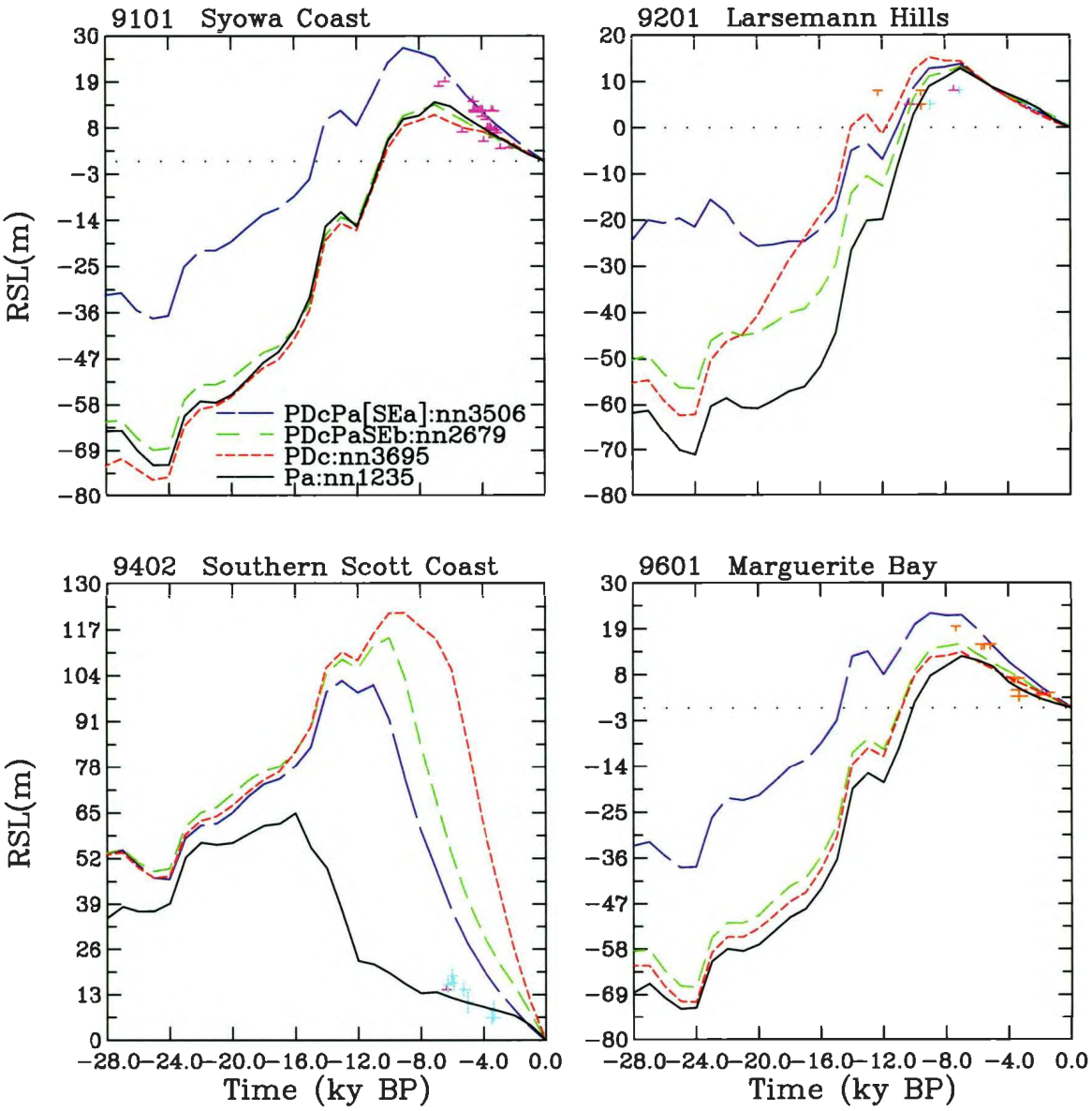


Figure 3.8: Plots showing representative RSL data points and sea level curves from RSL sites 9101, 9201, 9402 and 9601. Observed RSL data-points are colour coded according to the constraint they provide: light blue, two-way (type 1, dated sea level or type 3, close age), mauve, one-way lower-bounding (past sea level above: type 2a data of inundation or type 4a maximum age of beach) and orange, one-way upper bounding (past sea level below: type 2b, date of isolation or 4b, minimum age of beach). One-way error bars are generally indeterminate in their non-bounded direction, though not shown as such to avoid clutter. Note the runs are identical to those presented in Fig. 3.7.

present-day data. The two runs scored by schemes that combine both data-types fall between the only paleo-data or only present-day schemes, highlighting the benefits of employing each data-type. The plots also show how, generally, older data can provide a tighter constraint on the RSL curves. For example, the older data of site 9201 reduces the divergence in the late Holocene signals in comparison to the other sites. Alternatively, variation between RSL curves (or lack thereof) can also indicate the constraining potential that a site might provide, if all the trajectories followed the same track the site would provides less constraining potential than a site with large variation in the curves.

## 3.7 Summary, Future Work and outstanding issues

In this article we have presented a method to quantitatively evaluate model-derived deglaciation chronologies using observational data. This is part of a larger project to generate a deglacial probability distribution for the AIS. As such we have used the AIS as an example against which to develop the process. However the issues raised and the methods designed to tackle them are pertinent to the evaluation of any ice sheet reconstruction.

A diverse constraint database for the AIS has been compiled and is made available in spreadsheet form. We have been selective in including only data assessed to provide strong constraining potential (based on data-type, contemporaneous GSM resolution etc.). The authors would like to see AntICEdat move toward becoming an open-source, quality controlled constraint database, perhaps as a component of an AIS deglaciation chronology evaluation intercomparison process.

Each type of data has its specific challenges, limitations, and spatial-temporal regions of constraint. Present-day topographic data is from ALBMAP, whose largest

deficiency, as with other ice sheet topographic data sets, is the lack of uncertainty estimates. The data-point and site density of the paleo-data is unevenly distributed, predominantly located on the coast or, in the case of EXT data, off-shore. There is understandably very little paleo-data constraining the interior. The temporal constraint provided by the three paleo-data types predominantly covers the deglaciation period. The ELEV data-type, however, provides some coverage back towards the middle of the last glacial cycle.

Accurate and interpretable ice sheet reconstruction requires full accounting (as is possible) of all uncertainties present in the GSM and the data. The goal of capturing structural error in GSMs will remain an on-going challenge for the modelling community. On the data side, the community needs to more clearly and accurately document observational uncertainty, both due to measurement and interpretation. AntICEdat was compiled from many different sources and, in a number of cases, key information required for translating the observational data into a constraint data-point was unavailable, necessitating various assumptions.

The key considerations for translating data to a form suitable for model evaluation are listed below. The list is intended to provide guidance to data gatherers to ensure maximum constraint value can be extracted from the valuable data they collect and make available:

- Missing uncertainty information: It is essential that the uncertainties associated with raw observations and introduced post-collection (e.g. calibration processes, data interpretation) are quantified as accurately as possible and presented along with the data.

- Interpretation of data: If there are data-type specific conditions (*e.g.*, behavioral/environmental factors of dated fauna, site tidal ranges) that determine

how the data is to be interpreted this needs to be clearly stated in the source publication. For example, mollusc shells recovered in-situ are reported to reside at least 1-2 m below sea level. For the observational error model developed for this study, we have translated this into being a lower bound for past sea level of 2 m above the observation, and an upper ($1\sigma$) bound of an arbitrary 50 m. Thus we are making a number of assumptions that may be mis-interpreting the data.

- Missing location data: Each data-point requires location data. In some cases location data was not available with each data-point and had to be extracted from maps contained within the source publications.

- Aggregated data: If, in the analysis of the data-points, the authors deem it necessary to compute age-data by averaging a number of data-points, the associated averaged spatial data, and uncertainties, should also be made available.

- Provision of raw data for recalibration of ages: To ensure that the observational data is 'future-proof', sufficient raw data should be made available to ensure re-assessment/re-calibration can take place. This data incompleteness was predominantly an issue for ELEV data and has been identified as such in the cosmogenic-nuclide geochemical community (Dunai and Stuart, 2009).

- Accessibility: to ensure usage by modellers, data needs to be available online as a centralized community resource in digital format.

As noted earlier, explicit uncertainties need to be attributed to present-day topographic observations. If they were available, they could be exploited both during the evaluation process (*e.g.*, for scoring the modelled present-day topography) and to ensure uncertainties in boundary conditions are propagated into the uncertainty

estimation for the ensemble results.

Through data-weighting and observational error models, we account for observational uncertainty and partially account for structural error inherent in the GSM. We have assessed the sensitivity of the scoring to the different data-types and weightings; within plausible bounds the results from the schemes are robust. Choosing an uncertainty range for three scoring schemes PDcPaSEb (base set with weights as per volume of influence and narrow Eemian sieve), PDcPbSEb (base with doubled weight on paleo data and narrow Eemian sieve), and PDcPaSEa (base with wide Eemian sieve) gives a maximum LGM-to-present difference of 0.3 mESL between unweighted means of top 10 runs as selected by each scoring scheme.

Contributions of data-specific expertise are needed to refine the error models described herein. To augment the existing data, the published data types that are available (e.g. GRACE data, GPS uplift data, past ice elevations from ice cores) should be incorporated into AntICEdat. For use in ice chronology evaluation, error models for these data types also need to be specified. Finally, improvement in the estimation of structural uncertainty (and thereby better constrained data-weighting) is an ongoing project.

## Acknowledgements

We thank Pippa Whitehouse for extensive discussions and her very helpful and detailed review of an early draft. Detailed comments from an anonymous reviewer significantly improved clarity of the text. We also thank Dave Pollard for the provision and support of the PSU ice sheet model and Stephen Livingstone for providing his Marine Core database and clarifying the interpretation of the EXT data.

Support provided by Canadian Foundation for Innovation, the National Science

and Engineering Research Council, and ACEnet. Tarasov holds a Canada Research Chair. This article is a contribution to the INQUA sponsored Meltwater Ocean Cryosphere Atmospheric response network (MOCA) and has benefited from discussions within network workshops.

## 3.8 References

Ackert, R. P., Barclay, D. J., Borns, H. W., Calkin, P. E., Kurz, M. D., Fastook, J. L., Steig, E. J., 1999. Measurements of Past Ice Sheet Elevations in Interior West Antarctica. Science 286 (5438), 276 –280.

Anderson, J., 2002. The Antarctic Ice Sheet during the Last Glacial Maximum and its subsequent retreat history: a review. Quaternary Science Reviews 21, 49–70.

Balco, G., 2011. Contributions and unrealized potential contributions of cosmogenic-nuclide exposure dating to glacier chronology, 1990-2010. Quaternary Science Reviews 30, 3–27.

Baroni, C., Hall, B. L., 2004. A new Holocene relative sea-level curve for Terra Nova Bay, Victoria Land, Antarctica. Journal of Quaternary Science 19, 377–396.

Bassett, S. E., Milne, G. A., Bentley, M. J., Huybrechts, P., 2007. Modelling Antarctic sea-level data to explore the possibility of a dominant Antarctic contribution to meltwater pulse IA. Quaternary Science Reviews 26, 2113–2127.

Bentley, M., Fogwill, C. J., Kubik, P. W., Sugden, D. E., 2006. Geomorphological evidence and cosmogenic 10Be/26Al exposure ages for the Last Glacial Maximum and deglaciation of the Antarctic Peninsula Ice Sheet. Geological Society of America Bulletin 118 (9-10), 1149–1159.

Bentley, M. J., 2010. The Antarctic palaeo record and its role in improving predictions of future Antarctic Ice Sheet change. Journal of Quaternary Science 25 (1), 5–18.

Bentley, M. J., Fogwill, C. J., Le Brocq, A. M., Hubbard, A. L., Sugden, D. E., Dunai, T. J., Freeman, S. P. H. T., 2010. Deglacial history of the West Antarctic Ice Sheet in the Weddell Sea embayment: Constraints on past ice volume change. Geology 38 (5), 411–414.

Bentley, M. J., Hodgson, D. A., 2009. Antarctic Ice Sheet and climate history since the Last Glacial Maximum. Pages News 17 (1), 28–29.

Berkman, P., 1998. 226Ra/Ba ratios for dating Holocene biogenic carbonates in the Southern Ocean: preliminary evidence from Antarctic coastal mollusc shells. Chemical Geology 144 (3-4), 331–334.

Berkman, P. A., Forman, S. L., 1996. Pre-bomb radiocarbon and the reservoir correction for calcareous marine species in the Southern Ocean. Geophysical Research Letters 23 (4), 363.

Brooks, A., Edwards, R., 2006. The development of a sea-level database for Ireland. Irish Journal of Earth Sciences 24, 13–27.

Delmotte, M., Raynaud, D., Morgan, V., Jouzel, J., 1999. Climatic and glaciological information inferred from air-content measurements of a Law Dome (East Antarctica) ice core. Journal of Glaciology 45 (150), 255–263.

Dunai, T. J., Stuart, F. M., 2009. Reporting of cosmogenic nuclide data for exposure age and erosion rate determinations. Quaternary Geochronology 4 (6), 437–440.

Hall, B. L., 2009. Holocene glacial history of Antarctica and the sub-Antarctic islands. Quaternary Science Reviews 28, 2213–2230.

Hall, B. L., Denton, G. H., 1999. New relative sea-level curves for the southern Scott Coast, Antarctica: evidence for Holocene deglaciation of the western Ross Sea. Journal of Quartenary Science 14 (7), 641–650.

Hauser, T., Keats, A., Tarasov, L., 2011. Artificial neural network assisted Bayesian calibration of climate models. Climate Dynamics 39 (1-2), 137–154.

Heroy, D., Anderson, J., 2007. Radiocarbon constraints on Antarctic Peninsula Ice Sheet retreat following the Last Glacial Maximum (LGM). Quaternary Science Reviews 26 (25-28), 3286–3297.

Hillenbrand, C.-D., Smith, J. A., Kuhn, G., Esper, O., Gersonde, R., Larter, R. D., Maher, B., Moreton, S. G., Shimmield, T. M., Korte, M., 2010. Age assignment of a diatomaceous ooze deposited in the western Amundsen Sea Embayment after the Last Glacial Maximum. Journal of Quaternary Science 25, 280–295.

Huybrechts, P., 2002. Sea-level changes at the LGM from ice-dynamic reconstructions of the Greenland and Antarctic ice sheets during the glacial cycles. Quaternary Science Reviews 21 (1-3), 203–231.

Ingólfsson, Ó., Hjort, C., Berkman, P. A., Björck, S., Colhoun, E., Goodwin, I. D., Hall, B., Hirakawa, K., Melles, M., Möller, P., et al., 1998. Antarctic glacial history since the Last Glacial Maximum: an overview of the record on land. Antarctic Science 10 (3), 326–344.

Kluiving, S., van der Wateren, D., 2001. Antarctica Glaciological Geological Database (AGGD). http://www.antarctica.ac.uk/met/rcah/agdb/, Online; accessed 08-Feb-2012.

Kopp, R. E., 2012. Palaeoclimate: Tahitian record suggests Antarctic collapse. Nature 483 (7391), 549–550.

Kopp, R. E., Simons, F. J., Mitrovica, J. X., Maloof, A. C., Oppenheimer, M., 2009. Probabilistic assessment of sea level during the last interglacial stage. Nature 462, 863–867.

Lambeck, K., Purcell, A., Dutton, A., 2012. The anatomy of interglacial sea levels: The relationship between sea levels and ice volumes during the Last Interglacial. Earth and Planetary Science Letters 315–316, 4–11.

LeBrocq, A. M., Payne, A. J., Vieli, A., 2010. An improved Antarctic dataset for high resolution numerical ice sheet models (ALBMAP v1). Earth System Science Data 2 (3), 247–260.

Lisiecki, L. E., 2005. A Pliocene-Pleistocene stack of 57 globally distributed benthic $\delta$18O records. Paleoceanography 20, 1003.

Livingstone, S. J., O'Cofaigh, C., Stokes, C. R., Hillenbrand, C. D., Vieli, A., Jamieson, S. S., 2012. Antarctic palaeo–ice streams. Earth-Science Reviews 111 (1-2), 90–128.

Lythe, M. B., Vaughan the BEDMAP Consortium, D. G., 2001. BEDMAP: A new ice thickness and subglacial topographic model of Antarctica. Journal of Geophysical Research-Solid Earth 106, 11335–11352.

Mackintosh, A., 2007. Exposure ages from mountain dipsticks in Mac. Robertson Land, East Antarctica, indicate little change in ice-sheet thickness since the Last Glacial Maximum. Geology 6 (35), 551.

Martin, M. A., Winkelmann, R., Haseloff, M., Albrecht, T., Bueler, E., Khroulev, C., Levermann, A., 2010. The Potsdam Parallel Ice Sheet Model (PISM-PIK) - Part 2: Dynamic equilibrium simulation of the Antarctic ice sheet. The Cryosphere Discussions 4 (3), 1307–1341.

Martinerie, P., Lipenkov, V. Y., Raynaud, D., Chappellaz, J., Barkov, N. I., Lorius, C., 1994. Air content paleo record in the Vostok ice core (Antarctica): A mixed record of climate and glaciological parameters. Journal of Geophysical Research-Atmospheres 99, 10565.

Miura, H., Maemoku, H., Seto, K., Morikawa, K., 1998. Late Quaternary East Antarctic melting event in the Soya Coast region based on stratigraphy and oxygen isotopic ratio of fossil molluscs. Polar Geoscience 11, 260–274.

Overpeck, J. T., Otto-Bliesner, B. L., Miller, G. H., Muhs, D. R., Alley, R. B., Kiehl, J. T., 2006. Paleoclimatic evidence for future ice-sheet instability and rapid sea-level rise. Science 311 (5768), 1747–1750.

Parrenin, F., Dreyfus, G., Durand, G., Fujita, S., Gagliardini, O., Gillet, F., Jouzel, J., Kawamura, K., Lhomme, N., Masson-Delmotte, V., Ritz, C., Schwander, J., Shoji, H., Uemura, R., Watanabe, O., Yoshida, N., 2007. 1-D-ice flow modelling at EPICA Dome C and Dome Fuji, East Antarctica. Climate of the Past 3 (2), 243–259.

Peltier, W. R., 2004. Global glacial isostatic adjustment and the surface of the ice-age Earth: the ICE-5G(VM2) model and GRACE. Annual Review of Earth and Planetary Sciences 32, 111–149.

Pollard, D., DeConto, R. M., 2009. Modelling West Antarctic ice sheet growth and collapse through the past five million years. Nature 458, 329–332.

Price, S. F., Conway, H., Waddington, E. D., 2007. Evidence for late Pleistocene thinning of Siple Dome, West Antarctica. Journal of Geophysical Research-Earth Surface 112 (13).

Reimer, P., Baillie, M., Bard, E., Bayliss, A., Beck, J., Blackwell, P., Ramsey, C., Buck, C., Burr, G., Edwards, R., et al., 2009. IntCal09 and Marine09 radiocarbon age calibration curves, 0-50,000 years cal BP. Radiocarbon 51 (4), 1111–1150.

Rignot, E., Mouginot, J., Scheuchl, B., 2011. Ice Flow of the Antarctic Ice Sheet. Science 333 (6048), 1427–1430.

Ritz, C., Rommelaere, V., Dumas, C., 2001. Modeling the evolution of Antarctic ice sheet over the last 420,000 years: implications for altitude changes in the Vostok region. Journal of Geophysical Research-Atmospheres 106 (D23), 31943–31964.

Rutt, I. C., Hagdorn, M., Hulton, N. R. J., Payne, A. J., 2009. The Glimmer community ice sheet model. Journal of Geophysical Research-Earth Surface 114 (F13), 2004.

SCAR, 2006. Antarctic Digital Database, Scientific Committee on Antarctic Research (SCAR), Version 3.0. http://www.add.scar.org:8080/add/, Online; accessed Sep. 2011.

Schoof, C., 2007. Ice sheet grounding line dynamics: Steady states, stability, and hysteresis. Journal of Geophysical Research 112 (F3), F03S28.

Simpson, M. J. R., Milne, G. A., Huybrechts, P., Long, A. J., 2009. Calibrating a glaciological model of the Greenland ice sheet from the Last Glacial Maximum to present-day using field observations of relative sea level and ice extent. Quaternary Science Reviews 28, 1631–1657.

Steig, E. J., Fastook, J. L., Zweck, C., Goodwin, I. D., Licht, K. J., White, J. W. C., Ackert, R. P., 2001. West Antarctic Ice Sheet Elevation Changes. Antarctic Research Series 77, 75–99.

Storey, B., Fink, D., Hood, D., Joy, K., Shulmeister, J., Riger-Kusk, M., Stevens, M., 2010. Cosmogenic nuclide exposure age constraints on the glacial history of the Lake Wellman area, Darwin Mountains, Antarctica. Antarctic Science 22 (06), 603–618.

Stuiver, M., Reimer, P., Reimer, R., 2005. Calib 5.0. http://calib.qub.ac.uk/calib, Online; accessed 19-July-2008.

Tapley, B. D., Bettadpur, S., Watkins, M., Reigber, C., 2004. The gravity recovery and climate experiment: Mission overview and early results. Geophysical Research Letters 31, 9607.

Tarasov, L., Dyke, A. S., Neal, R. M., Peltier, W. R., 2012. A data-calibrated distribution of deglacial chronologies for the North American ice complex from glaciological modeling. Earth and Planetary Science Letters 315, 30–40.

Tarasov, L., Peltier, W. R., 2003. Greenland glacial history, borehole constraints and Eemian extent. Geophysical Research Letters 108 (83), 2124–2143.

Tarasov, L., Peltier, W. R., 2004. A geophysically constrained large ensemble analysis of the deglacial history of the North American ice sheet complex. Quaternary Science Reviews 23 (3–4), 359–388.

Thomas, I. D., King, M. A., Bentley, M. J., Whitehouse, P. L., Penna, N. T., Williams, S. D. P., Riva, R. E. M., Lavallee, D. A., Clarke, P. J., King, E. C., Hindmarsh, R. C. A., Koivula, H., 2011. Widespread low rates of Antarctic glacial isostatic adjustment revealed by GPS observations. Geophysical Research Letters 38, 22302.

Todd, C., Stone, J., Conway, H., Hall, B., Bromley, G., 2010. Late Quaternary evolution of Reedy Glacier, Antarctica. Quaternary Science Reviews 29 (11-12), 1328.

Verleyen, E., 2005. Relative sea-level history from the Lambert Glacier region, East Antarctica, and its relation to deglaciation and Holocene glacier readvance. Quaternary Research 63 (1), 45.

Weber, M. E., Clark, P. U., Ricken, W., Mitrovica, J. X., Hostetler, S. W., Kuhn, G., 2011. Interhemispheric Ice-Sheet Synchronicity During the Last Glacial Maximum. Science 334 (6060), 1265–1269.

Whitehouse, P. L., Bentley, M. J., Brocq, A. M. L., 2012. A deglacial model for Antarctica: geological constraints and glaciological modelling as a basis for a new model of Antarctic glacial isostatic adjustment. Quaternary Science Reviews 32 (16), 1–24.

Zhang, Q., Peterson, J. A., 1984. A geomorphology and Late Quaternary geology of the Vestfold Hills, Antarctica. Australian National Antarctic Research Expeditions Reports 133, 84.

Zwartz, D., 1998. Holocene sea-level change and ice-sheet history in the Vestfold Hills, East Antarctica. Earth and Planetary Science Letters 155 (1-2), 131.

# Connecting Text

The final research article first describes the distribution of the parameters used to generate the ensemble of reconstructions and, after application of the evaluation methodology, discusses how the probability distributions are computed. The scored results and probability distributions are then used to address objectives 3 and 4.

The research paper has been written with the intention of being submitted to *Quaternary Science Reviews.*

# Chapter 4

# A data-constrained large-ensemble analysis of Antarctica over the last glacial cycle

## 4.1 Abstract

Reconstructing the historical behaviour of the Antarctic Ice Sheet is essential for understanding and predicting climatic interactions, ice sheet sensitivities, and sea-level contributions. Furthermore, to interpret the reconstructions with any degree of confidence it is important that meaningful uncertainty estimates are attributed. Working toward this goal, this article presents results from a large-ensemble data-constrained study of Antarctic evolution over the last glacial cycle.

Ice sheet chronologies have been generated using a 3-D glacial systems model that includes sheet/stream/shelf flow; a parametrized basal drag coefficient (accounting for sub-grid topographic roughness, sediment likelihood, and systematic model-to-observation thickness misfits); a sub-grid grounding-line flux parametrization; a visco-elastic bedrock response component; heavily parametrized climate forcing (removing dependence on a single method); separate shelf and tidewater calving treatments; and a physically-motivated, empirically derived, sub-shelf melt component. There are 31 ensemble parameters to capture uncertainties in the glacial cycle climate, mass-balance processes, and ice dynamics. Once generated, the ensemble of reconstructions are constrained using a suite of observational data (including constraints on relative sea level, past ice thickness, and grounding line retreat data-points, as well as present-day ice volumes and configuration) and an evaluation methodology that produces a misfit-to-observations score for each run. Assuming variants of a Gaussian error model, the scores are used to generate probability distributions for the past evolution of the ice sheet.

Our reconstructions predict the Last Glacial Maximum (LGM) in Antarctica occurred at ~24 ka. The mean eustatic contribution from LGM until present-day is 8.9 m equivalent sea level (mESL), 5.8 mESL coming from WAIS. The maximal $1\sigma$ upper bound and the minimal $1\sigma$ lower bound from the generated distributions give a range

of 5.8 to 12.2 mESL. There is little change in the grounded ice volume from 24 ka until 16-17 ka at which time widespread deglaciation commences. The Ross and Weddell Sea sectors are the predominant sources of ice mass loss. The major period of grounding line retreat in the Weddell Sea sector, resulting in the present-day Ronne-Filchner shelf system, occurs after 12 ka; the grounding line in the Ross sea sector start its major retreat phase after 10 ka.

During the Eemian period, the minimum configuration of reconstructed ice sheets occurs at 114 ka and contributes between -0.2 to 3.4 mESL relative to present-day. The loss is principally due to a major retreat of the grounding line in the Ross Sea sector and a significantly thinner West Antarctic ice sheet.

In addition, we present standard deviation plots of the ensemble results for present day and at the LGM. In effect these plots highlight areas that would most benefit additional constraint and could provide a focus location for future field campaigns.

## 4.2 Introduction

The Antarctic Ice Sheet (AIS) is a key component in the global climate system, and has been identified as a major source of uncertainty to future sea level change (Meehl et al., 2007). It is also one of the slowest components; large tracts of the interior react on timescales greater than 10,000 yrs (Alley and Whillans, 1984; Ritz et al., 2001; Bamber et al., 2007). To understand and predict the contemporaneous and future behaviour of the ice sheet, and the resultant impact on sea level change, it is essential to understand the past evolution of the AIS. As such, there is a pressing requirement for quantitatively evaluated reconstructions of past evolution. In addition, it is crucial that the reconstructions have associated uncertainties to ensure that they can be interpreted with the appropriate degree of confidence.

In this study, the results from a data-constrained large-ensemble analysis of AIS evolution since the Eemian, with a particular focus on the deglaciation history from the Last Glacial Maximum (LGM) to present-day are presented and discussed.

Understanding these periods is important to address a number of distinct issues. Firstly, the sea level low stand during the LGM happened between 26.5 ka to 19.0 ka*. The far-field sea level records (Peltier and Fairbanks, 2006) are a globally integrated signal. They do not distinguish between the hemispheric, regional, or local glacial maximas (Clark et al., 2009). Accurate estimates of the local LGM timing (all subsequent usage of the term LGM refers to the local LGM of AIS) and the associated glacio-eustatic sea level contribution of the AIS will aid in constraining the timing and magnitudes of the other Quaternary ice sheets (Weber et al., 2011).

Secondly, extraction of present-day rates of Antarctic ice mass-change from geodetic and local gravity measurements requires removal of components from past and

*Throughout this text ka signifies calendar years before present and whereas kyr is a time period of 1000 yrs.

on-going glacial isostatic adjustment (Ivins and James, 2005; Bentley, 2010).

Thirdly, an accurate deglaciation chronology will facilitate understanding of the response of the AIS, and other ice sheets, to external forcing. This is especially important for deciphering the timing and provenance of rapid melt water pulses, determining the climatic events that trigger them, and disentangling the sensitivity of the various components in the climate system to rapid influxes of melt water (*e.g.*, Clark et al., 2002a,b; Weaver et al., 2003; Peltier and Fairbanks, 2006). Melt water pulse events are periods of accelerated sea level rise caused by rapid melting events. In the Barbados coral records the two most extreme examples of these events, meltwater pulse 1a and 1b (MWP-1a, MWP-1b), occurred around 14 ka and 11.3 ka. MWP-1a was characterised by a sea level rise of about 15 m or more in less than 500 yrs, the smaller MWP-1b by a rise of 5m in 400 yrs (Fairbanks, 1989; Bard et al., 1990). The timing, provenance–the predominant source of the MWP pulses has been attributed both to the northern hemisphere (Fairbanks, 1989; Peltier, 2005; Peltier and Fairbanks, 2006; Tarasov et al., 2012) and the southern hemisphere (Bard et al., 1996; Stanford et al., 2006)–and exact amplitudes of these events remains controversial, but the importance of correctly untangling the climatic interactions and potential triggers of such rapid events is incontrovertible (e.g. Clark, 2002; Bard et al., 2010; Deschamps et al., 2012).

Finally, paleo-climatic studies using coupled ocean-atmosphere models (*e.g.*, Paleo-Modelling Intercomparison Project II Braconnot et al., 2007)* require ice sheet reconstructions to provide essential boundary conditions and forcing such as orography and fresh water fluxes. The study of past climate periods that are analogous or partially analogous to predicted future climatic scenarios, *e.g.*, the Eemian, is of particular importance as a tool to assess potential climate system dynamics and guide climatic policy (Turney et al., 2006). The Eemian (last interglacial period) began approx-

*http://pmip2.lsce.ipsl.fr/

imately 129±1 ka and lasted until at least 118 ka (Overpeck et al., 2006); it was characterised by globally averaged warmer temperatures, (e.g. ~1.5 °C Turney and Jones, 2010)[†], sea levels higher than present-day (perhaps 6.6 - 9.4 m higher Kopp et al., 2009)[‡], a smaller Greenland Ice Sheet (GIS) and likely also a smaller West Antarctic ice sheet (WAIS)(Cuffey and Marshall, 2000; Overpeck et al., 2006; Kopp et al., 2009). Thus, the study of this period is of interest because of its similarity to predicted future climatic conditions and, being geologically recent, high resolution records are available against which models of future climate change can be tested (Overpeck et al., 2006; Meehl et al., 2007; Kopp et al., 2009).

To generate the reconstructions of AIS evolution that can be used, in part, to address these issues we employ a large ensemble analysis method. This follows on from similar work performed for the other major Quaternary ice sheets (Tarasov and Peltier, 2002, 2003; Tarasov et al., 2012). The ensemble technique exploits the parametrizations in the glacial systems model (as found in any complex numerical model) that are required to account for missing or poorly represented processes and the uncertainties due to boundary/forcing conditions.

The MUN/PSU GSM we use is based on the dynamical core of the Penn State university (PSU) ice sheet model (Pollard and DeConto, 2009, 2007, 2012a,b). There are 31 ensemble parameters to capture the uncertainties in the glacial cycle climate, mass-balance processes, and the ice dynamics Briggs et al. (2013). By sampling sets of parameters from the parameter space and generating a model run for each set, an ensemble of results can be constructed. Using a suite of observational data and an appropriate evaluation methodology a model-to-data misfit score is generated for each run (Briggs and Tarasov, 2012). A major strength of the ensemble method is that

[†]Other estimations range from 0.1 °C to >2 °C warmer than present.

[‡]Higher than 6.6 m with 95% certainty, higher than 8.0 m with 68% certainty and likely no more than 9.4 m (33 %).

probability distributions for data-fields of interest can be produced from the scored runs (with the probabilities derived from run scores), removing the reliance on results from a single run.

In this article the results from an ensemble of scored AIS reconstructions are described and evaluated. The Material and Methods section (Section 4.3) explains the approach taken to generate and score the ensemble and the subsequent computation of probability distributions. The ensemble results are then presented and discussed. First, the misfit to present-day observations and paleo-data is evaluated. Following this, the reconstructed LGM configuration of the AIS the AIS deglaciation evolution, and the predicted AIS contribution to MWP-1a and MWP-1b are presented. Standard deviation plots–which can be translated as regions that have the largest variance and would thus benefit further constraint data–of the ensemble results, at both present-day and the LGM are presented. Finally, the reconstructed Eemian configuration, the associated AIS contribution to sea level rise and a brief review of the evolution of AIS over the last glacial cycle until present-day are given.

## 4.3 Methods

The dynamical core of the glacial systems model (GSM) used in this study is based on the Penn State University (PSU) ice sheet model (Pollard and DeConto, 2007; Pollard and DeConto, 2009; Pollard and DeConto, 2012b) that has been modified for large ensemble analysis (Briggs et al., 2013). The MUN/PSU GSM has the following features: a diverse set of climate forcing mechanisms; a parametrized basal drag coefficient that accounts for sediment likelihood, boundary condition downscaling and systematic model-to-observation thickness misfit; tide water and ice-shelf calving functionality; and a newly developed physically-motivated empirically derived sub-shelf

melt component.

The model has 31 ensemble parameters that allow for exploration of the (as best can be done with 31 parameters) the uncertainty in the ice-physics, basal conditions, climate forcing, and ice-ocean interaction. The definition, justification, and usage of the parameters, and the associated sensitivity assessment, is described in (Briggs et al., 2013). Each of the parameters has a range of values that can produce plausible model output. The cumulative interaction of the parameters creates a parameter space. Extracting a sample parameter set from this space describes a unique model configuration from which its associated ice sheet reconstruction can be generated. Repeated sampling allows the creation of a large ensemble of reconstructions.

### 4.3.1 Parameter distributions and ensemble overview

The parameter ranges and associated sensitivity study described in Briggs et al. (2013) demonstrated that each of the 31 ensemble parameters has significant influence over at least one of six metrics. Exploration of the phase-space is made more efficient by generating distributions that reflect the non-uniform nature of the likely parameter values*. The Briggs et al. (2013) parameter ranges and distributions presented in this study have evolved in concert with the development of the MUN/PSU GSM and over the course of five developmental ensembles and evaluation exercises (identified as ANa through to ANe, in total more than 10,000 runs). The ensemble results are pertinent to a specific configuration of the GSM (as the model evolves the previous ensemble results become stale), however, analysis of previous results guides the set-up of future ensembles. Thus, the distributions are defined predominantly based

*With no computational resource restrictions the prior distribution of each parameter could be treated as uniform regardless of the plausibility of certain values, however, each run is computationally expensive taking between approximately 20 to 120 hrs. Defining distributions allows us to focus the efforts of the ensemble.

on past scoring experience and, in the case of physically based parameters, a priori information. For example, the default configuration of the PSU GSM uses a lapse-rate of 8.0 °C $km^{-1}$ (Pollard and DeConto, 2012b) whereas other studies have used a value of 9.14 °C $km^{-1}$ (Ritz et al., 2001; Pollard and DeConto, 2009). Development of the initial ensembles revealed that plausible results can be obtained over a range 5-11 °C $km^{-1}$ , as observed in high-latitude environments. As such, the distribution of lapse-rate parameter values has evolved into a beta distribution that is focused around the centre value of ~8.0 °C $km^{-1}$ but that has an upper and lower bound 3 °C $km^{-1}$ above and below the centre; this gives denser coverage of the likely parameter value(s) whilst still giving some coverage of less likely, but still plausible, values.

Distributions for each of the 31 parameters, presented in Figs. C.1 to C.4 of the Appendix, are generally beta distributions although some are simpler uniform distributions. The distributions are not rigorously defined, rather they are attempts to focus the ensemble. This study is the initial analysis that will progress into a full Bayesian calibration process (Hauser et al., 2011; Tarasov et al., 2012), the results from this assessment will be used to refine the parameter ranges from which further ensembles will be generated.

The ensemble of results analysed in this study (ANf) is an amalgam of two ensembles, a 'wide' ensemble of 1700 runs and a 'narrow' ensemble of 1300 runs. Each was generated using a random Latin hypercube†. The wide ensemble range is defined using the upper and lower values presented as part of the sensitivity study from Briggs et al. (2013); the narrow ensemble generates a second set of runs within the wide range, the narrow range developed from the scoring of earlier ensembles. The cumulative effect gives many more runs within the narrow set of likely parameter values, whilst still

†A statistical method for efficiently sampling from a multidimensional distribution. Each parameter range is divided into 'M' intervals, considered together the gridded parameters create a Latin hypercube. A parameter set is then sampled from the hypercube; each interval that has been sampled from is recorded, so it is not re-sampled, thus the whole sample space is efficiently explored.

providing coverage of the less likely values.

### 4.3.2 Ensemble scoring

From these two ensembles a total of 2929 runs completed successfully. A model-to-observation misfit score, $S_n$, was generated for each run in accordance with the constraint database and evaluation methodology detailed in Briggs and Tarasov (2012). This study addressed the challenges in applying heterogeneous observational data to GSM generated deglaciation chronologies. The constraint database they make available contains present data observations (PD), Eemian grounded ice volume estimates, relative sea level indicators (RSL), past ice sheet elevations (ELEV), and ice sheet extent data (EXT). For the paleo-data types, they use observational error models (which incorporate observational uncertainties and allow for model structural error) to compute a model-to-data misfit score for each paleo-data point. These are combined, using intra-data-type weighing to account for differences in site data-density*, into a data-type misfit score. A cumulative misfit score for each run is then computed using an inter-data-type weighting that adjusts the relative strength of the data-type scores based on a spatial and temporal volume of influence†. Prior to the final scoring, sieves may be used to filter out runs based on some key metric (*e.g.*, a run that has a larger, or smaller, grounded volume than the Eemian sieve would be rejected and not included in the final scoring).

The data-weighing methods Briggs and Tarasov (2012) use are an incomplete and provisional effort to account for the lack of a structural error model for the GSM. A structural error model would account for the model-to-measurement misfit that

*For example, if there are only two sites in the database, one in East Antarctica with 100 data points and one in West Antarctica with a single data point, without data-weighting the runs that more accurately model the EAIS site would dominate the scoring.

†Each data-type has incongruent spatial and temporal distributions *e.g.*, present-day ice thickness has a much larger spatial influence than a single 20 ka past ice sheet elevation data point.

cannot be attributed to observational uncertainty, nor to uncertainty in the model parameters, *i.e.*, the remaining uncertainties in the model due to missing processes, resolution issues etc. They performed a sensitivity assessment of the different scoring schemes; combinations of data-weightings and sieves. In addition, they explored the impact of the different data-types. Following their conclusion, for this study results from the composite schemes that employ all the constraint data are presented. Table 4.1 lists the main characteristics of the scoring schemes adopted; the same codification system is followed as Briggs and Tarasov (2012).

Table 4.1: Details of key scoring schemes from Briggs and Tarasov (2012). This study predominantly uses the schemes emphasised in bold.

| Scheme | Description | Number of runs scored | maximum score (largest misfit)[a] |
|---|---|---|---|
| PDc | baseline present-day | 2929 | 3.75 |
| PDcPa | PDc and paleo-data (Pa) | 2929 | 7.18 |
| **PDcPaSEa** | as PDcPa and with wide Eemian sieve (SEa) | 1868 | 6.35 |
| **PDcPaSEb** | as PDcPa and with narrow Eemian sieve(SEb) | 214 | 4.43 |
| **PDcbSEb** | as PDcPaSEb but with double paleo-data (Pb) weighting | 214 | 5.35 |

[a] Presented for comparison in Fig. 4.1 (score axis is clipped)

Except for obvious behaviour (*i.e.*, increasing precipitation increases grounded volume) a check for correlation between the ensemble parameters and the key metrics (*e.g.*, grounded volumes for AIS and WAIS at present-day and LGM) revealed no significant (<0.6) linear or non-linear (non-linear correlations where checked using scatter-plots between parameter values and key metrics) correlations.

### 4.3.3 Generation of distributions

Even the best runs (lowest scoring) selected by the scoring schemes will still have many deficiencies and will be imperfect representation of reality. In addition, the best run is only the lowest scoring run for a specific set of metrics and weighting defined in the scheme that scored the ensemble. If the scheme changes the best runs may change. Any 'single' run analysis must always be undertaken with such caveats.

The ensemble method provides a large sample of model runs from which statistical characteristics can be extracted. Run scores can be converted to relative weights (effectively probabilities), and one can then generate weighted means of, for example, ice volume or ice thickness chronologies. Critically, objective (in a restricted sense) uncertainty estimates can also be generated. More fundamentally, the set of ensemble runs with associated probabilities provides a probabilistic distribution of potential ice sheet chronologies.

A key challenge in defining such a probabilistic distribution is converting the set of model misfits to observations and allowances for structural error (all aggregated in our case into the misfit score) into an actual likelihood of the run corresponding to reality. This requires assumptions/choices as to the underlying statistical structure of the model misfit to the actual ice evolution over the last glacial cycle. Rougier (2007), delineates a rigorous Bayesian approach for defining such structure and using this structure to estimate probabilities. However, such a rigorous approach requires the elicitation of a complete variance covariance matrix for structural error (or corresponding parametric representations if a non-Gaussian structure is assumed).

As the actual statistical structure of the model misfit to truth is unknown, on the basis of the central limit theorem and tractability, we (as does Rougier (2007)) assume a nominal multivariate Gaussian structure. We have found it simpler and conceptually clearer to partially address structural error covariance through inter

and intra data weighting. Therefore, the structure reduces to a diagonal Gaussian distribution (*i.e.*, the corresponding variance/covariance matrix is diagonal). As data weighting effectively rescales the associated standard deviation for model-data misfit for each data constraint (cf chapter 3), an over-all scale for such weighting must be set. This scale determines how much "better" a run with (aggregate) mean square error (MSE) score of say 0.4 is compared to that of a run with score 0.6. Once this scaling is set in the form of a scaling factor, $\sigma_f$, the run probability, $P_n$, can be determined from the MSE misfit score, $Sn$, as

$$P_n = \frac{1}{C} e^{-(\frac{S_n}{\sigma_f{}^2})}, \tag{4.1}$$

where $S_n$ is the run score[†], as computed following Briggs and Tarasov (2012), for run number $_n$ and $C$ is the normalising factor that ensures $\sum_{n=1}^{N} P_n = 1$,

$$C = \sum_{n=1}^{N} e^{-(\frac{S_n}{\sigma_f{}^2})}. \tag{4.2}$$

The probabilities are then used to compute the mean of a variable ($x$) where,

$$\bar{x} = \sum_{n=1}^{N} P_n \cdot x_n \tag{4.3}$$

and the standard deviation

$$\sigma(\bar{x}) = \sqrt{\sum_{n=1}^{N} P_n \cdot (x_n - \bar{x}^2)}. \tag{4.4}$$

The appropriate value(s) for the scaling factor $\sigma_f$ is(are) unknown and must be determined experimentally/heuristically. We do this by assessing the sensitivity of

[†] The 31 parameter space is a continuous distribution from which a finite number of parameter sets is being sampled. Thus, regardless of the number of runs generated, the ensemble will always be an incomplete exploration of the phase space. As such the discrete form of the equations are presented here

mean grounded ice volume over a range of $\sigma_f$ values. Grounded ice volume is considered a key metric as the focus of the study is to assess sea level contribution from AIS; it is computed in metres equivalent sea level (mESL)[‡].

A set of incrementally increasing $\sigma_f$ values is generated from which, for each $\sigma_f$, the respective run probabilities and associated mean and standard deviation (error bars) are calculated. To further guide the choice of $\sigma_f$ two statistics – $P_{max}$, the probability of the best run and $P_{90}$, the number of runs required to achieve >90% coverage (of the total probability $P_{tot}$) – are computed and used along with two empirically derived targets. The targets have evolved from earlier large ensemble studies with the Greenland ice sheet (Tarasov and Peltier, 2004; Tarasov et al., 2012), the North American ice sheet (Tarasov and Peltier, 2006; Tarasov et al., 2012), and the Eurasia ice sheet complex (Tarasov et al, manuscript in preparation).

Accounting for the fact that most runs are poor (as expected from a random ensemble) balanced with ensuring that there is not an over-dominance of the best runs: target 1 requires that $P_{max}$ of the best run should contribute a maximum of 50% of the $P_{tot}$; target 2 requires that the number of runs that achieve $P_{90}$ be more than 10. This latter 'lower bound' target would be re-evaluated if there where a step change in the scores of the first few runs in comparison to the subsequent runs *i.e.*, there is a handful of exceptional runs. As can be seen in Fig. 4.1, PDcPaSEa exhibits a linear trend until ~600 runs, PDcPa until ~1000 (PDcPa does not have a sieve and is presented for comparison purposes). For PDcP[a/b]SEb the linear trend ceases at ~100 runs. As such, none of the schemes identify exceptionally good runs. The targets are used as guidelines and would likely be subject to change as the number of runs in the ensemble increases.

The incrementally increasing set of $\sigma_f$ values and the resultant $P_{max}$, $P_{90}$, mean

[‡]A conversion factor of 25.19 x $10^6$ $km^3$ of grounded ice = 1 mESL is used.

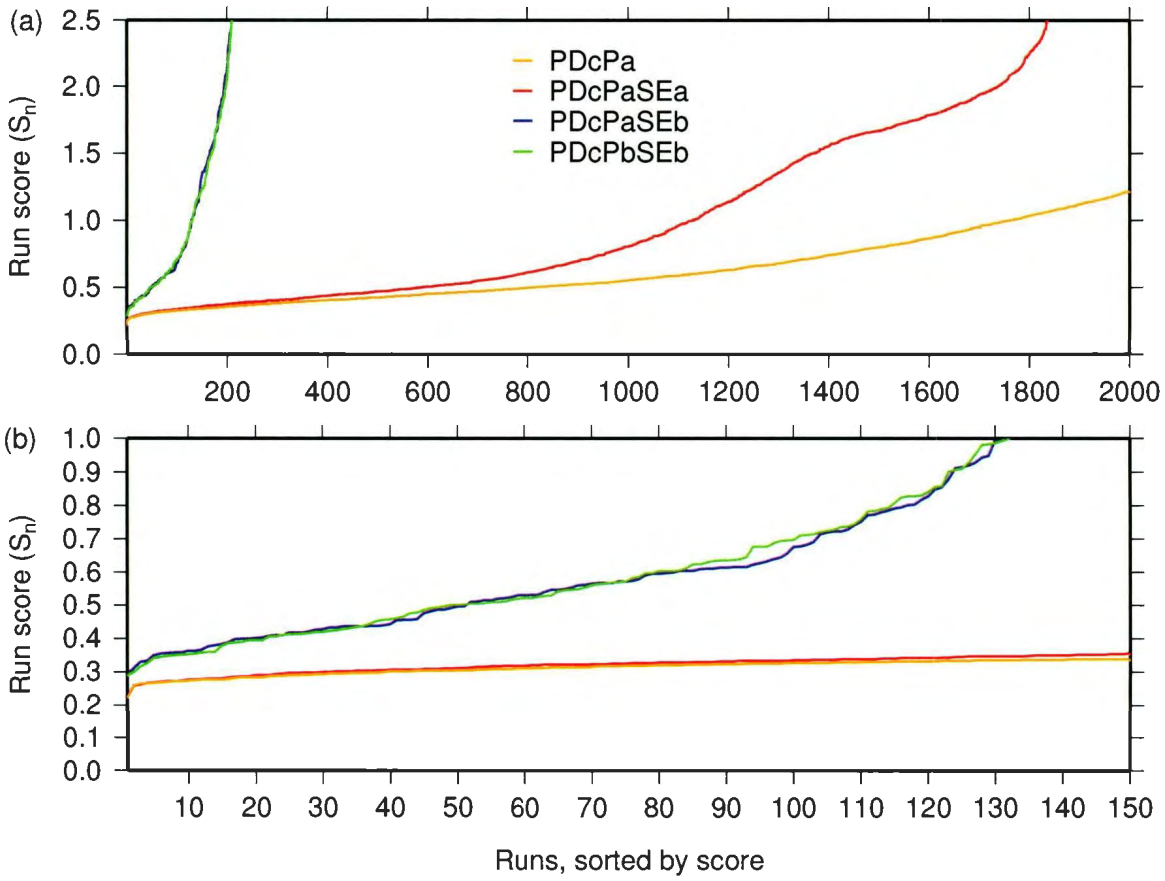


Figure 4.1: Distribution of scores for four schemes for the top 2000 runs (a) and the top 150 runs (b). To further focus on the lower scoring runs, both plots are clipped on the y-axis (See Table 4.1 for max values). Scheme PDcPa has no sieve, all 2929 runs are scored; it is presented for comparison. PDcPaSEa uses the wide sieve allowing only 1868 runs to be scored. Schemes PDcP[a/b]SEb both use the narrow sieve and only 214 runs are scored.

grounded ice volumes (for 0k and 20k), standard deviations, and locations of the thresholds in relation to $\sigma_f$ can be found in Table B.2a, b and c of the Appendix. To illustrate the impact of $\sigma_f$, a collection of mean grounded ice volumes, as computed from schemes PDcPaSEa (baseline weighting and wide Eemian sieve) and PDcPaSEb (baseline weighting and narrow Eemian sieve) for different $\sigma_f$ values, are presented in Fig. 4.2. The total number of runs scored by PDcPaSea is 1868 (64% of the ensemble), while for PDcPaSeb only 214 (7%) runs pass the sieve.

The upper plots of Fig. 4.2 present the distribution of probabilities generated from the $\sigma_f$ values that bracket the thresholds. As $\sigma_f$ is increased there is a reduction in the value of $P_{max}$ and a reciprocal increase in the number of runs required to achieve $P_{90}$. In the lower plots, the mean (and $1\sigma$ ) grounded ice volumes for 0k (vol0g) and 20k (vol20g) for the full set of $\sigma_f$ values are shown.

Given that our 2929 member random ensemble is unlikely to have many good fits to observations, we choose the smallest $\sigma_f$ that meet the criteria. This gives a $\sigma_f$ =0.09 for PDcPaSEa and a $\sigma_f$ =0.10 for PDcPaSEb. Applying a similar evaluation (not presented) to scheme PDcPbSEb yields a value of $\sigma_f$ =0.10. Subsequent results in this article are presented from the distributions computed using these schemes and $\sigma_f$ values, henceforth referred to as $W_{09}$ (wide sieve of PDcPaSEa), $N_{10}$ (narrow sieve of PDcPaSEb), and $N^*_{10}$ (narrow sieve of enhanced paleo-data weighing for PDcPbSEb) respectively.

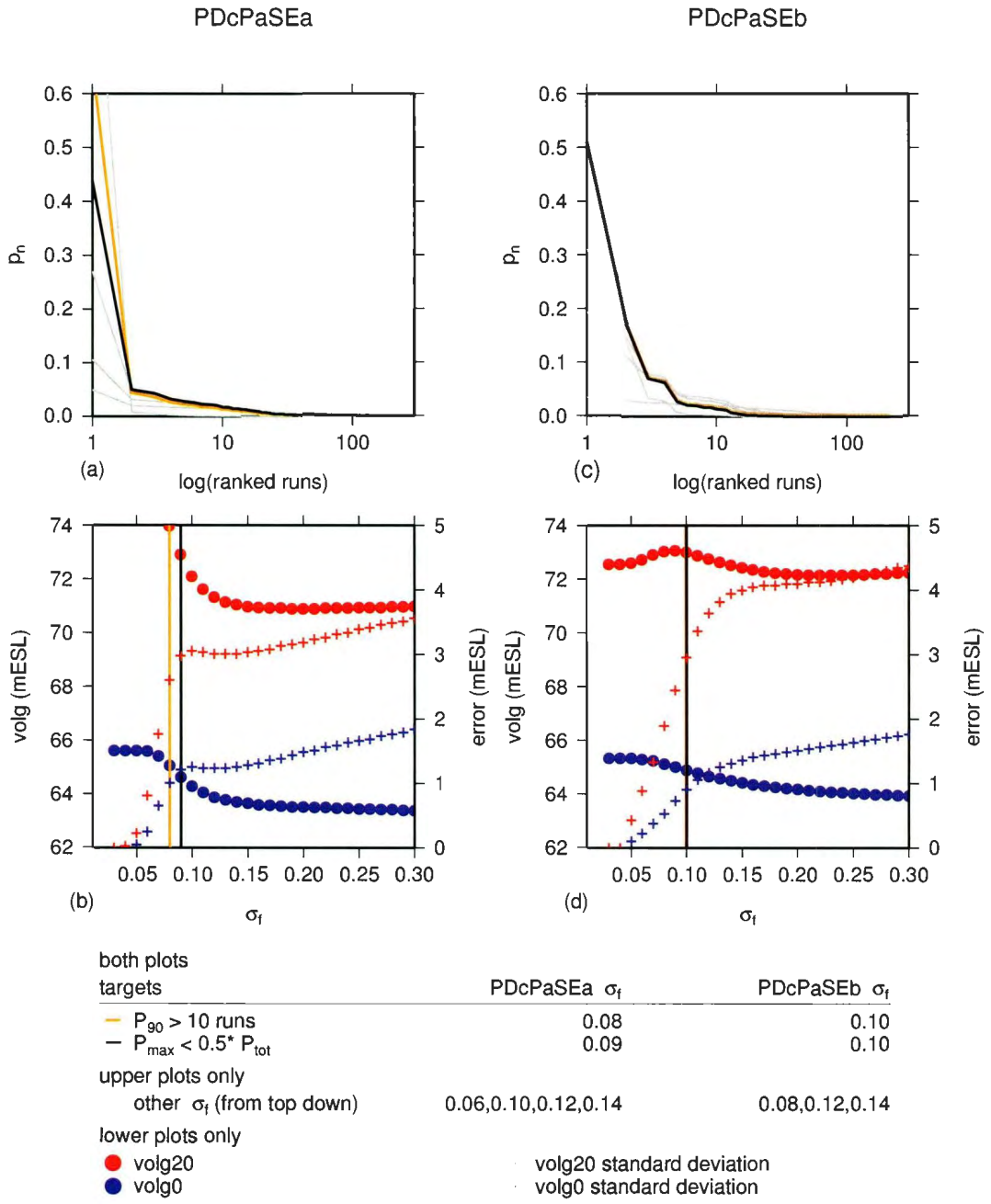


Figure 4.2: Exploration of $\sigma_f$ for schemes PDcPaSE[a/b]. Upper plots (a and c) show distribution of run probabilities, $P_n$ for ranked runs (sorted by $P_n$) for different values of $\sigma_f$, threshold values are highlighted in colour. Lower (b and d) plots show sensitivity plots of grounded ice volume at 20 k and 0 k (and associated errors) against $\sigma_f$. Coloured vertical lines represent the threshold $\sigma_f$ values.

## 4.4 Results

Probability distributions are not glaciologically self-consistent and can only be viewed as probabilistic descriptions. As such, results are presented from output derived from both the distributions, $W_{09}$ ,$N_{10}$ , $N^*_{10}$ and individual runs 2679 and 3506*

This section is structured as follows. The ensemble results for the modern day reconstructions are first presented (subsection 4.4.1), followed by the individual paleo-data type misfits (subsections 4.4.2, 4.4.3 and 4.4.4). The paleo-data site misfits are then evaluated on a sector by sector basis (subsection 4.4.5) followed by the resultant AIS deglaciation chronology, LGM configuration, and the LGM and MWP eustatic contributions (subsections 4.4.6 and 4.4.7). Finally the results for the Eemian configuration and subsequent evolution of AIS (subsections 4.4.8 and 4.4.9) are described.

All locations discussed in the text are shown on the composite bathymetry and basal/surface topography map plot of Fig. 4.3. See Fig. 1 of Briggs and Tarasov (2012) for a map and full description of each data-site.

### 4.4.1 Present-day reconstructions

The present-day configuration of run 2679 is compared with present-day observations in Fig. 4.4. Except for the observed surface velocity which are taken from the satellite derived Rignot et al. (2011) dataset re-gridded to 40 km, all present-day observational data are from ALBMAP (LeBrocq et al., 2010). ALBMAP is provided at a resolution of 5 km (herein named $ALB_5$ ). To be used as constraint data it must be upscaled to the model resolution of 40 km ($ALB_{40}$ ). The upscaling process to ensure grounding-line positions and key pinning points are preserved is documented in Briggs and Tarasov (2012). In making comparisons with present-day observations, it should be

* 2679 is the best run for PDcPaSEb, PDcPbSEb and ranked 18 by scheme PDcPaSEa. 3506 is the best run from PDcPaSEa, it is rejected by the narrow sieves

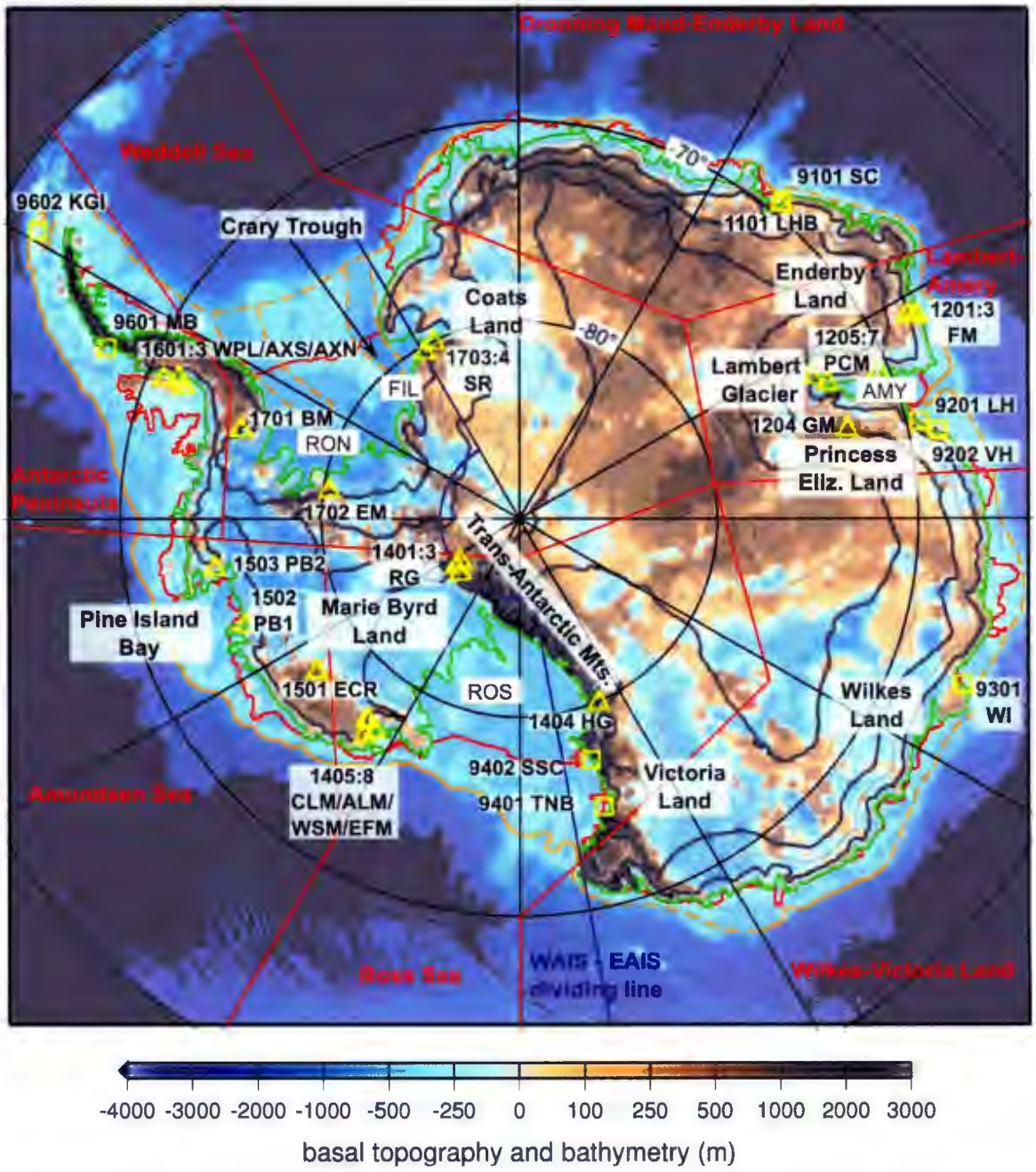


Figure 4.3: Composite map of names and locations of mentioned in the text, RSL (yellow squares) and ELEV (yellow triangles) constraint data points (with id numbers), and basal topography and bathymetry (colour filled image), contoured surface elevations (1000 m black, 500 m grey), present-day grounding line (green) and coastline (red). The orange lines are taken from the Livingstone et al. (2012) LGM grounding line extent reconstructions. Based on the data they compiled and assessed, the reconstructions were categorised into high confidence segments (solid orange line in this plot) and speculative segments (dotted orange).

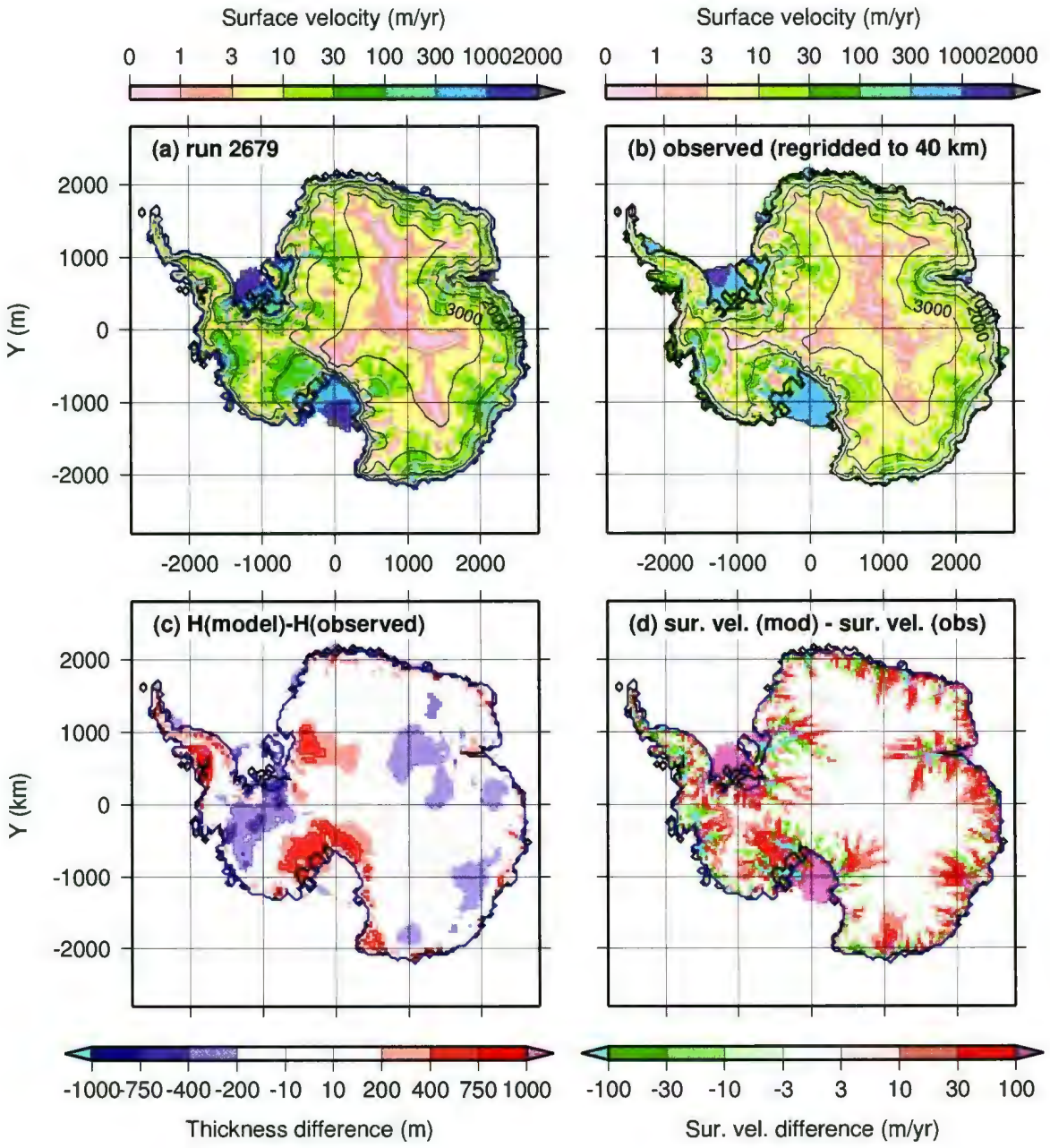


Figure 4.4: Present-day characteristics and differences for run 2679 and present day observation: (a) modelled magnitude of surface velocity overlaid with contours of surface elevation (1000 m thin black, 500 m light grey), (b) as (a) except using observations, (c) difference plot of modelled ice thickness minus observed ice thickness. (d) difference plot of modelled surface velocity and observed surface velocity. In both difference plots red indicates model overestimation. The present-day $ALB_{40}$ grounding line (black) and modelled grounding (blue) are show in all plots.

noted that there is uncertainty in the location of the observed grounding line (LeBrocq et al., 2010), at the ice margins (Bamber et al., 2009), and with the surface velocities (Rignot et al., 2011).

The upper plots present (a) the surface velocities overlain with surface elevation contours from 2679 and (b) the equivalent observations. The lower plots show (c) the differences between the modelled and observed ice thickness and (d) the modelled and observed surface velocities .

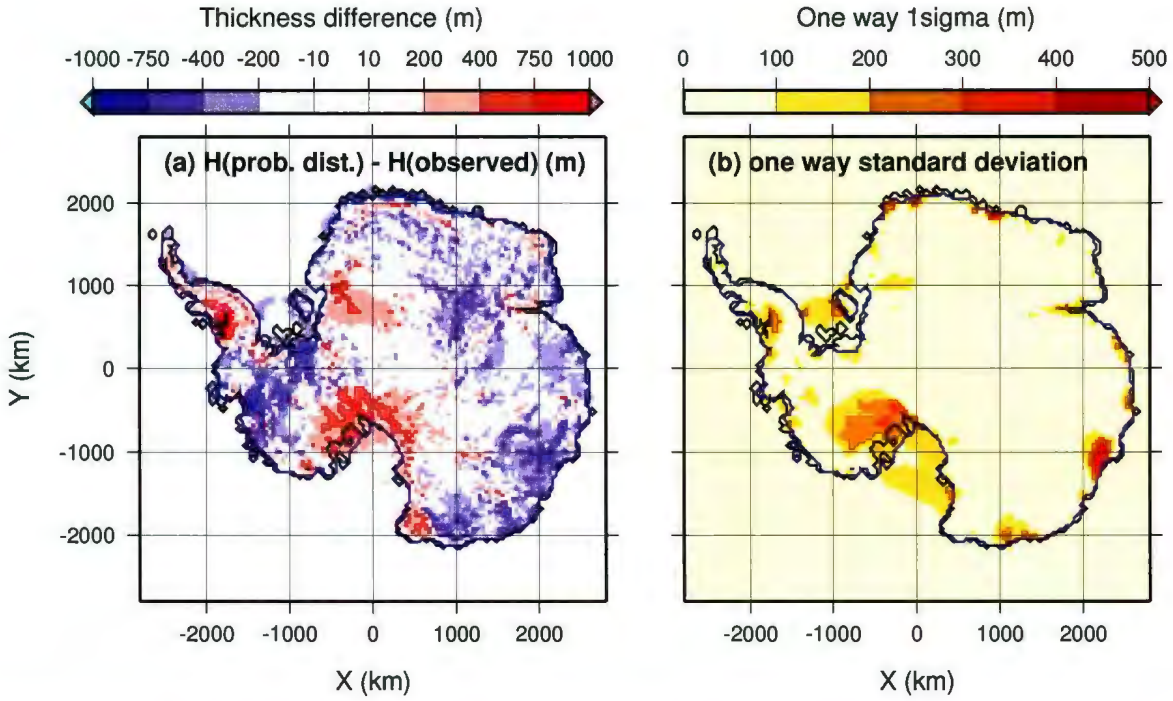


Figure 4.5: (a) difference between mean of the thickness field, as computed by $N_{10}$ , and $ALB_{40}$ (b) One way $1\sigma$ standard deviation.

This individual run underestimates, by more than 500 m in some locations, the measured ice thickness for the WAIS dome, around North Victoria and Wilkes Land, behind the Lambert Glacier and for the Ronne-Filchner Ice Shelf (RON-FIL). The thickness is overestimated, again by over 500 m in some cells, along some of the margins in the Transantarctic Mountains (TAM), the mountainous Antarctic Peninsula (AP), in the region south of Coats Land, and under the ice streams that nourish the

Ross Ice Shelf (ROS).

The reconstructed grounding line is within 1 grid cell of the observations for most of its length except behind the ROS and Ronne (RON) shelves (estimated from Fig. 4.14(a)). Behind the ROS ice shelf the modelled grounding line is further downstream (by up to ~250 km, 6 grid cells) than the observed location. Conversely the modelled RON ice shelf grounding line is located a maximum of ~250 km further upstream than the observations.

The velocity difference misfit (Fig. 4.14(b)) is very small (< 3 m/a) in the slow moving interior of EAIS and along the ice divides of WAIS and AP. The uncertainty of the velocity data estimated from table S1 in Rignot et al. (2011), over most of AIS is <4m/a with a maximum of >17m/a. Misfits rapidly increase in the tributaries and ice streams. At this scale it is difficult to distinguish if the stream velocities are underestimated and the slow moving ice in-between the streams is overestimated or *vice versa*. This pattern is to be expected given that the resolution of the model is at a scale comparable, or larger, than the width of most of the ice-streams in Antarctica. Inter-annual and decadal variability in ice stream velocities also introduces uncertainties into the data model comparisons that will eventually need to be assessed.

The differences between the modelled mean thickness field for $N_{10}$ and observed ice thickness is shown in Fig. 4.5 (a), the same pattern of over and under estimations from the difference plot for run 2679 is approximately replicated here (a consequence of either the best run having a strong influence on the estimated mean and/or the deficiencies being common through the contributing ensemble members). A similar pattern of thickness misfit is seen, to a greater or lessor degree in other contemporaneous resolution AIS reconstructions which operate at a higher grid resolution of 20 km (Pollard and DeConto, 2009; Martin et al., 2010; Whitehouse et al., 2012).

An uncertainty estimation ($1\sigma$ standard deviation) of the present-day thickness

field is shown in Fig. 4.5(b). The largest inter-run variations are seen behind the ROS and around the small outlet glaces along the EAIS margin (*e.g.*, Tottem Glacier in Wilkes land).

Table 4.2: Summary of present-day grounded volumes (mESL) for observations, key individual runs and from the mean of the distributions

| source | total (vol0g) | $1\sigma$ | WAIS (vol0gw) | $1\sigma$ | EAIS (vol0ge) | $1\sigma$ |
|---|---|---|---|---|---|---|
| $ALB_5$ | 62.8 | | 8.8 | | 53.9 | |
| $ALB_{40}$ | 62.7 | | 8.2 | | 54.5 | |
| $W_{09}$ | 63.3 | 1.3 | 8.8 | 0.4 | 54.4 | 0.9 |
| 3506 | 64.3 | | 9.1 | | 55.2 | |
| $N_{10}$ | 63.5 | 1.0 | 9.1 | 0.5 | 54.4 | 0.6 |
| $N^*_{10}$ | 63.4 | 1.0 | 9.0 | 0.5 | 54.4 | 0.7 |
| 2679 | 64.2 | | 9.5 | | 54.7 | |

Table 4.2 summarises the present-day grounded volume (vol0g) magnitudes, in mESL, for the total ice sheet (vol0g), the WAIS (vol0gw), and the EAIS (vol0ge)* for runs 2679, 3506 and the mean from $W_{09}$ , $N_{10}$ and $N^*_{10}$ . The 0.6 m discrepancy in regional volumes $ALB_5$ and $ALB_{40}$ should be taken into account as an added uncertainty. Using $ALB_{40}$ as the reference the largest vol0gw misfit is 1.4 mESL (from the $1\sigma$ upper bound of $N_{10}$ ) and for vol0ge is 0.8 mESL (from the $1\sigma$ upper bound of $W_{09}$ ). Scoring that used present-day configuration was performed against $ALB_{40}$ (Briggs and Tarasov, 2012). In all future plots the $ALB_{40}$ values are used as reference.

### 4.4.2 Paleo-data: RSL results

Relative sea level (RSL) data points provide proxy records of either an upper, a lower, or an exact bound of sea level at a specific time for a specific location. A set

*WAIS and EAIS are separated along a line-arc-line shown in Fig 4.3, defined as 30°W ->85°S ->170 °W .

of data points from the same site can be used to constrain a local RSL chronology. The constraint database (Briggs and Tarasov, 2012) used to evaluate the ensemble contains eight RSL sites, with a total of 96 data points. Four of the sites are located around EAIS (9101, 9201, 9202, 9301), two along the edge of the TAM and present-day ROS (9401, 9401), one is on the AP (9601), and one site is located in the South Shetland Islands (9602). The median age of constraint for the RSL data is 5.0 ka. The misfit scores were computed in accordance to the evaluation method described in Briggs and Tarasov (2012). The volume of influence calculation attributes the RSL data an inter-data weight of 8%.

The EAIS RSL data sites, with their respective constraints and reconstructed sea level curves from runs 2679, 3506 and the upper and lower $1\sigma$ error bars from $W_{09}$ are presented in Fig. 4.6. The remaining sites are presented in Fig. 4.7. The RSL error bars are computed by running the $1\sigma$ upper and lower bounded ice chronologies of the probability distributions thought the sea level solver (Tarasov and Peltier, 2004; Tarasov et al., 2012; Briggs et al., 2013). Thus they represent an RSL chronology that corresponds to a one $1\sigma$ upper or $1\sigma$ lower bound ice chronology for the ensemble (*i.e.*, at all locations and for all times) and therefore not to any actual member of the ensemble.

To avoid clutter in the figures whilst ensuring that both glaciologically consistent runs and the probabilistic reconstructions are represented, only one set of error bounds, $W_{09}$ , are presented. $W_{09}$ is chosen over $N_{10}$ because the sites where the RSL reconstructions have a tendency to be too high or too low, the $W_{09}$ upper or lower bounds are the closest to the observations. $W_{09}$ , therefore, gives the smallest misfit for the ensemble (given the caveats of a limited number of parameters and runs, the challenges in defining the evaluation method, and in producing the probability distribution). In addition, the $1\sigma$ upper and lower bounds for $W_{09}$ and $N_{10}$ follow

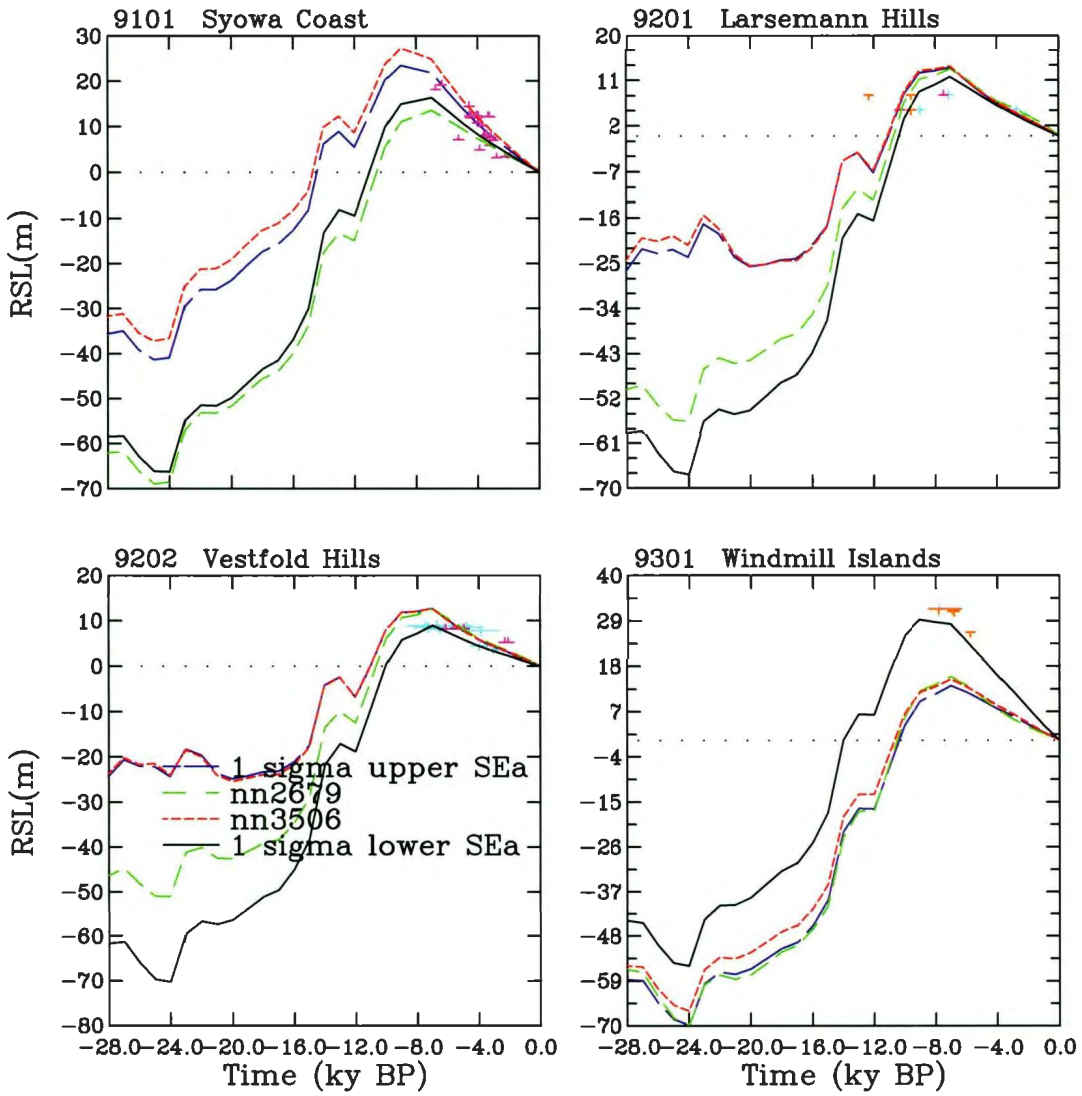


Figure 4.6: RSL data points and sea level curves for the EAIS sites. Observed RSL data points are colour coded according to the constraint they provide: two-way (light blue, dated past sea level); one-way lower-bounding (mauve, past sea level above or maximum age of beach) or one-way upper-bounding (orange, past sea level below or minimum age of beach). One-way error bars are generally indeterminate in their non-bounded direction, though not shown as such to avoid clutter. For a detailed description of the RSL dataset and its processing refer to Briggs and Tarasov (2012).

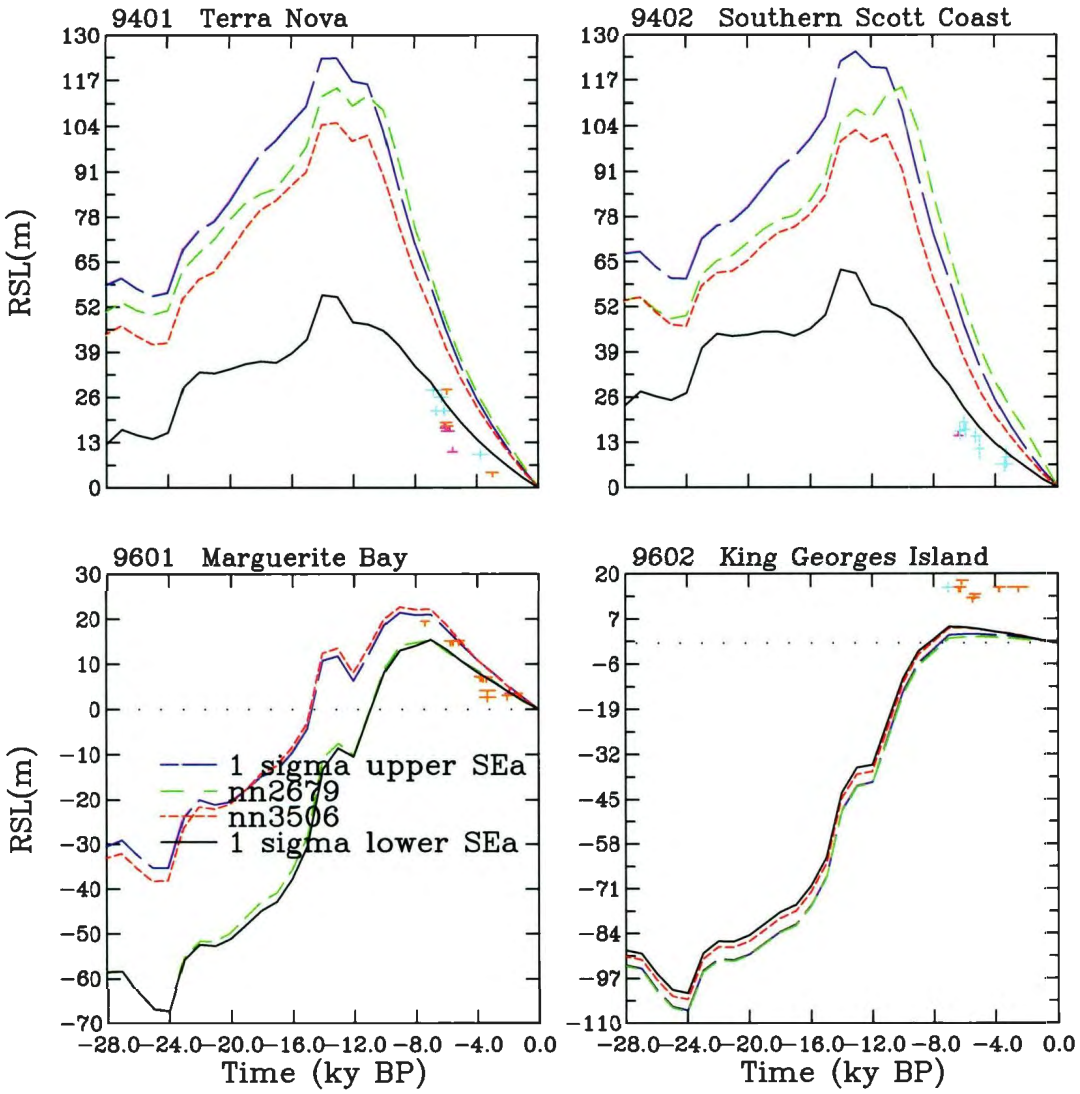


Figure 4.7: RSL data points and sea level curves for the TAM/ROS RSL sites (9401, 9402) and the Antarctic Peninsula sites (9601, 9602). Figure notes as for Fig. 4.6.

similar trajectories thus little qualitative information is lost in not presenting $N_{10}$ . Any noteworthy differences are mentioned in the text.

For the assessed reconstructions all but the two TAM/ROS sites present the same pattern of a sea level low-stand at ~24 ka that rises until 14-13 ka were there is a brief period, lasting until ~12 ka, of either decreasing sea level or, in the case of 9602 (South Shetland Islands), a large reduction in the rate of sea level increase. After ~12 ka the sea level again rises until a high stand at ~8 ka after which it falls smoothly until present-day. For the ROS sites the high stand occurs earlier. At site 9401 in the ROS, it occurs at ~14-13 ka, followed by a decrease in sea level until 12 ka. Then, depending on the reconstruction evaluated, the rate of sea level change reduces, levels off, or gradually increases until 11 ka, after which there is a smooth decrease until present-day. At site 9402, again depending on the reconstruction, either the above pattern is seen *i.e.*, high stand at 13 ka, or the high stand occurs earlier at 11-10 ka.

The TAM/ROS sites exhibit the largest, ~70 m, variation in RSL between the reconstructions at around 14 ka (this value is approximately the same for both the $W_{09}$ and $N_{10}$ distributions). In contrast, at this time, the maximum variability of the other sites is no more that ~15 m. During the period of the low stand at 24 ka, the variation at all but site 9602 is ~30-45 m. Note the mismatches are estimated from the plots.

### 4.4.3 Paleo-data: ELEV results

The ELEV data points are derived from surface exposure dating of glacially transported erratics and exposed striated bedrock. They provide two constraints, a paleo-ice thickness from the time when the sample was first exposed and a maximum ice

thickness constraint from the time they became exposed until present-day*. The observational error model used to compute the misfit score calculates the smallest misfit for all past ice surface elevations identified as being part of a thinning trend, thus both the temporal and elevation misfit is taken into account (Briggs and Tarasov, 2012). The constraint database contains 26 ELEV sites with a total of 106 data points and a median age of constraint = 9.6 ka. The volume of influence calculation attributes the ELEV data with an inter-data weight of 7% (Briggs and Tarasov, 2012).

The upper plots in Figs. 4.8 to 4.10 show the elevation of the ELEV observations, the modelled elevations (associated with the smallest misfit) from the ensemble and the $1\sigma$ upper and $1\sigma$ lower bounds for both $W_{09}$ and $N_{10}$ . The lower plots show the modelled to observed misfits. Age-altitude plots for each site can found in the Figs. C.5 to C.30 of the Appendix.

The sites can be categorised into 4 (approximates) types: sites with bounds that bracket the observations (ECR, PCM2); sites with a maximum upper or lower bound misfit that is less than ~300 m (FM1, FM2, FM3, GM, PCM1/2, CLM, ALM, EFR, ECR, PIB1/2, BM, EM); sites with maximum upper or lower bound misfit less than ~600 m (LHB, PCM2, WSM, SR1) and sites with the misfit >600 m misfit (RG1, RG2, RG3, HG, EFR, WPL, AXS, AXN, SR2). The sites that are >600 m misfit lie in the areas where the present-day difference plots have a large thickness mismatch *i.e.*, TAM, AP and south of Coats land. The maximum misfit, SR2, is 1139 m.

*The constraint is produced using surface exposure dating to calculate the amount of time that a glacially transported erratic or previously covered bedrock has been exposed to the atmosphere *i.e.*, uncovered by ice. Taken together with an elevation measurement for the sample this yields a paleo-ice surface elevation. A number of dated samples from a location, or along a transect, allows a thinning history to be reconstructed

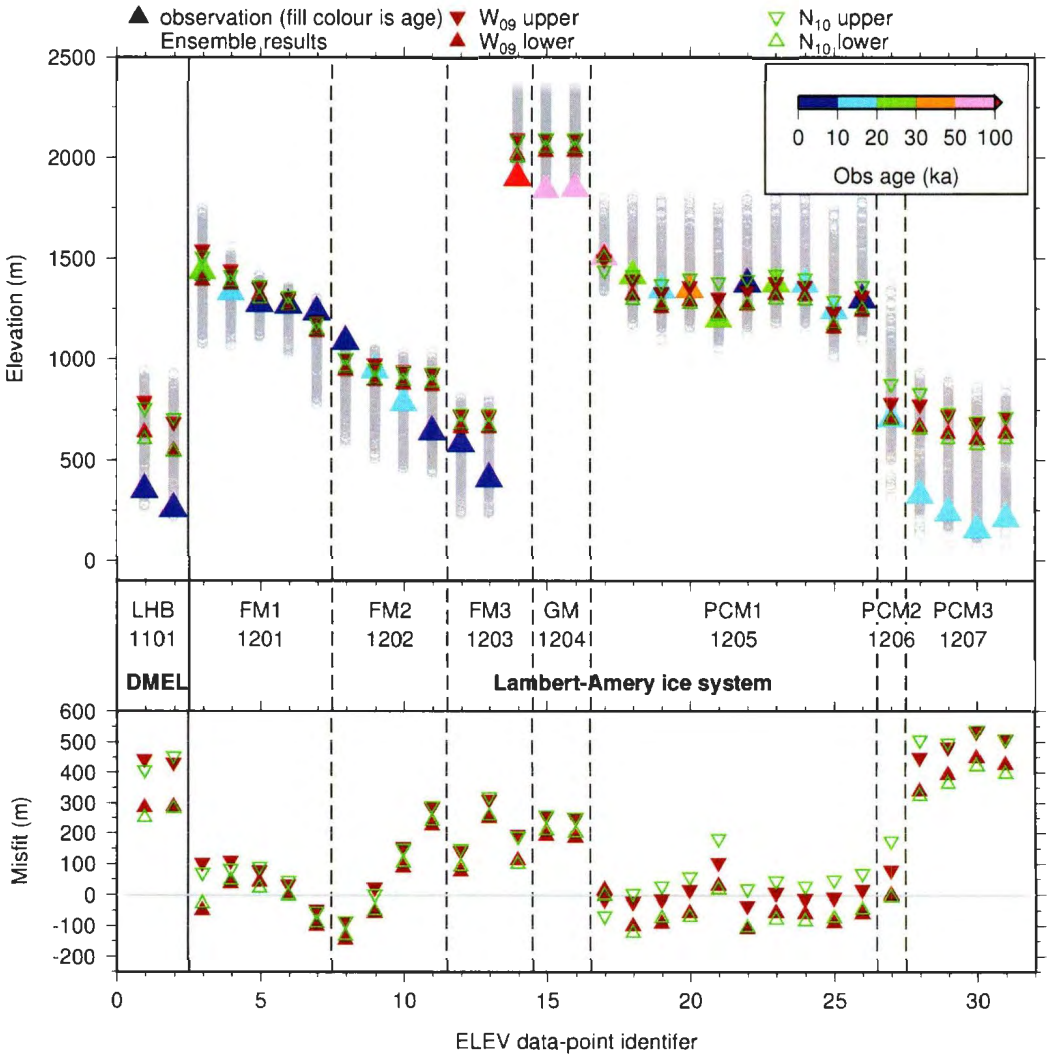


Figure 4.8: ELEV observations, ensemble results, upper and lower bounds from $W_{09}$ and $N_{10}$ , and computed misfits for Dronnig Maud and Enderby land (DMEL) and Lambert-Amery Ice Shelf (LAIS) sectors.

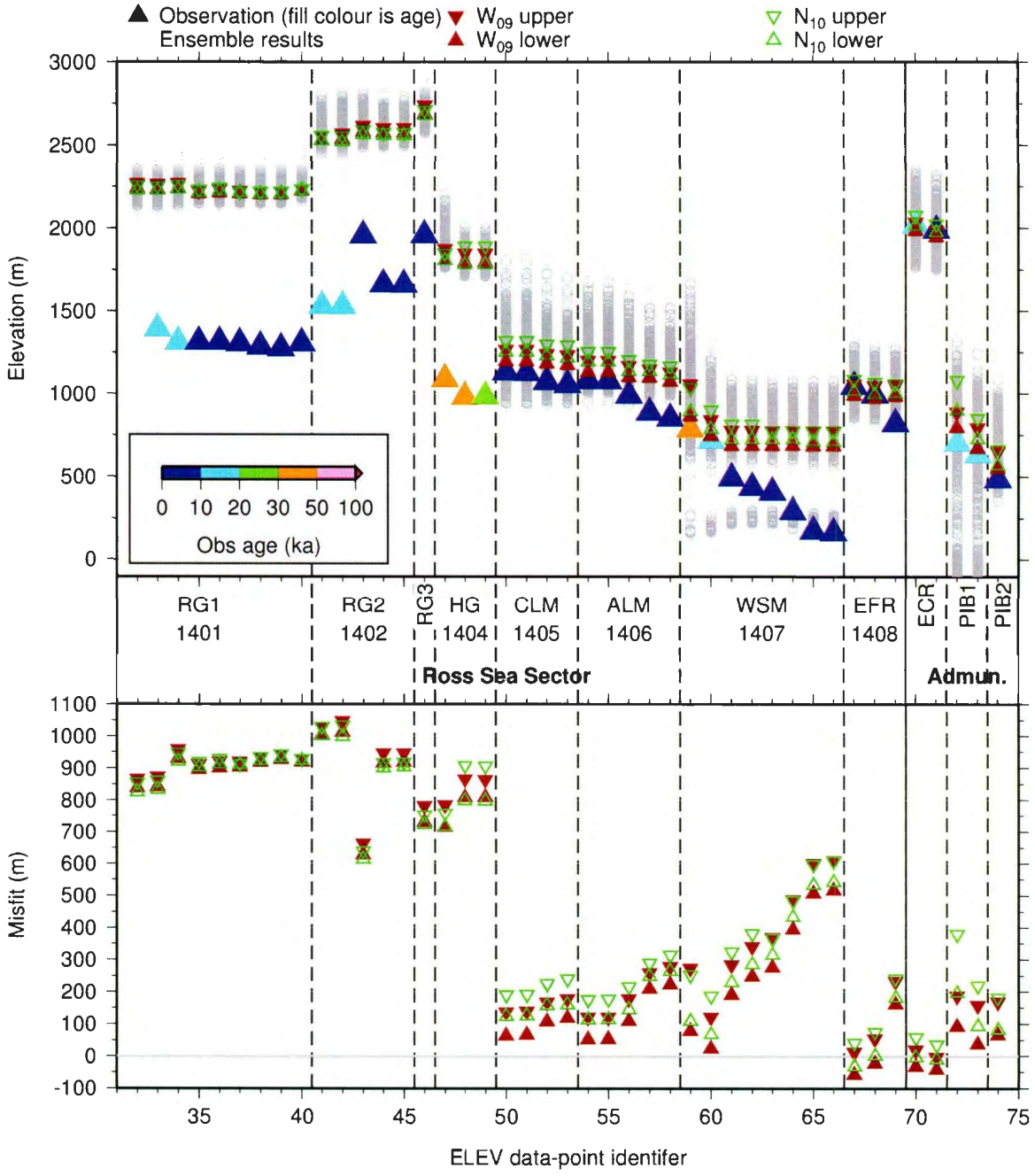


Figure 4.9: ELEV observations, ensemble results, upper and lower bounds from $W_{09}$ and $N_{10}$ , and computed misfits for Ross (ROS) and Admunsen sea (AS) sectors.

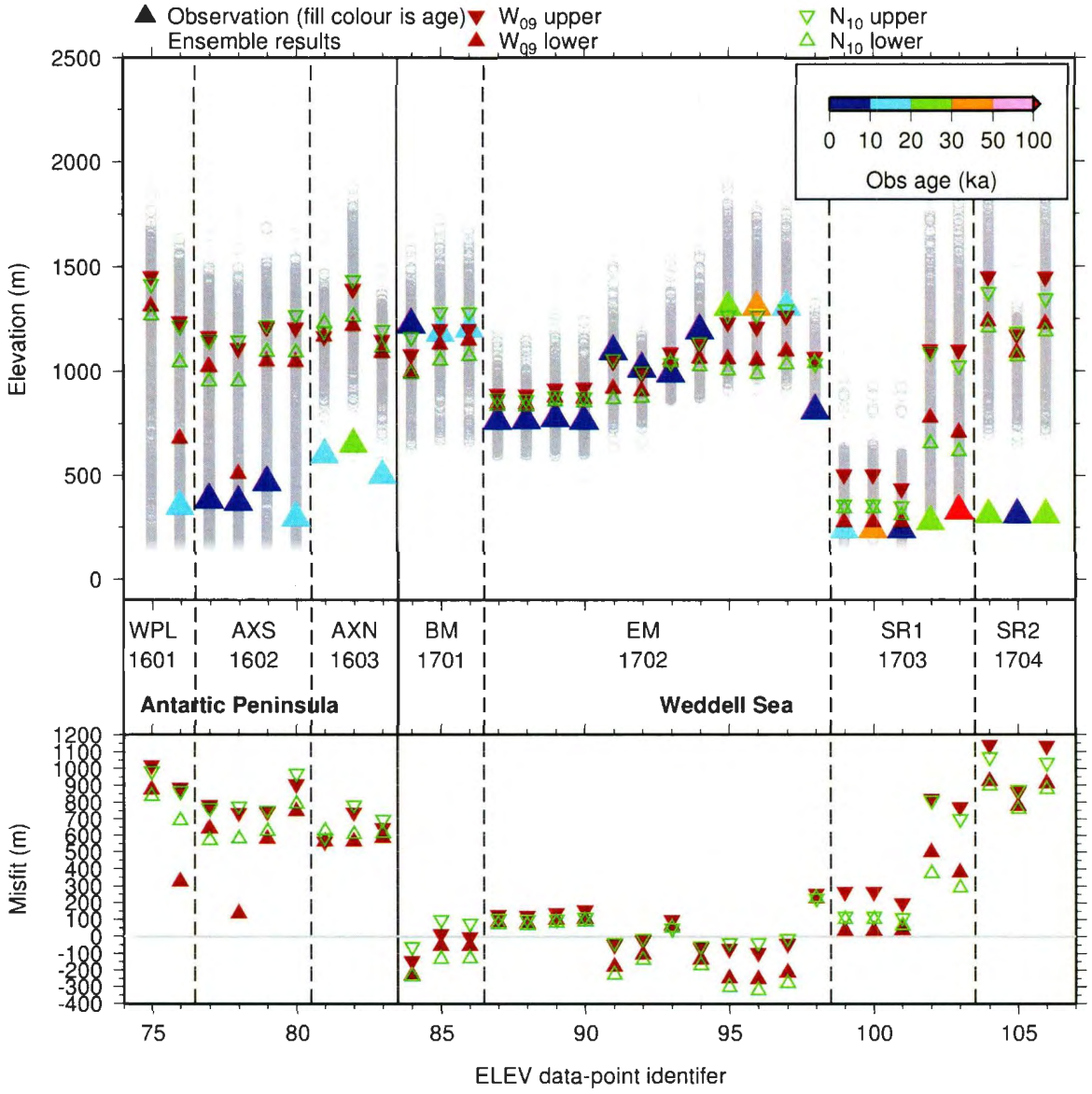


Figure 4.10: ELEV observations, ensemble results, upper and lower bounds from $W_{09}$ and $N_{10}$ , and computed misfits for Antarctic Peninsula (AP) and Weddell Sea (WS) sectors.

### 4.4.4 Paleo-data: EXT results

The EXT constraint type is derived from marine cores. Two types of constraint are presented in the Briggs and Tarasov (2012) database: the grounding line retreat data (GLR) constrains the age of the time when the grounding line retreated over a location; the open marine conditions (OMC) data provide an age that records the existence of open marine conditions at a location (as such they are a one-way bound, the data can only constrain the event of open ocean conditions existing at a given time but not when it started. GLR is a two-way bound). The database contains 21 GLR data points and 6 OMC data points, they are relatively well distributed around the AIS and have a median age of 16.6 ka. The models are scored by extracting the time of the modelled GLR or OMC event from the relevant site and computing the misfit to the observation; the volume of influence calculation for the inter-data type weighting attributed the EXT data with just 2% of the total weighting (Briggs and Tarasov, 2012).

The EXT observations, full set of ensemble results and top 10 and 40 runs (number of runs required to meet the $P_{90}$ target) for $W_{09}$ and $N_{10}$ are presented in Fig. 4.11. The temporal density of coverage for the ensemble results can be inferred from the concentration of the open circle symbols. A model result at 120 ka signifies either that the modelled retreat event happened at 120 ka or that the grounding line retreat event has not occurred at the modelled core location between 120 ka until present-day (the range over which scoring is performed) for that run. The oldest data point is 30.7 ka, thus either scenario is a poor reconstruction.

Only five of the GLR cores (2401, 2402, 2403, 2501 and 2503) produce runs with misfits that are <10 kyr. For the remaining cores, either the ensemble never reproduces a GLR event since 120 ka or none of the modelled events that are close to the observation were generated from the better runs. The OMC constraints all have runs

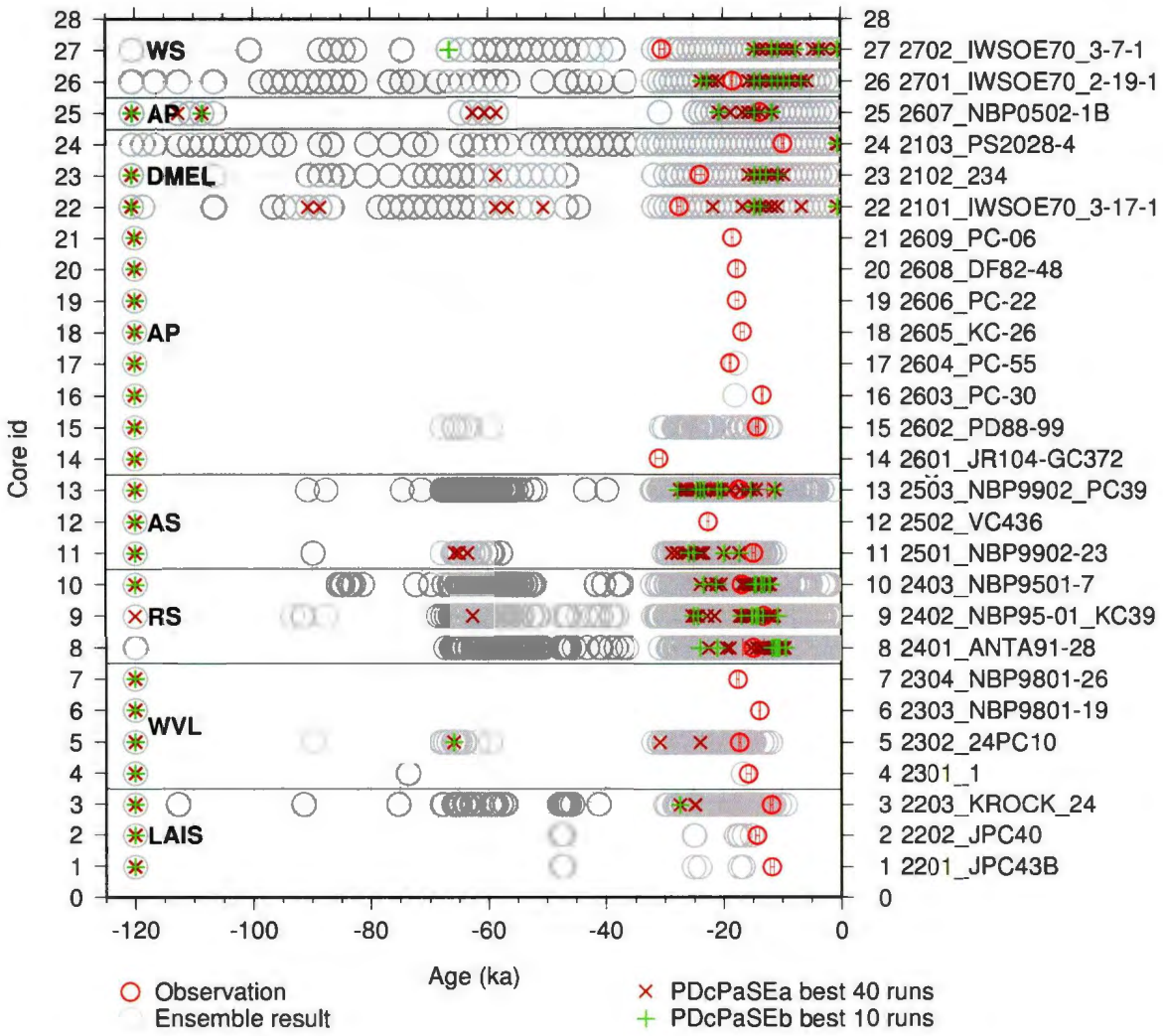


Figure 4.11: EXT observations and ensemble results. Core identifiers 1-21 are grounding line retreat (GLR) two-way constraint types, 22-27 are open marine conditions (OMC) one-way constraint. Black horizontal lines and associated labels segregate and identify the different sectors.

that bracket or recreate the observation but only one core has a run(s) that are <5 kyr misfit.

### 4.4.5 Paleo-data misfit by sector

The following paragraphs describe the pattern of misfits for the sites sector by sector. Only EXT observations that are reconstructed by the ensemble are mentioned. A summmary is provided in the discussion.

**Dronning Maud-Enderby Land (DMEL)** The two sites of this sector, RSL site 9101 and ELEV site 1101, are located adjacent to each other (same grid cell) and directly on the Syowa coast. ELEV observations record a thinning of ~100 m between 10 ka and ~6.5 ka, with no earlier data. The reconstructions in the $N_{10}$ age-altitude plots commence thinning after 16-17 ka, with ~300-400 m excess misfit. 9101 is derived from marine shells which provide a lower bound on decreasing sea level from ~7-3 ka. The excess ice of 1101 is reflected in the under-prediction of the RSL curves. The smallest misfit for both sites is from the $1\sigma$ lower bounds.

**Lambert-Amery ice sheet (LAIS)** The reconstructions of the Framnes Mts sites (120[1,2,3]), close to the DMEL sector and abutting the coast of EAIS, all begin deglaciating at around 16-17 ka. The beginning of deglaciation in the Prince Charles Mts sites (120[5,6,7]), upstream of the ice sheet is more difficult to distinguish and depends on the reconstruction assessed. The largest misfits, all less than 600m excess for the ELEV sites of this sector are found at sites PCM3, all other ELEV sites have misfits that are <300 m. The sites in the Framnes and Prince Charles Mts regions both follow the same pattern of small (<100) misfits at the upstream/higher site and larger misfits occurring closer toward the coast or ice sheet-ice shelf margin. There is

a marked reduction in the variance of the 120[1,2,3] reconstructions from 200-300 m at 15-16 ka to <100 m at 4 ka.

The two data points of site 1204, upstream of the Lambert Glacier and in the interior of EAIS, have misfits approaching 300 m. This is poor considering this site is far from the coast and is in a topographically simple region with slow moving ice. More noteworthy is the small (10-70 m depending on which chronology is assessed) subsequent over-riding of the site by the reconstructions at 25 ka. If the model is accurate (and the systematic over-prediction misfit ignored) this could be explained physically by the erratic receiving some of its cosmogenic dosage from elsewhere and subsequently being transported into is current location (Lilly et al., 2010). There is a period of little change or thickening between 23 ka and 16-17 ka, followed by continuous thinning.

The two RSL sites 9201 and 9202 are located within about 100 km of each other close to the Victoria-Wilkes sector. They both comprise a mixture of upper, lower and exact data points (isolation basins for both studies, 9202 augmented with mollusks). For site 9101 the misfits to the exact data point are small (<5m) and the high stand is ~5 m too high. Site 9202 has similar small mismatches (<5m) but the sea level curves are unable to reconstruct both the dated sea level and the sea level minimum observations.

For all sites except 9202 the $1\sigma$ lower bounds are closest to the observations; there is no distinction for site 9202

**Wilkes-Victoria Land (WVL)** A single RSL site is the only terrestrial dataset available in the (Briggs and Tarasov, 2012) database for constraining this sector of ice. Site 9301 on Windmill islands is a set of upper bounds and a single dated sea level point. The $1\sigma$ lower bounds (including $N_{10}$ , which follows $W_{09}$ at this site)

have the smallest misfit.

**Ross Sea (RS)** This sector is divided along the TAM. The east side is nourished from the East Antarctic ice sheet (EAIS) with ice flowing over and thought the TAM, the west side is nourished by the WAIS. On the EAIS side of the sector, the paleo-data sites (940[1,2], 140[1,2,3]) have either excess ice thickness or sea level. RSL sites 9401 in Terra Nova bay comprises maximum, minimum and close ages (from dated organic matter recovered from raised beaches). Site 9401, 200 km further south is similarly constrained. At both sites the smallest misfit is from the $1\sigma$ lower bound. There is a substantial (~>50 m) difference in the high stands between the $1\sigma$ lower bounds and the other three chronologies. The three ELEV sites in the TAM have some of the largest misfits fits to the data (500-1100 m) in the database and show little variability.

ELEV sites 1404 to 1408 are located in the E-SE Ford ranges of western Marie Byrd Land indicate a continuous thinning of 700 m over the past 10 ka (Stone et al., 2003). The sites are within 1-2 grid cells of each other, the reconstructions begin to deglaciate at around 17 ka. Collectively, the smallest misfit for the reconstructions occurs at the older higher sites and increases toward the younger/lower data points, in all cases there is insufficient thinning toward the end of the chronology. There is little variability in the chronologies (<300m at LGM), the $1\sigma$ lower bounds have the smallest misfit.

**Amundsen Sea (AS)** ELEV site 1501 is located at the most southerly end of the Executive Committee range in an area of gentle ice slopes. The upper and lower bounds bracket the observations, with $N_{10}$ lower and $W_{09}$ upper having the smallest misfit (< 50 m). In all but one of the chronologies there is a gentle thickening from pre-LGM until thinning begins at about 17 ka until present-day. The 10 ka high-stand generated from a modelling study discussed in the data source article Ackert et al.

(1999) is not seen in the reconstructions.

The observations at the two ELEV sites (150[2,3]) on opposite sides of Pine Island Bay are both overestimated. The $1\sigma$ bounds give the lowest misfits, ~<200 m. Both sites show a gradual thinning from pre-LGM until a sharp increase in thinning beginning between 17-11 ka, depending on the chronology assessed. The pulse of rapid thinning for these sites is well reflected in 4.15.

**Antarctic Peninsula (AP)** The present-day over-estimation of ice thickness in the AP is also seen in the ELEV sites, nearly all the chronologies have a >600 m over-estimation of the observations. The sites are all located within a few grid cells of each other, in a topographically complex region (the sites are located on each side of the George VI Sound) with many sub-grid features and steep gradients. Ignoring the thickness bias, the chronologies do capture the gradual thinning trend of deglaciation; the commencement of thinning at these sites occurs around 15 ka.

The sampled material for RSL site 9601, in Marguerite bay, provides maximum sea level constraints. The $W_{09}$ and $N_{10}$ $1\sigma$ lower (and run 2679) reconstructions are all on the correct side for all but two of observations *i.e.*, the reconstructed sea level falls within the one-way error bound. The misfit for the other reconstructions is small <10 m.

Site 9602 on King George Island contains a single exact age and a number of upper bounds. The reconstructions are all >15 m from the exact age point and have little variability (therefore this site provides little constraining potential). The island is a sub-grid feature in the model and is too small for sufficient ice growth, that can subsequently be removed, to enable enough isostatic adjustment to reconstruct the observation accurately.

**Weddell Sea (WS)** The reconstructed grounding line in this sector has a clear retreat signal, between the LGM and 12 ka the modelled LGM grounding line retreats continuously inland, along the Crary trough. The inland pockets of floating ice also increase in size. After 12 ka the grounded ice begins to disintegrate, by 8 ka the grounding line follows a similar path to the present-day configuration. The largest amount of thinning occurs between 12 and 10 ka.

The ELEV sites in the Weddell Sea sector constraint different regions of the sector. Site 1701, located on the east of the AP (ice flowing into the sides of the RON), records a thinning of ~300 m from about 7 ka, the reconstruction misfits are <300 m. Both the upper and the lower bounds predict the thinning to begin sometime after 15 ka. In addition, the $W_{09}$ upper bound (and run 3506) have a sharp increase in the thinning rate after 12 ka, when the grounding line has begun to retreat rapidly). The present-day reconstructed surface elevations have a small (<50 m) misfit. The $1\sigma$ upper bounds have the smallest misfits to all the data.

Site 1702 in the Ellsworth Mts constrains the ice flowing into the RON shelf. The observations record an unchanging elevation from 35 to 15 ka, after which thinning begins. The misfits are all < 400 m, the chronologies all under-predict the older, continuous surface elevation observations and over-predict the youngest group of observations. Deglaciation begins at around 14 ka for the upper bounds, the lower bounds see a period of thickening at around the time the grounding line is retreating. The $1\sigma$ upper bounds have the smaller misfits. The reconstructions all predict a thickening, of differing degrees, from present-day elevation levels at 40 ka until 14 ka.

The last two sites, 1703 and 1704, are from the Shackleton range along the edge of the Slessor glacier (which nourishes the FIL ice-shelf). Based on the constraint data these sites should see little change in the surface elevation, however, the results are peculiar. Firstly they are separated by a single grid cell, yet have very different

misfits. Site 1703 has <300 m misfits for 3 of the 4 data points. The minimum misfit for site 1704 is 700 m. Secondly, the reconstructions produce a substantial thickening prior to the deglaciation thinning. This is similar to 1702, the chronologies see a period prior to 34 ka with elevations similar to, or below present-day values, then a sharp increase in elevation at 34 ka. The age of deglaciation is ~16 ka after which the rapidly thinning begins.

### 4.4.6 Antarctic deglaciation chronology and LGM reconstruction

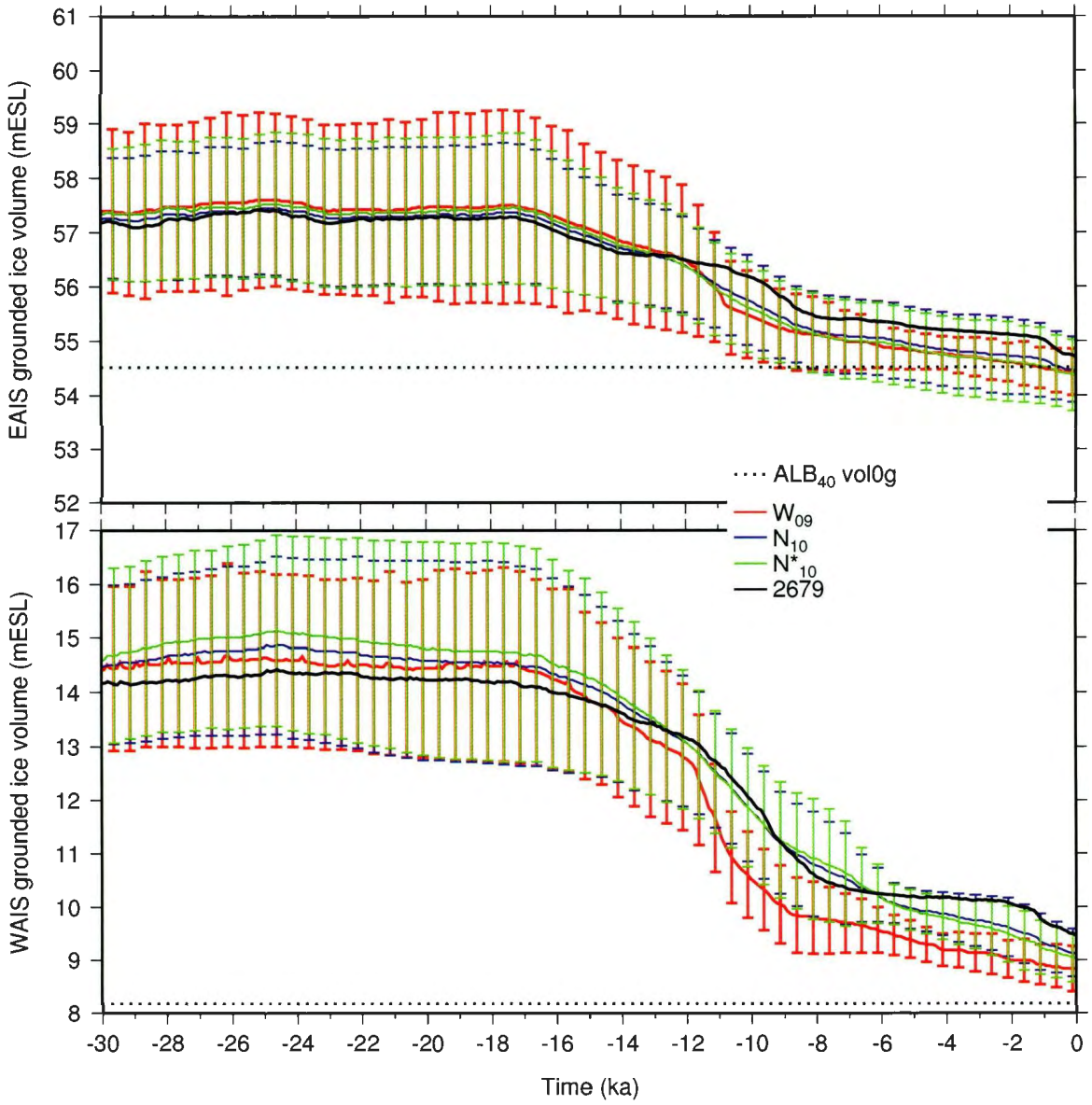


Figure 4.12: EAIS (upper) and WAIS (lower) grounded ice volume evolution with $1\sigma$ error bars generated from mean for $W_{09}$ , $N_{10}$ and $N^*_{10}$ .

Evolution of the WAIS and EAIS grounded ice volume (volgw, volge) from 30 ka to present-day, calculated from $W_{09}$ , $N_{10}$ and $N^*_{10}$ , is presented in Fig. 4.12. The

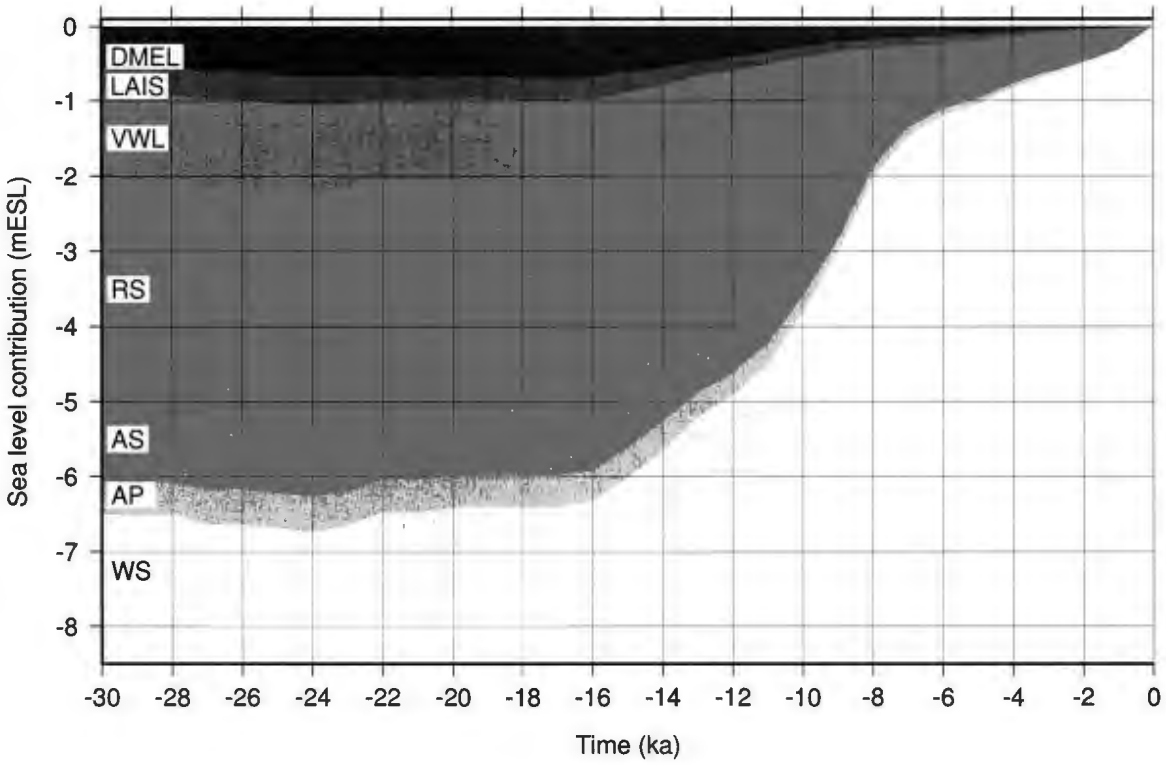


Figure 4.13: Eustatic sea level contributions, relative to present-day, from the drainage sectors computed from the $N_{10}$ mean.

impact of the narrow and wide sieves is clearly seen in the evolution of the volgw time series; runs rejected by the narrow sieve of $N_{10}$ but included in $W_{09}$ produce a signal that has a more rapid and larger magnitude decreasing trend between ~12 ka and 9 ka. The decrease from 9 ka to present day for $W_{09}$ is less steep than $N_{10}$ . There is little distinction between $N_{10}$ and $N^*_{10}$ in either volgw or volge. For the EAIS, there is a slight maxima between 24-25 ka and at about 17 ka after which deglaciation commences. In WAIS there is also a maxima between 24-25 ka (more pronounced for $N^*_{10}$ ) then a slow decrease in volgw until about 16-17 ka after which deglaciation accelerates until 12 ka, then accelerates again, until the signals diverge at 9 ka. The integrated grounded area evolution (not shown) shows a similar trend.

Defining the local LGM of AIS as occurring at 24 ka, the regional LGM contributions to eustatic sea level relative to present-day ($\Delta\xi_L$) from the three distributions

is presented in Table 4.3.

Table 4.3: Summary of the AIS, the WAIS, and the EAIS LGM (24 ka) contributions to eustatic sea level relative to present-day, $\Delta\xi$, from the $W_{09}$ , $N_{10}$ , and $N^*_{10}$ distributions.

| | AIS | | WAIS | | EAIS | |
|---|---|---|---|---|---|---|
| source | volg $\Delta\xi$ | $1\sigma$ | volgw $\Delta\xi$ | $1\sigma$ | volge $\Delta\xi$ | $1\sigma$ |
| $W_{09}$ | 8.9 | 2.5 | 5.8 | 1.4 | 3.1 | 1.2 |
| $N_{10}$ | 8.6 | 2.8 | 5.7 | 1.8 | 3.0 | 1.1 |
| $N^*_{10}$ | 9.2 | 3.0 | 6.0 | 1.9 | 3.1 | 1.2 |
| mean $\Delta\xi$ | 8.9 | - | 5.8 | - | 3.0 | - |

Using the regions that approximately demarcate the major drainage basins (shown in Fig 4.3 and defined in Briggs and Tarasov (2012)) allows a sector by sector eustatic sea level contribution estimation to be made, presented in Fig. 4.13. The estimations were computed using $N_{10}$ . The RS sector is the largest contributor providing ~3 mESL from LGM to present-day The WS sector, the other major ice shelf is the next largest contributing 1.5-2 mESL. Combined, the Admunsen sea (AS) and AP generate ~1.5 m. The VWL sector provides <1.5 mESL and, combined, the DMEL and LAIS sectors provide about 1 mESL.

#### 4.4.6.1 LGM (24 ka) reconstruction

The AIS LGM (24 ka) characteristics are shown in Fig. 4.14. As part of the Livingstone et al. (2012) review of AIS paleo-ice streams (from which the EXT data was also obtained (Briggs and Tarasov, 2012)) a reconstructed LGM grounding line map was created, shown in Fig. 4.14 (a). Using geomorphological evidence, they identified the maximum extent of the grounding line and therefore of the grounded component of the ice sheet at the LGM. Their ice extent map also identifies the sectors that are speculative due to little or no data.

In most locations, the modelled LGM grounding line never advances far enough

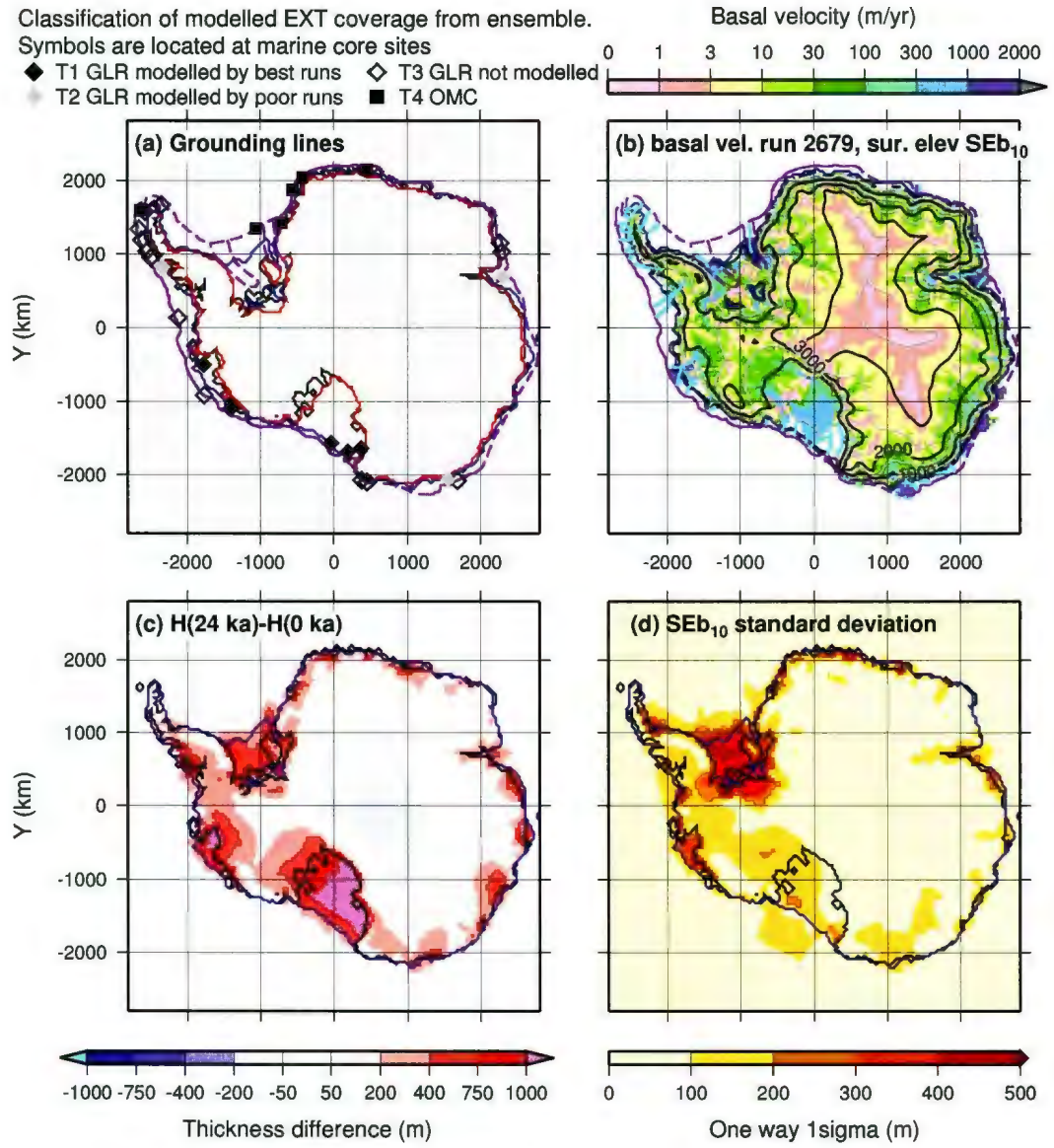


Figure 4.14: AIS LGM (24 ka) characteristics from $N_{10}$ and run 2679. For reference the modelled LGM grounding line (blue) is shown in all plots. (a) shows, in addition to the modelled LGM grounding line, the Livingstone et al. (2012) reconstructed (purple) and speculative (dashed purple, see text for details), LGM grounding line Livingstone et al. (2012), the observed (black) and modelled (red) present-day grounding line. To aid misfit estimates, the graticules have a resolution of 80 km, thus 2x model resolution. Symbols representing the ability of the ensemble to recreate the EXT observation are plotted at the location of the marine cores (see text for details of the typology). (b) magnitude of surface velocity (from run 2679) overlain with surface elevation (1000 m contours black, 500 m grey) from $N_{10}$ , modelled LGM grounding line (blue) and Livingstone et al. (2012) reconstructed grounding line (purple). Also shown are the Livingstone et al. (2012) paleo-ice-stream locations (cyan). (c) $N_{10}$ 20 ka ice thickness minus present-day (modelled) ice thickness, modelled LGM (blue) and observed present-day (black) grounding line. (d) One way $1\sigma$ standard deviation of $N_{10}$ . The cells with the largest variance are regions that would most benefit from additional constraint and could provide a focus location for future field campaigns.

onto the continental shelf to reproduce the Livingstone et al. (2012) reconstructed grounding line. As such, the modelled grounding line is unable to recreate the GLR observations (shown on the plot). The observations are represented as symbols, plotted at the locations of the marine cores, and are codified to represent how well the ensemble recreates each observation *i.e.*, if the observation was never recreated by any run in the ensemble, or only recreated by poor scoring runs etc. The observations that are never reproduced are located closer to the reconstructed Livingstone et al. (2012) LGM grounding line.

In the EAIS, the $N_{10}$ LGM grounding line is nearly always within 80 km (to aid misfit comparison the plot graticule is at 80 km, 2x the model resolution) of the Livingstone et al. (2012) reconstruction. The major areas of grounding line misfit in the EAIS are off-shore from AMY and along the coast of Victoria land (~<200 km misfit); these are, however, both segments of speculative LGM extent. In the WAIS the misfit increases along Marie Byrd land, past Pine Island Glacier until about half-way along the AP. On the Weddell Sea side of the AP, the modelled grounding line is largely unchanged from the present-day grounding line. The modelled LGM grounding line follows the contours of the Crary trough (>1000 m deep) alongside the coast of Coats land. There are also pockets of ungrounded ice further inland. The ROS grounding line has migrated until it is close to the continental shelf.

Distributions of surface velocities (run 2679), surface elevations (mean of $N_{10}$ ), and paleo ice stream locations are plotted in Fig 4.14(b). Paleo ice stream locations were also available as part of the Livingstone et al. (2012) data set and are plotted for comparative purposes. The model reproduces areas of faster ice flow (>30-100 m/a) that align with the larger paleo ice streams (which have a signal further upstream than the modelled LGM grounding line) *e.g.*, LAIS and the Crary trough. However, many of the smaller paleo streams are not replicated as they are located in the zone

that is not successfully reconstructed.

The difference between the reconstructed LGM $N_{10}$ and present-day $N_{10}$ ice thickness is shown in Fig 4.14(c). The LGM configuration has: a thinner interior EAIS; thicker margins around the whole continent; thick grounded ice in the locales where the shelves used to be (because of the migration of the ROS and RON-FIL grounding lines).

Fig. 4.14d shows the $1\sigma$ uncertainty estimation for $N_{10}$ at 24 ka (the distributions for the other means are visually similar). The cells with the greatest variance are located in regions that would most benefit from additional constraint. The largest variations are seen predominantly around the regions of fast flow (*e.g.*, LAIS, PIG) and in the areas of the marine basins of WAIS (under present-day WAIS dome, ROS ice streams, and behind RON-FIL) and EAIS (Victoria land and into Wilkes land).

#### 4.4.6.2 18 ka to present-day snapshots

The evolution of the surface elevation, migration of the grounding line, and WAIS and EAIS mESL contributions between time-slices from 18 ka to PD are shown in Fig. 4.15. The change from 24 and 18 ka is small. As such, this time-slice is not shown. In each subplot the 1000m surface contours and the grounding lines for each time-slice of the plot are shown. The largest magnitude of mass loss from both ice sheets occurs between 12 ka and 10 ka, then between 10 ka and 8 ka, predominantly sourced from ROS with a significant contribution from RON-FIL and the Pine Island Bay. The interior of the EAIS undergoes slight thickening at every stage, however, the margins thin (~<100m/2kyr) producing a net mass loss. The AP and AS sectors both deglaciate with a small (<100m/2kyr) continuous thinning trend apart from a few small regions. ROS and WS deglaciation is dominated by the grounding line retreat pattern.

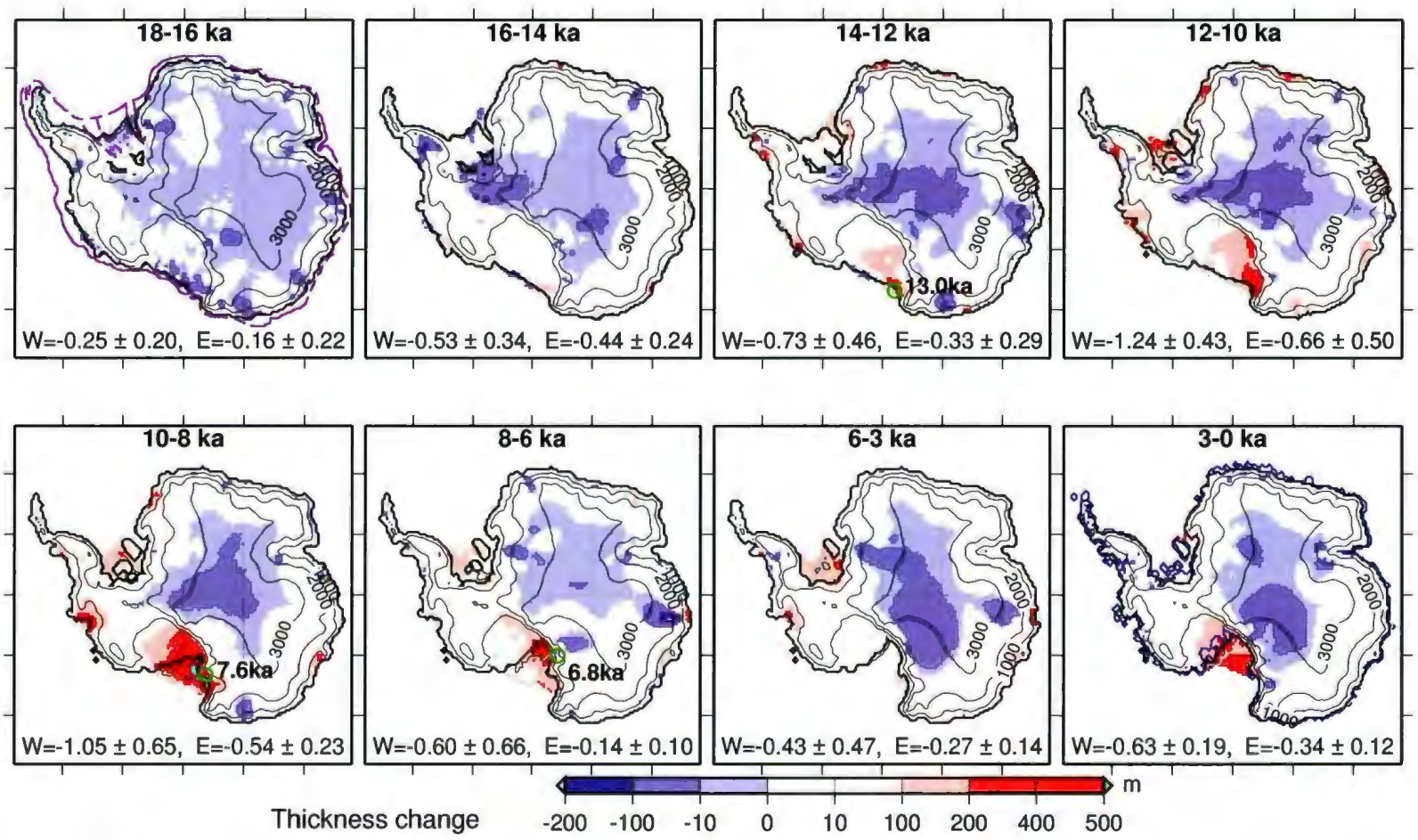


Figure 4.15: Antarctic deglaciation snapshots between time-slices from LGM to PD showing surface elevation, thickness change (Red indicates thinning), migration of the grounding line, and WAIS and EAIS eustatic contributions. The 1000 m surface contours and black grounding line are from the youngest time-slice of the given interval. The grey grounding line is extracted from the oldest time-slice in the interval. Sea level contribution (mESL) between time-slices is presented at the base of each plot for WAIS (W) and EAIS (E). All fields and scalars are computed from $N_{10}$ probability distribution. For reference, the LGM grounding line is presented in the 20-16 ka plot and the present-day observed grounding line is presented in the 3-0 ka plot. The dated green circles are grounding line retreat dates, see Discussion section (Section 4.5). Graticule is at 1000 km intervals.

### 4.4.7 Meltwater pulse 1a/b contributions

Figure 4.16 plots the run scores against the MWP-1a and 1b contributions for the $W_{09}$ wide and $N_{10}$ narrow schemes*; the runs that fall within the $P_{90}$ target are highlighted, by their fill colour, according to their ranking. There is no correlation between the modelled MWP-1a or MWP-1b predictions and the run scores, as such, the MWP contributions is estimated from the upper and lower values from the runs that fall within $P_{90}$ coverage.

For MWP-1a, ignoring the single low probability run at 1.8 mESL in Figure 4.16 (a), the likely maximum contribution is less than 1 mESL. The maximum contribution for MWP-1b from the wide scheme PDcPaSEa is ~1.5 mESL and <1 mESL from the narrow scheme PDcPaSEb.

*The MWP-1a contribution is computed as max(volg14.6 – volg14.0, volg14.5 – volg13.9, volg14.4 – volg13.8) where volgXX.X is the grounded ice volume at time XX.X (ka), the different periods allow flexibility as to when MWP-1a occurred. MWP-1b is computed as volg11.4-volg11.0.

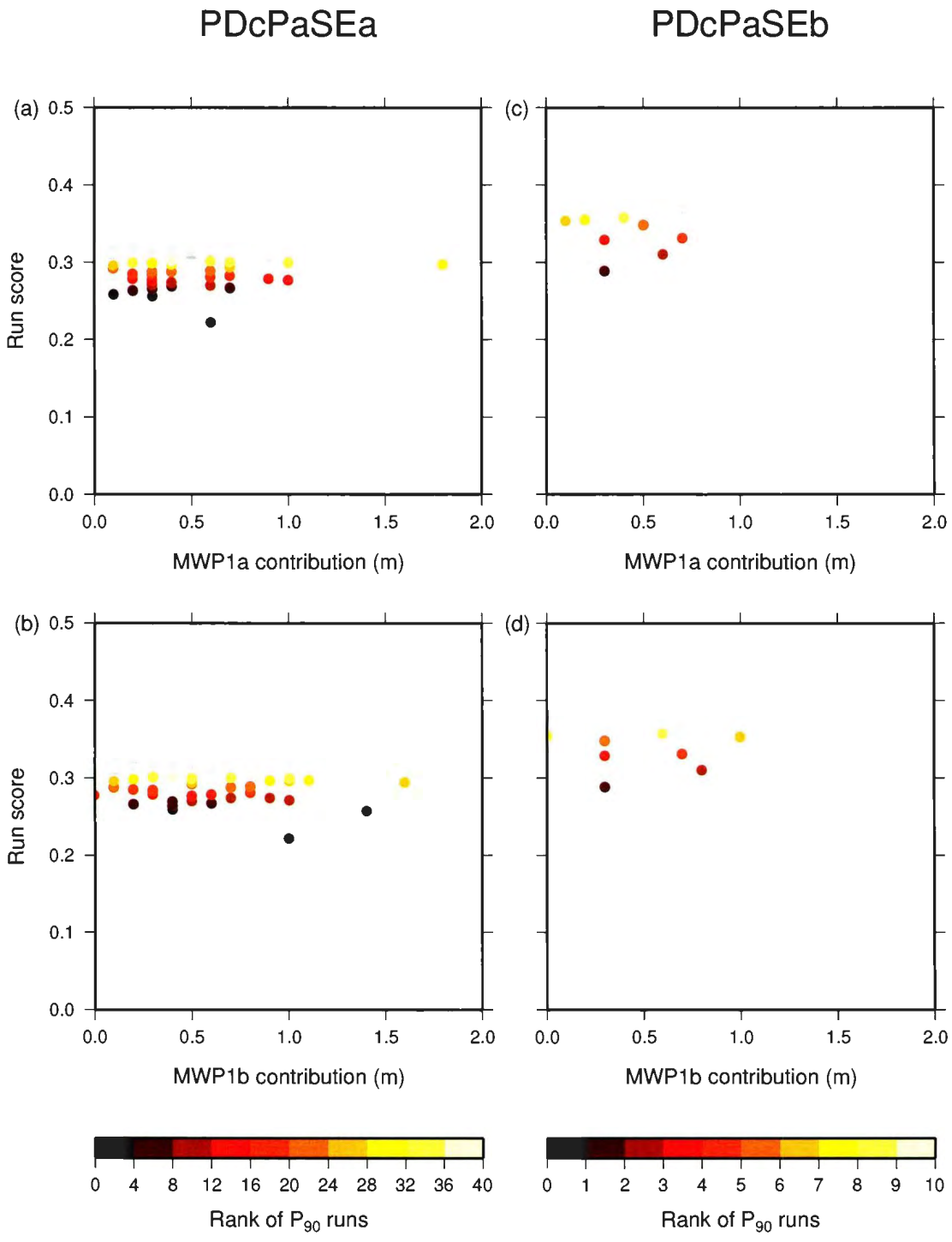


Figure 4.16: Run scores plotted against the MWP-1a and 1b contributions for the $W_{09}$ wide and $N_{10}$ narrow schemes. The crosses represent all the runs for each of the schemes, and circles are the runs that fall within the $P_{90}$ target, highlighted by their fill colour, according to their ranking.

### 4.4.8 Eemian configuration

The sea-level high stand of the Eemian, as with the LGM low stand, is a globally integrated signal, as such, there is uncertainty to the exact magnitude and timing of the sea-level rise attributed to each ice sheet. Previous studies (Cuffey and Marshall, 2000; Tarasov and Peltier, 2003; Kopp, 2012) have computed estimations of the Eemian contribution to sea level from AIS relative to present-day (subsequently refereed to as $\Delta\zeta$ in mESL). Note that $\Delta\zeta$ is inverse to $\Delta\xi$, the volume excess at LGM (*i.e.*, sea-level equivalent locked up in the larger LGM AIS configuration).

The narrow and wide sieves used in the scoring schemes employ the published $\Delta\zeta$ estimates (Cuffey and Marshall, 2000; Tarasov and Peltier, 2003; Kopp, 2012) as a basis to reject runs that produce an Eemian AIS configuration with a $\Delta\zeta$ outside of an upper and lower bound. In the evaluation schemes, the Eemian is identified as having occurred between 130 ka to 120 ka. The narrow sieves allow runs with a $\Delta\zeta$ between 1 and 8 mESL (thus an AIS configuration whose volume is less than present-day) to be accepted; runs outside this range are excluded from subsequent scoring. The wide sieve excludes runs with an $\Delta\zeta$ that is outside the range -1 mESL (*i.e.*, negative contribution indicating slightly larger configuration than present-day) to 10 mESL.

No runs produce an AIS with a $\Delta\zeta$ >6 mESL. The majority of the 1868 runs that pass the wide sieve contribute a maximum $\Delta\zeta$ that is <2 mESL. The narrow sieve schema rejects all but 218 runs. There is no correlation between the run ranking and the magnitude of $\Delta\zeta$. The runs that are included in the $P_{90}$ target are highlighted (circles represent the wide sieve, squares the narrow sieve), the colour scale representing their ranking by probability.

The $\Delta\zeta$ for the AIS, the WAIS, and the EAIS as computed from the three schemes are presented in Table 4.4. Taking the maximum ($N_{10}$ $\pm 1\sigma$ ) contribution to be at 114 ka (1.2 kyr beyond the 116.1±0.9 ka end of Marine Isotope Stage 5e proposed by

Shackleton (2003)) gives a maximum $\Delta\zeta$ from AIS of 3.4 mESL and a mean of 2.4 mESL. Fig. 4.17 shows the time series of $\Delta\zeta$ around the Eemian period.

Table 4.4: AIS $\Delta\zeta$ (maximum contribution to eustatic sea level relative to present-day) at 114 ka for the AIS, the WAIS, and the EAIS.

| | AIS | | WAIS | | EAIS | |
|---|---|---|---|---|---|---|
| source | volg $\Delta\zeta$ | $1\sigma$ | volgw $\Delta\zeta$ | $1\sigma$ | volge $\Delta\zeta$ | $1\sigma$ |
| $W_{09}$ | 0.5 | 0.7 | 0.2 | 0.6 | 0.2 | 0.2 |
| $N_{10}$ | 2.4 | 1.0 | 1.9 | 0.9 | 0.5 | 0.2 |
| $N^*_{10}$ | 2.1 | 1.0 | 1.7 | 0.9 | 0.4 | 0.2 |

Fig. 4.18 presents the $N_{10}$ surface elevation and thickness difference (past - present-day) snapshots from 126 ka, 120 k and at 114 ka. The surface elevation is relative to the global sea level record (computed from the stacked $\delta_{18}$ records of Lisiecki (2005))[†] at the appropriate time. The insert in the upper plots shows $\Delta\zeta$ from WAIS and EAIS. The mass loss is sourced primarily from WAIS.

[†]Interpolated between modern $\delta^{18}O$ corresponding to 0 m and LGM $\delta^{18}O$ corresponding to -125 m.

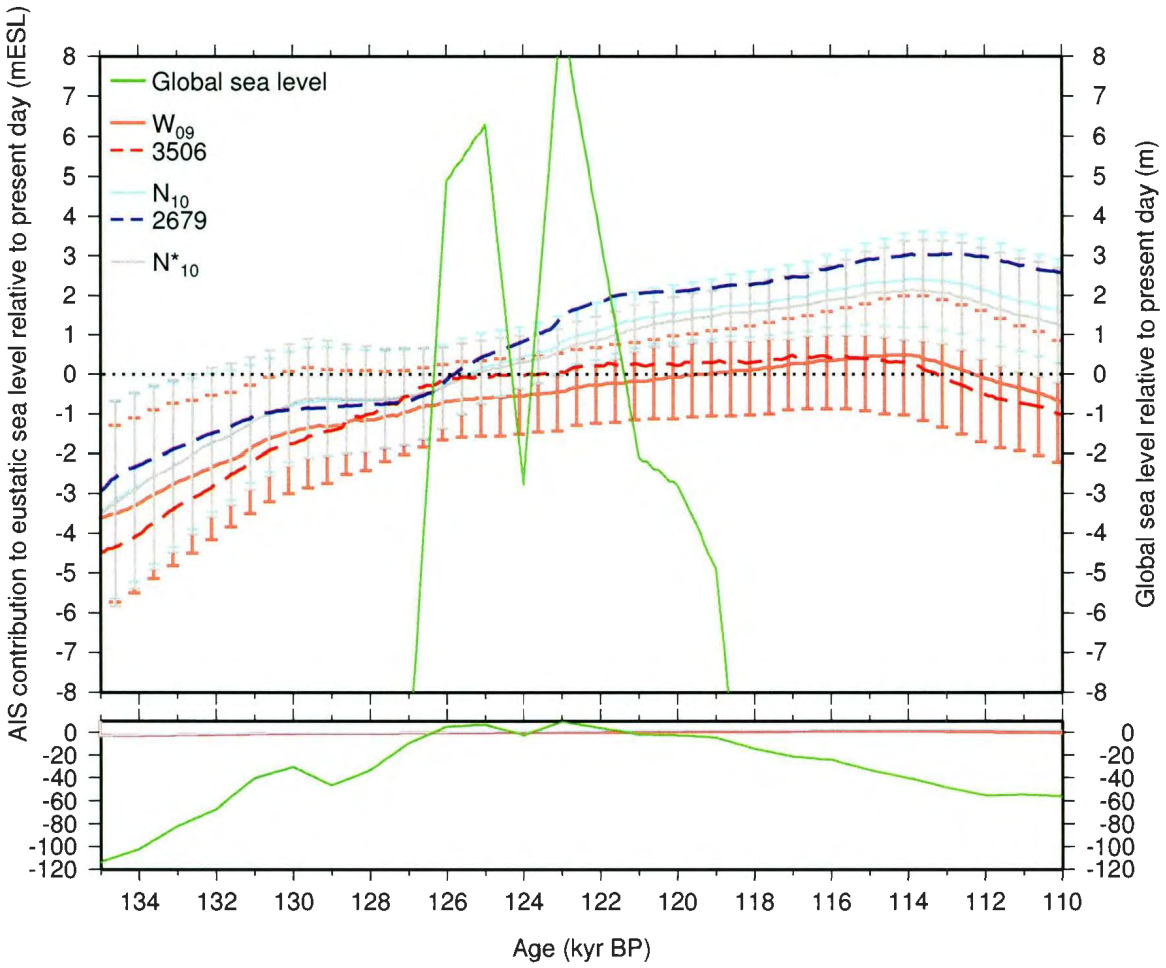


Figure 4.17: AIS evolution chronologies for the period before, during and after the Eemian presented as $\Delta\zeta$ (contribution to eustatic sea level relative to present-day). The global sea level departure from present (Lisiecki, 2005) is presented for timing and magnitude reference; for comparison the lower plot presents the full range of global sea level change over the same time period.

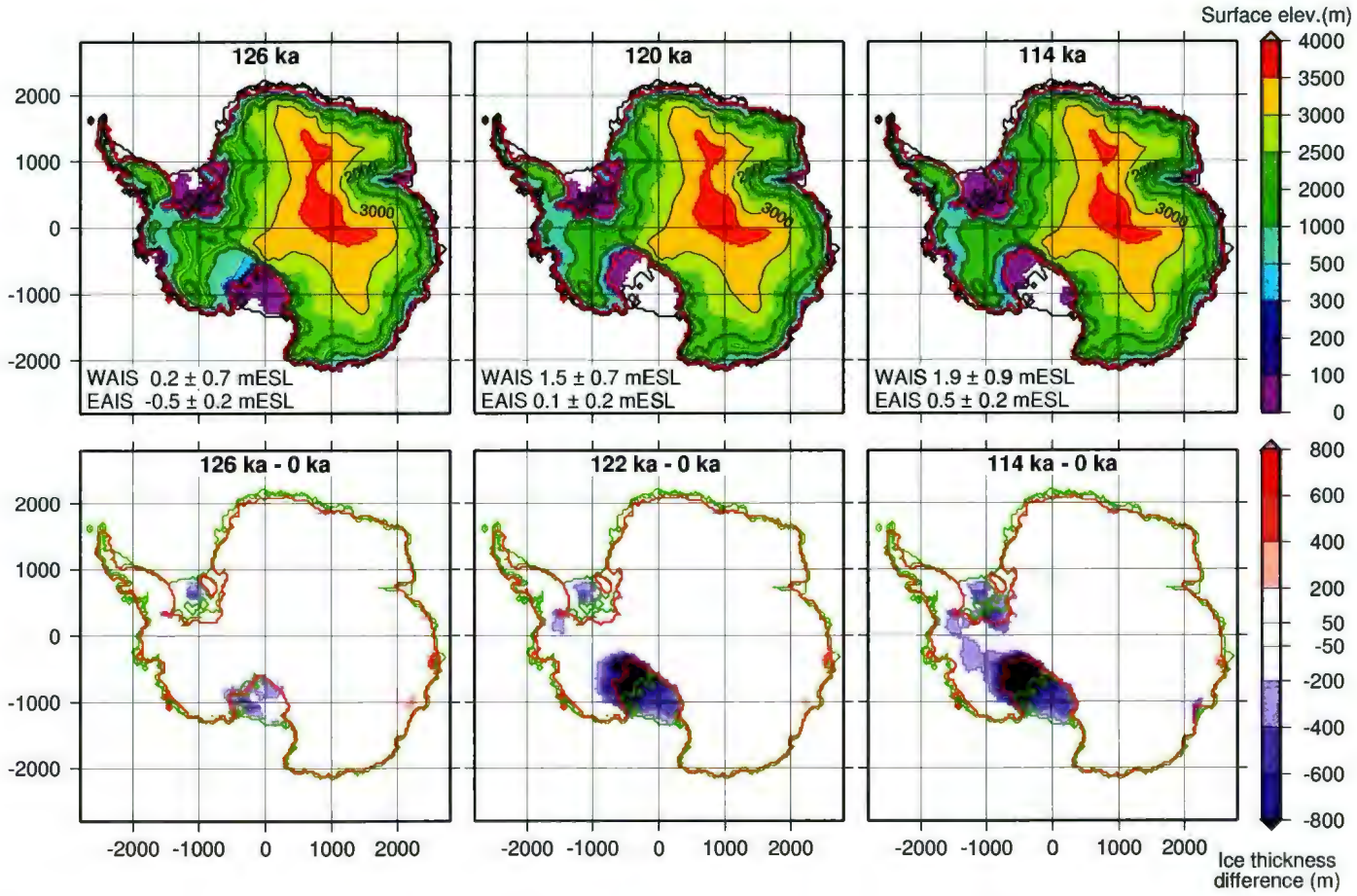


Figure 4.18: Upper plots show AIS surface elevation snapshots from $N_{10}$ , relative to global sea level inferred from the Lisiecki (2005) stacked $\delta_{18}$ records. Contribution to eustatic sea level from WAIS and EAIS is shown in each plot. Lower plots present thickness difference from the Eemian to present-day. Modelled grounding line position (red) is shown in all plots, and for reference, the present-day modelled $ALB_{40}$ (upper plots in black, lower plots in green) grounding line and shelf front. In the lower plots blue signifies thinner ice at Eemian.

### 4.4.9 Evolution of AIS since the Eemian

The final time series plots (Fig. 4.19) show the evolution, from -130 ka until present-day, of the eustatic sea level contribution of WAIS and EAIS in mESL relative to present-day. Also plotted are two of the time dependant climate forcing fields: sea level departure from present and the mean annual insolation departure from present-day (at 80°S), used as part of the set of parametrized climates of the GSM (Briggs and Tarasov, 2012).

Over the last glacial cycle EAIS changes approximately 6 mESL, WAIS is approaching 12 mESL (these estimates use the upper to the lower $1\sigma$ bound). The minimum contribution (relative to present-day, thus largest ice sheet configuration) is at the LGM. The maximum contribution from AIS occurs at 90 ka, ~4m±2 mESL. The surface elevation of AIS and the difference to present-day at this time is shown in Fig. 4.20. There is little contribution from EAIS whereas WAIS has undergone significant grounding line retreat and sufficient thinning to remove the grounded ice that separates the Weddell Sea from the Amundsen Sea. The $1\sigma$ upper and lower bounds for all the probability distributions have a greater or lessor degree of thinning but there is always an open passage between the Weddell and the Amundsen Sea.

## 4.5 Discussion

The MUN/PSU GSM (Briggs et al., 2013) configured through a wide and narrow set of parameter distributions was used to generate a 2929 member ensemble. Applying three composite scoring schemes from the Briggs and Tarasov (2012) evaluation methodology and constraint database generated three sets of scores; the wide sieve scheme scored 1848 runs, the narrow schemes 214 runs. The scores are converted into probabilities to compute the probability distribution, removing the dependence on a

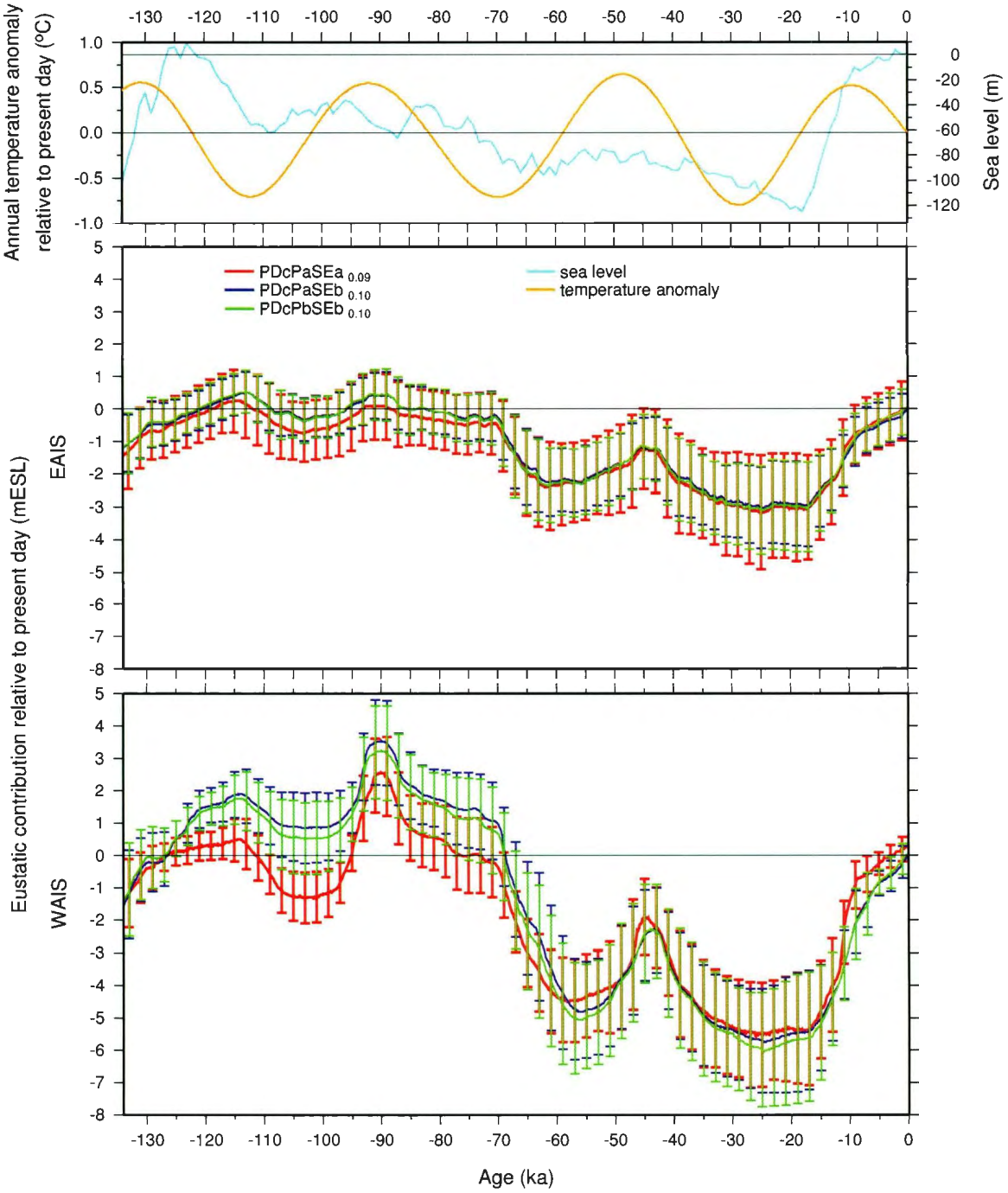


Figure 4.19: Grounded volume evolution of WAIS (lower) and EAIS (middle), represented as eustatic sea level contribution relative to present-day from $W_{09}$ ,$N_{10}$ and $N^*_{10}$ . Note the x-axes are the same range. Upper plot is the sea level departure from present (from stacked benthic $\delta^{18}O$ records of Lisiecki, 2005) and mean annual insolation departure from present (at 80°S).

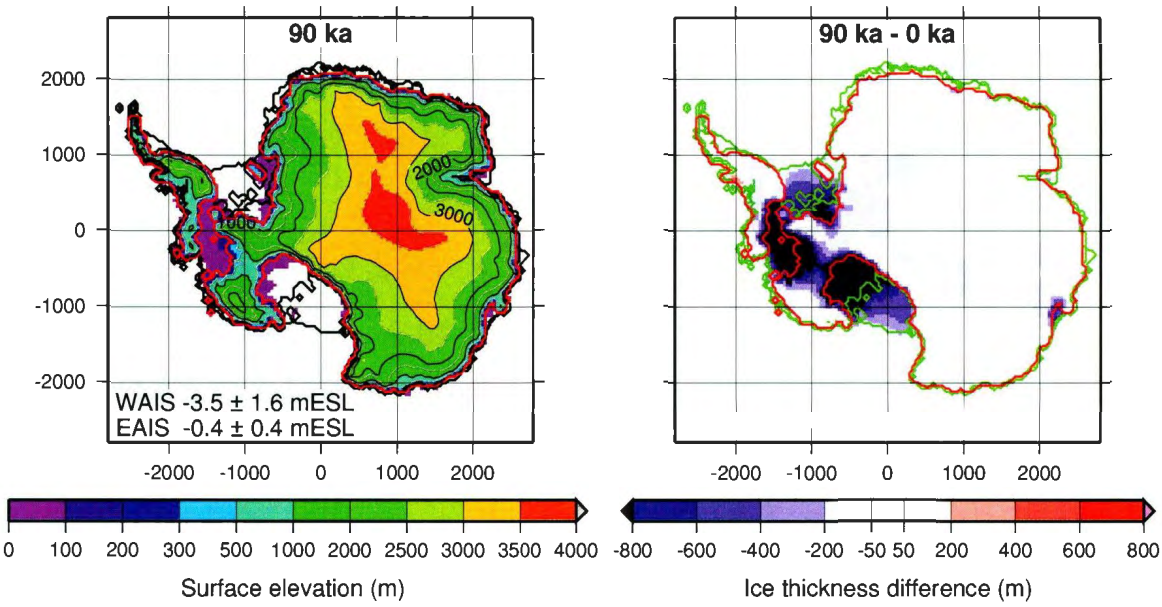


Figure 4.20: AIS surface elevation at 90 ka (left) and ice thickness difference between 90 ka and present-day. Modelled grounding line position (red) is shown in both plots. For reference, the present-day modelled $ALB_{40}$ (left plot in black, right plot in green) grounding line and shelf front. Blue signifies thinner ice at 90 ka.

single run (and generating uncertainty estimations). This requires the appropriate choice of a $\sigma_f$ to control the relative difference between runs. Based on empirical rules from past experience and analysis of grounded ice volumes generated from a suite of $\sigma_f$ values, a $\sigma_f$ value for each scheme was determined. To be conservative in our estimations (because $\sigma_f$ is determined empirically) all eustatic contributions presented in the discussion are taken from the maximum and minimum values from all three $1\sigma$ upper and lower bounds.

### 4.5.1 Reconstruction misfits

The modelled present-day grounding line closely tracks the observed line except under the ROS [RON] shelf were the predicted grounding lime is located downstream [upstream], the maximum misfit is ~6 grid cells (~240 km). The pattern and magnitude of the thickness misfits, exceeding 500 m at some locations, in the present-day thick-

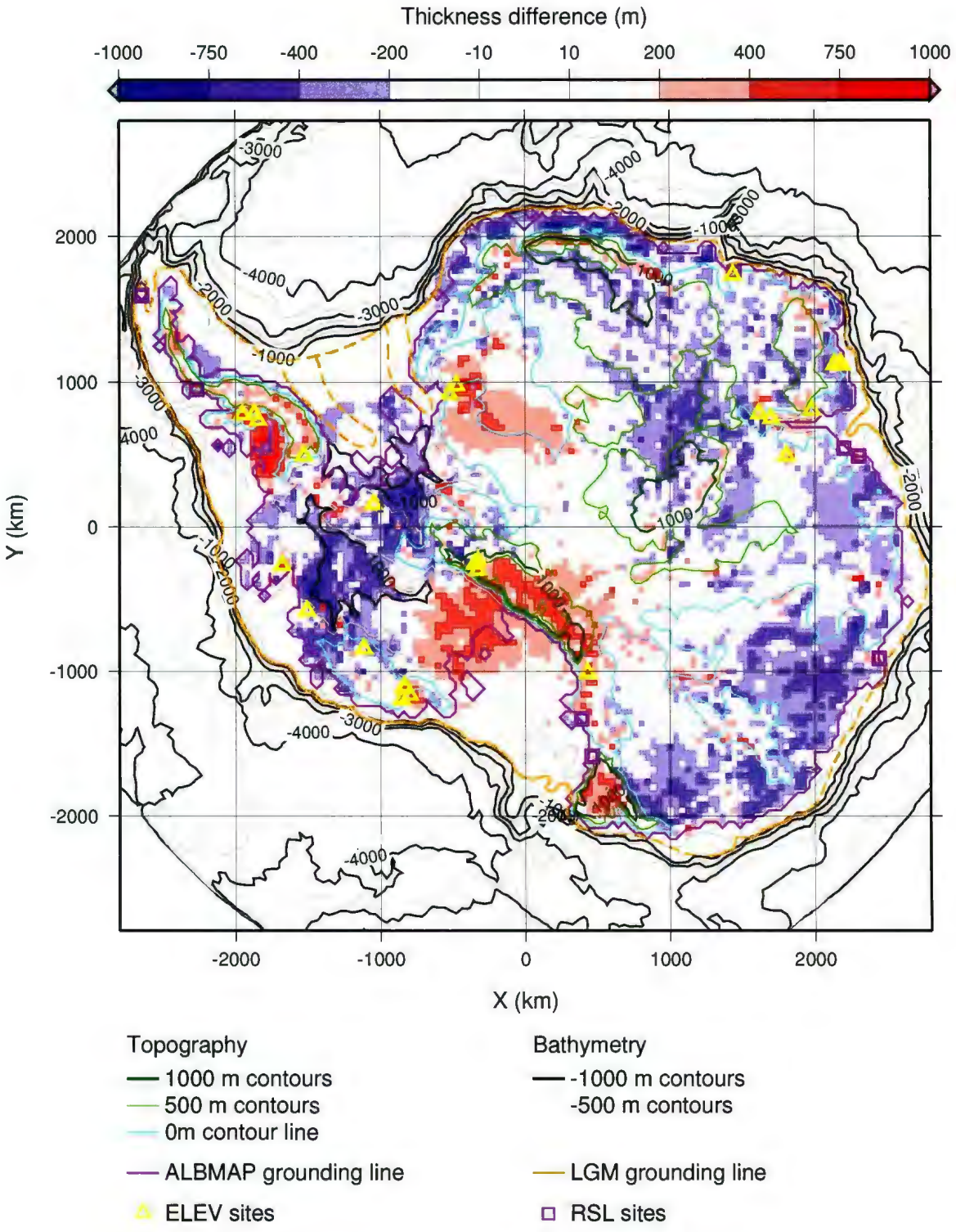


Figure 4.21: Thickness difference plot between mean $N_{10}$ and present-day, overlaid with topographic and bathymetric contours, present-day and LGM observed grounding lines and site locations for ELEV and RSL.

ness field are also seen in the results from other AIS GSMs (Pollard and DeConto, 2009; Martin et al., 2010; Whitehouse et al., 2012; Pollard and DeConto, 2012b).

The present-day model-to-observation thickness misfit field and the locations of the RSL and ELEV sites are shown in composite Figure 4.21. The plot is overlain with the bathymetry, topography and grounding line from ALBMAP and the Livingstone et al. (2012) LGM grounding line reconstruction.

The overly thin ice is found over marine basins (WAIS dome, around north Victoria and Wilkes land) but also at locations above present-day sea level (*e.g.*, behind the Lambert glacier). Equally, excess ice thickness is found both in high, mountainous regions (TAM and AP both have complex topography of glaciers flowing between rock outcrops and ridges with steep gradients that are poorly represented at 40 km resolution. Note that the contours in Fig. 4.21 have been smoothed, masking the more topographically complex areas seen in the topography of Fig. 4.3) and also in regions that are below sea level or over marine basins (Recovery basin, under the present-day ROS ice streams).

Recent work using an iterative inverse modelling technique (Pollard and DeConto, 2012b) has generated a distribution map of basal sliding that produces surface elevation differences of several 100's to a few 10's of m in most regions (a more sophisticated approach than the basal corrective map used in this GSM (Briggs et al., 2013)). The Pollard and DeConto (2012b) study also includes a sub-grid topographic parametrization which improved the misfit in mountainous regions. The MUN/PSU GSM has a similar sub-grid roughness parametrization. Whether a reduction in resolution (permitting narrower ice-streams to be resolved) improves the misfit in these topographically complex regions remains to be explored.

The ELEV and RSL observations are nearly all located in areas of excess ice misfit at present-day, for the majority of the ELEV and RSL sites the $1\sigma$ lower bound

reconstructions produce the smallest misfit to the observations. As such, the excess ice is a systematic error that continues back in time. It is important to note, however, that given that distributions and the lack of observations in regions of thin ice misfit, it would be erroneous to presume the lower bounds contribution estimations are more representative of reality.

### 4.5.2 LGM

The locations of the RSL and ELEV sites and the present-day model-to-observation thickness misfit field is shown in composite Figure 4.21. The plot is overlain with the bathymetry, topography and grounding line from ALBMAP and the Livingstone et al. (2012) LGM grounding line reconstruction.

Based on the sea-level equivalent time series plots for the reconstructions (Fig. 4.12 & 4.13), the local AIS LGM (*i.e.*, with respect maximum ice volume) occurs at 24 ka. Using the mean of the three distributions in Table 4.3 [and a lower and upper range from the minimal and maximal $1\sigma$ values] gives a $\Delta\xi_L$ (LGM contribution to eustatic sea level, relative to present-day) of 8.9 [5.8 to 12.2] mESL from AIS, 5.8 [3.9 to 7.9] mESL from WAIS and 3.0 [1.9 to 4.3] mESL from EAIS. These estimates are made with the caveat that there is likely insufficient grounding line migration, which, if remedied, would likely cause an increase in the predictions. However, given the worse region of grounding line migration is concentrated around the AP the increase would likely be small.

If the local AIS LGM is defined at 18 ka, these estimates are reduced by 0.1-0.2 mESL. $\Delta\xi_L$ from other, recent, modelling studies have included: 12 mESL (Pollard and DeConto, 2009); 10 mESL after 14 ka (Mackintosh et al., 2011, 14 ka identified as LGM in their study); 9±1.5 mESL, 8 mESL contribution from minimum misfit model (Whitehouse et al., 2012); 1.6 mESL (3.5 mESL from WAIS and -1.9 mESL

from EAIS, because of increased accumulation) (Pollard and DeConto, 2012b)).

Ross Sea and Weddell Sea are the predominant contributors to $\Delta\xi_L$. The estimate of 1.5-2 mESL from the Weddell Sea sector is in agreement with the minimum and maximum estimates of 1.4 to 2 mESL from the Bentley et al. (2010) Weddell Sea study. In the Amundsen Sea, the reconstruction predicts LGM excess ice volumes were <1mESL, comparable to the ~1.2 mESL estimate from Denton and Hughes (2002). Bassett et al. (2007) predict much higher values in Ross Sea, ~13.1 mESL, against our prediction of ~3 mESL. They predict the Weddell Sea contributes ~11.1 mESL; higher values in the Peninsula, ~2 mESL against 0.5 mESL; 0.5 mESL in the Amundsen Sea; and combined ~1 mESL from EAIS, less than our total EAIS estimation of ~2 mESL. The small (~0.5 mESL) Lambert-Amery sector contributions are similar in both studies. The Bassett et al. (2007) reconstructions employ a chronology generated from the Huybrechts (2002) ice sheet model that is subsequently deformed by hand to produce a number of different sea level reconstructions, as such it is not glaciologically self-consistent. Mackintosh et al. (2011) estimate a 1 mESL contribution from EAIS at the time of their 14 ka LGM.

Published reconstructions and observations (Bentley, 1999; Denton and Hughes, 2002; Anderson, 2002) of the large-scale LGM features consist of (i) a slightly thinner or unchanged EAIS interior (reduced accumulation due to extended sea ice coverage pushing the moisture source further away than at present-day (Huybrechts, 2002) and lower glacial temperatures in comparison to the interglacial temperatures) with thicker margins and a minor grounding line advance (ii) major migration of the ROS grounding line and an associated thickening (iii) grounding line advancement and limited thickening of the interior WAIS, (iv) thickening and migration of the grounding line onto the shelf for the AP, and (v) in the Weddell Sea/RON-FIL region, due to lack of evidence, there is uncertainty whether the present-day RON-FIL grounding line

was able to migrate to the continental shelf break or was hampered from advancing due to the presence of a deep troughs underneath and in front of the present-day ice shelf(Bentley et al., 2010; Hein et al., 2011). The latter hypothesis has been tested through a Weddell Sea sector focused modelling study (Bentley et al., 2010; LeBrocq et al., 2011). By prescribing different grounding line configurations, they found that a configuration which follows the contours of the deep troughs (rather than out at the continental shelf) is necessary to ensure the observations that constrain the ice nourishing the RON-FIL shelf (site 170[1,2,3,4]) are not over-ridden.

Apart from the limited grounding line advancement around the AP, the reconstruction captures these large-scale LGM features (Fig 4.14(c)). Furthermore, the modelled RON-FIL grounding line follows the contours of the Crary trough as hypothesised by (Bentley et al., 2010; LeBrocq et al., 2011). It is worth noting that although there is little constraint data on the interior of EAIS (Fig. 4.3), there is little variance in the model results in that region (Fig. 4.14). As such, additional data in that region would not significantly change the current results.

The $1\sigma$ uncertainty estimation plot Fig. 4.14(d) can be interpreted as highlighting regions where additional paleo-data would provide the most benefit for constraining the model during the LGM period. It can be compared directly with Fig. 6 of Whitehouse et al. (2012); the different modelling approaches give distinct uncertainty distributions. Much of the larger uncertainty (>200m) in the LGM reconstruction is seen in the RON-FIL region and Pine Island Bay. The Whitehouse et al. (2012) study also has large uncertainty in the AP, along the entire coast of the Amundsen Sea, around Victoria land and along much of the coast of EAIS.

### 4.5.3 LGM to present-day evolution

The time series plots (Fig. 4.12 & 4.13) show that all reconstructions across all sectors begin deglaciating (regional ice volume) between 16-17 ka. From the observational records deglaciation is thought to have generally started around 18 ka (Jouzel et al., 2001), however, regionally and locally there is variation in the times of grounding line retreat (ages range from 31-8 ka, with the majority of dates occurring between 18 and 8 ka (Livingstone et al., 2012)).

In the reconstructions, except for grounding lines of the ROS and RON-FIL shelves, the LGM grounding line does not advance far enough forward to the Livingstone et al. (2012) reconstructed maximum so that it can subsequently retreat and reconstruct the EXT data.

The 'swinging gate' migration of the grounding line in the Ross Embayment, however, is reconstructed by the model. It is thought to have occurred relatively smoothly from ~15 ka until it reached its present location at around ~3 ka (Conway et al., 1999; McKay et al., 2008). Three grounding line retreat dates are given in Fig. 4.15, 13.0 ka (marine core NBP95-01_KC39 (Domack et al., 1999), dated locations 7.6ka and 6.8ka (Conway et al., 1999)). Significant thinning starts after ~12 ka (Hall and Denton, 2000). The major retreat of the reconstructed ROS grounding line commences after 12 ka and continues until 6 ka. Between 6 ka until 3 ka the grounding line pauses, after which it continues to the present-day modelled location, up to 200 km downstream of the observed grounding line. The grounding line retreat over RSL sites 940[1,2] (the sites are located just north and south of the 7.6 ka marker in Fig. 4.15) and the thinning ice prior to the retreat at 14-12 ka and 12-10 ka (Fig. 4.15) are expressed in the high-stands of the RSL curves. The reconstructed grounding line in the Weddell Sea sector has a clear retreat phase, unfortunately there is little observational data to constraint the retreat (Bentley et al., 2011). Rapid retreat occurs after

12 ka.

Although there is little variation in the commencement of deglaciation across the sectors (Fig. 4.13), the reconstructed ELEV age-altitude plots (Figs. C.5 to C.30 of the Appendix.) show variation both between sites and between reconstructions within the sites. All the sites, except those with large misfits (in the TAM and AP), show variability in the timing and/or magnitude of the reconstructions.

For the EAIS sites, except for those directly upstream of the LAIS (PCM[1:3]), the onset of deglaciation is after about 17 ka for both the $1\sigma$ upper and lower bounds. The deglaciation of the PCM sites is immediately after the LGM for the $1\sigma$ upper reconstructions and as late as 12-14 ka for the $1\sigma$ lower bounds. The sites along the TAM reach their maximum thickness after ~14 ka, the latest time of all the sites. This coincides with the ~12-14 ka high stand of the nearby RSL sites.

In Marie Byrd Land, WAIS, there is little elevation change from ~26 ka until ~17 ka (for some reconstructions at some of the sites the maximum thickness occurs at 17-18ka, however there is <100m difference between 26 and 17-18 ka). After 17 ka all sites begin to thin. The two sites at Pine Island Bay both reach maximum altitude at ~24 ka. Slow deglaciation occurs until after 16-17 ka after, in nearly all of the reconstructions, the thinning rate increases. Apart from the ECR sites, the reconstructions for all the other sites have on-going thinning when they terminate at present-day.

The sites in the AP both have large misfits and, in addition, the reconstructions exhibit a sawtooth waveform pattern to the signal; this is likely due to them being situated in a region than is poorly resolved between ocean and land, probably with grid cells switching continuously between a grounded and floating state. Maximum thickness is reached prior to 26 ka and deglaciation occurs after 15-18 ka.

The Weddell Sea sites on the WAIS side of the RON-FIL reach maximum thick-

ness after 16-17ka then begin to thin. This is consistent with Bentley et al. (2010) reconstructions showing retreat from 15ka. The sites on the EAIS side of RON-FIL reach the maximum elevation at around 21 ka. The reconstructions for site 1703 (closer to the shelf) have a lot a variability, but when deglaciation does occur, as late as 11 ka for the $1\sigma$ upper, it is rapid, likely related to the RON-FIL shelf collapse at 12 ka.

It is worth highlighting that the reconstructions from site 1501 are good examples of (a) the GSM accurately reproducing the observations and (b) a site that provides valuable constraint *i.e.*, the observations lie between the reconstructions.

### 4.5.4 Meltwater pulses

There is no correlation between the MWP contributions and the lower scoring runs, as such, upper/lower bound estimations were made. Based on the reconstructions it is likely that the predicted contribution from MWP-1a is <1 mESL. For MWP-1b the predicted contribution is ~1.5 mESL from the wide scoring scheme and <1 mESL from the narrow scheme.

The under-predicted excess ice due to the apparently 'sticky' grounding line at LGM, may also provoke an increase in these estimates. In addition it should be noted that the largest contribution and therefore the most rapid deglaciation predicted by the whole ensemble is 3.0 mESL for MWP-1a and 3.7 mESL for MWP-1b (both generated by low scoring runs ranked 1284 and 1839 out of the total 1868 runs). Given this, it is unlikely that the AIS, based on our reconstructions contributed significantly to either MWP-1a or MWP-1b.

There is ongoing disagreement as to the hemispherical provenience of the source of MWP-1a (*e.g.*, Clark et al., 2002a; Peltier, 2005; Deschamps et al., 2012; Tarasov et al., 2012). The results from this study support the body of evidence that (a)

AIS did not have sufficient ice to provide a significant contribution and (b) that the evolution of AIS was a continuous rather that stepped deglaciation (as discussed in Bentley (2010)), precluding a predominant contribution from AIS. None of the magnitudes of LGM to present-day sea-level contributions from other Antarctica studies and discussed in the previous sections allow a significant contribution from the AIS for MWP-1a (Bentley et al., 2010; Mackintosh et al., 2011; Whitehouse et al., 2012; Pollard and DeConto, 2012b)

### 4.5.5 Eemian configuration and subsequent evolution

The maximum contribution from the AIS around the time of the Eemian occurs at 114 ka. The mean and maximum eustatic contribution at this time is 2.4 and 3.4 mESL respectively, predominantly sourced from the WAIS.

The probabilistic study by Kopp et al. (2009) concluded that the Southern Hemisphere contributed at least 2.5 m eustatic sea level increase. Through glaciological modelling, Tarasov and Peltier (2003) estimated the conservative contribution from Greenland to be 2-5.2 mESL with a more likely range of 2.7-4.5 mESL. Ignoring any synchronisation issues this requires a conservative minimum from AIS of 1.4 mESL and a more likely minimum of 2.1 mESL. Ackert et al. (2011) place constraints on WAIS geometry that limit the WAIS contribution to the higher sea levels observed during the last interglacial to ~3 mESL. The end of the Eemian has aligned to the end of Marine isotope stage 5e at 116.1±0.9 ka (Shackleton, 2003), as such our local minimum configuration occurring at ~114 ka is beyond the end of the Eemian but with magnitudes that are in good agreement with other studies.

At 126 ka, when the Eemian grounded volume is closest to present-day grounded volume, there is minimal difference between the respective configurations (Fig. 4.20 126 ka - 0ka). At minimum Eemian configuration, the ROS grounding line has re-

treated back into a significantly thinner WAIS as compared to that of present-day. The RON-FIL grounding line migrates little.

The minimum configuration of the AIS over the last glacial cycle occurs at 90 ka. The AIS contributes ~4m±2 mESL and the reconstructed configuration predicts a WAIS that has undergone significant grounding line retreat and sufficient thinning to remove the grounded ice that separates the Weddell Sea from the Amundsen Sea. At that time, the sea-level forcing in the model is in a period of falling sea level (approximately 60 m below present-day) and the temperatures are 0.5 °C warmer from present-day annual mean. The minimum configuration of the AIS at 90 ka is seen in the three model runs of the climate forcing sensitivity study of the PSU ISM (Pollard and DeConto, 2009). It is not seen in the glacial scale modelling studies of Huybrechts (1990); Ritz et al. (2001). There are contradictory hypotheses from observational and modelling studies as to whether WAIS did undergo a collapse (Macayeal, 1992; Pollard and DeConto, 2009; Scherer et al., 1998) or not (Hillenbrand et al., 2002). The collapses that are proposed to have occurred, however, all took place prior to the last glacial cycle.

## 4.6 Conclusion

Results from an ensemble of AIS reconstructions, generated using the MUN/PSU GSM (Briggs et al., 2013) and constrained using the evaluation methodology and observational database described in Briggs and Tarasov (2012) have been presented.

The following conclusions are made:

- LGM for the reconstructed AIS occurs at about 24 ka, with little change in the configuration until 17-18 ka. After 17 ka deglaciation commences in all sectors.
- AIS contribution to eustatic sea level rise from LGM to present-day is predicted

to be 8.9 mESL with a minimal and maximal $1\sigma$ range of 5.8 to 12.2 mESL. For the WAIS the mean is 5.8 mESL with a range of 3.9 to 7.9 mESL and for the EAIS the mean is 3.0 mESL with a range of 1.9 to 4.3 mESL.

- Ross and Weddell Sea sectors are the predominant sources of the mass loss, contributing ~3.5 and ~2 mESL respectively (not accounting for any uncertainty).
- The major period of grounding line retreat in the Weddell Sea sector, resulting in the present-day Ronne-Filchner shelf system, occurs after 12 ka; the grounding line in the Ross sea sector start its major retreat phase after 10 ka.
- The two relative sea level data sites of the Ross Sea sector predict a local sea level high stand at ~12 ka. The remaining six sites (4 in East Antarctica and 2 on the Antarctic Peninsula) predict a local high stand at ~8 ka.
- Maximum eustatic contribution for MWP-1a is likely <1 mESL, for MWP-1b is no more than ~1.5 mESL (more confidence in the accuracy of models ability to capture the grounding line migration could provoke a moderate increase in these estimates).
- Around the time of the Eemian the maximum contribution from AIS to eustatic sea level was 3.4 mESL, this occurred at 114 ka. A collapsed Ross Ice Shelf and retreat of the Siple Coast grounding line provide the majority of this ice mass loss.
- At ~90 ka, the model predicts a open seaway between the Weddell Sea and the Amundsen Sea. The associated thinning contributed between 2 and 6 mESL eustatic sea level rise, greater than during the Eemian.

There are two major deficiencies in the results and hence the GSM. The first is the over and under-estimation of ice thickness seen in the misfits to the present-day

observations (Fig. 4.4), and also in the majority of the RSL and ELEV sites. The locations and magnitudes (in places >500 m) are similar to those seen in other current, but higher resolution, AIS reconstructions and reflect difficulties in modelling the AIS in areas of complex topography and unknown basal conditions(Pollard and DeConto, 2009; Martin et al., 2010; Whitehouse et al., 2012; Pollard and DeConto, 2012a,b). The second deficiency is the limited ability of the GSM to advance the grounding line far beyond the present-day location, predominantly a problem in the Antarctic Peninsula. However, the reconstructions do reproduce the swinging gate retreat of the Ross Ice shelf grounding line (Conway et al., 1999; McKay et al., 2008) and, in the Filchner shelf region, the hypothesised LGM grounding line position that is restricted by the Crary trough (Bentley et al., 2010; LeBrocq et al., 2011). The reduced ability for the modelled grounding line to advance will likely cause the LGM contribution to increase, but given the misfit is predominately around the Antarctic Peninsula the magnitude is not estimated to be large (assuming the (Livingstone et al., 2012) LGM reconstructed grounding line is accurate). One-way variance plots were presented for present-day and LGM. The cells with the greatest variance are located in regions that would most benefit from additional constraint and could be used to guide future field campaigns.

Two steps are required for immediate improvement of the AIS reconstructions. The first, and most pressing, is to tackle the thickness misfits and the 'sticky' grounding line problem. Inclusion of the Pollard and DeConto (2012b) basal coefficient map as an extra parametrized boundary condition (or a similar approach) along with a doubling of the resolution would be one possible approach to explore. Further investigation is required to determine the cause of the grounding line behaviour. Secondly, full Bayesian calibration (Hauser et al., 2011; Tarasov et al., 2012) should improve the quality of model fits to observational constraints and provide much more robust

uncertainty estimates.

## 4.7 References

Ackert, R. P., Barclay, D. J., Borns, H. W., Calkin, P. E., Kurz, M. D., Fastook, J. L., Steig, E. J., 1999. Measurements of Past Ice Sheet Elevations in Interior West Antarctica. Science 286 (5438), 276 –280.

Ackert, R. P., Mukhopadhyay, S., Pollard, D., Deconto, R. M., Putnam, A. E., Borns, H. W., 2011. West Antarctic Ice Sheet elevations in the Ohio Range: Geologic constraints and ice sheet modeling prior to the last highstand. Earth and Planetary Science Letters 307, 83–93.

Alley, R. B., Whillans, I. M., 1984. Response of the East Antarctica Ice Sheet to Sea-Level Rise. Journal of Geophysical Research 89, 6487–6493.

Anderson, J., 2002. The Antarctic Ice Sheet during the Last Glacial Maximum and its subsequent retreat history: a review. Quaternary Science Reviews 21, 49–70.

Bamber, J. L., Alley, R. B., Joughin, I., 2007. Rapid response of modern day ice sheets to external forcing. Earth and Planetary Science Letters 257, 1–13.

Bamber, J. L., Gomez-Dans, J. L., Griggs, J. A., 2009. A new 1 km digital elevation model of the Antarctic derived from combined satellite radar and laser data. Part 1: Data and methods. The Cryosphere 3 (1), 101–111.

Bard, E., Hamelin, B., Arnold, M., Montaggioni, L., Cabioch, G., Faure, G., Rougerie, F., 1996. Deglacial sea-level record from Tahiti corals and the timing of global meltwater discharge. Nature 382, 241–244.

Bard, E., Hamelin, B., Delanghe-Sabatier, D., 2010. Deglacial meltwater pulse 1B and Younger Dryas sea levels revisited with boreholes at Tahiti. Science 327 (5970), 1235–1237.

Bard, E., Hamelin, B., Fairbanks, R. G., Zindler, A., 1990. Calibration of the 14C timescale over the past 30,000 years using mass spectrometric U/Th ages from Barbados corals. Nature 345, 405–410.

Bassett, S. E., Milne, G. A., Bentley, M. J., Huybrechts, P., 2007. Modelling Antarctic sea-level data to explore the possibility of a dominant Antarctic contribution to meltwater pulse IA. Quaternary Science Reviews 26, 2113–2127.

Bentley, M., 1999. Volume of Antarctic Ice at the Last Glacial Maximum, and its impact on global sea level change. Quaternary Science Reviews 18 (14), 1569–1595.

Bentley, M. J., 2010. The Antarctic palaeo record and its role in improving predictions of future Antarctic Ice Sheet change. Journal of Quaternary Science 25 (1), 5–18.

Bentley, M. J., Fogwill, C. J., Le Brocq, A. M., Hubbard, A. L., Sugden, D. E., Dunai, T. J., Freeman, S. P. H. T., 2010. Deglacial history of the West Antarctic Ice Sheet in the Weddell Sea embayment: Constraints on past ice volume change. Geology 38 (5), 411–414.

Bentley, M. J., Sugden, D. E., Fogwill, C. J., Brocq, A. M. L., Hubbard, A. L., Dunai, T. J., Freeman, S. P. H. T., 2011. Deglacial history of the West Antarctic Ice Sheet in the Weddell Sea embayment: Constraints on past ice volume change: REPLY. Geology 39 (5), e240–e240.

Braconnot, P., Otto-Bliesner, B., Harrison, S., Joussaume, S., Peterchmitt, J., Abe-Ouchi, A., Crucifix, M., Driesschaert, E., Fichefet, T., Hewitt, C. D., Kageyama,

M., Kitoh, A., Laine, A., Loutre, M., Marti, O., Merkel, U., Ramstein, G., Valdes, P., Weber, S. L., Yu, Y., Zhao, Y., 2007. Results of PMIP2 coupled simulations of the Mid-Holocene and Last Glacial Maximum - Part 1: experiments and large-scale features. Climate of the Past 3 (2), 261–277.

Briggs, R., Pollard, D., Tarasov., L., 2013. A glacial systems model configured for large ensemble analysis of Antarctica deglaciation. in prep.

Briggs, R., Tarasov, L., 2012. How to evaluate model derived deglaciation chronologies: A case study using Antarctica. Submitted to Quaternary Science Reviews.

Clark, P., 2002. Ice sheets and sea level of the Last Glacial Maximum. Quaternary Science Reviews 21, 1–7.

Clark, P. U., Dyke, A. S., Shakun, J. D., Carlson, A. E., Clark, J., Wohlfarth, B., Mitrovica, J. X., Hostetler, S. W., McCabe, A. M., 2009. The Last Glacial Maximum. Science 325 (5941), 710–714.

Clark, P. U., Mitrovica, J. X., Milne, G. A., Tamisiea, M. E., 2002a. Sea-level fingerprinting as a direct test for the source of global meltwater pulse 1A. Science 295, 2438–2441.

Clark, P. U., Pisias, N. G., Stocker, T. F., Weaver, A. J., 2002b. The role of the thermohaline circulation in abrupt climate change. Nature 415, 863–869.

Conway, H., Hall, B. L., Denton, G. H., Gades, A. M., Waddington, E. E., 1999. Past and future grounding-line retreat of the West Antarctic Ice Sheet. Science 286 (5438), 280–283.

Cuffey, K., Marshall, S., 2000. Substantial contribution to sea-level rise during the last interglacial from the Greenland ice sheet. Nature 404, 591–594.

Denton, G. H., Hughes, T. J., 2002. Reconstructing the Antarctic Ice Sheet at the Last Glacial Maximum. Quaternary Science Reviews 21 (1-3), 193–202.

Deschamps, P., Durand, N., Bard, E., Hamelin, B., Camoin, G., Thomas, A. L., Henderson, G. M., Okuno, J., Yokoyama, Y., 2012. Ice-sheet collapse and sea-level rise at the Bølling warming 14,600 years ago. Nature 483, 559–564.

Domack, E.W.and Jacobson, E., Shipp, S., Anderson, J., 1999. Late Pleistocene-Holocene retreat of the West Antarctic Ice-Sheet system in the Ross Sea: Part 2 - Sedimentologic and stratigraphic signature. Bulletin of the Geological Society of America 111 (10), 1517–1536.

Fairbanks, R. G., 1989. A 17,000-year glacio-eustatic sea level record: influence of glacial melting rates on the Younger Dryas event and deep-ocean circulation. Nature 342, 637–642.

Hall, B. L., Denton, G. H., 2000. Radiocarbon chronology of Ross Sea drift, eastern Taylor Valley, Antarctica: Evidence for a grounded ice sheet in the Ross Sea at the last glacial maximum. Geografiska Annaler: Series A, Physical Geography 82 (2/3), 305–336.

Hauser, T., Keats, A., Tarasov, L., 2011. Artificial neural network assisted Bayesian calibration of climate models. Climate Dynamics 39 (1-2), 137–154.

Hein, A. S., Fogwill, C. J., Sugden, D. E., Xu, S., 2011. Glacial/interglacial ice-stream stability in the Weddell Sea embayment, Antarctica. Earth and Planetary Science Letters 307, 211–221.

Hillenbrand, C.-D., Fütterer, D., Grobe, H., Frederichs, T., 2002. No evidence for a Pleistocene collapse of the West Antarctic Ice Sheet from continental margin sediments recovered in the Amundsen Sea. Geo-Marine Letters 22, 51–59.

Huybrechts, P., 1990. The Antarctic Ice Sheet during the last glacial-interglacial cycle: a three-dimensional experiment. Annals of Glaciology 14, 115–119.

Huybrechts, P., 2002. Sea-level changes at the LGM from ice-dynamic reconstructions of the Greenland and Antarctic ice sheets during the glacial cycles. Quaternary Science Reviews 21 (1-3), 203–231.

Huybrechts, P., 2002. Sea-level changes at the LGM from ice-dynamic reconstructions of the Greenland and Antarctic ice sheets during the glacial cycles. Quaternary Science Reviews 21, 203–231.

Ivins, E. R., James, T. S., 2005. Antarctic glacial isostatic adjustment: a new assessment. Antarctic Science 17 (04), 541.

Jouzel, J., Masson, V., Cattani, O., Falourd, S., Stievenard, M., Stenni, B., Longinelli, A., Johnsen, S. J., Steffenssen, J. P., Petit, J. R., Schwander, J., Souchez, R., Barkov, N. I., 2001. A new 27 ky high resolution East Antarctic climate record. Geophysical Research Letters 28, 3199–3202.

Kopp, R. E., 2012. Palaeoclimate: Tahitian record suggests Antarctic collapse. Nature 483 (7391), 549–550.

Kopp, R. E., Simons, F. J., Mitrovica, J. X., Maloof, A. C., Oppenheimer, M., 2009. Probabilistic assessment of sea level during the last interglacial stage. Nature 462, 863–867.

LeBrocq, A., Bentley, M., Hubbard, A., Fogwill, C., Sugden, D., Whitehouse, P., 2011. Reconstructing the Last Glacial Maximum ice sheet in the Weddell Sea embayment, Antarctica, using numerical modelling constrained by field evidence. Quaternary Science Reviews 30 (19-20), 2422–2432.

LeBrocq, A. M., Payne, A. J., Vieli, A., 2010. An improved Antarctic dataset for high resolution numerical ice sheet models (ALBMAP v1). Earth System Science Data 2 (3), 247–260.

Lilly, K., Fink, D., Fabel, D., Lambeck, K., 2010. Pleistocene dynamics of the interior East Antarctic ice sheet. Geology 38 (8), 703–706.

Lisiecki, L. E., 2005. A Pliocene-Pleistocene stack of 57 globally distributed benthic $\delta$18O records. Paleoceanography 20, 1003.

Livingstone, S. J., O'Cofaigh, C., Stokes, C. R., Hillenbrand, C. D., Vieli, A., Jamieson, S. S., 2012. Antarctic palaeo–ice streams. Earth-Science Reviews 111 (1-2), 90–128.

Macayeal, D. R., 1992. Irregular oscillations of the West Antarctic ice sheet. Nature 359, 29–32.

Mackintosh, A., Golledge, N., Domack, E., Dunbar, R., Leventer, A., White, D., Pollard, D., Deconto, R., Fink, D., Zwartz, D., Gore, D., Lavoie, C., 2011. Retreat of the East Antarctic ice sheet during the last glacial termination. Nature Geoscience 4, 195–202.

Martin, M. A., Winkelmann, R., Haseloff, M., Albrecht, T., Bueler, E., Khroulev, C., Levermann, A., 2010. The Potsdam Parallel Ice Sheet Model (PISM-PIK) - Part 2: Dynamic equilibrium simulation of the Antarctic ice sheet. The Cryosphere Discussions 4 (3), 1307–1341.

McKay, R., Dunbar, G., Naish, T., Barrett, P., Carter, L., Harper, M., 2008. Retreat history of the Ross Ice Sheet (Shelf) since the Last Glacial Maximum from deep-basin sediment cores around Ross Island. Palaeogeography, Palaeoclimatology, Palaeoecology 260 (1-2), 245–261.

Meehl, G., Stocker, T., Collins, W., Friedlingstein, P., Gaye, A., Gregory, J., Kitoh, A., Knutti, R., Murphy, J., Noda, A., Raper, S., Watterson, I., Weaver, A., Zhao, Z.-C., 2007. Climate Change 2007: The Physical Basis: Contributions of Working Group 1 to the Fourth Assessment Report of the Intergovernmental Panel on Climate Change. Cambridge University Press Cambridge, New York, Melbourne, Madrid, Cape Town, Singapore, São Paulo, Delhi, Ch. 10.

Overpeck, J. T., Otto-Bliesner, B. L., Miller, G. H., Muhs, D. R., Alley, R. B., Kiehl, J. T., 2006. Paleoclimatic evidence for future ice-sheet instability and rapid sea-level rise. Science 311 (5768), 1747–1750.

Peltier, W. R., 2005. On the hemispheric origins of meltwater pulse 1a. Quaternary Science Reviews 24 (14-15), 1655–1671.

Peltier, W. R., Fairbanks, F. G., 2006. Global Glacial Ice Volume and Last Glacial Maximum Duration from an Extended Barbados Sea Level Record. Quaternary Science Reviews 25 (23-24), 3322–3337.

Pollard, D., DeConto, R. M., 2007. A Coupled Ice-Sheet/Ice-Shelf/Sediment Model Applied to a Marine-Margin Flowline: Forced and Unforced Variations. Special Publication International Association of Sedimentologists 39, 37–52.

Pollard, D., DeConto, R. M., 2009. Modelling West Antarctic ice sheet growth and collapse through the past five million years. Nature 458, 329–332.

Pollard, D., DeConto, R. M., 2009. Modelling West Antarctic ice sheet growth and collapse through the past five million years-Supplementry. Nature 458 (7236), 329–32.

Pollard, D., DeConto, R. M., 2012a. A simple inverse method for the distribution of basal sliding coefficients under ice sheets, applied to Antarctica. The Cryosphere Discussions 6, 1405–1444.

Pollard, D., DeConto, R. M., 2012b. Description of a hybrid ice sheet-shelf model, and application to Antarctica. Geoscientific Model Development Discussions 5, 1077–1134.

Rignot, E., Mouginot, J., Scheuchl, B., 2011. Ice Flow of the Antarctic Ice Sheet. Science 333 (6048), 1427–1430.

Ritz, C., Rommelaere, V., Dumas, C., 2001. Modeling the evolution of Antarctic ice sheet over the last 420,000 years: implications for altitude changes in the Vostok region. Journal of Geophysical Research-Atmospheres 106 (D23), 31943–31964.

Rougier, J., 2007. Probabilistic inference for future climate using an ensemble of climate model evaluations. Climatic Change 81, 247–264.

Scherer, R. P., Aldahan, A., Tulaczyk, S., Possnert, G., Engelhardt, H., Kamb, B., 1998. Pleistocene Collapse of the West Antarctic Ice Sheet. Science 281, 82.

Shackleton, N., 2003. Marine Isotope Substage 5e and the Eemian Interglacial. Global and Planetary Change 36, 151–155.

Stanford, J. D., Rohling, E. J., Hunter, S. E., Roberts, A. P., Rasmussen, S. O., Bard, E., McManus, J., Fairbanks, R. G., 2006. Timing of meltwater pulse 1a and climate responses to meltwater injections. Paleoceanography 21, 4103.

Stone, J. O., Balco, G. A., Sugden, D. E., Caffee, M. W., Sass, L. C., Cowdery, S. G., Siddoway, C., 2003. Holocene deglaciation of Marie Byrd Land, West Antarctica. Science 299 (5603), 99–102.

Tarasov, L., Dyke, A. S., Neal, R. M., Peltier, W. R., 2012. A data-calibrated distribution of deglacial chronologies for the North American ice complex from glaciological modeling. Earth and Planetary Science Letters 315, 30–40.

Tarasov, L., Peltier, W. R., 2002. Greenland glacial history and local geodynamic consequences. Geophysical Journal International 150 (1), 198–229.

Tarasov, L., Peltier, W. R., 2003. Greenland glacial history, borehole constraints and Eemian extent. Geophysical Research Letters 108 (83), 2124–2143.

Tarasov, L., Peltier, W. R., 2004. A geophysically constrained large ensemble analysis of the deglacial history of the North American ice sheet complex. Quaternary Science Reviews 23 (3–4), 359–388.

Tarasov, L., Peltier, W. R., 2006. A calibrated deglacial drainage chronology for the North American continent: Evidence of an Arctic trigger for the Younger Dryas. Quaternary Science Reviews 25 (7-8), 659–688.

Turney, C. S. M., Jones, R. T., 2010. Does the Agulhas Current amplify global temperatures during super-interglacials? Journal of Quaternary Science 25, 839–843.

Turney, C. S. M., Kershaw, A. P., Lynch, A., 2006. Introduction: Integrating high-resolution past climate records for future prediction in the Australasian region. Journal of Quaternary Science 21, 679–680.

Weaver, A. J., Saenko, O. A., Clark, P. U., Mitrovica, J. X., 2003. Meltwater pulse 1A from Antarctica as a trigger of the Bolling-Allerod warm interval. Science 299 (5613), 1709–1713.

Weber, M. E., Clark, P. U., Ricken, W., Mitrovica, J. X., Hostetler, S. W., Kuhn, G., 2011. Interhemispheric Ice-Sheet Synchronicity During the Last Glacial Maximum. Science 334 (6060), 1265–1269.

Whitehouse, P. L., Bentley, M. J., Brocq, A. M. L., 2012. A deglacial model for Antarctica: geological constraints and glaciological modelling as a basis for a new model of Antarctic glacial isostatic adjustment. Quaternary Science Reviews 32 (16), 1–24.

# Chapter 5

# Conclusions

## 5.1 Summary

The four objectives listed in Section 1.4 were:

1. Development of a glacial systems model for large ensemble analysis of AIS evolution;

2. Development of a constraint database and associated evaluation methodology;

3. Evaluation of the characteristics and model-to-observation misfits in the reconstructions;

4. Investigation of AIS evolution using scored reconstructions.

Objective 1 was addressed in Chapter 2. A well tested contemporaneous continental-scale glacial-cycle ice sheet model has been heavily modified, including the definition of 31 ensemble parameters, to be used for large ensemble analysis. Except for a lack of a sub-glacial hydrology component, the included functionality addresses the major limitations that were generally lacking in the models used for the IPCC AR4 (Payne

et al., 2006; Meehl et al., 2007) *i.e.*, treatment of sheet/stream/shelf flow, grounding line migration, calving and sub-shelf melt. By using multiple climate generation methodologies the reliance on a single methodology has been removed. Using six metrics, a parameter sensitivity test was performed to verify that each parameter has significant impact on at least one of the metrics. This gives sufficient confidence that, collectivity and within the given parameter ranges, the parameter-space is being covered (as best can be done with 31 parameters) and warrants advancing to a full ensemble.

Accomplishment of objective 2 was described in Chapter 3. The article was written to address the challenges in using observational data to constraint GSM derived reconstructions, the AIS was used as an example but the issues broached must be considered for any ice sheet model reconstruction that requires the integration of different data types.

The constraint database contains present day configuration data, relative sea level (RSL) and past ice thickness indicators (ELEV), grounding line retreat (and open ocean conditions) data (EXT), and an Eemian eustatic contribution (relative to present day) sieve. The data was compiled and processed into a spreadsheet format facilitating automated processing. By making the database freely available as part of the supplement, it is envisioned that it will be useful to other researchers who might require a similar data-set (and thus avoid redundant work in re-collecting and re-processing the data). Apart from the ELEV cosmogenic dated observations, sufficient raw data was included to ensure the data can be re-calibrated as new radio-carbon calibration curves or marine correction factors become available.

Each type of data has specific issues that must be considered in their interpretation and usage. In addition, insofar as is possible, ice sheet reconstructions require complete accounting of the uncertainties in the data, the model and the parame-

ters. The second part of Chapter 3 discussed the challenges, and presented a number of methods (observational error models, intra- and inter- data type weightings), for applying the spatially and temporally diverse set of observations to reconstructions, whilst also capturing the observational uncertainty and accounting, to some degree, for structural error. To the authors best knowledge this is the first time such as study has been undertaken. A sensitivity study of the different combinations of data-types and weighting (defined in scoring schemes) was performed using, as a metric, the grounded ice volume computed from an unweighted mean of the 10 smallest misfit runs. Because the methods used to account for the heterogeneous data are a incomplete attempt at a full structural error model, caution must be taken in choosing one particular scoring scheme over another, however, within plausible bounds the results from the schemes were found to be robust. A list of recommendations was also made to ensure sufficient information is published in future data collection studies, thus ensuring maximum constraint potential is obtained from each piece of data collected.

The final two objectives were addressed in Chapter 4. Once generated (using predominantly beta distributions for each of the parameters), the ensemble was scored using the three preferred schemes (presented in Chapter 3) that employ all the paleo-data. The scores can be loosely interpreted as probabilities from which a probability distribution of the past evolution of the ice sheet can be constructed. Weighted mean values and uncertainty estimates of key model output (e.g. grounded ice volume) were computed.

The model has two major deficiencies: ice thickness misfits and poor grounding line advancement. The magnitudes (in excess of 500 m in some locations) and regions where the present-day misfits occur are also seen in other higher resolution AIS reconstructions (Pollard and DeConto, 2009; Martin et al., 2010; Whitehouse et al., 2012; Pollard and DeConto, 2012a,b). The restricted ability of the grounding line

to migrate forward is manifest in the inability of the model to reproduce the EXT data-points. The reconstructions do, however, recreate the grounding line (Conway et al., 1999; McKay et al., 2008) of the Ross Ice shelf and the hypothesised Crary Trough restricted grounding line position of the Weddell Sea sector (Bentley et al., 2010; LeBrocq et al., 2011).

The results predict that the Last Glacial Maximum in the AIS occurred at approximately 24 ka. The mean eustatic contribution from LGM until present day is 8.9 m mESL, the maximal $1\sigma$ upper bound and the minimal $1\sigma$ lower bound from the distributions give a range of 5.8 to 12.2 mESL. There is little change in the grounded ice volume from 24 ka until 16-17 ka at which time widespread deglaciation commences. The Ross and Weddell Sea sectors are the predominant sources of the ice mass loss. The maximum contribution to meltwater pulse 1a is predicted to be likely less than 1 mESL (an accurately modelled grounding line could see this estimate increase moderately). The major period of grounding line retreat in the Weddell Sea sector, resulting in the present day Ronne-Filchner shelf system, occurs after 12 ka; the grounding line of the Ross Sea sector starts its major retreat phase after 10 ka.

## 5.2 Future work

This thesis has documented a successful effort at building a framework for a data-calibrated large-ensemble analysis methodology for AIS evolution. This has been, however, an initial attempt; the following steps as seen as the priority in advancing the work.

**GSM improvements** As discussed at the end of Chapter 2, the two major deficiencies seen in the model must be addressed in future work. The major thickness misfits seen in this study are seen in other higher resolution AIS reconstructions (Pol-

lard and DeConto, 2009; Martin et al., 2010; Whitehouse et al., 2012; Pollard and DeConto, 2012b). The basal coefficient map derived from present day misfits (Briggs et al., 2013b) is similar to the iterative inverse modelling solution of Pollard and DeConto (2012a) (An iterative approach was not taken for this study). The Pollard and DeConto (2012b) GSM operated at resolution of 20 km and produced much smaller misfits (several 100's to a few 10's of m) that this study. As such, a doubling of resolution in the MUN/PSU GSM combined with the current basal coefficient map might improve the misfits we currently see. The use of the basal coefficient map must be caveated with the concern that the there is a degree of 'cancelling the errors' in the solution *i.e.*, the basal coefficient map masks other errors in the model caused by missing physics (hydrological and sedimentilogical processes) and other boundary conditions (geothermal heat flux) that effect sliding.

It remains to be seen if a doubling in resolution might improve the froward migration of the grounding line LGM. The GSM, as implemented, uses the Schoof grounding line flux condition, which is only defined for a power law form of the basal drag Schoof (2007); Pollard and DeConto (2007, 2012b). There is general consensus moving towards a Coulomb plastic basal drag law being more valid for subglacial sediment deformation (Cuffey and Paterson, 2010). The LGM grounding line misfit problem will certainly require further investigation.

Other improvements to the model that should be investigated in future work would be advancement of the climate forcing component, inclusion of a temperature dependant SSM component with associated ocean forcing components, and adoption of an adaptive grid techniques. Improvement of the climate forcing (avenues of exploration include coupled GSM-GCM ensembles using a fast GCM, or calibrated GCM runs being used to generate climate forcings) will be a long term goal both for the AIS and the other Quaternary ice sheets (Tarasov et al., 2012). Adaptive grids, *i.e.*, BISI-

CLES (Martin et al., 2012), allow a trade-off between increased resolution in areas that are highly dynamic (*e.g.*, in areas of ice streaming or topographically complex zones) whist maintaining coarse resolution in less dynamical areas.

**Constraint database and evaluation** The first step in improving the constraint database would be the inclusion of additional published data-types (*e.g.*, GRACE data, GPS uplift data, past ice elevations from ice cores) and the development, with the associated specialists, of the accompanying error models. The existing observational error models would also benefit review, and if required, refinement through the involvement of data-specific expertise. Improvement in the estimation of structural uncertainty (and thereby better constrained data-weighting) will be an on-going challenge for the community.

To better monitor the output from the model, it would be beneficial to add new metrics. The reconstructed grounding line was acquired after the model development, ensemble generation, and scoring had been concluded for this study, as such it could not be exploited for post scoring assessment. The inclusion of this dataset in the future development and sensitivity testing of the model will prove very valuable. In addition, monitoring of surface elevation or thickness metrics at a number of key locations *e.g.*, at the WAIS dome and in the areas of misfit in the EAIS would be a useful diagnostic.

Finally, full Bayesian calibration of the model (Hauser et al., 2011; Tarasov et al., 2012) will generate a more confident probability distribution for the model phase space given observational constraints and thereby generate better quality reconstructions.

# Bibliography

Ackert, R. P., Barclay, D. J., Borns, H. W., Calkin, P. E., Kurz, M. D., Fastook, J. L., Steig, E. J., 1999. Measurements of Past Ice Sheet Elevations in Interior West Antarctica. Science 286 (5438), 276 –280.

Ackert, R. P., Mukhopadhyay, S., Pollard, D., Deconto, R. M., Putnam, A. E., Borns, H. W., 2011. West Antarctic Ice Sheet elevations in the Ohio Range: Geologic constraints and ice sheet modeling prior to the last highstand. Earth and Planetary Science Letters 307, 83–93.

Albrecht, T., Martin, M., Haseloff, M., Winkelmann, R., Levermann, A., 2010. Parameterization for subgrid-scale motion of ice-shelf calving-fronts. The Cryosphere Discussions 4 (3), 1497–1523.

Alley, R. B., Clark, P. U., Huybrechts, P., Joughin, I., 2005. Ice-sheet and sea-level changes. Science 310 (5747), 456–460.

Alley, R. B., Horgan, H. J., Joughin, I., Cuffey, K. M., Dupont, T. K., Parizek, B. R., Anandakrishnan, S., Bassis, J., 2008. A Simple Law for Ice-Shelf Calving. Science 322, 1344.

Alley, R. B., Whillans, I. M., 1984. Response of the East Antarctica Ice Sheet to Sea-Level Rise. Journal of Geophysical Research 89, 6487–6493.

Amundson, J. M., Truffer, M., 2010. A unifying framework for iceberg-calving models. Journal of Glaciology 56 (199), 822–830.

Anderson, J., 2002. The Antarctic Ice Sheet during the Last Glacial Maximum and its subsequent retreat history: a review. Quaternary Science Reviews 21, 49–70.

Anderson, J. B., 1999. Antarctic marine geology. Cambridge University Press, Cambridge Univ Press.

Andrews, J. T., Jul. 1992. A case of missing water. Nature 358, 281.

Applegate, P. J., Kirchner, N., Stone, E. J., Keller, K., Greve, R., 2011. Preliminary assessment of model parametric uncertainty in projections of Greenland Ice Sheet behavior. The Cryosphere Discussions 5, 3175–3205.

Arthern, R. J., Winebrenner, D. P., Vaughan, D. G., 2006. Antarctic snow accumulation mapped using polarization of 4.3-cm wavelength microwave emission. Journal of Geophysical Research 111 (D10), 6107.

Balco, G., 2011. Contributions and unrealized potential contributions of cosmogenic-nuclide exposure dating to glacier chronology, 1990-2010. Quaternary Science Reviews 30, 3–27.

Bamber, J. L., 2000. Widespread Complex Flow in the Interior of the Antarctic Ice Sheet. Science 287 (5456), 1248–1250.

Bamber, J. L., Alley, R. B., Joughin, I., 2007. Rapid response of modern day ice sheets to external forcing. Earth and Planetary Science Letters 257, 1–13.

Bamber, J. L., Gomez-Dans, J. L., Griggs, J. A., 2009a. A new 1 km digital elevation model of the Antarctic derived from combined satellite radar and laser data. Part 1: Data and methods. The Cryosphere 3 (1), 101–111.

Bamber, J. L., Riva, R. E. M., Vermeersen, B. L. A., LeBrocq, A. M., 2009b. Reassessment of the potential sea-level rise from a collapse of the West Antarctic Ice Sheet. Science 324 (5929), 901–903.

Bard, E., Hamelin, B., Arnold, M., Montaggioni, L., Cabioch, G., Faure, G., Rougerie, F., 1996. Deglacial sea-level record from Tahiti corals and the timing of global meltwater discharge. Nature 382, 241–244.

Bard, E., Hamelin, B., Delanghe-Sabatier, D., 2010. Deglacial meltwater pulse 1B and Younger Dryas sea levels revisited with boreholes at Tahiti. Science 327 (5970), 1235–1237.

Bard, E., Hamelin, B., Fairbanks, R. G., Zindler, A., 1990. Calibration of the 14C timescale over the past 30,000 years using mass spectrometric U/Th ages from Barbados corals. Nature 345, 405–410.

Baroni, C., Hall, B. L., 2004. A new Holocene relative sea-level curve for Terra Nova Bay, Victoria Land, Antarctica. Journal of Quaternary Science 19, 377–396.

Bassett, S. E., Milne, G. A., Bentley, M. J., Huybrechts, P., 2007. Modelling Antarctic sea-level data to explore the possibility of a dominant Antarctic contribution to meltwater pulse IA. Quaternary Science Reviews 26, 2113–2127.

Beckmann, A., 2003. A parameterization of ice shelf-ocean interaction for climate models. Ocean Modelling 5 (2), 157–170.

Bentley, M., 1999. Volume of Antarctic Ice at the Last Glacial Maximum, and its impact on global sea level change. Quaternary Science Reviews 18 (14), 1569–1595.

Bentley, M., Fogwill, C. J., Kubik, P. W., Sugden, D. E., 2006. Geomorphological evidence and cosmogenic 10Be/26Al exposure ages for the Last Glacial Maximum

and deglaciation of the Antarctic Peninsula Ice Sheet. Geological Society of America Bulletin 118 (9-10), 1149–1159.

Bentley, M. J., 2005. Relative sea level curves for the South Shetland Islands and Marguerite Bay, Antarctic Peninsula. Quaternary Science Reviews 24, 1203–1216.

Bentley, M. J., 2010. The Antarctic palaeo record and its role in improving predictions of future Antarctic Ice Sheet change. Journal of Quaternary Science 25 (1), 5–18.

Bentley, M. J., Fogwill, C. J., Le Brocq, A. M., Hubbard, A. L., Sugden, D. E., Dunai, T. J., Freeman, S. P. H. T., 2010. Deglacial history of the West Antarctic Ice Sheet in the Weddell Sea embayment: Constraints on past ice volume change. Geology 38 (5), 411–414.

Bentley, M. J., Hodgson, D. A., 2009. Antarctic Ice Sheet and climate history since the Last Glacial Maximum. Pages News 17 (1), 28–29.

Bentley, M. J., Hodgson, D. A., Sugden, D. E., Roberts, S. J., Smith, J. A., Leng, M. J., Bryant, C., 2005. Early Holocene retreat of the George VI Ice Shelf, Antarctic Peninsula. Geology 33, 173.

Bentley, M. J., Sugden, D. E., Fogwill, C. J., Brocq, A. M. L., Hubbard, A. L., Dunai, T. J., Freeman, S. P. H. T., 2011. Deglacial history of the West Antarctic Ice Sheet in the Weddell Sea embayment: Constraints on past ice volume change: REPLY. Geology 39 (5), e240–e240.

Berger, A., Aug. 2002. An Exceptionally Long Interglacial Ahead? Science 297 (5585), 1287–1288.

Berkman, P., 1998. 226Ra/Ba ratios for dating Holocene biogenic carbonates in the Southern Ocean: preliminary evidence from Antarctic coastal mollusc shells. Chemical Geology 144 (3-4), 331–334.

Berkman, P. A., Forman, S. L., 1996. Pre-bomb radiocarbon and the reservoir correction for calcareous marine species in the Southern Ocean. Geophysical Research Letters 23 (4), 363.

Braconnot, P., Otto-Bliesner, B., Harrison, S., Joussaume, S., Peterchmitt, J., Abe-Ouchi, A., Crucifix, M., Driesschaert, E., Fichefet, T., Hewitt, C. D., Kageyama, M., Kitoh, A., Laine, A., Loutre, M., Marti, O., Merkel, U., Ramstein, G., Valdes, P., Weber, S. L., Yu, Y., Zhao, Y., 2007. Results of PMIP2 coupled simulations of the Mid-Holocene and Last Glacial Maximum - Part 1: experiments and large-scale features. Climate of the Past 3 (2), 261–277.

Briggs, R., Pollard, D., Tarasov., L., 2013a. A data-constrained large-ensemble analysis of Antarctica over the last glacial cycle. in prep.

Briggs, R., Pollard, D., Tarasov., L., 2013b. A glacial systems model configured for large ensemble analysis of Antarctica deglaciation. in prep.

Briggs, R., Tarasov, L., 2012. How to evaluate model derived deglaciation chronologies: A case study using Antarctica. Submitted to Quaternary Science Reviews.

Brooks, A., Edwards, R., 2006. The development of a sea-level database for Ireland. Irish Journal of Earth Sciences 24, 13–27.

Cazenave, A., Nerem, R. S., 2004. Present-day sea level change: Observations and causes. Reviews of Geophysics 42, 3001.

Church, J. A., White, N. J., Aarup, T., Wilson, W. S., Woodworth, P. L., Domingues, C. M., Hunter, J. R., Lambeck, K., 2008. Understanding global sea levels: past, present and future. Sustainability Science 3 (1), 9–22.

Clark, P., 2002. Ice sheets and sea level of the Last Glacial Maximum. Quaternary Science Reviews 21, 1–7.

Clark, P., Alley, R., Keigwin, L., Licciardi, J., Johnsen, S., Wang, H., 1996. Origin of the first global meltwater pulse following the last glacial maximum. Paleoceanography 11 (5), 563.

Clark, P. U., Dyke, A. S., Shakun, J. D., Carlson, A. E., Clark, J., Wohlfarth, B., Mitrovica, J. X., Hostetler, S. W., McCabe, A. M., 2009. The Last Glacial Maximum. Science 325 (5941), 710–714.

Clark, P. U., Mitrovica, J. X., Milne, G. A., Tamisiea, M. E., 2002a. Sea-level fingerprinting as a direct test for the source of global meltwater pulse 1A. Science 295, 2438–2441.

Clark, P. U., Pisias, N. G., Stocker, T. F., Weaver, A. J., 2002b. The role of the thermohaline circulation in abrupt climate change. Nature 415, 863–869.

Comiso, J. C., 2000. Variability and trends in antarctic surface temperatures from in situ and satellite infrared measurements. Journal of Climate 13 (10), 1674–1696.

Convey, P., Stevens, M. I., Hodgson, D. A., Smellie, J. L., Hillenbrand, C.-D., Barnes, D. K. A., Clarke, A., Pugh, P. J. A., Linse, K., Cary, S. C., Dec. 2009. Exploring biological constraints on the glacial history of Antarctica. Quaternary Science Reviews 28, 3035–3048.

Conway, H., Hall, B. L., Denton, G. H., Gades, A. M., Waddington, E. E., 1999. Past and future grounding-line retreat of the West Antarctic Ice Sheet. Science 286 (5438), 280–283.

Cuffey, K., Marshall, S., 2000. Substantial contribution to sea-level rise during the last interglacial from the Greenland ice sheet. Nature 404, 591–594.

Cuffey, K., Paterson, W., 2010. The Physics of Glaciers. Academic Press. Butterworth-Heinemann/Elsevier.

Davis, J. L., Mitrovica, J. X., 1996. Glacial isostatic adjustment and the anomalous tide gauge record of eastern North America. Nature 379, 331–333.

Delmotte, M., Raynaud, D., Morgan, V., Jouzel, J., 1999. Climatic and glaciological information inferred from air-content measurements of a Law Dome (East Antarctica) ice core. Journal of Glaciology 45 (150), 255–263.

Denton, G. H., Hughes, T. J., 2002. Reconstructing the Antarctic Ice Sheet at the Last Glacial Maximum. Quaternary Science Reviews 21 (1-3), 193–202.

Deschamps, P., Durand, N., Bard, E., Hamelin, B., Camoin, G., Thomas, A. L., Henderson, G. M., Okuno, J., Yokoyama, Y., 2012. Ice-sheet collapse and sea-level rise at the Bølling warming 14,600 years ago. Nature 483, 559–564.

Dinniman, M. S., Klinck, J. M., Smith, Jr., W. O., 2011. A model study of Circumpolar Deep Water on the West Antarctic Peninsula and Ross Sea continental shelves. Deep Sea Research Part II: Topical Studies in Oceanography 58, 1508–1523.

Domack, E., O'Brien, P., Harris, P., Taylor, F., Quilty, P. G., Santis, L. D., Raker, B., May 1998. Late Quaternary sediment facies in Prydz Bay, East Antarctica and

their relationship to glacial advance onto the continental shelf. Antarctic Science 10 (03).

Domack, E.W.and Jacobson, E., Shipp, S., Anderson, J., 1999. Late Pleistocene-Holocene retreat of the West Antarctic Ice-Sheet system in the Ross Sea: Part 2 - Sedimentologic and stratigraphic signature. Bulletin of the Geological Society of America 111 (10), 1517–1536.

Douglas, B. C., 1991. Global sea level rise. Journal of Geophysical Research 96, 6981–6992.

Douglas, B. C., Peltier, W. R., 2002. The puzzle of global sea-level rise. Physics Today 55 (3), 35–40.

Dunai, T. J., Stuart, F. M., 2009. Reporting of cosmogenic nuclide data for exposure age and erosion rate determinations. Quaternary Geochronology 4 (6), 437–440.

Dupont, T. K., Alley, R. B., 2005. Assessment of the importance of ice-shelf buttressing to ice-sheet flow. Geophysical Research Letters 32, 4503.

Fairbanks, R. G., 1989. A 17,000-year glacio-eustatic sea level record: influence of glacial melting rates on the Younger Dryas event and deep-ocean circulation. Nature 342, 637–642.

Fricker, H. A., Popov, S., Allison, I., Young, N., 2001. Distribution of marine ice beneath the Amery Ice Shelf. Geophysical Research Letters 28 (11), 2241–2244.

Goodwin, I., 1993. Holocene Deglaciation, Sea-Level Change, and the Emergence of the Windmill Islands, Budd Coast, Antarctica. Quaternary Research 40 (1), 55–69.

Goodwin, I., 2000. Glacio-isostasy and Glacial Ice Load at Law Dome, Wilkes Land, East Antarctica. Quaternary Research 53 (5), 285–293.

Grosfeld, K., Hellmer, H., Jonas, M., Sandhäger, H., Schulte, M., Vaughan, D., 1998. Marine ice beneath Filchner Ice Shelf Evidence from a multi-disciplinary approach. In: Jacobs, S., Weiss, R. (Eds.), Ocean, ice and atmosphere Interactions at the Antarctic continental margin. Vol. 75 of Antarct Res Ser. AGU, Washington DC,, pp. 319–339.

Hall, B., 2004. Holocene relative sea-level history of the Southern Victoria Land Coast, Antarctica. Global and Planetary Change 42 (1-4), 241–263.

Hall, B. L., 2009. Holocene glacial history of Antarctica and the sub-Antarctic islands. Quaternary Science Reviews 28, 2213–2230.

Hall, B. L., Denton, G. H., 1999. New relative sea-level curves for the southern Scott Coast, Antarctica: evidence for Holocene deglaciation of the western Ross Sea. Journal of Quartenary Science 14 (7), 641–650.

Hall, B. L., Denton, G. H., 2000. Radiocarbon chronology of Ross Sea drift, eastern Taylor Valley, Antarctica: Evidence for a grounded ice sheet in the Ross Sea at the last glacial maximum. Geografiska Annaler: Series A, Physical Geography 82 (2/3), 305–336.

Hanebuth, T., Stattegger, K., Grootes, P. M., 2000. Rapid flooding of the Sunda Shelf: a late glacial sea level record. Science 288 (5468), 1033–1035.

Hauser, T., Keats, A., Tarasov, L., 2011. Artificial neural network assisted Bayesian calibration of climate models. Climate Dynamics 39 (1-2), 137–154.

Hay, W. W., 1993. The role of polar deep water formation in global climate change. Annual Review of Earth and Planetary Sciences 21 (1), 227–254.

Hebeler, F., Purves, R. S., Jamieson, S. S. R., 2008. The impact of parametric uncertainty and topographic error in ice-sheet modelling. Journal of Glaciology 54 (188), 889–919.

Heimbach, P., Losch, M., 2012. Adjoint sensitivities of sub-ice-shelf melt rates to ocean circulation under the Pine Island Ice Shelf, West Antarctica. Annals of Glaciology 53, 59–69.

Hein, A. S., Fogwill, C. J., Sugden, D. E., Xu, S., 2011. Glacial/interglacial ice-stream stability in the Weddell Sea embayment, Antarctica. Earth and Planetary Science Letters 307, 211–221.

Heroy, D., Anderson, J., 2007. Radiocarbon constraints on Antarctic Peninsula Ice Sheet retreat following the Last Glacial Maximum (LGM). Quaternary Science Reviews 26 (25-28), 3286–3297.

Heroy, D. C., 2005. Ice-sheet extent of the Antarctic Peninsula region during the Last Glacial Maximum (LGM)—Insights from glacial geomorphology. Geological Society of America Bulletin 117 (11-12), 1497–1512.

Hillenbrand, C.-D., Fütterer, D., Grobe, H., Frederichs, T., 2002. No evidence for a Pleistocene collapse of the West Antarctic Ice Sheet from continental margin sediments recovered in the Amundsen Sea. Geo-Marine Letters 22, 51–59.

Hillenbrand, C.-D., Smith, J. A., Kuhn, G., Esper, O., Gersonde, R., Larter, R. D., Maher, B., Moreton, S. G., Shimmield, T. M., Korte, M., 2010. Age assignment of a diatomaceous ooze deposited in the western Amundsen Sea Embayment after the Last Glacial Maximum. Journal of Quaternary Science 25, 280–295.

Hiller, A., Wand, U., Kämpf, H., Stackebrandt, W., 1988. Occupation of the Antarctic continent by petrels during the past 35 000 years: Inferences from a 14C study of stomach oil deposits. Polar Biology 9 (2), 69–77.

Hindmarsh, R. C. A., 2006. The role of membrane-like stresses in determining the stability and sensitivity of the Antarctic ice sheets: back pressure and grounding line motion. Philosophical Transactions. Series A, Mathematical, Physical, and Engineering Sciences 364 (1844), 1733–67.

Hodgson, D. A., Verleyen, E., Vyverman, W., Sabbe, K., Leng, M. J., Pickering, M. D., Keely, B. J., 2009. A geological constraint on relative sea level in Marine Isotope Stage 3 in the Larsemann Hills, Lambert Glacier region, East Antarctica (31,366–33,228 cal yr BP). Quaternary Science Reviews 28 (25-26), 2689–2696.

Holland, D. M., Jacobs, S. S., Jenkins, A., 2003. Modelling the ocean circulation beneath the Ross Ice Shelf. Antarctic Science 15 (1), 13–23.

Holland, P. R., Jenkins, A., Holland, D. M., 2008. The Response of Ice Shelf Basal Melting to Variations in Ocean Temperature. Journal of Climate 21, 2558.

Hooyer, T. S., Iverson, N. R., 2002. Flow mechanism of the Des Moines lobe of the Laurentide ice sheet. Journal of Glaciology 48 (163), 575–586.

Horgan, H., Walker, R., Anandakrishnan, S., Alley, R., 2011. Surface elevation changes at the front of the Ross Ice Shelf: Implications for basal melting. Journal of Geophysical Research (Oceans) 116 (15), 2005.

Huybrechts, P., 1990. The Antarctic Ice Sheet during the last glacial-interglacial cycle: a three-dimensional experiment. Annals of Glaciology 14, 115–119.

Huybrechts, P., 1991. The Antartic ice sheet and enviromental change: a three-dimensional modelling study. Ph.D. thesis, Alfred Wegener Institute for Polar and Marine Research.

Huybrechts, P., 1993. Glaciological Modelling of the Late Cenozoic East Antarctic Ice Sheet: Stability or Dynamism? Geografiska Annaler. Series A, Physical Geography 75 (4), 221–238.

Huybrechts, P., 2002. Sea-level changes at the LGM from ice-dynamic reconstructions of the Greenland and Antarctic ice sheets during the glacial cycles. Quaternary Science Reviews 21, 203–231.

Huybrechts, P., 2002. Sea-level changes at the LGM from ice-dynamic reconstructions of the Greenland and Antarctic ice sheets during the glacial cycles. Quaternary Science Reviews 21 (1-3), 203–231.

Huybrechts, P., 2004. Antarctica: modelling. In: Bamber, J., Payne, A. (Eds.), Mass balance of the cryosphere: observations and modelling of contemporary and future changes. Cambridge: Cambridge University Press, pp. 491–523.

Huybrechts, P., Payne, A. J., Intercomparison, t. E., 1996. The EISMINT benchmarks for testing ice sheet models. Annals of Glaciology 23, 1–12.

Huybrechts, P., Wolde, J. d., 1999. The dynamic response of the Greenland and Antarctic ice sheets to multiple-century climatic warming. Journal of Climate 12, 2169–2188.

Ingólfsson, Ó., Hjort, C., Berkman, P. A., Björck, S., Colhoun, E., Goodwin, I. D., Hall, B., Hirakawa, K., Melles, M., Möller, P., et al., 1998. Antarctic glacial history since the Last Glacial Maximum: an overview of the record on land. Antarctic Science 10 (3), 326–344.

Ivins, E. R., James, T. S., 2005. Antarctic glacial isostatic adjustment: a new assessment. Antarctic Science 17 (04), 541.

Jacobs, S., Hellmer, H., Jenkins, A., 1996. Antarctic ice sheet melting in the Southeast Pacific. Geophysical Research Letters 23, 957–960.

Jacobs, S., Hellmer, H. H., Doake, C. S. M., Jenkins, A., Frolich, R., 1992. Melting of ice shelves and the mass balance of Antarctica. Journal of Glaciology 38(130), 375–387.

Jenkins, A., Doake, C. S. M., 1991. Ice-ocean interaction on Ronne Ice Shelf, Antarctica. Journal of Geophysical Research 96, 791–813.

Jenkins, A., Dutrieux, P., Jacobs, S. S., McPhail, S. D., Perrett, J. R., Webb, A. T., White, D., 2010. Observations beneath Pine Island Glacier in West Antarctica and implications for its retreat. Nature 3 (7), 468–472.

Johnson, J. S., Bentley, M. J., Gohl, K., 2008. First exposure ages from the Amundsen Sea Embayment, West Antarctica: The Late Quaternary context for recent thinning of Pine Island, Smith, and Pope Glaciers. Geology 36 (3), 223–226.

Joughin, I., Alley, R. B., Aug. 2011. Stability of the West Antarctic ice sheet in a warming world. Nature Geoscience 4, 506–513.

Joughin, I., Padman, L., 2003. Melting and freezing beneath Filchner-Ronne Ice Shelf, Antarctica. Geophysical Research Letters 30 (9), 1477.

Jouzel, J., Masson, V., Cattani, O., Falourd, S., Stievenard, M., Stenni, B., Longinelli, A., Johnsen, S. J., Steffenssen, J. P., Petit, J. R., Schwander, J., Souchez, R., Barkov, N. I., 2001. A new 27 ky high resolution East Antarctic climate record. Geophysical Research Letters 28, 3199–3202.

Jouzel, J., Masson-Delmotte, V., 2007. EPICA Dome C Ice Core 800KYr Deuterium Data and Temperature Estimates. IGBP PAGES/World Data Center for Paleoclimatology Data Contribution Series 2007-091.

King, J. C., Turner, J., 1997. Antarctic Meteorology and Climatology. Cambridge University Press, Cambridge.

Kluiving, S., van der Wateren, D., 2001. Antarctica Glaciological Geological Database (AGGD). , Online; accessed 08-Feb-2012.

Kopp, R. E., 2012. Palaeoclimate: Tahitian record suggests Antarctic collapse. Nature 483 (7391), 549–550.

Kopp, R. E., Simons, F. J., Mitrovica, J. X., Maloof, A. C., Oppenheimer, M., 2009. Probabilistic assessment of sea level during the last interglacial stage. Nature 462, 863–867.

Lambeck, K., Chappell, J., Apr 2001. Sea level change through the last glacial cycle. Science 292 (5517), 679–686.

Lambeck, K., Purcell, A., Dutton, A., 2012. The anatomy of interglacial sea levels: The relationship between sea levels and ice volumes during the Last Interglacial. Earth and Planetary Science Letters 315–316, 4–11.

Lambrecht, A., Sandhäger, H., Vaughan, D., Mayer, C., 2007. New ice thickness maps of Filchner-Ronne Ice Shelf, Antarctica, with specific focus on grounding lines and marine ice. Antarctic Science 19 (04).

Larour, E., Seroussi, H., Morlighem, M., Rignot, E., Mar. 2012. Continental scale, high order, high spatial resolution, ice sheet modeling using the Ice Sheet System Model (ISSM). Journal of Geophysical Research (Earth Surface) 117 (F16), 1022.

Laskar, J., Robutel, P., Joutel, F., Gastineau, M., Correia, A. C. M., Levrard, B., 2004. A long-term numerical solution for the insolation quantities of the Earth. Astronomy and Astrophysics 428, 261–285.

LeBrocq, A., Bentley, M., Hubbard, A., Fogwill, C., Sugden, D., Whitehouse, P., 2011. Reconstructing the Last Glacial Maximum ice sheet in the Weddell Sea embayment, Antarctica, using numerical modelling constrained by field evidence. Quaternary Science Reviews 30 (19-20), 2422–2432.

LeBrocq, A. M., Payne, A. J., Vieli, A., 2010. An improved Antarctic dataset for high resolution numerical ice sheet models (ALBMAP v1). Earth System Science Data 2 (3), 247–260.

Lilly, K., Fink, D., Fabel, D., Lambeck, K., 2010. Pleistocene dynamics of the interior East Antarctic ice sheet. Geology 38 (8), 703–706.

Lisiecki, L. E., 2005. A Pliocene-Pleistocene stack of 57 globally distributed benthic $\delta$18O records. Paleoceanography 20, 1003.

Liu, H., Jezek, K., Li, B., Zhao, Z., 2001. Radarsat antarctic mapping project digital elevation model version 2. Digital media., Boulder, CO: National Snow and Ice Data Center.

Liu, J. P., Milliman, J. D., 2004. Reconsidering melt-water pulses 1A and 1B: Global impacts of rapid sea-level rise. Journal of Ocean University of China 3, 183–190.

Livingstone, S. J., O'Cofaigh, C., Stokes, C. R., Hillenbrand, C. D., Vieli, A., Jamieson, S. S., 2012. Antarctic palaeo–ice streams. Earth-Science Reviews 111 (1-2), 90–128.

Loose, B., Schlosser, P., Smethie, W. M., Jacobs, S., 2009. An optimized estimate of glacial melt from the Ross Ice Shelf using noble gases, stable isotopes, and CFC transient tracers. Journal of Geophysical Research (Oceans) 114 (C13), 8007.

Lowe, A., Sep. 2002a. Reconstruction of the West Antarctic ice sheet in Pine Island Bay during the Last Glacial Maximum and its subsequent retreat history. Quaternary Science Reviews 21, 1879–1897.

Lowe, A., Sep. 2002b. Reconstruction of the West Antarctic ice sheet in Pine Island Bay during the Last Glacial Maximum and its subsequent retreat history. Quaternary Science Reviews 21, 1879–1897.

Lythe, M. B., Vaughan the BEDMAP Consortium, D. G., 2001. BEDMAP: A new ice thickness and subglacial topographic model of Antarctica. Journal of Geophysical Research-Solid Earth 106, 11335–11352.

Ma, Y., Gagliardini, O., Ritz, C., Gillet-Chaulet, F., Durand, G., Montagnat, M., 2010. Enhancement factors for grounded ice and ice shelves inferred from an anisotropic ice-flow model. Journal of Glaciology 56 (199), 805–812.

Macayeal, D. R., 1992. Irregular oscillations of the West Antarctic ice sheet. Nature 359, 29–32.

MacAyeal, D. R., 1997. EISMINT: Lessons in Ice-Sheet Modeling.

Mackintosh, A., 2007. Exposure ages from mountain dipsticks in Mac. Robertson Land, East Antarctica, indicate little change in ice-sheet thickness since the Last Glacial Maximum. Geology 6 (35), 551.

Mackintosh, A., Golledge, N., Domack, E., Dunbar, R., Leventer, A., White, D., Pollard, D., Deconto, R., Fink, D., Zwartz, D., Gore, D., Lavoie, C., 2011. Retreat

of the East Antarctic ice sheet during the last glacial termination. Nature Geoscience 4, 195–202.

Marshall, S. J., Dec. 2005. Recent advances in understanding ice sheet dynamics [rapid communication]. Earth and Planetary Science Letters 240, 191–204.

Marshall, S. J., James, T. S., Clarke, G. K. C., 2002. North American Ice Sheet reconstructions at the Last Glacial Maximum. Quaternary Science Reviews 21 (1-3), 175–192.

Martin, D. F., Cornford, S. L., Lipscomb, W. H., Price, S. F., Ranken, D. M., Ng, E. G., Payne, A. J., 2012. BISICLES: A High-performance Adaptive Ice Sheet Model. In: American Geophysical Union,Fall Meeting 2011,DI23A-2082.

Martin, M. A., Winkelmann, R., Haseloff, M., Albrecht, T., Bueler, E., Khroulev, C., Levermann, A., 2010. The Potsdam Parallel Ice Sheet Model (PISM-PIK) - Part 2: Dynamic equilibrium simulation of the Antarctic ice sheet. The Cryosphere Discussions 4 (3), 1307–1341.

Martinerie, P., Lipenkov, V. Y., Raynaud, D., Chappellaz, J., Barkov, N. I., Lorius, C., 1994. Air content paleo record in the Vostok ice core (Antarctica): A mixed record of climate and glaciological parameters. Journal of Geophysical Research-Atmospheres 99, 10565.

Maule, C. F., Purucker, M. E., Olsen, N., Mosegaard, K., 2005. Heat flux anomalies in Antarctica revealed by satellite magnetic data. Science 309 (5733), 464–467.

McGranahan, G., Balk, D., Anderson, B., 2007. The rising tide: assessing the risks of climate change and human settlements in low elevation coastal zones. Environment and Urbanization 19, 17–37.

McKay, R., Dunbar, G., Naish, T., Barrett, P., Carter, L., Harper, M., 2008. Retreat history of the Ross Ice Sheet (Shelf) since the Last Glacial Maximum from deep-basin sediment cores around Ross Island. Palaeogeography, Palaeoclimatology, Palaeoecology 260 (1-2), 245–261.

Meehl, G., Stocker, T., Collins, W., Friedlingstein, P., Gaye, A., Gregory, J., Kitoh, A., Knutti, R., Murphy, J., Noda, A., Raper, S., Watterson, I., Weaver, A., Zhao, Z.-C., 2007. Climate Change 2007: The Physical Basis: Contributions of Working Group 1 to the Fourth Assessment Report of the Intergovernmental Panel on Climate Change. Cambridge University Press Cambridge, New York, Melbourne, Madrid, Cape Town, Singapore, São Paulo, Delhi, Ch. 10.

Meier, M. F., Wahr, J. M., 2002. Sea level is rising: do we know why? Proceedings of the National Academy of Sciences 99 (10), 6524–6526.

Mercer, J. H., 1978. West Antarctic ice sheet and $CO_2$ greenhouse effect: a threat of disaster. Nature 271, 321–325.

Miura, H., Maemoku, H., Seto, K., Morikawa, K., 1998. Late Quaternary East Antarctic melting event in the Soya Coast region based on stratigraphy and oxygen isotopic ratio of fossil molluscs. Polar Geoscience 11, 260–274.

Neal, C. S., 1979. The dynamics of the Ross Ice Shelf revealed by radio echo-sounding. Journal of Glaciology 24, 295–307.

Newman, L., Convey, P., Gibson, J., Linse, K., 2009. Antarctic Paleobiology: Glacial refugia and constraints on past ice-sheet reconstructions. PAGES news 17 (1), 22–24.

Nicholls, K. W., Makinson, K., Robinson, A. V., 1991. Ocean circulation beneath the Ronne ice shelf. Nature 354, 221–223.

Nicholls, K. W., Østerhus, S., Makinson, K., Gammelsrød, T., Fahrbach, E., Jul. 2009. Ice-ocean processes over the continental shelf of the southern Weddell Sea, Antarctica: A review. Review of Geophysics 47 (3), RG3003.

O'Brien, P., Santis, L. D., Harris, P., Domack, E., Quilty, P., May 1999. Ice shelf grounding zone features of western Prydz Bay, Antarctica: sedimentary processes from seismic and sidescan images. Antarctic Science 11 (01).

Olbers, D., Hellmer, H., 2010. A box model of circulation and melting in ice shelf caverns. Ocean Dynamics 60, 141–153.

Oppenheimer, M., 1998. Global warming and the stability of the West Antarctic Ice Sheet. Nature 393, 325–332.

Overpeck, J. T., Otto-Bliesner, B. L., Miller, G. H., Muhs, D. R., Alley, R. B., Kiehl, J. T., 2006. Paleoclimatic evidence for future ice-sheet instability and rapid sea-level rise. Science 311 (5768), 1747–1750.

Parrenin, F., Dreyfus, G., Durand, G., Fujita, S., Gagliardini, O., Gillet, F., Jouzel, J., Kawamura, K., Lhomme, N., Masson-Delmotte, V., Ritz, C., Schwander, J., Shoji, H., Uemura, R., Watanabe, O., Yoshida, N., 2007. 1-D-ice flow modelling at EPICA Dome C and Dome Fuji, East Antarctica. Climate of the Past 3 (2), 243–259.

Pattyn, F., 2010. Antarctic subglacial conditions inferred from a hybrid ice sheet/ice stream model. Earth and Planetary Science Letters 295, 451–461.

Pattyn, F., Huyghe, A., De Brabander, S., De Smedt, B., Apr. 2006. Role of transition zones in marine ice sheet dynamics. Journal of Geophysical Research (Earth Surface) 111 (F10), 2004.

Pattyn, F., Perichon, L., Aschwanden, A., Breuer, B., De Smedt, B., Gagliardini, O., Gudmundsson, G. H., Hindmarsh, R., Hubbard, A., Johnson, J. V., et al., 2008. Benchmark experiments for higher-order and full Stokes ice sheet models (ISMIP-HOM). The Cryosphere 2 (2), 295–108.

Payne, A. J., Holland, P. R., Shepherd, A. P., Rutt, I. C., Jenkins, A., Joughin, I., 2007. Numerical modeling of ocean-ice interactions under Pine Island Bay's ice shelf. Journal of Geophysical Research (Oceans) 112 (C11), 10019.

Payne, A. J., Hunt, J. C. R., Wingham, D. J., 2006. Evolution of the Antarctic ice sheet: new understanding and challenges. Philosophical Transactions. Series A, Mathematical, Physical, and Engineering Sciences 364 (1844), 867–1872.

Payne, A. J., Vieli, A., Shepherd, A. P., Wingham, D. J., Rignot, E., 2004. Recent dramatic thinning of largest West Antarctic ice stream triggered by oceans. Geophysical Research Letters 31, 23401.

Peltier, W. R., 1998. Postglacial variations in the level of the sea: implications for climate dynamics and solid-earth geophysics. Review of Geophysics 36 (4), 603–689.

Peltier, W. R., 2004. Global glacial isostatic adjustment and the surface of the ice-age Earth: the ICE-5G(VM2) model and GRACE. Annual Review of Earth and Planetary Sciences 32, 111–149.

Peltier, W. R., 2005. On the hemispheric origins of meltwater pulse 1a. Quaternary Science Reviews 24 (14-15), 1655–1671.

Peltier, W. R., Drummond, R., 2008. Rheological stratification of the lithosphere: A direct inference based upon the geodetically observed pattern of the glacial isostatic adjustment of the North American continent. Geophysical Research Letters 35 (L16314), 16314.

Peltier, W. R., Fairbanks, F. G., 2006. Global Glacial Ice Volume and Last Glacial Maximum Duration from an Extended Barbados Sea Level Record. Quaternary Science Reviews 25 (23-24), 3322–3337.

Peltier, W. R., Tushingham, A. M., 1991. Influence of glacial isostatic adjustment on tide gauge measurements of secular sea level change. Journal of Geophysical Research 96, 6779–6796.

Pfeffer, W. T., Harper, J. T., O'Neel, S., 2008. Kinematic constraints on glacier contributions to 21st-century sea-level rise. Science 321 (5894), 1340–1343.

Pollard, D., DeConto, R. M., 2007. A Coupled Ice-Sheet/Ice-Shelf/Sediment Model Applied to a Marine-Margin Flowline: Forced and Unforced Variations. Special Publication International Association of Sedimentologists 39, 37–52.

Pollard, D., DeConto, R. M., 2009. Modelling West Antarctic ice sheet growth and collapse through the past five million years. Nature 458, 329–332.

Pollard, D., DeConto, R. M., 2009. Modelling West Antarctic ice sheet growth and collapse through the past five million years-Supplementry. Nature 458 (7236), 329–32.

Pollard, D., DeConto, R. M., 2012a. A simple inverse method for the distribution of basal sliding coefficients under ice sheets, applied to Antarctica. The Cryosphere Discussions 6, 1405–1444.

Pollard, D., DeConto, R. M., 2012b. Description of a hybrid ice sheet-shelf model, and application to Antarctica. Geoscientific Model Development Discussions 5, 1077–1134.

Price, S. F., Conway, H., Waddington, E. D., 2007. Evidence for late Pleistocene thinning of Siple Dome, West Antarctica. Journal of Geophysical Research-Earth Surface 112 (13).

Pritchard, H. D., Ligtenberg, S. R. M., Fricker, H. A., Vaughan, D. G., van den Broeke, M. R., Padman, L., 2012. Antarctic ice-sheet loss driven by basal melting of ice shelves. Nature 484 (7395), 502–505.

Pudsey, C. J., Barker, P. F., Larter, R. D., Dec. 1994. Ice sheet retreat from the Antarctic Peninsula shelf. Continental Shelf Research 14, 1647–1675.

Rasmussen, S. O., Andersen, K. K., Svensson, A. M., Steffensen, J. P., Vinther, B. M., Clausen, H. B., Siggaard-Andersen, M.-L., Johnsen, S. J., Larsen, L. B., Dahl-Jensen, D., Bigler, M., Röthlisberger, R., Fischer, H., Goto-Azuma, K., Hansson, M. E., Ruth, U., 2006. A new Greenland ice core chronology for the last glacial termination. Journal of Geophysical Research (Atmospheres) 111 (D10), 6102.

Reddy, T. E., Holland, D. M., Arrigo, K. R., 2010. Ross ice shelf cavity circulation, residence time, and melting: Results from a model of oceanic chlorofluorocarbons. Continental Shelf Research 30, 733–742.

Reimer, P., Baillie, M., Bard, E., Bayliss, A., Beck, J., Blackwell, P., Ramsey, C., Buck, C., Burr, G., Edwards, R., et al., 2009. IntCal09 and Marine09 radiocarbon age calibration curves, 0-50,000 years cal BP. Radiocarbon 51 (4), 1111–1150.

Rignot, E., Bamber, J. L., van den Broeke, M. R., Davis, C., Li, Y., van de Berg, W. J., van Meijgaard, E., 2008. Recent Antarctic ice mass loss from radar interferometry and regional climate modelling. Nature Geoscience 1, 106–110.

Rignot, E., Jacobs, S. S., 2002. Rapid Bottom Melting Widespread near Antarctic Ice Sheet Grounding Lines. Science 296, 2020–2023.

Rignot, E., Mouginot, J., Scheuchl, B., 2011. Ice Flow of the Antarctic Ice Sheet. Science 333 (6048), 1427–1430.

Ritz, C., Rommelaere, V., Dumas, C., 2001. Modeling the evolution of Antarctic ice sheet over the last 420,000 years: implications for altitude changes in the Vostok region. Journal of Geophysical Research-Atmospheres 106 (D23), 31943–31964.

Rougier, J., 2007. Probabilistic inference for future climate using an ensemble of climate model evaluations. Climatic Change 81, 247–264.

Rutt, I. C., Hagdorn, M., Hulton, N. R. J., Payne, A. J., 2009. The Glimmer community ice sheet model. Journal of Geophysical Research-Earth Surface 114 (F13), 2004.

Sanderson, T., 1979. Equilibrium profile of ice shelves. Journal of Glaciology 22 (88), 435–460.

SCAR, 2006. Antarctic Digital Database, Scientific Committee on Antarctic Research (SCAR), Version 3.0. , Online; accessed Sep. 2011.

Scherer, R. P., Aldahan, A., Tulaczyk, S., Possnert, G., Engelhardt, H., Kamb, B., 1998. Pleistocene Collapse of the West Antarctic Ice Sheet. Science 281, 82.

Schoof, C., 2007. Ice sheet grounding line dynamics: Steady states, stability, and hysteresis. Journal of Geophysical Research 112 (F3), F03S28.

Shackleton, N., 2003. Marine Isotope Substage 5e and the Eemian Interglacial. Global and Planetary Change 36, 151–155.

Shapiro, N. M., Ritzwoller, M. H., 2004. Inferring surface heat flux distributions guided by a global seismic model: particular application to Antarctica. Earth and Planetary Science Letters 223 (1-2), 213–224.

Shipp, S., Anderson, J. B., Domack, E. W., 1999. Late Pleistocene–Holocene retreat of the West Antarctic Ice-Sheet system in the Ross Sea: Part 1—Geophysical results. Geological Society of America Bulletin 111 (10), 1486–1516.

Siegert, M. J., 2001. Ice sheets and Late Quaternary environmental change. John Wiley, Chichester; New York.

Simpson, M. J. R., Milne, G. A., Huybrechts, P., Long, A. J., 2009. Calibrating a glaciological model of the Greenland ice sheet from the Last Glacial Maximum to present-day using field observations of relative sea level and ice extent. Quaternary Science Reviews 28, 1631–1657.

Smethie, Jr., W., Jacobs, S., 2005. Circulation and melting under the Ross Ice Shelf: estimates from evolving CFC, salinity and temperature fields in the Ross Sea. Deep Sea Research Part II: Topical Studies in Oceanography 52, 959–978.

Stanford, J. D., Rohling, E. J., Hunter, S. E., Roberts, A. P., Rasmussen, S. O., Bard, E., McManus, J., Fairbanks, R. G., 2006. Timing of meltwater pulse 1a and climate responses to meltwater injections. Paleoceanography 21, 4103.

Steig, E. J., Fastook, J. L., Zweck, C., Goodwin, I. D., Licht, K. J., White, J. W. C., Ackert, R. P., 2001. West Antarctic Ice Sheet Elevation Changes. Antarctic Research Series 77, 75–99.

Stone, E. J., Lunt, D. J., Rutt, I. C., Hanna, E., 2010. Investigating the sensitivity of numerical model simulations of the modern state of the Greenland ice-sheet and its future response to climate change. The Cryosphere, Volume 4, Issue 3, 2010, pp.397-417 4, 397–417.

Stone, J. O., Balco, G. A., Sugden, D. E., Caffee, M. W., Sass, L. C., Cowdery, S. G., Siddoway, C., 2003. Holocene deglaciation of Marie Byrd Land, West Antarctica. Science 299 (5603), 99–102.

Storey, B., Fink, D., Hood, D., Joy, K., Shulmeister, J., Riger-Kusk, M., Stevens, M., 2010. Cosmogenic nuclide exposure age constraints on the glacial history of the Lake Wellman area, Darwin Mountains, Antarctica. Antarctic Science 22 (06), 603–618.

Stuiver, M., Braziunas, T., 1985. Complication of isotopic dates from Antarctica. Radiocarbon 27, 117–304.

Stuiver, M., Reimer, P., Reimer, R., 2005. Calib 5.0. , Online; accessed 19-July-2008.

Sugden, D. E., Bentley, M. J., O'Cofaigh, C., 2006. Geological and geomorphological insights into Antarctic ice sheet evolution. Philosophical Transactions. Series A, Mathematical, Physical, and Engineering Sciences 364 (1844), 1607–1625.

Takada, M., 2003. ESR dating of fossil shells in the Lützow-Holm Bay region, East Antarctica. Quaternary Science Reviews 22 (10-13), 1323–1328.

Tapley, B. D., Bettadpur, S., Watkins, M., Reigber, C., 2004. The gravity recovery and climate experiment: Mission overview and early results. Geophysical Research Letters 31, 9607.

Tarasov, L., Dyke, A. S., Neal, R. M., Peltier, W. R., 2012. A data-calibrated distribution of deglacial chronologies for the North American ice complex from glaciological modeling. Earth and Planetary Science Letters 315, 30–40.

Tarasov, L., Peltier, W. R., 2002. Greenland glacial history and local geodynamic consequences. Geophysical Journal International 150 (1), 198–229.

Tarasov, L., Peltier, W. R., 2003. Greenland glacial history, borehole constraints and Eemian extent. Geophysical Research Letters 108 (83), 2124–2143.

Tarasov, L., Peltier, W. R., 2004. A geophysically constrained large ensemble analysis of the deglacial history of the North American ice sheet complex. Quaternary Science Reviews 23 (3–4), 359–388.

Tarasov, L., Peltier, W. R., 2006. A calibrated deglacial drainage chronology for the North American continent: Evidence of an Arctic trigger for the Younger Dryas. Quaternary Science Reviews 25 (7-8), 659–688.

Thomas, I. D., King, M. A., Bentley, M. J., Whitehouse, P. L., Penna, N. T., Williams, S. D. P., Riva, R. E. M., Lavallee, D. A., Clarke, P. J., King, E. C., Hindmarsh, R. C. A., Koivula, H., 2011. Widespread low rates of Antarctic glacial isostatic adjustment revealed by GPS observations. Geophysical Research Letters 38, 22302.

Thyssen, F., Bombosch, A., Sandhäger, H., 1993. Elevation, ice thickness and structure mark maps of the central part of the Filchner-Ronne Ice Shelf. Polarforschung 62 (1), 17–26.

Todd, C., Stone, J., Conway, H., Hall, B., Bromley, G., 2010. Late Quaternary evolution of Reedy Glacier, Antarctica. Quaternary Science Reviews 29 (11-12), 1328.

Turney, C. S. M., Jones, R. T., 2010. Does the Agulhas Current amplify global temperatures during super-interglacials? Journal of Quaternary Science 25, 839–843.

Turney, C. S. M., Kershaw, A. P., Lynch, A., 2006. Introduction: Integrating high-resolution past climate records for future prediction in the Australasian region. Journal of Quaternary Science 21, 679–680.

Verleyen, E., 2005. Relative sea-level history from the Lambert Glacier region, East Antarctica, and its relation to deglaciation and Holocene glacier readvance. Quaternary Research 63 (1), 45.

Vieli, A., Payne, A. J., Jan. 2005. Assessing the ability of numerical ice sheet models to simulate grounding line migration. Journal of Geophysical Research (Earth Surface) 110 (F9), 1003.

Walker, R. T., Dupont, T. K., Parizek, B. R., Alley, R. B., Sep. 2008. Effects of basal-melting distribution on the retreat of ice-shelf grounding lines. Geophysical Research Letters 35 (17), L17503.

Weaver, A. J., Saenko, O. A., Clark, P. U., Mitrovica, J. X., 2003. Meltwater pulse 1A from Antarctica as a trigger of the Bolling-Allerod warm interval. Science 299 (5613), 1709–1713.

Weber, M. E., Clark, P. U., Ricken, W., Mitrovica, J. X., Hostetler, S. W., Kuhn, G., 2011. Interhemispheric Ice-Sheet Synchronicity During the Last Glacial Maximum. Science 334 (6060), 1265–1269.

Wen, J., Jezek, K. C., ó, B. M. C., Herzfeld, U. C., Farness, K. L., Huybrechts, P., 2007. Mass budgets of the Lambert, Mellor and Fisher Glaciers and basal fluxes beneath their flowbands on Amery Ice Shelf. Science in China Series D: Earth Sciences 50 (11), 1693–1706.

White, D. A., Fink, D., Gore, D. B., 2011. Cosmogenic nuclide evidence for enhanced sensitivity of an East Antarctic ice stream to change during the last deglaciation. Geology 39 (1), 23–26.

Whitehouse, P. L., Bentley, M. J., Brocq, A. M. L., 2012. A deglacial model for Antarctica: geological constraints and glaciological modelling as a basis for a new

model of Antarctic glacial isostatic adjustment. Quaternary Science Reviews 32 (16), 1–24.

Williams, M., Grosfeld, K., Warner, R., Gerdes, R., Determann, J., 2001. Ocean circulation and ice-ocean interaction beneath the Amery Ice Shelf, Antarctica. Journal of Geophysical Research 106, 22383–22400.

Yamane, M., Yokoyama, Y., Miura, H., Maemoku, H., Iwasaki, S., Matsuzaki, H., 2011. The last deglacial history of Lützow-Holm Bay, East Antarctica. Journal of Quaternary Science 26, 3–6.

Yu, J., Liu, H., Jezek, K. C., Warner, R. C., Wen, J., 2010. Analysis of velocity field, mass balance, and basal melt of the Lambert Glacier-Amery Ice Shelf system by incorporating Radarsat SAR interferometry and ICESat laser altimetry measurements. Journal of Geophysical Research (Solid Earth) 115 (B14), 11102.

Zhang, Q., Peterson, J. A., 1984. A geomorphology and Late Quaternary geology of the Vestfold Hills, Antarctica. Australian National Antarctic Research Expeditions Reports 133, 84.

Zotikov, I. A., Zagorodnov, V. S., Raikovsky, J. V., 1980. Core Drilling through the Ross Ice Shelf (Antarctica) Confirmed Basal Freezing. Science 207, 1463–1465.

Zwartz, D., 1998. Holocene sea-level change and ice-sheet history in the Vestfold Hills, East Antarctica. Earth and Planetary Science Letters 155 (1-2), 131.

# Appendix A

# A glacial systems model configured for large ensemble analysis of Antarctica deglaciation

## A.1 Supplementary tables

Table A.1: Table of symbols and (non ensemble) model parameters discussed in the text

| Symbol | Definition | Units | Value |
|---|---|---|---|
| $calvrate_{Ts}$ | Ice-shelf calving rate | m $yr^{-1}$ | |
| $crh$ | basal sliding co-efficient (between bed and ice) | m $a^{-1}Pa^{-2}$ | |
| $crhcrit$ | SSA-SIA critical threshold | m $a^{-1}Pa^{-2}$ | $10^{-10}$ |
| $\dot{C}$ | Calving rate | m $yr^{-1}$ | |
| $H$ | ice thickness | m | |
| $H_{flot}$ | maximum buoyant thickness for tidewater calving | m | |
| $hb$ | basal elevation, relative to sea level | m | |
| $hs$ | ice surface elevation | m | |
| $hs_{PD}$ | reference present day ice surface elevation | m | |
| $I$ | glacial index, derived from either $T_{epica}$ | | |
| $n_{edge}$ | no. grid-cell edges that meet tidewater conditions (see Sec. 2.3.10.1) | | |
| $\dot{M}g$ | Sub shelf melt (SSM) rate for grounding line zone | m $yr^{-1}$ | |
| $\dot{M}g_{AMY}$ | reference SSM rate for AMY grounding line zone | m $yr^{-1}$ | |
| $\dot{M}g_{RON}$ | reference SSM rate for RON grounding line zone | m $yr^{-1}$ | |
| $\dot{M}a$ | SSM rate for accumulation zone | m $yr^{-1}$ | |
| $\dot{M}s$ | SSM rate for shelf front zone | m $yr^{-1}$ | |
| $P$ | interpolated (blended) precipitation | m $yr^{-1}$ | |
| $P_{LGM}$ | reference LGM precipitation field | m $yr^{-1}$ | |
| $P_{PD}$ | reference PD precipitation field | m $yr^{-1}$ | |
| $Pave_{LGM}$ | PMIPII average LGM precipitation field | m $yr^{-1}$ | |
| $Peof1,2_{LGM}$ | PMIPII reference LGM precipitation EOFs | m $yr^{-1}$ | |
| $Pf_{1,2,3}$ | individual precipitation fields | m $yr^{-1}$ | |
| $Pfac$ | scaled precipitation glacial index | | |
| $Se$ | sediment presence exponent | | |
| $Slk$ | sediment likelihood parameter | | |
| $t$ | time | yr | |
| $T$ | interpolated (blended) temperature | C | |
| $T_m$ | melting temperature of ice | C | 0 |
| $T_s$ | sea-surface mean summer temperature | C | |
| $T_{LGM}$ | reference LGM temperature field | C | |
| $T_{PD}$ | reference PD temperature field | C | |
| $Tave_{LGM}$ | PMIPII averaged LGM temperature | C | |
| $Teof_{LGM}$ | PMIPII LGM temperature EOFs | C | |
| $Tf_{1,2,3}$ | individual temperature fields | C | |
| $T_{Cmn}$ | minimum critical $T_s$ for tidewater calving | C | -5 |
| $T_{Cmx}$ | maximum critical $T_s$ for tidewater calving | C | 2 |
| $u, v$ | total horizontal velocities | $ms^{-1}$ | |
| $u_b, v_b$ | horizontal basal velocities | $ms^{-1}$ | |
| $U_c$ | tidewater calving velocity | km $yr^{-1}$ | |
| $U_{Cmx}$ | maximum calving velocity | km $yr^{-1}$ | |
| $(\mathbf{X})$ | horizontal dimensions | m | |
| $z$ | vertical dimension dimensions (positive upwards) | m | |
| $zcrhMN$ | minimum basal sliding co-efficient | $ma^{-1}Pa^{-2}$ | $5x10^{-11}$ |
| $zcrhMX$ | maximum basal sliding co-efficient | $ma^{-1}Pa^{-2}$ | $6x10^{-5}$ |
| $zcrhslid$ | basal sliding co-efficient for hard bed (bare rock) | $ma^{-1}Pa^{-2}$ | $10^{-10}$ |
| $zcrhsed$ | basal sliding co-efficient for soft bed (sediment) | $ma^{-1}Pa^{-2}$ | $10^{-6}$ |
| $\Delta_{\text{Halb}}$ | ice thickness model -obs misfit | | |
| $\Delta s$ | $\delta^{18}$O O sea level departure from present | | |
| $\Delta q_s$ | annual orbital insolation anomaly from present day at 80 S | W $m^{-2}$ | |
| $\epsilon_{shf}$ | shelf aspect ratio | | |
| $\epsilon_{AMY}$ | AMY shelf aspect ratio | | |
| $\epsilon_{RON}$ | RON shelf aspect ratio | | |
| $\sigma_{hb}$ | sediment roughness | | |
| $\tau_b$ | basal stress | Pa | |
| $\lvert\phi\rvert$ | latitude | South | |

| Distance from grounding line (km) | H (m) | Melt rate (m $yr^{-1}$) |
|---|---|---|
| 0 | 1600 | -1 |
| 25 | 1540 | -4.5 |
| 50 | 1400 | -4.5 |
| 75 | 1220 | -2.5 |
| 100 | 1200 | -0.65 |
| 125 | 1150 | -0.45 |
| 150 | 1020 | -0.7 |
| 170 | 1010 | -0.1 |
| 185 | 980 | -0.5 |
| 210 | 930 | -1.25 |
| 230 | 900 | -0.75 |
| 260 | 860 | -0.4 |
| 280 | 750 | -0.5 |
| 310 | 700 | 0.15 |
| 325 | 660 | 0.25 |
| 350 | 650 | -0.1 |
| 375 | 640 | 0.0 |
| 400 | 590 | 0.25 |
| 425 | 575 | 0.25 |
| 450 | 530 | 0.25 |
| 475 | 510 | 0.2 |
| 510 | 490 | 0.0 |
| 550 | 480 | 0.25 |
| 590 | 450 | 0.05 |
| 640 | 450 | 0.0 |
| 680 | 420 | -0.05 |
| 720 | 400 | -1.6 |
| 750 | 250 | -6 |

(a)

| Distance from grounding line (km) | H (m) | Melt rate (m $yr^{-1}$) |
|---|---|---|
| 0 | 2300 | - |
| 20 | - | -22.5 |
| 40 | 2000 | - |
| 60 | - | -11 |
| 75 | 1640 | - |
| 90 | - | -6.5 |
| 110 | 1300 | - |
| 130 | - | -3 |
| 140 | 1040 | - |
| 165 | - | -2.5 |
| 180 | 920 | - |
| 200 | - | -1.5 |
| 220 | 840 | - |
| 235 | - | -1.5 |
| 255 | 760 | - |
| 265 | - | -1 |
| 280 | 720 | - |
| 300 | - | -0 |
| 315 | 700 | - |
| 345 | 640 | - |
| 335 | - | 0.5 |
| 360 | - | 1 |
| 375 | 600 | - |
| 390 | - | 1.5 |
| 410 | 520 | - |
| 430 | 480 | - |
| 420 | - | 0.5 |
| 430 | 480 | - |
| 450 | - | 0 |
| 470 | 440 | - |
| 485 | - | 1.5 |
| 495 | 380 | - |
| 505 | - | 1.5 |
| 510 | 360 | - |
| 520 | - | 1.5 |
| 525 | 300 | - |
| 530 | - | -2.0 |
| 540 | 280 | - |

(b)

Table A.2: Tables of thickness (H) and melt rates for the (a) AMY and (b) RON ice shelves. The AMY data was extracted from Fig. 4 and Fig. 6 in Wen et al. (2007). The RON data from Fig 9. and Fig. 10 in Jenkins and Doake (1991).

Table A.3: SSM observations as extracted from the literature

| Shelf | Reference | Type of data | Value | Method |
|---|---|---|---|---|
| AMY | | | | |
| | Jacobs et al. (1996) | Average rate (all Jacobs et al. (1996) estimates ± 50%) | 0.65 m $yr^{-1}$ | Measurement |
| | Jacobs et al. (1996) | Net melt | 23 Gt $yr^{-1}$ | " |
| | Williams et al. (2001) | Total melt | 5.8 Gt $yr^{-1}$ and 18.0 Gt $yr^{-1}$ | Model |
| | Rignot and Jacobs (2002) | at grounding line | 31.5 m $yr^{-1}$ | InSAR |
| | Wen et al. (2007) | Mean melt near the southern grounding line | 23.0± 3.5 m $yr^{-1}$ | In-situ and remote sensing |
| | Wen et al. (2007) | Freezing rates | 0.5 ± 0.1 to 1.5 ± 0.2 m $yr^{-1}$ | " |
| | Wen et al. (2007) | Total basal melting | 50.3 ± 7.5 Gt $yr^{-1}$ | " |
| | Wen et al. (2007) | Total refreezing | 7.0 ± 1.1 Gt $yr^{-1}$ | " |
| | Wen et al. (2007) | Net basal melting | 43.3± 6.5 Gt $yr^{-1}$ | |
| | Yu et al. (2010) | Net basal melting | 27.0 ± 7.0 Gt $yr^{-1}$ | In-situ and remote sensing |
| ROS | | | | " |
| | Jacobs et al. (1996) | Average rate (excluding 100 km of shelf front) | 0.22 m $yr^{-1}$ | Measurement |
| | Jacobs et al. (1996) | Net melt (excluding 100 km of shelf front) | 81 Gt $yr^{-1}$ | " |
| | Holland et al. (2003) | Estimated from Fig 10, max melt at GL | 0.12 m $yr^{-1}$ | Model |
| | Holland et al. (2003) | Estimated from Fig 10, average freeze cm | 0.02 m $yr^{-1}$ | " |
| | Loose et al. (2009) | avergae basal melt rate of | 33-50 $km^3/a$ | Noble gases, stable isotopes, and CFC transient tracers |
| | Reddy et al. (2010) | average basal melt rates of (including a seasonal signal) | 0.1 m $yr^{-1}$ | CFC tracers |
| | Horgan et al. (2011) | Melt law for shelf front (40 km by 760 km) | 16 $km^3/a$ | Remote sensing |
| | | within the front km | 2.8 ± 1.0 m $yr^{-1}$ | " |
| FIL-RON | | | | |
| | Jacobs et al. (1996) | Average rate (excluding 100 of shelf front) | 0.55 m $yr^{-1}$ | Measurement |
| | Jacobs et al. (1996) | Net melt (excluding 100 of shelf front) | 202 Gt $yr^{-1}$ | " |
| | Grosfeld et al. (1998) | Net melt for FIL | 0.35 m $yr^{-1}$ | Model |
| | Rignot and Jacobs (2002) | at grounding line | 2-14 m $yr^{-1}$ | InSAR |
| | Joughin and Padman (2003) | Total net melt rate for FIL-RON | 83.4 ± 24.8 Gt $yr^{-1}$ | Remote-sensing data sets |
| | Joughin and Padman (2003) | RON grounding line melt | 50.4 Gt $yr^{-1}$ | " |
| | Joughin and Padman (2003) | RON freeze-on | 55.6 Gt $yr^{-1}$ | " |
| | Joughin and Padman (2003) | RON front melt | 54.8 Gt $yr^{-1}$ | " |
| | Joughin and Padman (2003) | FIL melt | 20.6 Gt $yr^{-1}$ | " |
| | Joughin and Padman (2003) | FIL freeze-on | 16.1 Gt $yr^{-1}$ | " |
| | Joughin and Padman (2003) | Downstream of Foundation Ice Stream | 24.8 Gt $yr^{-1}$ | " |
| Other shelves | | | | |
| | Jacobs et al. (1996) | Total estimate - (AMY+ROS+FIL+RON) | 450 Gt $yr^{-1}$ | Measurement |

Table A.4: Processed SSM observational data used for verification purposes. Values in italics for RON-FIL shelf system are converted or derived quantities (density of ice = 917 kg $m^3$, area of RON= $341.4 \times 10^3$ $km^2$, FIL= $71.7 \times 10^3$ $km^2$ and assuming the 24.8 Gt $yr^{-1}$ downstream of Foundation Ice Stream is split between RON and FIL). Melt rate or magnitude estimations for grounding line area melt or freeze-on are not calculated because of the uncertainties in estimating the area over which it occurs

| Shelf | Melt type | Rate m $yr^{-1}$ | ± | Mass loss Gt $yr^{-1}$ | ± | Notes | Reference |
|---|---|---|---|---|---|---|---|
| AMY | net melt | 0.65 | 0.325 | 23.3 | 11.5 | | Jacobs et al. (1996) |
| | net melt | | | 43.0 | 6.5 | | Wen et al. (2007) |
| | net melt | 0.51 | 0.13 | 27.0 | 7.0 | | Yu et al. (2010) |
| | freeze on | 0.5 → 1.5 | | 7.0 | 1.1 | | Wen et al. (2007) |
| ROS | net melt | 0.22 | 0.11 | 81 | 40.5 | | Jacobs et al. (1996) |
| | net melt | | | 48.5 | 18.6 | | Loose et al. (2009) |
| | net melt | 0.1 | | | | | Reddy et al. (2010) |
| | grounding area | 0.12 | | | | max | Holland et al. (2003) |
| | freeze-on | 0.02 | | | | ave | Holland et al. (2003) |
| | freeze-on | 0 → 0.24 | | | | ave | Reddy et al. (2010) |
| | freeze-on | 0 → 0.48 | | | | max | Reddy et al. (2010) |
| | shelf front | 2.8 | 1 | 14.67 | | 40 x 760 km | Horgan et al. (2011) |
| RON-FIL | | | | | | | |
| | net melt | 0.55 | | 202 | 101 | | Jacobs et al. (1996) |
| | net melt | *0.20* | | 83.4 | 24.8 | | Joughin and Padman (2003) |
| RON | | | | | | | |
| | net melt | *0.19* | | 62.0 | 24.8 | | Joughin and Padman (2003) |
| | grounding area | | | 50.4 | | | Joughin and Padman (2003) |
| | freeze on | | | 55.6+1.1 | | | Joughin and Padman (2003) |
| | shelf front | | | 55.9 | | | Joughin and Padman (2003) |
| FIL | | | | | | | |
| | net melt | 0.35 | | *22.8* | | | Grosfeld et al. (1998) |
| | net melt | *0.25* | | 16.9 | 24.8 | | Joughin and Padman (2003) |
| | grounding area | | | 20.6 | | | Joughin and Padman (2003) |
| | freeze-on | | | 16.1 | | | Joughin and Padman (2003) |
| OTHERS | | | | | | | |
| | net melt | | | 450 | 225 [1] | | Jacobs et al. (1996) |

[1] 50 % error reported for all the shelves (Jacobs et al., 1996) is repeated here.

## A.2 References

Grosfeld, K., Hellmer, H., Jonas, M., Sandhäger, H., Schulte, M., Vaughan, D., 1998. Marine ice beneath Filchner Ice Shelf Evidence from a multi-disciplinary approach. In: Jacobs, S., Weiss, R. (Eds.), Ocean, ice and atmosphere Interactions at the Antarctic continental margin. Vol. 75 of Antarct Res Ser. AGU, Washington DC,, pp. 319–339.

Holland, D. M., Jacobs, S. S., Jenkins, A., 2003. Modelling the ocean circulation beneath the Ross Ice Shelf. Antarctic Science 15 (1), 13–23.

Horgan, H., Walker, R., Anandakrishnan, S., Alley, R., 2011. Surface elevation changes at the front of the Ross Ice Shelf: Implications for basal melting. Journal of Geophysical Research (Oceans) 116 (15), 2005.

Jacobs, S., Hellmer, H., Jenkins, A., 1996. Antarctic ice sheet melting in the Southeast Pacific. Geophysical Research Letters 23, 957–960.

Jenkins, A., Doake, C. S. M., 1991. Ice-ocean interaction on Ronne Ice Shelf, Antarctica. Journal of Geophysical Research 96, 791–813.

Joughin, I., Padman, L., 2003. Melting and freezing beneath Filchner-Ronne Ice Shelf, Antarctica. Geophysical Research Letters 30 (9), 1477.

Loose, B., Schlosser, P., Smethie, W. M., Jacobs, S., 2009. An optimized estimate of glacial melt from the Ross Ice Shelf using noble gases, stable isotopes, and CFC transient tracers. Journal of Geophysical Research (Oceans) 114 (C13), 8007.

Reddy, T. E., Holland, D. M., Arrigo, K. R., 2010. Ross ice shelf cavity circulation, residence time, and melting: Results from a model of oceanic chlorofluorocarbons. Continental Shelf Research 30, 733–742.

Rignot, E., Jacobs, S. S., 2002. Rapid Bottom Melting Widespread near Antarctic Ice Sheet Grounding Lines. Science 296, 2020–2023.

Wen, J., Jezek, K. C., ó, B. M. C., Herzfeld, U. C., Farness, K. L., Huybrechts, P., 2007. Mass budgets of the Lambert, Mellor and Fisher Glaciers and basal fluxes beneath their flowbands on Amery Ice Shelf. Science in China Series D: Earth Sciences 50 (11), 1693–1706.

Williams, M., Grosfeld, K., Warner, R., Gerdes, R., Determann, J., 2001. Ocean circulation and ice-ocean interaction beneath the Amery Ice Shelf, Antarctica. Journal of Geophysical Research 106, 22383–22400.

Yu, J., Liu, H., Jezek, K. C., Warner, R. C., Wen, J., 2010. Analysis of velocity field, mass balance, and basal melt of the Lambert Glacier-Amery Ice Shelf system by incorporating Radarsat SAR interferometry and ICESat laser altimetry measurements. Journal of Geophysical Research (Solid Earth) 115 (B14), 11102.

# Appendix B

# How to evaluate model derived deglaciation chronologies: A case study using Antarctica

## B.1 Interpolation of ALBMAP

ALBMAP is resampled from 5 km resolution ($\text{ALBMAP}_5$) to 40 km resolution ($\text{ALBMAP}_{40}$) using the Ferret (v6.5) data visualization and analysis software package. The bathymetry, as defined by $\text{ALBMAP}_5$, under the Ross Ice shelf is relatively shallow. Using the Ferret default interpolation method causes the grounding line to migrate toward the ocean (shown in Fig. B.1b). Using this method would mean the target areas for the computation of the MSE metrics (volume of WAIS grounded ice [Wg], volume of WAIS floating ice [Wf] and total volume of EAIS ice [Et]) would be incorrect. To ensure that the low resolution data is self-consistent and that the position of the grounding line is maintained after re-sampling, the following interpolation scheme is adopted,

$$h_{40} = h_5[@AVE] \tag{B.1}$$

$$hb_{40} = \begin{cases} hb_5[@AVE] & \text{if grounded ice, } H_5\left(\frac{\rho_i}{\rho_o}\right) \geq -hb_5 \\ 0.75hb_5[@AVE] + 0.25hb_5[@MIN] & \text{if floating ice, } H_5\left(\frac{\rho_i}{\rho_o}\right) < -hb_5 \end{cases} \tag{B.2}$$

$$H_{40} = \begin{cases} h_{40} - hb_{40} & \text{if grounded ice, } H_5\left(\frac{\rho_i}{\rho_o}\right) \geq -hb_5 \\ H_5[@AVE] & \text{if floating ice, } H_5\left(\frac{\rho_i}{\rho_o}\right) < -hb_5 \end{cases} \tag{B.3}$$

Where $h$ is surface elevation (subscript $_5$ is high (5 km) resolution data, $_{40}$ is the resampled low (40 km) resolution data), $hb$ is basal topography (+ve up), $H$ is ice thickness, $\rho_i$ is the density of ice (910 kg/m$^3$), $\rho_o$ is density of the sea-water (1024 kg/m$^3$) and @AVE (average) and @MIN (minimum) are Ferret interpolation

functions. The ratio of 0.75:0.25 for computing $hb_{40}$ was calculated to give the lowest misfit when comparing the areas of the different data-sets. The plots in Fig B.1 shows location of resampled grounding line using @AVE and @AVE+@MIN functions.

Three other adjustments where made to the low resolution bathymetry. The Crary Ice Rise (82.93 S, 172.50W) and Roosevelt Island (-79.41S, 162.00W) are under-represented in ALBMAP$_5$ (Fig.B.1a & b) . These pinning points provide important back stress for the Ross ice-shelf. Topographic adjustments were estimated from information in SCAR Composite Gazetteer Antarctica (accessed May 2011). Roosevelt Island is described as 80 mi long in a NW-SE direction and 40 mi wide, with a central ridge about 550 m above sea level. Crary has no elevation information in the Gazetteer. The pre and post-adjustment values are shown in Table A.1. The grounding line of the Lambert Glacier-Amery ice-shelf system was also adjusted to recreate the trough/ridge/trough that is lost in the transform from $hb_{40}$ to $hb_5$, see Fig. B.1c.

Table A.1: Grid locations and pre/post-adjustment values of $hb_{40}$

| x | y | pre-adjustment value of $hb_{40}$ | post-adjustment value of $hb_{40}$ |
|---|---|---|---|
| Crary Ice Rise | | | |
| -280 | -880 | -418.9 | 25 |
| | | | |
| Roosevelt Island | | | |
| -400 | -1040 | -458.5 | 0 |
| -400 | -1080 | -354.5 | 100 |
| -360 | -1080 | -235.8 | 400 |
| -360 | -1120 | -204.8 | 400 |
| -320 | -1120 | -313.6 | 100 |
| -320 | -1160 | -493.1 | 100 |
| | | | |
| Lambert Glacier - Amery Ice shelf grounding line | | | |
| 1600 | 720 | -319.1 | -600 |
| 1640 | 720 | -308.7 | -1300 |
| 1680 | 720 | -927.0 | -300 |
| 1720 | 720 | -1455.0 | -1620 |
| 1760 | 720 | -1156.0 | -1400 |

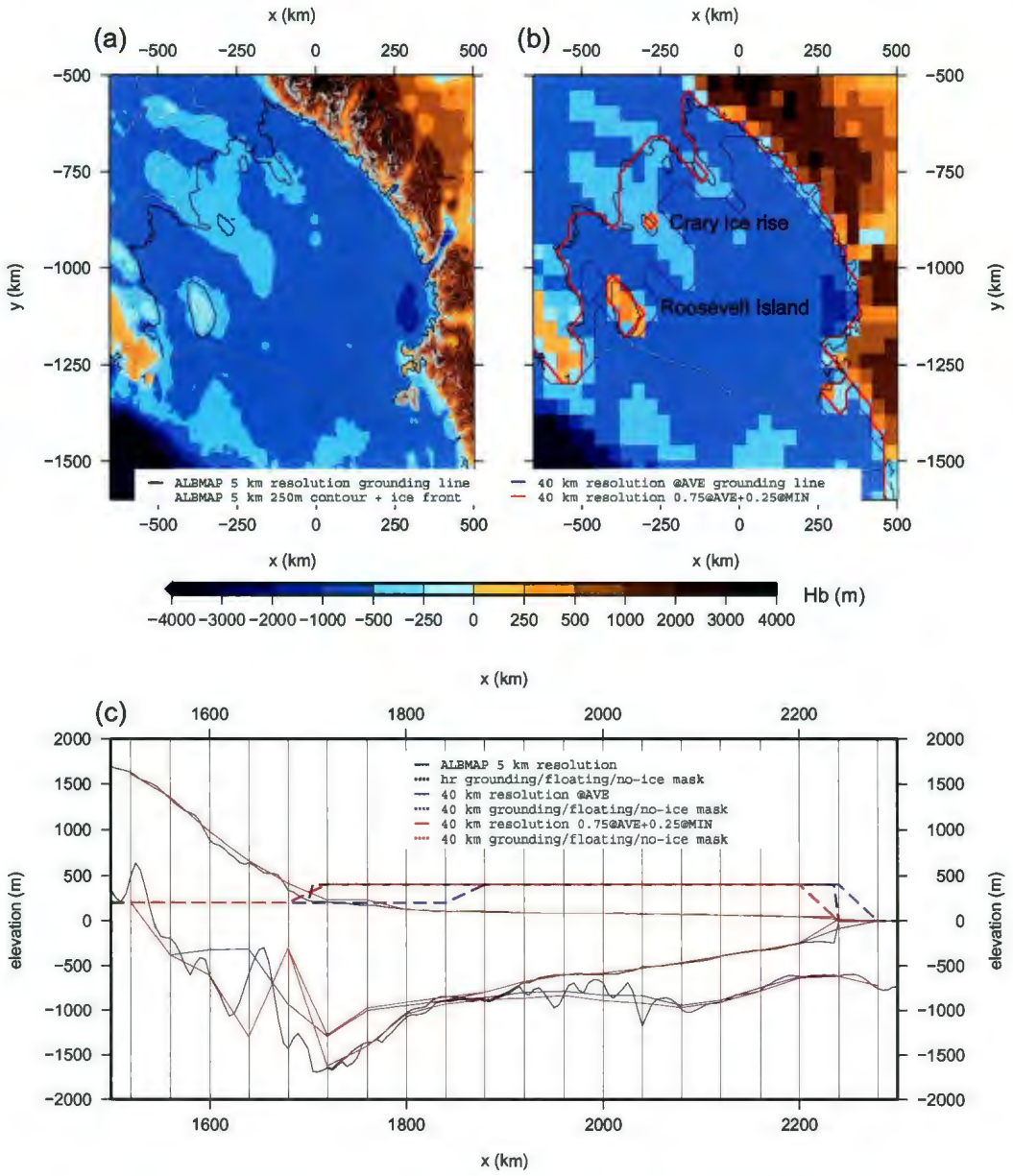


Figure B.1: Plots showing impact of interpolation, and adjustments made by hand, to $\text{ALBMAP}_{40}$ generated from $\text{ALBMAP}_5$, on the Ross ice-shelf (a & b) and Amery ice-shelf (c). $\text{ALBMAP}_5$ grounding line (black) migrates forward with the average interpolation function (blue), show in (b). This is corrected using average+minimum blended interpolation (red). Roosevelt Island and Crary ice rise, which provide important pinning points and back stresses are under-represented in $\text{ALBMAP}_5$ (a). They are hand inserted in $\text{ALBMAP}_{40}$ (b). Plot (c) shows the deep trough (black) just behind the grounding line of the Lambert Glacier-Amery ice-shelf system that is lost during interpolation (blue), adjusted by hand after interpolation (red). Migration of grounding line with unadjusted $\text{ALBMAP}_{40}$ can also be see (dashed blue). See text for details.

## B.2 Site notes

### B.2.1 RSL sites

Table B.2: RSL site notes

| id | Location | Reference | Notes |
|---|---|---|---|
| 9101 | Enderby Land, Syowa Coast (SC) | Miura et al. 1998 | Site is located in Lützow-Holm bay on the Syowa Coast. Data derived from in-situ marine shells (*Laternula Elliptica*) collected from excavated trenches in raised beaches, providing a sea level minimum. The data, including lat/lon, were taken from AGGD (Kluiving and van der Wateren, 2001). The samples fall into two ages, late Pleistocene (30-46 ka BP) and Holocene (3-7 ka BP). Takada (2003) performed a study to compare Electro Spin Resonance (ESR) derived dates with the AMS $^{14}$C dates. They found that with a reservoir effect for marine fossils of 420-1600 yr (Stuiver and Braziunas, 1985) the ESR and AMS $^{14}$C for the older samples may be underestimated, but the Holocene ages (based on a single sample) were similar. The reservoir correction used in this study, 1300±100 yr falls within the 420-1600 yr bounds. Only the younger samples have been employed here. No elevation error provided so use default value. |

*Continued on next page...*

Table B.2 – *Continued from previous page*

| id | Location | Reference | Notes |
|---|---|---|---|
| 9201 | Lambert Glacier region, Larsemann Hills (LH) | Verleyen 2005 | Larsemann Hills adjacent to the Lambert Glacier-Amery Ice Shelf system is derived from AMS dated sediment from three cores taken in three isolation basins, Pup Lagoon, Heart Lake, and Kirisjes Pond. Lat/lon taken from Fig. 2 in the publication. Ages date back to ~15 ka BP. Sill elevations taken from Fig.3. Sill elevation error given in publication. All data points used. One of the lacustrine-marine transitions has a reservoir correction applied, repeated here. |

*Continued on next page...*

Table B.2 – *Continued from previous page*

| id | Location | Reference | Notes |
|---|---|---|---|
| 9202 | Lambert Glacier region, Vestfold Hills (VH) | Zwartz 1998 | Located about 100km to the north of Larsemann Hills. Study is based on sediment cores from isolation basins and in-situ shells (isolation basins were sampled by authors for the study, in-situ shells from an earlier study, Zhang and Peterson (1984)). In Table . 8, the researchers present temporal ranges for the ML or LM transition derived from the source measurements (Table. 6). The RSL curve they present in Fig. 6 is based on these derived transitions and adopted here (the date and uncertainty in the database is derived from the upper and lower bound they present). The derived ML/LM transitions are based on either M sediments (Anderson), L sediments (Watts, Druzhby, Anderson), or in three cases both types(Organic, Highway, Ace). In those latter cases, to simplify processing, the following assumptions are made (See Fig. 6 in source publication):<br>1) Organic Lake. Because of the minimum constraint provided by the shells M dated ML transition is highly unlikely. Younger L derived ML transition is used.<br>2) Highway Lake. Older M dated ML transition is much more likely, furthermore only 40 yrs of L dated ML transition is being lost.<br>3) Ace. M dated ML transition would required a very steep RSL change (approaching 1 m in 0-250 yr) and would ignore/exclude Druzhby transition so highly unlikely. Older L dated ML transition most likely. Lat/lon taken from (AGGD)Kluiving and van der Wateren (2001). Sill height errors from Zwartz (1998); default error used for shell samples from Zhang and Peterson (1984), only youngest/limiting shell samples selected. Ages go back ~7 ka BP. |

Table B.2 – *Continued from previous page*

| id | Location | Reference | Notes |
|---|---|---|---|
| 9301 | Wilkes Land, Windmill Islands (WI) | Goodwin 2000 | Based on a re-interpretation of an earlier study (Goodwin, 1993). Data extracted from AGGD (Kluiving and van der Wateren, 2001). The data points are a collection of bulk $^{14}C$ measurements of marine and lake sediments in isolation basins. Elevation uncertainty taken from Goodwin (2000). Ages date back to ~8 ka BP. |
| 9401 | Victoria Land, Terra Nova Bay (TNB) | Baroni and Hall 2004 | Terra Nova Bay adjacent to the Ross Sea. Samples of penguin guano, penguin remains, shells and seal skin from raised beaches provide beach age maximum, minimum and close ages. Data ages to ~8 ka BP. The authors present a comprehensive analysis of the data. Because of the high quality of the data, the numerous samples and the detailed analysis only the data points that are close to the published RSL curve, (Fig. 6 Baroni and Hall (2004)) are used. Lat/lon taken from Fig. 2 in Baroni and Hall (2004)), site is small < ~4 km x ~5 km and, given resolution of the figure only one lat/lon is used for all data points. Elevation error based on error stated at end of introduction. |

*Continued on next page...*

Table B.2 – *Continued from previous page*

| id | Location | Reference | Notes |
|---|---|---|---|
| 9402 | Scott Coast, Southern Scott Coast (SSC) | Hall 2004 | Also on the Ross Sea ~200 km south of Terra Nova Bay, site is derived from samples of crushed marine shells, seal skin and elephant seal taken from storm beaches, providing maximum, minimum and close ages of the beach. Ages to ~7 ka BP. As with Site 9401 authors present a comprehensive analysis of the data and because of the high quality of the data, the numerous samples and the detailed analysis only the data points that are close to the published RSL curve, (Fig. 2 Hall (2004)) are used. Lat/lon estimated from Fig. 1 Hall (2004). Elevation errors extracted from publication. |
| 9601 | West Antarctic Peninsula, Marguerite Bay (MB) | Bentley 2005 | Also 9602. Sites are an amalgam of new and previously published $^{14}C$ dates. Marguerite Bay site comprises freshwater and marine sediment from isolation basins and penguin bones (Bentley 2005 and references therein). Only data points that are close to the published RSL (Fig. 3 Bentley (2005)) curve are used. Lat/lon estimated from Fig. 2(a) Bentley (2005). Elevation error of 0.2m, taken from publication. |

*Continued on next page...*

Table B.2 – *Continued from previous page*

| id | Location | Reference | Notes |
|---|---|---|---|
| 9602 | South Shetland Islands, King George Island (KGI) | Bentley 2005 | Part of the South Shetland Islands. Data points selected here are ∼<1000 yr age and are derived from penguin bone, freshwater sediment and freshwater moss (indicating marine isolation). See comment below about whale bone. Only data points that are close to the published RSL (Fig. 5 Bentley (2005)) curve are used. Lat/lon estimated from Fig. 2(c) Bentley (2005). Elevation error of 0.2m is taken from publication.<br>Note: In the South Shetland Islands there are two sites, the second is only ∼100 km away, located on Livingstone Is. Bentley (2005) combines these two locations into a single site but makes the observation that there may be significant local differences in the RSL history. In the RSL modelling/data comparison work of Bassett et al. (2007) the two locations are treated as separate RSL sites to account for the spacial variation seen in the sea level predictions for that region (Bassett et al., 2007). All the samples from Livingstone Island (and some from King George Island) are from dated whalebone collagen that was recovered from beaches. The samples were large and buried several tens of centimeters deep in the sediment, so likely not deposited by wave activity, rather they provide a maximum age. However it is unclear what adjustment factor to apply in this case. Furthermore, Bentley (2005) found applying the Berkman and Forman (1996) 1434±200 correction factor produces modern ages and thus little constraint. The smaller correction factor of 500-600 yrs (Curl1980) was applied to recover more useful dates. Given the uncertainty in the age of the samples, the adjustment factor, the dimensions of the islands in relation to model resolution (∼100km x ∼20km ) and the proximity to the King George Islands. The |

Table B.2 – *Continued from previous page*

| id | Location | Reference | Notes |
|---|---|---|---|

## B.2.2 ELEV sites

Table B.3: ELEV site notes

| id | Location (code) | Reference | Notes |
|---|---|---|---|
| 1101 | Dronning Maud Land, Lutzow-Holm Bay (LHB) | Yamane et al. 2011 | Six cosmo dated samples collected from Skarvsnes and Skallen oases on the Syowa Coast. Two rejected (SK2, SV11) as having complex history. The four remaining are all located <5 km apart. Two, SV4-2 and SV7-2, dated at ~10 ka separated by 400m local elevation and two, SV3-1 and SV9-2, at ~6ka, 100m altitude apart. Only the higher samples have been employed here. No altitude errors given, default applied. |
| 1201 | MacRobertson Land, Framnes Mtns. (FM1) | Mackintosh 2007 | Also 1202 and 1203. Framnes Mts. are a N-S oriented range that extend from the coast of MacRobertson Land ~50 km inland, forming a transect perpendicular to the ice-sheet margin. Study site split into three sites from S to N, 1201, 1202, 1203. The study is based on a collection of dated erratics. Authors identify samples with complex histories. Only highest and youngest samples used, based on Fig. 2, anomalous high sample, FM-NMas-1-2 excluded as recommended. No altitude errors given, default used. |
| 1202 | MacRobertson Land, Framnes Mtns. (FM2) | Mackintosh 2007 | See 1201 |

*Continued on next page...*

| id | Location (code) | Reference | Notes |
|---|---|---|---|
| 1203 | MacRobertson Land, Framnes Mtns. (FM3) | Mackintosh 2007 | See 1201 |
| 1204 | Interior EA., Grooves Mts. (GM) | Lilly et al. 2010 | Groove Mts., upstream of Lambert Glacier in interior of EA. Vast majority of samples are ~100 ka old thus too old with current evaluation set-up. Two samples, GR01, GR13 are 53, 51 ka respectively (minimum $^{10}Be$ age used as these are ages discussed in text). Located just above the present day ice-sheet. One other, GR06, (plus a repeat GR06r of with similar age) at 104 ka is also used. No altitude measurement errors given, default used. |
| 1205 | MacRobertson Land, South Prince Charles Mts. (PCM1) | White et al. 2011 | Also 1206 and 1207. Located in the Lambert Glacier-Amery Ice Shelf system. Study site split into three constraint sites. Data is spread along ~500 km working down from Mt. Ruker, south PCM, via Mt. Stinear and Mt. Rymill to Loewe Massif on edge of LAIS. For Mt. Rucker, all samples are used except for 3; Ruk-251 is complex and Ruk-249, Ruk-227 beyond oldest age limit. No altitude measurement errors given, default used. |
| 1206 | MacRobertson Land, Central Prince Charles Mts. (PCM2) | White et al. 2011 | See 1205 also. Mt Stinear and Mt Rymill is a complex chronology. Site 154 is identified as the most representative sample (pers comms). No altitude measurement errors given, default used. |

*Continued on next page...*

| id | Location (code) | Reference | Notes |
|---|---|---|---|
| 1207 | MacRobertson Land, North Prince Charles Mts. (PCM3) | White et al. 2011 | See 1205 also. Loewe Massif, authors identify four key samples (LM-C12a, LM-C8b, LM-C3, LM-C14b) that provide a chronostratigraphic-consistent sequences from 18->12 ka. No altitude measurement errors given, default used. |

*Continued on next page...*

| id | Location (code) | Reference | Notes |
|---|---|---|---|
| 1401 | Queen Maud Mts., Reedy Glacier (RG1) | Todd et al. 2010 | See also 1402, 1403. Comprises data points located along the margins of the Reedy Glacier. A 120 km long glacier flowing northwards on the WA side of the Trans-Antarctic mountains, is the main tributary to the Mercer Ice stream (itself flowing to the Ross Ice Shelf). Glacial erratics were dated from the head of the glacier and from above the margins. Samples were taken from five sites (Quartz Hills, Caloplaca Hills, Mims Spur, Hatcher Bluffs, Polygon Spur) working up the glacier, with exposure ages increasing up stream, thus the glacier underwent thickening attributed to (a) grounding and thickening of RIS causing a wave of thickening to propagate upstream and (b) increased snow accumulation on EA plateau. The study makes use of both upper limit (max elevation ice-sheet attained) and recessional deposits (deposited as ice retreated). Altitude uncertainty stated as typically 3-4 m, unless stated otherwise in following descriptions, 4 m is used. Study site is split into three constraint sites working up the glacier<br>Quartz hills: upper limit age constraint is based on 6 of 12 samples (remaining are too old). Authors publish a weighted mean age, but not an altitude/location. The upper limit persisted for ~3ka. The oldest and youngest samples are used as bounds. All recessional deposits identified as representative are used.<br>All other samples are identified as complex thus are rejected. |

*Continued on next page...*

| id | Location (code) | Reference | Notes |
|---|---|---|---|
| 1402 | Queen Maud Mts., Reedy Glacier (RG2) | Todd et al. 2010 | See 1401. Caloplaca Hills only have upper limit deposits. Again they are presented as a weighted mean, but not a weighted altitude. As for Quartz hills the oldest and youngest sample altitudes are used here as bounds. Mims Spur. Upper limit data presented as weighted mean, authors wary to state upper or lower bound. The weighted mean age is used here. Altitude is lower alt + 0.5(upper alt - lower alt). Altitude uncertainty is calculated as 0.5(upper alt - lower alt) Not enough confidence in recessional deposits sample to use as constraint. Polygon Spur: Four recessional deposits, 2 identified as complex. Remaining two used here. |
| 1403 | Queen Maud Mts., Reedy Glacier (RG3) | Todd et al. 2010 | See 1401. Hatcher: One sample at 3.5 ka recommended in text. |
| 1404 | Darwin Range, Hatherton Glacier (HG) | Storey et al. 2010 | Hatherton glacier drains ice from TAM into lower Darwin Glacier, then from Darwin Glacier into Ross ice shelf). Samples taken from two transects at Lake Wellman. Total of 25 erratics, giving a pre-LGM of ~600m thicker at 2.2 Ma. Complex mix of dates promote detailed analysis concluding with maximum and minimum assessments. Relevant here, author identifies five erratics from transect BB' that are clustered around 37 ka and presents them as a mean. Youngest/highest hypothesis applied here. $^{10}$Be and $^{26}$Al ages are measured but not merged together, discussion uses on $^{10}$Be dates. No altitude measurement errors given, default used. |

*Continued on next page...*

| id | Location (code) | Reference | Notes |
|---|---|---|---|
| 1405 | Marie Byrd Land, Ford Ranges (CLM) | Stone et al. 2003 | See 1406, 1407, 1408 also. Ford ranges are formed by a number of peaks oriented east-southeast from Eastern Fosdicks near Sulzeberger Bay following an approximate transect ~80km inland along Sarnoff-Allegheny-Clark Mts. Samples from glacially transported cobbles dated with $^{10}$Be. Study site is split into four constraint sites. I select data from the margins of the study area, Eastern Fosdick, Western Sarnoff and Clark and Allegheny Mts. This site is Clark Mts. Transect(s) have correct chrono-stratigraphical sequence. Youngest/highest hypothesis applied to reduce number of points. No altitude measurement errors given, default used. |
| 1406 | Marie Byrd Land, Ford Ranges (ALM) | Stone et al. 2003 | See 1405 for details. Allegheny Mts. |
| 1407 | Marie Byrd Land, Ford Ranges (WSM) | Stone et al. 2003 | See 1405 for details. Western Sarnoff Mts. |
| 1408 | Marie Byrd Land, Ford Ranges (EFR) | Stone et al. 2003 | See 1405 for details. Eastern Fosdick Mts. |

*Continued on next page...*

| id | Location (code) | Reference | Notes |
|---|---|---|---|
| 1501 | Marie Byrd Land, Executive Committee Range (ECR) | Ackert et al. 1999 | Lateral moraine located on Mt. Waesche in Marie Byrd Land, WA. Site is a collection of closely dated erratics (dated using $^{3}He$ and $^{36}Cl$ SED). Dates taken from a lower lateral moraine band. Eight samples from four locales, authors reject one old age, plus after further discussion remove two younger samples, leaving five; four clustered at 10.ka and a single sample at 7.4 ka . All other dates rejected by authors. Youngest/highest taken from the cluster, leaving two samples. No altitude measurement errors given, default used. Lat/lon estimated from plot. |
| 1502 | Amundsen Sea Embayment, Pine Island Bay (PIB1) | Johnson et al. 2008 | Also 1503. Three dated glacial deposits from Turtle Rock on the margins of the Pope and Smith Glaciers in the Amundsen Sea Embayment, WA. One sample, TR3, identified as embedded in till lower and older than others thus rejected. No altitude measurement errors given, default used. |
| 1503 | Amundsen Sea Embayment, Pine Island Bay (PIB2) | Johnson et al. 2008 | Also 1502. Two dated glacial deposits from Mt. Mante overlooking Pine Island Glacier in the Amundsen Sea Embayment, WA. Only MM2 used. MM1 possibly has inheritance given TR1, TR2. No altitude measurement errors given, default used. |

*Continued on next page...*

| id | Location (code) | Reference | Notes |
|---|---|---|---|
| 1601 | Batterbee Mts., West Palmer Land (WPL) | Bentley et al. 2006 | Also 1602, 1603, 1701. Comprehensive study across the Antarctic Peninsula using both geomorphological evidence and dated erratics. Only dated erratics used in this database. Data points are taken from age altitude plots of Fig 4 (and from notes in the text). Table 1 is already filtered by erosion island thus identifying quality points. For Batterbee Mts., youngest/highest used. Altitude error is 2% of altitude. N.B. Ablation valley not mentioned (and young) so not used. Fergusson nunataks give old dates and are rejected. |
| 1602 | Two Step Cliffs, Alexander Island South (AXS) | Bentley et al. 2006; Hodgson et al. 2009 | See 1601 also. From Bentley et al. (2006) two samples, TSC1 and TSC2 are reliable. Altitude error is 2% of altitude. From Hodgson et al. (2009) Citadel Bastion, four $^{10}Be$ boulder samples, two from the summit, two from an adjacent col. See Table. 2. Youngest/highest used. |
| 1603 | Moutonnée Valley, Alexander Island North (AXN) | Bentley et al. 2006 | See 1601 also. Clear sequence from MV2, MV1, MV5. Altitude error is 2% of altitude. |

*Continued on next page...*

| id | Location (code) | Reference | Notes |
|---|---|---|---|
| 1701 | East Palmer Land, Berhrendt Mts. (BM) | Bentley et al. 2006 | See 1601 also. Located on the east side of the AP, constraining Weddell Sea. The author only favours the three samples from the Berhrendt Mts (at 7.2 ka ice surface <300 m thicker than present), explicitly rejecting Mount Dewe, Fergusson and (inferring) the same for Sweeney. Altitude error is 2% of altitude. |
| 1702 | Ellsworth Land, Ellsworth Mountains (EM) | Bentley et al. 2010 | Study comprises of 69 SED from two sites in SW Weddell Sea Embayment. Clearly presented in Fig 2 and supplement. Youngest/highest selected. Sample elevation error quoted in supplement as ± 10 m. |
| 1703 | Shackleton Range, Shackleton Range1 (SR1) | Hein et al. 2011 | See 1704 also. Study from Slessor and Recovery Glaciers (that drain into Filchner Ice Shelf). Results show that there has been no significant change in ice height between PD and LGM, hypothesizing, because Filchner could not advance forward due to deep bathymetric depression of Thiel/Crary Trough. Based on discussion, at Mt. Provender, the concordant bedrock and erratic ages suggest the ice margin lowered to its present elevation of 240 m by 41 ka. Three samples described in discussion used. At Mt. Skidmore, the two youngest exposure ages (one of them the only dating for the LGM) come from the modern ice margin with ages of 27 ka and 120 ka.<br>No altitude measurement errors given, default used. |

*Continued on next page...*

| id | Location (code) | Reference | Notes |
|---|---|---|---|
| 1704 | Shackleton Range, Shackleton Range2 (SR2) | Hein et al. 2011 | See 1703. At Mt. Sheffield the three youngest exposure ages are the only ones dating to the LGM. Retrieved from the modern ice margin with ages of 3 ka, 23 ka and 25 ka. No altitude measurement errors given, default used. |

## B.3 Site maps and age-altitude plots

The following figures show, in the lower pane, a map of the region around each site with the topographic details (Contours taken from 1 km RAMP-DEM (Liu et al., 2001)). Flowlines, rock outcrops and coastline from 1:10,000,000 scale dataset from Antarctic Digital Database (SCAR, 2006), in the upper pane, an age-altitude plot with the observations and an inset showing the location of the site on the AIS. There is a figure per site. The figures are centred on the site position, the region is approximately 200 km x 200 km. The red overlay is a 40 km resolution grid, representing the model domain. The data-points for the site are shown as red diamonds. In some cases, if close enough, other sites can be seen on the map, these data-points are show as black triangles. These data-points are not plotted on the age altitude plots.

### B.3.1 RSL sites

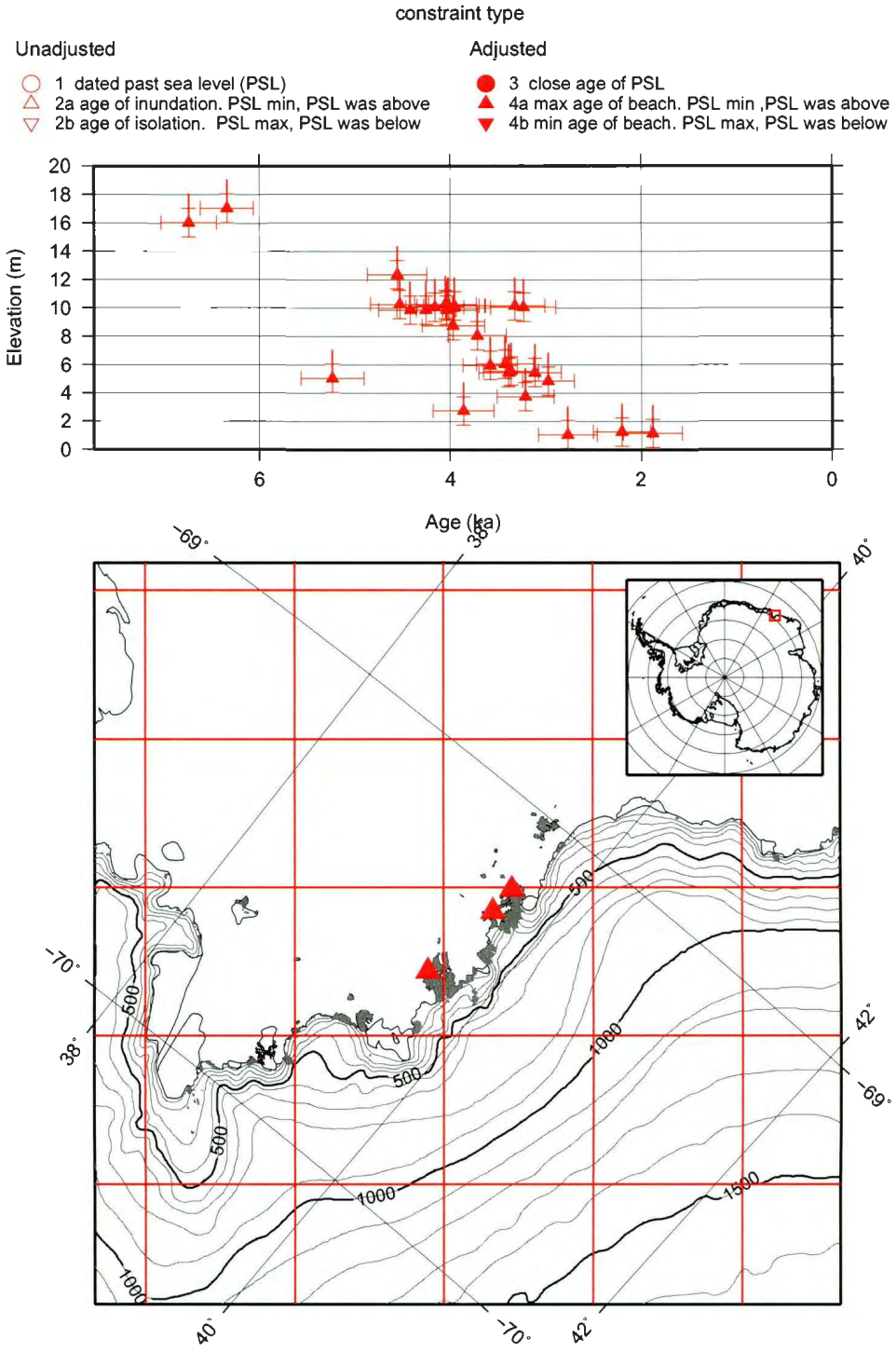


Figure B.2: RSL site:9101 Syowa Coast (SC)

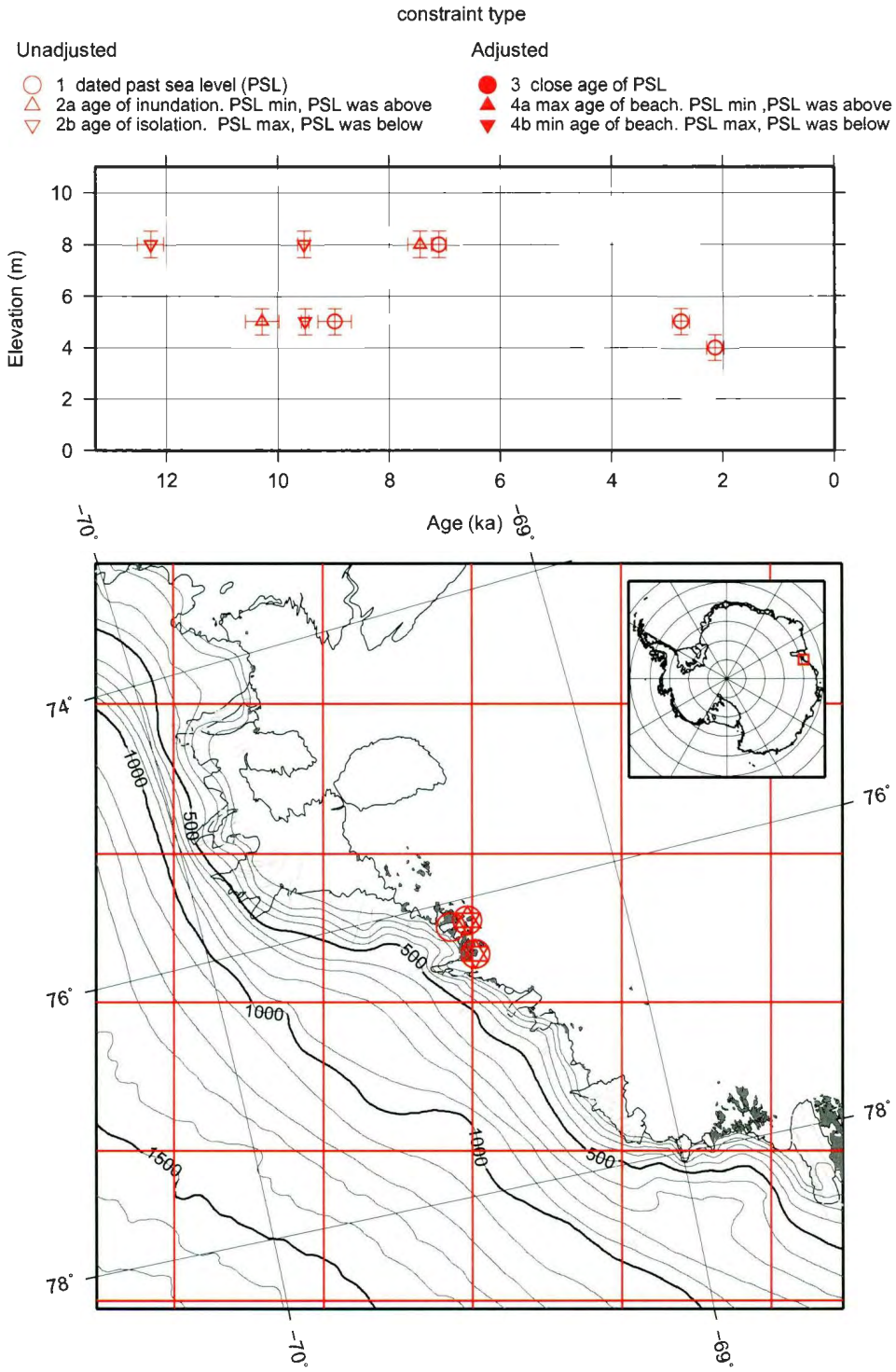


Figure B.3: RSL site:9201 Larsemann Hills (LH)

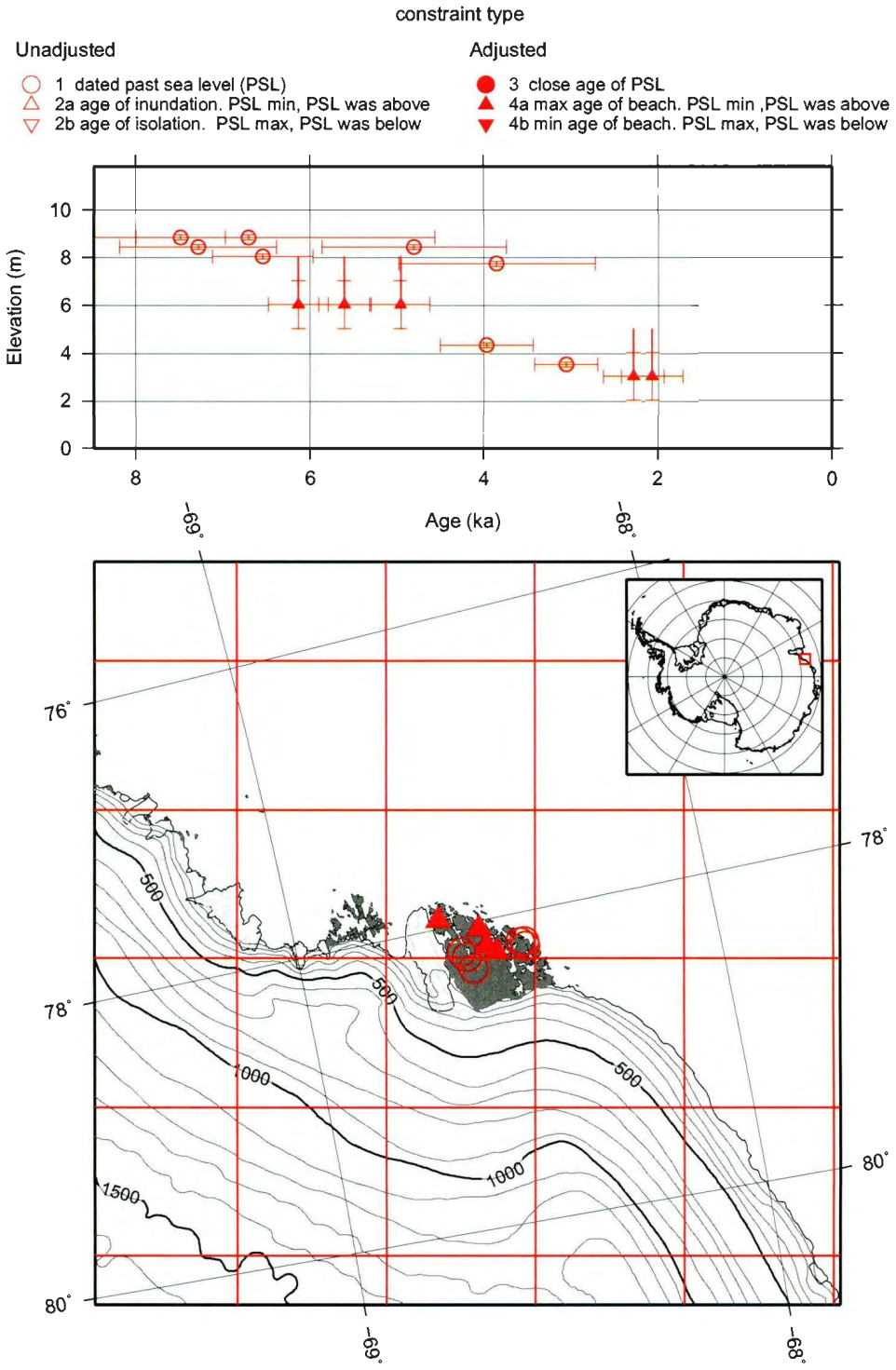


Figure B.4: RSL site:9202 Vestfold Hills (VH)

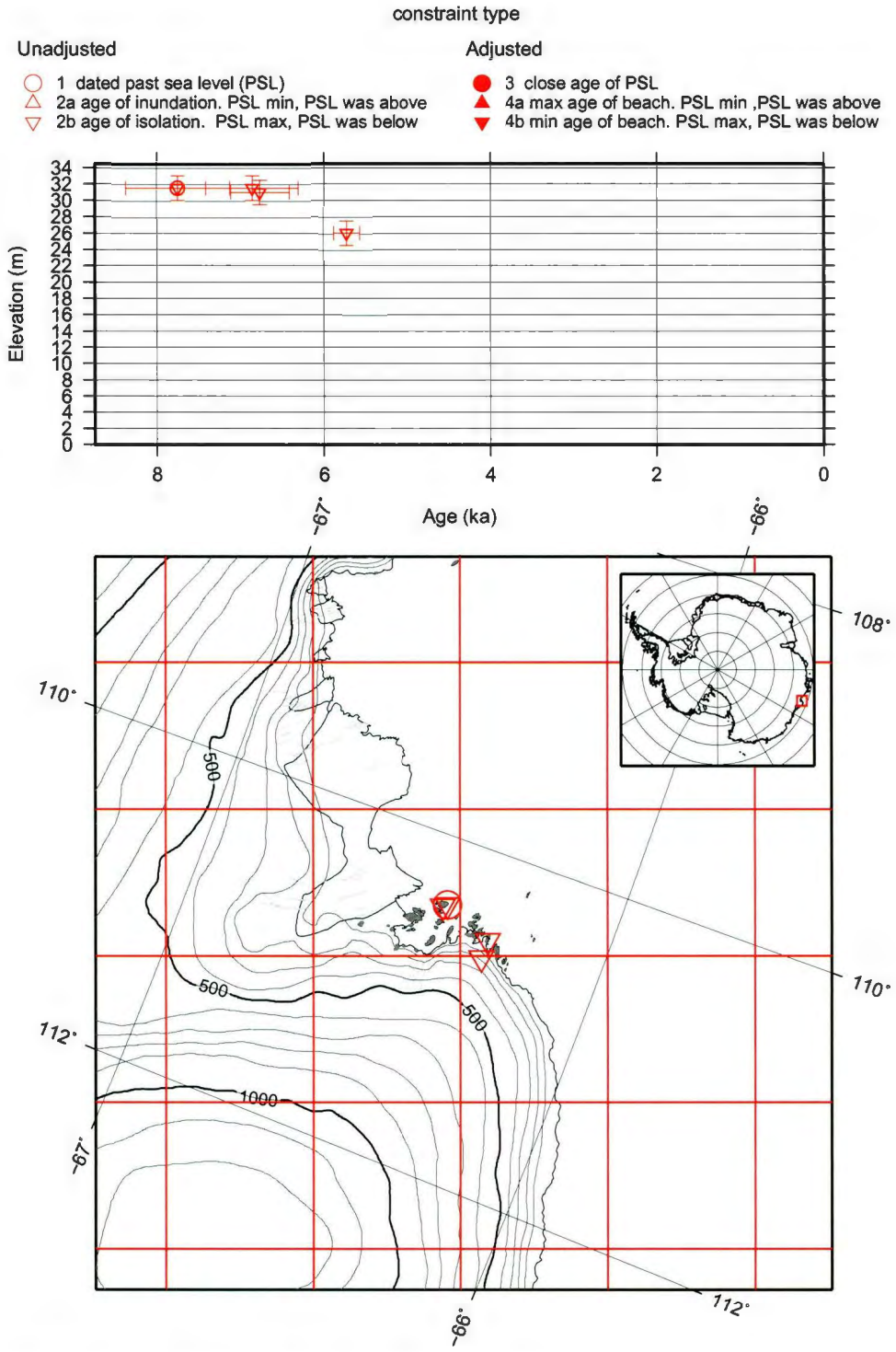


Figure B.5: RSL site:9301 Windmill Islands (WI)

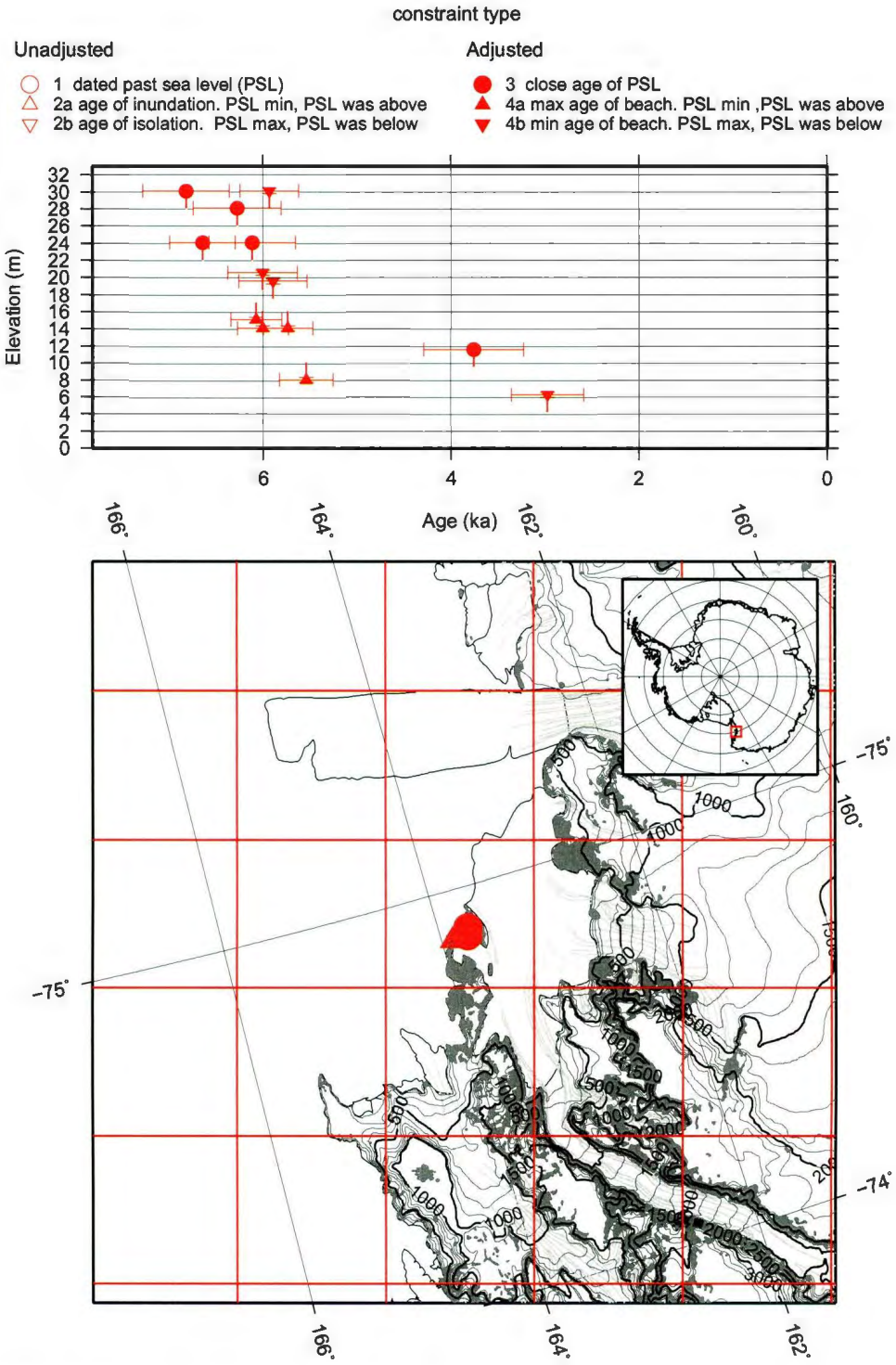


Figure B.6: RSL site:9401 Terra Nova Bay (TNB)

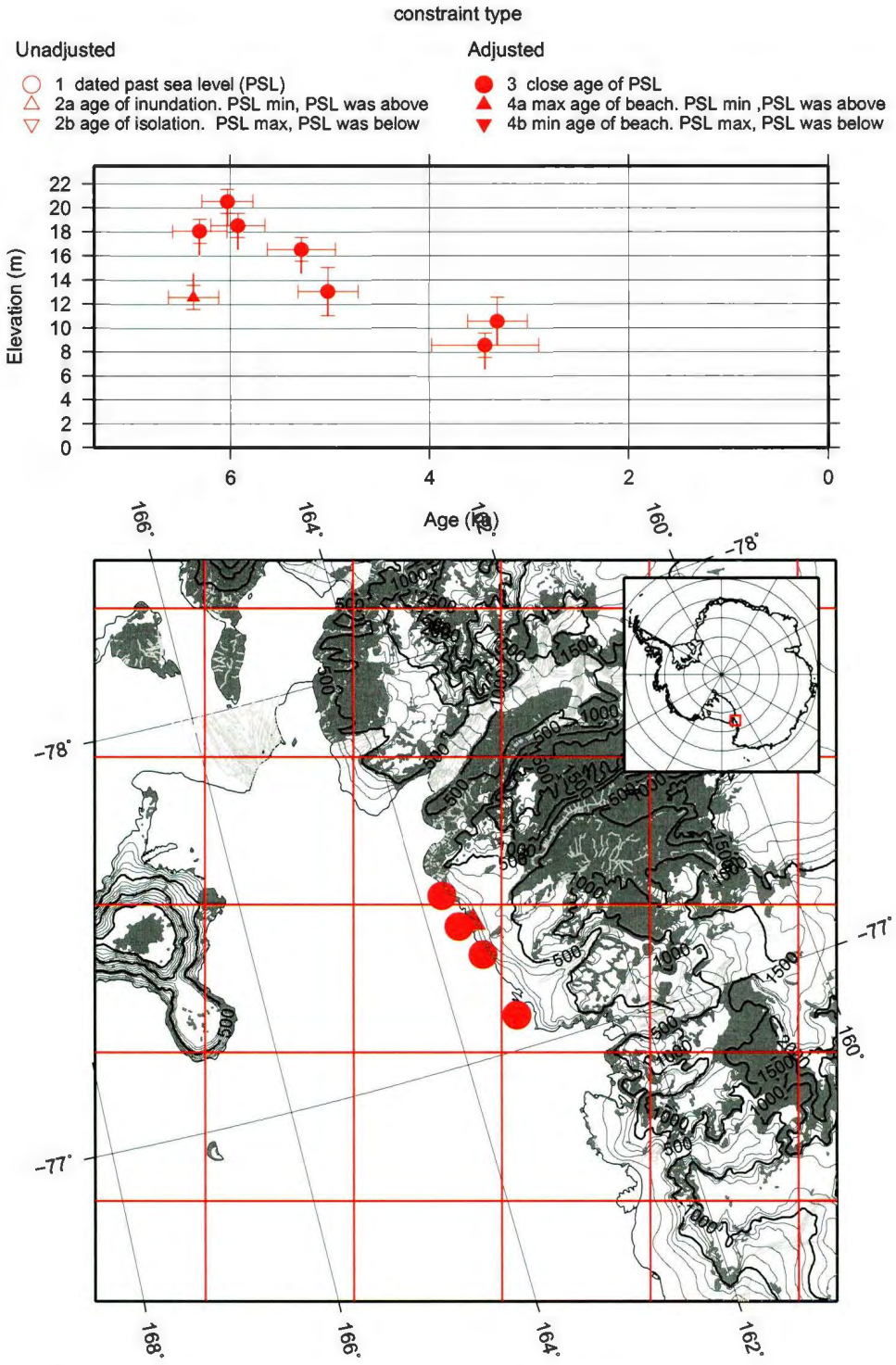


Figure B.7: RSL site:9402 Southern Scott Coast (SSC)

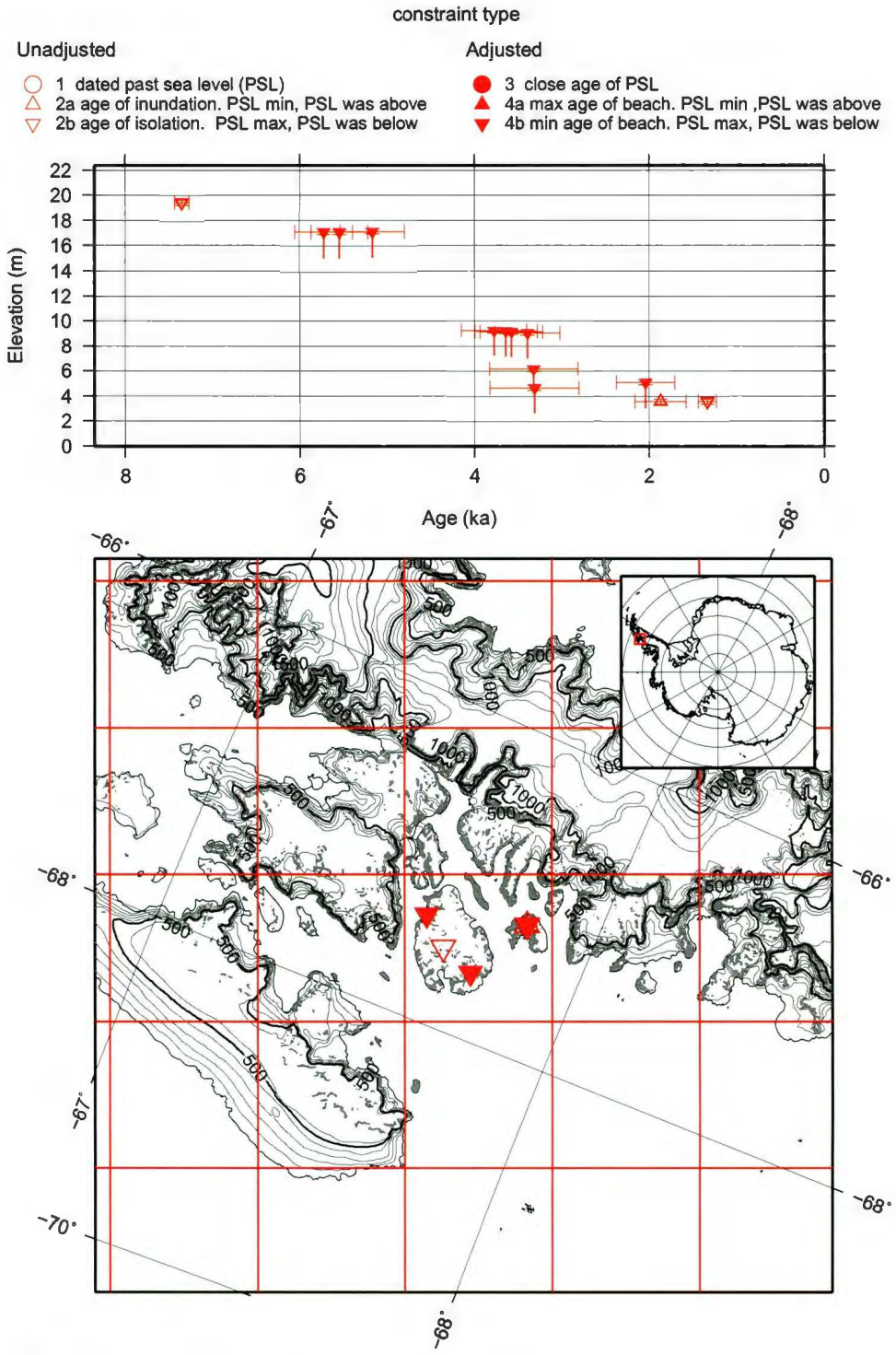


Figure B.8: RSL site:9601 Marguerite Bay (MB)

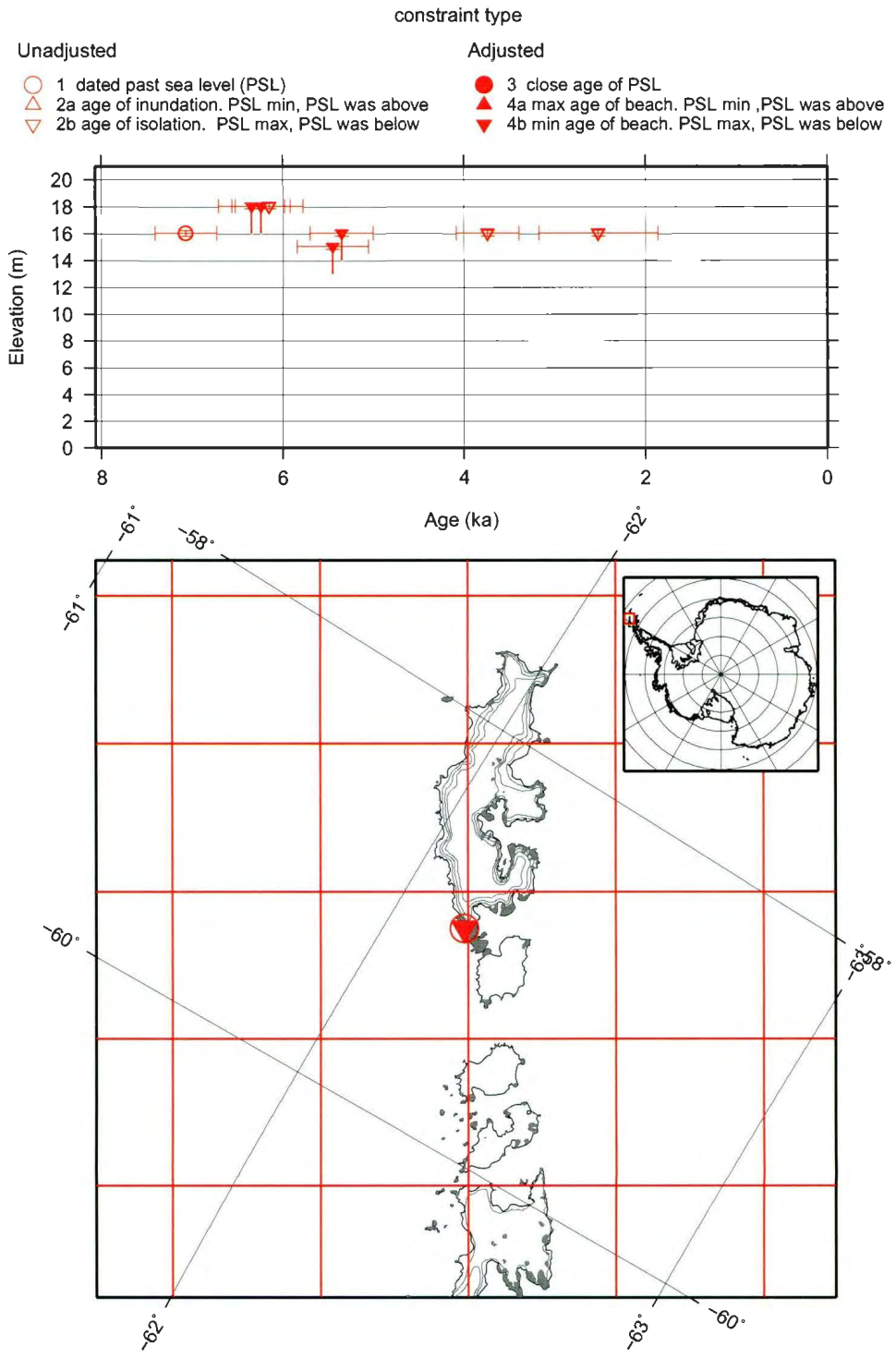


Figure B.9: RSL site:9602 King George Island (KGI)

### B.3.2 ELEV sites

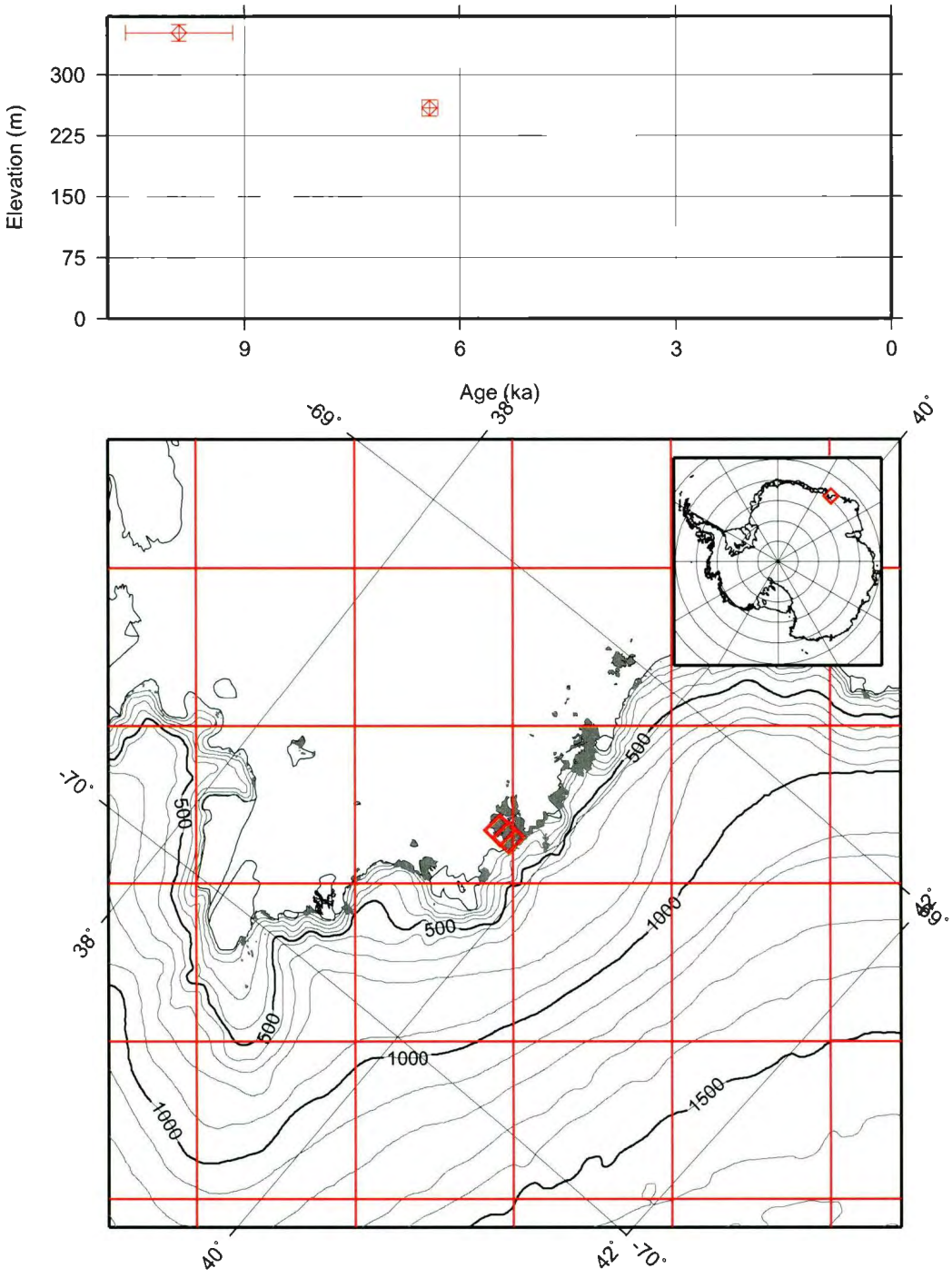


Figure B.10: PHS site:1101 Lutzow-Holm Bay (LHB)

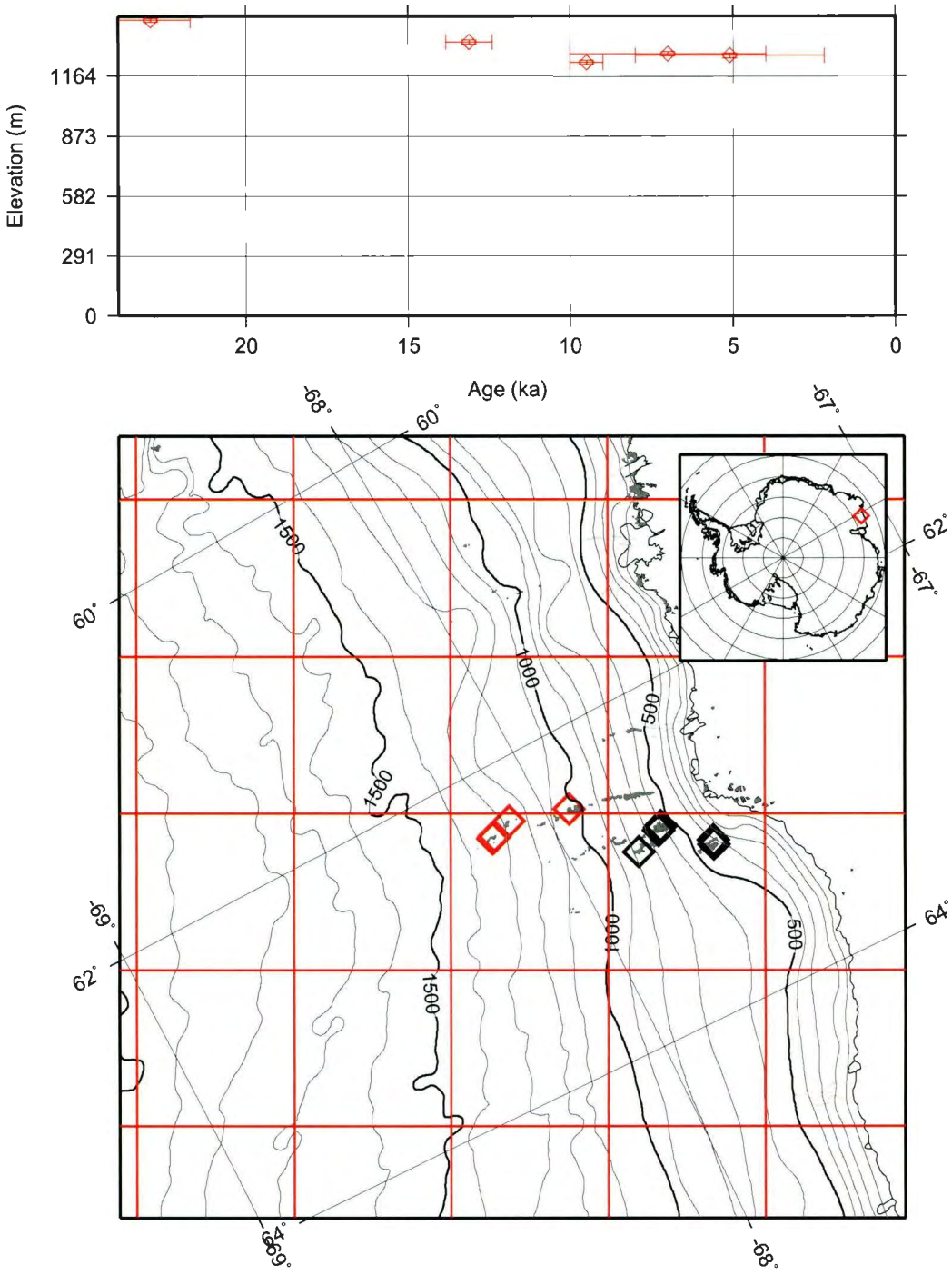


Figure B.11: PHS site:1201 Framnes Mts. 1 (FM1)

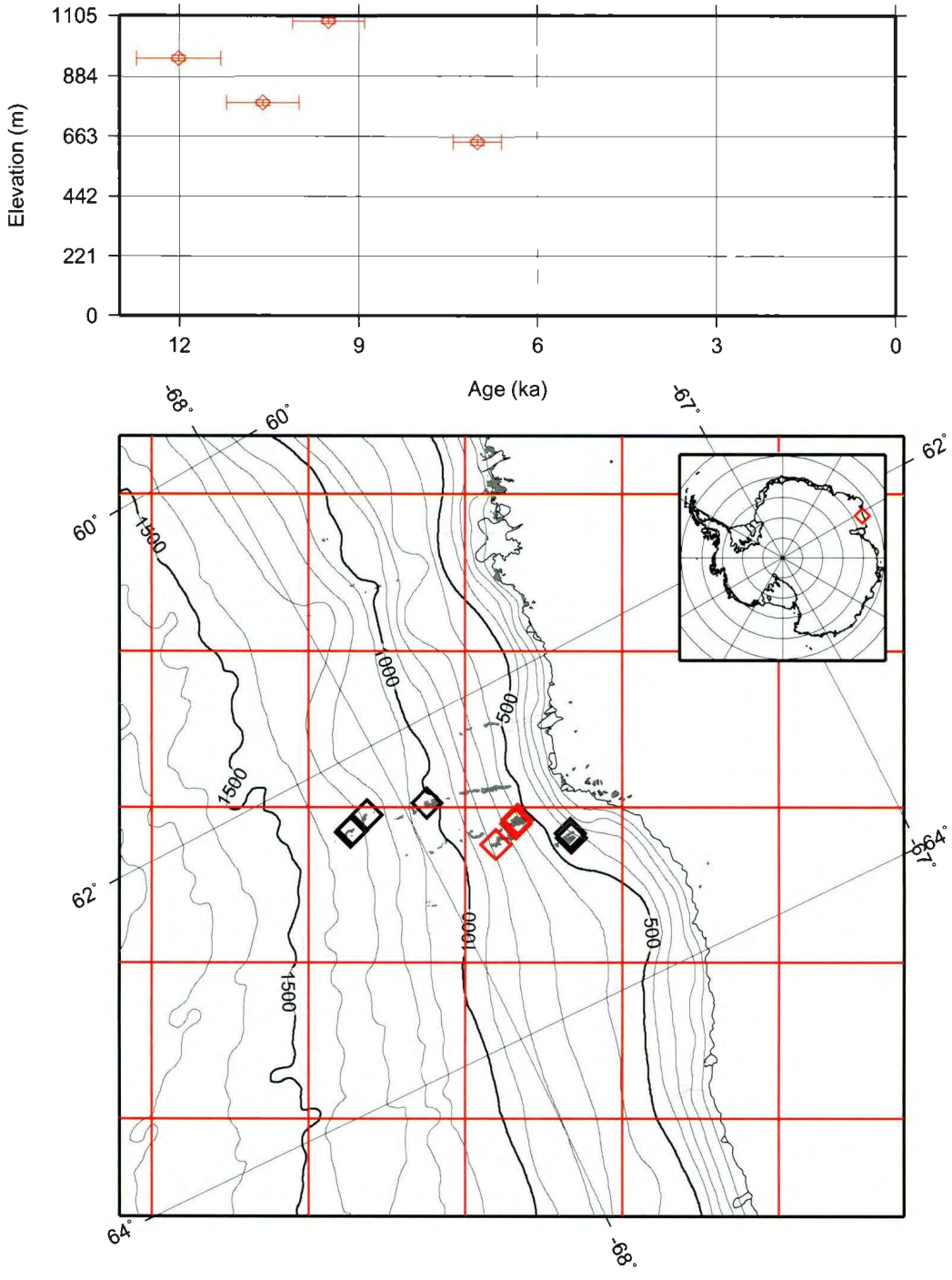


Figure B.12: PHS site:1202 Framnes Mts. 2 (FM2)

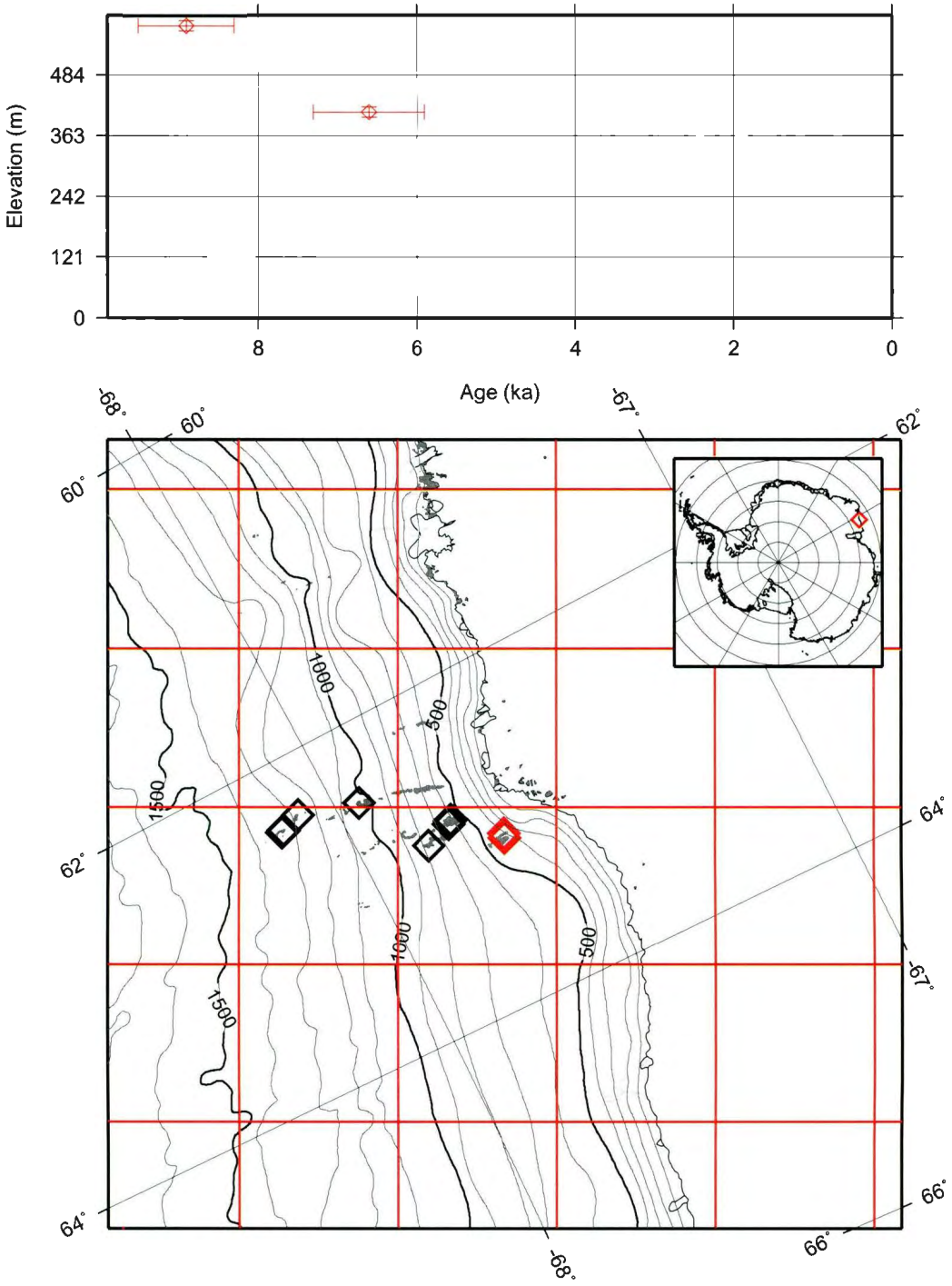


Figure B.13: PHS site:1203 Framnes Mts. 3 (FM3)

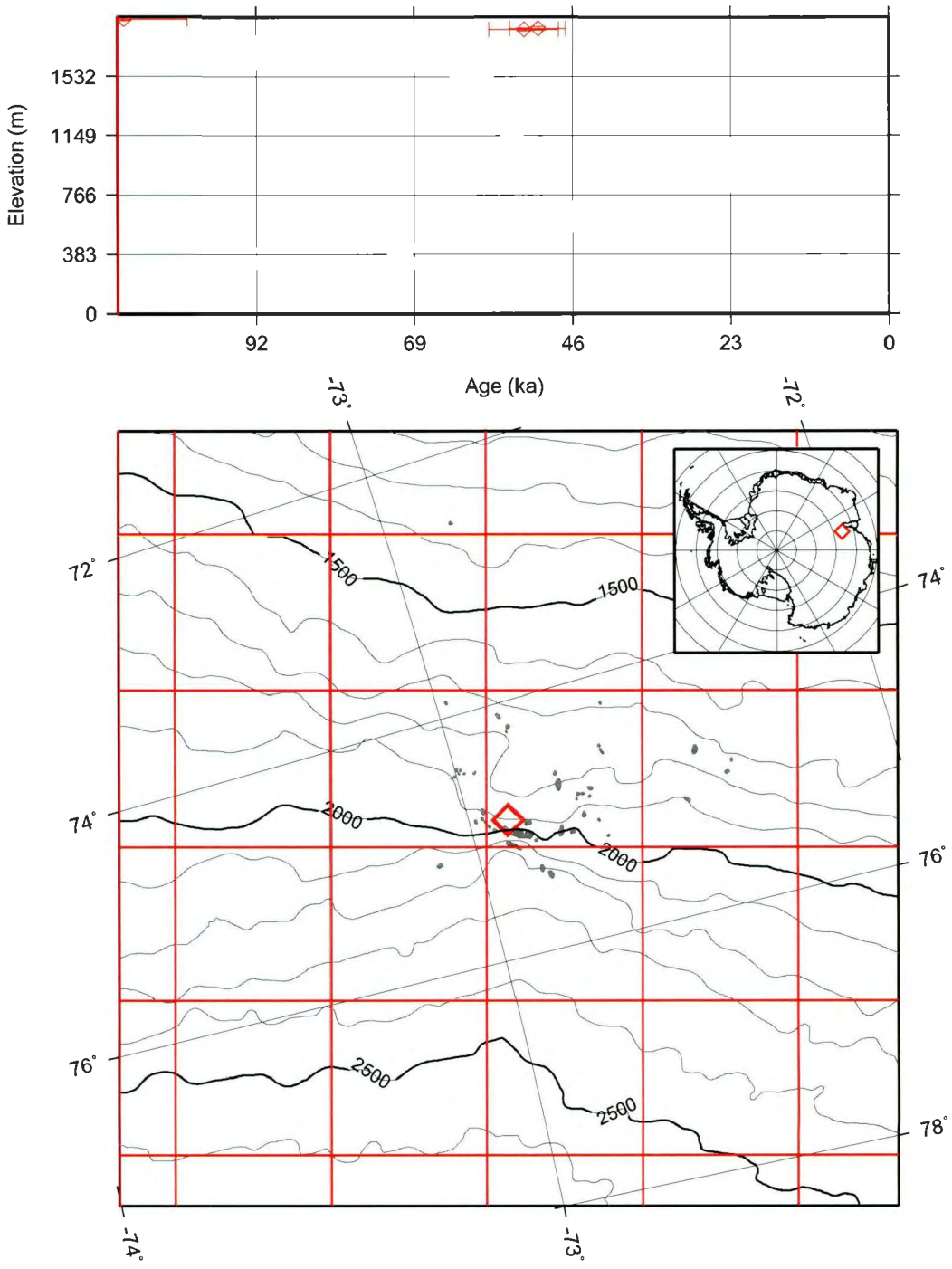


Figure B.14: PHS site:1204 Grove Mts. (GM)

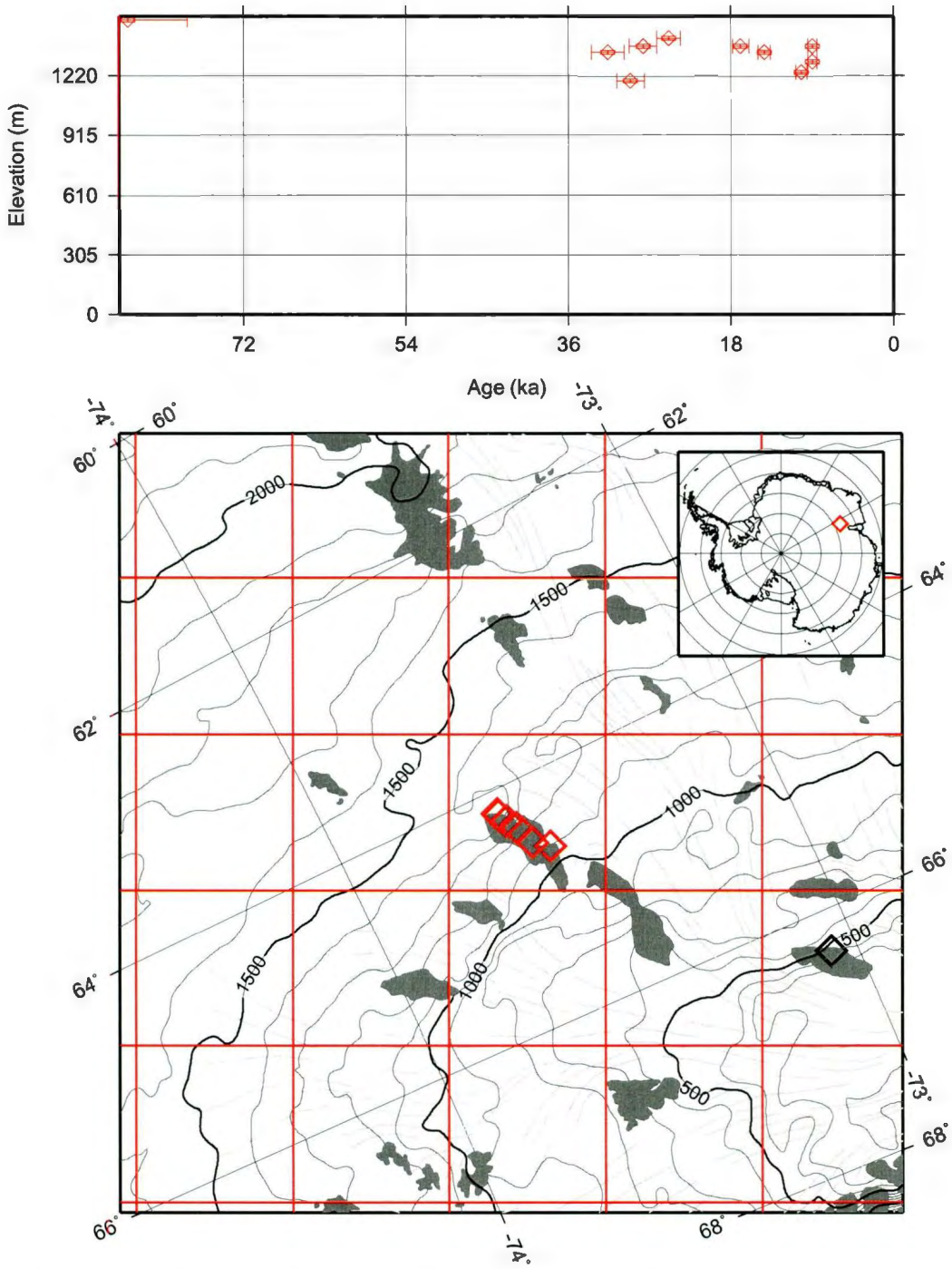


Figure B.15: PHS site:1205 Prince Charles Mts. 1 (PCM1)

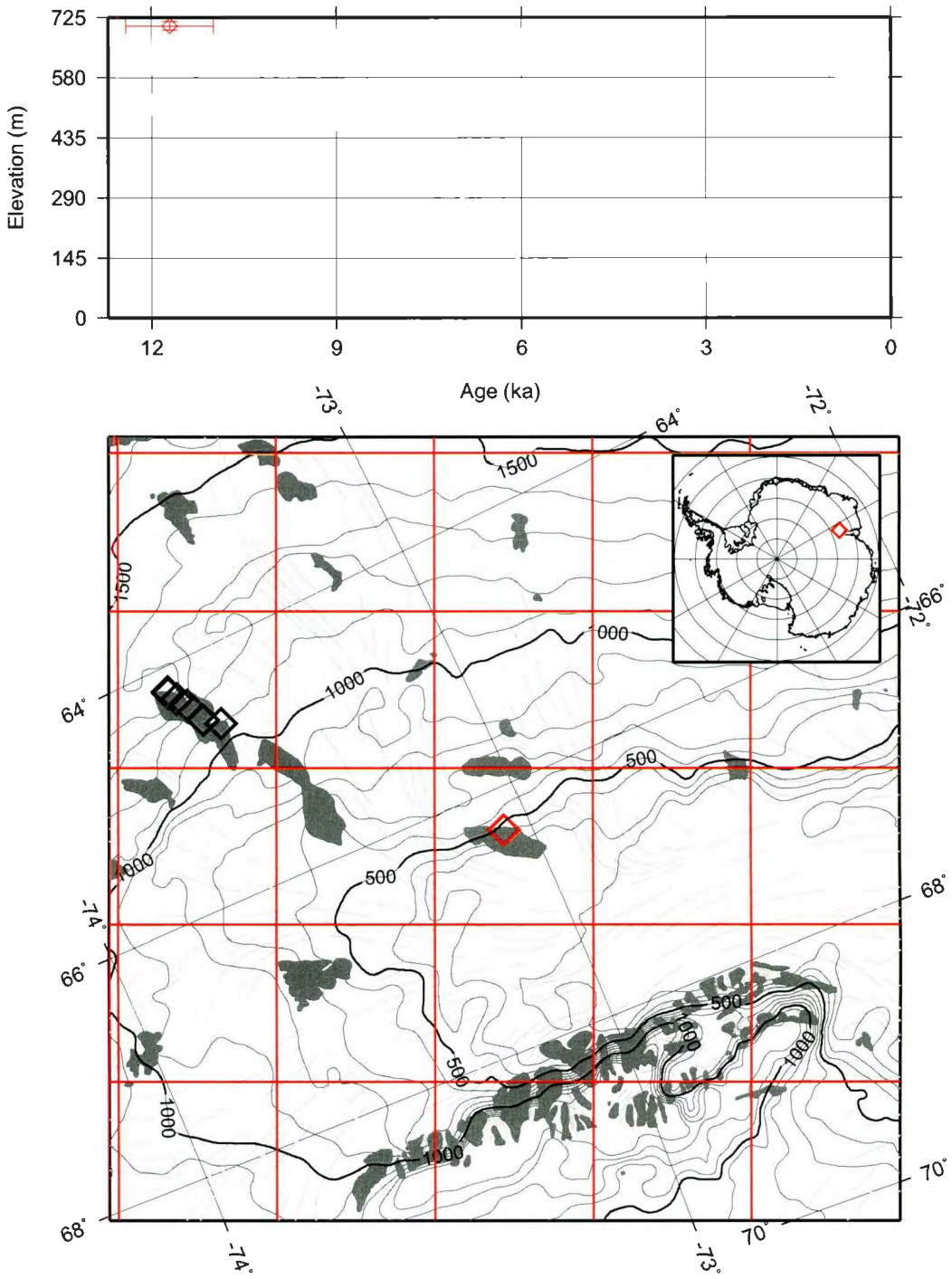


Figure B.16: PHS site:1206 Prince Charles Mts. 2 (PCM2)

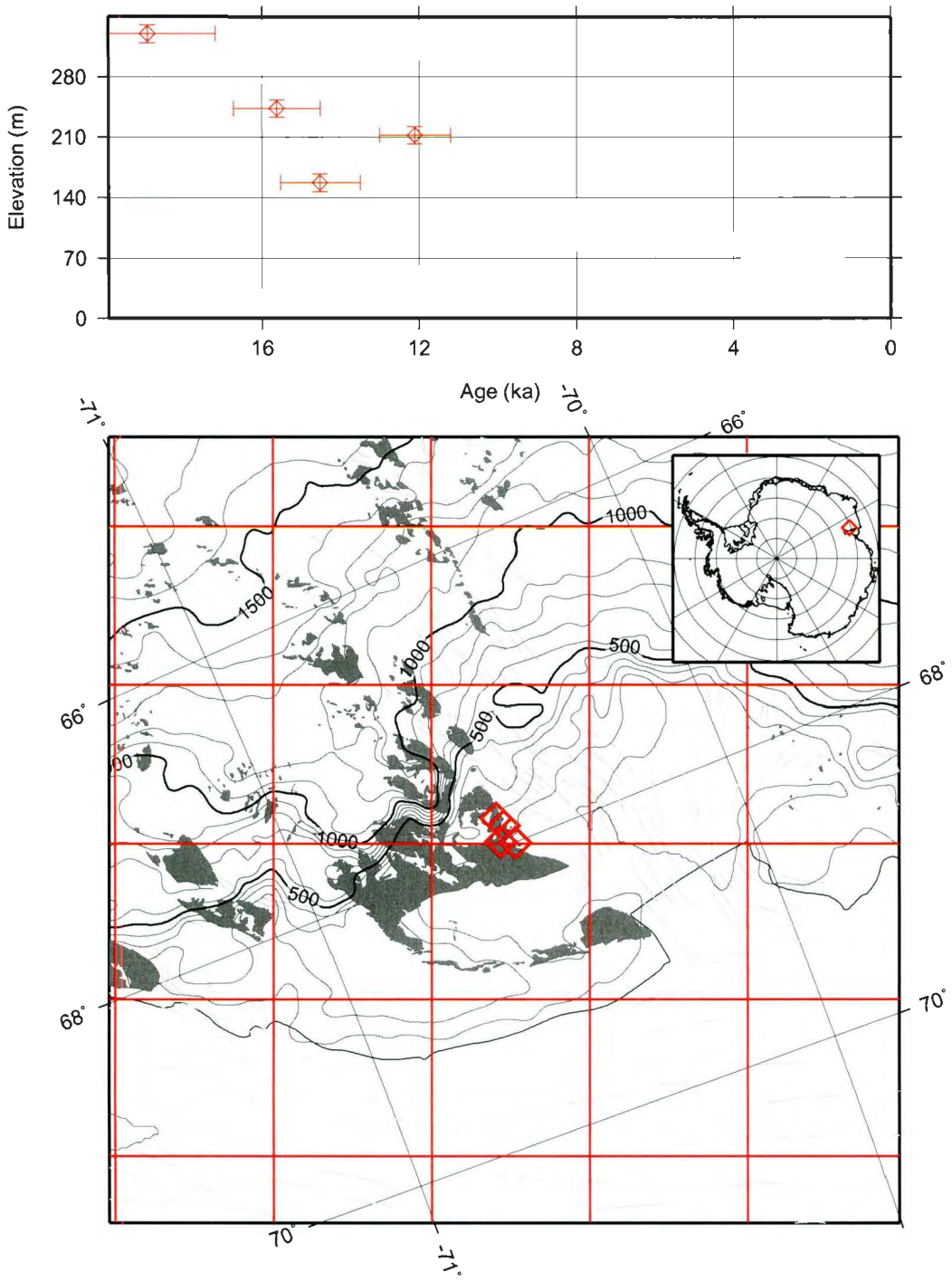


Figure B.17: PHS site:1207 Prince Charles Mts. 3 (PCM3)

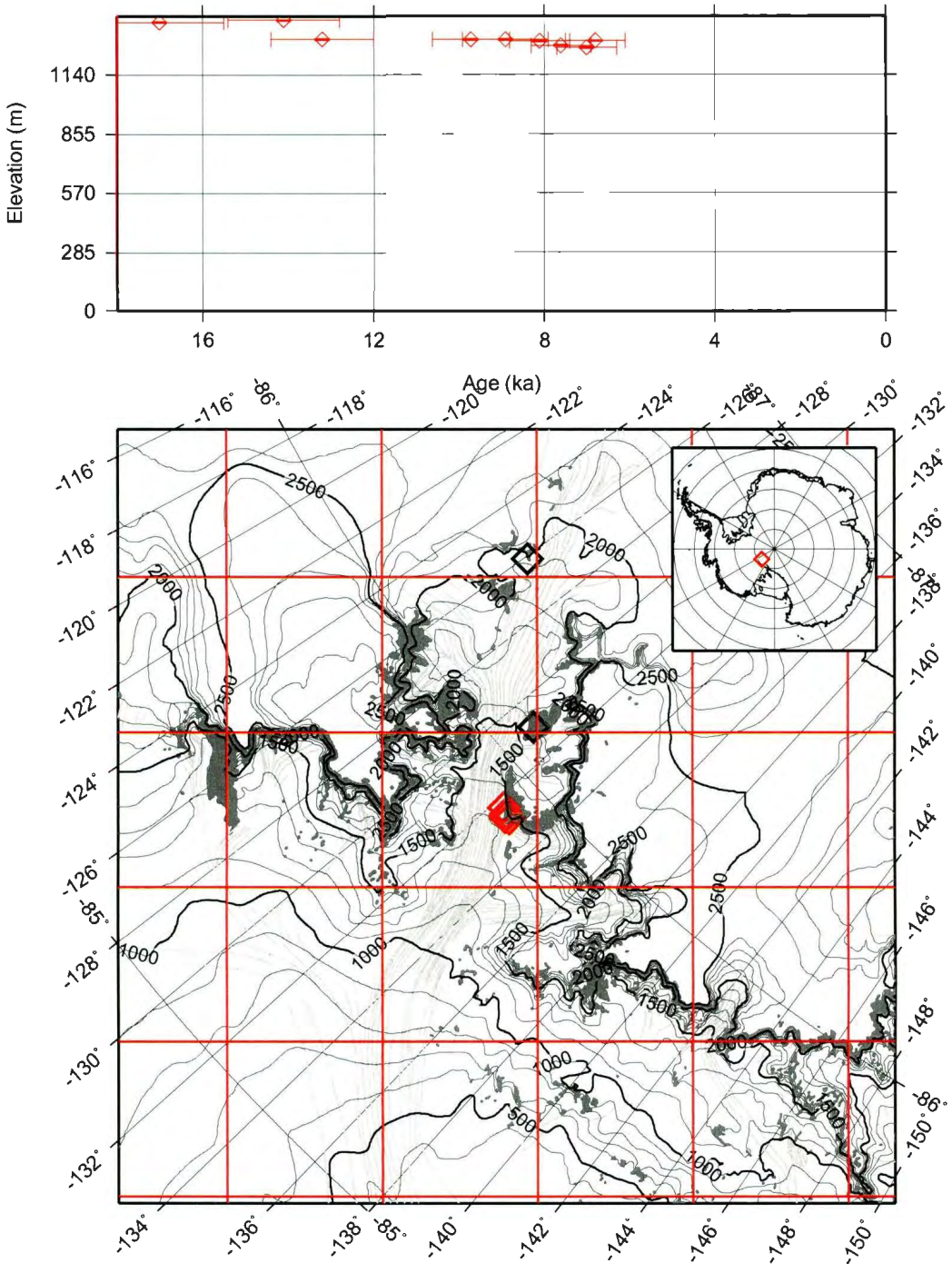


Figure B.18: PHS site:1401 Reedy Glacier 1 (RG1)

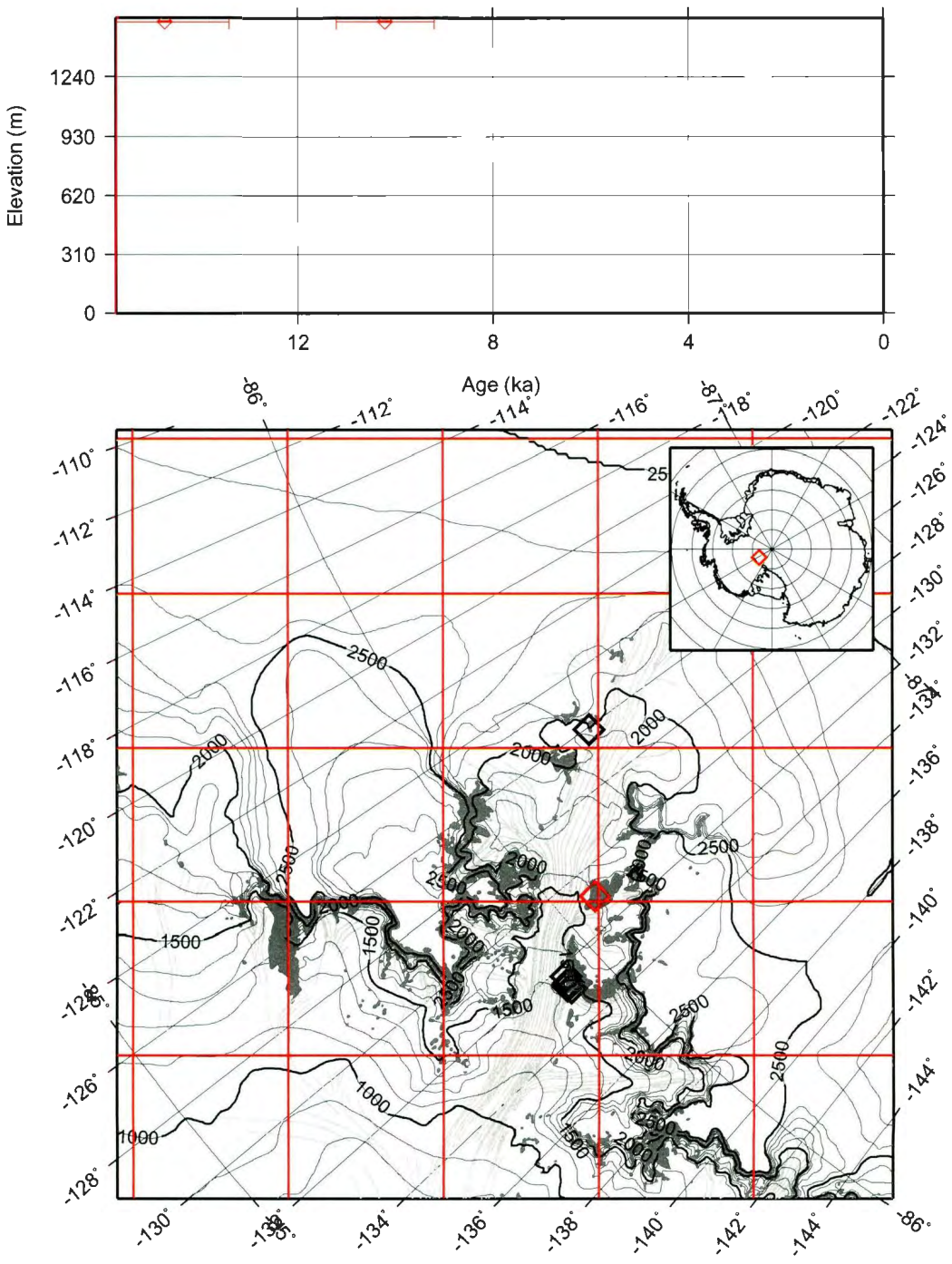


Figure B.19: PHS site:1402 Reedy Glacier 2 (RG2)

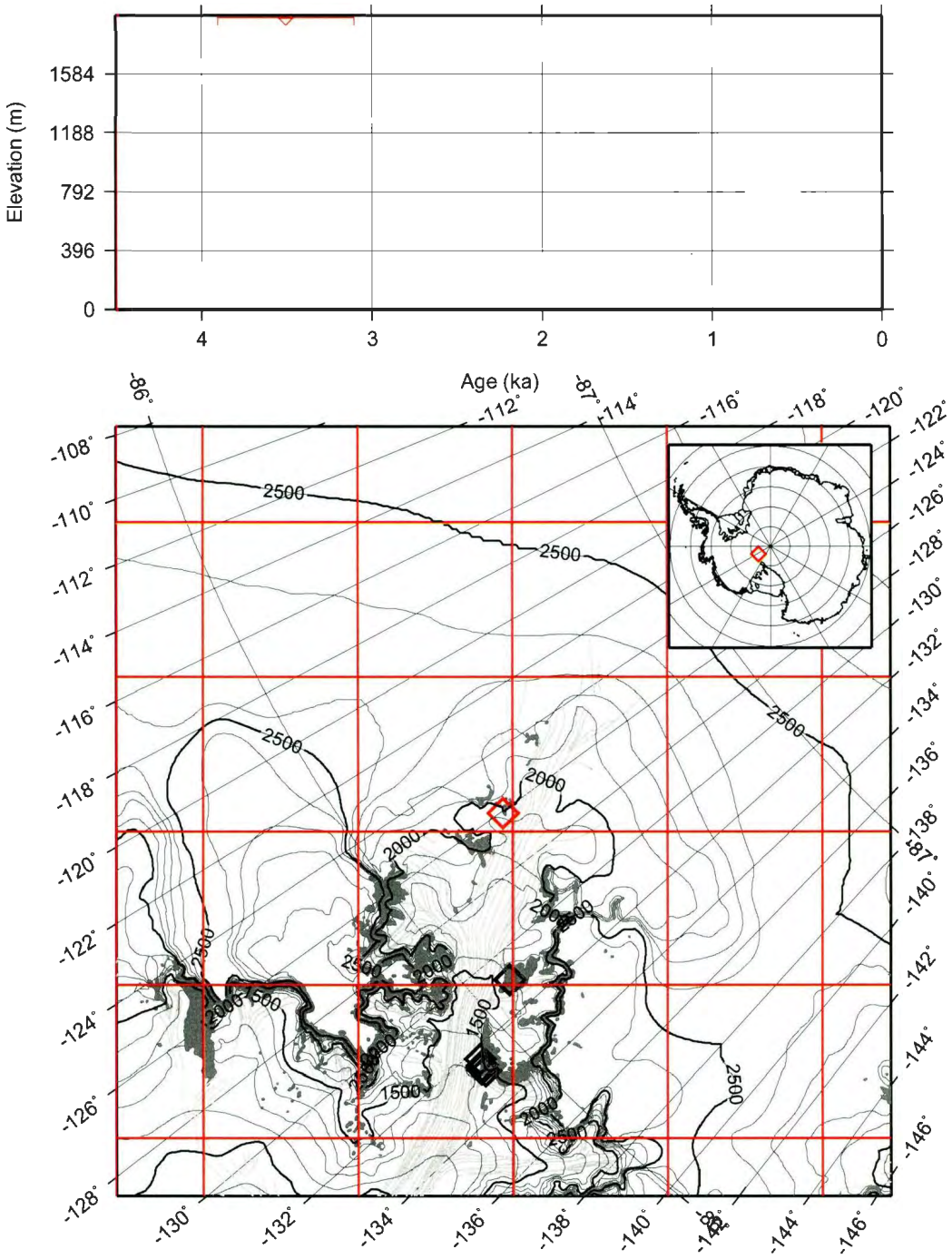


Figure B.20: PHS site:1403 Reedy Glacier 3 (RG3)

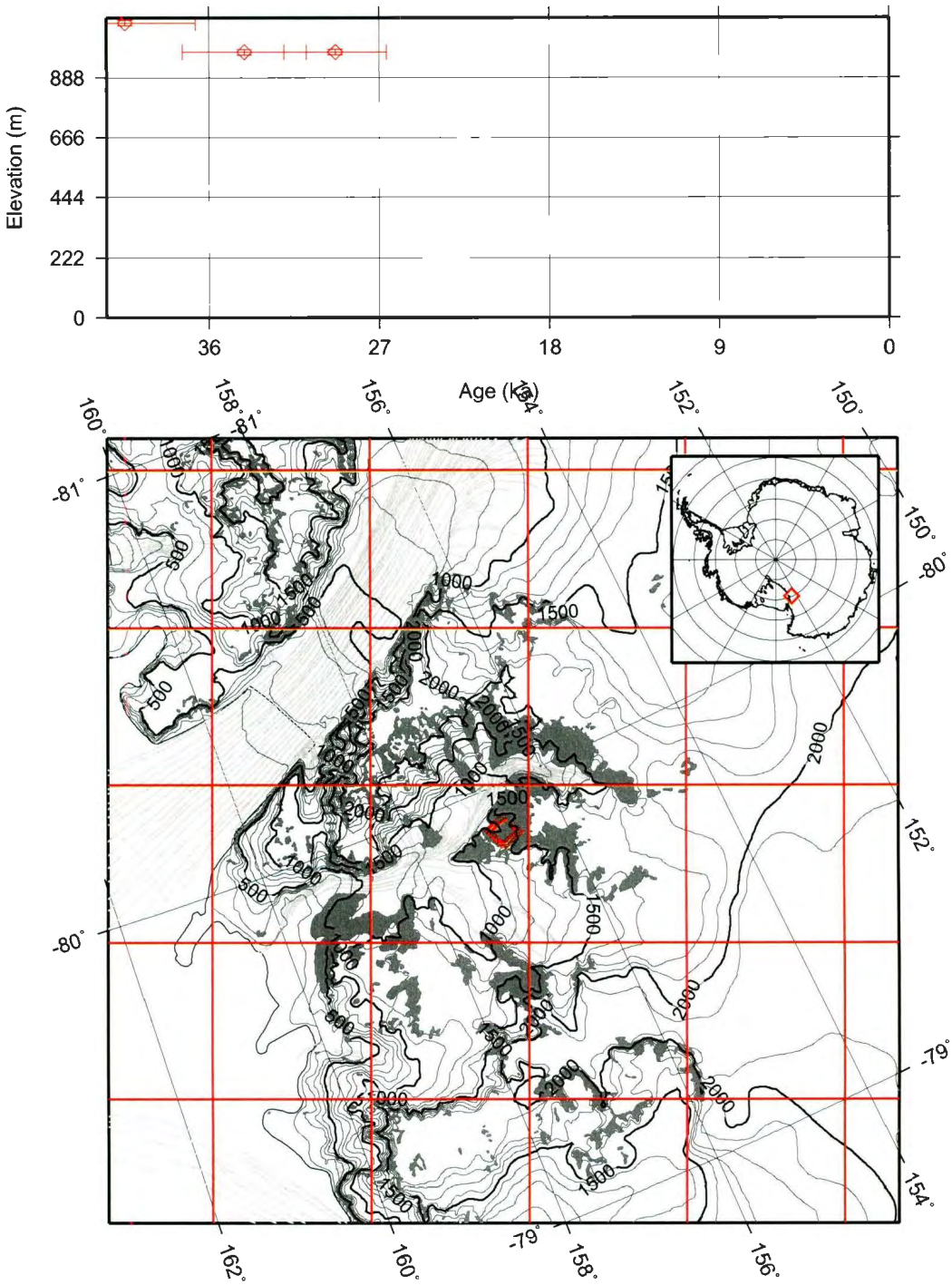


Figure B.21: PHS site:1404 Hatherton glacier (HG)

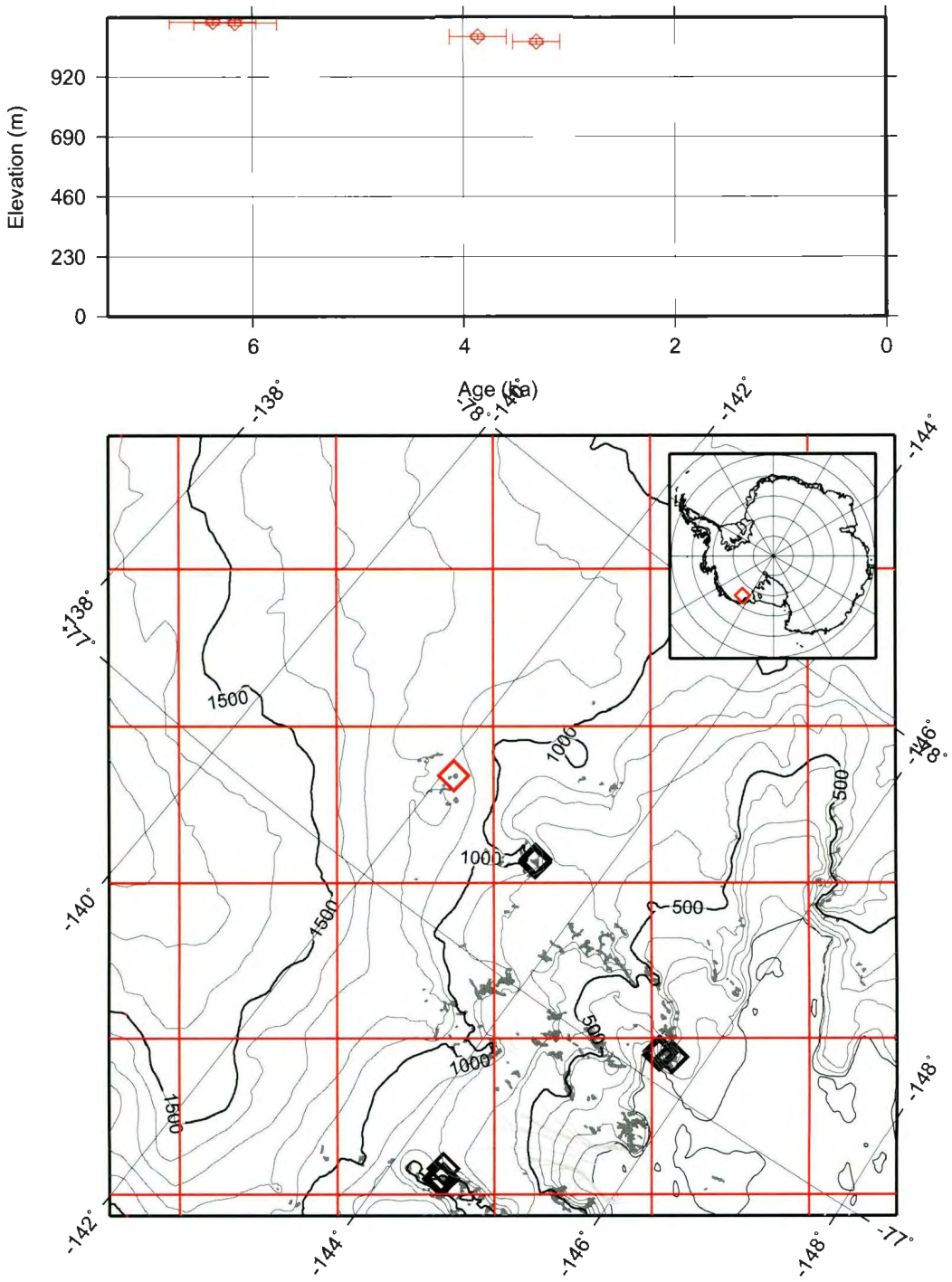


Figure B.22: PHS site:1405 Clark Mtn (CLM)

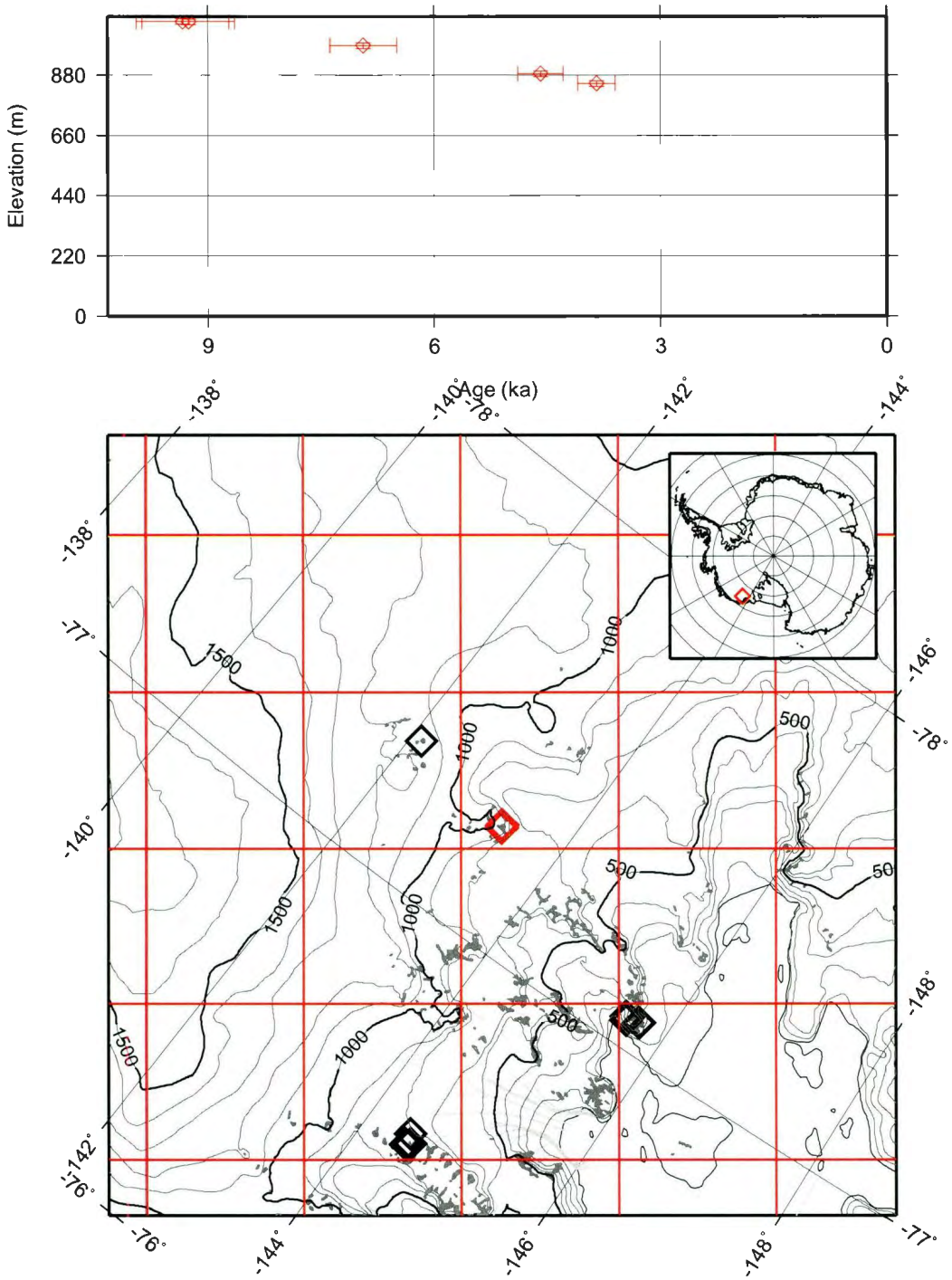


Figure B.23: PHS site:1406 Allegheny Mtn (ALM)

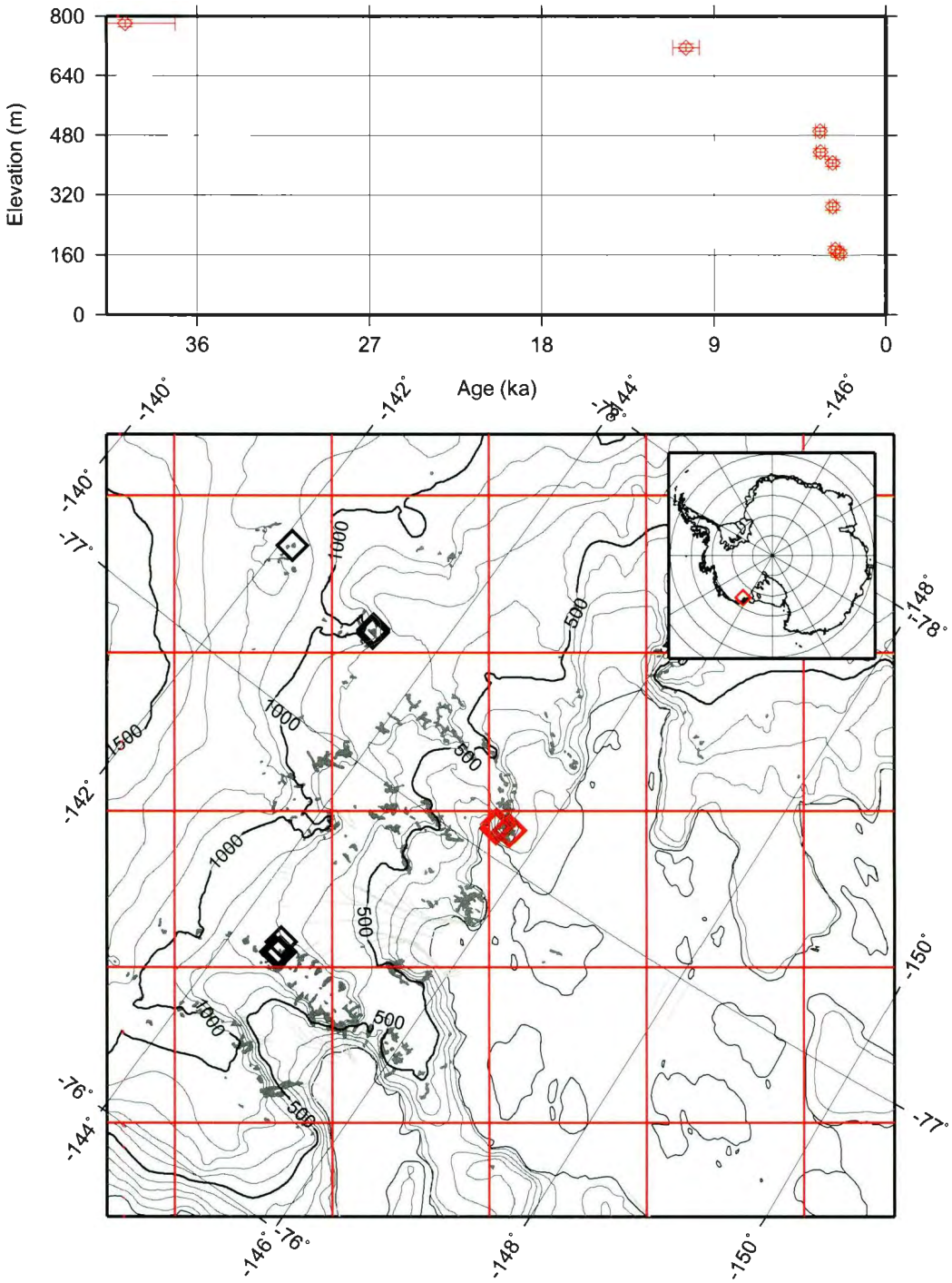


Figure B.24: PHS site:1407 Western Sarnoff Mts (WSM)

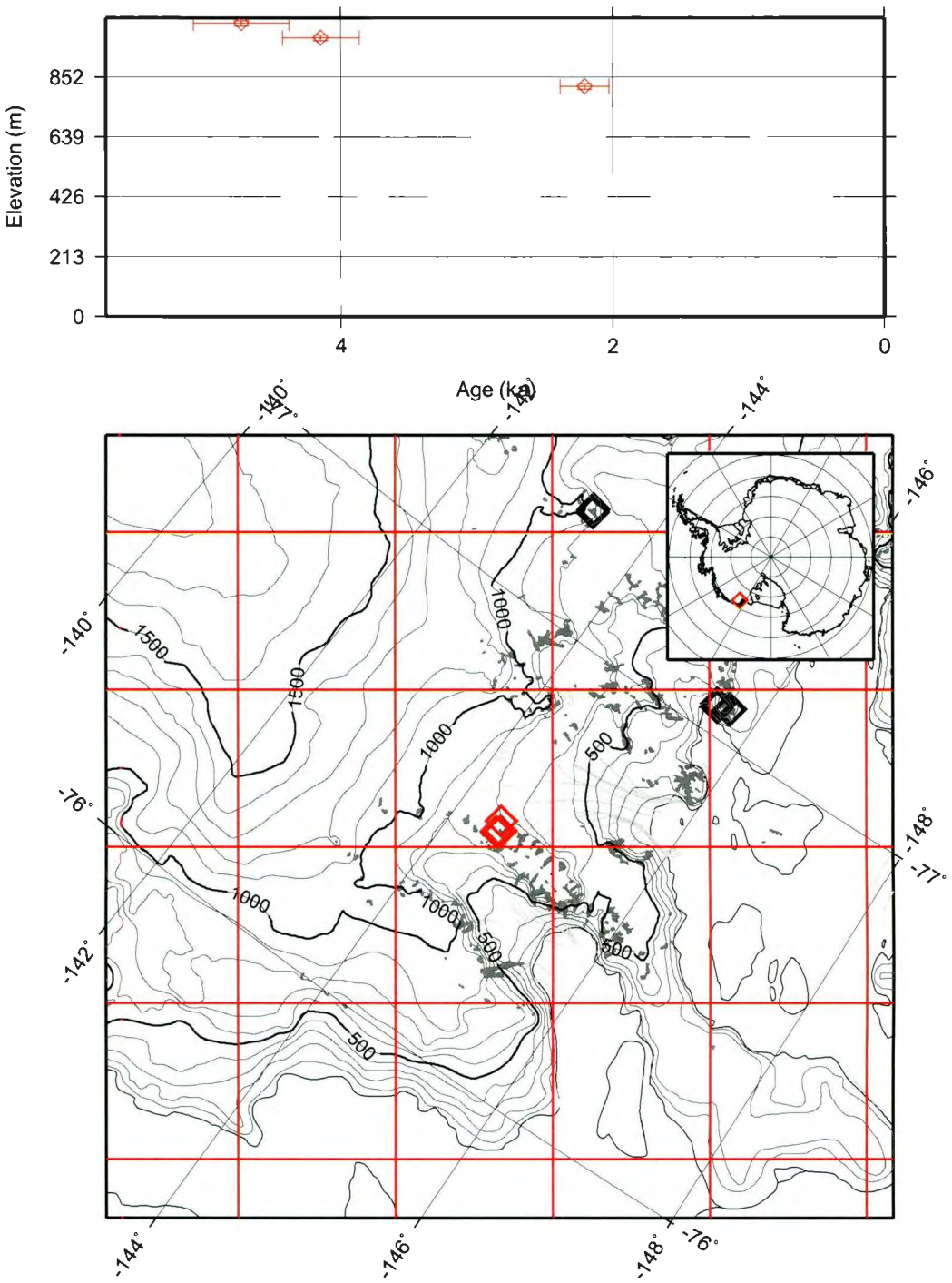


Figure B.25: PHS site:1408 Eastern Fosdick Mts (EFR)

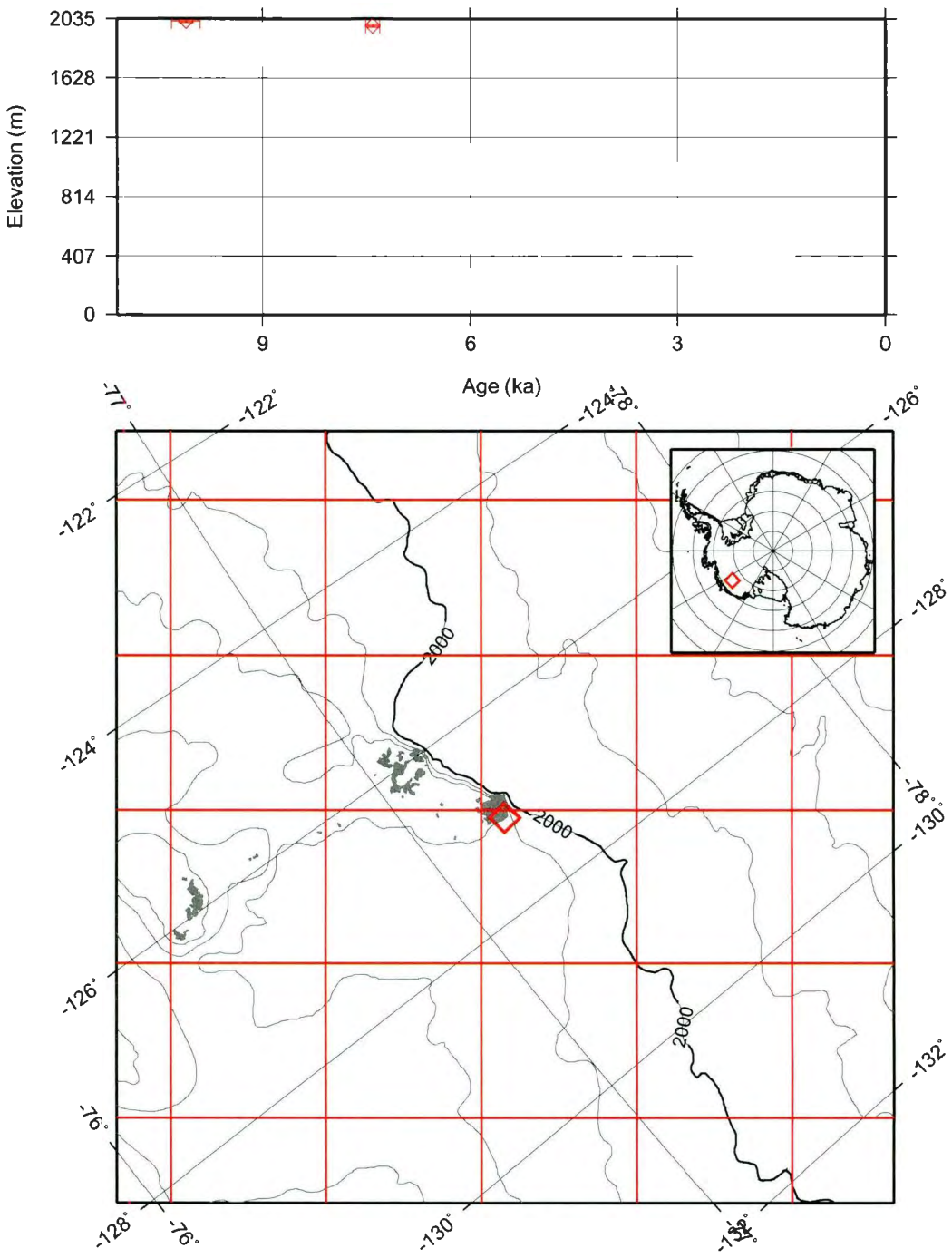


Figure B.26: PHS site:1501 Executive Committee Range (ECR)

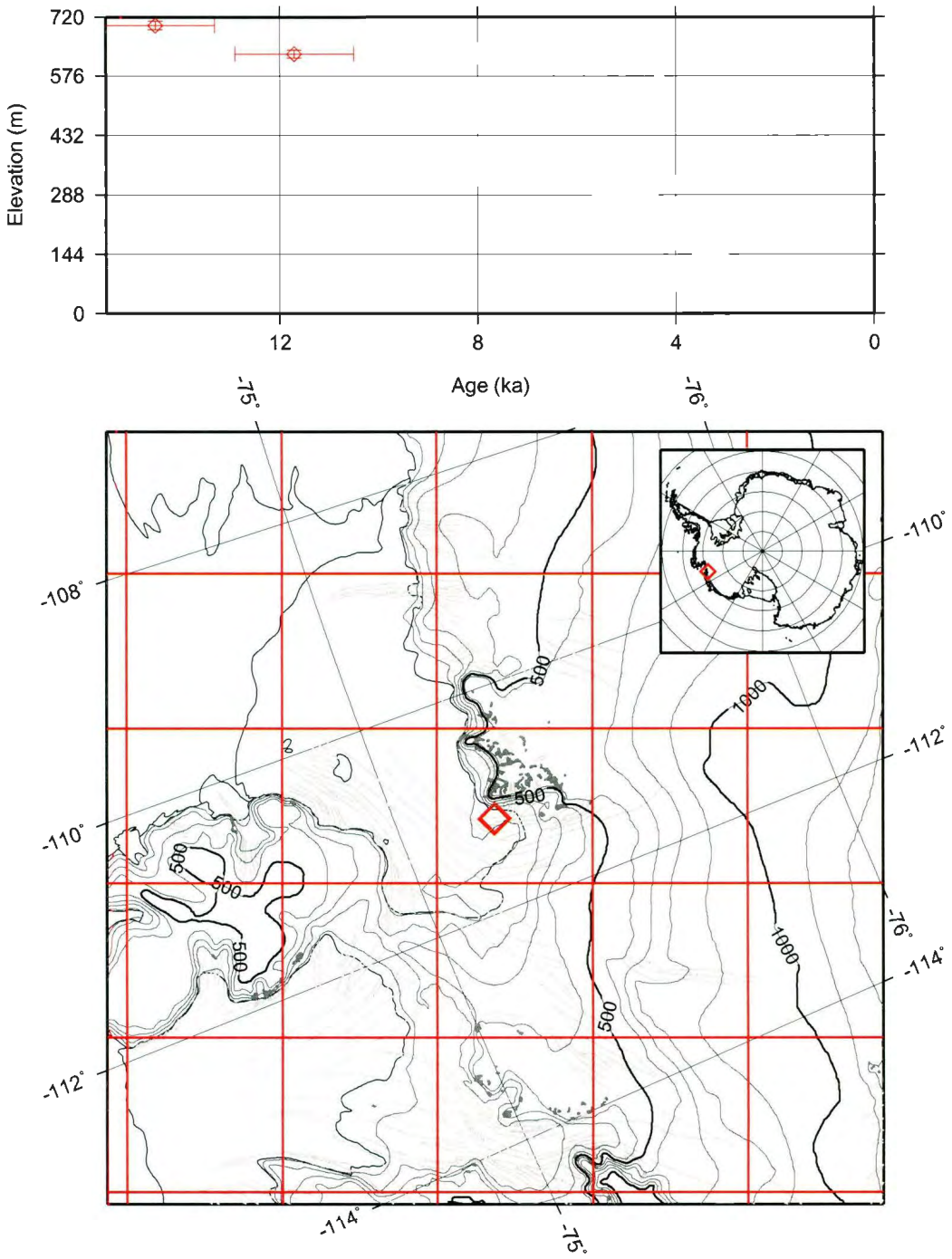


Figure B.27: PHS site:1502 Pine Island Bay 1 (PIB1)

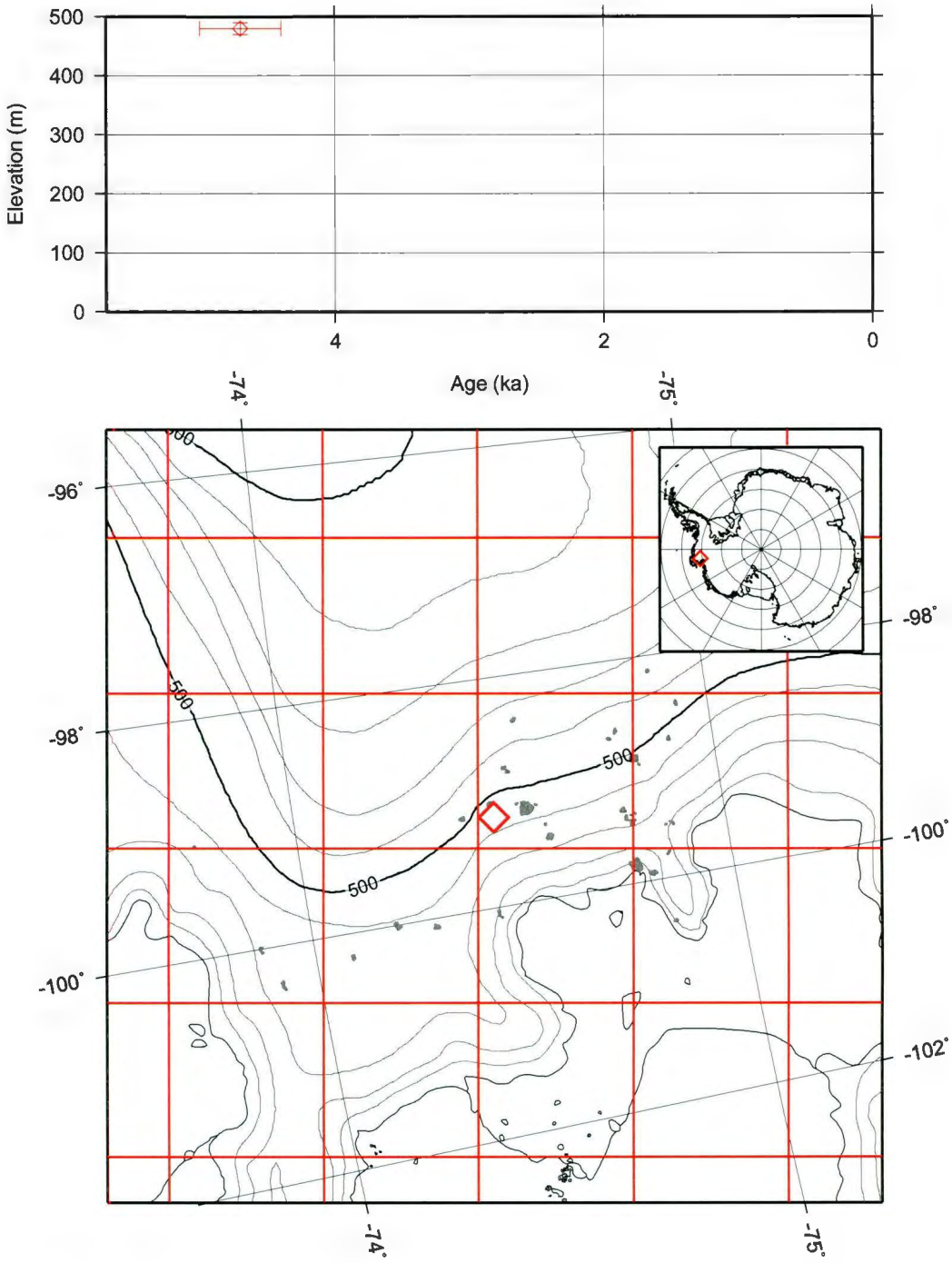


Figure B.28: PHS site:1503 Pine Island Bay 2 (PIB2)

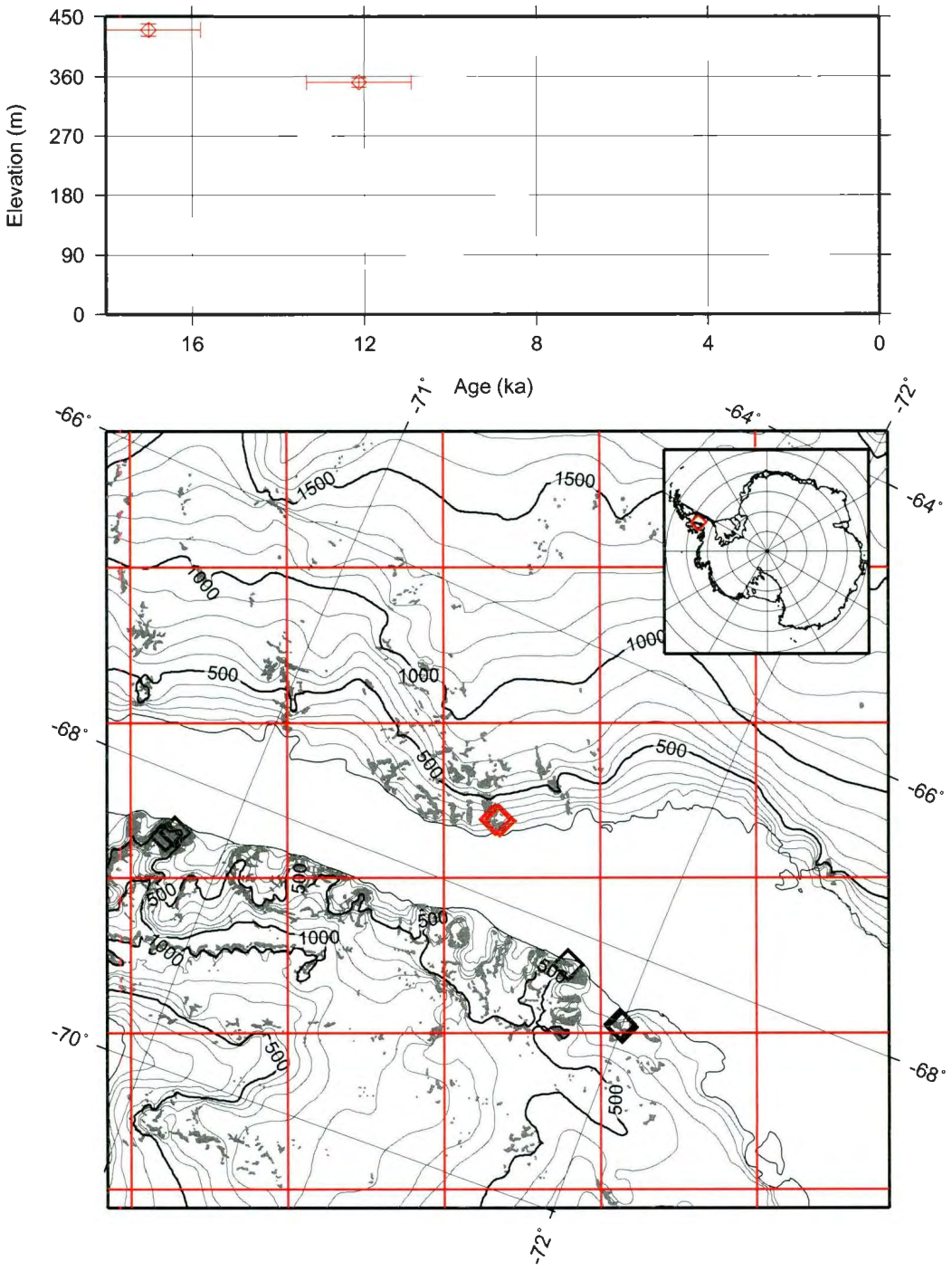


Figure B.29: PHS site:1601 West Palmer Land (WPL)

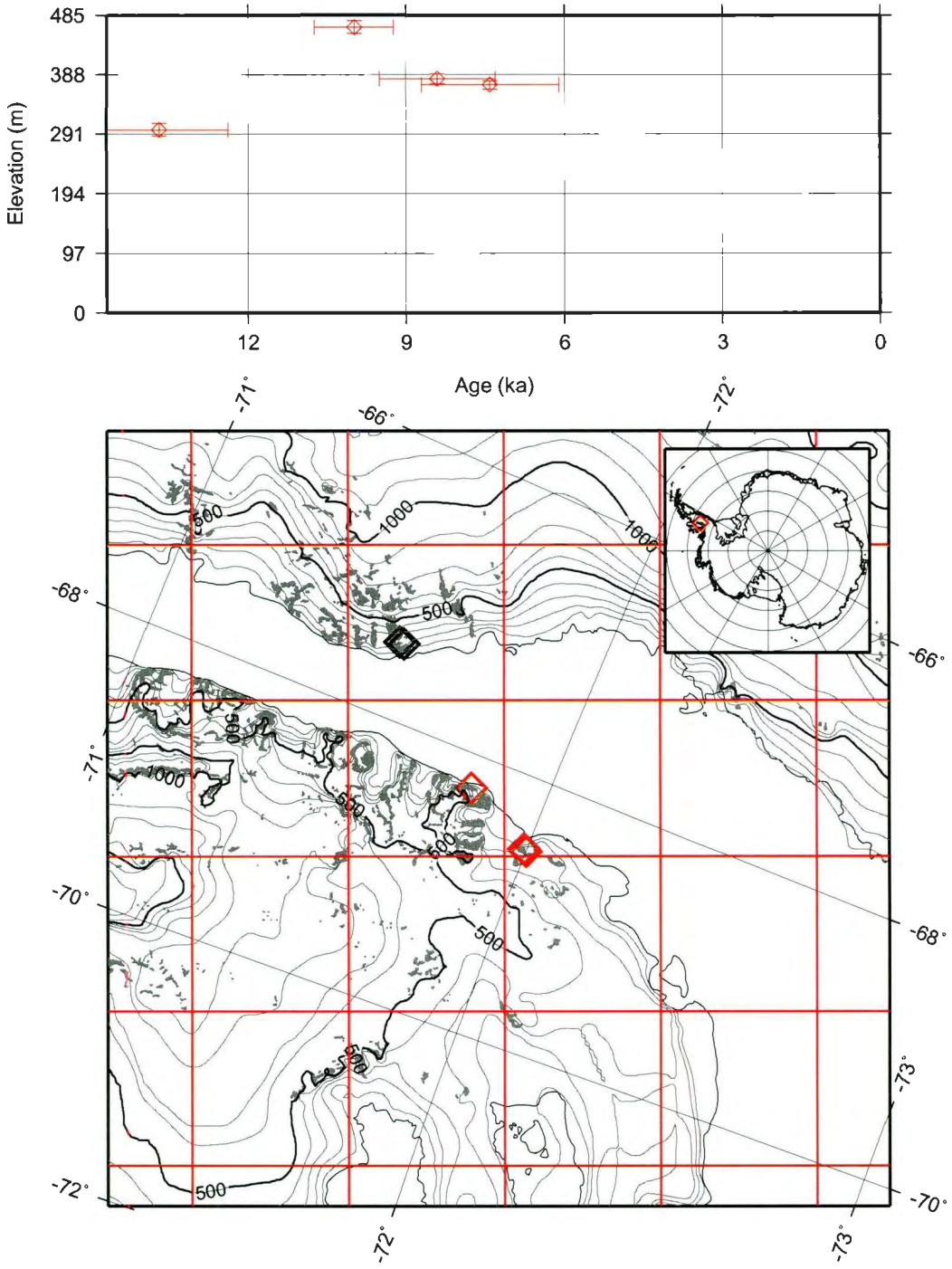


Figure B.30: PHS site:1602 Alexander Island South (AXS)

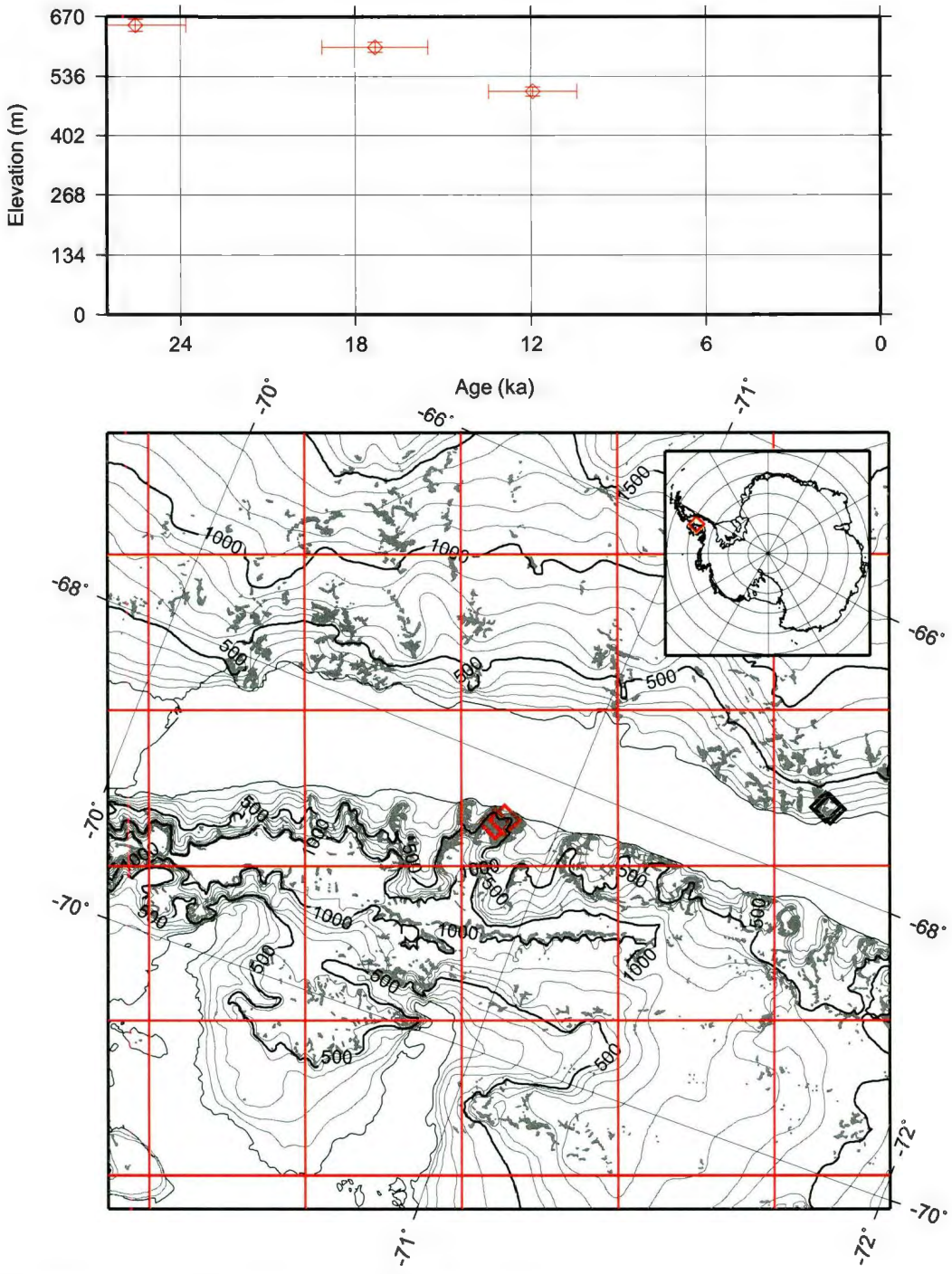


Figure B.31: PHS site:1603 Alexander Island North (AXN)

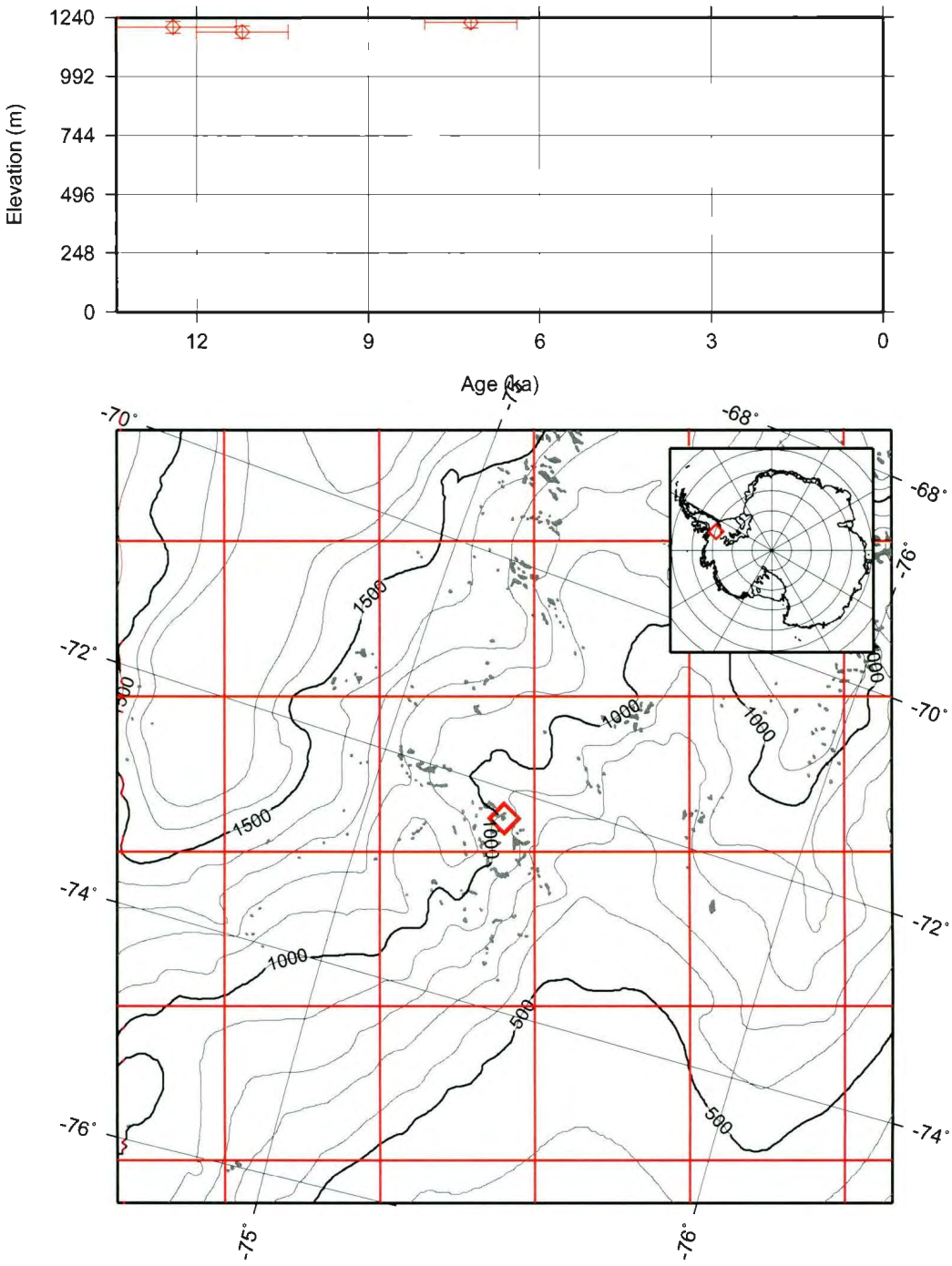


Figure B.32: PHS site:1701 Behrendt Mts (BM)

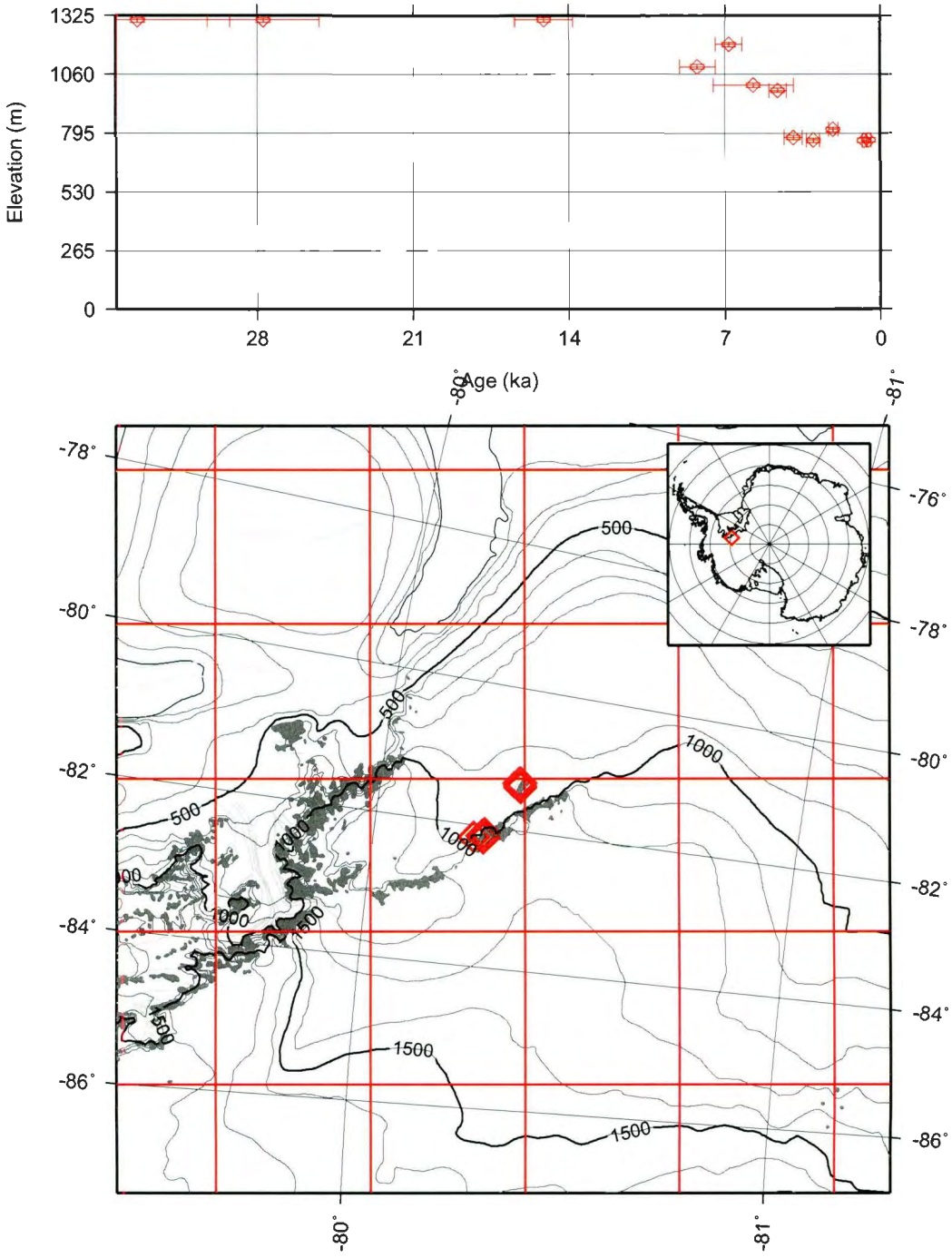


Figure B.33: PHS site:1702 Ellsworth Mts. (EM)

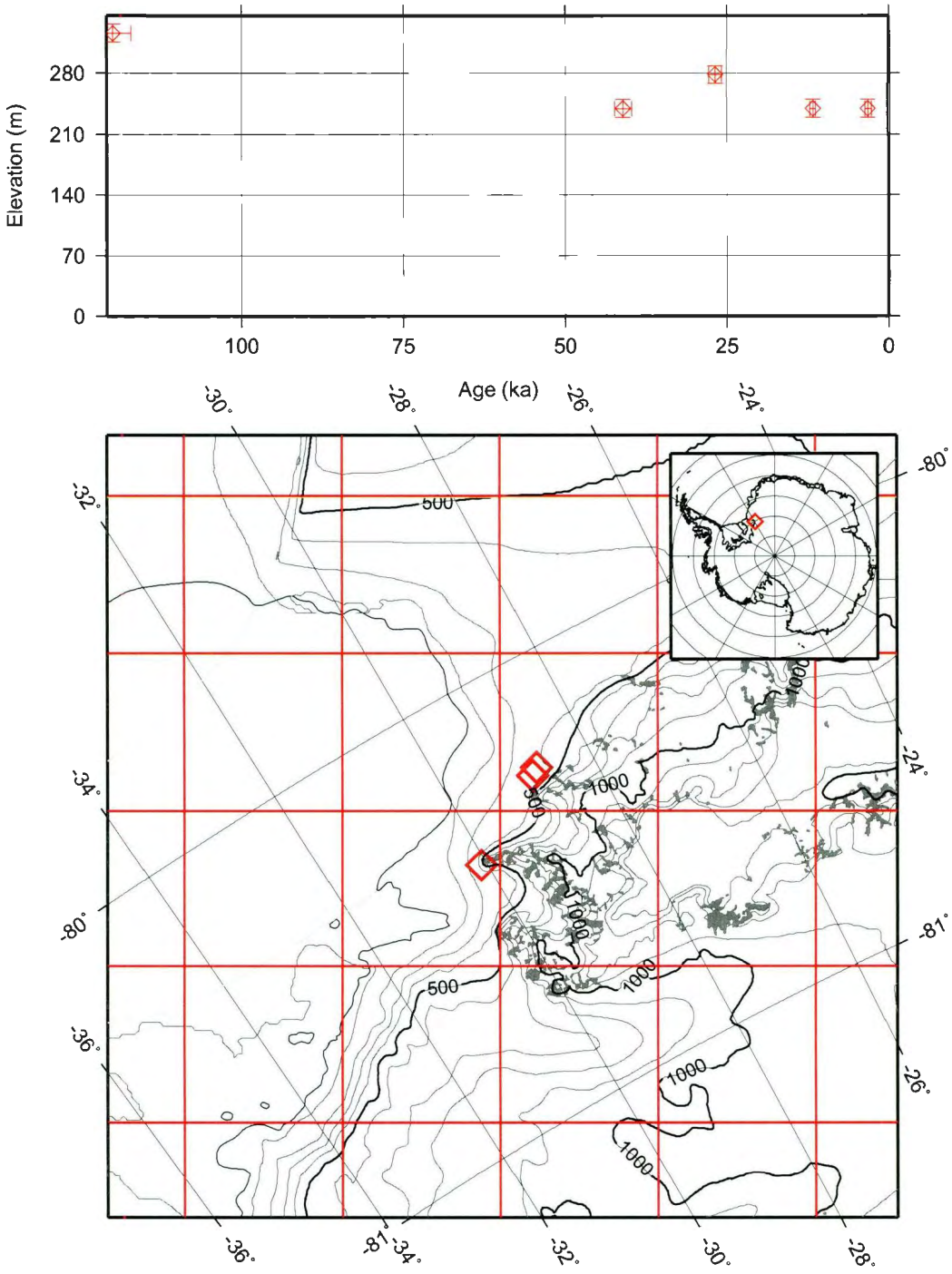


Figure B.34: PHS site:1703 Shackleton Range 1 (SR1)

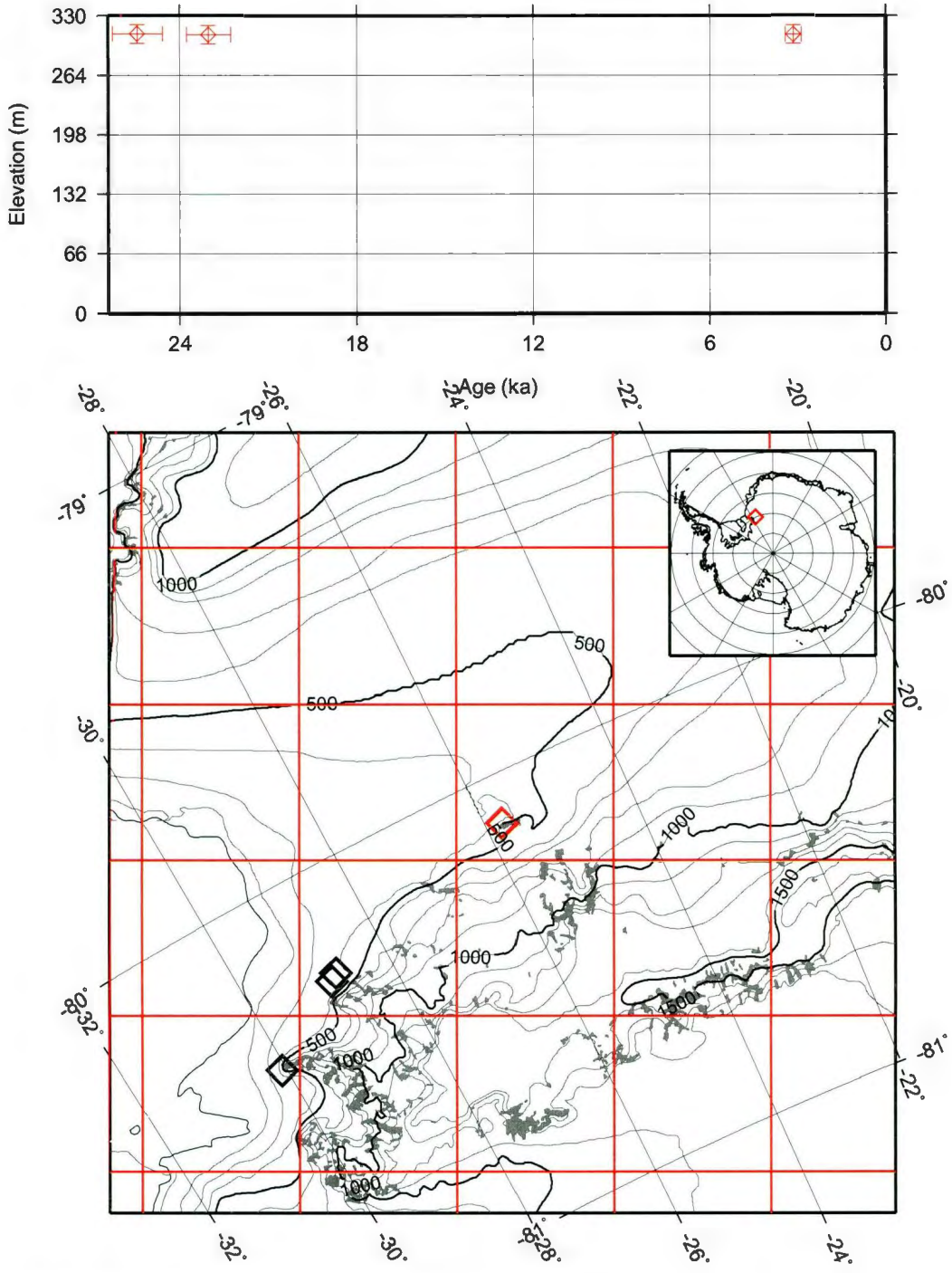


Figure B.35: PHS site:1704 Shackleton Range 2 (SR2)

## B.4 References

Ackert, R. P., Barclay, D. J., Borns, H. W., Calkin, P. E., Kurz, M. D., Fastook, J. L., Steig, E. J., 1999. Measurements of Past Ice Sheet Elevations in Interior West Antarctica. Science 286 (5438), 276 –280.

Baroni, C., Hall, B. L., 2004. A new Holocene relative sea-level curve for Terra Nova Bay, Victoria Land, Antarctica. Journal of Quaternary Science 19, 377–396.

Bassett, S. E., Milne, G. A., Bentley, M. J., Huybrechts, P., 2007. Modelling Antarctic sea-level data to explore the possibility of a dominant Antarctic contribution to meltwater pulse IA. Quaternary Science Reviews 26, 2113–2127.

Bentley, M., Fogwill, C. J., Kubik, P. W., Sugden, D. E., 2006. Geomorphological evidence and cosmogenic 10Be/26Al exposure ages for the Last Glacial Maximum and deglaciation of the Antarctic Peninsula Ice Sheet. Geological Society of America Bulletin 118 (9-10), 1149–1159.

Bentley, M. J., 2005. Relative sea level curves for the South Shetland Islands and Marguerite Bay, Antarctic Peninsula. Quaternary Science Reviews 24, 1203–1216.

Bentley, M. J., Fogwill, C. J., Le Brocq, A. M., Hubbard, A. L., Sugden, D. E., Dunai, T. J., Freeman, S. P. H. T., 2010. Deglacial history of the West Antarctic Ice Sheet in the Weddell Sea embayment: Constraints on past ice volume change. Geology 38 (5), 411–414.

Berkman, P. A., Forman, S. L., 1996. Pre-bomb radiocarbon and the reservoir correction for calcareous marine species in the Southern Ocean. Geophysical Research Letters 23 (4), 363.

Goodwin, I., 1993. Holocene Deglaciation, Sea-Level Change, and the Emergence of the Windmill Islands, Budd Coast, Antarctica. Quaternary Research 40 (1), 55–69.

Goodwin, I., 2000. Glacio-isostasy and Glacial Ice Load at Law Dome, Wilkes Land, East Antarctica. Quaternary Research 53 (5), 285–293.

Hall, B., 2004. Holocene relative sea-level history of the Southern Victoria Land Coast, Antarctica. Global and Planetary Change 42 (1-4), 241–263.

Hein, A. S., Fogwill, C. J., Sugden, D. E., Xu, S., 2011. Glacial/interglacial ice-stream stability in the Weddell Sea embayment, Antarctica. Earth and Planetary Science Letters 307, 211–221.

Hodgson, D. A., Verleyen, E., Vyverman, W., Sabbe, K., Leng, M. J., Pickering, M. D., Keely, B. J., 2009. A geological constraint on relative sea level in Marine Isotope Stage 3 in the Larsemann Hills, Lambert Glacier region, East Antarctica (31,366–33,228 cal yr BP). Quaternary Science Reviews 28 (25-26), 2689–2696.

Johnson, J. S., Bentley, M. J., Gohl, K., 2008. First exposure ages from the Amundsen Sea Embayment, West Antarctica: The Late Quaternary context for recent thinning of Pine Island, Smith, and Pope Glaciers. Geology 36 (3), 223–226.

Kluiving, S., van der Wateren, D., 2001. Antarctica Glaciological Geological Database (AGGD). , Online; accessed 08-Feb-2012.

Lilly, K., Fink, D., Fabel, D., Lambeck, K., 2010. Pleistocene dynamics of the interior East Antarctic ice sheet. Geology 38 (8), 703–706.

Liu, H., Jezek, K., Li, B., Zhao, Z., 2001. Radarsat antarctic mapping project digital elevation model version 2. Digital media., Boulder, CO: National Snow and Ice Data Center.

Mackintosh, A., 2007. Exposure ages from mountain dipsticks in Mac. Robertson Land, East Antarctica, indicate little change in ice-sheet thickness since the Last Glacial Maximum. Geology 6 (35), 551.

Miura, H., Maemoku, H., Seto, K., Morikawa, K., 1998. Late Quaternary East Antarctic melting event in the Soya Coast region based on stratigraphy and oxygen isotopic ratio of fossil molluscs. Polar Geoscience 11, 260–274.

SCAR, 2006. Antarctic Digital Database, Scientific Committee on Antarctic Research (SCAR), Version 3.0. , Online; accessed Sep. 2011.

Stone, J. O., Balco, G. A., Sugden, D. E., Caffee, M. W., Sass, L. C., Cowdery, S. G., Siddoway, C., 2003. Holocene deglaciation of Marie Byrd Land, West Antarctica. Science 299 (5603), 99–102.

Storey, B., Fink, D., Hood, D., Joy, K., Shulmeister, J., Riger-Kusk, M., Stevens, M., 2010. Cosmogenic nuclide exposure age constraints on the glacial history of the Lake Wellman area, Darwin Mountains, Antarctica. Antarctic Science 22 (06), 603–618.

Stuiver, M., Braziunas, T., 1985. Complication of isotopic dates from Antarctica. Radiocarbon 27, 117–304.

Takada, M., 2003. ESR dating of fossil shells in the Lützow-Holm Bay region, East Antarctica. Quaternary Science Reviews 22 (10-13), 1323–1328.

Todd, C., Stone, J., Conway, H., Hall, B., Bromley, G., 2010. Late Quaternary evolution of Reedy Glacier, Antarctica. Quaternary Science Reviews 29 (11-12), 1328.

Verleyen, E., 2005. Relative sea-level history from the Lambert Glacier region, East Antarctica, and its relation to deglaciation and Holocene glacier readvance. Quaternary Research 63 (1), 45.

White, D. A., Fink, D., Gore, D. B., 2011. Cosmogenic nuclide evidence for enhanced sensitivity of an East Antarctic ice stream to change during the last deglaciation. Geology 39 (1), 23–26.

Yamane, M., Yokoyama, Y., Miura, H., Maemoku, H., Iwasaki, S., Matsuzaki, H., 2011. The last deglacial history of Lützow-Holm Bay, East Antarctica. Journal of Quaternary Science 26, 3–6.

Zhang, Q., Peterson, J. A., 1984. A geomorphology and Late Quaternary geology of the Vestfold Hills, Antarctica. Australian National Antarctic Research Expeditions Reports 133, 84.

Zwartz, D., 1998. Holocene sea-level change and ice-sheet history in the Vestfold Hills, East Antarctica. Earth and Planetary Science Letters 155 (1-2), 131.

# Appendix C

# A data-constrained large-ensemble analysis of Antarctica over the last glacial cycle

# C.1 Appendix: Parameter distribution

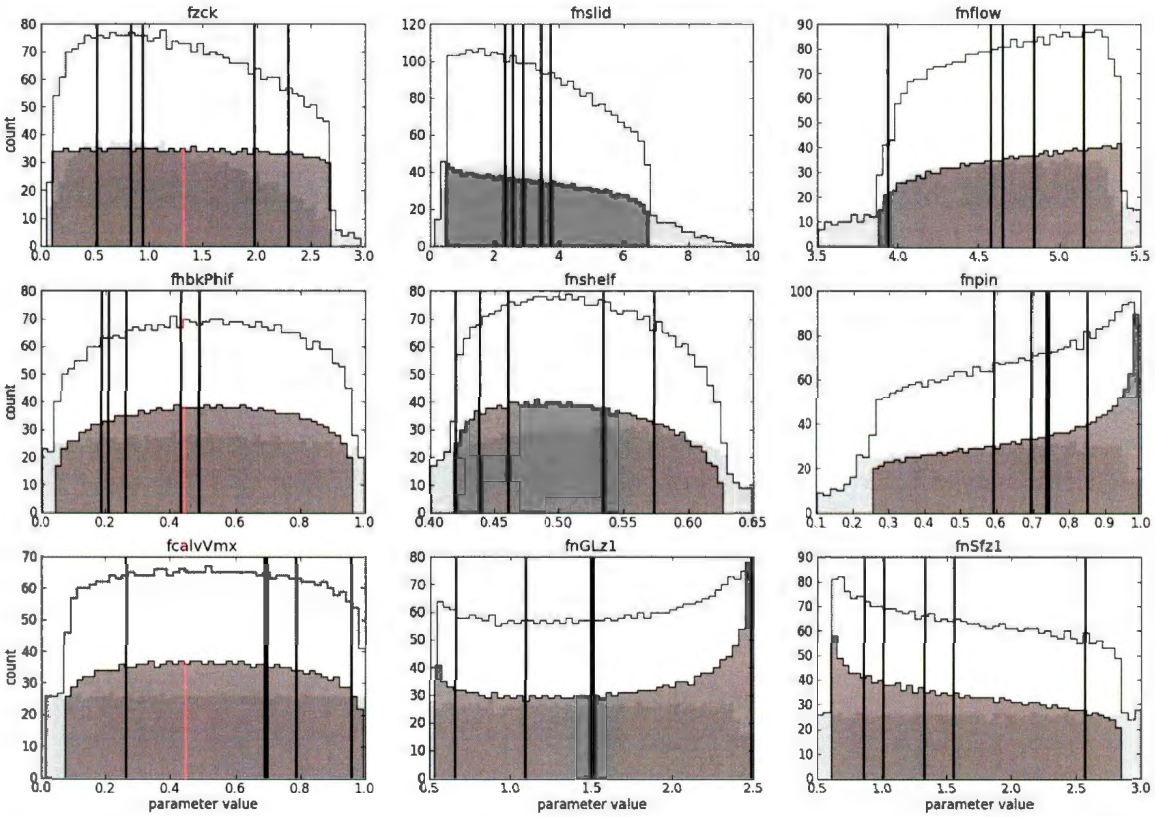


Figure C.1: Parameter distributions I. Histograms bin size=50. Light grey is the wide ensemble set, dark grey is the narrow set. The cumulative total is the stepped black line. Vertical black lines represent the value of the paramter for the best four runs as scored by PDcPbSEb and run 3506. For a complete explanation of the paramters refer to Briggs et al. (2013).

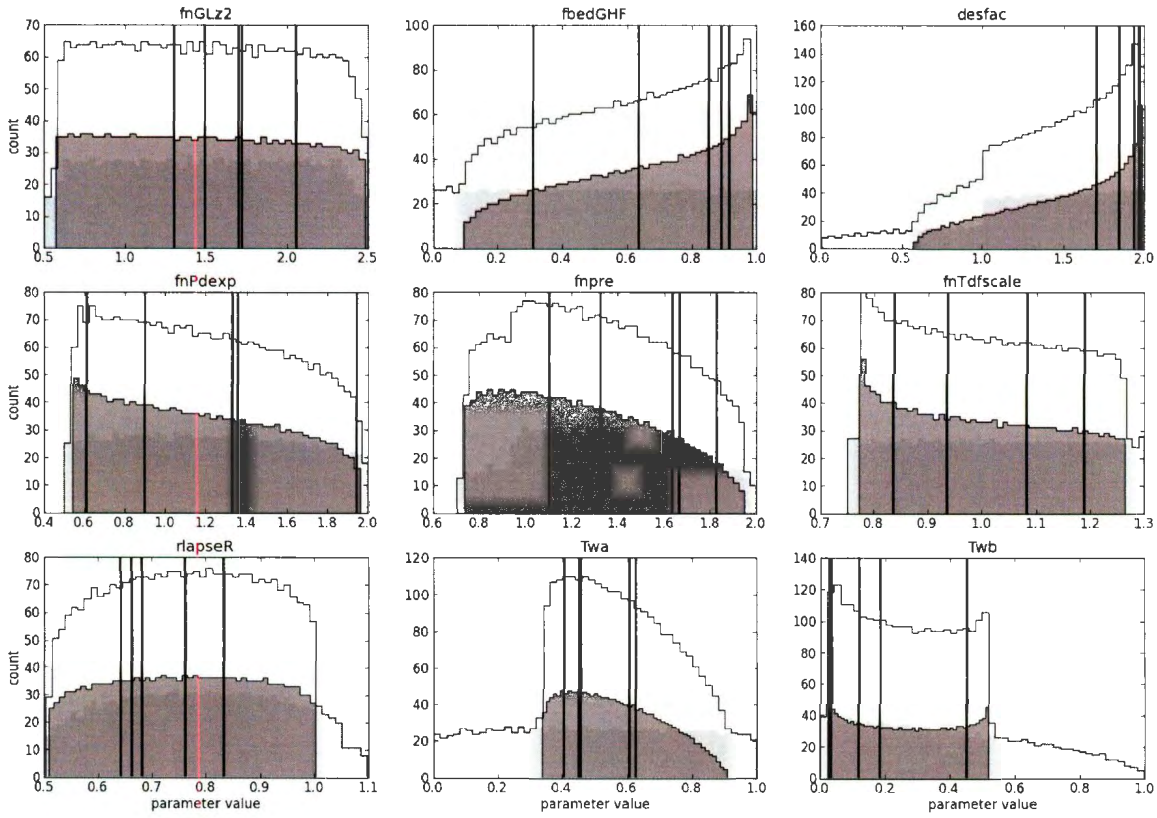


Figure C.2: Parameter distributions II (see Fig. C.1 caption for notes).

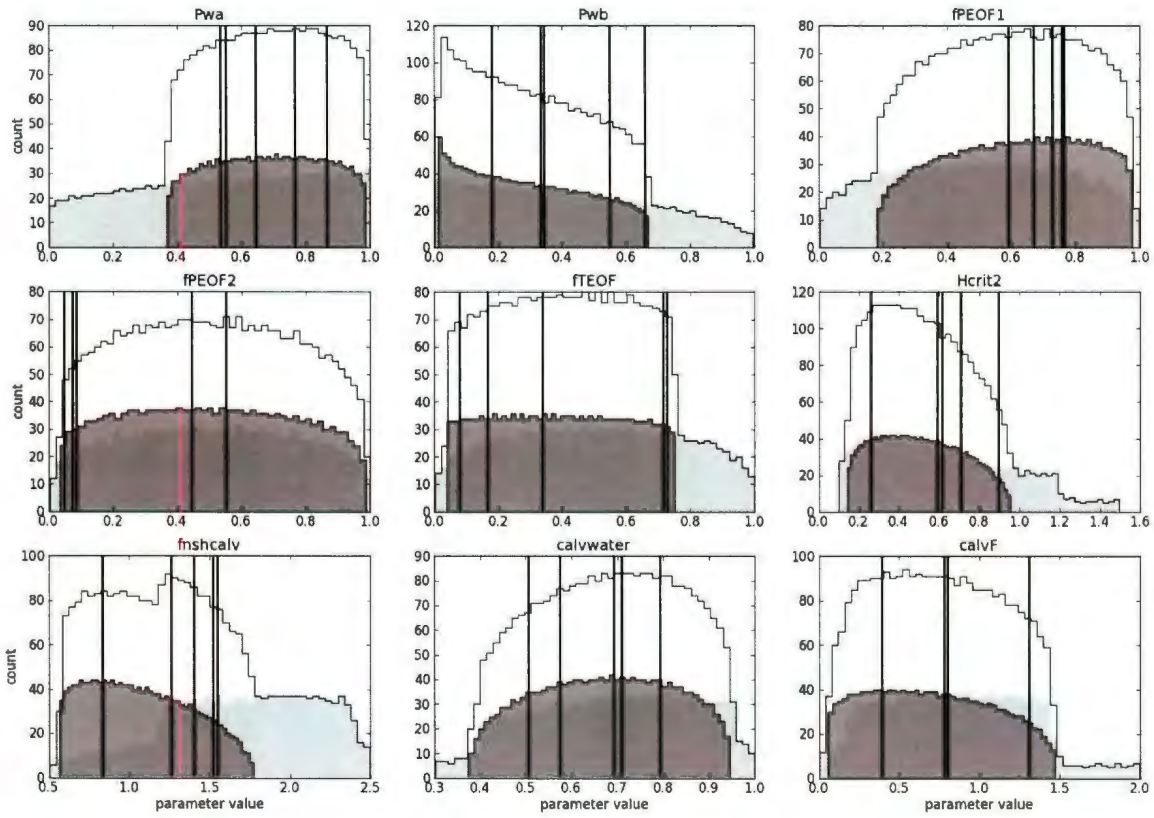


Figure C.3: Parameter distributions III (see Fig. C.1 caption for notes).

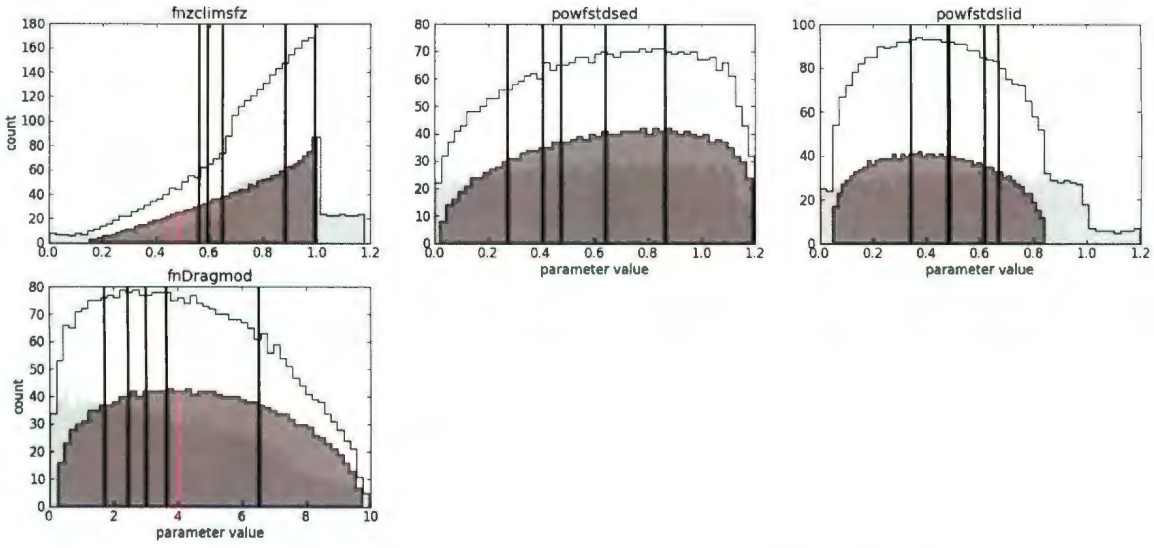


Figure C.4: Parameter distributions IV (see Fig. C.1 caption for notes).

## C.2 Appendix: Exploration of $\sigma_f$ for generation of weighted average - Probability Distribution

Table B.1: Range of $\sigma_f$ values (only results until $\sigma_f$ =0.25 are tabulated) and the resultant probabilities and volg metrics for scoring scheme PDcPaSea and PDcPaSeb. Bold font indicates the sigma values that are used in Fig. 4.2 and discussed in Section 4.3.3.

(a) PDcPaSea (total number of scored runs=1868)

| $\sigma_f$ | $P_{max}$ | $P_{90}$ | volg20k | err | volg0k | err |
|---|---|---|---|---|---|---|
| 0.06 | 0.973 | 1 | 74.5 | 0.8 | 64.2 | 0.3 |
| 0.07 | 0.869 | 3 | 74.0 | 1.9 | 64.1 | 0.7 |
| target 1:$P_{90} > 10$ runs | | | | | | |
| 0.08 | 0.664 | 15 | 73.0 | 2.7 | 63.7 | 1.1 |
| target 2:$P_{max} < 0.5 \times P_{tot}$ | | | | | | |
| **0.09** | 0.439 | 37 | 71.9 | 3.1 | 63.3 | 1.3 |
| 0.10 | 0.271 | 69 | 71.0 | 3.2 | 62.9 | 1.3 |
| 0.11 | 0.167 | 106 | 70.5 | 3.2 | 62.6 | 1.3 |
| 0.12 | 0.106 | 144 | 70.2 | 3.1 | 62.4 | 1.3 |
| 0.13 | 0.071 | 188 | 70.0 | 3.1 | 62.3 | 1.3 |
| 0.14 | 0.049 | 235 | 69.9 | 3.1 | 62.2 | 1.3 |
| 0.15 | 0.035 | 281 | 69.8 | 3.1 | 62.2 | 1.3 |
| 0.16 | 0.026 | 324 | 69.7 | 3.1 | 62.1 | 1.3 |
| 0.17 | 0.020 | 365 | 69.7 | 3.1 | 62.1 | 1.4 |
| 0.18 | 0.016 | 406 | 69.7 | 3.2 | 62.0 | 1.4 |
| 0.19 | 0.013 | 446 | 69.7 | 3.2 | 62.0 | 1.4 |
| 0.20 | 0.011 | 481 | 69.7 | 3.2 | 62.0 | 1.5 |
| 0.21 | 0.009 | 514 | 69.7 | 3.3 | 62.0 | 1.5 |
| 0.22 | 0.008 | 545 | 69.7 | 3.3 | 61.9 | 1.5 |
| 0.23 | 0.007 | 573 | 69.7 | 3.4 | 61.9 | 1.6 |
| 0.24 | 0.006 | 600 | 69.7 | 3.4 | 61.9 | 1.6 |
| 0.25 | 0.005 | 625 | 69.7 | 3.4 | 61.9 | 1.6 |

(b) PDcPaSeb (total number of scored runs=214)

| $\sigma_f$ | $P_{max}$ | $P_{90}$ | volg20k | err | volg0k | err |
|---|---|---|---|---|---|---|
| 0.06 | 0.945 | 1 | 71.7 | 0.8 | 64.1 | 0.3 |
| 0.07 | 0.868 | 2 | 71.8 | 1.3 | 64.0 | 0.5 |
| 0.08 | 0.760 | 2 | 71.9 | 1.9 | 63.9 | 0.7 |
| 0.09 | 0.634 | 4 | 71.9 | 2.4 | 63.7 | 0.8 |
| **0.10** | 0.509 | 9 | 71.9 | 3.0 | 63.5 | 1.0 |
| target 1:$P_{max} < 0.5 \times P_{tot}$ 0.509 is | | | | | | |
| acceptable as next highest $\sigma_f$ gives 0.4 | | | | | | |
| target 2:$P_{90} > 10$ runs ( acceptable) | | | | | | |
| 0.11 | 0.400 | 12 | 71.7 | 3.4 | 63.4 | 1.1 |
| 0.12 | 0.312 | 16 | 71.6 | 3.7 | 63.3 | 1.2 |
| 0.13 | 0.245 | 22 | 71.4 | 3.8 | 63.2 | 1.3 |
| 0.14 | 0.194 | 27 | 71.3 | 4.0 | 63.1 | 1.4 |
| 0.15 | 0.156 | 32 | 71.2 | 4.0 | 63.0 | 1.4 |
| 0.16 | 0.128 | 36 | 71.1 | 4.0 | 62.9 | 1.4 |
| 0.17 | 0.106 | 40 | 71.0 | 4.1 | 62.8 | 1.5 |
| 0.18 | 0.090 | 44 | 71.0 | 4.1 | 62.8 | 1.5 |
| 0.19 | 0.077 | 48 | 70.9 | 4.1 | 62.7 | 1.5 |
| 0.20 | 0.066 | 53 | 70.9 | 4.1 | 62.7 | 1.5 |
| 0.21 | 0.058 | 58 | 70.9 | 4.1 | 62.7 | 1.6 |
| 0.22 | 0.051 | 62 | 70.9 | 4.1 | 62.6 | 1.6 |
| 0.23 | 0.046 | 66 | 70.9 | 4.1 | 62.6 | 1.6 |
| 0.24 | 0.041 | 71 | 70.9 | 4.1 | 62.6 | 1.6 |
| 0.25 | 0.038 | 74 | 70.9 | 4.1 | 62.6 | 1.7 |

| $\sigma_f$ | $P_{max}$ | $P_{90}$ | volg20k | err | volg0k | err |
|---|---|---|---|---|---|---|
| 0.06 | 0.745 | 2 | 72.4 | 1.6 | 63.8 | 0.6 |
| 0.07 | 0.650 | 2 | 72.6 | 1.9 | 63.7 | 0.7 |
| 0.08 | 0.555 | 3 | 72.6 | 2.3 | 63.6 | 0.8 |
| 0.09 | 0.462 | 6 | 72.4 | 2.8 | 63.5 | 0.9 |
| threshold for $P_{max} = 0.5 \times P_{tot}$ | | | | | | |
| **0.10** | 0.377 | 9 | 72.2 | 3.2 | 63.4 | 1.0 |
| threshold for $P_{90} > 10$ runs | | | | | | |
| 0.11 | 0.305 | 12 | 71.9 | 3.5 | 63.3 | 1.1 |
| 0.12 | 0.246 | 15 | 71.6 | 3.7 | 63.2 | 1.2 |
| 0.13 | 0.199 | 20 | 71.4 | 3.8 | 63.1 | 1.3 |
| 0.14 | 0.163 | 24 | 71.2 | 3.9 | 63.0 | 1.4 |
| 0.15 | 0.135 | 29 | 71.0 | 4.0 | 62.9 | 1.4 |
| 0.16 | 0.113 | 33 | 70.9 | 4.0 | 62.8 | 1.4 |
| 0.17 | 0.096 | 37 | 70.8 | 4.0 | 62.8 | 1.5 |
| 0.18 | 0.082 | 41 | 70.8 | 4.0 | 62.7 | 1.5 |
| 0.19 | 0.071 | 46 | 70.7 | 4.0 | 62.7 | 1.5 |
| 0.20 | 0.063 | 51 | 70.7 | 4.0 | 62.6 | 1.6 |
| 0.21 | 0.055 | 56 | 70.6 | 4.0 | 62.6 | 1.6 |
| 0.22 | 0.049 | 60 | 70.6 | 4.0 | 62.5 | 1.6 |
| 0.23 | 0.045 | 64 | 70.6 | 4.0 | 62.5 | 1.6 |
| 0.24 | 0.040 | 67 | 70.6 | 4.0 | 62.5 | 1.7 |
| 0.25 | 0.037 | 71 | 70.6 | 4.0 | 62.5 | 1.7 |

Table B.2: Results of incremental changes to $\sigma_f$ and resultant probabilities and volg metrics for scoring scheme PDcPbSeb

## C.3 Appendix: ELEV site maps and age-altitude plots

Figs. C.5 to C.30 that follow, present, for each ELEV site, a map of the surrounding region with topographic details (contours taken from 1 km RAMP-DEM (Liu et al., 2001). Flowlines, rock outcrops and coastline are from the 1:10,000,000 scale Antarctic Digital Database (SCAR, 2006)) and an age-elevation plot with the observations and reconstructed surface elevations relative to present day basal elevation. The inset shows the location of the site on the AIS. The maps are centred on the site position, the region is approximately 200 km x 200 km. The red overlay is a 40 km resolution grid, representing the model domain. Data-points for the site are shown as red diamonds, with temporal and elevation uncertainty bars. In some cases the data from sites in close proximity, plotted as black triangles, can be seen. These data-points are not plotted on the age-altitude plots.

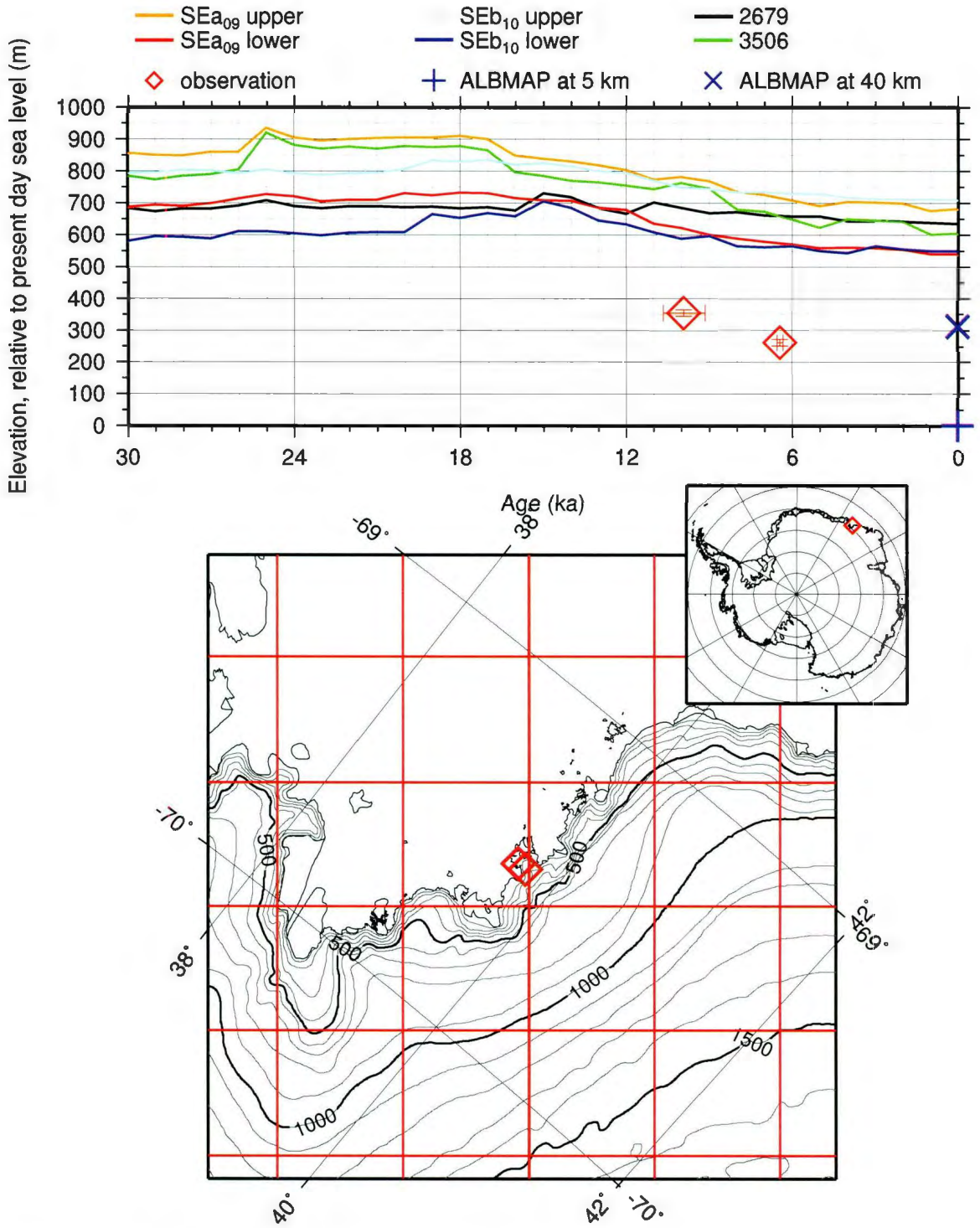


Figure C.5: PHS siteMisfit:1101 Lutzow-Holm Bay (LHB)

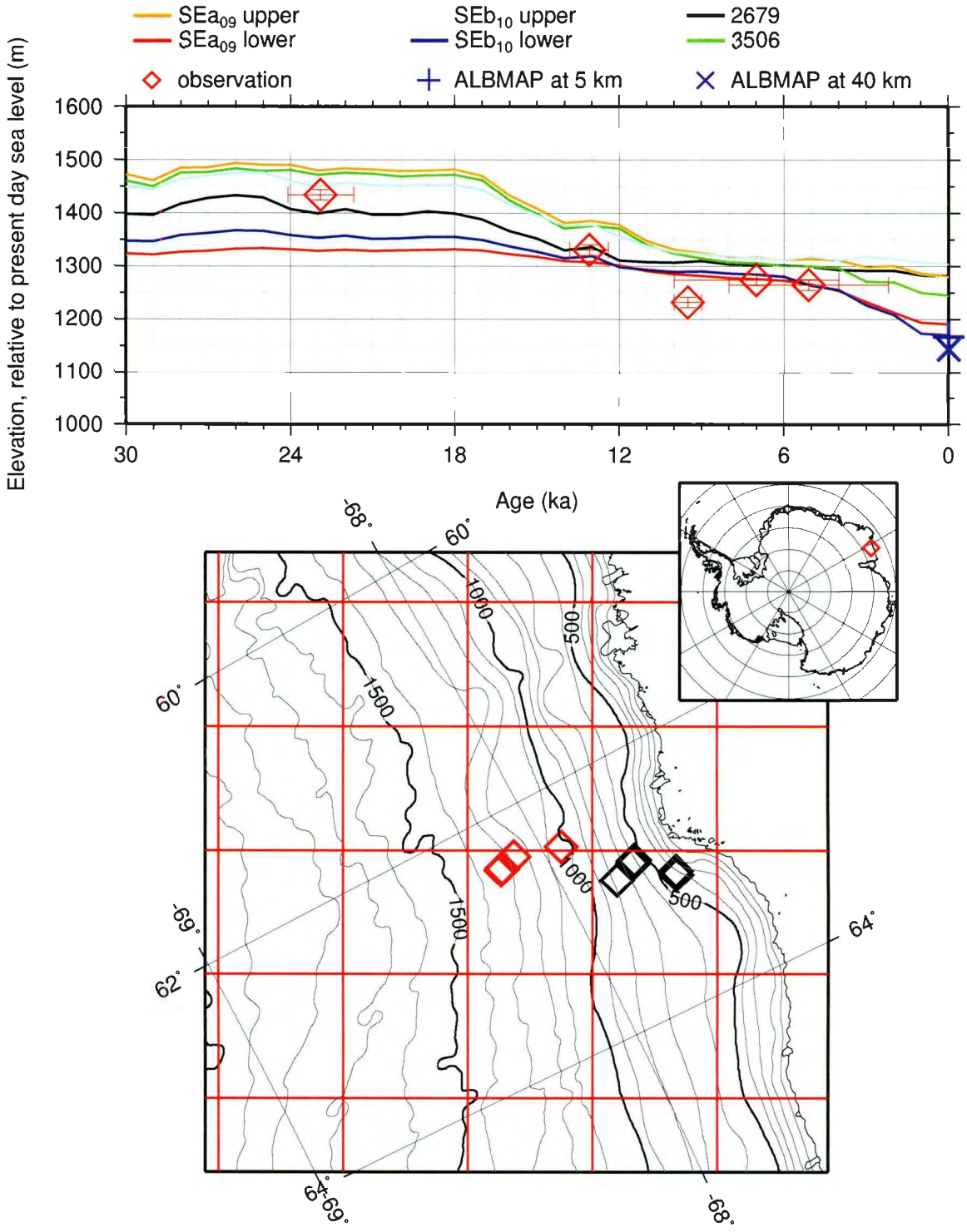


Figure C.6: PHS siteMisfit:1201 Framnes Mts. 1 (FM1)

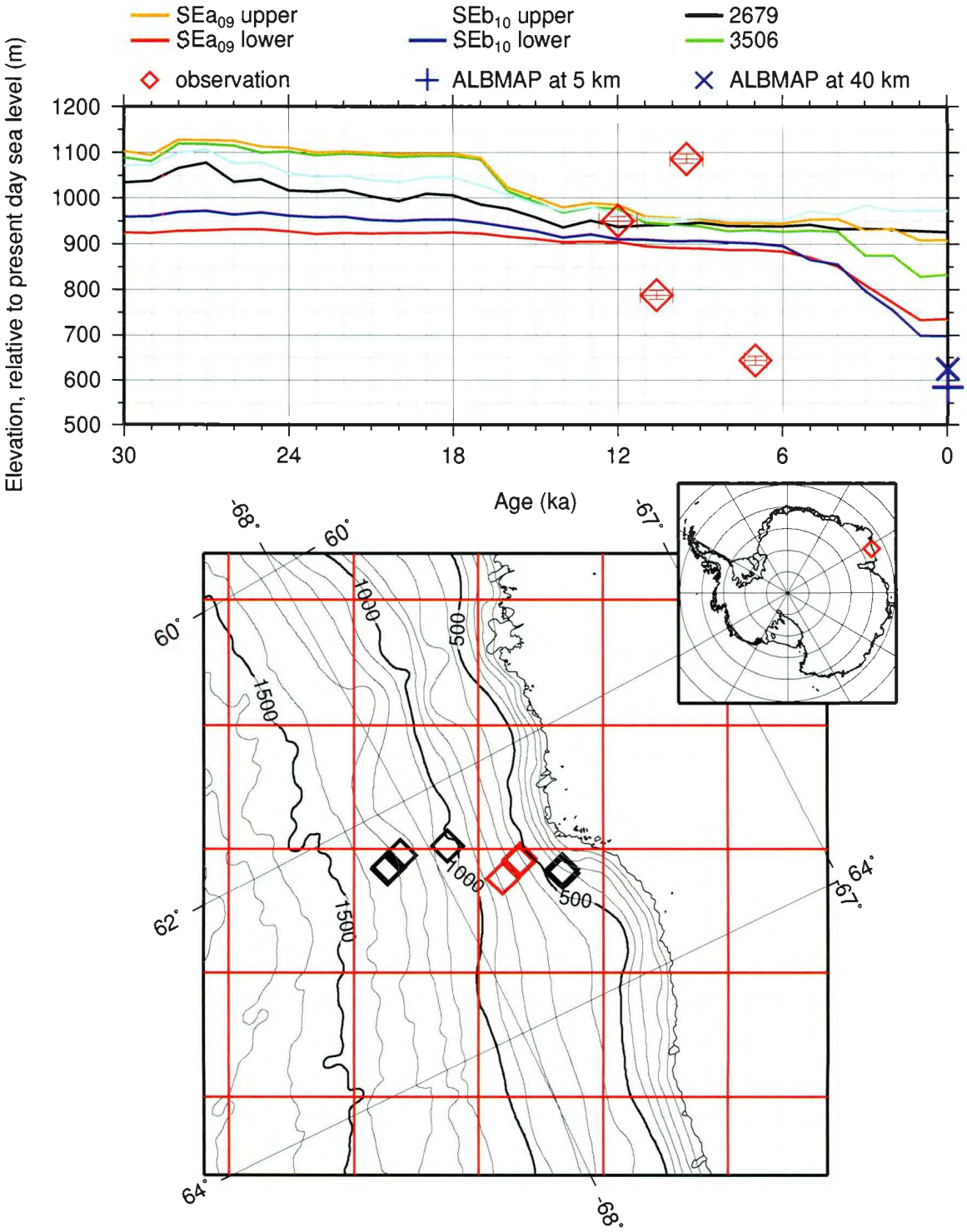


Figure C.7: PHS siteMisfit:1202 Framnes Mts. 2 (FM2)

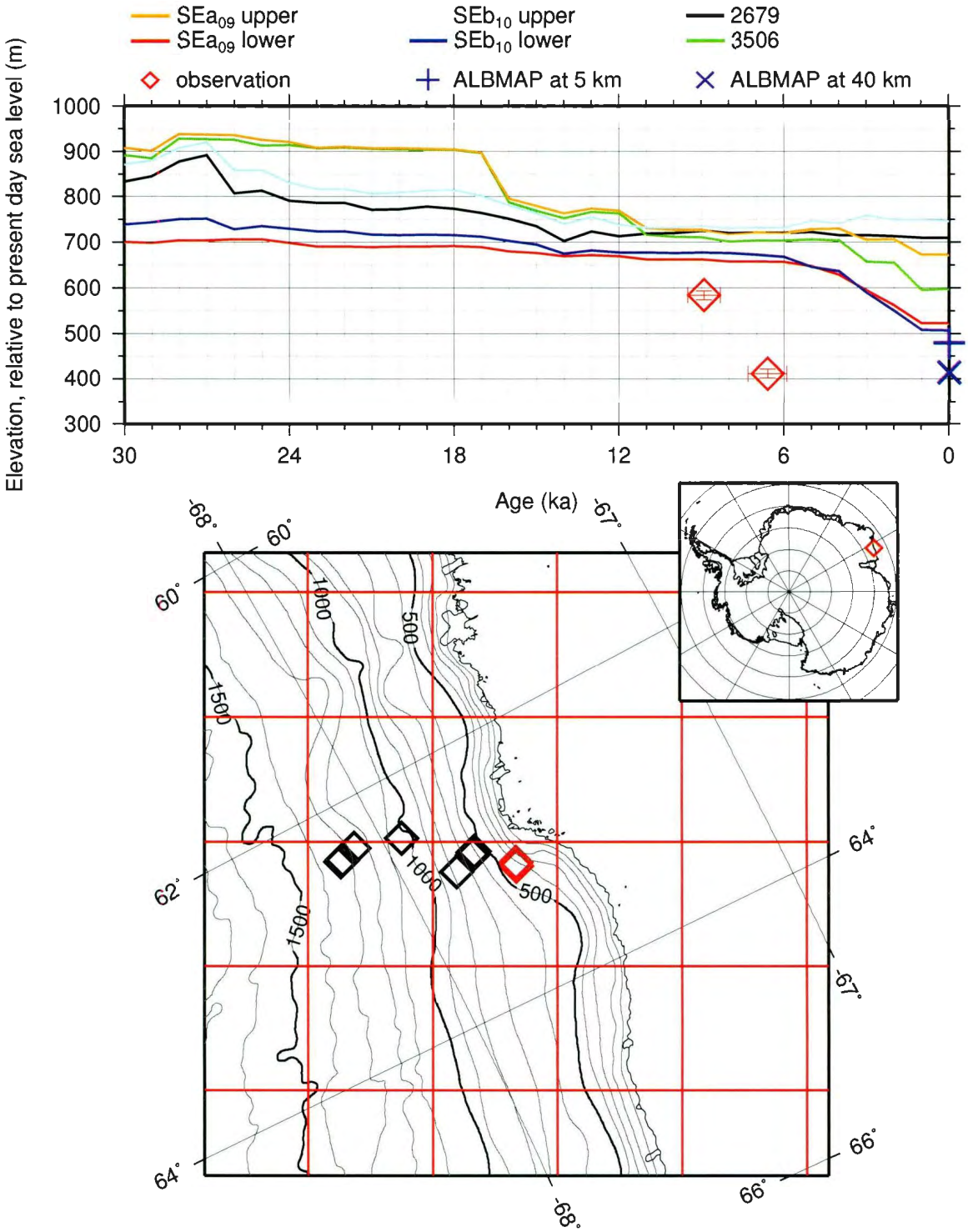


Figure C.8: PHS siteMisfit:1203 Framnes Mts. 3 (FM3)

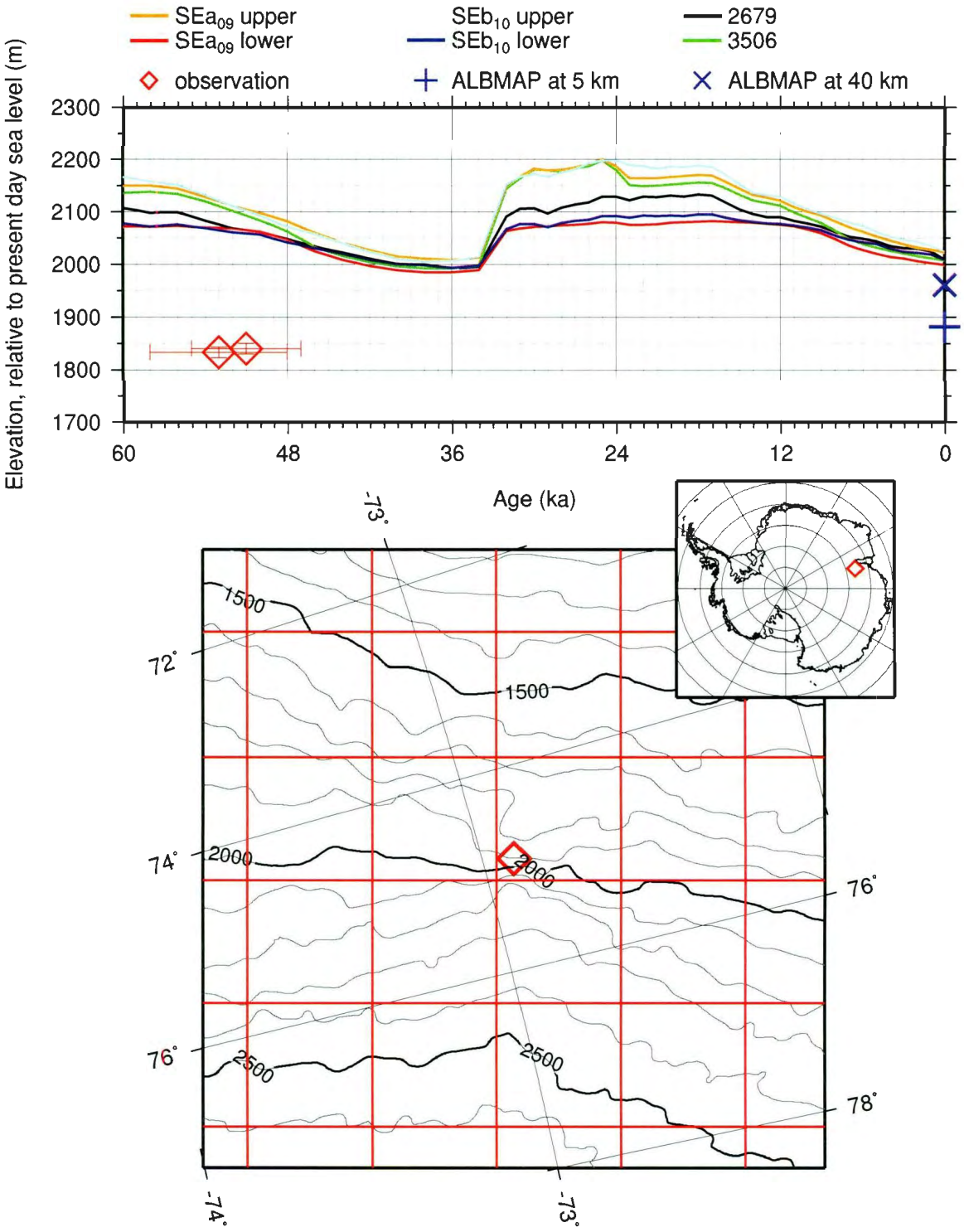


Figure C.9: PHS siteMisfit:1204 Grove Mts. (GM)

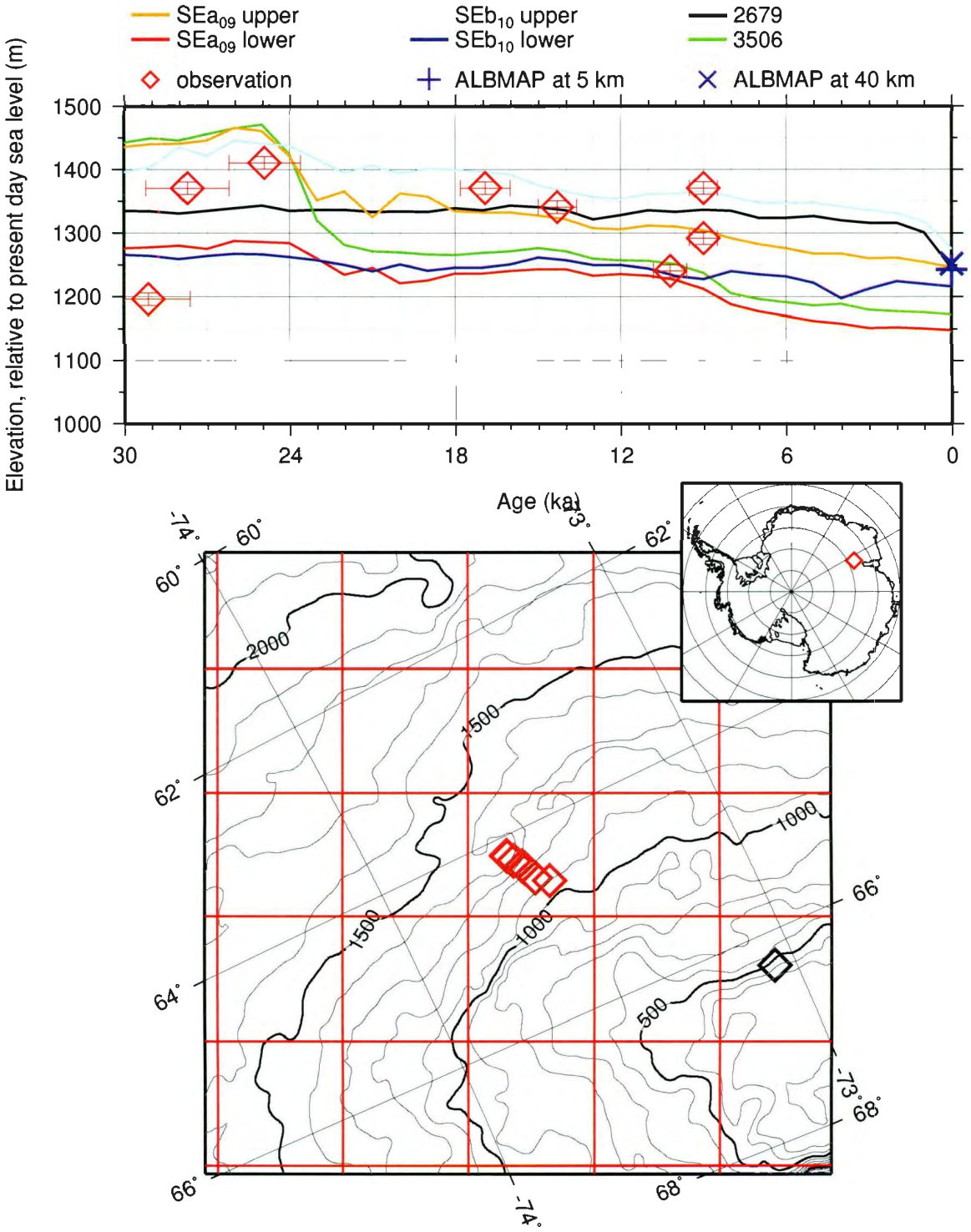


Figure C.10: PHS siteMisfit:1205 Prince Charles Mts. 1 (PCM1)

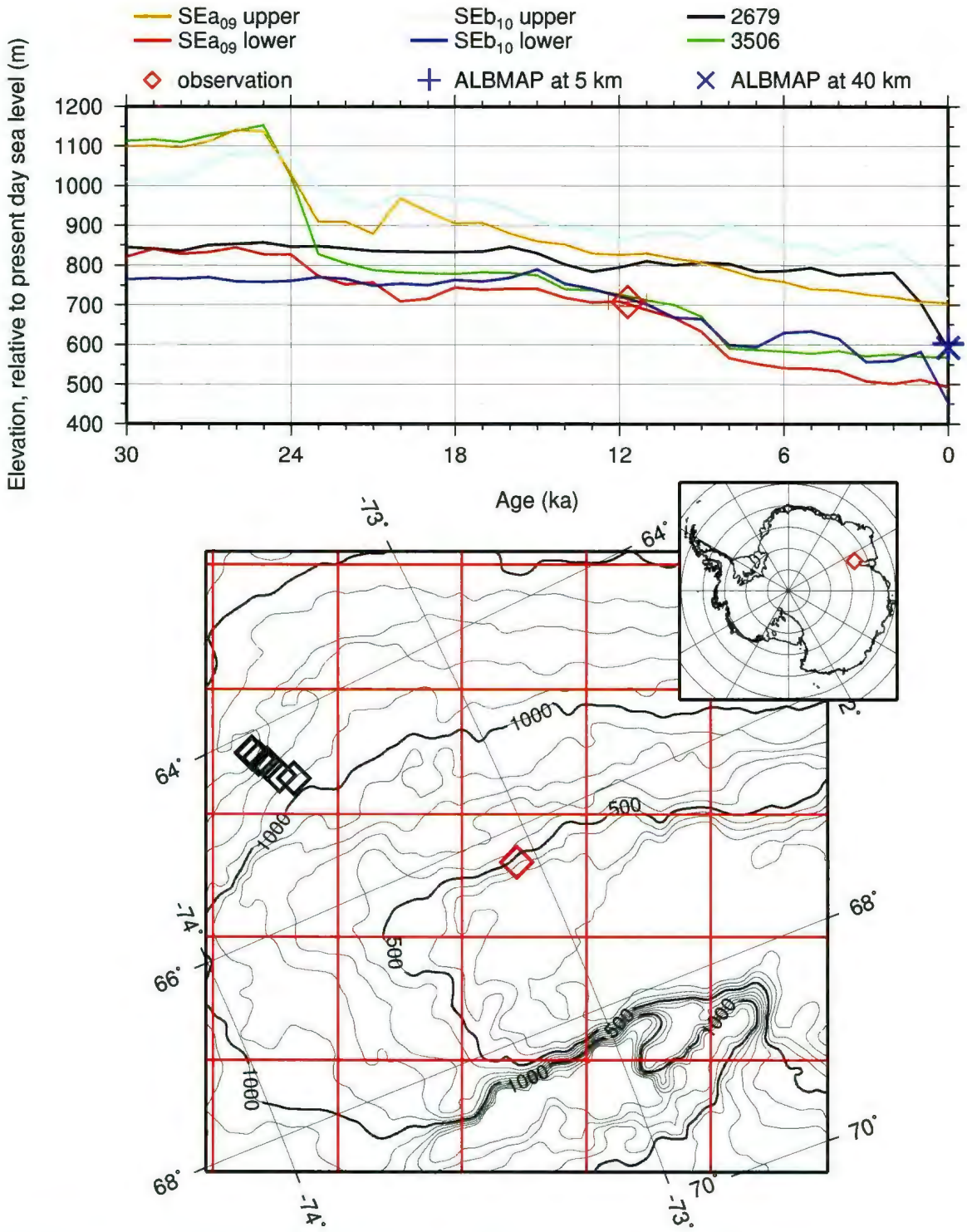


Figure C.11: PHS siteMisfit:1206 Prince Charles Mts. 2 (PCM2)

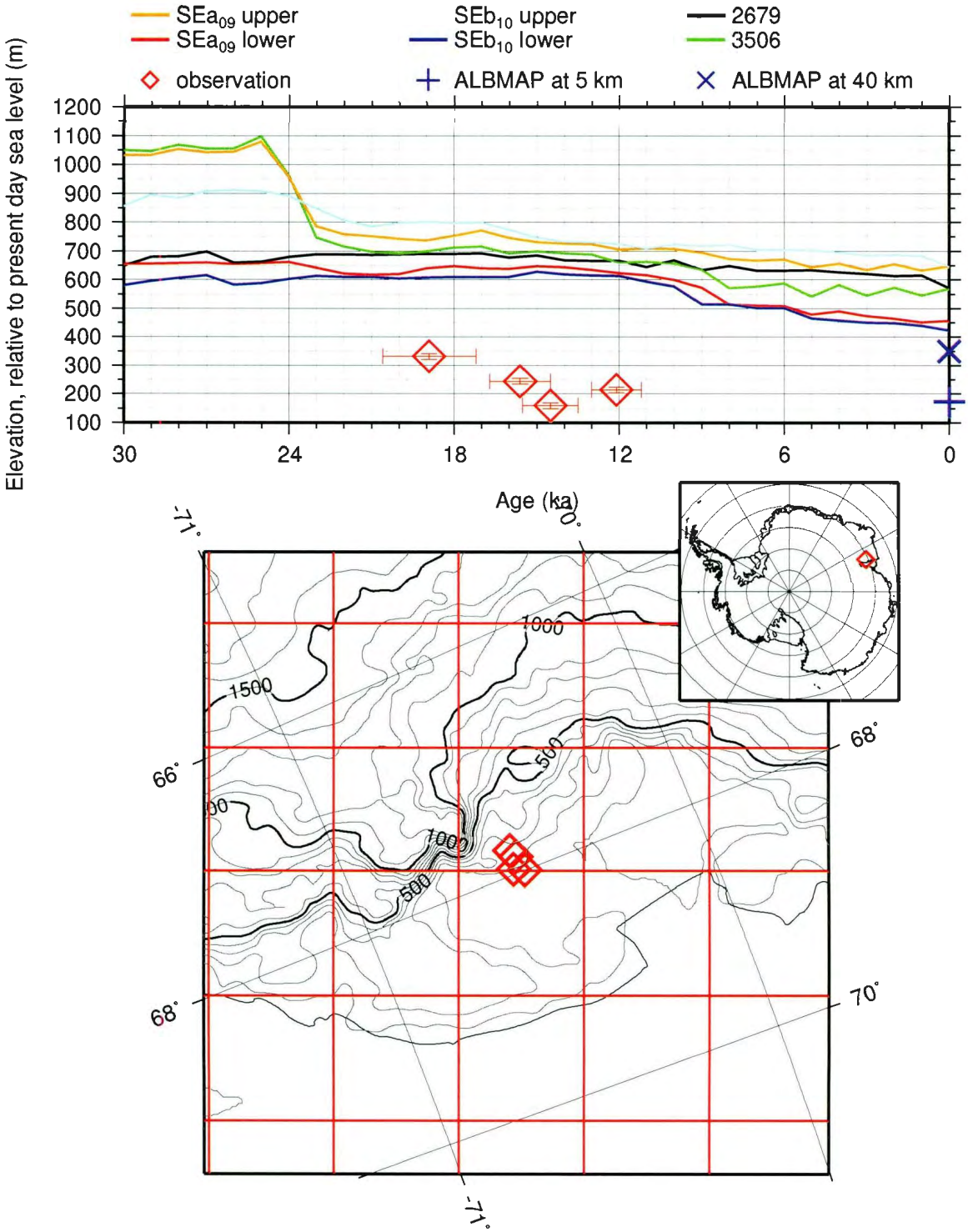


Figure C.12: PHS siteMisfit:1207 Prince Charles Mts. 3 (PCM3)

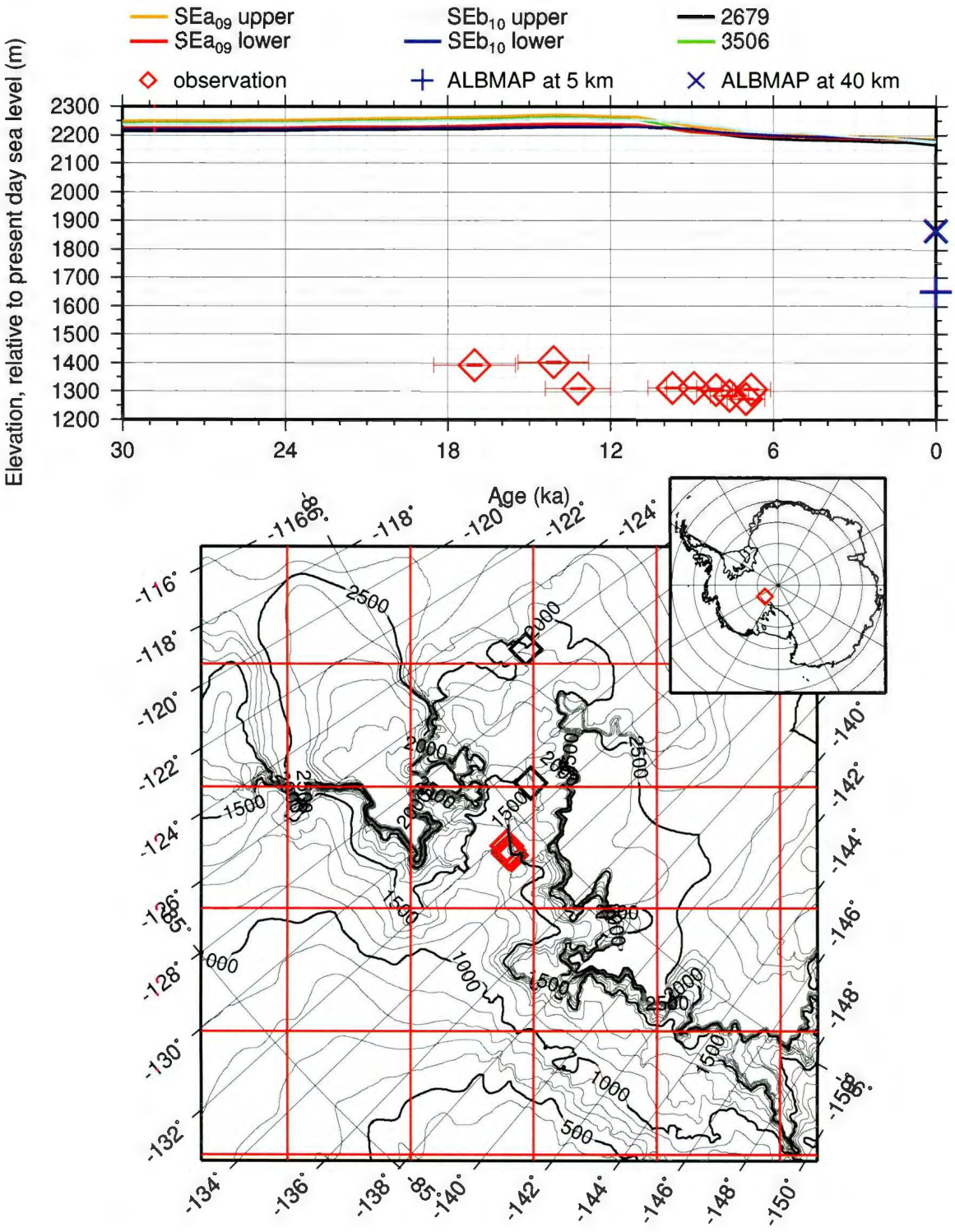


Figure C.13: PHS siteMisfit:1401 Reedy Glacier 1 (RG1)

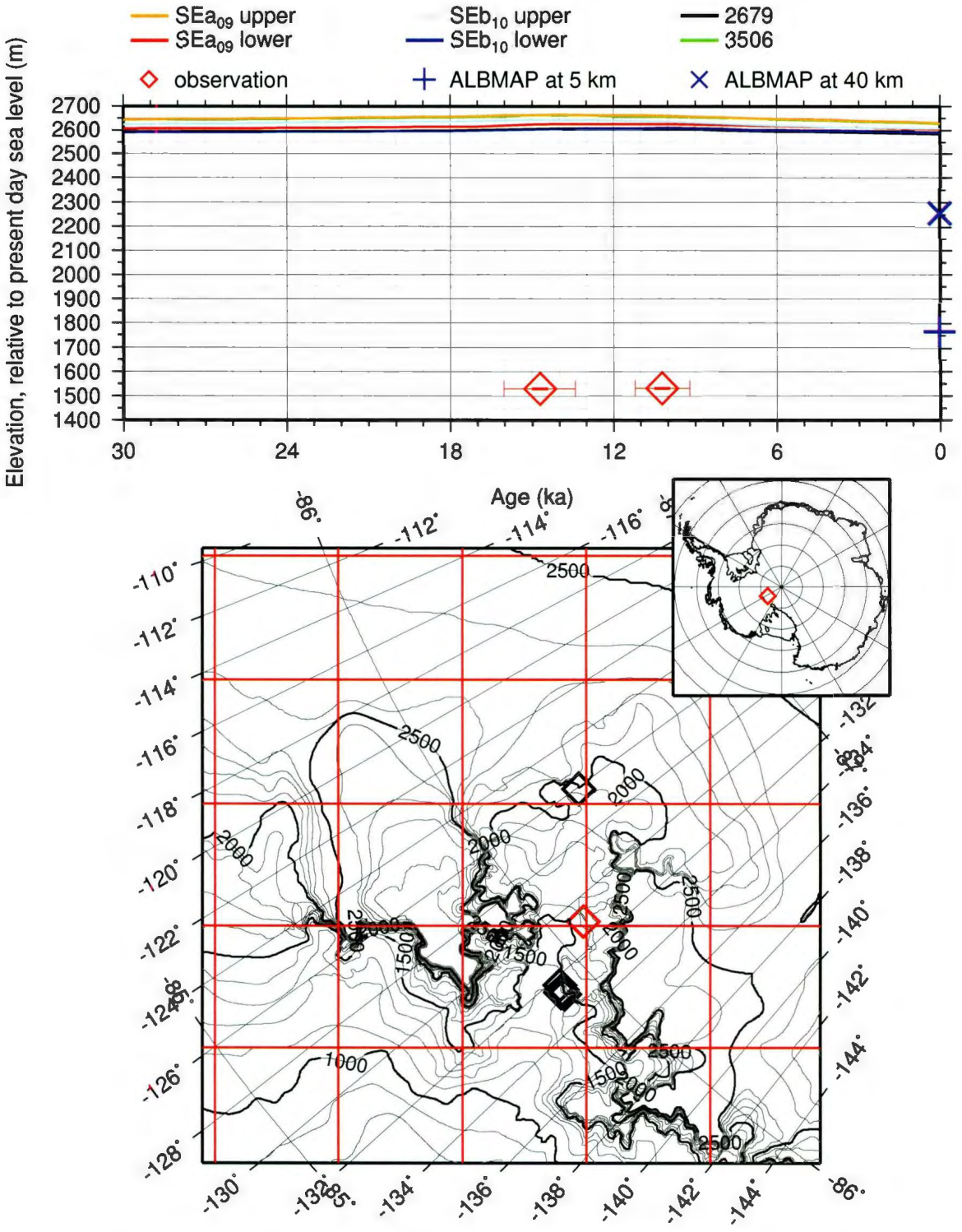


Figure C.14: PHS siteMisfit:1402 Reedy Glacier 2 (RG2)

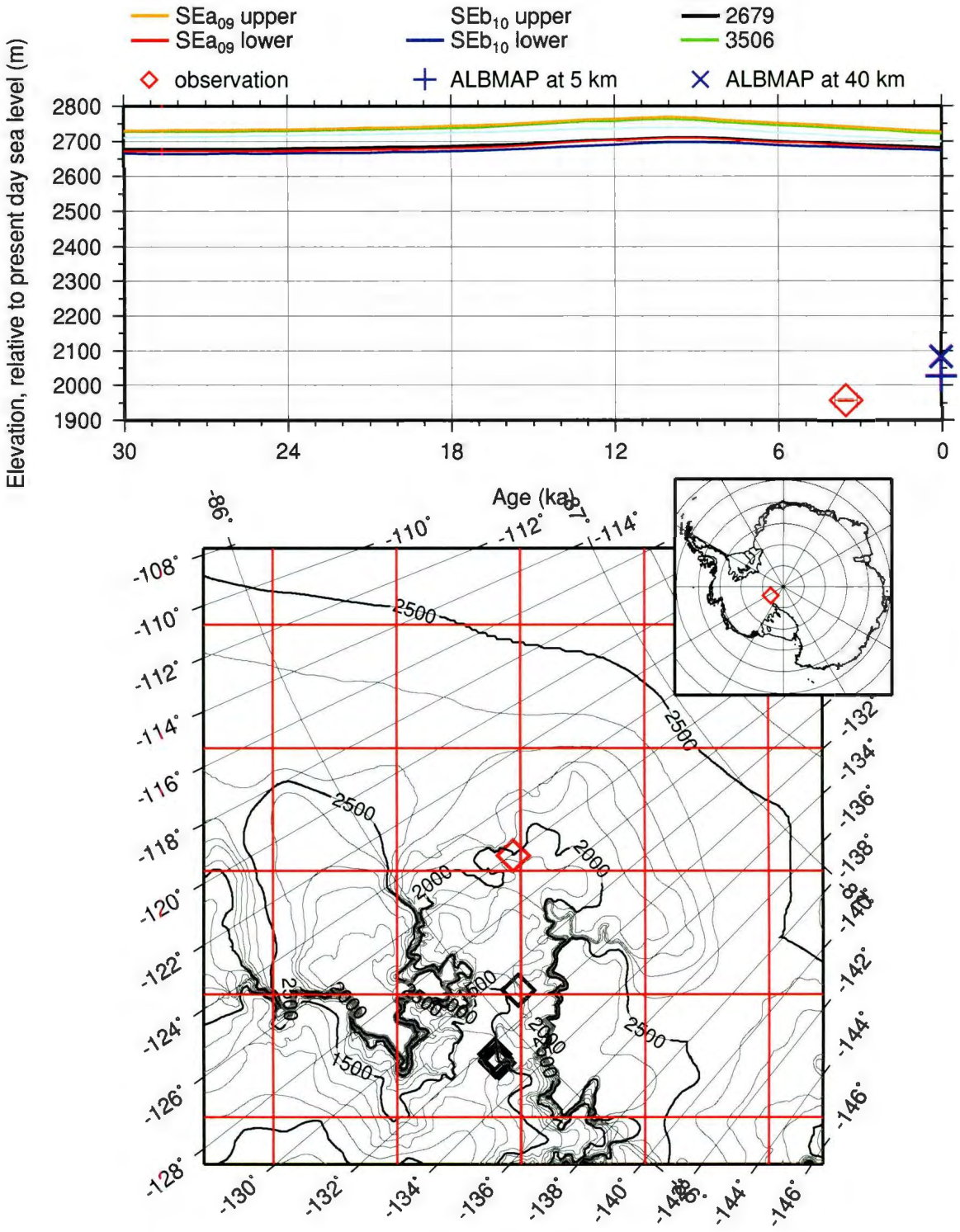


Figure C.15: PHS siteMisfit:1403 Reedy Glacier 3 (RG3)

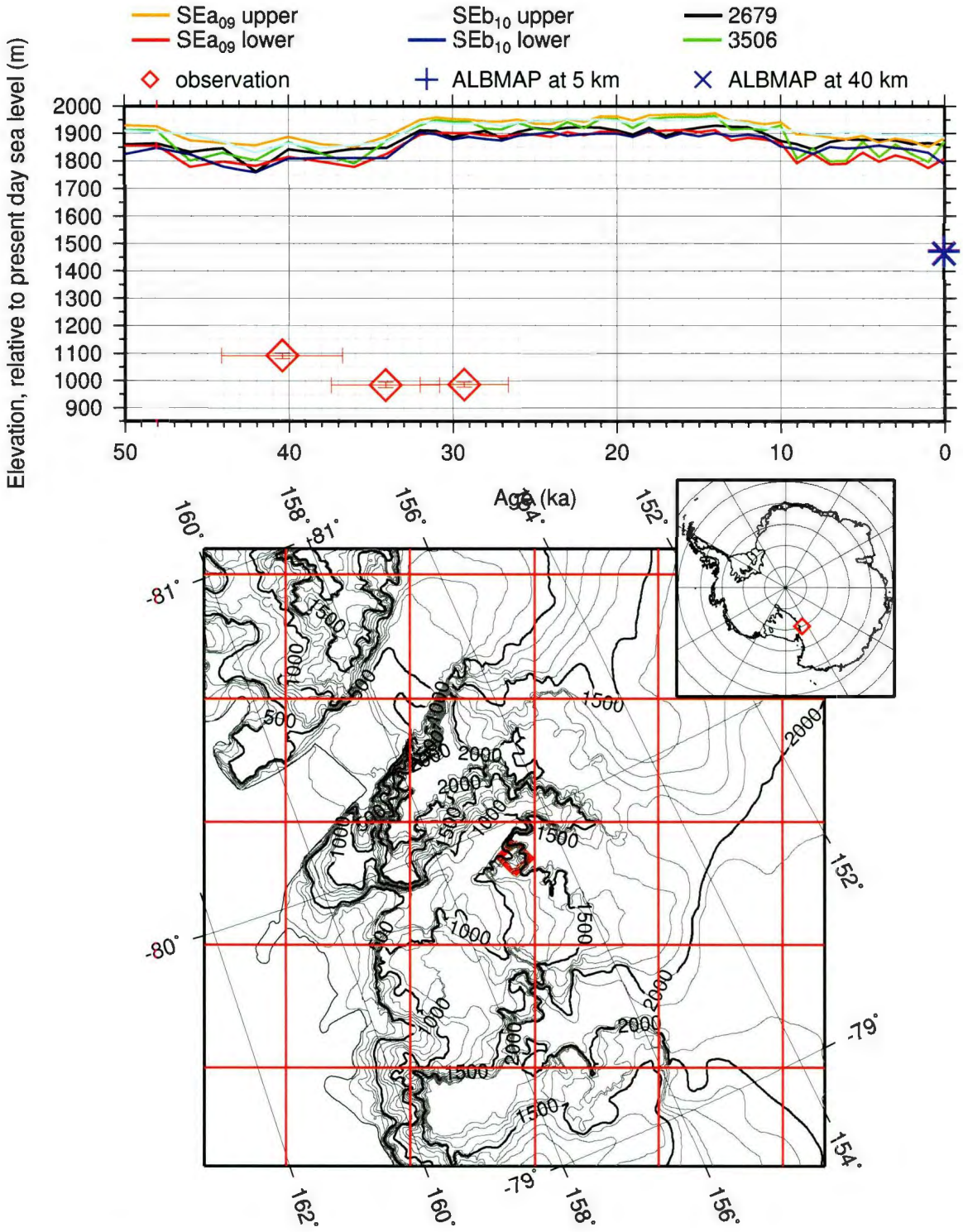


Figure C.16: PHS siteMisfit:1404 Hatherton glacier (HG)

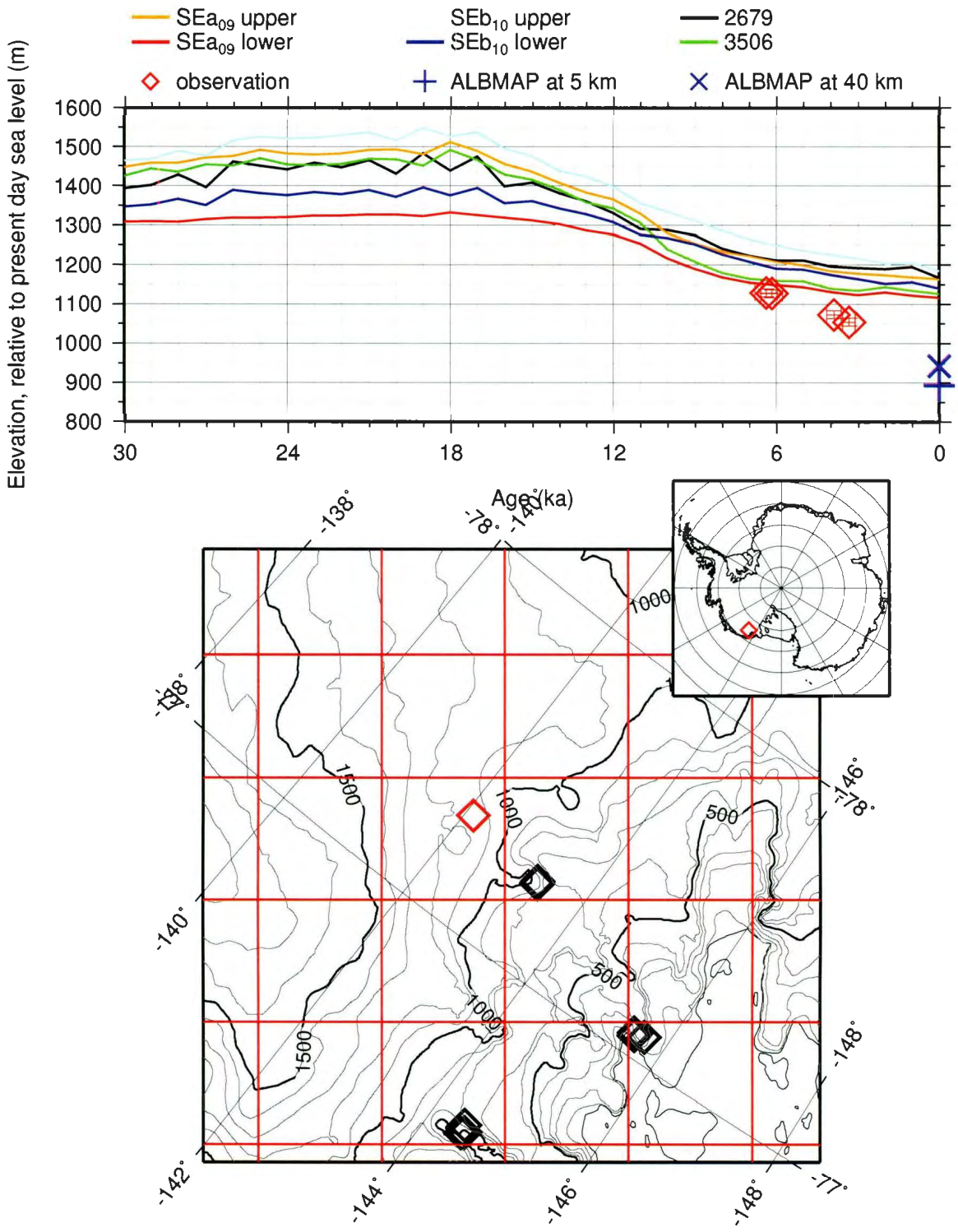


Figure C.17: PHS siteMisfit:1405 Clark Mtn (CLM)

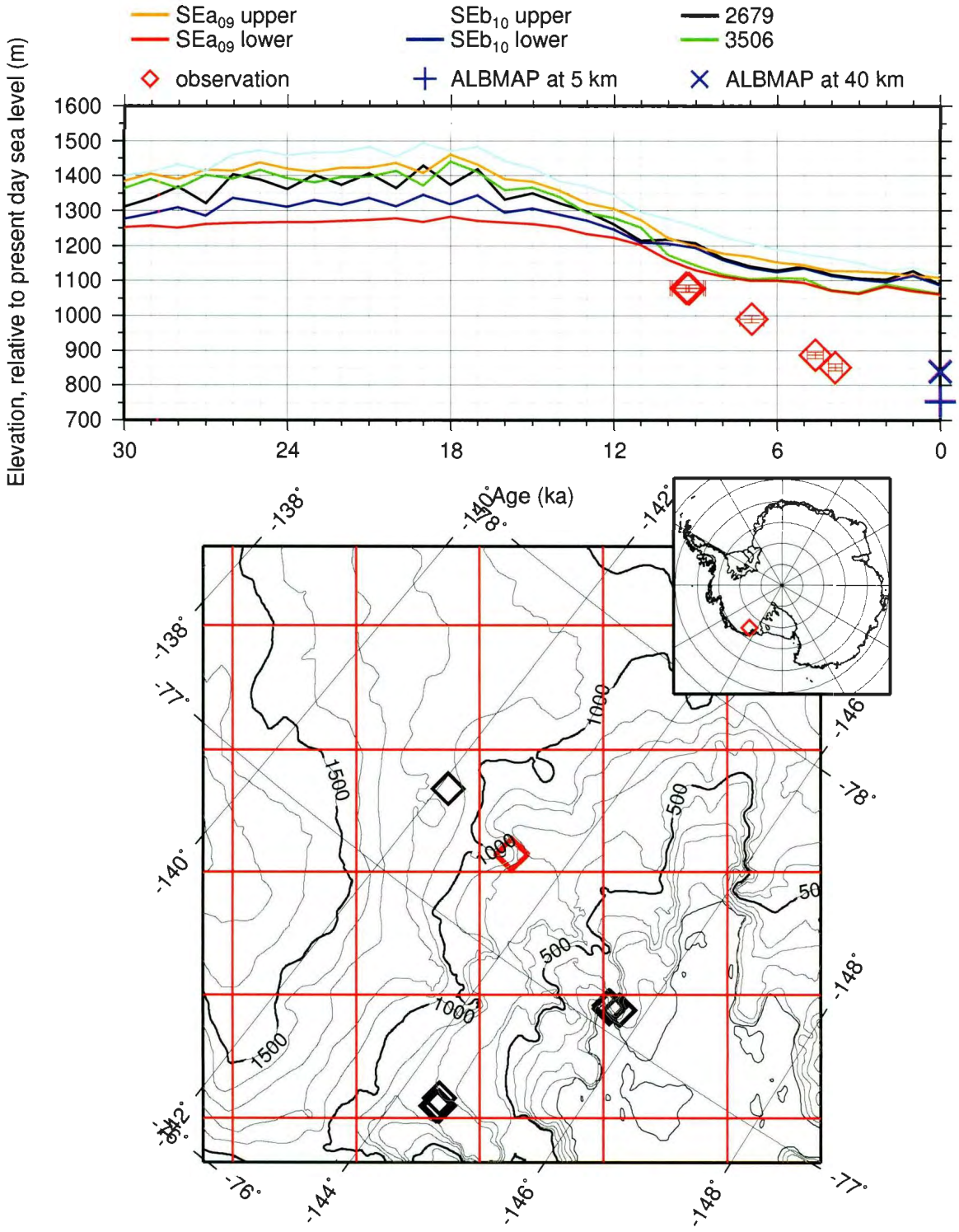


Figure C.18: PHS siteMisfit:1406 Allegheny Mtn (ALM)

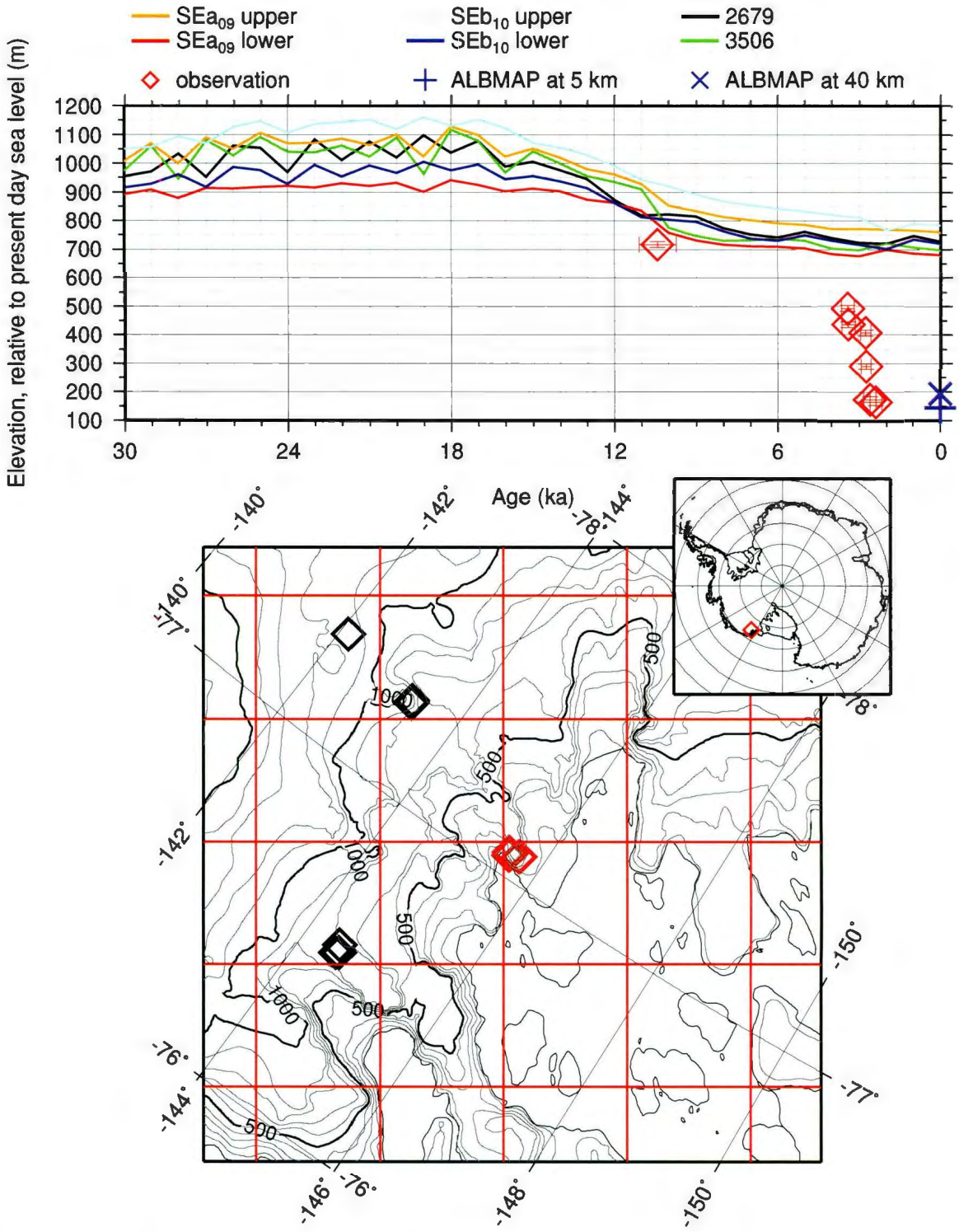


Figure C.19: PHS siteMisfit:1407 Western Sarnoff Mts (WSM)

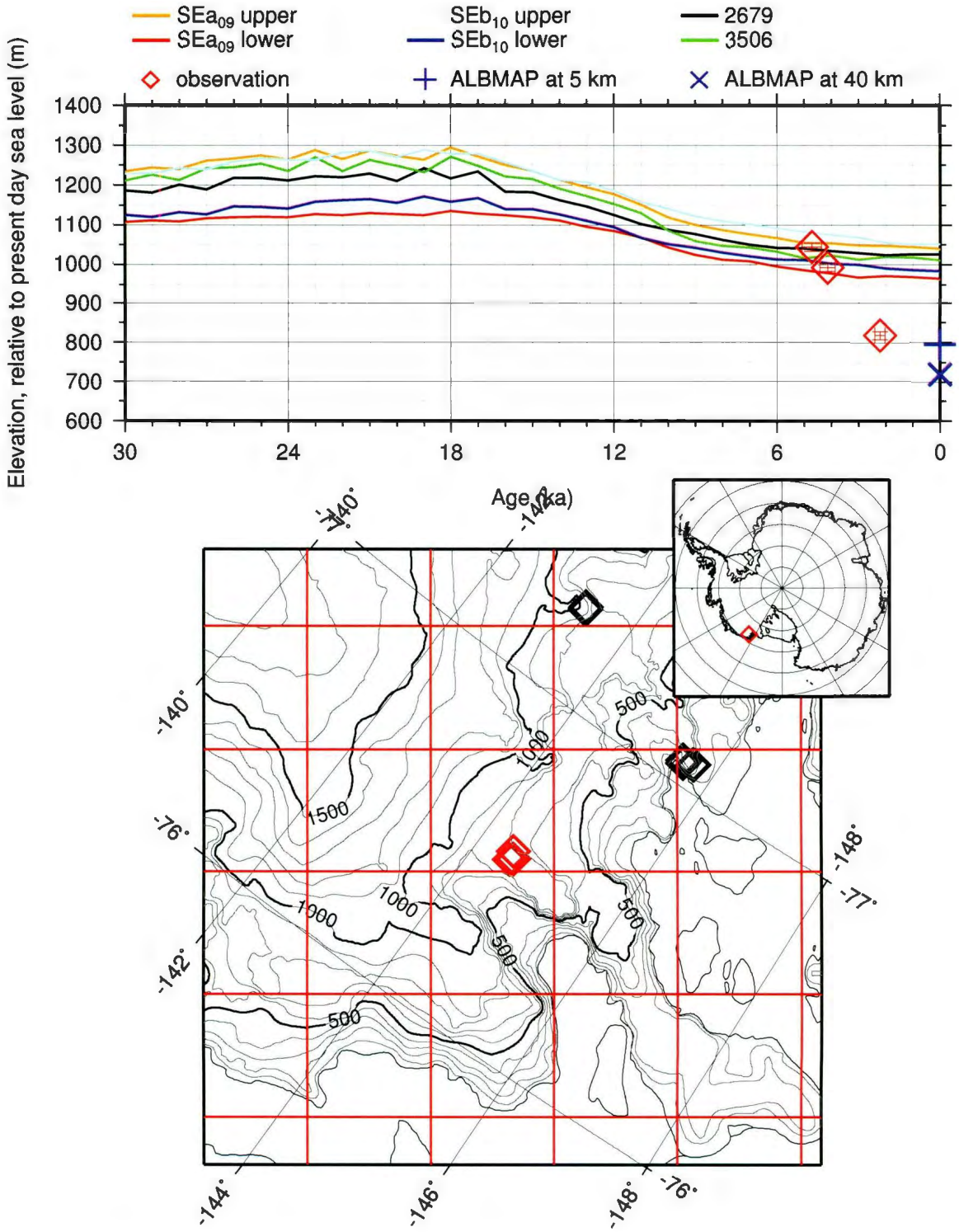


Figure C.20: PHS siteMisfit:1408 Eastern Fosdick Mts (EFR)

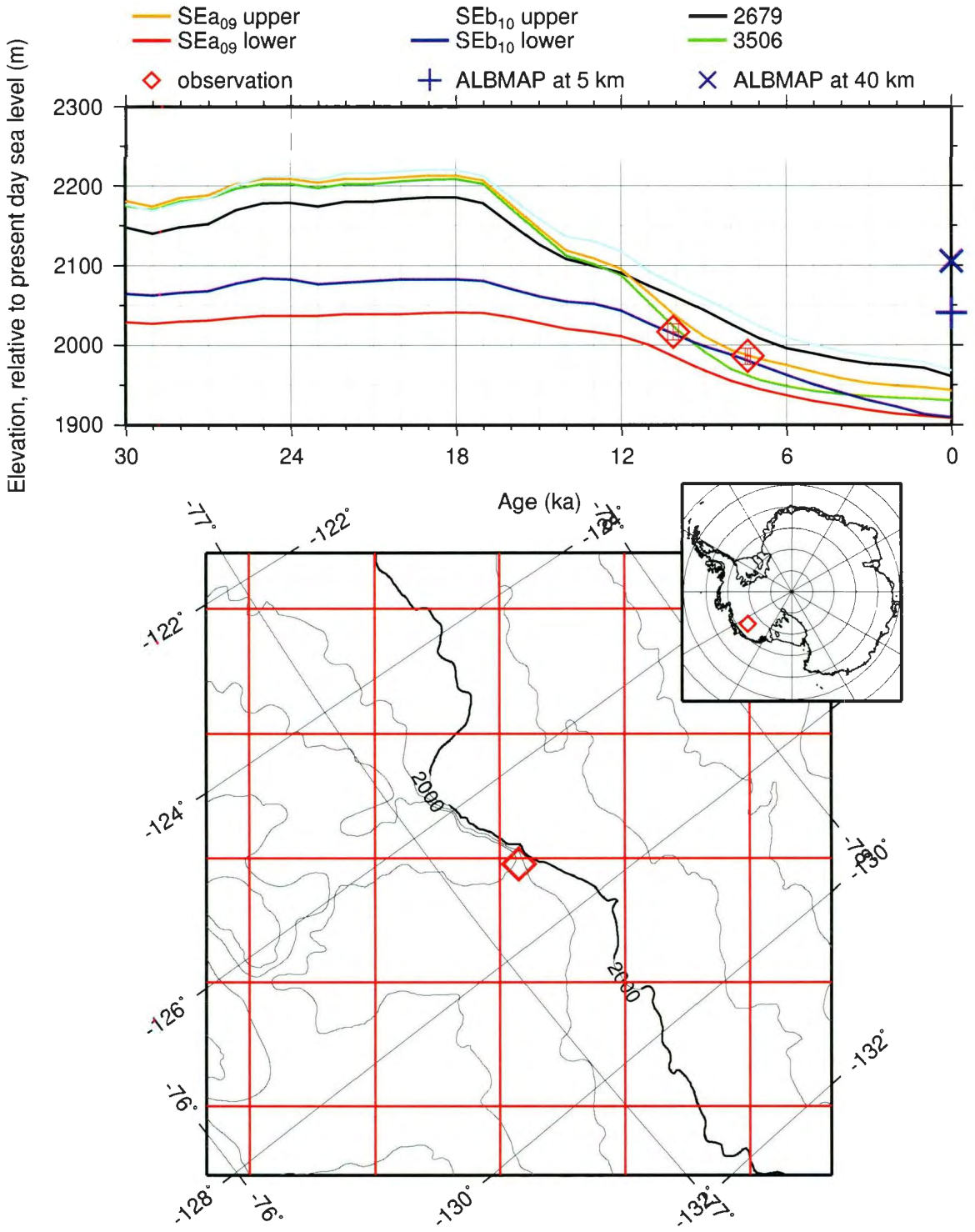


Figure C.21: PHS siteMisfit:1501 Executive Committee Range (ECR)

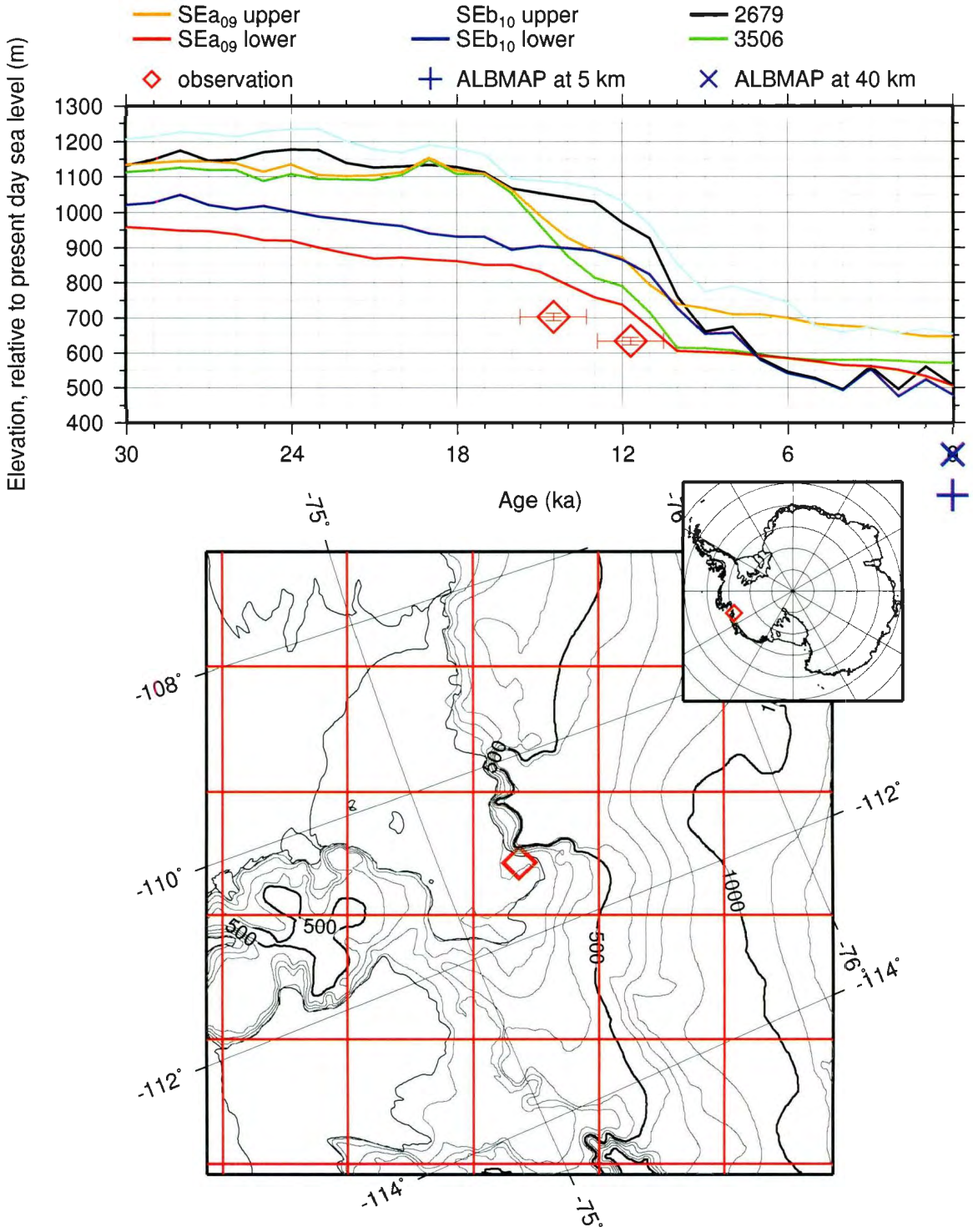


Figure C.22: PHS siteMisfit:1502 Pine Island Bay 1 (PIB1)

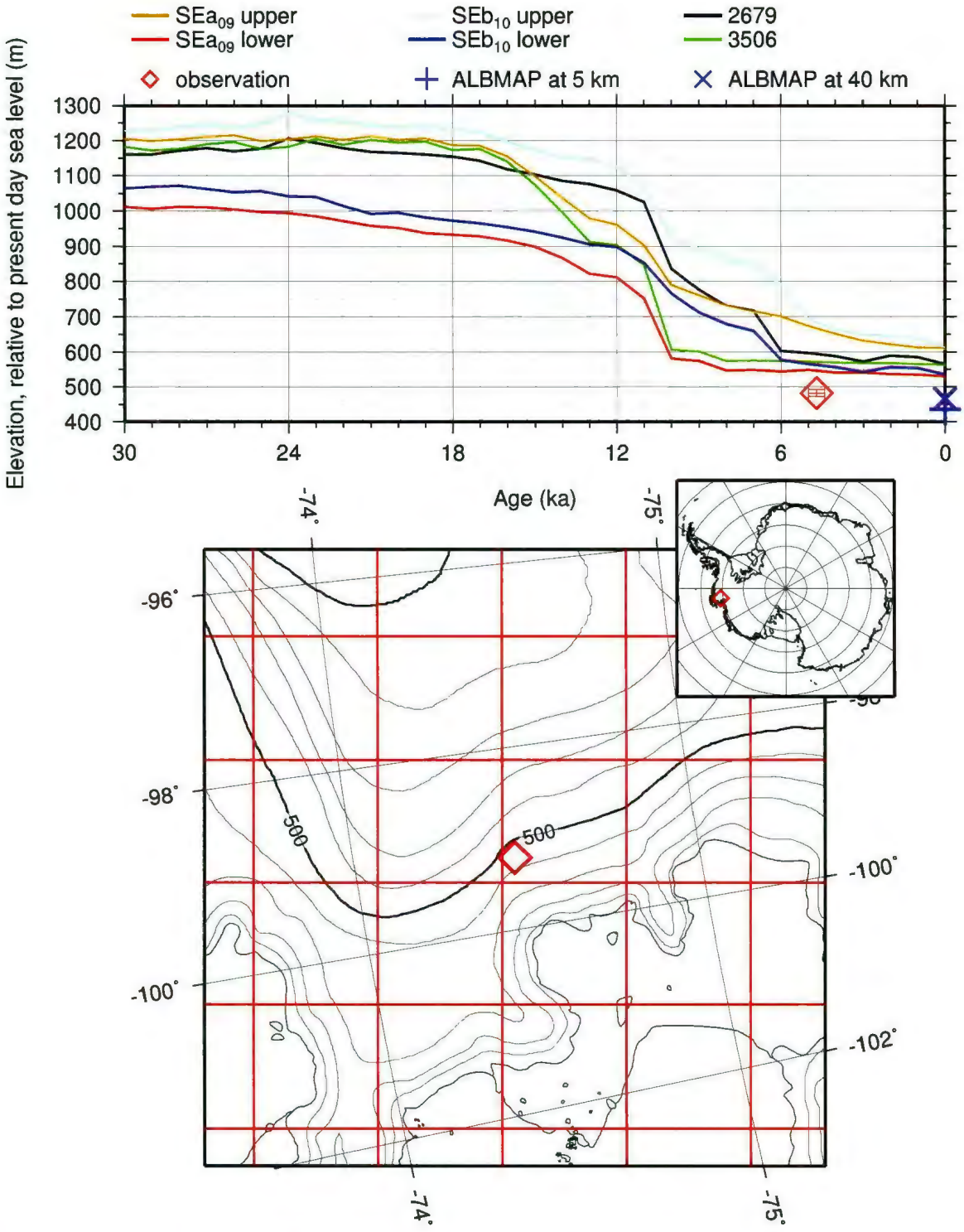


Figure C.23: PHS siteMisfit:1503 Pine Island Bay 2 (PIB2)

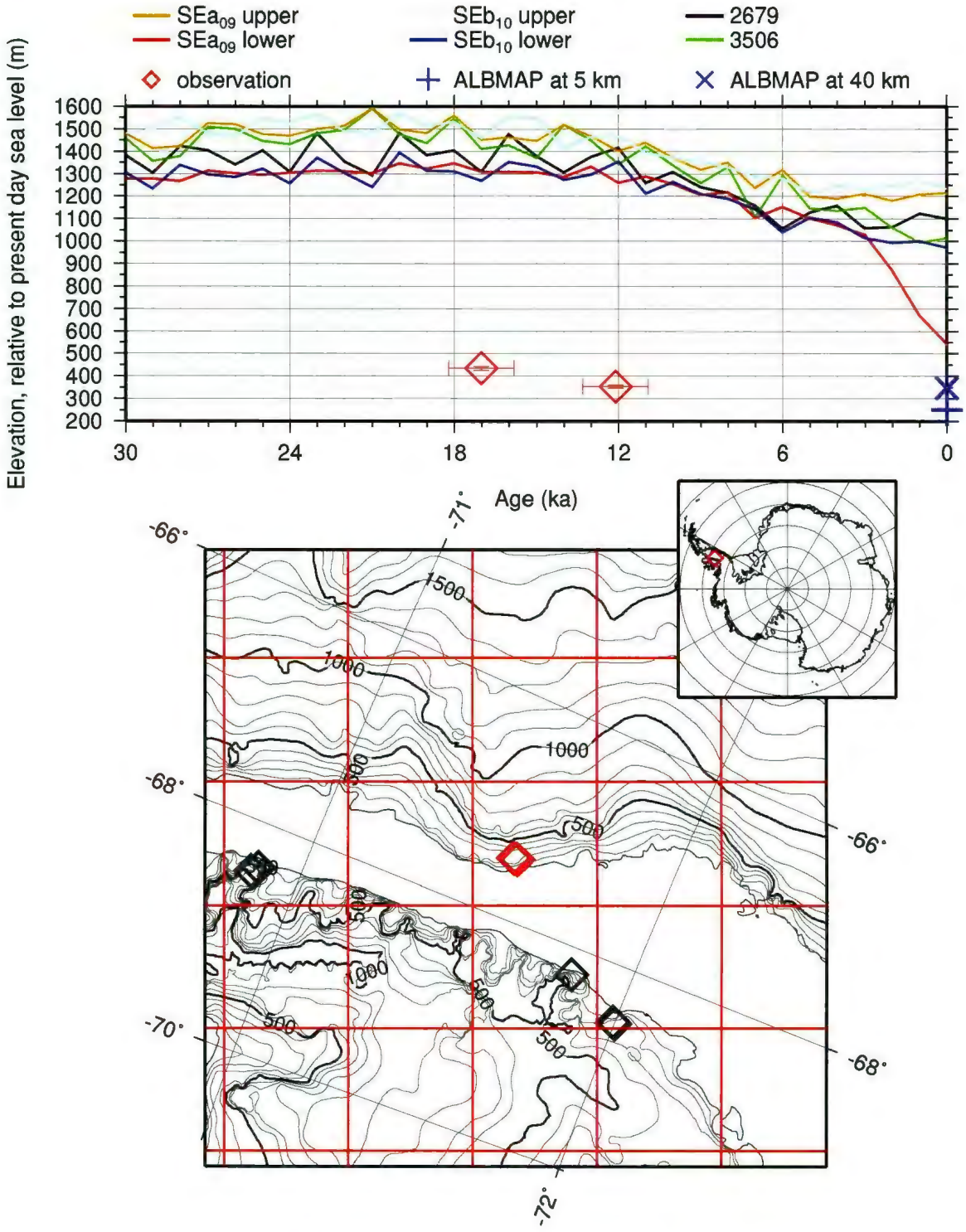


Figure C.24: PHS siteMisfit:1601 West Palmer Land (WPL)

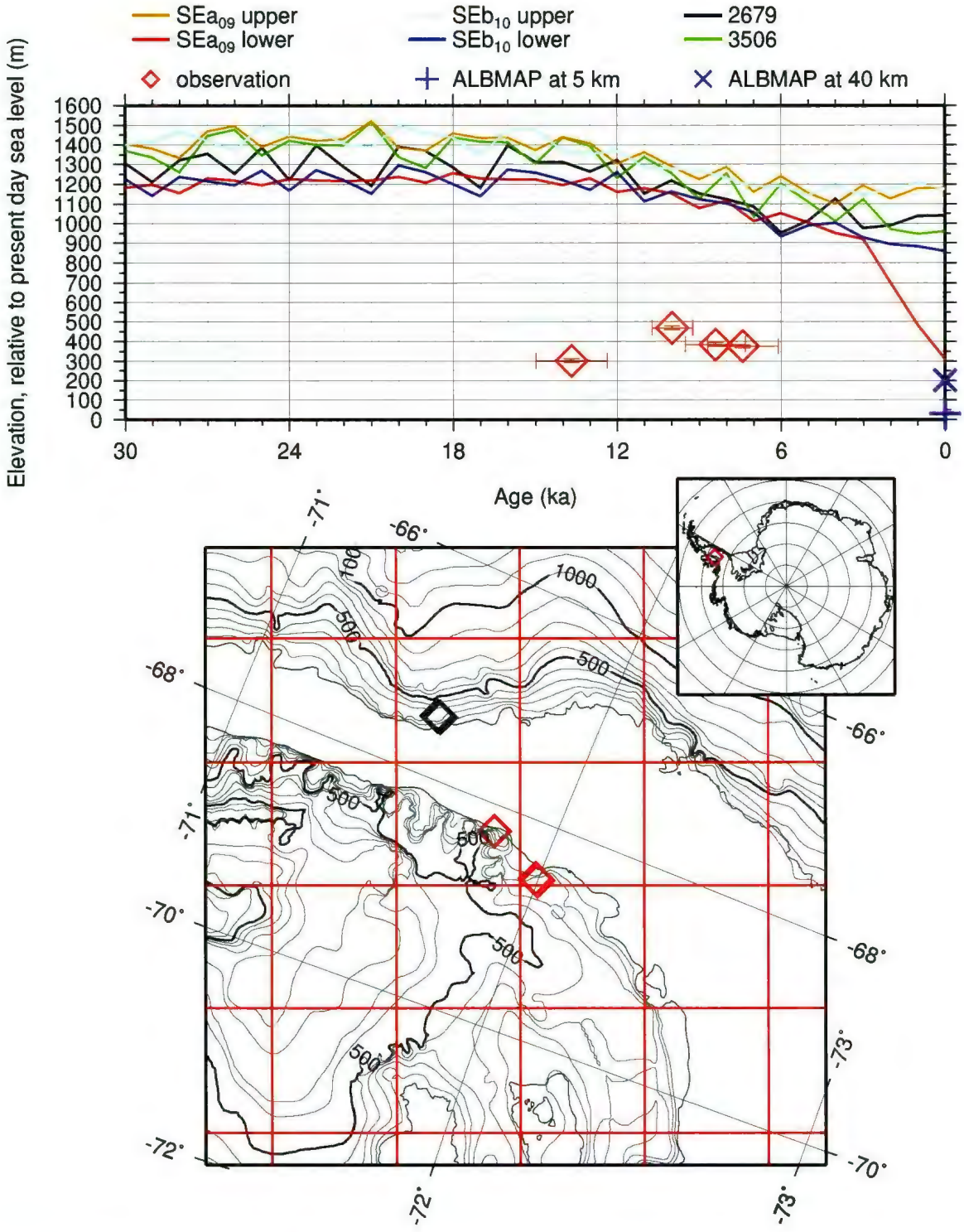


Figure C.25: PHS siteMisfit:1602 Alexander Island South (AXS)

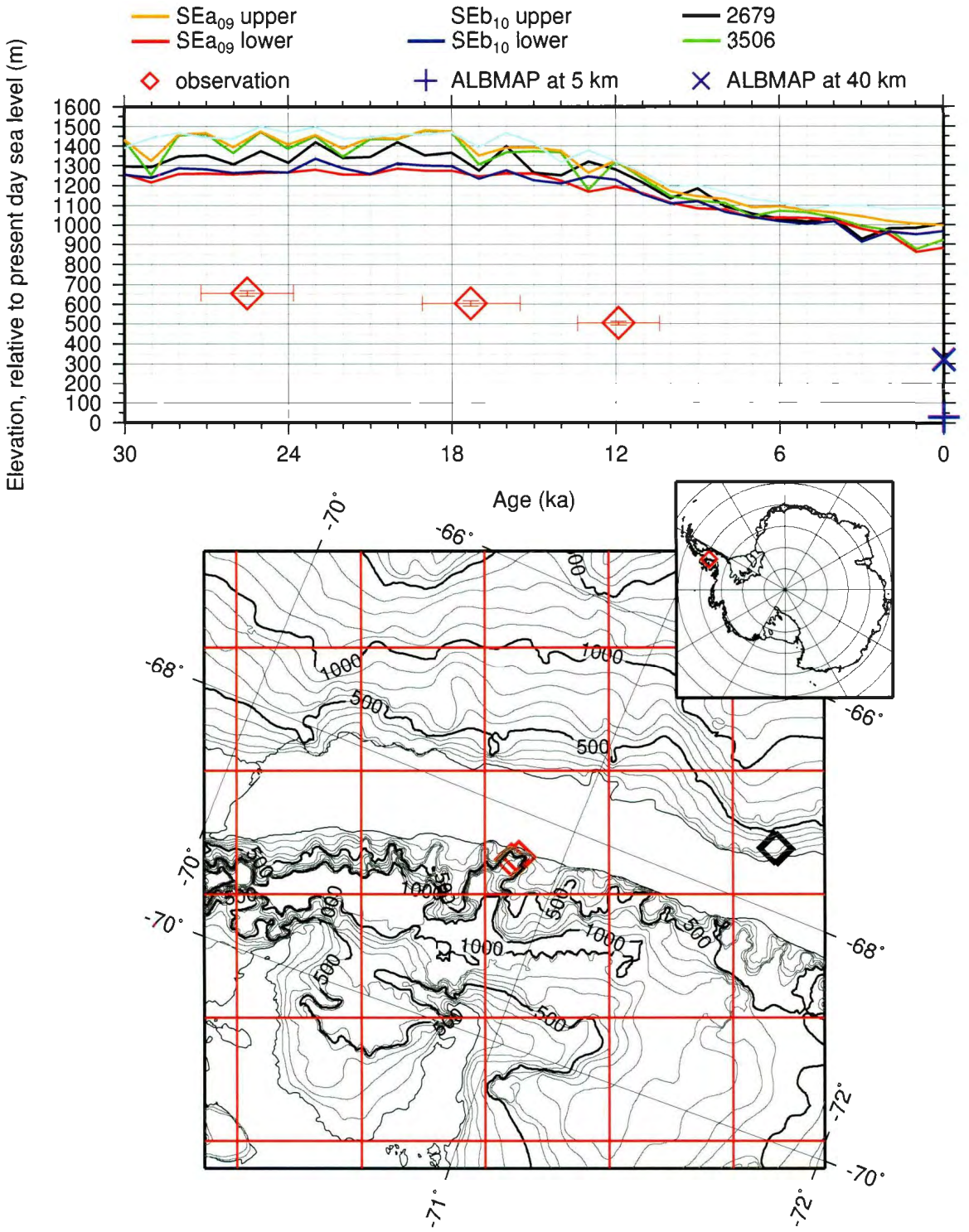


Figure C.26: PHS siteMisfit:1603 Alexander Island North (AXN)

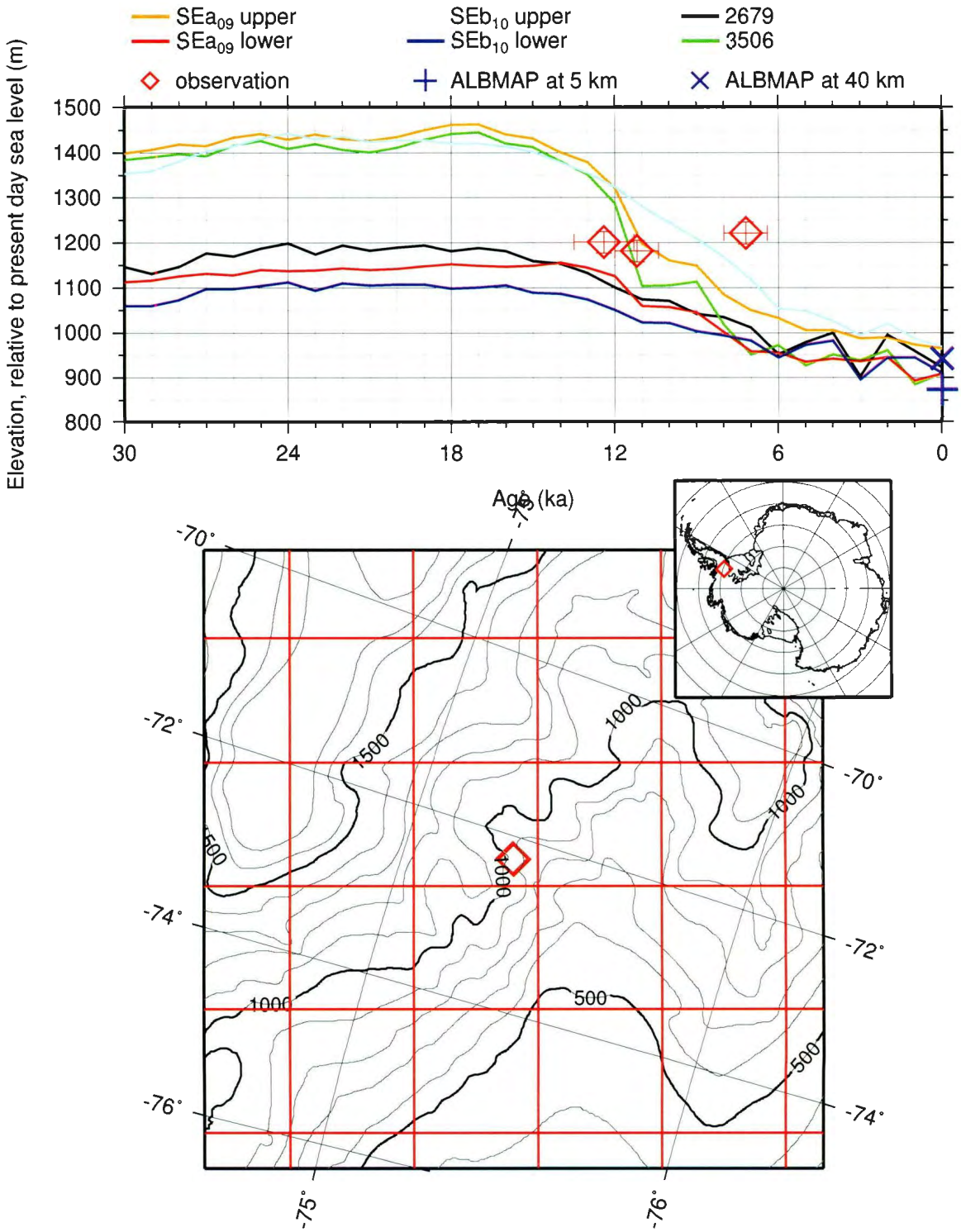


Figure C.27: PHS siteMisfit:1701 Behrendt Mts (BM)

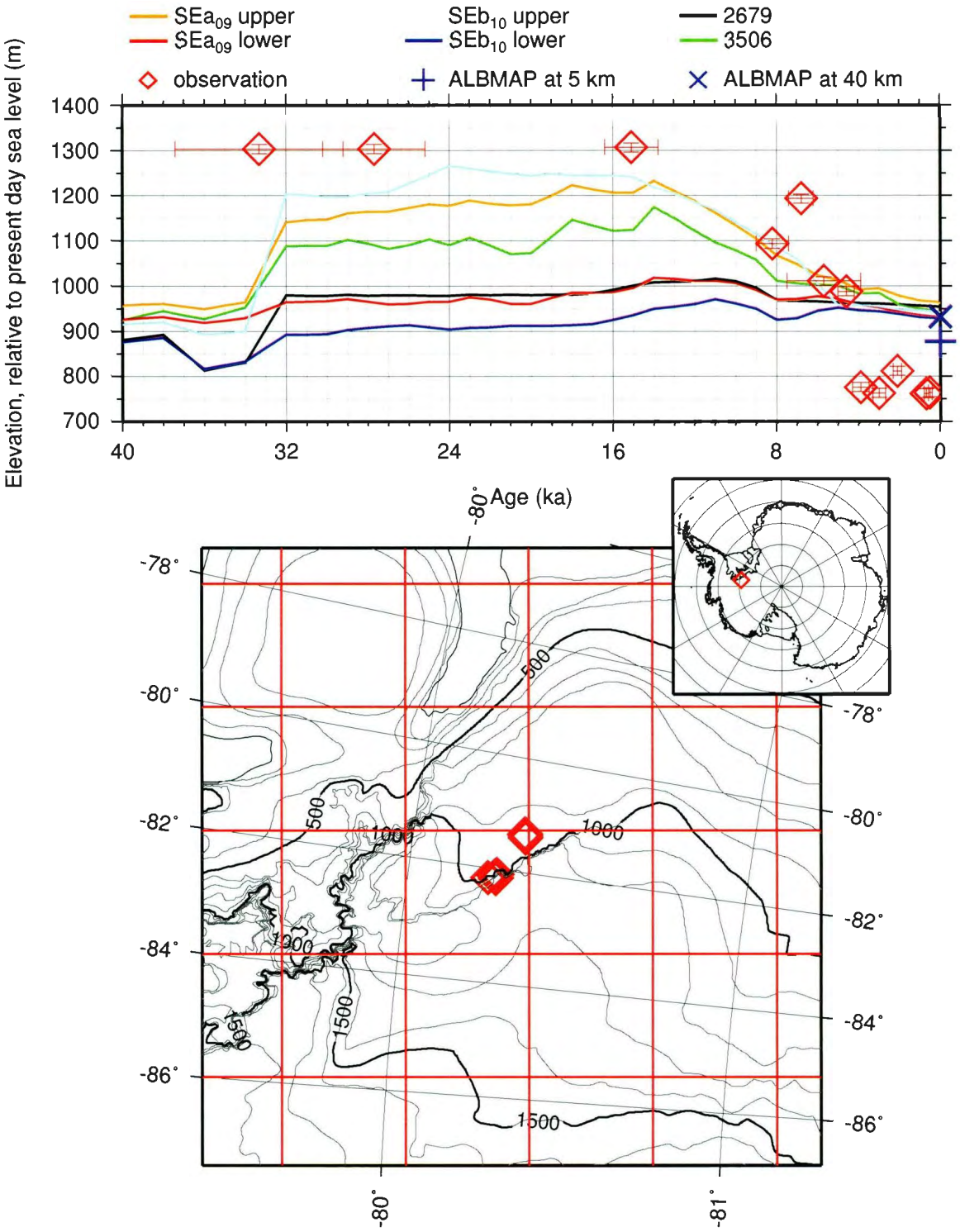


Figure C.28: PHS siteMisfit:1702 Ellsworth Mts. (EM)

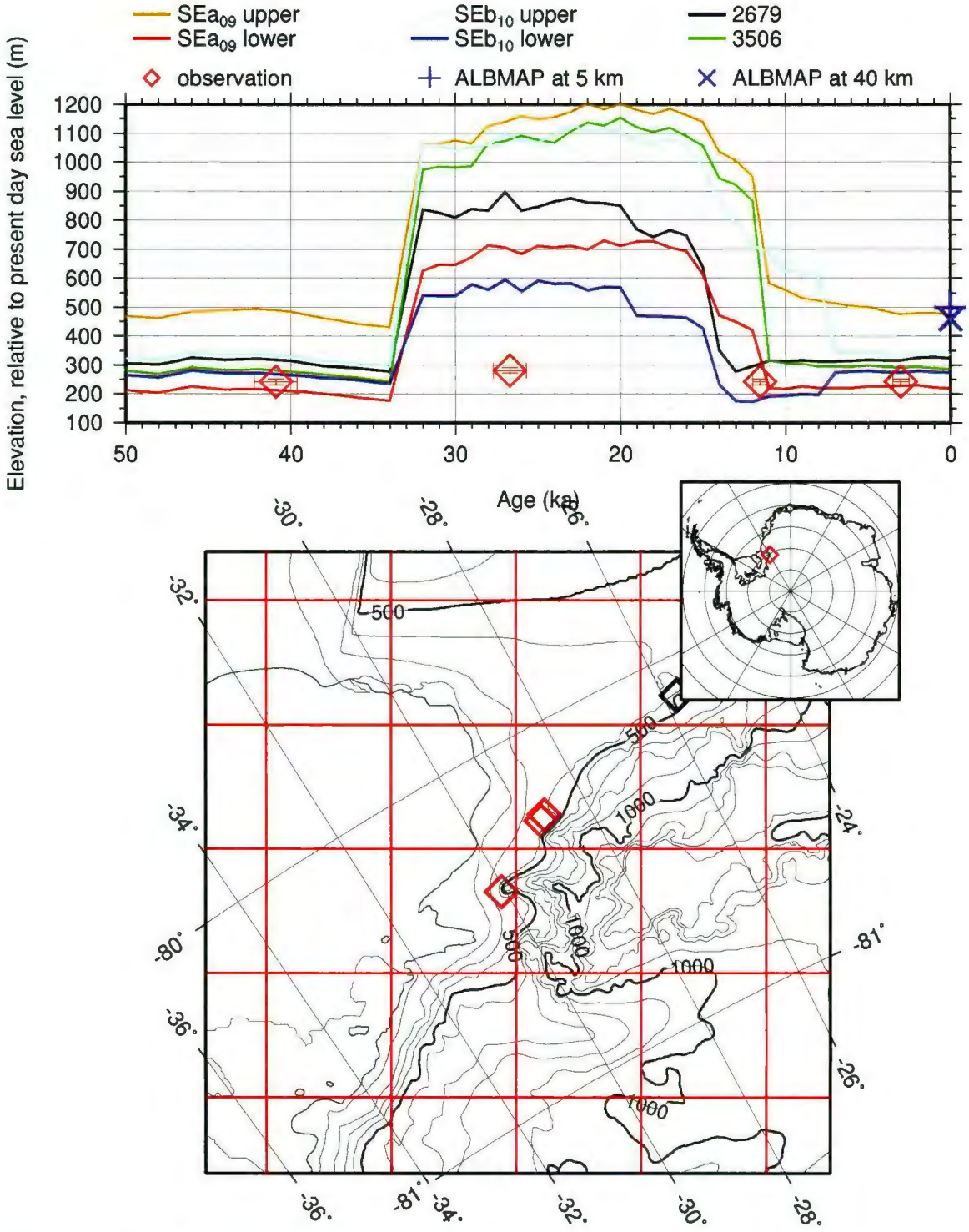


Figure C.29: PHS siteMisfit:1703 Shackleton Range 1 (SR1)

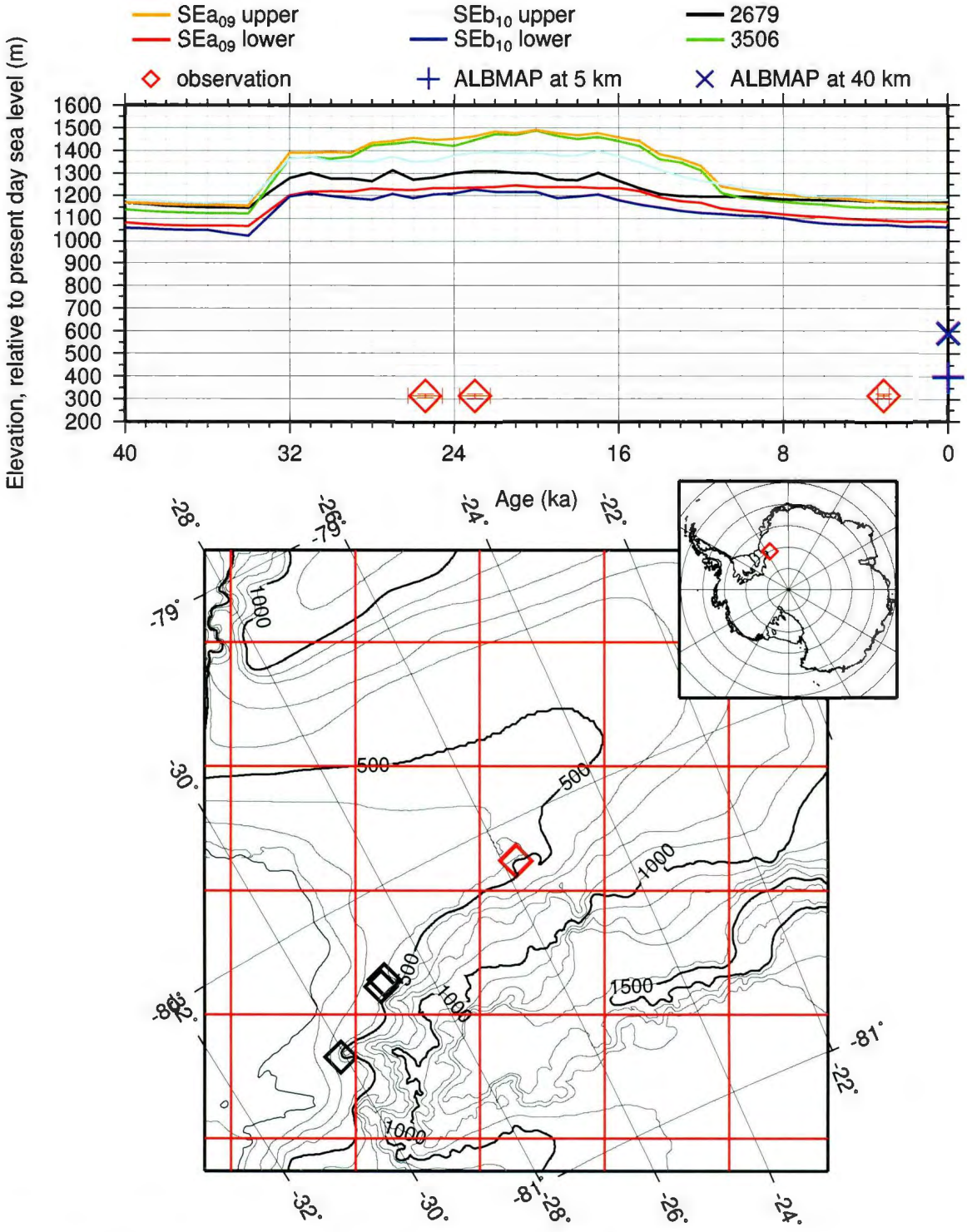


Figure C.30: PHS siteMisfit:1704 Shackleton Range 2 (SR2)

## C.4 References

Briggs, R., Pollard, D., Tarasov., L., 2013. A glacial systems model configured for large ensemble analysis of Antarctica deglaciation. in prep.

Liu, H., Jezek, K., Li, B., Zhao, Z., 2001. Radarsat antarctic mapping project digital elevation model version 2. Digital media., Boulder, CO: National Snow and Ice Data Center.

SCAR, 2006. Antarctic Digital Database, Scientific Committee on Antarctic Research (SCAR), Version 3.0. , Online; accessed Sep. 2011.